Topics in Current Chemistry 306

Jerry C.C. Chan *Editor*

Solid State NMR

Springer

306

Topics in Current Chemistry

Topics in Current Chemistry

Recently Published and Forthcoming Volumes

Solid State NMR
Volume Editor: Jerry C. C. Chan
Vol. 306, 2012

Prion Proteins
Volume Editor: Jörg Tatzelt
Vol. 305, 2011

Microfluidics: Technologies and Applications
Volume Editor: Bingcheng Lin
Vol. 304, 2011

Photocatalysis
Volume Editor: Carlo Alberto Bignozzi
Vol. 303, 2011

Computational Mechanisms of Au and Pt Catalyzed Reactions
Volume Editors: Elena Soriano, José Marco-Contelles
Vol. 302, 2011

Reactivity Tuning in Oligosaccharide Assembly
Volume Editors: Bert Fraser-Reid, J. Cristóbal López
Vol. 301, 2011

Luminescence Applied in Sensor Science
Volume Editors: Luca Prodi, Marco Montalti, Nelsi Zaccheroni
Vol. 300, 2011

Chemistry of Opioids
Volume Editor: Hiroshi Nagase
Vol. 299, 2011

Electronic and Magnetic Properties of Chiral Molecules and Supramolecular Architectures
Volume Editors: Ron Naaman, David N. Beratan, David H. Waldeck
Vol. 298, 2011

Natural Products via Enzymatic Reactions
Volume Editor: Jörn Piel
Vol. 297, 2010

Nucleic Acid Transfection
Volume Editors: Wolfgang Bielke, Christoph Erbacher
Vol. 296, 2010

Carbohydrates in Sustainable Development II
Volume Editors: Amélia P. Rauter, Pierre Vogel, Yves Queneau
Vol. 295, 2010

Carbohydrates in Sustainable Development I
Volume Editors: Amélia P. Rauter, Pierre Vogel, Yves Queneau
Vol. 294, 2010

Functional Metal-Organic Frameworks: Gas Storage, Separation and Catalysis
Volume Editor: Martin Schröder
Vol. 293, 2010

C-H Activation
Volume Editors: Jin-Quan Yu, Zhangjie Shi
Vol. 292, 2010

Asymmetric Organocatalysis
Volume Editor: Benjamin List
Vol. 291, 2010

Ionic Liquids
Volume Editor: Barbara Kirchner
Vol. 290, 2010

Orbitals in Chemistry
Volume Editor: Satoshi Inagaki
Vol. 289, 2009

Glycoscience and Microbial Adhesion
Volume Editors: Thisbe K. Lindhorst, Stefan Oscarson
Vol. 288, 2009

Solid State NMR

Volume Editor: Jerry C. C. Chan

With Contributions by

S. Afonin · M. Berditsch · J.C.C. Chan · C. Fernandez · M. Ieronimo · K. Koch · H. Koller · A.B. Nielsen · N. Chr. Nielsen · M. Pruski · L.A. Strassø · A.S. Ulrich · M. Weiß · J.P. Yesinowski

Springer

Editor
Prof. Jerry C. C. Chan
Department of Chemistry
National Taiwan University
No. 1, Section 4
Roosevelt Road, Taipei
Taiwan
chanjcc@ntu.edu.tw

ISSN 0340-1022 e-ISSN 1436-5049
ISBN 978-3-642-24802-3 e-ISBN 978-3-642-24803-0
DOI 10.1007/978-3-642-24803-0
Springer Heidelberg Dordrecht London New York

Library of Congress Control Number: 2011939195

Volume Editor

Prof. Jerry C. C. Chan

Department of Chemistry
National Taiwan University
No. 1, Section 4
Roosevelt Road, Taipei
Taiwan
chanjcc@ntu.edu.tw

Editorial Board

Topics in Current Chemistry Also Available Electronically

Topics in Current Chemistry is included in Springer's eBook package *Chemistry and Materials Science*. If a library does not opt for the whole package the book series may be bought on a subscription basis. Also, all back volumes are available electronically.

For all customers with a print standing order we offer free access to the electronic volumes of the series published in the current year.

If you do not have access, you can still view the table of contents of each volume and the abstract of each article by going to the SpringerLink homepage, clicking on "Chemistry and Materials Science," under Subject Collection, then "Book Series," under Content Type and finally by selecting *Topics in Current Chemistry*.

You will find information about the

– Editorial Board
– Aims and Scope
– Instructions for Authors
– Sample Contribution

at springer.com using the search function by typing in *Topics in Current Chemistry*.

Color figures are published in full color in the electronic version on SpringerLink.

Aims and Scope

The series *Topics in Current Chemistry* presents critical reviews of the present and future trends in modern chemical research. The scope includes all areas of chemical science, including the interfaces with related disciplines such as biology, medicine, and materials science.

The objective of each thematic volume is to give the non-specialist reader, whether at the university or in industry, a comprehensive overview of an area where new insights of interest to a larger scientific audience are emerging.

Thus each review within the volume critically surveys one aspect of that topic and places it within the context of the volume as a whole. The most significant developments of the last 5–10 years are presented, using selected examples to illustrate the principles discussed. A description of the laboratory procedures involved is often useful to the reader. The coverage is not exhaustive in data, but rather conceptual, concentrating on the methodological thinking that will allow the non-specialist reader to understand the information presented.

Discussion of possible future research directions in the area is welcome.

Review articles for the individual volumes are invited by the volume editors.

In references *Topics in Current Chemistry* is abbreviated *Top Curr Chem* and is cited as a journal.

Impact Factor 2010: 2.067; Section "Chemistry, Multidisciplinary": Rank 44 of 144

Preface

For such a diverse field as solid-state NMR, it is always a difficult matter to decide what should be covered in a single book of a reasonable page limit. Hopefully, many would agree that biological research and material science are the two major research themes in solid-state NMR. Also, a good understanding of the basic theory is mandatory before one could fully exploit the power of solid-state NMR to its fullest extent. With this in mind, the present volume of Topics in Current Chemistry starts with the chapter by Nielsen and co-workers, which focuses on the design principles of dipolar recoupling techniques. In a very succinct way, the authors have covered many techniques with potential applications in biological research, where the prominent features of different classes of recoupling pulse sequences are discussed incisively. In Chapter 2, the applications of solid-state NMR are illustrated in the context of amyloid fibrils. The techniques highlighted are mainly taken from the literature of amyloid research. These two chapters together provide a complementary account for the current status of biological solid-state NMR under magic-angle spinning conditions. In Chapter 3, Ulrich and co-workers review the latest progress in solid-state NMR of ^{19}F-labeled membrane-active peptides bound to oriented native biomembranes. The authors generously share many practical hints in sample preparation and membrane alignment. The unique opportunity of ^{19}F NMR in the progress towards *in-cell* NMR is well illustrated.

The theme of the second half of this volume is shifted to material science. The review by Fernandez and Pruski (Chapter 4) gives a timely account for the rapid advancing field of NMR of quadrupole nuclei. A vast collection of techniques addressing different important issues such as sensitivity and resolution enhancement are discussed in a very organized fashion. This chapter forms an excellent common ground for the discussion of NMR studies of different kinds of materials. Koller and co-workers describe in Chapter 5 the NMR of silica-based micro- and mesoporous materials, with particular emphasis on the different facets of zeolite research. The authors have compiled the literature in the past ten years to give a nice overview of the field, demonstrating clearly the power of solid-state NMR in the studies of catalytic materials. In the last chapter of the book Yesinowski discusses solid-state NMR of semiconductors (Chapter 6). Following a broad overview of the

general field, various relevant internal interactions constituting the overall spin Hamiltonian are discussed in detail, which provides a coherent framework for the critical evaluation of a large body of literature on bulk and nanoscaled semiconductors. This comprehensive review will not only serve as a roadmap for new comers, but also alert the experienced researchers to other important topics and issues of which they may not have been aware.

Overall, the contributors to this volume have provided first-hand accounts of various important research topics in solid-state NMR. Being the editor, I feel very privileged to work with my very distinguished colleagues, who have been at the frontier of their fields for many years. Thanks to their painstaking efforts I am very much convinced that this volume will be a useful reference for researchers and students who are interested in the principles and applications of solid-state NMR spectroscopy.

Fall 2011 Jerry C. C. Chan

Contents

Top Curr Chem (2012) 306: 1–45
DOI: 10.1007/128_2011_129

Published online: 22 April 2011

Dipolar Recoupling

Niels Chr. Nielsen, Lasse A. Strassø, and Anders B. Nielsen

Abstract We describe the principles and applications of dipolar recoupling in solid-state NMR spectroscopy as a means to access information about molecular structure and transfer magnetization between spins. In this manner, dipolar recoupling forms an essential basis for multiple-dimensional solid-state NMR experiments from which information about structure and dynamics can be extracted. We introduce the basic formalism needed to understand such experiments, present some powerful design principles, and on this basis describe in a coherent way a series of homo- and heteronuclear dipolar recoupling experiments. These experiments serve to highlight design strategies, the gradual development of increasingly advanced and powerful methods, and reflect the application of dipolar recoupling in biological solid-state NMR spectroscopy.

Keywords Dipolar recoupling · Dynamics · Protein structure · Solid-state NMR

Contents

N.C. Nielsen (✉), L.A. Strassø, and A.B. Nielsen
Center for Insoluble Protein Structures (inSPIN), Interdisciplinary Nanoscience Center (iNANO) and Department of Chemistry, Aarhus University, Aarhus C 8000 Aarhus, Denmark
e-mail: ncn@chem.au.dk

1 Introduction

Besides constant development of increasingly powerful NMR instrumentation with stronger and stronger magnetic field strengths, advanced multiple-channel rf probes, and stators for fast sample rotation, the rapid progress of biological solid-state NMR spectroscopy owes its current state to the development of advanced pulse sequences. These are of key importance for handling and exploitation of the information-rich albeit complex isotropic and anisotropic nuclear spin Hamiltonians governing the spin dynamics for solid samples. For biological solids, two major avenues [1–4] have been taken methodologically to combine the needs for high resolution along with extraction of information about structure and dynamics from anisotropic interactions. One approach has been oriented-sample solid-state NMR spectroscopy where one exploits macroscopic or magnetic uniaxial sample alignment to obtain "single-crystal-like" spectra with high resolution [1, 3, 5, 6]. This method has proved to be very useful for studying peptides and proteins embedded in biological (or most often reconstituted into phospholipid bilayer) membranes. The other approach uses magic-angle-spinning (MAS) [7–9] to average anisotropic interactions to first order, thereby promoting high-resolution spectra in the detection dimension(s) while using so-called recoupling techniques (for reviews, see [2, 10–19]) to reintroduce selectively anisotropic interactions to mediate coherence/polarization transfer or obtain information about structure and dynamics (e.g., internuclear distances and torsion angles) in other periods of the experiment. The latter approach, with particular focus on recoupling of dipole–dipole coupling interactions between spins, will be the topic of this review.

Dipolar recoupling is a discipline of fundamental importance for biological solid-state NMR – but also, to an increasing extent, to other areas such as solid-state NMR studies of polymers, supramacromolecular structures, bioorganic compounds, and materials – as a means to transfer coherence between spins or probe nuclear interactions. The concept of dipolar recoupling was introduced through experiments such as double-cross polarization (DCP) [20], rotational resonance [21], rotational echo double resonance (REDOR) [22], and dipolar recovery at the magic angle (DRAMA) [23]. These methods – although based on previous concepts – paved the way for the "art" of interfering with MAS averaging through rf pulsing, continuous rf irradiation, or chemical shift modulation which formed the basic elements of a discipline that, to date, have led to hundreds of different pulse sequences being

relevant through different characteristics on implementation or performance for a wide area of applications. To name a few, the methods involved early pulse techniques (see explanations for abbreviations later) such as RFDR [24] and TEDOR [25], rotary resonance methods such as HORROR [26] and heteronuclear rotary resonance [27], adiabatic methods such as DREAM [28], windowless variants of DRAMA such as DRAWS [29], symmetry-based pulse sequences such as C7 [30], POST-C7 [31] and numerous other CN, RN, and related pulse sequences [32–37], rf-driven spin-diffusion methods such as DARR [38] and MIRROR [39], optimal control recoupling sequences [40–43], and recently third-spin assisted [44, 45] and multi-oscillating field techniques [46–49]. The various methods have different merits per se, but are in many respects very similar through their origin from the same design strategies.

In the following sections, we will introduce the basic theory to understand the development of dipolar recoupling experiments, describe some of the most commonly used design/analysis strategies, and provide a description of distinct classes of recoupling experiments in a short and condensed fashion. The aim is to provide a coherent understanding of recoupling phenomena in a relatively easily accessible manner and simultaneously provide knowledge of the most common techniques currently used for structural analysis of proteins and bioorganic compounds. The aim is not to provide detailed descriptions of all current methods (which would be far beyond the volume of this review) but rather, through appropriately selected examples, to provide a flavor of dipolar recoupling from a technological and functional point of view.

2 Theory

In comparison with other spectroscopic techniques, NMR is blessed with short-range interactions that render it possible to characterize and influence the spin evolution over relatively long periods of time without excessive loss from dissipative processes. This implies that the spin evolution to a large extent (but certainly not exclusively) may be described as unitary evolution of coherence/polarization potentially supplemented with corrections due to relaxation.

2.1 Equation of Motion

Ignoring relaxation, the spin evolution is governed by the Liouville-von-Neumann equation

$$\dot{\rho}(t) = -i[H(t), \rho(t)], \tag{1}$$

where $\rho(t)$ represents the density matrix for the system and $H(t)$ the Hamiltonian inducing the motion. Equation (1) has the formal solution

$$\rho(t) = U(t)\rho(0)U^{+}(t), \tag{2}$$

where $\rho(0)$ is the initial density operator and $U(t)$ the propagator (i.e., exponential operator) for the motion

$$U(t) = \hat{T}e^{-i\int_0^t H(t')\mathrm{d}t'} \tag{3}$$

with $\hat{T}$ denoting the so-called Dyson time ordering operator.

2.2 Hamiltonians and Transformation Formula

The Hamiltonian generally takes the form

$$H(t) = H_{\mathrm{int}}(t) + H_{\mathrm{ext}}(t), \tag{4}$$

where the internal Hamiltonian $H_{\mathrm{int}}(t)$ may conveniently be expressed in terms of irreducible spherical tensor operators

$$H_{\mathrm{int}}(t) = \sum_{\lambda} H_{\lambda}(t); \quad H_{\lambda}(t) = C^{\lambda}\sum_{j=0}^{2}\sum_{m=-j}^{j}(-1)^{m}\left(R^{\lambda}_{j,-m}\right)^{L}T^{\lambda}_{j,m} \tag{5}$$

with λ denoting relevant nuclear spin interactions (such as chemical shift, J coupling, dipole–dipole coupling, and quadrupolar coupling). Expressions for the fundamental constant C^{λ}, the spatial part of the Hamiltonian $\left(R^{\lambda}_{j,-m}\right)^{P}$, and the spin part of the Hamiltonian $T^{\lambda}_{j,m}$ can be found in Table 1.

Table 1 NMR interactions in irreducible spherical tensor form

λ	σ	J	IS	Q
C^{λ}	γ_{σ}	1	$-2\gamma_I\gamma_S\hbar$	$eQ/[2I\hbar(2I-1)]$
$\left(R^{\lambda}_{0,0}\right)^{P}$	$\delta^{\mathrm{iso}}_{\sigma}$	$\delta^{\mathrm{iso}}_{J}$	0	0
$\left(R^{\lambda}_{2,0}\right)^{P}$	$\delta^{\mathrm{aniso}}_{\sigma}\sqrt{\frac{3}{2}}$	$\delta^{\mathrm{aniso}}_{J}\sqrt{\frac{3}{2}}$	$\sqrt{\frac{3}{2}}\frac{\mu_0}{4\pi}\frac{1}{r^3}$	$eq\sqrt{\frac{3}{2}}$
$\left(R^{\lambda}_{2,\pm1}\right)^{P}$	0	0	0	0
$\left(R^{\lambda}_{2,\pm2}\right)^{P}$	$-\frac{1}{2}\delta^{\mathrm{aniso}}_{\sigma}\eta^{\sigma}$	$-\frac{1}{2}\delta^{\mathrm{aniso}}_{j}\eta^{J}$	0	$-eq\frac{\eta^{Q}}{2}$
$T^{\lambda}_{0,0}$	B_0I_z	$I\cdot S$	0	0
$T^{\lambda}_{2,0}$	$\sqrt{\frac{2}{3}}B_0I_z$	$\frac{1}{\sqrt{6}}(3I_zS_z - I\cdot S)$	$\frac{1}{\sqrt{6}}(3I_zS_z - I\cdot S)$	$\frac{1}{\sqrt{6}}\left[3I_z^2 - I(I+1)\right]$
$T^{\lambda}_{2,\pm1}$	$\mp\frac{1}{2}B_0I_{\pm}$	$\mp\frac{1}{2}(I_{\pm}S_z + I_zS_{\pm})$	$\mp\frac{1}{2}(I_{\pm}S_z + I_zS_{\pm})$	$\mp\frac{1}{2}(I_{\pm}I_z + I_zI_{\pm})$
$T^{\lambda}_{2,\pm2}$	0	0	$\frac{1}{2}I_{\pm}S_{\pm}$	$\frac{1}{2}I_{\pm}^2$

Fundamental constants (C^{λ}), spatial tensors in the principal axis frame ($(R^{\lambda}_{m,m'})^{P}$), and spin tensors ($T^{\lambda}_{j,m}$) for chemical shielding (σ), J coupling (J), dipole–dipole (IS), and quadrupolar coupling (Q) nuclear spin interactions (for more detailed definition of symbols refer to [50])

Addressing specifically the dipole–dipole coupling interaction, the Hamiltonian in the high-field approximation takes the form

$$H_{IS}(t) = C^{IS}\left(R^{IS}_{2,0}\right)^{L} T^{IS}_{2,0}, \tag{6}$$

with the fundamental constant $C^{IS} = -2\hbar\gamma_I\gamma_S$ and the spin part given by $T^{IS}_{2,0} = \frac{1}{\sqrt{6}}(3I_zS_z - I\cdot S)$. The spatial part monitored in the laboratory frame (L) is related to the spatial tensor in the principal axis frame (P) typically through transformations through a crystal (or molecule) fixed frame (C) and a rotor fixed frame (R) according to

$$\left(R^{\lambda}_{2,m}\right)^{L} = \sum_{m',m'',m'''}\left(R^{\lambda}_{2,m''}\right)^{P} D^{(2)}_{m''',m''}\left(\Omega^{\lambda}_{PC}\right) D^{(2)}_{m'',m'}\left(\Omega^{\lambda}_{CR}\right) D^{(2)}_{m',m}\left(\Omega^{\lambda}_{RL}\right), \tag{7}$$

where we introduced the standard transformation of irreducible spherical tensor operators [51, 52]

$$T^{F2}_{j,m} = \sum_{m'=-j}^{j} T^{F1}_{j,m'} D^{(j)}_{m',m}\left(\Omega^{\lambda}_{F1F2}\right) \tag{8}$$

using Wigner $D^{(j)}_{m'm}(\Omega) = e^{-im'\alpha} d^{(j)}_{m'm}(\beta) e^{-im\gamma}$ or reduced Wigner ($d^{(j)}_{m'm}(\beta)$) rotation matrices (Table 2) depending on the Euler angles $\Omega = \{\alpha, \beta, \gamma\}$ corresponding to each of the transformations in (7). We note that the transformation formula in (8) obviously applies for transformation of both spatial- and spin-space irreducible tensor operators on the Hamiltonian and density operator level. We also note that the spin operators may sometimes conveniently be transformed using standard Cartesian product operator formula [53] of the type

$$e^{-i\phi B} A e^{i\phi B} = c_\phi A - s_\phi i[B, A] = c_\phi A - s_\phi C, \tag{9}$$

Table 2 Reduced irreducible tensor operators $d^{(j)}_{m,m'}(\beta)$

j	$m'\|m$	-2	-1	0	1	2
1	-1		$\frac{1}{2}(1+c_\beta)$	$\frac{1}{\sqrt{2}}s_\beta$	$\frac{1}{2}(1-c_\beta)$	
	0		$-\frac{1}{\sqrt{2}}s_\beta$	c_β	$\frac{1}{\sqrt{2}}s_\beta$	
	1		$\frac{1}{2}(1-c_\beta)$	$-\frac{1}{\sqrt{2}}s_\beta$	$\frac{1}{2}(1+c_\beta)$	
2	-2	$\frac{1}{4}(1+c_\beta)(1+c_\beta)$	$\frac{1}{2}(1+c_\beta)s_\beta$	$\sqrt{\frac{3}{8}}s^2_\beta$	$\frac{1}{2}(1-c_\beta)s_\beta$	$\frac{1}{4}(1-c_\beta)(1-c_\beta)$
	-1	$-\frac{1}{2}(1+c_\beta)s_\beta$	$-\frac{1}{2}(1-c_\beta)+c^2_\beta$	$\sqrt{\frac{3}{8}}s_{2\beta}$	$\frac{1}{2}(1+c_\beta)-c^2_\beta$	$\frac{1}{2}(1-c_\beta)s_\beta$
	0	$\sqrt{\frac{3}{8}}s^2_\beta$	$-\sqrt{\frac{3}{8}}s_{2\beta}$	$\frac{1}{2}\left(3c^2_\beta-1\right)$	$\sqrt{\frac{3}{8}}s_{2\beta}$	$\sqrt{\frac{3}{8}}s^2_\beta$
	1	$-\frac{1}{2}(1-c_\beta)s_\beta$	$\frac{1}{2}(1+c_\beta)-c^2_\beta$	$-\sqrt{\frac{3}{8}}s_{2\beta}$	$-\frac{1}{2}(1-c_\beta)+c^2_\beta$	$\frac{1}{2}(1+c_\beta)s_\beta$
	2	$\frac{1}{4}(1-c_\beta)(1-c_\beta)$	$-\frac{1}{2}(1-c_\beta)s_\beta$	$\sqrt{\frac{3}{8}}s^2_\beta$	$-\frac{1}{2}(1+c_\beta)s_\beta$	$\frac{1}{4}(1+c_\beta)(1+c_\beta)$

applying for operators A, B, and C fulfilling cyclic commutation (i.e., $[A,B] = iC$, $[B,C] = iA$, $[C,A] = iB$). A typical scenario would be $\rho(0) = A, H(t) = \omega(t)B$, and $\phi = \int_0^t \omega(t')\mathrm{d}t'$.

Within this framework, the dipolar coupling between two spins I and S may be described in terms of the Hamiltonian

$$H_{IS}(t) = \omega_{IS}(t)\sqrt{6}T_{2,0}^{IS} = \omega_{IS}(t)(3I_zS_z - I \cdot S) \tag{10}$$

with the sample-spinning parameterized through the Fourier series

$$\omega_{IS}(t) = \sum_{m=-2}^{2} \omega_{IS}^{(m)} e^{im\omega_r t}; \quad \omega_{IS}^{(m)} = b_{IS} e^{im\gamma_{PR}} d_{0,-m}^{(2)}(\beta_{PR}) d_{-m,0}^{(2)}(\beta_{PL}), \tag{11}$$

where, for simplicity, we ignored the C to R spatial transformation and introduced the dipole–dipole coupling constant $b_{IS} = -\gamma_I\gamma_S\hbar\mu_0/\left(4\pi r_{IS}^3\right)$ relating to the internuclear distance r_{IS}. For the subsequent description of dipolar recoupling, it is relevant to write out the dependencies of the involved Fourier components

$$\omega_{IS}^{(0)} = 0; \quad \omega_{IS}^{(1)} = \omega_{IS}^{(-1)^*} = -\frac{1}{2\sqrt{2}} b_{IS} s_{2\beta_{PR}} e^{i\gamma_{PR}}; \quad \omega_{IS}^{(2)} = \omega_{IS}^{(-2)^*} = \frac{1}{4} b_{IS} s_{\beta_{PR}}^2 e^{i2\gamma_{PR}}, \tag{12}$$

using the shorthand notation $c_x = \cos(x)$, $s_x = \sin(x)$.

The external Hamiltonian $H_{\mathrm{ext}}(t)$ described above contains in the high-field approximation (taking out the dependency of the external static magnetic field) the rf irradiation Hamiltonian of the form

$$H_{\mathrm{ext}}(t) = H_{\mathrm{rf}}(t) = \omega_{\mathrm{rf}}^I(t) I_{\phi_I(t)} + \omega_{\mathrm{rf}}^S(t) S_{\phi_S(t)} \tag{13}$$

using the abbreviation $I_{\phi_I(t)} = e^{-i\phi_I(t)I_z} I_x e^{i\phi_I(t)I_z}$ and similar for the S-spin operator.

2.3 Design Principles

On basis of the Hamiltonians described above, it is possible to design systematically solid-state NMR experiments which, through appropriate combination of sample spinning and rf irradiation, tailor the internal Hamiltonian to a specific shape. This may be used to emphasize desired parts of the Hamiltonian while suppressing effects from undesired parts [54]. Using, in particular, three design strategies, dozens of dipolar recoupling experiments have been designed over the past three decades. The three design strategies are effective (or average) Hamiltonian theory, Floquet theory, and numerical experiment design that in recent years has involved optimal control methods.

2.3.1 Effective Hamiltonian Theory

Average or effective Hamiltonian theory, as introduced to NMR spectroscopy by Waugh and coworkers [55] in the late 1960s, has in all respects been the most important design tool for development of dipolar recoupling experiments (and many other important experiments). In a very simple and transparent manner, this method facilitates delineation of the impact of advanced rf irradiation schemes on the internal nuclear spin Hamiltonians. This impact is evaluated in an ordered fashion, enabling direct focus on the most important terms and, in the refinement process, the less dominant albeit still important terms in a prioritized manner.

Prior to an effective Hamiltonian analysis it is, in order to get this converging to the lowest orders, typical to remove the dominant rf irradiation from the description by transforming the internal Hamiltonian into the interaction frame of the rf irradiation. This procedure is well established and also used in the most simple description of NMR experiments by transforming the Hamiltonian into the rotating frame of the Zeeman interaction (the so-called Zeeman interaction frame). In the Zeeman interaction frame the time-modulations of the rf terms are removed and the internal Hamiltonian is truncated to form the secular high-field approximated Hamiltonian – all facilitating solution of the Liouville-von-Neumann equation in (1) and (2). The transformation into the rf interaction frame is given by

$$\tilde{H}(t) = U_{\mathrm{rf}}^{+}(t)H(t)U_{\mathrm{rf}}(t) - iU_{\mathrm{rf}}^{+}(t)\frac{d}{\mathrm{d}t}U_{\mathrm{rf}}(t) = \tilde{H}_{\mathrm{int}}(t), \tag{14a}$$

$$\tilde{\rho}(t) = U_{\mathrm{rf}}^{+}(t)\rho(t)U_{\mathrm{rf}}(t), \tag{14b}$$

where the last term in (14a) is the so-called Coriolis term, taking away the dominant rf interaction from the interaction frame Hamiltonian. The transformation of the Hamiltonian in (14a) is useful in cases where continuous periods of rf irradiation are considered.

In cases where ideal (i.e., instantaneously short) rf pulses are used, it is useful instead to use a so-called toggling frame approach where the Hamiltonian by each pulse is toggled to another frame. For the case where N ideal rf events have occurred, the Hamiltonian for the free precession period following the Nth pulse is described by

$$H_N^T = U_1^{+} \cdots U_N^{+} H(t) U_N \cdots U_1, \tag{15}$$

where the superscript T denotes the toggling frame and U_i the propagator for the ith rf pulse.

The effective (or average) Hamiltonian is generally expressed as

$$\overline{\tilde{H}} = \overline{\tilde{H}}^{(1)} + \overline{\tilde{H}}^{(2)} + \ldots \tag{16}$$

with the lowest-order terms in the Magnus expansion defined as

$$\overline{\tilde{H}}^{(1)} = \frac{1}{\tau_c} \int_0^{\tau_c} \tilde{H}(t) \mathrm{d}t, \tag{17a}$$

$$\overline{\tilde{H}}^{(2)} = \frac{1}{2i\tau_c} \int_0^{\tau_c} \mathrm{d}t \int_0^t \left[\tilde{H}(t), \tilde{H}(t')\right] \mathrm{d}t', \ldots \tag{17b}$$

where τ_c is the cycle period of the rf irradiation.

In cases where the Hamiltonians (typically due to phase or amplitude switching in the rf fields) are discontinuously time-dependent, the average Hamiltonian may conveniently be set up using the semi-continuous Baker-Campbell-Hausdorff (scBCH) expansion [56] as

$$\overline{\tilde{H}}^{(1)} = \frac{1}{\tau_c} \sum_{i=1}^{n} \tau_i \overline{\tilde{H}}_i^{(1)}, \tag{18a}$$

$$\overline{\tilde{H}}^{(2)} = \frac{1}{\tau_c} \sum_{i=1}^{n} \tau_i \overline{\tilde{H}}_i^{(2)} + \frac{1}{2i\tau_c} \sum_{i>j} \tau_i \tau_j \left[\overline{\tilde{H}}_i^{(1)}, \overline{\tilde{H}}_j^{(1)}\right], \ldots, \tag{18b}$$

where we assume n pulse sequence elements, each characterized by a period τ_i over which the standard Magnus expansion (17) is applied to generate the element effective Hamiltonians $\overline{\tilde{H}}_i^{(r)}$ to order r.

It applies for both formulations above that the expansion in principle contains an infinite number of terms. The convergence to a few lowest order terms relies on the ability to orderly separate influences of the dominant rf irradiation terms (through a suitable interaction frame) from the less dominant internal terms of the Hamiltonian. In principle, this may be overcome using the spectral theorem (or the Caley–Hamilton theorem [57]) providing a closed (i.e., exact) solution to the Baker–Campbell–Hausdorf problem with all dependencies included in n terms where n designates the dimension of the Hilbert-space matrix representation (e.g., 2 for a single spin-1/2, 4 for a two-spin-1/2 system) [58, 59].

2.3.2 Floquet Theory

Floquet theory [60] represents a powerful method to analyze and describe NMR experiments including, in the present context, methods for dipolar recoupling. In particular the bimodal variants are promising in the sense that they may handle perturbations/interactions involving multiple time periodicities, as for example induced by combined sample spinning and rf irradiation in the case of dipolar

recoupling. While the vast majority of dipolar recoupling experiments have been designed using effective Hamiltonian theory, Floquet theory has so far mainly been used to analyze and describe new details of earlier experiments rather than as a direct tool in the design process. This is despite the fact that the method also holds promise for experiment design. For this reason, and because of its somewhat different notation calling for a longer account than possible here, we will not describe the underlying principles and merits of this method in this review. We will rather focus attention on a very recent review on the topic by Vega and coworkers [61] that provides a couple of examples using bimodal Floquet theory to describe dipolar recoupling experiments, a topic also addressed recently by, e.g., Ernst and coworkers [62], Scholz et al. [63] and Ramachandran et al. [64]

2.3.3 Optimal Control Theory

It is clear that pulse sequences may not only be designed by analytical means, they may also be designed numerically (see, e.g., reviews on numerical aspects of solid-state NMR in [54, 65, 66]) using standard nonlinear optimization to well-defined analytical expressions [67, 68], by optimizing pulse sequences directly on the spectrometer [69], or by optimal control procedures [70–72] to name but a few of the possibilities. We will in this review restrict ourselves to optimal control design procedures that recently in analytical and numerical form have formed a new basis for efficient NMR experiment design.

A general quest for experiment design is to develop an experiment that optimizes the transfer of a given initial state A [e.g., $\rho(0)$ in (2)] into a given final state C [e.g., a certain operator for $\rho(t)$ in (2)]. In the case without relaxation this corresponds to optimizing the propagator to realize this demand. Another task could be to optimize the rf irradiation to provide a certain desired effective Hamiltonian H_D or the corresponding propagator U_D. Within the formalism of optimal control [73–75] one defines a cost function

$$J = \Phi - \frac{\alpha}{2} \sum_{k=1}^{2N} \int_0^T \omega_k^2(t) \mathrm{d}t \tag{19}$$

for a pulse sequence of length T and with $2N$ rf pulse amplitudes being involved in the pulse sequence (N rf pulses with x- and y-phase amplitudes). The first term in (19) is referred to as the final cost, which for optimization of a state transfer $A \rightarrow C$ and optimization of an effective propagator U_D takes the forms

$$\Phi = \langle C \,|\, \rho(t) \rangle = Tr\{C^+ \rho(t)\}, \tag{20a}$$

$$\Phi = \left| Tr\left\{ U_D^+ U(T) \right\} \right|^2, \tag{20b}$$

respectively. Based on this cost function, the rf field may be changed iteratively according to [72]

$$\omega_k(t_j) \rightarrow \omega_k(t_j) + \varepsilon\big(Tr\{\lambda^+(t_j)[-iI_k, \rho(t_j)]\} - \alpha\omega_k(t_j)\big), \tag{21a}$$

$$\omega_k(t_j) \rightarrow \eta\omega_k(t_j) + \frac{1-\eta}{\alpha} Tr\{\lambda^+(t_j)[-iI_k, \rho(t_j)]\}, \tag{21b}$$

for the gradient ascent pulse engineering (GRAPE) [70] and Krotov type algorithms [76, 77], respectively, as frequently used in optimal control design of NMR experiments. The former method has been implemented as part of the open-source SIMPSON software package [50] for "automatized" experiment design, e.g., in solid-state NMR [71]. In (21), we used the forward and backwards transformed operators $\rho(t_j) = U_j \cdots U_1 \rho(0) U_1^+ \cdots U_j^+$ and $\lambda^+(t_j) = U_{j+1}^+ \cdots U_N^+ C^+ U_N \cdots U_{j+1}$.

3 Homo- and Heteronuclear Dipolar Recoupling Techniques

In this section we will illustrate the design of dipolar recoupling techniques using the theory described above and introduce the reader to various powerful techniques within a historical and a practical point-of-view perspective. Focus is, for some of the methods, devoted to a basic understanding of the techniques, laying the ground for evolutionary developments, while others are mainly included to cover certain powerful methods without going into too much detail. We will not distinguish strongly between homo- and heteronuclear methods, but rather distinguish the methods through their mode of design/operation.

3.1 Pulsed Recoupling Methods: REDOR, DRAMA

The art of pulsed dipolar recoupling was introduced to heteronuclear and homonuclear spins through methods such as REDOR [22] and DRAMA [23], respectively, which in an elegant manner demonstrated that coherent averaging of dipole–dipole coupling interactions may be prevented by altering the sign encoding from the spatial terms using appropriately placed rf pulses operating in spin space. For both methods we assume at present ideal rf pulses, implying that we use a toggling (rather than interaction) frame approach to define the Hamiltonians in the individual periods of the experiment.

The REDOR experiment (Fig. 1a), introduced by Gullion and Schaefer in 1989 [22], invokes a strong π pulse for one of the spin species (e.g., the I spin in an I-S spin system) in the middle of each rotor period τ_r – in addition to one π pulse at each rotor echo on the S-spin channel to refocus isotropic chemical shift effects and

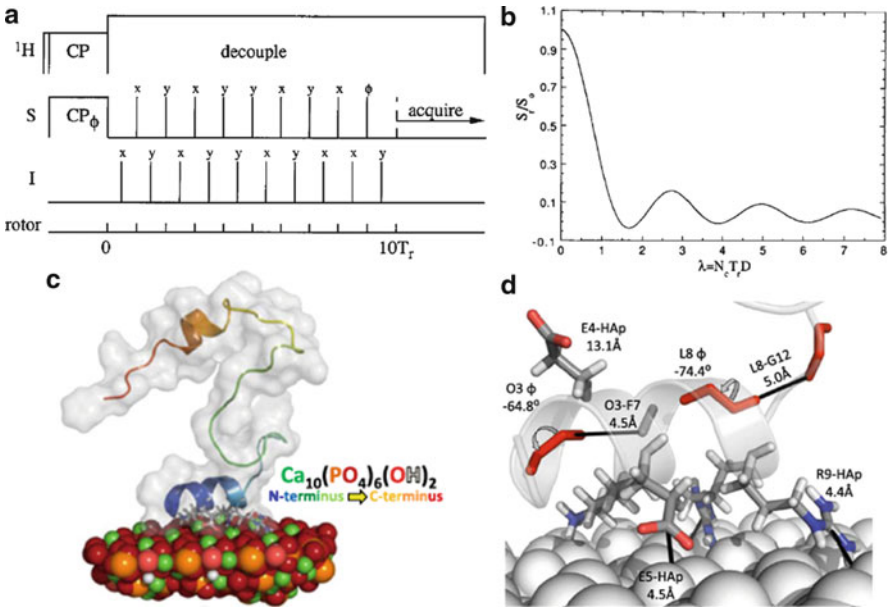

Fig. 1 (**a**) REDOR experiment and (**b**) typical REDOR dephasing curve (D designates the dipole–dipole coupling, τ_r the rotor period, and N_c the number of rotor cycles for the REDOR experiment) (reproduced from [78] with permission). (**c**, **d**) REDOR based determination of statherin binding to a hydroxyapatite surface (reproduced from [79] with permission)

avoid cancellation of the dipolar coupling interaction by opposite signs in the toggling frames of subsequent rotor periods. The recoupling I-spin π pulse transforms the heteronuclear dipole–dipole coupling Hamiltonian (transverse components truncated by the large shift difference in heteronuclear spin systems)

$$H_{IS}(t) = \sum_{m=-2}^{2} \omega_{IS}^{(m)} e^{im\omega_r t} 2I_z S_z, \tag{22}$$

which otherwise would be averaged by sample spinning $\bar{H}_{IS}(t) = \frac{1}{\tau_r} \int_{}^{\tau_r} H_{IS}(t)\mathrm{d}t = 0$ (since all finite Fourier components are modulated by $\pm\omega_r t$ or ${}^0\pm 2\omega_r t$), into toggling frame Hamiltonians [see (15)] $H_{IS}^T(t) = H_{IS}(t)$ for $t \in [0, \tau_r/2]$ and $H_{IS}^T(t) = e^{i\pi S_x} H_{IS}(t) e^{-i\pi S_x} = -H_{IS}(t)$ for $t \in [\tau_r/2, \tau_r]$. Using (18a), the first-order effective Hamiltonian over one rotor period takes the form [using (12)]

$$\begin{aligned} \overline{\tilde{H}}_{IS}^{(1)} &= \frac{1}{\tau_r} \left(\int_0^{\tau_r/2} H_{IS}(t)\mathrm{d}t - \int_{\tau_r/2}^{\tau_r} H_{IS}(t)\mathrm{d}t \right) \\ &= \frac{2i}{\pi} \left(\omega_{IS}^{(1)} - \omega_{IS}^{(-1)} \right) 2I_z S_z = \frac{\sqrt{2}}{\pi} b_{IS} s_{2\beta_{PR}} s_{\gamma_{PR}} 2I_z S_z \,. \end{aligned} \tag{23}$$

This Hamiltonian leads to dephasing of the S-spin signal recorded as function of time (increasing number of rotor periods N_c in the REDOR experiment) as illustrated in Fig. 1b. REDOR has been a key experiment in biological solid-state NMR, as for example used recently for determination of statherin binding to biomineral surfaces as illustrated in Fig. 1c, with numerous REDOR determined internuclear distances high-lighted in Fig. 1d [79].

The REDOR experiment has formed the basis for a large number of "ideal pulse" type recoupling experiments, and later finite pulse variants, for heteronuclear dipolar recoupling. These include experiments such as frequency selective REDOR (FS-REDOR) [80], TEDOR (Transferred Echo DOuble Resonance) [25], and 3D variants of TEDOR [81, 82], which have found important applications, e.g., for measurement of internuclear ^{13}C–^{15}N distances in biological solids. We should also mention that rotor-encoded variants of TEDOR, such as REPT, HDOR [83], and REREDOR [84], have been proposed for ^{1}H–^{13}C dipolar recoupling under high-speed MAS conditions.

For the homonuclear case, it is for general applications not possible to apply a π pulse selectively on one of the spins in the middle of the rotor period and in this manner obtain recoupling. In this case, the DRAMA experiment (Fig. 2a, top) proposed by Tycko and Dabbagh [23], may be used. In its standard form, this experiment contains a $(\pi/2)_{\mathrm{x}}$ pulse at $\tau_{\mathrm{r}}/4$ and a $(\pi/2)_{-\mathrm{x}}$ pulse at $3\tau_{\mathrm{r}}/4$. These induce the toggling frame Hamiltonians $H_{IS}^{T}(t) = H_{IS}^{zz}(t)$ for $t \in [0, \tau_r/4]$, $H_{IS}^{T}(t) = H_{IS}^{yy}(t)$ for $t \in [\tau_r/4, 3\tau_r/4]$, and $H_{IS}^{T}(t) = H_{IS}^{zz}(t)$ for $t \in [3\tau_r/4, \tau_r]$, with the superscript denoting the phase of the first spin component in (10) (we note that the $I \cdot S$ component is invariant to rotations in spin space). In this case, the first-order effective Hamiltonian takes the form

$$\begin{aligned}\overline{\tilde{H}}_{IS}^{(1)} &= \frac{1}{\tau_r}\left(\int_0^{\tau_r/4} H_{IS}^{zz}(t)\mathrm{d}t + \int_{\tau_r/4}^{3\tau_r/4} H_{IS}^{yy}(t)\mathrm{d}t + \int_{3\tau_r/4}^{\tau_r} H_{IS}^{zz}(t)\mathrm{d}t\right) \\ &= \frac{3}{\pi}\left(\omega_{IS}^{(1)} + \omega_{IS}^{(-1)}\right)(I_zS_z - I_yS_y) = -\frac{3}{\pi\sqrt{2}} b_{IS} s_{2\beta_{PR}} c_{\gamma_{PR}} (I_zS_z - I_yS_y), \end{aligned} \quad (24)$$

readily identified as a double-quantum (DQ) two-spin Hamiltonian in a frame rotated by $\pi/2$ around y. DRAMA may be used to transfer x-phase coherence between spins characterized by a frequency-domain powder spectrum depending on the dipolar coupling (and thereby the internuclear distance) as illustrated by a numerical simulation in Fig. 2a (bottom).

We note that DRAMA has also formed the basis for refined variants such as the chemical-shift-compensated MELODRAMA [85], windowless DRAWS [29], and the DRAMA-XY4 [86] experiments, finding important applications for example for measurement of ^{13}C–^{13}C distances involving carbonyl spins. We should also note the existence of many other important pulsed homonuclear recoupling experiments such as the widely used Radio Frequency Driven Dipolar Recoupling (RFDR) [24] and Back-to-Back (BaBa) [87] experiments.

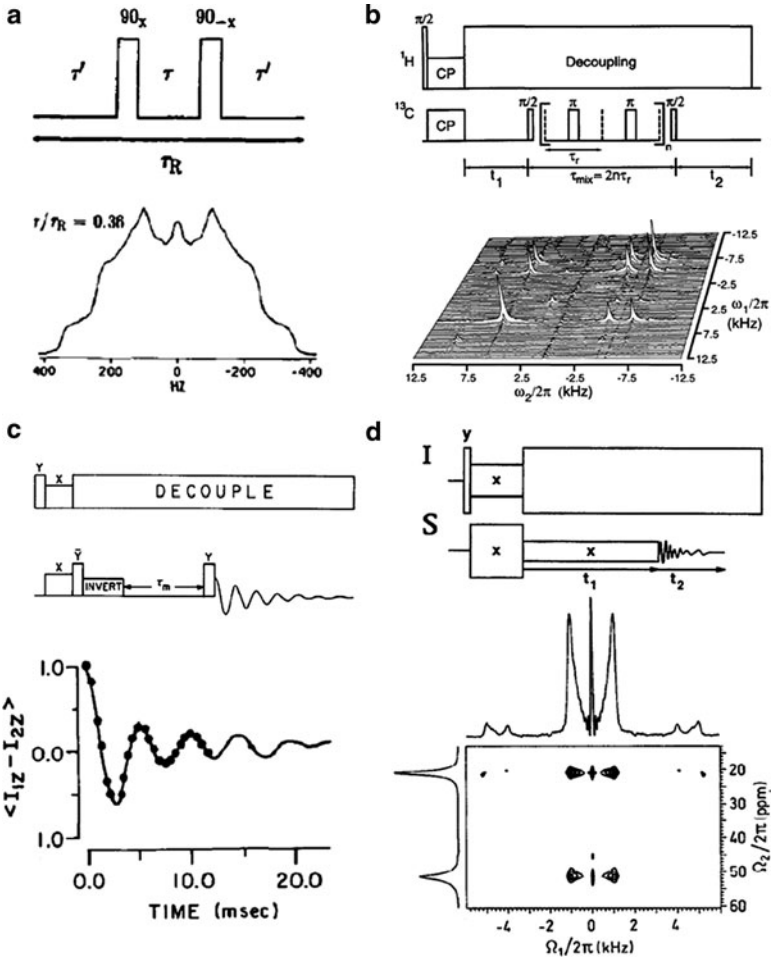

Fig. 2 (**a**) DRAMA pulse sequence (using $\tau' = \tau/2 = \tau_r/4$ in the text) and a representative calculated dipolar recoupled frequency domain spectrum (reproduced from [23] with permission). (**b**) RFDR pulse sequence inserted as mixing block in a 2D ^{13}C–^{13}C chemical shift correlation experiment, along with an experimental spectrum of ^{13}C-labeled alanine (reproduced from [24] with permission). (**c**) Rotational resonance inversion sequence along with an $n = 3$ rotational resonance differential dephasing curve for ^{13}C-labeled alanine (reproduced from [21] with permission). (**d**) Double-quantum HORROR experiment along with a 2D HORROR nutation spectrum of $^{13}C_2$-2,3-L-alanine (reproduced from [26] with permission)

3.2 From Infinite to Finite Pulsed Recoupling: RFDR and fpRFDR

The RFDR experiment (Fig. 2b), here serving to illustrate the incorporation of finite rf pulse effects into the design or refinement process, was first introduced by Griffin,

Vega, and coworkers as a sequence of well-placed ideal (i.e., infinitely strong) π-pulses serving to reintroduce the zero-quantum (ZQ) part of the homonuclear dipole–dipole coupling operator in a homonuclear two-spin system. The coherent averaging due to MAS is in the toggling frame of the π-pulses partially disrupted by a differential chemical shift term and thereby recoupling takes place.

The basic RFDR element consists of two π-pulses each centered in the middle of each rotor period in two consecutive rotor periods leading to a cyclic rf field. In the toggling frame of ideal (i.e., infinitely strong) π-pulses, the Hamiltonian of the chemical shift terms and the homonuclear dipolar coupling interaction is split up into three commuting parts:

$$\begin{aligned}\tilde{H}_{0a} &= \frac{1}{2}(\omega_I(t)+\omega_S(t))\theta(t)(I_z+S_z)\\ \tilde{H}_{0b} &= \omega_{IS}(t)2I_zS_z\\ \tilde{H}_1 &= \frac{1}{2}(\omega_I(t)-\omega_S(t))\theta(t)(I_z-S_z)-\omega_{IS}(t)(I_xS_x+I_yS_y)\\ &= \Delta\omega(t)\theta(t)I_z^{23}-\omega_{IS}(t)I_x^{23}\end{aligned} \tag{25}$$

where $\theta(t)$ equals 1 or -1 after an even or odd number of π-pulses, respectively, $\Delta\omega(t)=\omega_I(t)-\omega_S(t)$, and we make use of the fictitious spin$-1/2$ operators [88, 89] $I_x^{23}=I_xS_x+I_yS_y$, $I_y^{23}=I_yS_x-I_xS_y$, and $I_z^{23}=\frac{1}{2}(I_z-S_z)$. Over the full period, a spin echo is obtained (also refocusing chemical shielding anisotropies) and $\overline{\tilde{H}}_{0b}=0$. $\tilde{H}_1$ is not self-commuting at all times and effective Hamiltonian theory is therefore applied to gain physical insight.

The calculation of the effective Hamiltonian is greatly simplified by only considering the isotropic chemical shift difference, $\Delta\omega^{\mathrm{iso}}=\omega_I^{\mathrm{iso}}-\omega_S^{\mathrm{iso}}$, leading to

$$\begin{aligned}\overline{\tilde{H}}_{IS}^{(1)} &= -\left(\frac{1}{\pi}(\omega_{IS}^{(1)}+\omega_{IS}^{(-1)})\frac{a}{1-a^2}s_{\pi a}-\frac{1}{\pi}(\omega_{IS}^{(2)}+\omega_{IS}^{(-2)})\frac{a}{4-a^2}s_{\pi a}\right)I_x^{23}\\ &= \frac{2}{\pi}\left(\frac{1}{2\sqrt{2}}b_{IS}s_{2\beta_{PR}}c_{\gamma_{PR}}\frac{a}{1-a^2}+\frac{1}{4}b_{IS}s_{\beta_{PR}}^2c_{2\gamma_{PR}}\frac{a}{4-a^2}\right)s_{\pi a}I_x^{23}\end{aligned} \tag{26}$$

with $a=\Delta\omega^{\mathrm{iso}}/\omega_r$. This effective Hamiltonian to first order, proportional to the ZQ operator, can be used to transfer longitudinal magnetization in, e.g., correlation spectroscopy as exemplified in Fig. 2b (bottom). We note that experiments are typically implemented with an XY-8 phase scheme for the π pulses rather than in the XX-scheme, as implied in the effective Hamiltonian calculation [24].

The ideal π-pulses approximation used in RFDR is acceptable when the pulse length is much shorter than the rotor period and the spinning frequency is much larger than the dipole–dipole coupling frequency. For moderate to high MAS frequencies, the approximation breaks down and a refined theoretical description is needed. The finite pulse RFDR (fpRFDR) experiment of Ishii [90] serves this need. Assuming π-pulses of width τ_w with constant amplitude and no phase modulation, the effective Hamiltonian in the interaction frame of the finite rf pulse (e.g., implemented with a XY-8 phase cycling scheme) takes the form

$$\overline{\tilde{H}}_{IS}^{(1)} = \frac{3}{2t_r} \int_{\tau}^{\tau+\tau_w} \omega_{IS}(t) s^2_{\omega_{rf}t} (2I_zS_z - I_xS_x - I_yS_y) \mathrm{d}t. \tag{27}$$

Upon using a π-pulse centered in the middle of each rotor period τ_r and lasting one-third of a rotor period, the first-order effective Hamiltonian is

$$\begin{aligned} \overline{\tilde{H}}_{IS}^{(1)} &= \left(\frac{-27\sqrt{3}}{64\pi} \left(\omega_{IS}^{(1)} + \omega_{IS}^{(-1)} \right) + \frac{27\sqrt{3}}{80\pi} \left(\omega_{IS}^{(2)} + \omega_{IS}^{(-2)} \right) \right) (2I_zS_z - I_xS_x - I_y S_y) \\ &= \left(\frac{27}{64\pi} \sqrt{\frac{3}{2}} b_{IS} s_{2\beta_{PR}} c_{\gamma_{PR}} + \frac{27\sqrt{3}}{160\pi} b_{IS} s^2_{\beta_{PR}} c_{2\gamma_{PR}} \right) (2I_zS_z - I_xS_x - I_yS_y). \end{aligned} \tag{28}$$

We immediately recognize the difference in the effective operator of fpRFDR compared to that of RFDR. In RFDR, a pure ZQ operator is recoupled, while for fpRFDR it is an effective operator proportional to the native homonuclear dipole–dipole coupling operator. Furthermore, for RFDR the scaling factor depends on the isotropic chemical shift difference while the scaling factor of fpRFDR does not. The recoupling of the dipole–dipole coupling interaction in fpRFDR originates in the spin evolution during the π-pulses, i.e., the mechanism of recoupling in fpRFDR is different from that of RFDR. It should finally be mentioned that fpRFDR can easily be implemented at very high MAS frequencies and potentially with very little or no ^{1}H decoupling [90]. Also, we should mention that refined versions such as RFDR using adiabatic π pulses have been proposed [91]. An example of the applicability of low-power fpRFDR along with paramagnetic doping of proteins for nanomole-scale (or speed-accelerated) biological solid-state NMR is illustrated in Fig. 3. The figure illustrates the paramagnetic effect of Cu in the water phase and a 2D PACC (paramagnetic relaxation-assisted condensed data collection) spectrum of 1.8 mg uniformly ^{13}C-labeled ubiquitin recorded using 40 kHz sample spinning, 7 kHz rf field strength for ^{1}H decoupling, and 0.7 s repetition delay [92].

3.3 *Mechanical or Chemical-Shift-Based Recoupling: Rotational Resonance*

As demonstrated by Griffin, Levitt, and coworkers in the late 1980s [21, 93], it is also possible to recouple homonuclear dipolar couplings through interference between isotropic chemical shifts and the rotor revolution. This phenomenon, called rotational resonance, occurs when the spinning frequency is adjusted to a submultiple of the isotropic chemical shift difference, i.e., $n\omega_r = \left| \omega_I^{\mathrm{iso}} - \omega_S^{\mathrm{iso}} \right|$. To understand this experiment, the dipolar coupling Hamiltonian in (10) is transformed

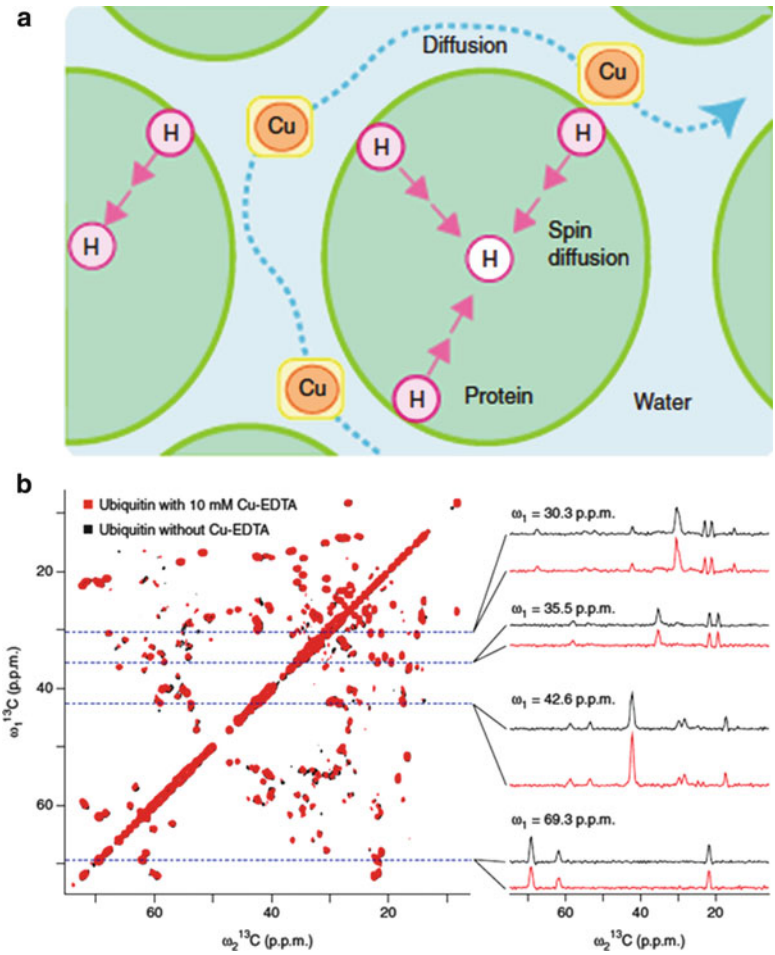

Fig. 3 (**a**) Proposed mechanism of paramagnetic ^{1}H T_1 relaxation enhancement in the PACC experiment enabling reduction of the repetition time to 0.7 s. (**b**) PACC 2D ^{13}C–^{13}C correlated spectrum of a uniformly ^{13}C-labeled microcrystalline sample of ubiquitin (1.8 mg) containing 10 mM Cu-EDTA recorded using 40 kHz spinning and fpRFDR mixing with 7 kHz ^{1}H decoupling (reproduced from [92] with permission)

[by Cartesian operations as in (9)] into the interaction frame of the isotropic chemical shifts on the two spins

$$\begin{aligned}\tilde{H}_{IS}(t) &= e^{i\omega_I^{\mathrm{iso}} t I_z} e^{i\omega_S^{\mathrm{iso}} t S_z} H_{IS}(t) e^{-i\omega_S^{\mathrm{iso}} t S_z} e^{-i\omega_I^{\mathrm{iso}} t I_z} \\ &= \omega_{IS}(t)\left[2I_zS_z - c_{\Delta\omega^{\mathrm{iso}}t}(I_xS_x + I_yS_y) - s_{\Delta\omega^{\mathrm{iso}}t}(I_xS_y - I_yS_x)\right] \\ &= \sum_{m=-2}^{2} \omega_{IS}^{(m)}\left[e^{im\omega_r t} 2I_zS_z - \frac{1}{2}\left(e^{i(n+m)\omega_r t} + e^{-i(n-m)\omega_r t}\right) I_x^{23}\right. \\ &\quad \left. + \frac{1}{2i}\left(e^{i(n+m)\omega_r t} - e^{-i(n-m)\omega_r t}\right) I_y^{23}\right] \end{aligned} \tag{29}$$

assuming $\Delta\omega^{\mathrm{iso}} = \omega_I^{\mathrm{iso}} - \omega_S^{\mathrm{iso}} = n\omega_r$ and where the fictitious spin−1/2 operators (see above) indicates that the recoupling in this case is mediated through a ZQ effective Hamiltonian. This becomes evident through the first-order effective Hamiltonian

$$\overline{\tilde{H}}_{IS}^{(1)} = -\frac{1}{2}\left(\omega_{IS}^{(-n)} + \omega_{IS}^{(n)}\right)I_x^{23} + \frac{1}{2i}\left(\omega_{IS}^{(-n)} - \omega_{IS}^{(n)}\right)I_y^{23}, \tag{30}$$

revealing a static dipolar Hamiltonian in cases where $n = \pm 1$ or $n = \pm 2$, corresponding to the case where the sample spinning frequency is adjusted to the isotropic chemical shift difference or half of it, respectively. For the $n = 1$ case, the Hamiltonian takes the form

$$\overline{\tilde{H}}_{IS}^{(1)} = \frac{1}{2\sqrt{2}} b_{IS} s_{2\beta_{PR}} \left(c_{\gamma_{PR}} I_x^{23} + s_{\gamma_{PR}} I_y^{23}\right), \tag{31}$$

which effectively operates on the differential shift operator $I_z^{23} = \frac{1}{2}(I_z - S_z)$. This explains why distance measurements using rotational resonance typically proceeds via pulse sequences where the polarization of one of the two spins is inverted selectively prior to evolution under the rotational resonance operator as illustrated in Fig. 2c along with a dephasing curve obtained for the $n = 3$ rotational resonance of doubly-^{13}C-labeled Zn-acetate.

The rotational resonance experiment has, for example, found important applications for measurement of internuclear distances in selectively ^{13}C-labeled proteins [94], as a means to excite DQ coherences [95], and for establishment of one-bond ^{13}C–^{13}C correlations in 2D experiments for assignment purposes [96]. We note that many variants of the rotational resonance experiment exist, such as rotational resonance with spinning-speed switching [97], adiabatic versions of rotational resonance by ramping the spinning speed [98], the rotational resonance tickling experiment [99] reducing the sensitivity towards zero-quantum relaxation, RRTR [100] and BroBaRR [101] using rf irradiation to make the experiment more broadbanded, and the constant time rotational resonance width experiment [102].

3.4 *Continuous rf Irradiation Recoupling: DCP, HORROR, and Composite Recoupling*

Dipolar recoupling may also be accomplished using continuous rf irradiation as demonstrated in the heteronuclear and homonuclear case by the CP at MAS conditions (or for low-γ heteronuclear spins called double-cross-polarization, DCP [103]) and HORROR (homonuclear rotary resonance) [26] experiments, respectively. These experiments may easily be described by transforming the description into the interaction frame of the rf irradiation using (14a) exploiting

either Cartesian [cf. (9)] or irreducible spherical tensor operations (8). For variation, we take the latter approach here.

Addressing first the heteronuclear case (i.e., the DCP experiment introduced by Schaefer and coworkers in 1984), the dipolar coupling may be expressed as in (10) that upon heteronuclear truncation of the transverse terms may be recast in irreducible tensor operator form ($I_z = T^I_{1,0}$, $S_z = T^S_{1,0}$) as

$$H_{IS}(t) = 2\omega_{IS}(t) T^I_{1,0} T^S_{1,0}, \tag{32}$$

which we influence with rf irradiation of the form $H_{\mathrm{rf}} = p\omega_r I_x + q\omega_r S_x$ (i.e., simple continuous wave rf irradiation at both channels). Here we assume $\omega^I_{\mathrm{rf}} = p\omega_r$ and $\omega^S_{\mathrm{rf}} = q\omega_r$ without any restrictions so far on p and q. In this case, transformation into the interaction frame of the rf irradiation conveniently goes first through a $-\pi/2$ rotation around y which in terms of Wigner rotations takes us to the tilted frame T

$$H^T_{IS}(t) = 2\omega_{IS}(t) \sum_{\mu,\mu'=-1}^{1} T^I_{1,\mu} T^S_{1,\mu'} d^{(1)}_{\mu,0}\left(-\frac{\pi}{2}\right) d^{(1)}_{\mu',0}\left(-\frac{\pi}{2}\right) \tag{33}$$

that, by noting that the rf field is now along the I_z and S_z axes, transforms into

$$\tilde{H}^T_{IS}(t) = 2 \sum_{m=-2}^{2} \sum_{\mu,\mu'=-1}^{1} \omega^{(m)}_{IS} T^I_{1,\mu} T^S_{1,\mu'} d^{(1)}_{\mu,0}\left(-\frac{\pi}{2}\right) d^{(1)}_{\mu',0}\left(-\frac{\pi}{2}\right) e^{i(m+p\mu+q\mu')\omega_r t}, \tag{34}$$

also introducing the Fourier expansion from (11). Equation (34) offers a wide variety of recoupling conditions (see, e.g., [104]), among which we will focus here on the most typical ZQ version with $\mu = -\mu' = \pm 1$ which, using $d^{(1)}_{\mu,0}\left(-\frac{\pi}{2}\right) d^{(1)}_{-\mu,0}\left(-\frac{\pi}{2}\right) = -\frac{1}{2}$, leads to the interaction frame Hamiltonian

$$\tilde{H}^T_{IS}(t) = -\sum_{m=-2}^{2} \sum_{\mu=-1}^{1} \omega^{(m)}_{IS} T^I_{1,\mu} T^S_{1,-\mu} e^{i(m+\mu(p-q))\omega_r t}, \tag{35}$$

having static components for $p - q = \pm m$. Taking the $p - q = 1$ case (offering the highest dipolar scaling factor), the effective Hamiltonian is given by

$$\begin{aligned} \overline{\tilde{H}}^{(1)T}_{IS} &= \frac{1}{2\sqrt{2}} b_{IS} s_{2\beta_{PR}} \left(T^I_{1,1} T^S_{1,-1} e^{-i\gamma_{PR}} + T^I_{1,-1} T^S_{1,1} e^{i\gamma_{PR}} \right) \\ &= -\frac{1}{2\sqrt{2}} b_{IS} s_{2\beta_{PR}} \left(I^{23}_x c_{\gamma_{PR}} + I^{23}_y s_{\gamma_{PR}} \right), \end{aligned} \tag{36}$$

where the fictitious spin−1/2 operators (see above) illuminates the ZQ nature of the recoupled Hamiltonian in the tilted frame. This Hamiltonian may be used to transfer

polarization (in the tilted frame; x-phase coherence in the non-tilted frame) from spin I to S as demonstrated by

$$\rho^T(t) = U^T(t)I_z\big(U^T(t)\big)^+ = I_z^{14} + c_{\omega_D t}I_z^{23} - s_{\omega_D t}\Big(c_{\gamma_{PR}}I_y^{23} - s_{\gamma_{PR}}I_x^{23}\Big), \tag{37}$$

where we assumed $\rho^T(0) = I_z = I_z^{14} + I_z^{23}$ using $I_z^{14} = \frac{1}{2}(I_z + S_z)$. With $S_z = I_z^{14} - I_z^{23}$ it is evident that complete transfer of polarization is obtained for $\omega_D t = \frac{1}{2\sqrt{2}} b_{IS} s_{2\beta_{PR}} t = \pi$.

The DCP experiment is in standard form [103], using ramping of the rf field on one of the channels [105], in adiabatic form [106], in form of the frequency-selective SPECIFIC sequence [107], or using various kinds of phase- and amplitude modulation such as in the SPICP [108], RFDRCP [109], *i*DCP [110], GATE [104], and PATCHED [111] protocols, a standard element in most biological solid-state NMR experiments. Recently, it has also been demonstrated that such experiments can be used without decoupling to facilitate applications at higher spinning frequencies and with reduced rf induced sample heating [112].

The so-called HORROR experiment by Nielsen and coworkers [26] introduced continuous rf irradiation recoupling to homonuclear spin-pairs and initiated the later very widely used concept of γ-encoded recoupling. Using a irreducible spherical approach as described above, the HORROR experiment (Fig. 2d) is readily described as starting out with the dipolar coupling Hamiltonian in (10) and x-phase rf irradiation in the form $H_{\mathrm{rf}} = n\omega_r(I_x + S_x)$, also here without initial constraint on n. The dipolar coupling Hamiltonian transforms into tilted frame (rotation $-\pi/2$ around $I_y + S_y$)

$$H_{IS}^T(t) = \sqrt{6}\omega_{IS}(t)\sum_{\mu=-2}^{2} T_{2,\mu}d_{\mu,0}^{(2)}\Big(-\frac{\pi}{2}\Big), \tag{38}$$

and into the interaction frame of the rf field (now directed along $I_z + S_z$)

$$\tilde{H}_{IS}^T(t) = \sqrt{6}\sum_{m=-2}^{2}\sum_{\mu=-2}^{2}\omega_{IS}^{(m)}T_{2,\mu}d_{\mu,0}^{(2)}\Big(-\frac{\pi}{2}\Big)e^{i(m+n\mu)\omega_r t}. \tag{39}$$

In this case, the most efficient recoupling is obtained by adjusting the rf field strength to half the spinning frequency and selecting the $m = \pm 1$ terms leading to the effective DQ Hamiltonian over two rotor periods

$$\begin{aligned}\overline{\tilde{H}}_{IS}^{(1)T} &= \frac{3}{2}\Big(\omega_{IS}^{(-1)}T_{2,2}^{IS} + \omega_{IS}^{(1)}T_{2,-2}^{IS}\Big)\\ &= -\frac{3}{4\sqrt{2}}b_{IS}s_{2\beta_{PR}}\Big(T_{2,2}^{IS}e^{-i\gamma_{PR}} + T_{2,-2}^{IS}e^{i\gamma_{PR}}\Big).\end{aligned} \tag{40}$$

Using the relations $T^{IS}_{2,\pm 2} = \frac{1}{2} I^{\pm} S^{\pm} = \frac{1}{2} I^{14}_{\pm}$, the density operator evolves as

$$\rho^T(t) = U^T(t) I_z \left(U^T(t)\right)^+ = I_z^{23} + c_{\omega_D t} I_z^{14} - s_{\omega_D t}\left(c_{\gamma_{PR}} I_y^{14} - s_{\gamma_{PR}} I_x^{14}\right), \qquad (41)$$

introducing the fictitious DQ operators $I_x^{14} = I_x S_x - I_y S_y$, $I_y^{14} = I_y S_x + I_x S_y$, and $I_z^{14} = \frac{1}{2}(I_z + S_z)$. It is seen that HORROR effectuates transfer of polarization from I_z to $-S_z$ for $\omega_D t = \frac{3}{4\sqrt{2}} b_{IS} s_{2\beta_{PR}} t = \pi$. We note that this transfer is demonstrated in the tilted frame, implying that the weak x-phase rf irradiation adjusted to the HORROR match condition is typically bracketed by strong $\pi/2$ pulses of phase y and $-y$ (the former often provided by a CP element with x-phase spin lock on the ^{13}C channel) in consistency with the pulse scheme in Fig. 2d.

While introducing rf driven coherence transfer between spins of the same species, the HORROR experiment itself has not been very widely used for homonuclear recoupling due to its sensitivity to resonance offsets and rf inhomogeneity. But the experiment has formed a highly recognized foundation in terms of a basic recoupling match condition and for numerous later important recoupling experiments. These includes, for example, the DARR experiment [38] using HORROR (typically using the MSD-HORROR [113] or heteronuclear rotary resonance $\omega_{\mathrm{rf}} = \omega_r$ matching condition) as a qualitative base to drive spin diffusion between protons (see below), the adiabatic HORROR-variant DREAM [98], and through introduction of γ-encoded recoupling which has been an important source of inspiration for numerous later recoupling experiments such as the symmetry-based CN [30–32] and RN [33, 114] experiments [37] and multiple-oscillating field techniques [46–49] discussed later in this review.

Through introduction of γ-encoding [26], the efficiency of transfer of coherence between spins in powder samples increased from around 50% in "standard" experiments such as DRAMA and RFDR to more than 70% through elimination of the dependency on the γ_{PR} powder angle. This concept has lately been elaborated further on through reduction of the dependency of the β_{PR} powder angle through composite dipolar recoupling [43, 115] and by exploiting the γ_{PR} powder angle dependency in so-called γ-preparation experiments [116] leading to sensitivity enhanced 2D experiments capturing both x- and y-phase coherences involving in the indirect dimension.

We will here address attention to the COMB ("compensated for beta") experiment, which illustrates a useful relation between normal rf pulses and dipolar recoupling and uses this feature to compensate for the effect of variations in the β_{PR} crystallite angles in a powder. This variation comes through via a dipolar coupling scaling factor $\omega_D = -\frac{\kappa}{2\sqrt{2}} b_{IS} s_{2\beta_{PR}}$ in, e.g., DCP ($\kappa = 1$) or HORROR ($\kappa = 3/2$) recoupling experiments. To illustrate this, and understand how appropriately placed rf correction pulses may be used for such compensation, it is most convenient to describe the recoupling experiments in the normal non-tilted frame (i.e., a frame not rotated by $-\pi/2$ around $I_y + S_y$ as used above for DCP and HORROR) for which the "ZQ" (superscript $-$) and "DQ" (superscript $+$) fictitious spin$-1/2$ operators take the form $X^{\pm} = \frac{1}{2}(I_x \pm S_x)$, $Y^{\pm} = I_z S_y \pm I_y S_z$, and

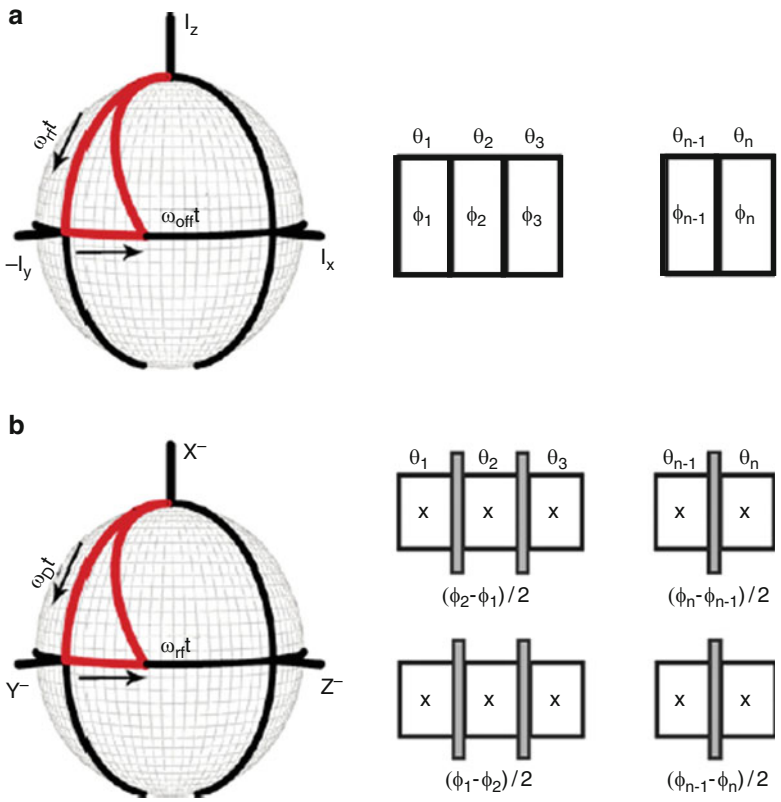

Fig. 4 Analogy between (**a**) rf pulses and (**b**) dipolar recoupling as illustrated through transformation in the involved 3D operator subspaces (*left*) and a general composite rf pulse and the translation to a corresponding general composite dipolar recoupling sequence (*right*) offering the possibility to design recoupling experiments through development of composite rf pulses (reproduced from [43] with permission)

$Z^{\pm} = I_z S_z \mp S_y I_y$. Using these definitions and standard notation for rf pulses we obtain the Hamiltonians

$$H_{\text{pulse}} = \omega_{\text{rf}} I_x + \omega_{\text{off}} I_z \tag{42a}$$

$$H^{\pm}_{\text{recouple}} = \omega_D \left(c_{\gamma_{PR}} Z^{\pm} + s_{\gamma_{PR}} Y^{\pm} \right) + \Delta\omega_{\text{rf}} X^{\pm} \xrightarrow{\gamma_{PR}=0} \omega_D Z^{\pm} + \Delta\omega_{\text{rf}} X^{\pm} \tag{42b}$$

where $\omega_{\text{rf}} = \omega^{\text{nom}}_{\text{rf}} + \Delta\omega_{\text{rf}}$ is the rf field strength (with nominal value and inhomogeneity), ω_{off} the resonance offset, and, for simplicity, we assumed $\gamma_{PR} = 0$ in the right-hand side of (42b). We note that the formulation in (42b) assumes both spins to be on resonance. The two Hamiltonians lead to transformations of the type

$$I_z \xrightarrow{H_{\text{pulse}}\tau} aI_z + bI_x + cI_y \tag{43a}$$

$$X^{\pm} \xrightarrow{H^{\pm}_{\text{recouple}}\tau} aX^{\pm} + bZ^{\pm} + cY^{\pm}, \quad X^{\mp} \xrightarrow{H^{\pm}_{\text{recouple}}\tau} X^{\mp} \tag{43b}$$

using $a = c_\vartheta^2 + c_\theta s_\vartheta^2$, $b = s_\vartheta c_\vartheta (1 - c_\theta)$, and $c = s_\vartheta s_\theta$ with $\vartheta = \tan^{-1}(\omega_{\text{rf}}/\omega_{\text{off}})$, $\theta = \tau\sqrt{\omega_{\text{rf}}^2 + \omega_{\text{off}}^2}$ for pulses and $\vartheta = \tan^{-1}(\omega_D/\Delta\omega_{\text{rf}})$, $\theta = \tau\sqrt{\Delta\omega_{\text{rf}}^2 + \omega_D^2}$ for recoupling. Equations (42) and (43) clearly demonstrate the formal analogy between pulses and recoupling (cf. Fig. 4), in the sense that the rf field strength for pulses is replaced by the dipolar coupling in recoupling and that offset in the case of pulses is replaced by rf inhomogeneity for recoupling. This implies that composite pulses such as $\left(\frac{\pi}{2}\right)_y(\pi)_{\bar{x}}\left(\frac{\pi}{2}\right)_y$ and $\left(\frac{3\pi}{2}\right)_{\bar{x}}(2\pi)_x\left(\frac{\pi}{2}\right)_y\left(\frac{3\pi}{2}\right)_{\bar{y}}(2\pi)_y\left(\frac{\pi}{2}\right)_x$ compensating for both rf inhomogeneity and resonance offset [117] may be translated into so-called COMB_3 and COMB_6 recoupling sequences compensating for β_{PR}-dependent variations in ω_D and rf inhomogeneity [115]. The COMB_3DCP (superscript −) or COMB_3HORROR (superscript +) sequences are characterized by the propagators

$$U = e^{-iH^{\pm}_{\text{recouple}}t_{\pi/2}} e^{-i(\pi/2)X^{\pm}} e^{-iH^{\pm}_{\text{recouple}}t_{\pi}} e^{i(\pi/2)X^{\pm}} e^{-iH^{\pm}_{\text{recouple}}t_{\pi/2}}, \tag{44}$$

demonstrating the use of pulses along the $X^{\pm}$ axis to effectuate the phase shifts of the composite rf pulses. Such composite recoupling sequences, and more advanced versions obtained using optimal control [43] (see below), have improved the theoretical transfer efficiency from the ca. 70% from γ-encoded experiments to around 90%, and in practice sensitivity gains in the order of 50% have been obtained due to additional better compensation for rf inhomogeneity.

3.5 *Symmetry-Based Dipolar Recoupling: CN and RN Sequences*

In the mid-1990s it was clear that methods like HORROR (and for the heteronuclear case DCP) were not sufficiently stable towards rf inhomogeneity and sufficiently broadbanded to facilitate universal recoupling in uniformly labeled samples often displaying large dispersion in chemical shifts. This motivated Levitt, Nielsen, and coworkers to develop symmetry-based dipolar recoupling experiments (reviewed in [37] and [118]), initially in the form of the $C7_2^1$ [30] and soon after the more broadbanded, permutation-offset-stabilized POST-$C7_2^1$ [31] experiment, followed by a large number of specific CN_n^v [32] and later RN_n^v [33, 34] pulse sequences designed for different purposes. The symmetry-based sequences, also adapted by other groups through sequences such as CMR7 [35] and SPC-5 [36], combined the attractive concept of γ-encoded recoupling from the HORROR experiment with elegant recipes for symmetry-based tailoring of the pulse sequences to eliminate/reduce effects from undesired nuclear spin and rf interactions such as offsets, rf inhomogeneity, and unwanted couplings.

To describe these experiments, introducing new degrees of freedom to manipulate systematically both spin and spatial tensor components, it proves convenient to recast the internal Hamiltonian in (5) in the form

$$H^{\Lambda}_{lm\lambda 0}(t) = \sum_{\Lambda,l,m,\lambda} \omega^{\Lambda}_{lm}(t) T^{\Lambda}_{\lambda,0}, \tag{45}$$

where Λ designates a given nuclear spin interaction with $\Lambda = \mathrm{D}$ dipole–dipole coupling, $\Lambda = J$ scalar coupling and $\Lambda = \delta$ chemical shift. l and λ denote the ranks for the spatial and spin tensors with the components $m = -l, -l+1, \ldots l$ and $\mu = -\lambda, -\lambda+1, \ldots \lambda$, respectively. In (45), the latter index, μ, is set to zero under free precession in the standard high-field approximation. The angular frequency amplitude is given by $\omega^{\Lambda}_{lm}(t) = \omega^{\Lambda}_{lm} e^{im\omega_r t}$, here expressing the Fourier components as $\omega^{\Lambda}_{lm} = \left[R^{\Lambda}_{lm}\right]^R d^{(l)}_{m0}(\beta_{RL}) e^{-im\alpha_0}$ with $\left[R^{\Lambda}_{lm}\right]^R$ being the mth component of the spatial tensor in the rotor-fixed frame R.

Using this notation, Levitt and coworkers introduced two classes of symmetry-based recoupling experiments CN^{ν}_{n} and RN^{ν}_{n} both specified by three symmetry numbers N, ν, and n; n is the number of rotor periods the whole sequence is spanning, N describes the number of elements for the sequence each having a duration of $\tau_e = n\tau_r/N$, and ν is the winding number corresponding to a phase increment between each element. The latter is given by an addition of $2\pi\nu/N$ for each element for CN^{ν}_{n} and by a change in sign between each element for RN^{ν}_{n} with the phase given by $\pi\nu/N$. For the CN^{ν}_{n} symmetry, the overall rf field is cyclic for each element, while for the RN^{ν}_{n} symmetry each element corresponds to a π-rotation of resonant spins. The basic setup of the CN^{ν}_{n} and RN^{ν}_{n} recoupling sequences are illustrated in Fig. 5a, b, respectively.

Upon entering the interaction frame of the rf irradiation for the CN^{ν}_{n} or RN^{ν}_{n} sequences [cf. (14)] and taking the first-order effective Hamiltonians [cf. (17a) and (18a)], it is possible to establish the following selection rules for the averaging (and conversely recoupling) of the various interactions described in (45) as

$$\overline{H}^{\Lambda(1)}_{lm\lambda\mu} = \frac{1}{\tau_c} \int_0^{\tau_c} \tilde{H}^{\Lambda}_{lm\lambda\mu}(t)\mathrm{d}t = 0 \tag{46}$$

applying for

$$CN^{\nu}_{n}: \; mn - \mu\nu \neq NZ, \quad \text{where } Z \text{ is integer} \tag{47a}$$

$$RN^{\nu}_{n}: \; mn - \mu\nu \neq \frac{N}{2} Z_{\lambda}, \quad \text{where } Z_{\lambda} \text{ is integer with same parity as } \lambda. \tag{47b}$$

with $\tau_c = 2\pi n/\omega_r$ being the cycle time for the symmetry. These selection rules may be used systematically to design sequences that recouple/decouple various interactions characterized by different (l,λ) numbers: Homonuclear dipole–dipole

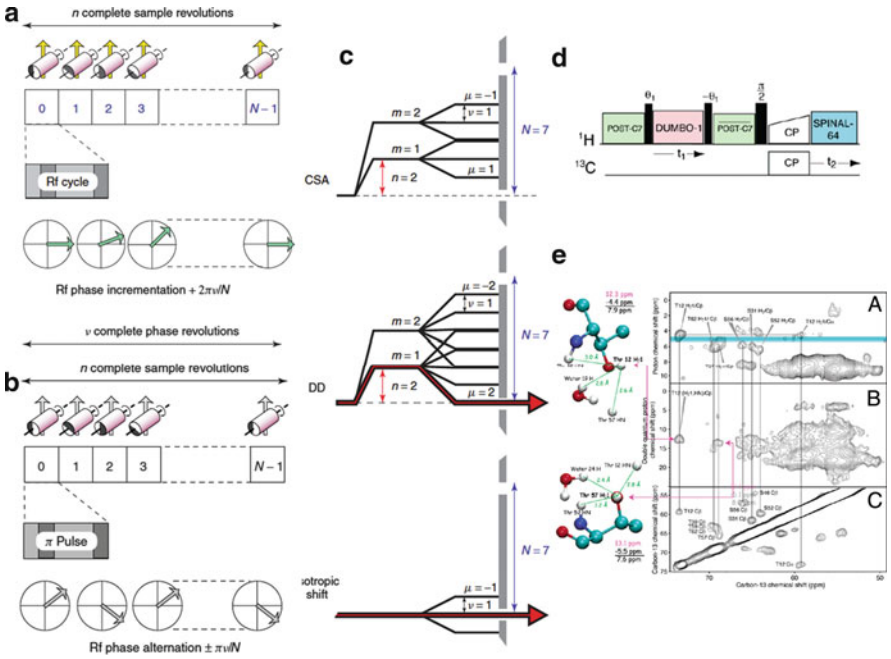

Fig. 5 Symmetry-based dipolar recoupling illustrated in terms of pulse sequences for the CN_n^ν (**a**) and RN_n^ν (**b**) pulse sequences, a spin-space selection diagram for the $C7_2^1$ symmetry (**c**) (reproduced from [118] with permission). Application of POST-$C7_2^1$ [31] as an element in a ^{1}H–^{1}H double-quantum vs ^{13}C chemical shift correlation experiment (**d**) used as elements (B panel) in a study of water binding to polycrystalline proteins (reproduced from [119] with permission)

coupling (2,2), homonuclear J coupling (0,0), isotropic chemical shift (0,1), and chemical shift anisotropy and heteronuclear dipole–dipole coupling (2,1). An example is given in Fig. 5c for the original $C7_2^1$ pulse sequence [30], where pathways entering a "wall" are averaged (according to (47a), as is the case for chemical shift anisotropy, CSA), while those passing through the gaps (as is the case for the dipole–dipole coupling, DD, in addition to the isotropic chemical shift) are not – and thereby recoupled. Using (47) or space-spin selection diagrams as in Fig. 5c, a large variety of sequences have been introduced to offer, e.g., recoupling of dipole– dipole couplings [30–34, 37], anisotropic chemical shielding [120], or for decoupling [33, 121–123]. An example illustrating the application of symmetry-based dipolar recoupling to establish information about the location of water in protein crystals through intermolecular ^{1}H–^{1}H dipole couplings is given in Fig. 5e using the pulse sequence in Fig. 5d with POST-$C7_2^1$ as driver of coherence transfer between protons.

A large variety of solid-state NMR re- and decoupling experiments have been developed using the concept of symmetry-based pulse sequence design. Many of those come directly from selecting sequences with appropriate values of N, ν, and n in a first-order approach as given by (47). With regard to biological solid-state

NMR, we should mention that not only symmetry-based experiments for magnetization transfer between spins via recoupled dipolar couplings have been proposed, but also experiments such as TOBSY [124] using symmetry-based elements to facilitate transfer via J couplings have been proposed. Many experiments have been designed using additional higher-order terms in the effective Hamiltonian and using refined selection rules based on these. In addition, the symmetry-based scaffold for the sequences has been further developed using supercycling schemes to cancel higher-order terms systematically in experiments with longer duration [32, 118, 125].

Finally, we should note that not only the symmetry-based scaffold of the pulse sequence is important but also the basic pulse sequence element, notably explaining the widely different performance of $C7_2^1$ [30] and POST-$C7_2^1$ [31] originating only in the replacement of the $2\pi_x 2\pi_{-x}$ element (which is somewhat compensating with respect to shielding effects relative to the simpler $2\pi_x$ element) by the permuted POST element $(\pi/2)_x(2\pi)_{-x}(3\pi/2)_x$. Likewise, RN_n^v sequences have been presented with π_x as well as various composite π pulses, such as $(\pi/2)_{-x}(2\pi)_x(3\pi/2)_{-x}(\pi/2)_x$ as the basic element. By appropriate choice of element, it is possible not only to alter the suppression of non-desired interactions/effects (e.g., resonance offsets and rf inhomogeneity) but also to alter the scaling factor of the desired interactions [126, 127]. It is also possible to alter the ease of operation through reduction of the demands to the rf irradiation field strength, originally being quite high for symmetry-based recoupling experiments. We mention as examples off-resonance irradiation procedures simultaneously increasing the dipolar scaling factor and reducing the rf demands [128] and the use of optimal control [129] (see below), nonlinear optimization [130, 131], and exponentially modulated fields [132] (see below) to lower the rf power demands. This facilitates operation at higher spinning frequencies and/or reduces the demands to the associated high-power ^{1}H decoupling, e.g., in the interest of reduced rf-induced sample heating.

3.6 Spin-Diffusion and Third-Spin-Assisted Recoupling

In general the recoupling techniques discussed above relied on first-order effective Hamiltonian theory in a two-spin-system approach. Recently, increasing attention has been devoted to recoupling experiments involving an assistant third spin (typically a proton) and spin diffusion techniques. Such methods are important as means to establish long-range distance information for assignment and structure determination (see, e.g., [45, 133–135]). To describe such methods, including some of the most popular recoupling techniques for structure determination, one needs to look at higher-order terms in the effective Hamiltonian.

Magnetization transfer via proton-driven-spin-diffusion (PDSD) in MAS NMR is not by any means a new experiment. It was introduced in the early 1980s by Maciel and coworkers [136] and later used, described, and analyzed by numerous groups in relation to, e.g., biological solid-state NMR. In its original form, the experiment consists of a couple of oppositely phase $\pi/2$ pulses bringing the low-γ

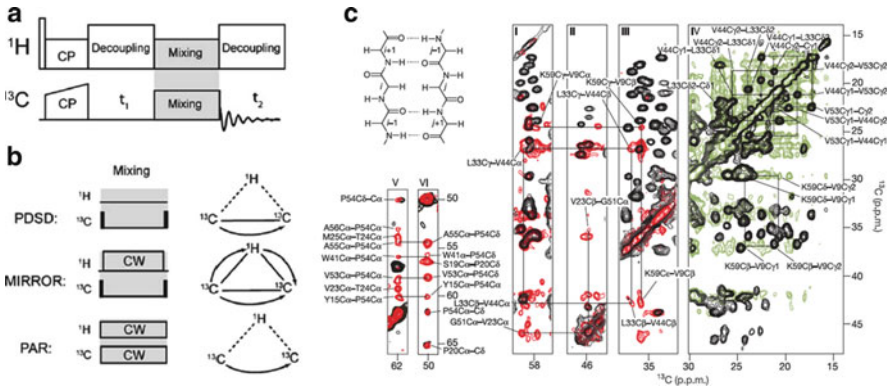

Fig. 6 A general pulse sequence (**a**) for spin diffusion or third-spin assisted mixing for polarization transfer between carbons (as shown) or carbon and nitrogen along with examples of homonuclear mixing elements and illustration of activated parts of ^{1}H–^{13}C–^{13}C spin systems for PDSD, MIRROR, and PAR (**b**) (taken from [18] with permission). (**c**) Example of the application of PDSD for structure determination of the α-spectrin SH3 domain (taken from [133] with permission)

coherence to the longitudinal axis and back, in between which a period without ^{1}H decoupling facilitates the spin diffusion driven by protons (Fig. 6a, b top). While a deeper insight into the spin diffusion mechanism in this experiment, often seen in biological solid-state NMR with an evolution time over hundreds of milliseconds, most likely requires a many-spin system approach, it turns out that many of the concepts relating to distance measurements may be explored in small spin systems. Taking a three-spin approach involving two carbon spins (S_1 and S_2) and a proton spin (I), it is found that second-order dipole–dipole cross-terms between interactions of the type [using (10) and (11)]

$$H_D(t) = \sum_{m=-2}^{2} \omega_{S_1S_2}^{(m)} e^{im\omega_r t}(3S_{1z}S_{2z} - S_1 \cdot S_2) + \sum_{m=-2}^{2} \omega_{S_1I}^{(m)} e^{im\omega_r t} 2S_{1z}I_z \qquad (48)$$

lead to non-averaged terms through which coherence transfer may migrate. For the simple three-spin systems such terms may take the form

$$\bar{H}_{DD}^{(2)} = \frac{1}{\omega_r}\left[\mathrm{Im}\left(\omega_{S_1S_2}^{(1)}\omega_{S_1I}^{(-1)}\right) + \frac{1}{2}\mathrm{Im}\left(\omega_{S_1S_2}^{(2)}\omega_{S_1I}^{(-2)}\right)\right] 2I_z\left(S_{1x}S_{2y} - S_{1y}S_{2x}\right) \qquad (49)$$

revealing that PDSD under MAS conditions may promote zero-quantum polarization transfer between the two S spins. A deeper analysis of this experiment is beyond the scope of this review, but may be found, e.g., in a recent paper by Ernst and coworkers [137]. The PDSD experiment has been a very important driver for establishing biological solid-state NMR spectroscopy as a powerful protein structure determination tool as illustrated by some of the pioneering spectra of SH3 by Oschkinat and coworkers [133] in Fig. 6c.

Along the same lines, it has been demonstrated that one could speed up the spin-diffusion/magnetization transfer by irradiation on the proton channel. Such experiments, typically using a HORROR-like rotary resonance rf field with amplitude $\omega_{rf}^{I} = \omega_r$ on the proton spins in the diffusion period, are known as dipolar-assisted rotational resonance (DARR) [38] or radiofrequency field assisted diffusion (RAD) [138] experiments. At high spinning speeds and high static magnetic fields, the efficiency of PDSD and DARR experiments are compromised which may be overcome using experiments such as phase-alternated recoupling irradiation scheme (PARIS) [139] and mixed rotational and rotary resonance (MIRROR) [39]. In the MIRROR experiment (Fig. 6b, middle), for example, the proton rf field is matched to the spinning frequency and to the isotropic chemical shift difference of ^{13}C spins, $\omega_{\mathrm{rf}} = n\omega_r \pm \Delta\omega_{\mathrm{iso}}$, and by using amplitude or phase alternation, the sequence is made more broad-banded. In this case, it may be shown that the effective Hamiltonian arising from cross-terms between homo- and heteronuclear dipolar couplings is proportional to the three-spin operator $I_a^{\mp} S_q^{\pm} S_p^{\mp}$. This Hamiltonian promotes homonuclear ZQ transfer while also activating heteronuclear ZQ and DQ polarization transfer.

Recently a new type of proton assisted recoupling experiments has been developed for coherence transfer where rf irradiation is taking place on all involved rf channels. This embraces the homonuclear proton assisted recoupling (PAR) [45, 140, 141] and the later resonant second-order transfer (RESORT) [142] experiments, as well as the heteronuclear proton assisted insensitive nuclei (PAIN) cross polarization [44] experiments. In PAR and PAIN, spin-lock CW irradiation is applied on both passive (^{1}H) and active spins (^{13}C, ^{15}N) without matching rotary resonance conditions. In RESORT a phase alternation irradiation scheme for the passive spins is used.

The PAR experiment may be described by considering two heteronuclear dipolar coupling interactions with one proton (I) in common, i.e., a Hamiltonian of the type

$$H_D(t) = \sum_{m=-2}^{2} \omega_{S_1 I}^{(m)} e^{im\omega_r t} 2S_{1z} I_z + \sum_{m'=-2}^{2} \omega_{S_2 I}^{(m')} e^{im'\omega_r t} 2S_{2z} I_z, \tag{50}$$

where S_1 and S_2 denote two ^{13}Cs. In the interaction frame of the rf irradiation $H_{\mathrm{rf}}(t) = p\omega_r(S_{1x} + S_{2x}) + q\omega_r I_x$ (upon transforming the description into a tilted frame around $\frac{\pi}{2}\left(I_y + S_{1y} + S_{2y}\right)$ as used for HORROR and DCP), the Hamiltonian to first-order is averaged out, $\bar{H}_D^{T(1)} = 0$, in the case where no rotary resonance conditions are met. A static ZQ Hamiltonian involving the two heteronuclear dipolar couplings in (50), however, may be found to second order [45]

$$\bar{\bar{H}}_{DD}^{T(2)} = \frac{1}{\omega_r} \left[\begin{array}{l} \left[\mathrm{Re}\left(\omega_{S_1 I}^{(1)} \omega_{S_2 I}^{(-1)}\right) \lambda(1,p,q) + \mathrm{Re}\left(\omega_{S_1 I}^{(2)} \omega_{S_2 I}^{(-2)}\right) \lambda(2,p,q) \right] 2I_z S_x^{S_1 S_2(23)} \\ + i \left[\mathrm{Im}\left(\omega_{S_1 I}^{(1)} \omega_{S_2 I}^{(-1)}\right) \sigma(1,p,q) + \mathrm{Im}\left(\omega_{S_1 I}^{(2)} \omega_{S_2 I}^{(-2)}\right) \sigma(2,p,q) \right] 2I_z S_y^{S_1 S_2(23)} \end{array} \right] \tag{51}$$

unless p takes the values 0, 1/2, 1, 3/2, and 2. In (51) we used fictitious spin−1/2 operators on the S spins and

$$\lambda(m,p,q) = \frac{p-q}{m^2-(q-p)^2} - \frac{p+q}{m^2-(p+q)^2} \tag{52a}$$

and

$$\sigma(m,p,q) = \frac{m}{m^2-(q+p)^2} - \frac{m}{m^2-(q-p)^2}. \tag{52b}$$

From (51) it is seen that, in the tilted frame, the PAR experiment (and similar for RESORT) can mediate S_{1z} to S_{2z} transfer through an effective Hamiltonians of the form $I_z S_1^{\mp} S_2^{\pm}$, which effectively indicates that the experiment may be used for transferring x magnetization between carbon spins in the normal frame. For PAIN a similar formalism may be used with, e.g., $I = {}^1\mathrm{H}$, $S_1 = {}^{13}\mathrm{C}$, and $S_2 = {}^{15}\mathrm{N}$, leading to second-order DQ ($H_z C_p^{\mp} N_q^{\mp}$) or ZQ ($H_z C_p^{\mp} N_q^{\pm}$) effective Hamiltonians depending on the rf field strength. The operators in the tilted frame are similar to those for PDSD in (49) but the scaling factor for the residual dipolar coupling is in general higher for PAR/RESORT/PAIN than for PDSD. Figure 7 illustrates the use of PAR by Griffin and coworkers to establish information about internuclear distances above 4 Å for a uniformly $^{13}\mathrm{C}$,$^{15}\mathrm{N}$-labeled sample of the N-*f*-MLF-OH three-peptide [45].

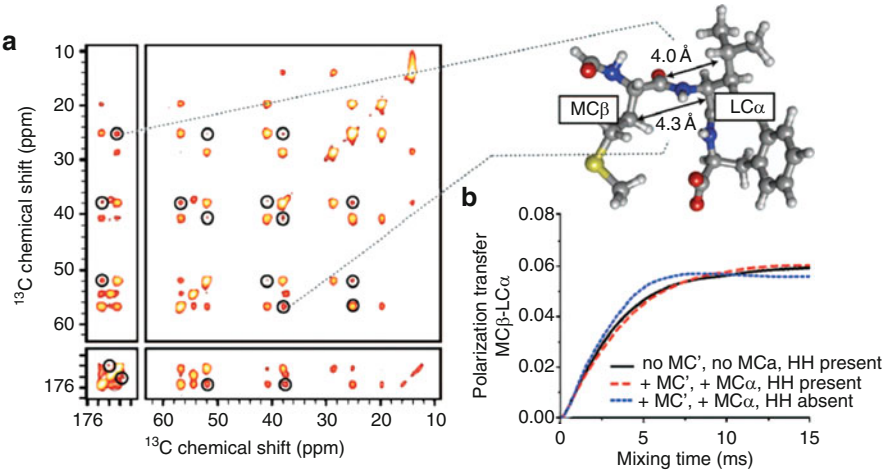

Fig. 7 (**a**) 2D PAR spectrum of uniformly $^{13}\mathrm{C}$, $^{15}\mathrm{N}$-labeled N-*f*-MLF-OH (structure inserted) diluted to 10% in natural abundance providing cross peaks (*circled*) corresponding to internuclear $^{13}\mathrm{C}$–$^{13}\mathrm{C}$ distances of more than 4 Å. (**b**) Simulations supporting that the transfer is dominated by the MC-[^{1}H]-LC third-spin assisted transfer, i.e., relayed transfer is negligible (reprinted from [45] with permission)

Finally, we should also mention that assisted spin recoupling is by no means restricted to ^{1}H, ^{13}C, and ^{15}N spin species but may also be used to facilitate ^{1}H and ^{2}H to low-γ spin transfers. This may be exploited in extensively deuterated samples using rf fields on ^{1}H and ^{2}H which are matched to a rotary resonance condition to facilitate spin-diffusion between ^{13}C spins in a longitudinal mixing process. This was recently demonstrated by van Rossum and coworkers in terms of the double-nucleus enhanced recoupling (DONER) experiment [143].

3.7 *Multiple-Oscillating Field Techniques: Dipolar Truncation, Recoupling of Native Dipolar Coupling, and Recoupling Without Decoupling*

While progressing rapidly towards increasingly powerful experiments, a number of outstanding challenges still remain. These include, among others, the long debated problem of dipolar truncation, which effectively prevents determination of long-range distances between homonuclear spins in uniformly or densely labeled samples – and thereby loss of a large potential for extraction of structural constrains in biological solid-state NMR. A second, and related, problem is that the vast majority of present recoupling experiments, through the exploitation of the same design principles, are associated with Hamiltonians of the same character such as the strongly prevailing DQ and ZQ Hamiltonians. These Hamiltonians are not necessarily optimal, in the sense that they may complicate extraction of the two phase components in phase-sensitive multiple-dimensional experiments, cause signal cancellation due to signals of opposite sign (for DQ Hamiltonians), etc. A third kind of problems is operational and sample-heating issues relating to the use of strong rf field irradiation on the ^{1}H spins for decoupling in concert with dipolar recoupling.

Dipolar truncation, which occurs when non-commuting dipole–dipole coupling interactions cause truncation of the effects from weak coupling interactions by larger coupling interactions, has been debated extensively since the introduction of the very first homonuclear recoupling experiments. The reason for this debate is obvious. The weak couplings bear important information about long-range distances that are very important in structure determination. Furthermore, the truncation effect is most pronounced for the easiest attainable uniformly isotope labeled samples and in particular when using broadband recoupling methods to optimize the amount of information to few experiments. The problem of dipolar truncation is illustrated in Fig. 8a by a typical three-spin system where the aim is to observe the dipole–dipole coupling interaction between spins 3 and 1, through dephasing on spin 3, in presence of the much stronger coupling between spins 1 and 2. The upper weakly modulated curve illustrates that such dephasing cannot be observed if one uses standard planar (DQ or ZQ) recoupling sequences.

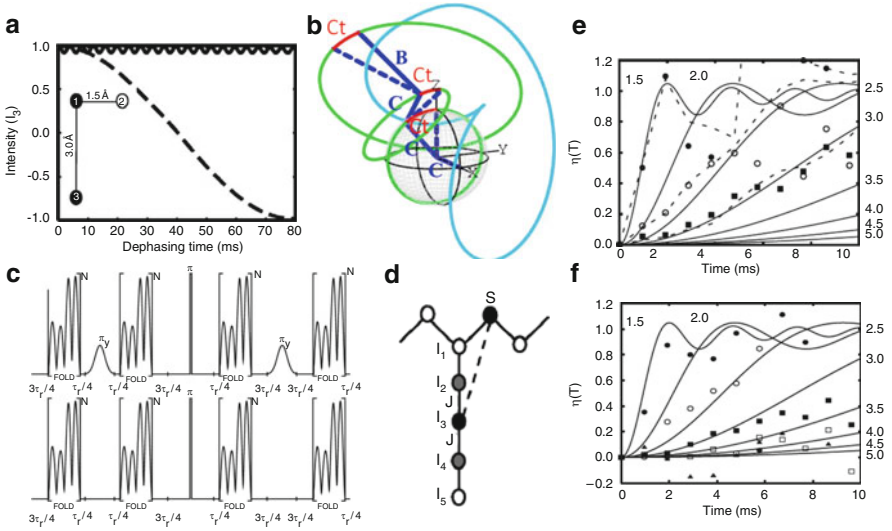

Fig. 8 (**a**) Schematic illustration of the dipolar truncation problem for a three-spin system where the aim is to observe dephasing between 1 and 3 in presence of 2. The curve at the top illustrates that no dephasing is observed due to dipolar truncation when using a planar mixing sequence while dephasing (lower curve) is observed upon using recoupling leading to an Ising operator. (**b**) Rf trajectory for the FOLD experiment, (**c**) main (*top*) and reference (*bottom*) FOLD pulse sequences with the selective pulses in-between the FOLD elements adjusted to invert, e.g., the ^{13}C' spins as indicated by *S* in (**d**). (**e**, **f**) Experimental dephasing curves plotted in a theoretical Fresnel type distance grid (see distances in Å to the right) for $^{13}C_{\alpha}$ (*filled circles*), $^{13}C_{\beta}$ (*open circles*), $^{13}C_{\gamma}$ or $^{13}C_{\gamma 2}$ (*filled squares*), $^{13}C_{\gamma 1}$ (*open squares*), and $^{13}C_{\delta 1}$ (*filled triangles*) for uniformly ^{13}C,^{15}N-labeled samples of L-threonine (**e**) and ubiquitin (**f**). (**a**, **d** reproduced from [46] with permission; **c**, **e**, **f** reproduced from [47] with permission)

One solution to the dipolar truncation of small coupling interactions by larger coupling interactions is to use sparsely labeled samples, e.g., using differently ^{13}C-labeled glycerol in the expression as now used frequently for solid-state NMR structure determination, despite the need for more costly samples and extraction of structural parameters from several samples (which accordingly need to be identical). This approach has, along with recommendations on experimental protocols, recently been analyzed by Bayro et al. [144].

Addressing the problem from a spin engineering point of view, the task could be to transform the spin part of dipolar coupling in (10) including both longitudinal ($2I_zS_z$) and planar ($-I_xS_x - I_yS_y$) terms into a form containing only the former term (the so-called Ising operator). Ising operators commute between different spin pairs facilitating dephasing as illustrated by the dashed line in Fig. 7a. Exactly this feature has been extensively exploited for measurement of heteronuclear dipolar couplings, where dipolar truncation is not a problem. Along these lines, Levitt and coworkers recently proposed a symmetry-based recoupling experiment facilitating truncation of planar terms of the homonuclear dipolar coupling interaction [145]. This experiment, however, suffers from simultaneous recoupling of

heteronuclear dipolar couplings to protons and accordingly was demonstrated on deuterated samples. Tycko and coworkers introduced several methods to circumvent/reduce the effects of dipolar truncation, including stochastic dipolar recoupling [146, 147], that remove dipolar truncation effects, although at the expense of an r_{IS}^{-6} distance dependency – as in liquid-state NMR – rather than the more favorable r_{IS}^{-3} dependence typically encountered in solid-state NMR. This obviously may affect the upper limit for distances that can be measured using such techniques. Other experiments include frequency selective SEASHORE [148] and zero-quantum ZQ-SEASHORE [149]. As an example, Fig. 9 shows the ZQ-SEASHORE pulse sequence (formed by recoupling building blocks similar to those described above) along with 2D spectra and long-range distance information extracted from MB(i+4)EK with uniform ^{13}C,^{15}N labeling on Ala9 and Ala10 as presented in [149].

In an alternative approach, which as we shall see in this section also serves to improve on some of the other problems in addition to dipolar truncation, the groups of Khaneja and Nielsen introduced a novel approach for dipolar recoupling involving multiple-oscillating fields [46–49]. The first of these experiments involved the

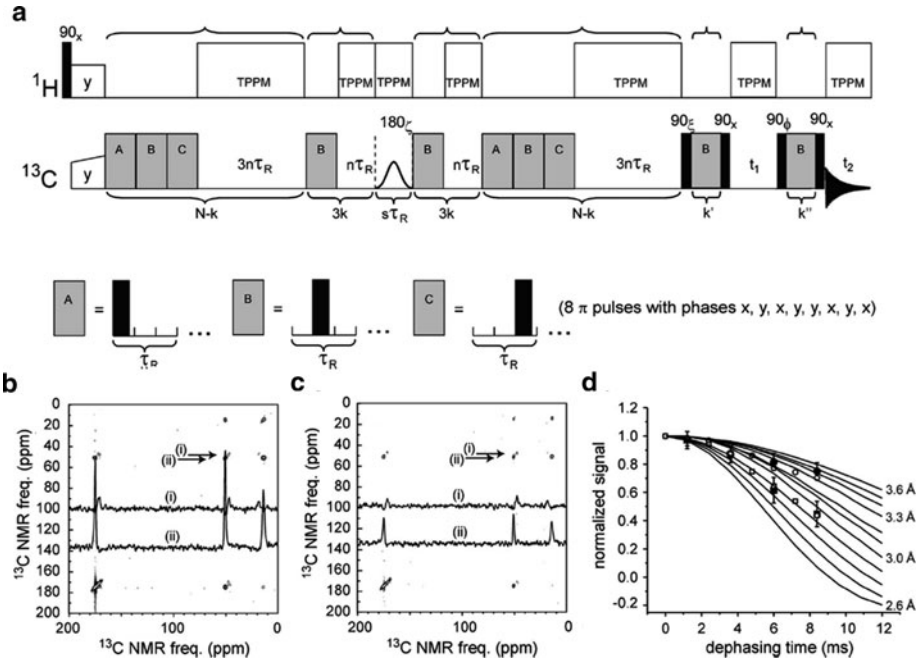

Fig. 9 (**a**) Constant-time frequency-selective pulse sequence used for indirect measurement of $^{13}C'$–$^{13}C'$ distances in MB(i + 4)EK with uniformly ^{15}N,^{13}C-labeled L-alanine at Ala9 and Ala10. The 2D spectra in (**b**) and (**c**) and the extracted data points in (**d**) show that the dephasing is more rapid, with hence a shorter internuclear distance, for $^{13}C'$ nuclei in the helical conformation (represented by *squares*) than for those in the non-helical conformation (represented by *circles*) (reproduced from [149] with permission)

triple-oscillating field technique TOFU [46] using three orthogonal rotating fields to recouple the dipole–dipole coupling interactions, average effects from anisotropic shielding and heteronuclear dipolar coupling, while maintaining (scaled) isotropic chemical shifts operators. The TOFU rf field, introducing a new way to design efficient re- and decoupling experiments systematically, takes the form

$$H_{\mathrm{rf}}(t) = CF_x + Ce^{-iCtF_x}F_y e^{iCtF_x} + Be^{-iCtF_x}e^{-iCtF_y}F_z e^{-iCtF_y}e^{-iCtF_x}, \qquad (53)$$

where, for brevity, we introduced the spin-pair operators $F_q = I_q + S_q$ ($q = x,y,z$). This formulation renders a stepwise transformation into the interaction frame of the rf field using (14) straightforward: for each step one uses the static component to remove an exponential modulation of the following terms and the Coriolis term removes the static term in the process. In the last frame all modulating terms are removed and the residual rf Hamiltonian takes the form of BF_z. Upon setting the amplitude B much larger than ω_r and C, this residual term ensures that the effective Hamiltonian commutes with the total angular momentum about the z-axis.

By choosing $C = \omega_r/4$, the first-order effective Hamiltonian in a homonuclear two-spin system looks as follows:

$$\overline{\tilde{H}}_{IS}^{(1)} = \frac{1}{2}\omega_I^{(0)}I_z + \frac{1}{2}\omega_S^{(0)}S_z - \frac{3}{32\sqrt{2}}b_{IS}s_{2\beta_{PR}}c_{\gamma_{PR}}(2I_zS_z - I_xS_x - I_yS_y). \qquad (54)$$

The differential chemical shift operator in this Hamiltonian truncates the planar terms of the recoupled dipole–dipole coupling interaction, leaving only the desired Ising operator. By refocusing the chemical shift operators using a strong π pulse in the center of the overall TOFU period, the transverse magnetization dephases under Ising operators of the type $2I_zS_z$ which commute for different spin-pairs, whereby dipolar truncation is prevented.

To avoid rapid dephasing due to strong dipolar couplings to neighboring nuclei in multiple-spin systems that in practice will obscure all information from distant Hamiltonian-wise recovered spin-pairs, the experiment is implemented in such a way that two rotor-synchronized TOFU blocks are shifted by half a rotor period relative to one another. This shift changes the sign of the TOFU-recoupled $m = \pm 1$ Fourier components of the dipole–dipole coupling interaction (a phase change for these terms in the exponentials in (11)), implying that the relevant dipole–dipole coupling interactions are refocused. We refer to this rotor assisted dipolar refocusing as RADAR [46]. A selective pulse can once again change the sign of selected dipole–dipole coupling interactions and those affected by both the shift in rotor synchronization and the selective pulse remain recoupled while all other terms get refocused.

A typical example is to apply the selective pulse to the carbonyl (or methyl) spins implying that the magnetization measured at the surrounding spins exclusively reflects dephasing due to interaction with exactly this spin (or spin type) while couplings to other nearby spins are refocused – forming the basis for, e.g.,

$^{13}C'$–$^{13}C_x$ distance measurements as illustrated in Fig. 8d. Typically, two experiments are recorded, one as the main experiment with ($S_m(t)$) and one as the reference experiment without ($S_r(t)$) the encoding selective pulse. The normalized difference between data from the two experiments provides a Fresnel like (to first order) functionality

$$\eta(T) = \frac{S_r(t) - S_m(t)}{S_r(t)} = 1 - \int \cos(\omega_{IS} T), \tag{55}$$

from which the internuclear distances can be extracted much like the typical procedure for REDOR experiments (see above).

Before describing the overall experiment and presenting exemplifying results, we note that the dipolar scaling factor of the TOFU experiment is significantly reduced relative to typical homonuclear recoupling experiments through attenuation during all modulation steps of the experiment. This obviously reduces the potential for measuring long ^{13}C–^{13}C distances. To increase the scaling factor, Strassø et al. [47] recently proposed the four oscillating field technique (FOLD) using four appropriately adjusted modulating fields rather than the three used in TOFU. The rf field trajectory produced by the four fields is illustrated in Fig. 8b, while pulse sequences for the main (top) and reference (bottom) experiments both including RADAR elements are shown in Fig. 8c. The FOLD extension facilitates refocusing of otherwise defocused parts of the internal Hamiltonian whereby the scaling factor may be increased relative to TOFU. The first-order Hamiltonian of FOLD for a homonuclear spin system looks as follows:

$$\overline{\tilde{H}}^{(1)} = \frac{1}{2}\omega_I^{(0)} I_z + \frac{1}{2}\omega_S^{(0)} S_z - \frac{15}{64\sqrt{2}} b_{IS} s_{2\beta_{PR}} c_{\gamma_{PR}} (2I_z S_z - I_x S_x - I_y S_y), \tag{56}$$

which displays an improvement of the dipolar scaling by a factor 5/2. In this manner the potential to measure long distances is significantly increased, but it obviously also sets higher demands on the "truncating" effect of the chemical shift terms which now need to remove planar terms scaled up by the same factor of 5/2. Figure 8e, f shows experimental Fresnel type distance measurements for $^{13}C'$–$^{13}C_x$ spin-pairs in uniformly ^{13}C,^{15}N-labeled samples of threonine and ubiquitin, respectively, obtained using the pulse sequences in Fig. 8c with selective pulses on the $^{13}C'$ spins.

The concept and attractive/transparent design principles in multiple-oscillating field techniques are obviously not restricted to solving the dipolar truncation problem. They may also be used to address some of the other challenges listed at the start of this section: generating Hamiltonians of specific form and avoiding excessive sample heating from strong ^1H decoupling. Addressing the first point through recoupling of the dipolar coupling in native form, the double oscillating field technique (DUO) [49] uses the following rf field Hamiltonian:

$$H_{\mathrm{rf}}(t) = CF_x + Be^{-iCtF_x} F_z e^{iCtF_x}. \tag{57}$$

By setting $C = \omega_r/2$ and $B = 7\omega_r/2$, the CF_x term averages the chemical shift operators over a reasonable bandwidth while simultaneously recoupling the dipole–dipole coupling interactions with a relative large scaling factor. In the recoupling frame, the residual rf field Hamiltonian, BF_z, averages all non-secular terms in the internal Hamiltonian and furthermore opens up for improved stability towards rf inhomogeneity and miscalibration of the rf field amplitude (these effects can be eliminated to first order concatenating DUO elements with opposite sign of B). The first-order effective Hamiltonian for DUO in a two-spin system takes the form

$$\bar{\tilde{H}}^{(1)} = \frac{-3}{8\sqrt{2}} b_{IS} s_{2\beta_{PR}} c_{\gamma_{PR}} (2I_z S_z - I_x S_x - I_y S_y), \tag{58}$$

being proportional to the native dipole–dipole coupling interaction in the high-field approximation. Mediated by the planar terms, this operator can be used to transfer longitudinal magnetization.

In this regard, the DUO Hamiltonian provides two-dimensional (2D) correlation spectra with identical sign for peaks between directly and more remotely coupled spins as characteristic for ZQ recoupling techniques. This is opposed to the most frequent DQ Hamiltonians (as observed, e.g., for the HORROR and $C7_2^1$ experiments) that give a distinct pattern with sequential transfers characterized by positive and negative signals. One may argue that the DUO experiment in this respect does not make a difference relative to techniques such as RFDR [24] and in particular its finite pulse version fpRFDR [90] also recoupling a native type dipolar coupling Hamiltonian (see above). This is not the case, however, in the sense that the scaling factor of the DUO experiment is significantly larger than that for fpRFDR, thereby mediating faster transfer of polarization. Furthermore, the experiment is substantially more robust towards rf inhomogeneity.

A lot of attention has recently been devoted to the problem of rf-induced sample heating, which may be a severe problem in biological solid-state NMR where expensive isotope-labeled proteins may be destroyed by heating. Heating may also be a problem even for samples that can stand it since variations in temperature may cause line broadening due to temperature dependent chemical shift variation. As these problems arise from the electric field component of the electromagnetic irradiation during the pulses (in particular at high frequency, implying that the ^{1}H irradiation is the major source to the problem), the solution to the problem may take several directions. One is a hardware-based way, eliminating the E-field component of the irradiation through design of shielded/compensated rf coils for the ^{1}H channel [150, 151] or using very small rotors to exploit very fast spinning in combination with weak rf pulse irradiation for ^{1}H decoupling [152–155]. Another solution is to base the structure determination on samples not containing protons to a large extent. A third approach is to design experimental procedures not relying on irradiation on the ^{1}H channel – or reducing the irradiation as much as possible. The latter avenue has been taken in relation to homonuclear dipolar recoupling in terms of the RFDR without decoupling [90, 156], cosine modulated adiabatic recoupling (CMAR) [157], and variants of these experiments [111]. In relation to heteronuclear

recoupling, methods without decoupling so far include DCP without decoupling [112] and the exponentially modulated recoupling technique (EXPORT) [48].

We draw attention here to the EXPORT experiment which, using a double-oscillating field, recouples the dipolar interaction between, say, ^{13}C and ^{15}N, and simultaneously efficiently removes all offset effects (making the experiment broadband) and heteronuclear dipolar couplings to protons, thereby removing the need for ^{1}H irradiation during recoupling. We note that the experiment is universal and may also be used straightforwardly for homonuclear recoupling without decoupling. The rf field Hamiltonian of the EXPORT experiment takes the form

$$H_{\mathrm{rf}}(t) = C_I I_x + C_S S_x + B_I e^{-iC_I t I_x} I_y e^{iC_I t I_x} + B_S e^{-iC_S t S_x} S_y e^{iC_S t S_x}, \tag{59}$$

where I may denote a ^{15}N spin and S a ^{13}C spin. This Hamiltonian may be expressed in terms of amplitude $A_K(t) = \sqrt{C_K^2 + B_K^2 c_{C_K t}^2}$ and phase $\phi_K(t) = \tan^{-1}(B_K c_{C_K t}/C_K) + (B_K/C_K)(c_{C_K t} - 1)$ with $K = I,S$ for easy implementation on the spectrometer.

In the simplest setup, the two strong field components may be set identical to $C_I = C_S = C$. The relatively large CI_x or CS_x term averages isotropic and anisotropic chemical shift effects as well as the heteronuclear dipolar coupling interaction between ^{15}N or ^{13}C and ^{1}H. The difference of – or the sum of – the B coefficients selects the form of the recoupled heteronuclear dipole–dipole coupling interaction, as expressed in terms of the effective Hamiltonian in the interaction frame of the rf irradiation

$$\overline{\overline{H}}_{IS}^{(1)}(B_I \pm B_S = n\omega_r) = \omega_{D,n}\left[c_{n\gamma_{PR}}(I_z S_z \mp I_x S_x) + s_{n\gamma_{PR}}(I_x S_z \pm I_z S_x)\right] \tag{60}$$

taken over the period $4\pi/|B_I - B_S|$ (assuming $|B_I - B_S| \neq 0$) and using $\omega_{D,\pm 1} = -\frac{1}{4\sqrt{2}} b_{IS} s_{2\beta_{PR}}$ and $\omega_{D,\pm 2} = \frac{1}{8} b_{IS} s_{\beta_{PR}}^2$.

The average Hamiltonian of EXPORT opens up the possibility of γ-encoded ZQ or DQ dipolar recoupling depending on the choice of B coefficients. Figure 10 shows the rf trajectory of the EXPORT experiment (Fig. 10a), the EXPORT pulse sequence (Fig. 10b), the offset and rf field inhomogeneity/tolerance relative to previous DCP and band-selective $^{\mathrm{OC}}$DCP (see below) experiments (Fig. 10c), and an experimental demonstration for uniformly ^{13}C,^{15}N-labeled GB1 (Fig. 10d) recorded at 16.4 T using EXPORT with $C = 3\omega_r$, $B_I = \frac{3}{8}\omega_r$ and $B_S = \frac{5}{8}\omega_r$, 23.8 kHz spinning, and no ^{1}H decoupling. We note that EXPORT is typically implemented in an rf inhomogeneity compensating manner using a phase-alternation scheme similar to that used by Khaneja and coworkers in relation to the PAMORE experiment [111], here implemented with a change in phase of 180° for the CI_x and CS_x terms every $2\pi/C$ period. Relative to the commonly used and technically very simple DCP experiment, also recently implemented without decoupling [112], the EXPORT experiment demonstrates a very broad excitation profile, strong robustness towards rf field mismatch (thereby facilitating easy setup and ensuring robustness in long-term experiments) and rf inhomogeneity, and good

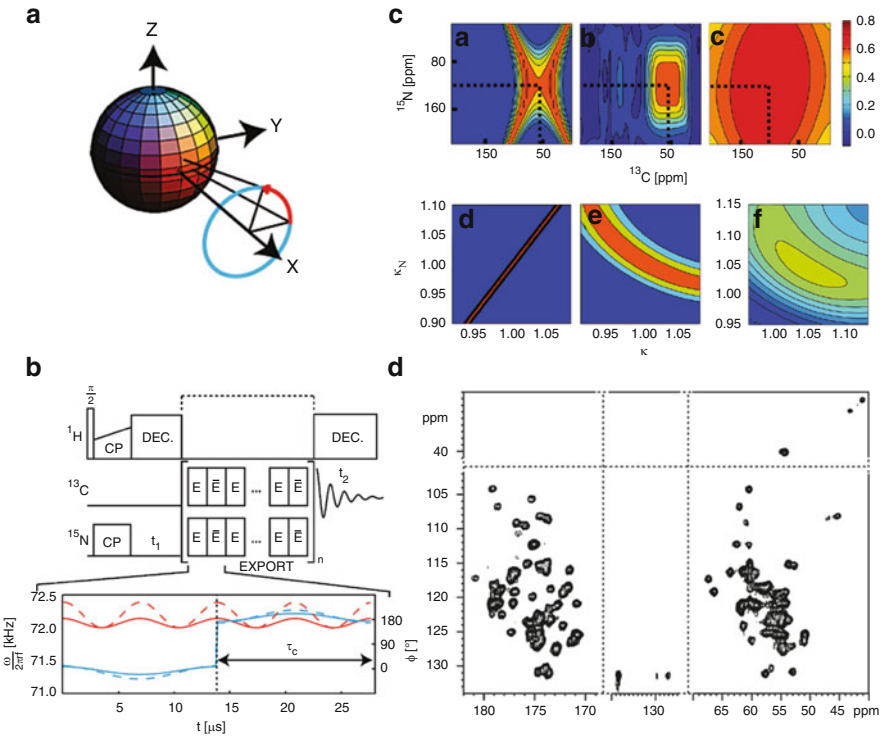

Fig. 10 (**a**) Rf trajectory, (**b**) pulse sequence, (**c**) offset (*upper*) and rf inhomogeneity (*lower*) profile for EXPORT (**c** subpanels c, e, f) relative to DCP (**c** subpanels a, d) and optimal control DCP (**c** subpanel b), along with a 2D ^{13}C–^{13}C correlation spectrum of GB1 obtained using EXPORT with 23.8 kHz spinning and no ^{1}H decoupling (reproduced from [48] with permission)

performance without ^{1}H decoupling. By choosing a small C coefficient (but still larger than the B coefficients and ω_r) or a large C coefficient, one can set up experiments with or without ^{1}H decoupling. Hence EXPORT offers great flexibility with respect to MAS frequency and rf fields on the various channels.

As mentioned above, the concept of multiple-oscillating field techniques and symmetry-based dipolar recoupling has recently been merged in terms of the EXPORT-CN experiment offering new possibilities for low-power dipolar recoupling [132].

3.8 *Optimal Control Recoupling Methods*

While all methods described above have been derived by analytical means, we will in this section describe the design of recoupling experiments by numerical means in an optimal control setting. The idea behind the use of alternative design strategies

is, obviously, to design optimum experiments reflecting given spin systems and experimental parameters in the best possible way. A secondary, and equally important, motivation is to explore the potential for obtaining new insight into what can be achieved and how this potentially may be accomplished, i.e., learn new tricks for experiment design.

In relation to dipolar recoupling this may be formulated in two different ways. One strategy involves the design of an experiment that, mediated by dipole–dipole couplings, drives the most efficient transfer from a given state A to another state C. The other strategy would be to design pulse sequence elements with an effective Hamiltonian (or an effective propagator) that as closely as possible matches a desired Hamiltonian (e.g., Ising, planar, isotropic, etc.). In both cases the aim is to reach the maximum transformation efficiency as, in the absence of relaxation, may be formulated through unitary bounds on spin dynamics [158–160]. For recoupling applications such bounds should be considered in the light of the additional challenges associated with anisotropic nuclear spin interactions (e.g., the dipole–dipole coupling used to drive polarization/coherence transfer) in samples with uniformly distributed powder angles. In addition, the optimal experiment should generally be designed to be as short as possible, be as gentle as possible with respect to rf power consumption, be robust towards instrumental errors such as rf inhomogeneity, and display robustness towards variation of parameters (e.g., offsets) over desired ranges tailored to a given application. These constraints are also of concern in the analytical experiment design, but typically it is difficult to handle them all simultaneously in an experiment of finite duration (often error terms are handled in recursive fashion leading to rapid increase in experiment duration). It appears intuitively reasonable that methods like optimal control may find better solutions through efficient exploitation of hundreds of pulse parameters associated with pulse sequences with a big array of pulses distributed over the duration of the experiment and adapted for optimal performance. We will in the following give three examples of which two relate directly to some of the analytically-derived experiments described above while the latter exemplifies an application so far not reached analytically.

The first example, also being the example introducing optimal control to solid-state NMR [40] and further elaborated on later [161], is optimal control versions of the DCP experiment. This experiment was a natural choice for numerical improvements as it is widely used and it is well known that this experiment is sensitive to offsets, rf mismatch relative to the MAS-modified Hartmann-Hahn condition, and rf inhomogeneity. In particular the two latter effects may reduce significantly the performance of ^{15}N to ^{13}C transfers, severely complicate setup of such experiments, and render these critically sensitive to altered tuning/rf conditions in the course of potentially long experiments for biological samples.

Optimal control offers the possibility to obtain an optimal solution to a given problem, as described by a Hamiltonian and a set of supplementary conditions reflecting the problem, either analytically or numerically. As dipolar recoupling is associated with time-modulated anisotropic parameters and spread of parameters due to different orientation of the individual crystallites, attempts to use optimal

control in solid-state NMR have so far been numerically alone. This is by any standard also the simplest approach for the ordinary spectroscopist, and, by using the optimal control software as provided [71] through the open-source SIMPSON simulation package [50, 162] (facilitated by use of auxiliary open-source programs such as SIMMOL [163] to define typical spin system parameters), one may automatically design NMR experiments for given purposes. This applies even if the user is not familiar with Hamiltonian theory. The only input is the initial state, the final state (either spin states or Hamiltonians), the spin system, its parameters (or ranges for them), and parameters for external conditions (spinning, rf fields, etc.). For the work with proteins this is particularly simple as many of the spin system parameters and their variation are well-known, such as, for example, those applying to NCO (i.e., ^{15}N to ^{13}C') and NCA (i.e., ^{15}N to $^{13}C_{\alpha}$) transfers being the major objective with regard to the DCP experiment for biological applications.

In setting up an optimization of a DCP experiment, it is important to define the goal and set that in reference to previous experiments. One could be, at any cost, to generate an experiment providing 100% transfer of coherence. Another could be to generate an experiment which in a given period of time generates very good transfer but with very low cost in terms of rf field amplitudes (e.g., to facilitate combination with ^{1}H decoupling of modest strength) and robustness towards rf inhomogeneity and offsets in a range matching the experimental conditions. Experiments of the former category may include already existing adiabatic experiments, which over 6–10 ms of relatively strong rf irradiation on the two rf channels concerned reach very high transfer efficiency. The second goal is more compatible with most usage of DCP today, a shorter experiment with less power involved. To meet this need, Kehlet et al. developed so-called ^{OC}DCP experiments for ^{15}N to ^{13}C transfers [40] with focus on NCO and NCA experiments [161] using SIMPSON with optimal control procedures (typical input files can be found in [71]) leading to rf waves for the so-called ^{OC}NCO experiment. This method is illustrated as the ^{15}N to ^{13}C transfer element in Fig. 11a, transfer efficiencies optimized for a given offset (Fig. 11b) and rf inhomogeneity (Fig. 11c) ranges, and demonstrated experimentally in terms of a 2D ^{OC}NCO spectrum of uniformly-^{13}C,^{15}N-labeled ubiquitin in Fig. 11d in comparison with DCP (lower projection to the left in Fig. 11d as compared to the higher projection from the ^{OC}NCO experiment). The OC experiments are typically characterized by low rf field strengths, on the order of 1–1.5 times the spinning frequency, being substantially lower than those typically used for DCP and adiabatic variants.

The experiments illustrated in Fig. 11 were optimized for a specific set of parameters in terms of spinning speed (which is unique for the solution), magnetic field strength, etc., and one might argue that the flexibility in analytical solutions such as DCP is desirable, although the experiment suffers from sensitivity to rf inhomogeneity and offsets. One may, however, combine the wishes for the use of a certain experiment and optimal control improvement of sensitivity and robustness, for example, using the pulse-recoupling analogy described in Sect. 3.4 leading to optimal control COMB experiments as demonstrated recently by Hansen et al. [43].

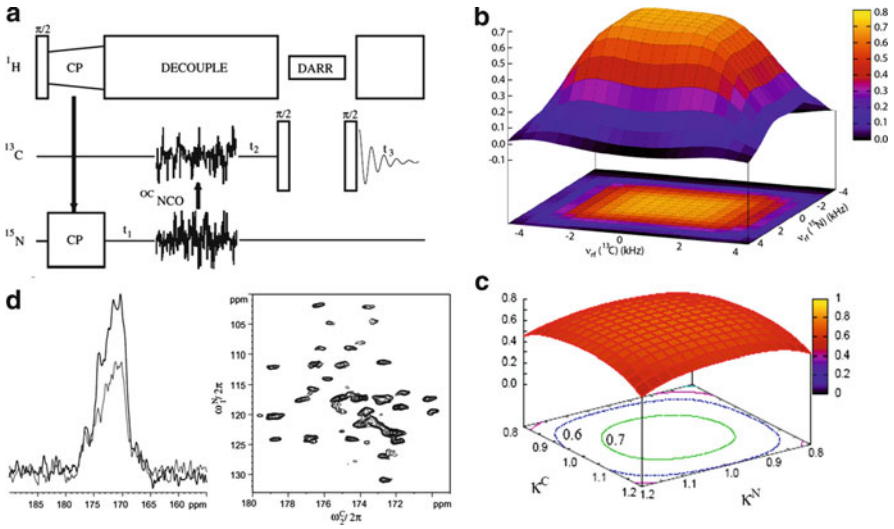

Fig. 11 (**a**) 2D NCO experiment with optimal control element inserted for $^{15}N \rightarrow {}^{13}C'$ transfer. Transfer efficiencies for the ^{OC}NCO experiment optimized for 12 kHz spinning speed as function of (**b**) resonance offsets for $^{13}C'$ and ^{15}N and (**c**) rf inhomogeneity/adjustment in terms of scaling factors on the nominal rf field strengths for ^{13}C and ^{15}N. (**d**) Experimental ^{OC}NCO 2D spectrum of uniformly $^{13}C,^{15}N$-labeled ubiquitin with the projections to the left comparing ^{OC}NCO experiment (*most intense*) and DCP (*less intense*) based NCO experiments [reproduced with permission from [161] (**a**, **d**) and [164] (**c**)]

This leads in a very simple and computational fast way to experiments of high quality in the sense that optimal control is used to optimize an rf pulse (a simple one-spin, two-level system) which is robust towards offsets (which for recoupling corresponds to rf inhomogeneity) and rf inhomogeneity (which for recoupling corresponds to variation in the dipole–dipole coupling due to the powder angle). The resulting composite pulse is subsequently translated into a recoupling experiment (two-spin, four-level system) using a DCP experiment with "phase-inducing" correction pulses inserted between each pulse in the composite refocusing experiment as illustrated in Fig. 4. Figure 12a illustrates the rf and recoupling trajectories of the $COMB_{30}DCP$ experiment, while Fig. 12b, c illustrates the performance of the experiment in terms of transfer efficiencies (compared with DCP and previous COMB DCP experiments in cases without, upper, and with 5% Lorentzian rf inhomogeneity, lower) and an experimental demonstration on uniformly-$^{13}C,^{15}N$-labeled ubiquitin. The projections in Fig. 12c reveal almost a doubling in sensitivity for $COMB_9DCP$ relative to the standard DCP experiment upon which the COMB experiment is formed (only difference is a number of correction pulses in between DCP elements as illustrated in Fig. 4b).

The final optimal control example addresses the possibility to design experiments characterized by a specific Hamiltonian. We consider the well-established

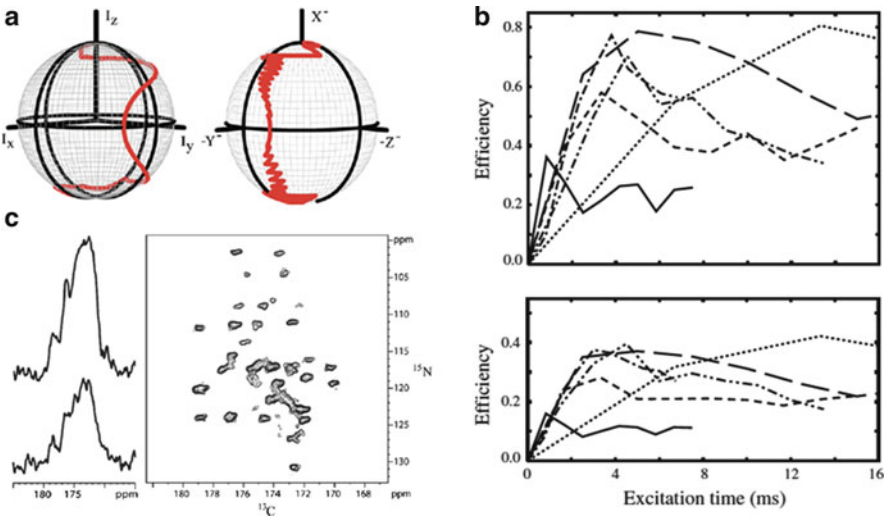

Fig. 12 (**a**) Rf pulse (*left*) and recoupling (*right*) trajectories for the $COMB_{30}DCP$ experiment. (**b**) Simulated transfer efficiencies of DCP (*solid line*), $COMB_3DCP$ (*dashes*), $COMB_6DCP$ (*dotted*), $COMB_9DCP$ (*dash-dot*), $COMB_{18}DCP$ (*dash-dot-dot*), and $COMB_{30}DCP$ (*long dashes*) without (*top*) and with 5% Lorentzian rf inhomogeneity. (**c**) Experimental comparison (projections to the *left*) of $COMB_9DCP$ and standard DCP experiments for uniformly ^{13}C,^{15}N-labeled ubiquitin (reproduced from [43] with permission)

problem that planar Hamiltonians (e.g., the ZQ operator $I_xS_x + I_yS_y$ or the DQ operator $I_xS_x - I_yS_y$) only transfer one spin component (e.g., I_z to S_z). This essentially means that, in 2D experiments, mixing with a planar sequence will only facilitate transfer of either I_x or I_y through the transfer element, effectively leading to a loss in sensitivity by a factor $1/\sqrt{2}$. Such loss would be avoided if the planar mixing sequence was replaced by an isotropic mixing sequence characterized by the operator $I_xS_x + I_yS_y + I_zS_z$ facilitating equal transfer of I_x and I_y. This represents a quite obvious way to improve the efficiency of multi-dimensional solid-state NMR recoupling experiments. The problem, however, is that no recoupling experiments have so far been developed analytically to provide an isotropic operator. This need, however, has been demonstrated by optimal control by Tosner et al. [42] through the development of isotropic mixing sequences realizing sensitivity enhancements by a factor of $1/\sqrt{2}$ in 2D ^{13}C–^{13}C correlation spectra.

We note that optimal control is a universal tool for experiment design and has also, in solid-state NMR spectroscopy, found additional applications in the design of homonuclear dipolar recoupling [41], broadband rf pulses and quantum gates [71], building blocks of symmetry-based recoupling experiments [129], quadrupolar multiple-quantum MAS experiments [165], and improved pulses for quadrupolar nuclei [166]. Numerous references to further applications with regard to liquid-state NMR can be found in [72].

4 Conclusions and Outlook

We have in the review described one of the most fascinating, powerful, fundamentally important facets of solid-state NMR spectroscopy, namely the combination of the high-resolution facets of magic-angle-spinning NMR and the information-bearing reintroduction of specific interactions in certain periods of the experiment via recoupling.

We have specifically addressed dipolar recoupling, but do note that recoupling may also apply to all other anisotropic interactions. The ability to maintain high resolution in the detection dimension(s) of solid-state NMR experiments while, as efficiently and well-controlled as possible, reintroducing dipolar couplings to obtain structural information (distances, torsion angles, etc.) or drive coherences between spins is fundamental for essentially all applications of solid-state NMR in relation to structure and dynamics. We have presented the underlying principles and tools for their design and we have within this framework described the most fundamental and widely used experiments. This provides the unfamiliar reader with an easy overview, the more trained reader with simple tools and examples of the development of dipolar recoupling experiments, and the interested user with a basis for designing their own experiments for given applications. Dipolar recoupling, as representative of the art of tailoring Hamiltonians in coherent spectroscopy, is by no means a finished area of research. Ever since the first experiments were introduced, more and more recoupling experiments are carried out every year. The reason is simple – they form in many cases the heart of the pulse sequences, and that has to be evolved to perfection. In addition, new areas of solid-state NMR, e.g., the intensive use of new labeling schemes, constantly provide new challenges for which recoupling experiments have to be designed. Thus this review will by no means be the last word on dipolar recoupling, the underlying principles, and design.

Acknowledgements We acknowledge support from the Danish National Research Foundation in terms of support to the inSPIN research center. We are grateful to numerous coworkers and colleagues for contributing to the basic results reviewed in this chapter.

References

1. Opella SJ (1997) Nature Struct Biol 4:845
2. Griffin RG (1998) Nature Struct Biol 5:508
3. Davis JH, Auger M (1999) Prog Nucl Magn Reson Spectrosc 35:1
4. Nielsen NC, Malmendal A, Vosegaard T (2004) Mol Membr Biol 21:129
5. Kovacs FA, Cross TA (1997) Biophys J 73:2511
6. Bechinger B, Sizun C (2003) Concepts Magn Reson 18A:130
7. Andrew ER, Bradbury A, Eades RG (1959) Nature 183:1802
8. Lowe IJ (1959) Phys Rev Lett 2:285
9. Maricq MM, Waugh JS (1979) J Chem Phys 70:3300

10. Bennett AE, Griffin RG, Vega S (1994) NMR basic principles and progress, vol 33. Springer, Berlin, p 1
11. Griffiths JM, Bennett AE, Griffin RG (1997) Encyclopedia of magnetic resonance. Wiley, Chichester
12. Baldus M, Geurts DG, Meier BH (1998) Solid State Nucl Magn Reson 11:157
13. Dusold S, Sebald A (2000) Annu Rep NMR Spectrosc 41:185
14. Baldus M (2002) Prog Nucl Magn Reson Spectrosc 41:1
15. Bjerring M, Vosegaard T, Malmendal A, Nielsen NC (2003) Concepts Magn Reson 18A:111
16. Schnell I (2004) Prog Nucl Magn Reson Spectrosc 45:145
17. Schaefer J (2007) Encyclopedia of magnetic resonance. Wiley, Chichester
18. Ladizhansky V (2009) Solid State Nucl Magn Reson 36:119
19. Jaroniec CP (2009) In: Harris RK, Wasylischen RE (eds) Encyclopedia of magnetic resonance. Wiley, Chichester
20. Schaefer J, Mckay RA, Stejskal EO (1979) J Magn Reson 34:443
21. Raleigh DP, Levitt MH, Griffin RG (1988) Chem Phys Lett 146:71
22. Gullion T, Schaefer J (1989) J Magn Reson 81:196
23. Tycko R, Dabbagh G (1990) Chem Phys Lett 173:461
24. Bennett AE, Ok JH, Griffin RG, Vega S (1992) J Chem Phys 96:8624
25. Hing AW, Vega S, Schaefer J (1992) J Magn Reson 96:205
26. Nielsen NC, Bildsøe H, Jakobsen HJ, Levitt MH (1994) J Chem Phys 101:1805
27. Oas TG, Griffin RG, Levitt MH (1988) J Chem Phys 89:692
28. Verel R, Ernst M, Meier BH (2001) J Magn Reson 150:81
29. Gregory DM, Mitchell DJ, Stringer JA, Kiihne S, Shiels JC, Callahan J, Mehta MA, Drobny GP (1995) Chem Phys Lett 246:654
30. Lee YK, Kurur ND, Helmle M, Johannessen OG, Nielsen NC, Levitt MH (1995) Chem Phys Lett 242:304
31. Hohwy M, Jakobsen HJ, Eden M, Levitt MH, Nielsen NC (1998) J Chem Phys 108:2686
32. Brinkmann A, Eden M, Levitt MH (2000) J Chem Phys 112:8539
33. Carravetta M, Eden M, Zhao X, Brinkmann A, Levitt MH (2000) Chem Phys Lett 321:205
34. Brinkmann A, Levitt MH (2001) J Chem Phys 115:357
35. Rienstra CM, Hatcher ME, Mueller LJ, Sun BQ, Fesik SW, Griffin RG (1998) J Am Chem Soc 120:10602
36. Hohwy M, Rienstra CM, Jaroniec CP, Griffin RG (1999) J Chem Phys 110:7983
37. Levitt MH (2008) J Chem Phys 128:052205
38. Takegoshi K, Nakamura S, Terao T (2003) J Chem Phys 118:2325
39. Scholz I, Huber M, Manolikas T, Meier BH, Ernst M (2008) Chem Phys Lett 460:278
40. Kehlet CT, Sivertsen AC, Bjerring M, Reiss TO, Khaneja N, Glaser SJ, Nielsen NC (2004) J Am Chem Soc 126:10202
41. Kehlet C, Vosegaard T, Khaneja N, Glaser SJ, Nielsen NC (2005) Chem Phys Lett 414:204
42. Tosner Z, Glaser SJ, Khaneja N, Nielsen NC (2006) J Chem Phys 125:184502
43. Hansen JØ, Kehlet C, Bjerring M, Vosegaard T, Glaser SJ, Khaneja N, Nielsen NC (2007) Chem Phys Lett 447:154
44. Lewandowski JR, De Paepe G, Griffin RG (2007) J Am Chem Soc 129:728
45. De Paepe G, Lewandowski JR, Loquet A, Bockmann A, Griffin RG (2008) J Chem Phys 129:245101
46. Khaneja N, Nielsen NC (2008) J Chem Phys 128:015103
47. Straasø LA, Bjerring M, Khaneja N, Nielsen NC (2009) J Chem Phys 130:225103
48. Nielsen AB, Straaso LA, Nieuwkoop AJ, Rienstra CM, Bjerring M, Nielsen NC (2010) J Phys Chem Lett 1:1952
49. Straasø LA, Nielsen NC (2010) J Chem Phys 133:064501
50. Bak M, Rasmussen JT, Nielsen NC (2000) J Magn Reson 147:296
51. Mehring M (1983) Principles of high resolution NMR in solids. Springer, New York
52. Spiess HW (1978) Rotations of molecular and nuclear spin relaxation. Springer, Berlin

53. Sørensen OW, Eich GW, Levitt MH, Bodenhausen G, Ernst RR (1983) Prog Nucl Magn Reson Spectrosc 16:163
54. Nielsen NC, Vosegaard T, Malmendal A (2006) In: Webb GA (ed) Modern magnetic resonance. Applications in chemistry, biological and marine sciences, vol 1. Springer, Dordrecht, The Netherlands, p 679
55. Haeberle U, Waugh JS (1968) Phys Rev 175:453
56. Hohwy M, Nielsen NC (1998) J Chem Phys 109:3780
57. Cayley A (1858) Philos Trans R Soc Lond 148:17
58. Untidt TS, Nielsen NC (2002) Phys Rev E 65
59. Siminovitch D, Untidt T, Nielsen NC (2004) J Chem Phys 120:51
60. Floquet G (1883) Ann Sci Ec Norm Sup 12:47
61. Leskes M, Madhu PK, Vega S (2010) Prog Nucl Magn Reson Spectrosc 57:345
62. Ernst M, Samoson A, Meier BH (2005) J Chem Phys 123:064102
63. Scholz I, van Beek JD, Ernst M (2010) Solid-State Nucl Magn Reson 37:39
64. Ramachandran R, Lewandowski JR, van der Wel PCA, Griffin RG (2006) J Chem Phys 124:214107
65. Sivertsen AC, Bjerring M, Kehlet CT, Vosegaard T, Nielsen NC (2005) Annu Rep NMR Spectrosc 54:243
66. Nielsen NC (2006) In: Ramamoorthy A (ed) NMR spectroscopy of biological solids. CRC/ Taylor & Francis, New York, p 261
67. Nielsen NC, Bildsøe H, Jakobsen HJ (1988) J Magn Reson 80:149
68. Liu H, Glaser SJ, Drobny GP (1990) J Chem Phys 93:7543
69. Elena B, de Paepe G, Emsley L (2004) Chem Phys Lett 398:532
70. Khaneja N, Reiss T, Kehlet C, Schulte-Herbruggen T, Glaser SJ (2005) J Magn Reson 172:296
71. Tosner Z, Vosegaard T, Kehlet C, Khaneja N, Glaser SJ, Nielsen NC (2009) J Magn Reson 197:120
72. Nielsen NC, Kehlet C, Glaser SJ, Khaneja N (2010) Encyclopedia in magnetic resonance. Wiley, Chichester
73. Pontryagin LS (1962) The mathematical theory of optimal processes. Interscience, New York
74. Bryson AE, Ho Y-C (1975) Applied optimal control: optimization, estimation, and control. Hemisphere Publishing/distributed by Halsted Press, Washington
75. Krotov VF (1995) Global methods in optimal control theory. Marcel Dekker, New York
76. Maximov II, Tosner Z, Nielsen NC (2008) J Chem Phys 128:184505
77. Maximov II, Salomon J, Turinici G, Nielsen NC (2010) J Chem Phys 132
78. Gullion T (1998) Concepts Magn Reson 10:277
79. Masica DL, Ash JT, Ndao M, Drobny GP, Gray JJ (2010) Structure 18:1678
80. Jaroniec CP, Tounge BA, Herzfeld J, Griffin RG (2001) J Am Chem Soc 123:3507
81. Michal CA, Jelinski LW (1997) J Am Chem Soc 119:9059
82. Jaroniec CP, Filip C, Griffin RG (2002) J Am Chem Soc 124:10728
83. Saalwachter K, Graf R, Spiess HW (1999) J Magn Reson 140:471
84. Saalwachter K, Schnell I (2002) Solid State Nucl Magn Reson 22:154
85. Sun BQ, Costa PR, Kocisko D, Lansbury PT, Griffin RG (1995) J Chem Phys 102:702
86. Chou FC, Tsai TWT, Lee HK, Chan JCC (2009) Solid State Nucl Magn Reson 36:177
87. Feike M, Demco DE, Graf R, Gottwald J, Hafner S, Spiess HW (1996) J Magn Reson A 122:214
88. Vega S (1978) J Chem Phys 68:5518
89. Wokaun A, Ernst RR (1977) J Chem Phys 67:1752
90. Ishii Y (2001) J Chem Phys 114:8473
91. Leppert J, Heise B, Ohlenschlager O, Gorlach M, Ramachandran R (2003) J Biomol NMR 26:13
92. Wickramasinghe NP, Parthasarathy S, Jones CR, Bhardwaj C, Long F, Kotecha M, Mehboob S, Fung LWM, Past J, Samoson A, Ishii Y (2009) Nat Meth 6:215

93. Levitt MH, Raleigh DP, Creuzet F, Griffin RG (1990) J Chem Phys 92:6347
94. Creuzet F, McDermott A, Gebhard R, van der Hoef K, Spijker-Assink MB, Herzfeld J, Lugtenburg J, Levitt MH, Griffin RG (1991) Science 251:783
95. Nielsen NC, Creuzet F, Griffin RG, Levitt MH (1992) J Chem Phys 96:5668
96. Seidel K, Lange A, Becker S, Hughes CE, Heise H, Baldus M (2004) Phys Chem Chem Phys 6:5090
97. Nielsen NC, Creuzet F, Griffin RG (1993) J Magn Reson A 103:245
98. Verel R, Baldus M, Nijman M, van Os JWM, Meier BH (1997) Chem Phys Lett 280:31
99. Costa PR, Sun BQ, Griffin RG (1997) J Am Chem Soc 119:10821
100. Takegoshi K, Nomura K, Terao T (1995) Chem Phys Lett 232:424
101. Chan JCC, Tycko R (2004) J Chem Phys 120:8349
102. Ramachandran R, Ladizhansky V, Bajaj VS, Griffin RG (2003) J Am Chem Soc 125:15623
103. Schaefer J, Stejskal EO, Garbow J, McKay DB (1984) J Magn Reson 59:150
104. Bjerring M, Rasmussen JT, Krogshave RS, Nielsen NC (2003) J Chem Phys 119:8916
105. Metz G, Wu XL, Smith SO (1994) J Magn Reson A 110:219
106. Baldus M, Geurts DG, Hediger S, Meier BH (1996) J Magn Reson A 118:140
107. Baldus M, Petkova AT, Herzfeld J, Griffin RG (1998) Mol Phys 95:1197
108. Wu XL, Zilm KW (1993) J Magn Reson A 104:154
109. Sun BQ, Costa PR, Griffin RG (1995) J Magn Reson A 112:191
110. Bjerring M, Nielsen NC (2003) Chem Phys Lett 382:671
111. Lin J, Bayro MJ, Griffin RG, Khaneja N (2009) J Magn Reson 197:145
112. Bjerring M, Nielsen AB, Tosner Z, Nielsen NC (2010) Chem Phys Lett 494:326
113. Bak M, Nielsen NC (1997) J Chem Phys 106:7587
114. Brinkmann A, Schmedt auf der Gunne J, Levitt MH (2002) J Magn Reson 156:79
115. Khaneja N, Kehlet C, Glaser SJ, Nielsen NC (2006) J Chem Phys 124:114503
116. Khaneja N (2006) J Magn Reson 183:242
117. Levitt MH (1986) Prog Nucl Magn Reson Spectrosc 18:61
118. Levitt MH (2002) In: Grant DM, Harris RK (eds) Encyclopedia of nuclear magnetic resonance, vol 9. Wiley, Chichester, p 165
119. Lesage A, Emsley L, Penin F, Bockmann A (2006) J Am Chem Soc 128:8246
120. Brouwer DH, Ripmeester JA (2007) J Magn Reson 185:173
121. Eden M, Levitt MH (1999) J Chem Phys 111:1511
122. Paul S, Thakur RS, Goswami M, Sauerwein AC, Mamone S, Concistre M, Forster H, Levitt MH, Madhu PK (2009) J Magn Reson 197:14
123. Paul S, Schneider D, Madhu PK (2010) J Magn Reson 206:241
124. Hardy EH, Detken A, Meier BH (2003) J Magn Reson 165:208
125. Kristiansen PE, Carravetta M, van Beek JD, Lai WC, Levitt MH (2006) J Chem Phys 124:234510
126. Eden M (2003) Chem Phys Lett 378:55
127. Chou FC, Lee HK, Chan JCC (2010) J Chem Phys 133:114503
128. Bjerring M, Nielsen NC (2003) Chem Phys Lett 370:496
129. Nielsen AB, Bjerring M, Nielsen JT, Nielsen NC (2009) J Chem Phys 131:025101
130. Herbst C, Herbst J, Kirschstein A, Leppert J, Ohlenschlager O, Gorlach M, Ramachandran R (2009) J Biomol NMR 44:175
131. Herbst C, Herbst J, Carella M, Leppert J, Ohlenschlager O, Gorlach M, Ramachandran R (2010) J Biomol NMR 47:7
132. Nielsen AB, Jain SK, Nielsen NC (2011) Chem Phys Lett 503:310
133. Castellani F, van Rossum B, Diehl A, Schubert M, Rehbein K, Oschkinat H (2002) Nature 420:98
134. Manolikas T, Herrmann T, Meier BH (2008) J Am Chem Soc 130:3959
135. Bertini I, Bhaumik A, De Paepe G, Griffin RG, Lelli M, Lewandowski JR, Luchinat C (2010) J Am Chem Soc 132:1032
136. Szeverenyi NM, Sullivan MJ, Maciel GE (1982) J Magn Reson 47:462

137. Grommek A, Meier BH, Ernst M (2006) Chem Phys Lett 427:404
138. Morcombe CR, Gaponenko V, Byrd RA, Zilm KW (2004) J Am Chem Soc 126:7196
139. Weingarth M, Bodenhausen G, Tekely P (2009) J Am Chem Soc 131:13937
140. Lewandowski JR, De Paepe G, Eddy MT, Griffin RG (2009) J Am Chem Soc 131:5769
141. Lewandowski JR, De Paepe G, Eddy MT, Struppe J, Maas W, Griffin RG (2009) J Phys Chem B 113:9062
142. Scholz I, Meier BH, Ernst M (2010) Chem Phys Lett 485:335
143. Akbey U, Oschkinat H, van Rossum BJ (2009) J Am Chem Soc 131:17054
144. Bayro MJ, Huber M, Ramachandran R, Davenport TC, Meier BH, Ernst M, Griffin RG (2009) J Chem Phys 130:114506
145. Marin-Montesinos I, Mollica G, Carravetta M, Gansmuller A, Pilelo G, Bechmann M, Sebald A, Levitt MH (2006) Chem Phys Lett 432:572
146. Tycko R (2007) Phys Rev Lett 99:187601
147. Tycko R (2008) J Phys Chem B 112:6114
148. Paravastu AK, Tycko R (2006) J Chem Phys 124
149. Hu KN, Tycko R (2009) J Chem Phys 131:045101
150. Stringer JA, Bronnimann CE, Mullen CG, Zhou DH, Stellfox SA, Li Y, Williams EH, Rienstra CM (2005) J Magn Reson 173:40
151. McNeill SA, Gor'kov PL, Shetty K, Brey WW, Long JR (2009) J Magn Reson 197:135
152. Ernst M, Samoson A, Meier BH (2003) J Magn Reson 163:332
153. Kotecha M, Wickramasinghe NP, Ishii Y (2007) Magn Reson Chem 45:S221
154. Wickramasinghe NP, Kotecha M, Samoson A, Past J, Ishii Y (2007) J Magn Reson 184:350
155. Scholz I, Hodgkinson P, Meier BH, Ernst M (2009) J Chem Phys 130:114510
156. Bayro MJ, Ramachandran R, Caporini MA, Eddy MT, Griffin RG (2008) J Chem Phys 128:052321
157. De Paepe G, Bayro MJ, Lewandowski J, Griffin RG (2006) J Am Chem Soc 128:1776
158. Sørensen OW (1990) J Magn Reson 86:435
159. Glaser SJ, Schulte-Herbrüggen T, Sieveking M, Schedletzky O, Nielsen NC, Sørensen OW, Griesinger C (1998) Science 280:421
160. Stoustrup J, Schedletzky O, Glaser SJ, Griesinger C, Nielsen NC, Sørensen OW (1995) Phys Rev Lett 74:2921
161. Kehlet C, Bjerring M, Sivertsen AC, Kristensen T, Enghild JJ, Glaser SJ, Khaneja N, Nielsen NC (2007) J Magn Reson 188:216
162. Vosegaard T, Malmendal A, Nielsen NC (2002) Monatsh Chem 133:1555
163. Bak M, Schultz R, Vosegaard T, Nielsen NC (2002) J Magn Reson 154:28
164. Kehlet C, Nielsen NC (2007) Bruker Spin Report 157:31
165. Vosegaard T, Kehlet C, Khaneja N, Glaser SJ, Nielsen NC (2005) J Am Chem Soc 127:13768
166. O'dell LA, Harris KJ, Schurko RW (2010) J Magn Reson 203:156

Top Curr Chem (2012) 306: 47–88
DOI: 10.1007/128_2011_154

Published online: 1 June 2011

Solid-State NMR Techniques for the Structural Determination of Amyloid Fibrils

Jerry C.C. Chan

Abstract This review discusses the solid-state NMR techniques developed for the study of amyloid fibrils. Literature up to the end of 2010 has been surveyed and the materials are organized according to five categories, viz. homonuclear dipolar recoupling and polarization transfer via J-coupling, heteronuclear dipolar recoupling, correlation spectroscopy, recoupling of chemical shift anisotropy, and tensor correlation. Our emphasis is on the NMR techniques and their practical aspects. The biological implications of the results obtained for amyloid fibrils are only briefly discussed. Our main objective is to showcase the power of NMR in the study of biological unoriented solids.

Keywords Amyloid fibrils · Backbone torsion angle · Correlation spectroscopy · CSA · Dipolar recoupling · H/D exchange · J-coupling · Tensor correlation

Contents

J.C.C. Chan
Department of Chemistry, National Taiwan University, No. 1, Section 4, Roosevelt Road, Taipei, Taiwan
e-mail: chanjcc@ntu.edu.tw

1 Introduction

Amyloid fibrils are filamentous insoluble protein aggregates closely related to many fatal neurodegenerative diseases including Alzheimer's disease, type II diabetes, Huntington's disease, and prion diseases [1, 2]. The molecular structure of amyloid fibrils is known to contain β-sheets that extend over the length of the fibril, created by intermolecular hydrogen bonding of β-strand peptide segments that run perpendicular to the fibril axis, which is commonly referred to as the cross-β motif. It has been known for some years that the amyloid fibrils formed by peptide sequences of very different biophysical properties have many structural features in common [1]. To unravel the physical principles governing this interesting phenomenon, which can provide significant mechanistic insights into the self-assembly process of macromolecules, it is necessary to determine the molecular structures of amyloid fibrils formed by a large variety of proteins or their fragments. Since the pioneering work by Griffin and co-workers [3], solid-state NMR has been established as the major analytical tool to unravel the structural details of amyloid fibrils at the molecular level [4, 5]. Over the years, solid-state NMR studies of amyloid fibrils have been reviewed regularly [4–9, 11, 12]. Many cleverly designed solid-state NMR strategies have been developed to probe the hydrogen-bond registry of β-sheet layer, the spatial organization of the various β-sheet segments of the peptide chain, the existence of salt bridge, the side-chain–side-chain interactions, the quaternary contacts between β-sheet layers, the staggering of neighboring β strands, and the motional dynamics of the backbone. The review by Naito and Kawamura has also included a nice exposition of the interaction between amyloidogenic protein and membranes [12].

Biological solid-state NMR is such an active research field that many new techniques and notions have been reported in the past few years. It is simply beyond the scope of the present review to include all the techniques which may find fruitful applications in the study of amyloid fibrils. Given the page limit, we will only focus on the NMR techniques which have already been applied to the study of unoriented solid-state samples of amyloid fibrils. As implied from the title, our emphasis will be placed on the NMR techniques and the implications of the results obtained for

amyloid fibrils will only be briefly discussed. Our purpose is to present "what has been done" so that one may consider "what could be done." On a more general note, we hope that the applications discussed for amyloid fibrils can showcase the power of NMR in the study of biological solids. Most of the techniques discussed are under the condition of magic-angle spinning (MAS), which consists of radiofrequency (rf) pulse sequences that are applied in synchrony with the MAS sample rotation. Our discussion is largely descriptive and will include some practical hints on the experimental aspect. For a more in-depth discussion of the techniques and theories, readers are referred to the original literature.

2 Homonuclear Dipolar Recoupling and J-Coupling Based Techniques

In the cross-β structural motif, the registry of the hydrogen bonds between the β strands is determined by a delicate balance of multiple side-chain–side-chain interactions. Experimentally, the organization of the β-sheet structure can be determined by measuring the distance between two selected residues in adjacent β strands. Some very useful homonuclear dipolar recoupling techniques for distance measurements and spin counting will be discussed. In addition, homonuclear polarization transfer techniques mediated by the scalar spin–spin coupling (J-coupling) will also be covered in the following section. The dipolar recoupling techniques developed for homonuclear correlation spectroscopy are discussed in Sect. 4.

2.1 Rotational Resonance

Rotational resonance (R^2) is the first solid-state NMR technique applied to study amyloid fibrils [3, 13–15]. One common implementation is to set the spinning frequency equal to the chemical shift difference of the spin pair of interest, say, I and S. To the lowest order, the average Hamiltonian contains the zero-quantum (ZQ) flip-flop term ($I_+S_- + I_-S_+$) [16, 17]. Therefore, the density operator of the spin system would oscillate between the terms of I_z–S_z and of the ZQ coherence ($I_+S_- - I_-S_+$). After a selective inversion of either polarization to the $-z$ axis, which would maximize the initial polarization difference, the amplitude of I_z–S_z can be monitored as a function of the mixing time. From the time course of the exchange in Zeeman order, the internuclear distance could be extracted if the T_2 relaxation of the ZQ coherence (T_2^{ZQ}) is known. Usually, T_2^{ZQ} is approximated by the T_2 relaxations of I and S, according to the equation $(T_2^{ZQ})^{-1} = (T_2^{I})^{-1} + (T_2^{S})^{-1}$. Interestingly, it has been suggested that T_2^{ZQ} can be measured directly in a Hahn-echo like experiment, where the ZQ coherence can be refocused by the

composite $(\pi/2)_x - (\pi/2)_y - (\pi/2)_x$ pulse [18]. Because the chemical shift difference of the carbonyl and aliphatic regions is about130–160 ppm, distances of the spin pairs of C′–C^{α}, C′–C^{β}, or C′–C^{γ} can be estimated conveniently by R^2. This strategy has been applied in the study of the fibrils formed by $PrP_{106–126}$ [19], where it has been shown that the fibril structure comprises a close stacking of two neighboring β-sheets adopting the structural motif of the class 1 steric zipper [20]. Recently, a constant-time version of the R^2 experiment has been developed [21, 22], where the dynamics of the magnetization transfer is monitored as a function of the spinning frequency. This so-called rotational resonance width (R^2W) technique has the advantage that its data analysis allows an independent extraction of the internuclear distance and the T_2^{ZQ} parameter [21, 23]. Previously, it has been shown that the fibrils formed by the peptide GNNQQNY have three different polymorphs [24]. For the fibril sample formed by a 50/50 (by mass) mixture of the peptides of [^{13}C′-Gly]-NNQQNY and [$^{13}C^{\alpha}$-Gly]-NNQQNY, the intermolecular ^{13}C–^{13}C distance has been determined by the technique of R^2W [25]. The results lie in the range of 4.5–4.9 Å (with an error of ±1.0 Å), consistent with the in-register parallel β-sheet structure.

2.2 Dipolar Dephasing

The technique of dipolar recoupling with a windowless sequence (DRAWS) has been developed to recouple homonuclear dipole–dipole interaction under MAS conditions [26, 27]. The lowest-order average Hamiltonian of DRAWS is proportional to the terms of $\left(I_xS_x - I_yS_y\right)$ and $(3I_zS_z - I \cdot S)$. When the transverse magnetization is allowed to evolve under DRAWS, the dephasing rate of the signal will depend on the dipolar coupling constants and the T_2 relaxation. By measuring the crystalline compound of adipic acid, the upper limit of ^{13}C–^{13}C distances measurable by DRAWS was established to be ca. 6 Å [18]. In an early application of DRAWS to the study of amyloid fibrils, the organization of the β-sheet structure for $A\beta_{10–35}$ fibrils has been shown to be in-register parallel [28]. In addition, the secondary structure of the peptide monomer has been verified to adopt β-sheet structure by measuring the $C'_{(i)}$–$C'_{(i+1)}$ distances at selected residues [18]. To mimic the spin evolution of an "infinite" long chain as anticipated for fibrils of a few microns in length, each of the spins in a linear chain was set to have two coupled neighbors [18]. In particular, the spins at the two ends are "coupled" as if they were neighbors. This implementation of periodic boundary conditions has been shown to be an effective approach to eliminate the "edge effect" [18, 29]. DRAWS can also be used to prepare a double-quantum filter (DQF) [30]. The advantage of the resulting DQF–DRAWS technique is that the dipolar coupling and the relaxation parameters can be independently extracted from the excitation profile of the DQ signal [29]. Hence, it is possible to determine accurately by DQF–DRAWS the interstrand distances in amyloid fibrils [25, 29, 31, 32]. While DRAWS is very well compensated for the effect of chemical shift anisotropy (CSA) [33], the required rf

field is 8.5 times the spinning frequency, which has precluded its application in the fast spinning regime. In addition, the implementation of windowless pulse sequences is not trivial if phase transient problems are severe. Sometimes a damping resistor has to be added in parallel to the sample coil in order to reduce the detrimental effect of phase glitches [18, 34].

The homonuclear dipolar recoupling technique of radio frequency-driven recoupling (RFDR) involves a hard π pulse per rotor period and its recoupling mechanism is based on the modulation of chemical shift difference [35–37]. When the delta-pulse approximation is relaxed so that the pulse width of the π pulse is about one-third of the rotor period, the so-called finite-pulse RFDR (fpRFDR) could selectively reintroduce the homonuclear dipole–dipole interaction under fast MAS conditions [38]. Because the recoupling mechanism of fpRFDR does not require the presence of chemical shift difference, it can be applied to study samples with a singly labeled site. For the study of amyloid fibrils, the technique of fpRFDR is usually applied in a constant-time framework (see below).

2.3 Constant-Time Dipolar Dephasing

To minimize the effects of various experimental imperfections such as rf inhomogeneity and T_2 relaxation, it is highly desirable to design a recoupling experiment where the number of rf pulses and the total pulse sequence duration are maintained constant [39]. It has been shown that the average Hamiltonian of the fpRFDR recoupling sequence has the same operator form as the static homonuclear dipole–dipole interaction [38]. Hence, the classical WAHUHA sequence developed for homonuclear decoupling under static condition [40], viz. $\tau - (\pi/2)_x - \tau - (\pi/2)_y - 2\tau - (\pi/2)_{-y} - \tau - (\pi/2)_{-x} - \tau$, can be exploited as shown in Fig. 1 to achieve homonuclear dipolar recoupling in a constant-time manner [41]. That is, the total duration of the pulse sequence is kept constant and the effective dipolar dephasing time is varied by adjusting the positions of the WAHUHA pulses. In other words, we combine two pulse sequences which have opposite effects. While fpRFDR will reintroduce the homonuclear dipole–dipole interaction, WAHUHA will suppress it, so that the net dipolar dephasing occurs as a result of "controlled" cancellation. This technique, which has the acronym fpRFDR-CT, has been successfully applied to probe the β-sheet organization of amyloid fibrils [4, 42].

For the amyloid fibrils formed by proteins or polypeptides with more than 20 amino acid residues, the fibril core usually comprises in-register parallel β-sheets [19, 28, 43–50], although it has also been shown that a polymorph of the D23N-Aβ40 fibrils may have an antiparallel β-sheet structure [51]. The fpRFDR-CT technique is well suited to verify whether or not a fibril system adopts the organization of in-register parallel β-sheets. For a single β-sheet layer, significant signal dephasings of the C' and C^{β} labeled at two different residues will provide strong evidence for in-register parallel organization. In particular, shifting the hydrogen bond registry away from in-register alignment by one residue in either direction will

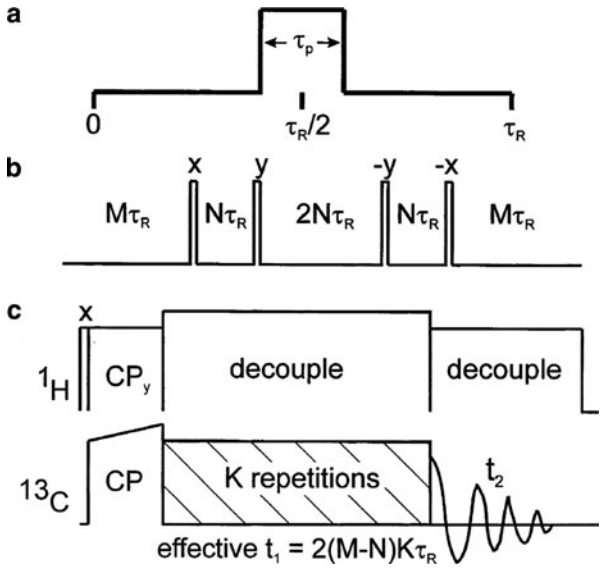

Fig. 1 Pulse sequence for fpRFDR-CT measurements. (**a**) The fpRFDR sequence consists of a single π pulse of length τ_p centered in each MAS rotation period τ_R. (**b**) The fpRFDR sequence is incorporated into a multiple pulse cycle based on the WAHUHA cycle, by insertion of four π/2 pulses with the indicated phases. Homonuclear dipole–dipole couplings generated by fpRFDR are scaled by a factor of $(M - N)/(M + 2N)$. (**c**) In the full 2D technique, ^{13}C magnetization created by CP evolves under ^{13}C–^{13}C dipole–dipole couplings for an effective t_1 period $2(M - N)K\tau_R$ is kept constant. ^{1}H–^{13}C couplings are removed by proton decoupling fields during t_1 and t_2. (Figures and caption adapted from [41]. Copyright (2001), with permission from Elsevier)

increase the nearest distance between two labeled C^{β} atoms to ca. 7 Å, for which there will be no significant signal dephasing observed in the fpRFDR-CT experiment. To quantify the spacing between the neighboring β-strands (d), the fpRFDR-CT data can be compared with simulations on a linear chain of six spins with d varied from 4 to 7 Å. To reduce the "edge effect" of a finite spin system, the initial density operator may include only the polarization of the central two spins, whereas the detection operator includes all six spins [45]. Furthermore, the contribution from the background signals must be corrected for to warrant a meaningful comparison between the experimental and simulation data (see below) [44]. However, if there are two β-sheets closely interdigitated, as in the case of steric zipper [20], the interpretation of the fpRFDR-CT data would be less straightforward [52]. Also, the fpRFDR-CT data of C^{α} is difficult to analyze quantitatively because of its fast T_2 relaxation.

2.3.1 Correction of Background Signals

To illustrate the procedure of background signal correction, let us consider a hypothetical fibril system formed by polypeptides containing 21 residues, where a

chosen residue is ^{13}C labeled at the carbonyl site. Assuming that 100% of the molecules are fibrillized and that the natural abundance signals do not dephase at all, the uncorrected C′ fpRFDR-CT data can be written as

$$\frac{S_{\mathrm{raw}}(\tau)}{S_{\mathrm{raw}}(0)} = \frac{S^{\mathrm{l,f}}(\tau) + S^{\mathrm{na,u}}}{S^{\mathrm{l,f}}(0) + S^{\mathrm{na,u}}}, \tag{1}$$

where τ denotes the effective dipolar dephasing time, and $S^{\mathrm{l,f}}$ and $S^{\mathrm{na,u}}$ indicate the signals arising from the labeled sites in fibrillar state and the sites of natural abundance (undephased), respectively. Accordingly, the C′ fpRFDR-CT data are corrected as

$$\frac{S^{\mathrm{l,f}}(\tau)}{S^{\mathrm{l,f}}(0)} = \frac{S_{\mathrm{raw}}(\tau) - S_{\mathrm{raw}}(0) \times \frac{20\times 1.1\%}{(1+20\times 1.1\%)}}{S_{\mathrm{raw}}(0) \times \left(1 - \frac{20\times 1.1\%}{(1+20\times 1.1\%)}\right)}. \tag{2}$$

In a more general case, some signals from natural abundance ^{13}C nuclei will dephase ($S^{\mathrm{na,d}}$) because of the finite probability that they are in close proximity of other ^{13}C nuclei. Furthermore, some labeled peptide molecules are unfibrillized and we assume that their signals will not dephase ($S^{\mathrm{l,u}}$). Consequently, we can write

$$\frac{S_{\mathrm{raw}}(\tau)}{S_{\mathrm{raw}}(0)} = \frac{S^{\mathrm{l,f}}(\tau) + S^{\mathrm{l,u}} + S^{\mathrm{na,d}}(\tau) + S^{\mathrm{na,u}}}{S^{\mathrm{l,f}}(0) + S^{\mathrm{l,u}} + S^{\mathrm{na,d}}(0) + S^{\mathrm{na,u}}}. \tag{3}$$

An estimation of the $S^{\mathrm{na,d}}$ signal can be obtained by measurements of the unlabeled fibril sample. For convenience, here we assume that 10% of the natural abundance signal will dephase, i.e., $S^{\mathrm{na,d}} = S^{\mathrm{na,u}} \times 0.1/0.9$, so that we can write

$$\frac{\left(\frac{0.1}{0.9} + 1\right) S^{\mathrm{na,u}}}{S_{\mathrm{raw}}(0)} = \frac{20 \times 1.1\%}{1 + 20 \times 1.1\%}. \tag{4}$$

Similarly, we can obtain

$$\frac{\left(\frac{1-x_{\mathrm{u}}}{x_{\mathrm{u}}} + 1\right) S^{\mathrm{l,u}}}{S_{\mathrm{raw}}(0)} = \frac{1}{1 + 20 \times 1.1\%}, \tag{5}$$

where the factor x_{u} denotes the fraction of the unfibrillized samples. For a sufficiently long dephasing time (ca. 70 ms), the fraction of the residual ^{13}C signal that does not decay to zero becomes

$$\frac{S_{\mathrm{residual}}}{S_{\mathrm{raw}}(0)} = \frac{S^{\mathrm{l,u}} + S^{\mathrm{na,u}}}{S_{\mathrm{raw}}(0)}. \tag{6}$$

On the basis of (4)–(6) we can estimate x_u experimentally:

$$x_u = \frac{1}{0.82}\left(\frac{S_{\text{residual}}}{S_{\text{raw}}(0)} - 0.18 \times 0.9\right). \tag{7}$$

Consequently, the signal fractions of $S^{l,f}(\tau)/S^{l,f}(0)$ can be calculated and compared with simulations. For samples prepared by bacterial expression, correction of the background signals can be carried out in a similar fashion [48, 53, 54]. It is noteworthy that spin geometries deviated from linearity, which may occur in the side-chain ^{13}C nuclei such as C^{β}, would produce more rapid signal decays and smaller residual signal fraction [55].

2.3.2 Torsion Angle Determination

The backbone torsion ϕ angle is defined as the dihedral angle of $C'_{(i-1)}N_{(i)}C^{\alpha}{}_{(i)}C'_{(i)}$. Therefore, the ϕ angle of the residue i can be determined by measuring the distance between $C'_{(i-1)}$ and $C'_{(i)}$ [56] and the most sensitive region of $|\phi|$ is from 40 to 140° [57]. This strategy, together with other techniques based on tensor correlations (Sect. 6), has been applied to characterize the secondary structure of the bend region of $A\beta_{1-40}$ fibrils [57]. In a similar fashion, the backbone torsion ψ angle of the residue i, which is defined as the dihedral angle of $N_{(i)}C^{\alpha}{}_{(i)}C'_{(i)}N_{(i+1)}$, can be determined by measuring the distance between $N_{(i)}$ and $N_{(i+1)}$. Not surprisingly, the most sensitive region for $|\psi|$ determination is quite comparable to that of $|\phi|$ [47, 55]. For the measurements of multiple $N_{(i)}$–$N_{(i+1)}$ distances, one could exploit the idea of C^{α}-detection or the resolution enhancement provided by the C'–C^{α} and C^{α}–C^{β} correlations [55]. For the fibril samples formed by islet amyloid polypeptides, the ψ angle of the residue Phe23 extracted from the C^{α}-detected ^{15}N fpRFDR-CT data is consistent with a bend structure in the region of residues 18–27 [47].

2.3.3 PITHIRDS-CT

Although fpRFDR-CT is a constant-time technique, the effect of T_2 relaxation is different as the positions of the WAHUHA pulses vary. Furthermore, a strong rf field is required to achieve the hard pulse approximation for WAHUHA, which could present a stringent condition for proton decoupling. As an alternative to the use of WAHUHA pulses, Tycko has developed a new approach to construct the constant-time version of fpRFDR [55]. In general, the cyclic time displacement of an arbitrary recoupling sequence by τ_n will introduce a phase factor $\exp(im\omega_r\tau_n)$ and will rotate the average Hamiltonian as follow [55]:

$$\bar{H}_n = e^{im\omega_r\tau_n}\left\{U_{\text{rf}}(M\tau_r - \tau_n, 0)\bar{H}U_{\text{rf}}(M\tau_r - \tau_n, 0)^{-1}\right\}, \tag{8}$$

where $M\tau_r$ denotes the cycle time of the sequence and U_{rf} is the unitary operator defined by the rf field. We now consider the pulse sequence of fpRFDR and set $\tau_n = 2\pi n/3\omega_R$, where $n = 0, 1, 2$. Because each of the π pulses in fpRFDR has a duration of one-third of the rotor period, it can be shown that the corresponding operator of $U_{rf}(M\tau_r - \tau_n, 0)$ is a unity operator. Consequently, if we concatenate $\bar{H}_0$, $\bar{H}_1$, and $\bar{H}_2$, we will have

$$\bar{H}_0 + \bar{H}_1 + \bar{H}_2 = \left\{1 + e^{im\omega_r\tau_1} + e^{im\omega_r\tau_2}\right\}\bar{H} = 0. \tag{9}$$

The novelty of (9) is that the net homonuclear dipolar dephasing can be controlled by a systematic variation of the number of the $\bar{H}_0$, $\bar{H}_1$, and $\bar{H}_2$ blocks. This technique has the acronym of PITHIRDS-CT [55] and has the virtues that the effect of T_2 is identical for all data points and that the rf field of all the pulses is only 1.67 times the spinning frequency. The only experimental concern is that very stable spinning or active rotor synchronization may be required for the implementation of PITHIRDS-CT.

2.4 Multiple-Quantum NMR

As discussed above, dipolar dephasing experiments can provide very valuable structural information for the study of amyloid fibrils. However, for a given dephasing rate, it is not trivial to deduce the number of spins constituting the spin cluster. In this regard, multiple-quantum (MQ) NMR is a powerful technique for spin counting because the observation of an n-quantum signal implies that there must be at least n spins coupled in a spin network [58]. The first application of MQ NMR to the study of amyloid fibrils was carried out under static condition [59]. With an excitation time of 14.4 ms, signals up to 5Q were observed for two singly labeled $A\beta_{1-40}$ fibril samples (Ala21-$^{13}C^{\beta}$ and Ala30-$^{13}C^{\beta}$). These observations have firmly established that the β-sheet structure of the $A\beta_{1-40}$ fibrils is in-register parallel [59]. At a magnetic field of 9.4 T, the total experimental time for each sample (10–15 mg) is approximately 100 h, with a recycle delay of 1 s. In addition to the issue of poor sensitivity, MQ NMR measurements for C′ under static condition are very inefficient because of the large CSA. To tackle these problems, Oyler and Tycko have incorporated the fpRFDR sequence into some MQ NMR techniques developed for static solids [60]. The design principle is quite similar to that of fpRFDR-CT. For a singly labeled $A\beta_{1-40}$ fibril sample (Val39-$^{13}C'$), signals up to 3Q were observed with an excitation time of 31.1 ms under a spinning frequency of 18.519 kHz. The total experimental time is ca. 28 h for 8 mg of the sample. Although the sensitivity has greatly improved under MAS condition, the downscaling of the effective Hamiltonian leads to a substantially longer excitation time. On the other hand, the intramolecular 3Q signal has been observed in a uniformly ^{13}C labeled fibril sample with an excitation time of 1.2 ms [60].

This observation illustrates an interesting possibility of probing torsion angles by a controlled evolution of the intramolecular MQ signals, just as discussed by Levitt and co-workers [61].

2.5 Polarization Transfer Via Homonuclear J-Coupling

Under the high-resolution condition provided by MAS, it is possible to probe the correlations between different nuclei via the dipole–dipole interaction or the J-coupling [62, 63]. It is of great interest to pursue J-coupling mediated polarization transfer in SSNMR [64–76] both because of the selectivity offered by this through-bond interaction and because of the 100% theoretical transfer efficiency for a two-spin system. To realize polarization transfer via J-coupling, other internal interactions such as chemical shifts and homonuclear dipole–dipole coupling must be efficiently suppressed. A very successful pulse sequence for this purpose is total through-bond-correlation spectroscopy (TOBSY) [65]. A typical TOBSY sequence would create the following average Hamiltonian to the lowest order:

$$\bar{H} = 2\pi J_{\mathrm{iso}} I \cdot S. \tag{10}$$

However, typical polarization transfer efficiency reported for ^{13}C–^{13}C TOBSY measurements of polypeptides is significantly less than the theoretical maximum. One of the major reasons is due to the requirement of high power ^{1}H decoupling during the polarization transfer, which is usually set to be three times larger than the recoupling field [37, 77].

Many years ago, Yannoni et al. demonstrated that separate proton decoupling is in principle unnecessary for ^{13}C nutation spectroscopy [78]. Recently, it has been shown in a ^{13}C homonuclear dipolar recoupling experiment that MAS alone is sufficient for good ^{1}H decoupling when the spinning frequency is high enough [38]. A systematic study has also shown that significant excitation of ^{13}C homonuclear double-quantum coherence can be acquired without ^{1}H decoupling [79]. This no-decoupling approach, coined as NO-DEC by Baldus and co-workers [79], was first tested for dipolar recoupling experiments. Intuitively, this NO-DEC approach can be immediately incorporated into most existing TOBSY-like sequences [65, 66, 70–73]. By numerical simulations we found that proton decoupling is indeed not necessary for the so-called R-TOBSY method, as long as the rf recoupling field is high enough. Experimentally, a good $C' \rightarrow C^{\alpha}$ polarization transfer efficiency (>50%) in a uniformly labeled noncrystalline polypeptide has been achieved without ^{1}H decoupling, for which the rf field was set to 125 kHz at a spinning frequency of 25 kHz [80] (Fig. 2). Although the chemical shift difference between C' and C^{α} becomes larger at higher magnetic field, numerical simulations based on the R-TOBSY technique shows that the transfer efficiency at a field strength of 18.8 T is nearly identical to that at 7.05 T.

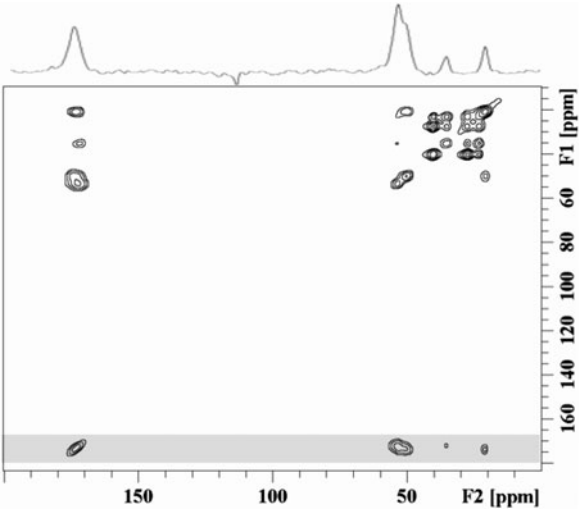

Fig. 2 ^{13}C–^{13}C correlation spectrum measured for the MB(i + 4)EK polypeptides at 7.05 T under 25 kHz MAS spinning. The projection of the *shaded region* is shown to highlight the excellent $C' \rightarrow C_\alpha$ transfer efficiency. (Figures and caption adapted from [80]. Copyright (2006), with permission from Elsevier)

2.6 *Frequency-Selective Polarization Transfer*

To achieve a more selective polarization transfer, e.g., $C' \leftrightarrow C^\alpha$, the so-called multiple chemical shift precession (MCSP) could be employed to achieve frequency selective polarization transfer based on J-coupling [81]. The design principle of MCSP has a close analogy to the DANTE concept in the zero-quantum subspace. Consider the ZQ coherence excited by a TOBSY pulse block. Under free precession, the ZQ coherence will evolve at a frequency equal to the chemical shift difference (Δ) of the two interacting spins. As an analogy to the DANTE concept, a train of TOBSY pulse blocks can be used to excite selectively the desired ZQ coherence in a multiple-spin system, provided that the free precession period between two TOBSY blocks is set equal to the integer multiples of $1/\Delta$. That is, for other spin pairs whose chemical shift difference is different from Δ, the flip-flop term of the average Hamiltonian will be truncated. Figure 3 shows the experimental results obtained for [U–^{13}C, ^{15}N]-alanine. The upper trace represents the regular TOBSY experiment, in which a significant portion of the C' polarization has been transferred to C^α and C^β. As we set the precession period equal to $1/\Delta$ and increase the N from 1 to 4, a significant increase in the C^α polarization is produced at the expense of the C^β polarization. The selectivity of the MCSP approach depends on the number of precession periods. An optimum value for N has to be determined experimentally.

The idea of frequency selectivity is certainly not restricted to J-coupling mediated polarization transfer. Furthermore, frequency selective polarization transfer can also be realized by DQ recoupling techniques. For the technique of shift-evolution-assisted selective homonuclear recoupling (SEASHORE), which employs POST-C7 to construct an effective DQ coupling [82, 83], frequency selective polarization can be achieved when the transmitter offset is set to the

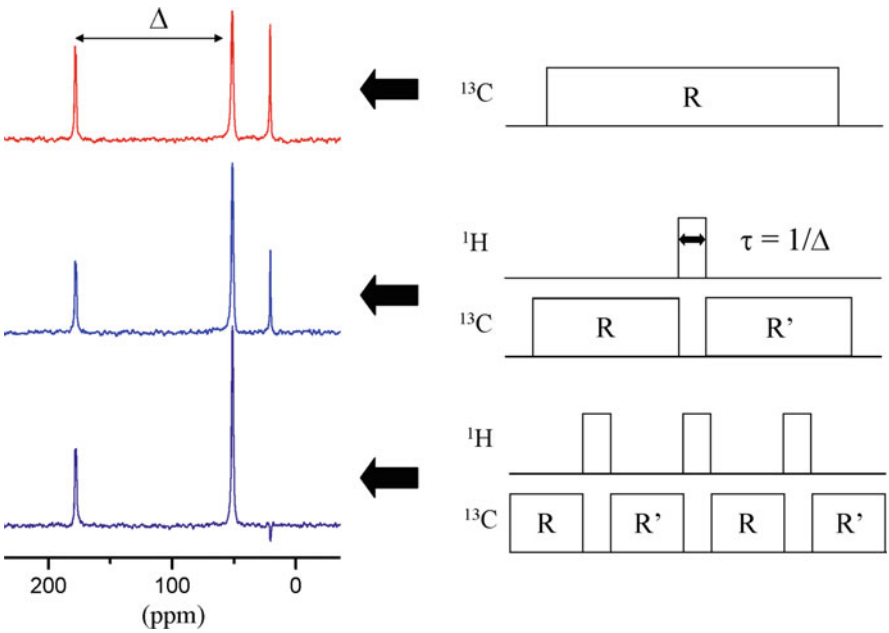

Fig. 3 Experimental results measured for [U–^{13}C, ^{15}N]-alanine based on the MCSP approach. The polarization of C^{α} after the mixing period increases as the number of R-TOBSY mixing periods increases to four. Accordingly, the C^{β} is nullified eventually. (Figure and caption adapted from [81]. Copyright (2006), with permission from Elsevier)

midpoint of the chemical shifts of the spin pair of interest, i.e., $(\omega_I + \omega_S) = 0$ [84]. In comparison, the frequency selectivity of MCSP depends on the duration of the free precession period, whereas SEASHORE may rely only on the transmitter position for its selectivity. The latter approach has the advantage that the free precession period can be set to multiples of the rotor period. Strictly speaking, the frequency selectivity is achieved in SEASHORE when the phase factor $(\omega_I + \omega_S)n\tau_r$ is zero or a multiple of 2π, where $n\tau_r$ is the duration of the free precession period [84]. Very recently, the technique of fpRFDR has been incorporated in the framework of SEASHORE [85]. The resultant technique, viz. ZQ-SEASHORE, can achieve frequency selective dipolar recoupling under very fast MAS condition (40 kHz).

3 Heteronuclear Dipolar Recoupling Techniques

3.1 REDOR

Rotational echo double resonance (REDOR) [86] is one of the most important techniques developed for solid-state NMR spectroscopy. The theory of REDOR is

well understood [87, 88] and requires no further discussion in this review. It has been shown that the distances along the peptide backbone obtained by $^{13}C\{^{15}N\}$ REDOR measurements can provide useful constraints on the backbone torsion angles [89]. Another important application of REDOR in the studies of amyloid fibrils is the determination of the H-bond registry of the β-sheets. We will discuss some specific details relevant to this application in the following section.

To avoid the interference from intramolecular REDOR dephasing, peptides with $^{15}NH_i$ labels could be mixed with peptides with $^{13}CO_j$ labels in a 1:1 ratio before fibrillization, where i and j denote the residues with isotopic enhancement at the amide and carbonyl sites, respectively. If an in-register parallel β-sheet is considered as the hypothetical structure, the most adequate model for the analysis of the $^{13}C\{^{15}N\}$ REDOR data measured for the case of $i = j$ should be a ^{15}N–^{13}C–^{15}N spin system, where the NCN angle is ca. 127° and the two ^{15}N–^{13}C distances are 5.3 and 5.5 Å (Fig. 4a). For the case of $i = j + 1$, the NCN angle should be 154° and the two ^{15}N–^{13}C distances 4.2 and 5.6 Å. Other combinations of i and j for an

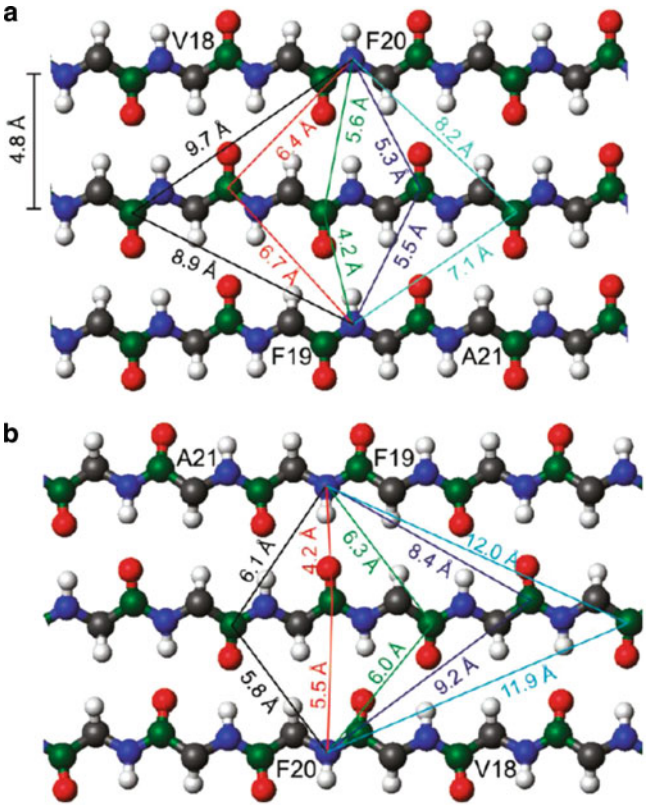

Fig. 4 (**a**) Model for an in-register parallel β-sheet for REDOR simulations. Only the backbone is shown and the residue labels correspond to the sequence of $A\beta_{1-40}$. Relevant distances between Phe20 amide nitrogens (*blue* in color) and backbone carbonyl sites (*dark green* in color) are shown. (**b**) Model for an antiparallel β-sheet with $17 + k \leftrightarrow 21 - k$ registry. (Figure and caption adapted from [51]. Copyright 2009 American Chemical Society)

in-register parallel β-sheet are not likely to produce any REDOR fraction ($\Delta S/S_0$) larger than 0.1 [51]. For an antiparallel β-sheet (Fig. 4b), if the $^{15}NH_i$ makes a hydrogen bond to the $^{13}CO_j$ on a neighboring peptide chain, the REDOR dephasing can be analyzed based on the ^{15}N–^{13}C–^{15}N spin system where the NCN angle is ca. 180° and the two ^{15}N–^{13}C distances are 4.2 and 5.5 Å. Furthermore, if the residues *i* and *j* are not hydrogen bonded, the corresponding REDOR fractions will be significantly smaller. Consequently, measurements of the $^{13}C\{^{15}N\}$ REDOR data of the judiciously labeled samples can be carried out to determine the H-bond registry. Although the spin systems are based on idealized geometry, the agreement between the experimental and simulation data are usually quite satisfactory, provided that the contribution of the ^{13}C signals arising from the unlabeled sites has been properly accounted for. A very detailed discussion of the procedure for background signal correction has been documented in the literature [44]. Because the ^{13}C–^{15}N distances targeting in our REDOR experiments are in the range of 4.5–5.5 Å, the required dephasing time is usually up to 50 ms. To minimize the T_2 relaxation of the $^{13}C'$ signals, we find that the REDOR pulse sequence developed by Anderson et al. [90], where the rotor synchronized π pulses are alternating between the dephasing and observe channels, is most suitable for the study of amyloid fibrils. Although a train of π pulses are applied in the ^{13}C channel, the recoupling of ^{13}C homonuclear dipole–dipole interaction should be negligible for the cross-β motif because the closest ^{13}C–^{13}C distance within the same β-sheet layer is greater than 9 Å, provided that the peptides with ^{15}N labels and those with ^{13}C labels are well mixed before fibrillization. The situation is somewhat more complicated for those fibril samples formed by the polypeptides which contain the AGAAAAGA sequence. If this palindrome sequence is located in the core region of the fibrils, it is very likely that the two neighboring β-sheets would be closely packed to form the so-called steric zipper [20, 91]. As such, the interlayer distance could be as close as 5 Å [52]. In any case, one can monitor the attenuation of the reference signal (S_0) as a function of the dephasing time to verify if there is any sizable homonuclear dipolar interaction among the ^{13}C spins.

3.2 Frequency-Selective REDOR

Frequency-selective REDOR (fsREDOR) is a very powerful technique developed for the study of ^{13}C and ^{15}N uniformly labeled peptides or proteins [92]. The basic idea of this technique is to combine REDOR and soft π pulses to recouple a selected ^{13}C–^{15}N dipole–dipole interaction in a multiple-spin system. Usually one could use Gaussian shaped pulses to achieve the required selective π inversions. Other band selective shaped pulses have been developed for a more uniform excitation profile [93]. In its original implementation, fsREDOR was used to extract the internuclear distances of several model crystalline compounds [92]. In the past few years, this technique has proven to be very useful for the study of amyloid fibrils as well. For the Ure2p$_{10–39}$ fibril samples containing ^{13}C and ^{15}N uniformly

labeled Gln, ^{13}C detected fsREDOR was used to assign the ^{15}N signals arising from the side chain (111 ppm) and backbone amide sites (125 ppm), without measuring the more time-consuming $^{13}C/^{15}N$ correlation spectrum. Experimentally, selective inversion of the ^{15}N peak at 111 ppm produced greater dephasing of the Gln18 δ-carbon and selective inversion of the ^{15}N NMR peak at 125 ppm produced greater dephasing of the $^{13}C^{\alpha}$ signal [45]. For the WT $A\beta_{1-40}$ fibril samples with uniform ^{15}N and ^{13}C labeling at F20, D23, V24, K28, G29, A30, and I30, one can use fsREDOR to probe selectively the salt bridge resulting from the close proximity between D23 and K28 [51]. The viability of this method stems from the fact that the C_{γ} signal of D23 and N_{ξ} of K28 are well resolved from other backbone C′ and amide ^{15}N signals, respectively. In addition to these applications, fsREDOR has been incorporated in other newly developed techniques as discussed below.

3.3 DSQ-REDOR

Amyloid fibrils formed by peptides and proteins that are rich in glutamine or asparagine residues are of particular interest, both because of their involvement in neurodegenerative disorders such as Huntingon's disease [94] and because of the hypothesis put forward by Perutz that these fibrils are stabilized by linear chains of hydrogen bonds among the side-chain amide groups of glutamine or asparagine. Perutz coined the phrase "polar zippers" to describe the putative side-chain hydrogen bonding interactions [95, 96]. However, it is not trivial to provide direct experimental evidence for the formation of polar zippers in amyloid fibrils. For each side chain the intraresidue ^{15}N–^{13}C dipole–dipole coupling amounts to 1,280 Hz, corresponding to a chemical bond distance of 1.338 Å [97]. If a linear chain of hydrogen bonds among the amide groups of glutamine is formed, the interresidue ^{15}N–^{13}C dipole–dipole coupling would be 25–78 Hz (3.4–5.0 Å nearest-neighbor ^{15}N–^{13}C distance). For ^{13}C and ^{15}N uniformly labeled samples, it is very difficult to characterize the relatively weak interresidue ^{15}N–^{13}C dipolar coupling in the presence of the strong intraresidue ^{15}N–^{13}C coupling by regular $^{13}C\{^{15}N\}$ REDOR.

Very recently, a novel solid-state NMR technique has been developed by Tycko et al. to probe the formation of polar zippers in amyloid fibrils [45]. This technique is an extension of the fsREDOR techniques. Referring to Fig. 5, a short fsREDOR pulse train is applied during the pulse sequence period τ_1 to prepare intraresidue, heteronuclear "double single-quantum" (DSQ) coherences between directly-bonded $^{13}C/^{15}N$ pairs in side-chain amide groups. DSQ coherences are represented by spin density operator terms of the form $I_{1x}S_{1x}$ in the standard product operator formalism [100]. It is easy to show that the coherence $I_{1x}S_{1x}$ is unaffected by the Hamiltonian of the form $I_{1z}S_{1z}$. In other words, the intraresidue DSQ coherences are unaffected by intraresidue ^{15}N–^{13}C couplings during the longer fsREDOR dephasing period τ_d, but can decay due to intermolecular ^{15}N–^{13}C couplings pairs if such couplings are present. DSQ coherences at the end of τ_d are converted to observable

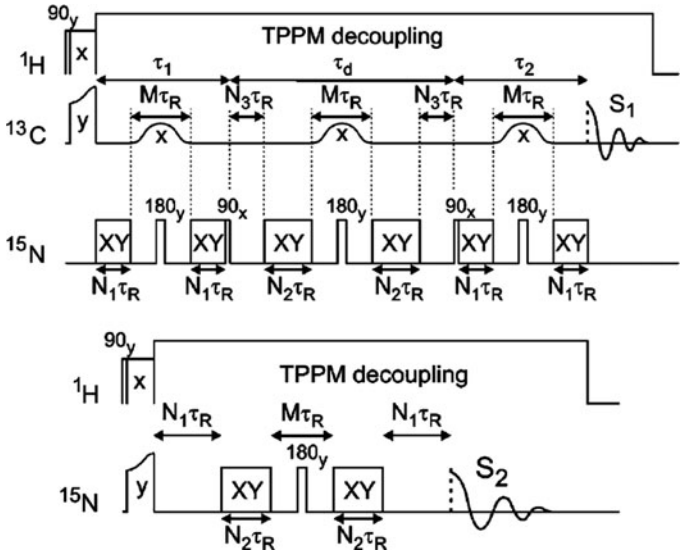

Fig. 5 Radio frequency pulse sequences for measurements of S_1 and S_2 in DSQ-REDOR experiments. The MAS period τ_R is 100 μs. XY represents a train of ^{15}N π pulses with XY-16 phase patterns [98]. TPPM represents two-pulse phase modulation [99]. In these experiments, $M = N_1 = 4$, $N_2 + N_3 = 48$, and N_2 is incremented from 0 to 48 to produce effective dephasing times from 0 to 9.6 ms. Signals arising from intraresidue ^{15}N–^{13}C DSQ coherence (S_1) are selected by standard phase cycling. Signal decay due to the pulse imperfection of ^{15}N pulses is estimated by S_2. Decay due to the intermolecular ^{15}N–^{13}C dipole–dipole couplings is calculated as $S_1(N_2)/S_2(N_2)$. The phase cycling scheme can be found in the original figure and caption. (Figure and caption adapted from [45])

carbonyl ^{13}C nuclear spin polarization by the final fsREDOR pulse train during period τ_2. ^{13}C NMR signals that arise from the DSQ coherences are selected by appropriate phase cycling of rf pulses in τ_1 and τ_2. This technique has the acronym DSQ-REDOR. The DSQ-REDOR data obtained for the fibril sample formed by the fragment of Ure2p prion protein (^{13}C and ^{15}N uniformly labeled at Gln18) are consistent with the structural motif of polar zipper [45]. In addition, DSQ-REDOR can also be used to determine the backbone ϕ and ψ angles for peptide samples with uniform ^{13}C and ^{15}N labels at two consecutive residues [101]. The idea is to create the DSQ coherences for the $^{13}CO_i$–$^{15}NH_{i+1}$ pair. The excited DSQ coherences are then evolved under the influence of the dipolar interactions of the $^{15}NH_i$–$^{13}CO_i$ and $^{15}NH_{i+1}$–$^{13}CO_{i+1}$. Thus, the dephasing of the DSQ coherence has an implicit dependence on the backbone torsion angles of ϕ_{i+1} and ψ_i.

3.4 Band-Selective TEDOR

Another useful technique which is closely related to fsREDOR is the band-selective transferred echo double resonance (BASE TEDOR) [102]. As shown in Fig. 6, the

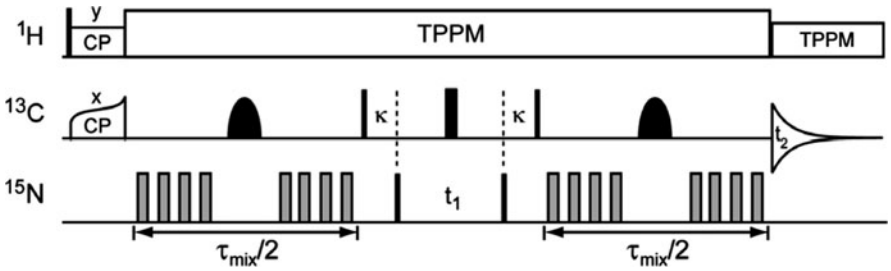

Fig. 6 Pulse sequence of 3D band-selective TEDOR. The selective ^{13}C pulses were applied in either the C^{α} region (~54 ppm) or the C' region (~174 ppm). The short delays κ ensure that the total delay between the first and second REDOR periods is equal to an integer number of rotor cycles. For all sequences, the $\pi/2$ and π pulses are represented by *thin* and *thick black rectangles*, respectively, and have phase *x*. The π REDOR pulses on the ^{15}N channel (*gray rectangles*) were phase cycled according to the XY-4 scheme [98]. (Figure and caption adapted from the Supporting Information of [103]. Copyright 2010 American Chemical Society)

^{13}C antiphase coherence generated in the first fsREDOR period is converted into the ^{15}N antiphase coherence by a pair of $\pi/2$ pulses on the ^{15}N and ^{13}C spins. With the middle band-selective π pulse applied in the C^{α} (or C') region, the coherence transfer would occur between the amide nitrogen and C^{α} (or C') only. In addition, the selective ^{13}C π pulse can refocus the J-couplings between the excited spins and other ^{13}C spins which are outside the bandwidth of the selective pulse. After the chemical shift evolution in the ^{15}N dimension (t_1 evolution), the ^{15}N antiphase coherence is then transferred back to the ^{13}C antiphase coherence by the second fsREDOR period [102, 103]. As discussed in the foregoing section, ^{15}N fpRFDR-CT or PITHIRDS-CT can be used to probe the backbone ψ angle when two consecutive amide sites are ^{15}N labeled. However, the spectral resolution of the amide ^{15}N is rather poor compared to that of C^{α}. Therefore, one can employ the BASE TEDOR technique to transfer the ^{15}N signals to the directly bonded C^{α} for detection, when the samples are ^{15}N and ^{13}C uniformly labeled at multiple sites [55]. The $^{13}C^{\alpha}$-detected ^{15}N fpRFDR-CT data have been acquired for fibril samples formed by islet amyloid polypeptide, from which it has been shown that the Phe23 residue adopts a non-β-strand conformation [47]. By a systematic variation of the fsREDOR period, the BASE TEDOR technique can be used to probe internuclear bond distances. In particular, the effective ^{15}N–$^{13}C'$ and ^{15}N–$^{13}C^{\alpha}$ one-bond dipolar couplings of selected residues of huPrP$_{23–144}$ fibrils were determined at a MAS frequency of 11.111 kH. A variant of BASE TEDOR, known as z-filtered TEDOR, has also been employed to determine a few dozen of the one-bond and two bond C–N distances of the fibrils formed by the 11-residue fragment of human transthyretin [104].

3.5 ^{1}H–*X Dipolar Couplings*

Any heteronuclear dipolar recoupling techniques developed for systems containing multiple ^{1}H spins must have the property to suppress actively the ^{1}H–^{1}H dipolar

interaction. There are several methods to achieve this goal. In addition to the frequency-switched LG (FSLG) technique [105, 106], symmetry-based methods [107, 108] have also been developed for the characterization of C–H and N–H bond lengths. Site specific one-bond dipolar couplings of ^{15}N–^{1}H and $^{13}C^{\alpha}$–^{1}H have been characterized for residues in the amyloid core region of huPrP$_{23–144}$ fibrils [103]. Together with the results of the effective ^{15}N–$^{13}C'$ and ^{15}N–$^{13}C^{\alpha}$ one-bond dipolar couplings, it has been deduced that the structural dynamics at the sub-microsecond time scale are approximately identical for residues located in different parts of the amyloid core [103]. Other applications of the recoupling techniques for ^{15}N–$^{1}H^{N}$ and $^{13}C^{\alpha}$–$^{1}H^{\alpha}$ can be found in the tensor correlation methods for the measurements of backbone torsion angles (see Sect. 6).

4 Correlation Spectroscopy

Correlation spectroscopy is of paramount importance in solid-state NMR studies of biological solids. On the basis of the ^{13}C and ^{15}N chemical shifts, it is possible to estimate the backbone torsion angles if the secondary structure is in the α-helix or β-sheet regions. This feature is particularly useful for the study of amyloid fibrils. Furthermore, the signal line widths can provide a reliable measure on the structural order. For well ordered fibrils, the line widths are usually in the region of 2–3 ppm for lyophilized samples, whereas the line widths would become 0.5–1.5 ppm for hydrated samples. Although one could rely on multidimensional techniques to enhance spectral resolution, very often one can also reduce the ambiguities in data analyses by comparing spectra obtained for the samples prepared with different labeling schemes. For example, by comparing the spectra of uniformly labeled samples with those of "diluted" samples (mixture of labeled and unlabeled samples), one can distinguish the distant constraints arising from intra- or intermolecular contacts. In this section, we will discuss some correlation techniques which have been successfully applied to the studies of amyloid fibrils.

4.1 Spectral Assignment

The ^{13}C signals within a uniformly labeled residue can be assigned by broadband ^{13}C homonuclear correlation spectroscopy. NMR techniques commonly employed for the spectral assignments of fibril samples include proton-driven spin diffusion (PDSD) [109], RFDR [36, 37], fpRFDR [38], dipolar assisted rotational resonance/rf assisted diffusion (DARR/RAD) [110–112], dipolar recoupling enhanced by amplitude modulation (DREAM) [113], and TOBSY [65, 71, 73, 114]. It should be noted that there does not exist a universal technique optimized for all kinds of samples. The choice of technique largely depends on the peptide sequence, the isotopic labeling scheme, the desired measurement temperature, the inherent signal

line width, the static field strength, and the accessibility of the desired probe head. Below we will discuss some illustrative examples taken from the literature of amyloid fibrils.

The simplest techniques for ^{13}C homonuclear correlation spectroscopy are the PDSD and DARR, for which the polarization-transfer mechanism is illustrated in Fig. 7. The MAS frequency for PDSD is usually adjusted to be smaller than one half of the chemical shift difference between the carbonyl and aliphatic regions, and the mixing time is in the range of 20–50 ms [115–117]. For DARR, the MAS frequency is adjusted in such a way that the carbonyl and aliphatic signals are close to but not exactly on rotational resonance, and the mixing time is in the range of 5–20 ms [19, 118], depending on whether cross peaks due to multiple-bond connectivity are desired. Both techniques have been applied to the study of amyloid fibrils in high field ($\geq$14.1 T). Because the MAS frequency is relatively low (ca. 10 kHz), a stable spinning can be maintained at relatively low temperature [119]. Other techniques listed above such as fpRFDR require the rf irradiation in the ^{13}C channel and they have much higher efficiency for one-bond polarization transfer than PDSD and DARR. The mixing time is usually in the range of 2–3 ms. The technique of fpRFDR is a viable option for the study of amyloid fibrils formed by relatively

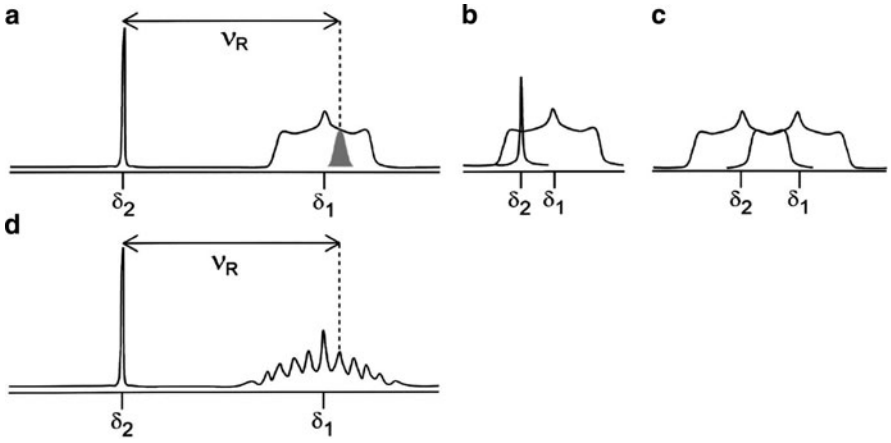

Fig. 7 Schematic ^{13}C MAS spectra of two ^{13}C spins under ^{13}C–^{1}H recoupling, showing various types of spectral overlap necessary for energy conservation in ^{13}C–^{13}C polarization transfer. Spectrum (**a**) represents two resonances of C^{ali} at δ_1 and C′ at δ_2, where C^{ali} denotes any methine, methylene, and methyl carbons. The *hatched peak* denotes one of the spinning sidebands of the C′ peak, being overlapped with the recovered ^{13}C–^{1}H dipolar powder pattern of the C^{ali} resonance. Spectrum (**b**) shows spectral overlap for a pair of spins whose chemical shift difference is smaller than the ^{13}C–^{1}H dipolar broadening. Spectrum (**c**) shows the case when spectral overlap occurs between two ^{13}C–^{1}H dipolar powder patterns. Spectrum (**d**) is similar to (**a**), but the ^{13}CH resonance shows a sideband pattern induced by modulation of the ^{13}C–^{1}H dipolar interaction under suitable ^{1}H rf irradiation. Spectral overlap is achieved for one of the spinning sidebands of the C′ peak and one of the modulation-induced sidebands of the C^{ali} resonance. The *vertical dotted lines* denote the position of the spinning sideband of the C′ peak. (Figure and caption adapted from [111]. Copyright [2003], American Institute of Physics)

short peptide sequence or full-length protein [54, 120], where the spinning frequency is usually in the range of 18–22 kHz. The DREAM technique is highly optimized for probing connectivity of the carbon signals in the aliphatic region under fast MAS frequency (25 kHz), whereas the transfer between C' and C^{α} can also be realized under very fast MAS (40 kHz at a static field of 14.1 T) [121]. An interesting feature of the RFDR approach is that it could be applied without proton decoupling if the ^{13}C recoupling field is around 120 kHz under fast spinning conditions [122]. Another NO-DEC technique developed for high-field and fast spinning conditions is cosine modulated adiabatic recoupling (CMAR) [123]. Both techniques have been applied to the study of amyloid fibrils [124, 125].

Recently, the use of paramagnetic relaxation enhancement (PRE) in biological solid-state NMR has received considerable attention [126–128]. On the basis of PRE, Ishii et al. have developed a very efficient strategy to carry out the ^{13}C homonuclear correlation experiments (paramagnetic relaxation-assisted condensed data collection, PACC), for which convincing results have been obtained for amyloid fibrils [129]. In the presence of paramagnetic species (e.g., Cu-EDTA), the proton T_1 relaxation of the $A\beta_{1-40}$ and $A\beta_{1-42}$ fibril samples can be shortened substantially. Under the condition of 40 kHz MAS, a very weak ^{1}H decoupling (7 kHz, TPPM) is sufficient to provide a decent spectral resolution. Overall, the experimental recycle delay for PACC can be cut down to 0.2 s, rendering the measurements of fibril samples at the nanomole scale possible at 9.4 T. We note in passing that the effect of PRE on the ^{13}C CPMAS spectra has also been used to probe the solvent exposed regions of $PrP_{106-126}$ fibrils and oligomers [130].

For fibril samples comprising relatively short peptides prepared by solid-phase synthesis, the ^{13}C–^{13}C correlation spectra alone could provide site-specific ^{13}C chemical shifts because the sequence positions of the labeled residues are known. However, for samples prepared by bacterial expression, techniques such as NCOCA and NCACX are required to carry out sequential assignment [121]. The coherence transfer between ^{15}N and ^{13}C nuclei is the basic step for sequential assignment techniques. There are two transfer mechanisms developed for the ^{13}C–^{15}N coherence transfer. For the technique of SPECIFIC CP, the ^{13}C spin locking field is adjusted to be comparable to the resonance offset so that the matching of the Hartmann–Hahn conditions would depend on the position of the ^{13}C transmitter [131]. As an illustration, the coherence transfer from ^{15}N to C^{α} and ^{15}N to C' can be selected by placing the ^{13}C transmitter at ca. 44 and 162 ppm, respectively, when the ^{13}C and ^{15}N rf fields are set to 5 and 30 kHz, respectively, under a MAS frequency of 25 kHz [121]. Alternatively, using the technique of BASE TEDOR or ZF-TEDOR, frequency selective ^{13}C–^{15}N coherence transfer can also be achieved [125, 132]. As shown in a study of $A\beta_{1-40}$ fibrils, an evolution period of 2.87 ms could result in strong intraresidue $^{13}C^{\alpha}/^{15}N$ cross-peaks [132]. On the other hand, a mixing period of 6 ms is optimized for two-bond $^{15}N_{(i+1)}$–$^{13}C_{(i)}$ transfer, which can facilitate sequential assignment of the backbone signals [124].

The aforementioned assignment techniques based on dipole–dipole interactions are sufficient for the fibril samples with limited structural dynamics. In the presence of substantial dynamics, which may significantly attenuate the dipole–dipole

interactions between neighboring nuclei, the $^{13}C\{^{1}H\}$ CP signals of some residues may become missing in the dipolar-based correlation spectra. As discussed earlier, the homonuclear polarization transfer of TOBSY proceeds through chemical bonds. Consequently, the TOBSY sequences have the same selectively towards both the mobile and rigid parts of the system. This feature is an advantage in the study of hydrated fibril samples formed by sizable proteins or polypeptides. Using INEPT or CP as the preparation step for the subsequent TOBSY polarization transfer, one can select the ^{13}C signals corresponding to either the mobile or the rigid parts, respectively [133]. The latter are usually originated from the core region of the amyloid fibrils [115, 134–136] and the mobile region is presumably solvent exposed [125]. To detect the signal arising from the mobile region of fibrils and to alleviate the interference of the signals from monomers, one can incorporate a T_2 filter before the $^{13}C\{^{1}H\}$ CP step as shown in Fig. 8 [5, 134].

It is well known that the fibrils formed by different fragments of the β-amyloid peptide could have different molecular structures [4]. While the studies of the fibril structures formed by a variety of protein fragments can deepen our understanding of the underlying biophysical principles of protein folding and misfolding, the fibrils formed by bona fide proteins remain to be the most biological relevant targets. Very often, these targets such as prion protein have to be prepared by bacterial expression. Although the carbon sources of 1,3-^{13}C-glycerol and 2-^{13}C-glycerol could be used to enhance the spectral resolution, signal overlap may remain a severe problem when the molecular mass of the fibril-forming monomer becomes too large. In particular, when the number of cross-peaks is considerably smaller than the number of residues in the protein sequence, manual sequential assignment may become very difficult. Furthermore, it is important to check for the existence of any alternative sets of assignments which are consistent with the same set of spectra. To tackle this problem, Tycko et al. have developed a computer protocol based on a

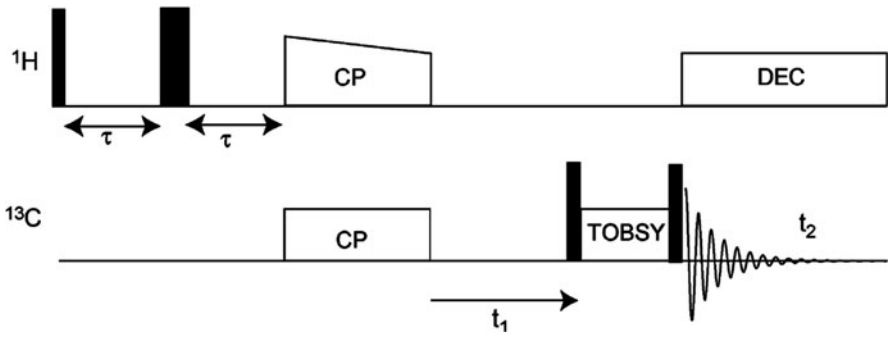

Fig. 8 Pulse sequence for the measurement of homonuclear correlation spectra with T_2 filtering. *Narrows bars* indicate π/2 pulses and *broad bars* indicate π pulses. Experimental conditions employed for α-synuclein fibrils samples: static field strength 9.4 T; temperature −5 °C; spinning frequency 8 kHz; T_2 filter 100 ms; CP contact time 2.5 ms; TOBSY mixing time 6 ms. The rf phases can be found in the original figure and caption. (Figure and caption adapted from the Supporting Information of [134]. Copyright (2005) National Academy of Sciences, USA)

Monte Carlo/simulated annealing (MC/SA) algorithm for sequential assignment in uniformly ^{13}C, ^{15}N-labeled proteins [137]. The two-dimensional (2D) NCACX and NCOCX spectra measured for the fibril samples of full-length Syrian hamster prion protein (residues 23–231) have been analyzed by the MC/SA protocol, from which it has been concluded that the fibril core is formed primarily in the region of residues 173–224 [54].

4.2 Distance Constraints

When site specific ^{13}C and ^{15}N chemical shifts are available, preliminary structural conformation of the individual polypeptide strand can be obtained by TALOS calculations [138, 139], from which one can easily identify the β-sheet regions of the protein sequence. To refine the backbone conformation, one can use the proton-mediated techniques [140], viz. NHHC and CHHC, to probe the short-range H^N–H^α and H^α–H^α contacts ($\leq$3 Å). Consider the framework of the NHHC pulse sequence. After the initial $^{15}N\{^1H\}$ CP, the polarizations of H^N are prepared by the $^1H\{^{15}N\}$ CP with a contact time of ca. 150 μs. Then, a very brief ^1H–^1H spin diffusion period (ca. 200 μs) is used to allow the contacts of H^N–H^α, if any. Finally, the H^α polarizations are transferred to C^α for detection by another brief $^{13}C\{^1H\}$ CP (150 μs). The CHHC experiment can be carried out in a similar fashion. As discussed by Baldus et al. [141], the sequential $H^N_{(i+1)}$–$H^\alpha_{(i)}$ distance is less than 2.6 Å for the β-sheet conformation, whereas the distance is about 3 Å for α-helices. Therefore, NHHC spectra are very useful for the identification of the core regions of amyloid fibrils [49, 134]. For fibril systems with antiparallel β-sheet organization, the CHHC experiment is well suited to determine the H-bond registry because the nearest distance of the H^αs between the aligned residues is ca. 2.1 Å [10]. Furthermore, for the fibrils formed by an equimolar mixture of ^{13}C labeled and ^{15}N labeled monomers, only intermolecular contacts will be observed in the NHHC spectrum [49]. Both intermolecular and nonsequential intramolecular contacts obtained by NHHC and CHHC experiments are very important for structural determination [49].

To determine long-range homonuclear distance constraints, the techniques of PDSD and DARR are most commonly employed. Indeed, the PDSD technique has been employed to derive distance constraints for the first protein structure determined by solid-state NMR at 17.6 T [142]. When the mixing time is in the range of 250–1,500 ms, long-range contacts up to ca. 6 Å become detectable in DARR or PDSD experiments [132]. In the DARR spectra measured for $A\beta_{1-42}$ fibrils, the cross peaks corresponding to the side-chain contacts between Phe19 and Leu34 have been observed, whereas the contact between Phe19 and Gly38 is missing [143]. This observation shows that the mature $A\beta_{1-42}$ fibrils have a similar β-turn-β structure as $A\beta_{1-40}$ fibrils, which is not consistent with a previous conclusion based on mutagenesis results [144]. Nonetheless, it is well known that a slight difference in incubation conditions can result in different molecular structures for amyloid fibrils [145]. From the DARR spectra of the samples prepared by a 1:1 mixture of

two differently labeled $A\beta_{1-42}$ peptides, where one peptide was labeled at the $^{13}C^{\delta}$-Gln15 and the other at the $^{13}C^{\alpha}$-Gly37, the observation of the cross-peak between C^{δ}-Gln15 and C^{α}-Gly37 indicates that β-strand staggering occurs in $A\beta_{1-42}$ fibrils [143], just as observed for $A\beta_{1-40}$ fibrils [132]. Note that for a nonstaggered geometry, the predicted distance between the labeled sites would be longer than the detection limit of DARR.

The architecture of β-sheet is also very important in the determination of fibril structures. Given that the side chains of even-numbered and odd-numbered residues in the same β-sheet point in opposite directions, any side-chain contacts between odd-numbered and even-numbered residues observed in PDSD or DARR spectra may indicate bend structures or intersheet contacts. With this consideration, the quaternary contacts of the basic cross-β units have been found to be different for two morphologically distinct $A\beta_{1-40}$ fibrils [132, 146]. As another example, the quaternary contacts between β-sheets of the nonfibrillar oligomers formed by $PrP_{106-126}$ are found to be similar to those in fibrillar state [130]. Very recently, it has been shown that the band selective RFDR (BASE RFDR), where selective π pulses are used in the RFDR recoupling pulse train, is significantly more efficient than DARR for probing long-range contacts [147]. Another useful technique for the measurement of long-range ^{13}C–^{13}C or ^{15}N–^{15}N distances is the proton assisted recoupling (PAR) technique [148]. The transfer mechanism of PAR is based on the higher order effect, for which the dipolar truncation effect [149] is largely attenuated. The PAR technique has been used to probe the intermolecular backbone contacts of GNNQQNY fibrils and the results are consistent with an in-register parallel alignment [25].

For the determination of heteronuclear long-range contacts, ZF-TEDOR with long mixing time is a promising approach [150]. This method has been used to study the fibrils formed by a 50:50 mixture of [^{15}N,^{12}C]- and [^{14}N,^{13}C]-labeled β_2-microglobulin monomers [151]. At a mixing time of 16 ms, a number of intermolecular ^{13}C–^{15}N distances in the range of 5–5.5 Å have been detected. The results prove that the fibrils adopt an in-register parallel β-sheet structure [151].

4.3 H/D Exchange Detected by Correlation Spectroscopy

We have shown that correlation spectroscopy is of great utility for spectral assignments and for measurement of distance constraints. Here, we show that the ^{13}C–^{15}N correlation spectroscopy can also be exploited to monitor hydrogen/deuterium (H/D) exchange experiments. H/D exchange can be used to identify solvent-protected backbone amide protons in amyloid fibrils [144, 152, 153]. In brief, the amyloid fibrils are first incubated in deuterated buffer. After quenching the H/D exchange, the fibrils must be disaggregated into monomers. The residues at which the amide protons are exchanged to deuterons can then be detected by mass spectrometry [154] or solution-state NMR spectroscopy [155]. The most challenging step is the rapid conversion of the fibrils into the corresponding

monomers for subsequent detection. Although *d*6-DMSO is a reliable solvent for the dissolution of amyloid fibrils, it is not trivial to minimize the effect of backward exchange [155]. Different solvent mixtures have been suggested for different amyloid systems, showing that it is largely an empirical task to prepare the quenching buffer for an H/D exchange experiment [156]. Recently, we find that the dissolution of the amyloid fibrils is not necessary when ^{13}C–^{15}N correlation spectroscopy is used as the detection method [50]. That is, the technique of $^{15}N\{^{1}H\}$ CPMAS can be used to select the signals of the nitrogen atoms which are in close proximity to protons. In particular, when the CP contact time is set to 100 μs, the ^{15}N signals of the deuterated amide groups would be largely suppressed. By this simple strategy, the in situ characterization of H/D exchange in amyloid fibrils could be realized.

As a proof-of-principle experiment, we measured the $^{15}N\{^{1}H\}$ CP spectra of the amyloid fibrils formed by $huPrP_{127–147}$ (Ac-GYMLGSAMSRPIIHFGSDYED-NH_2), which is ^{15}N and ^{13}C labeled at P137 and S143. Figure 9 shows the spectra of the fibril sample (without any H/D exchange) obtained at two contact times, viz. 2 ms and 100 μs. For the 2-ms spectrum, two amide nitrogen signals are observed, in which the peaks at 135 and 117 ppm are assigned to the amide nitrogen of P137 and S143, respectively [89]. When the CP contact time is reduced to 100 μs, the $^{15}N\{^{1}H\}$ CP signal would be dominated by the one-bond ^{1}H–^{15}N transfer, which is referred to as the $^{15}N^{H}$ signal in the subsequent discussion. Accordingly, the $^{15}N^{H}$ signal of P137 is not detectable because proline does not have any amide proton. As expected, the $^{15}N^{H}$ signal of S143 is still observable under the same experimental condition, which has approximately the same intensity as the 2-ms $^{15}N\{^{1}H\}$ signal. Therefore, it is plausible to monitor the H/D exchange of amide protons by measuring the corresponding $^{15}N^{H}$ signals without disassembling the fibrils into monomers. We first define the protection factor of the amide proton as the ratio of the $^{15}N^{H}$ signal intensities of the sample with and without H/D exchange. After

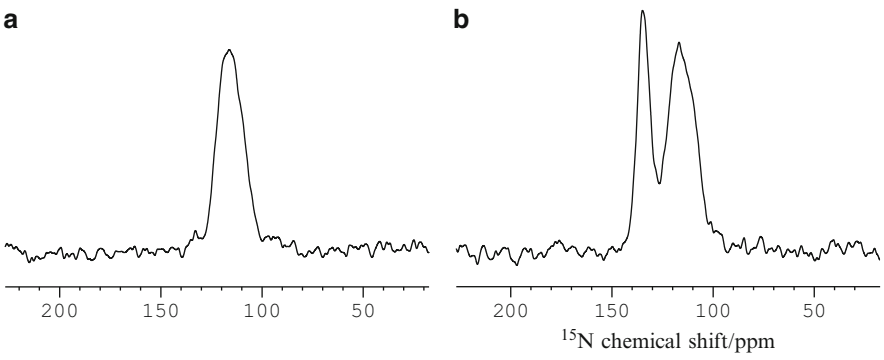

Fig. 9 $^{15}N\{^{1}H\}$ CPMAS spectra of the fibril sample formed by $huPrP_{127–147}$ (^{15}N labeled at P137 and S143) at a spinning frequency of 20 kHz. (**a**) Contact time of 100 μs. (**b**) Contact time of 2 ms. (Figure and caption adapted from [50]. Copyright 2010 WILEY-VCH Verlag GmbH & Co. KGaA, Weinheim)

42-h H/D exchange, the protection factors were found to be 0.07 ± 0.03 and 0.6 ± 0.3 for S143 and I138, respectively. The relatively large errors are mainly due to the uncertainty of the amount of salts left in the samples. To alleviate this problem, we redefine the protection factor as the ratio of the signal intensities of $^{15}N^{H}$ and ^{15}N, where the contact time of the corresponding $^{15}N\{^{1}H\}$ CP experiments were set to 100 μs and 2 ms, respectively. The thus obtained protection factor for I138 is 0.65 ± 0.1. The error bar was determined by the root-mean-square noise of the spectrum. For measurements on uniformly labeled fibril samples, our strategy can be easily combined with 2D $^{13}C\{^{15}N\}$ correlation spectroscopy [50].

5 Recoupling of Chemical Shift Anisotropy

Under MAS alone, anisotropic interactions such as CSA and dipole–dipole couplings are averaged to zero, provided that the spinning frequency is sufficiently high. Since anisotropic interactions usually have a direct or indirect dependence on molecular structure, numerous techniques have been developed to reintroduce these interactions under MAS. Various CSA recoupling techniques have been proposed and their merits have been briefly discussed by Schmidt-Rohr and co-workers [157]. Many of these CSA recoupling methods are not applicable to homonuclear dipole–dipole coupled systems or at MAS frequencies higher than 15 kHz, either because finite-pulse effects become dominant or because the required rf fields become too high to be practical. In this section, we describe the technique of recoupling of chemical shift anisotropy (ROCSA) [158]. The major advantages of ROCSA are: (1) that the effects of homonuclear dipole–dipole interactions are strongly suppressed; (2) that the lineshape of the recoupled CSA pattern is identical to the corresponding static powder pattern; (3) that the required rf field (in kHz) is only about four times the MAS frequency; (4) that only phase shifts in multiples of 90° are required.

5.1 Theory of ROCSA

Under MAS at frequency $\omega_r = 2\pi\nu_r$, the high-field Hamiltonian of a spin-1/2 system takes the following form in the rotating frame:

$$H(t) = H_{\mathrm{rf}}(t) + H_{\mathrm{int}}(t), \tag{11}$$

$$H_{\mathrm{int}}(t) = \sum_{\Lambda m\lambda} \omega_m^{\Lambda} \exp(\mathrm{i}m\omega_r t) T_{\lambda 0}^{\Lambda}, \tag{12}$$

where Λ represents various internal interactions, ω_m^{Λ} are the orientation-dependent coefficients of the Fourier components of the spatial functions ($-2 \leq m \leq 2$), and

$T_{\lambda 0}^{\Lambda}$ are irreducible tensor operators of rank λ. The Hamiltonian of a static powder sample can be easily derived from the MAS Hamiltonian by setting $\omega_r = 0$:

$$H_{\text{int}} = \sum_{\Lambda m \lambda} \omega_m^{\Lambda} T_{\lambda 0}^{\Lambda}. \tag{13}$$

ROCSA makes use of the CN_n^v sequences [82, 159] to generate a static CSA powder pattern under MAS condition. The average Hamiltonian for a CN_n^v sequence is [159]

$$\begin{aligned} \bar{H}(t_q) = & \sum_{\Lambda L m \lambda \mu} (i)^{\mu} \omega_{Lm\lambda\mu}^{\Lambda} \exp(\mathrm{i}m\omega_r t_0)\, d_{\mu 0}^{\lambda}(-\beta_{rf}) \\ & \times \sum_{q} \exp\left(+\mathrm{i}q\frac{2\pi}{N}(mn-\mu v)\right) T_{\lambda\mu}^{\Lambda}. \end{aligned} \tag{14}$$

All the symbols carry their usual meanings. If we want to create an average Hamiltonian similar to the static one, we just need to keep the terms associated with T_{20}^{CS}. Furthermore, the scaling factors of those terms should be identical. With the pulse sequence of Cn_n^1 [160, 161], the symmetry allowed terms are $(m = 0, \pm 1, \pm 2; \mu = 0)$ for $n \geq 3$. For convenience we define the following scaling factors:

$$\chi_m^{\lambda} = \frac{1}{\tau_r} \int_0^{\tau_r} d_{00}^{\lambda}(-\beta_{rf}) \exp(\mathrm{i}m\omega_r t)\mathrm{d}t. \tag{15}$$

We want to derive a specific subcycle for Cn_n^1 such that the scaling factors χ_m^{λ} are identical for m equal to ± 1 and ± 2. In general, we have $\chi_m^{\lambda} = \left(\chi_{-m}^{\lambda}\right)^*$ and therefore the conditions $\chi_m^{\lambda} = \chi_{-m}^{\lambda}$ are equivalent to the conditions that χ_m^{λ} are real numbers. In particular, if we have a mirror symmetry of

$$\beta_{\text{rf}}(t) = \beta_{\text{rf}}(\tau_r - t), \tag{16}$$

for $0 \leq t \leq \tau_r$, we can obtain

$$\chi_m^{\lambda} = \frac{1}{\tau_r} \left\{ \int_0^{\tau_r/2} d_{00}^{\lambda}(-\beta_{\text{rf}}(t)) \exp(\mathrm{i}m\omega_r t)\mathrm{d}t + \int_{\tau_r/2}^{\tau_r} d_{00}^{\lambda}(-\beta_{\text{rf}}(\tau_r - t')) \exp(\mathrm{i}m\omega_r t')\mathrm{d}t' \right\}. \tag{17}$$

Setting $\tau_r - t' = t$ for the second integral, we then have

$$\chi_m^{\lambda} = \frac{1}{\tau_r} \times \left\{ \int_0^{\tau_r/2} d_{00}^{\lambda}(-\beta_{\mathrm{rf}}(t)) \exp(\mathrm{i}m\omega_r t)\mathrm{d}t - \int_{\tau_r/2}^{0} d_{00}^{\lambda}(-\beta_{\mathrm{rf}}(t)) \exp(\mathrm{i}m\omega_r(\tau_r - t))\mathrm{d}t \right\}, \tag{18}$$

$$\chi_m^{\lambda} = \frac{2}{\tau_r} \left\{ \int_0^{\tau_r/2} d_{00}^{\lambda}(-\beta_{\mathrm{rf}}(t)) \cos(m\omega_r t)\mathrm{d}t \right\}. \tag{19}$$

Consequently, under the mirror symmetry described in (16), χ_m^{λ} must be real because

$$d_{00}^{\lambda}(\beta) = \sum_{k=0}^{\lambda} (-1)^k \frac{(\lambda)!(\lambda)!}{(\lambda-k)!k!(\lambda-k)!(k)!} \left(\cos\tfrac{\beta}{2}\right)^{2(\lambda-k)} \left(\sin\tfrac{\beta}{2}\right)^{2k}, \tag{20}$$

where k is an integer.

Now consider the pulse sequence in Fig. 10. Each repetition of C spans one rotor period. Between 0 and $\tau_r/2$, the composite "0π" pulse $90_0360_{180}270_0$ is applied. This composite pulse, which has been commonly referred to as POST, is chosen because it has been shown to compensate for effects of rf inhomogeneity [83]. The mirror-image composite pulse is applied between $\tau_r/2$ and τ_r. With this particular design of ROCSA, the homonuclear dipole–dipole interaction is considerably suppressed relative to the CSA.

5.2 ROCSA Spectra of Amyloid Fibrils

It has been shown both theoretically and experimentally that C^{α} CSA values are useful parameters to probe the local structures of biological systems [162, 163]. By comparison of the experimental CSA values with the calculated shielding surfaces, one may obtain an estimation of the backbone torsion angles of the corresponding residues. As an illustration, Fig. 11 shows the ROCSA spectra measured for the $A\beta_{11-25}$ fibril sample which was uniformly ^{13}C, ^{15}N-labeled at Val18 [158]. Isotropic ^{13}C chemical shift data indicate that Val18, Phe19, Phe20, and Ala21 adopt β-strand conformations in $A\beta_{11-25}$ fibrils. The C^{α} CSA values obtained by ROCSA measurements are consistent with β-strand conformations at these residues. As illustrated in the studies of microcrystalline proteins, ROCSA can be used to obtain structural constraints on the secondary structure by characterizing the chemical shift tensors of the backbone carbons [163]. We expect that such an approach should also find fruitful applications in the study of amyloid fibrils.

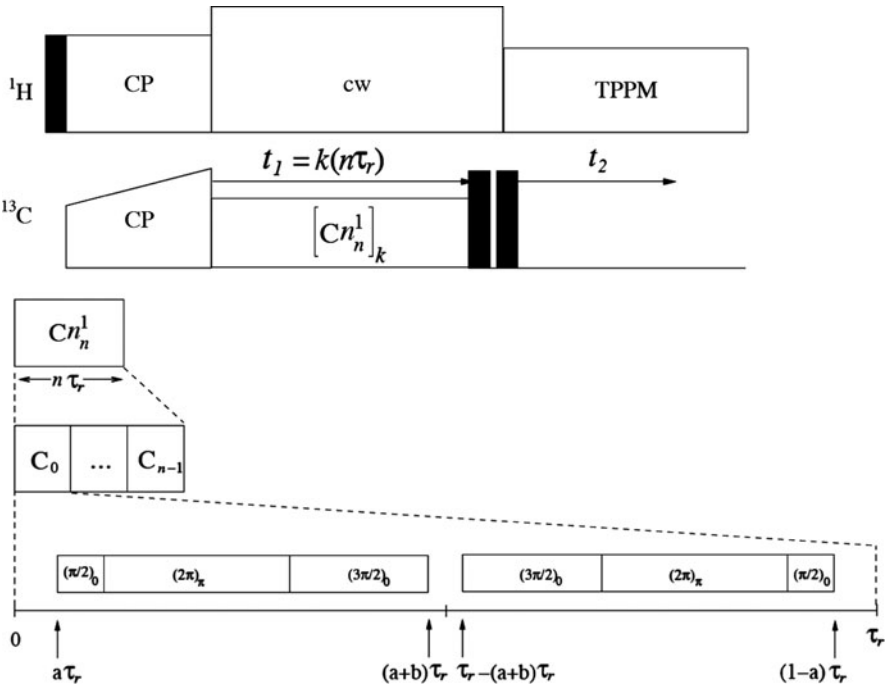

Fig. 10 ROCSA pulse sequence based on Cn_n^1 symmetry. The *rectangular blocks* in *black* represent $\pi/2$ pulses. The recoupling period (t_1) comprises k cycles of Cn_n^1. Each complete cycle of Cn_n^1 spans n rotor periods ($n\tau_R$). The rf phase of each C_q subcycle is set equal to $2\pi q/n$, where q is an index running from 0 to $n - 1$. Within each C_q subcycle, $a\tau_R$ and $b\tau_R$ indicate the position and the duration of the POST composite pulse, respectively. We find that the solution $(a, b) = (0.0329, 0.467)$ is a favorable choice for the suppression of the homonuclear dipole–dipole interaction. The *bracketed* and *subscripted values* indicate the pulse length and rf phase in radians, respectively. (Figure and caption adapted from [158]. Copyright [2003], American Institute of Physics)

For polypeptides with inherent structural disorders, the ^{13}C signals in the carbonyl region are usually poorly resolved. Therefore, the characterization of the C′ CSA, which is sensitive to the C = O. . .HN hydrogen bond strength, will become very difficult if more than one carbonyl carbon are ^{13}C labeled. Because the C^α signals of polypeptides are usually better resolved than the C′ signals, one may transfer the C′ CSA patterns to the neighboring C^α for subsequent detection. This "C^α-detection" scheme has been developed on the basis of ROCSA and R-TOBSY [164]. That is, the C′ CSA is first recoupled by ROCSA and then the pattern is transferred to C^α for detection by R-TOBSY. Dipolar-based polarization transfer techniques such as fpRFDR are not suitable in the present context because the C′–C^α dipolar interaction will modulate the C′ CSA pattern and such modulation may depend on the relative orientation of the C′ and C^α chemical shift tensors, which is usually unknown. Figure 12 shows the C^α-detected C′ CSA patterns of the amyloid fibrils formed by the peptide fragment of $PrP_{109–122}$, in which the residues

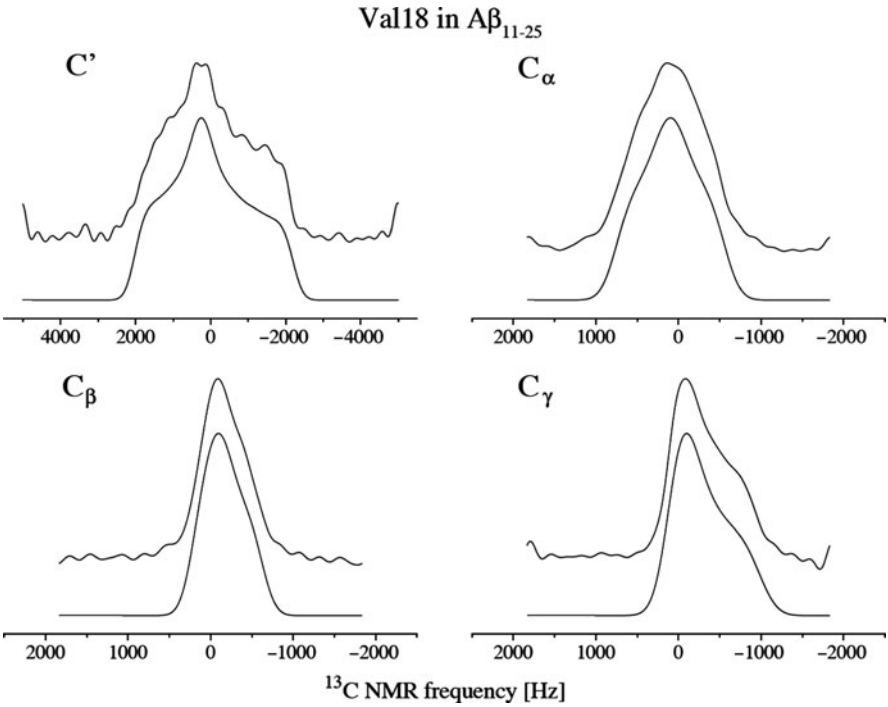

Fig. 11 ROCSA spectra for Val-18 of $A\beta_{11-25}$ fibrils. The C′ spectrum was measured at 9.39 T under a MAS frequency of 20 kHz. The other spectra were measured at 14.09 T under the frequency of 11 kHz. *Upper traces* are experimental spectra. *Lower traces* are best-fit simulations for one-spin system. The rf carrier frequency is at 0 Hz. (Figure and caption adapted from [158]. Copyright [2003], American Institute of Physics)

Ala113, Gly119, and Val122 are uniformly ^{13}C- and ^{15}N-labeled [164]. The C′ signals of Ala113 and Val122 are overlapping but their C^{α} signals are well resolved. The minor distortion of the C′ CSA pattern of Val122 may be attributed to the structural disorder at the C terminus of the polypeptide. Studies on other model compounds indicate that the C^{α}-detection scheme for C′ CSA pattern is a robust one, as long as the spin-lattice relaxation times of the C′ and C^{α} signals are significantly longer than the polarization transfer period. Again, the idea of C^{α}-detection can be incorporated easily in existing homonuclear correlation techniques.

6 Tensor Correlation Methods

Tensor correlation methods refer to the selection of two anisotropic interactions so that the pattern of the 2D correlation spectrum can reveal the magnitudes and relative orientation of the two tensorial interactions. Below we will discuss many different SSNMR techniques suggested for the determination of peptide backbone

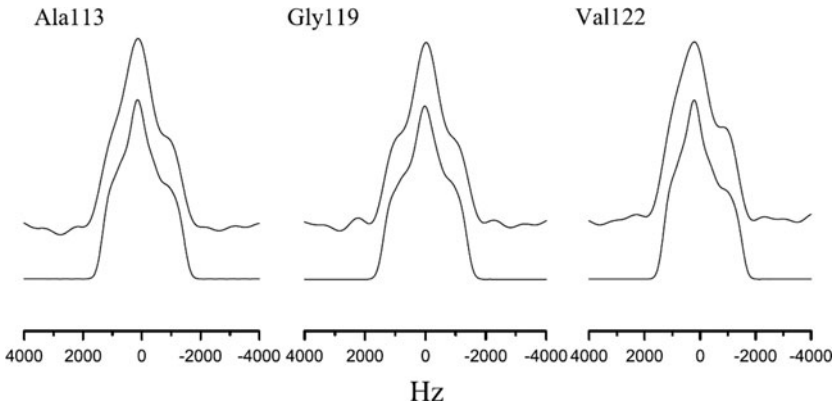

Fig. 12 C_α-detected C′ CSA patterns of the $SHPrP_{109–122}$ fibril sample. The *upper* and *lower traces* correspond to the experimental and simulated spectra, respectively. Simulations correspond to the evolution of a one-spin system under the ROCSA sequence. The only variables are the chemical shift anisotropy and the asymmetry parameter. A Gaussian window function of 400 Hz was applied to the simulated spectrum before the Fourier transformation. (Figure and caption adapted from [164]. Copyright (2007), with permission from Elsevier)

torsion angles ϕ and ψ under MAS. These techniques are all based on the principle of tensor correlation [165–167].

6.1 Backbone Phi–Psi Angle Determination

The correlation of the chemical shift tensors of two neighboring carbonyl carbons, say, $C'_{(i)}$ and $C'_{(i+1)}$, can be exploited to determine the backbone torsion ϕ and ψ angles of the residue $i + 1$. Because of the symmetry properties of the C′ chemical shift tensor and the peptide plane, this approach cannot distinguish the conformations corresponding to (ϕ, ψ) and $(-\phi, -\psi)$ [168]. That is, a unique solution for (ϕ, ψ) is not warranted in general, unless the alternative solution is not allowed sterically. The first technique which exploits this correlation approach is the 2D MAS exchange experiment [168, 169]. Other useful techniques include DQDRAW [56, 170] and DQCSA [171]. The utility of these methods relies on the assumption that the orientation of the C′ chemical shift tensor with respect to the peptide plane is insensitive to the variation of the peptide conformation and the formation of hydrogen bonds. Theoretical calculations carried out for a model glycyl–glycine dipeptide at the DFT-IGLO level lend strong support to this basic assumption [172]. On the other hand, it has been shown by NMR measurements on model peptides that the most shielded principal component (δ_{33}) is always perpendicular to the peptide plane, whereas the orientation of the principal components lying in the peptide plane has a variation of about 25° [173–179]. A more comprehensive discussion of this issue can be found in a recent review [180]. Thus, the systematic

errors of the backbone torsion angles determined by the $C'_{(i)}$–$C'_{(i+1)}$ approach are mainly due to the uncertainty in the tensor orientation of the C′ carbon. Nonetheless, the intrinsic structural inhomogeneity commonly found in amyloid fibrils would presumably render this uncertainty immaterial. The major disadvantage of this method is that each labeled sample can allow the determination of one pair of ϕ and ψ angles only.

For the study of $A\beta_{1-40}$ fibrils, it is very important to characterize the conformation of the non-β-sheet region (residues 25–29) in order to construct the molecular model for the fibrils. On the basis of the measurements of 2D MAS exchange and DQCSA, site specific torsion angles were obtained for the bend region of $A\beta_{1-40}$ fibrils [57]. Because of the multiplicity in the sign choices for the obtained ϕ and ψ angles, however, dimensional constraints obtained from EM images and the structural constraint that corresponds to the salt bridge formed between D23 and K28 are required to deduce a unique molecular conformation for the bend region [57].

6.2 Backbone Psi Angle Determination

A direct determination of the backbone ψ angle can be obtained by the tensor correlation of the $N_{(i)}$–$C^{\alpha}_{(i)}$ and $C'_{(i)}$–$N_{(i+1)}$ vectors. One possibility is to excite the DQ coherence between $C^{\alpha}_{(i)}$ and $C'_{(i)}$ and then let the DQ coherence evolve under the influence of the heteronuclear ^{13}C–^{15}N dipole–dipole interaction [181, 182]. The virtue of this design is that it can be easily combined with other resolution enhancement technique such as INADEQUATE [183]. Alternatively, the magnetization of $C'_{(i)}$ dephased under the ^{13}C–^{15}N dipolar coupling can be transferred to $C^{\alpha}_{(i)}$ for another period of ^{13}C–^{15}N dipolar dephasing [183]. This idea can be combined with the NCOCA experiment so that the superior resolution provided by the $C^{\alpha}_{(i)}$–$N_{(i+1)}$ correlation could be exploited. The overall efficiency, however, is relatively low due to the use of two polarization-transfer steps, viz. $^{15}N \rightarrow {}^{13}C$ and $^{13}C \rightarrow {}^{13}C$ [183]. In comparison with the $C'_{(i)}$–$C'_{(i+1)}$ techniques, the advantage of the $N_{(i)}$–$C^{\alpha}_{(i)}$–$C'_{(i)}$–$N_{(i+1)}$ is that multiple ψ angles can be obtained from a uniformly labeled system [183]. Note that this so-called NCCN experiment cannot distinguish the sign of ψ and the most sensitive region is $|\psi|$ equal to 140–180° [181]. To remove the sign ambiguity in ψ, one can resort to the correlation experiments of different symmetries such as $H^{\alpha}_{(i)}$–$C^{\alpha}_{(i)}$–$N_{(i+1)}$–$H^{N}_{(i+1)}$ [184]. Strictly speaking, the correlation of the $H^{\alpha}_{(i)}$–$C^{\alpha}_{(i)}$ and $N_{(i+1)}$–$H^{N}_{(i+1)}$ vectors would depend on both the backbone ψ and ω angles, but the deviation of ω from the ideal values, i.e., 180° for *trans* and 0° for *cis* conformations, should be very small in most cases. The above pulse frameworks are very general and different heteronuclear or homonuclear dipolar recoupling schemes can be incorporated in them for the backbone or side-chain torsion angle determinations [184]. The NCCN technique has been applied to study the backbone ψ angles of the GNNQQNY fibrils [25]. The results indicate that there is a localized non-β-sheet structure at residue N8 in one of the three fibril conformers.

All the techniques we have discussed thus far for ψ determination require isotopic labeling of two consecutive residues. Nevertheless, it has been demonstrated that the backbone torsion ψ angle can be determined within a single ^{13}C uniformly-labeled residue [185, 186]. The method, with the acronym RACO for relayed anisotropy correlation, comprises three basic modules, viz. the CSA recoupling of C′, the polarization transfer from C′ to C^{α}, and the heteronuclear $^{13}C^{\alpha}$–$^{1}H^{\alpha}$ dipolar recoupling [186]. That is, the backbone torsion ψ angle can be determined by correlating the carbonyl ^{13}C chemical shift and the $^{13}C^{\alpha}$–$^{1}H^{\alpha}$ dipolar tensors within a single ^{13}C uniformly-labeled residue. In its original implementation, RACO requires the acquisition of a series of 2D spectra under the heteronuclear dipolar recoupling condition and therefore is not applicable for systems with multiple uniformly ^{13}C labeled residues. This limitation of RACO can be easily alleviated by separating the heteronuclear dipolar recoupling and the t_2 acquisition periods, and by choosing recoupling pulse sequences designed for fast MAS [187]. However, without a detailed understanding of the basic principles of tensor correlation, it is not trivial to obtain the optimized implementation of RACO by trial and error because there are many different recoupling pulse sequences reported in the literature [63].

6.2.1 Echo Formation Between Two Correlated Anisotropic Interactions

In the following, we present a simple physical picture to illustrate some general features of the RACO approach. As mentioned above, the backbone ψ angle can be determined by correlating the C′ chemical shift anisotropy and the C^{α}–H^{α} dipolar interaction. Both interactions are anisotropic, i.e., the NMR signal evolving under the influence of either interaction will decay (or dephase) to zero in a powder sample. After the polarization transfer between C′ and C^{α}, the signal dephased in the first period may be partially refocused in the second period. The extent of the "echo" formation depends on whether the orientation dependence of the average Hamiltonians during the CSA and dipolar recoupling periods are in close resemblance [188]. In other words, the "echo" amplitude depends on: (1) the orientation dependence of the average Hamiltonian; (2) the durations of the two dephasing periods; (3) the relative orientation of the two internal interactions, which is implicitly related to the backbone ψ angle. When the recoupling pulse sequences for the CSA and the heteronuclear dipolar interactions are γ-encoded where the spatial parts $m = 2$ are selected, the extent of the resemblance of the two average Hamiltonians has a strong dependence on the ψ angle, and one could then accurately determine the ψ angle by comparing the experimental echo amplitude and the results simulated based on the model spin system, which is usually set as C′–C^{α}–H^{α}. For convenience, experimentally we chose to use the FSLG technique which is a non-γ-encoded sequence for heteronuclear dipolar recoupling. Nevertheless, γ-encoded sequences such as $R18_2^5$ should be a good alternative option [108, 189]. Furthermore, to ensure the closest resemblance of the two average Hamiltonians, the homonuclear polarization transfer inserted

between the two recoupling periods should be isotropic. That is, the R-TOBSY sequence is a favorable choice for the homonuclear polarization transfer in the present context.

The experimental strategy discussed above was applied to determine the dihedral angle of uniformly ^{13}C and ^{15}N labeled L-alanine and *N*-acetyl-D,L-valine (NAV) samples. The $^{13}C' \rightarrow C^{\alpha}$ peak intensities of three separate experiments corresponding to zero, one, and two complete cycles of CSA recoupling were measured while the dipolar recoupling period was fixed at three rotor periods [188]. The experimental data were normalized by the first data point (no CSA recoupling) and then compared with the numerical simulations carried out in the same fashion as discussed earlier. Due to the symmetry properties of the C′ CSA and the C^{α}–H^{α} dipolar interactions, the plot of squared deviations (χ^2) between experimental and simulation data will have reflection symmetries about −150, −60, 30, and 120° [186]. Minimum χ^2 values for L-alanine and NAV occur at ψ equal to 160 (161.5) and 175 (178.2)°, respectively, where the bracketed values correspond to the crystallographic data obtained by diffraction techniques [190, 191].

For the fibril samples formed by the H1 fragment of the Syrian hamster prion protein ($SHPrP_{109–122}$, Ac-MKHMAGAAAAGAVV-NH_2), the backbone ψ angles of the alanine residues in the AGAAAAGA region were determined by the tensor correlation method based on the RACO approach [52]. The C′ CSA of A113 was characterized by the ROCSA incorporated with the C^{α}-detection scheme [164] and it was assumed that the C′ CSAs of all the alanine residues with β-strand conformation are approximately the same. Additional simulations show that the ψ angle determination is indeed not sensitive to the C′ CSA. As a matter of the inherent symmetry of the tensors being correlated, there are two set of ψ angles which have the best agreement with the experimental data. One is in the range of 75–100°, whereas another one is in the β-sheet region. In this particular case, the secondary chemical shift (δ–δ_{random}) data have shown that the AGAAAAGA region has the β-sheet conformation. Consequently, the ψ angles of the palindrome region were obtained with high precision, which had been used as the benchmark data for the subsequent molecular dynamics simulations [52].

6.3 Backbone Phi Angle Determination

The backbone ϕ angle can be determined by the correlation of the N–H^N and C^{α}–H^{α} dipolar tensors [184, 192, 193]. The strategy of the earliest attempt is to create the ^{15}N–^{13}C multiple-quantum coherence by REDOR and then let the coherence evolve under the scaled heteronuclear dipole–dipole interaction generated by MREV-8 [193]. As the technique of MREV-8 is designed for applications under static conditions, the phase evolution will be modulated by MAS. In other words, the dipolar dephasing during the first half of the rotor period will be refocused in the second half. Consequently, the spinning frequency must be less than 3 kHz so that the dephasing period is long enough to reveal the angular

dependence on ϕ with sufficient resolution. As a logical extension of the original approach, it has been shown that the effective dephasing time of MREV-8 can be lengthened by insertion of rotor-synchronized π pulses in the ^{13}C or ^{15}N channels [192]. The idea is quite similar to REDOR because the average Hamiltonian of the heteronuclear dipole–dipole interaction generated by MREV-8 has the operator form of I_zS_z [193]. Consequently, the double coupling scheme can be applied under moderate spinning condition as long as the quasi-static approximation is still valid (ca. 10 kHz). For higher spinning frequency, the time modulation of the spatial part of the Hamiltonian (due to MAS) will interfere with the averaging process of MREV-8 in the spin part. That is, the averaging of the undesired homonuclear dipole–dipole interaction will become less effective. Because the one-bond dipolar coupling constant of $N–H^N$ is smaller than that of $C^\alpha–H^\alpha$ by approximately a factor of 2, the correlation of the two tensors will have a stronger dependence on the ϕ angle when the dipolar dephasing period of $N–H^N$ is doubled compared with that of $C^\alpha–H^\alpha$. This double coupling scheme has been realized by preparing two separate dephasing periods for the corresponding antiphase signals [192].

Taking the MREV-8 as a basic C element (duration $= \tau_r/5$), one can generate a γ-encoded [194] version of MREV-8 by concatenating the five C elements with an rf phase set equal to $k \times 2\pi/5$, where $k = 0$–4 [107]. The averaged Hamiltonian calculated to the lowest order for this so-called T-MREV method has the following form:

$$\bar{H}_{IS} = \{\kappa\bar{\omega}_{m=-1}I_+ + \kappa^*\bar{\omega}_{m=+1}I_-\}S_z, \tag{21}$$

where $I_\pm$ denote the spin operators for protons, κ is the scaling factor of the pulse sequence, and $\bar{\omega}_m$ denotes the spatial part of the average Hamiltonian [107]. The advantage of (21) is that the time dependence of both the spatial and spin parts has been considered and therefore the dephasing of the magnetization is cumulative over the whole irradiation period. As the T-MREV is constructed based on MREV-8, its application is also limited to spinning frequency under 10 kHz. This drawback can be alleviated by using recoupling sequence such as $R18_2^5$ [108, 189]. In general, the use of γ-encoded sequences for the heteronuclear dipolar recoupling requires a proper account of the different T_2 relaxation rates of the I and S states [107]. Based on T-MREV, a 3D $^1H–^{15}N–^{13}C–^1H$ dipolar chemical shift experiment has been constructed for the ϕ angle determination as shown in Fig. 13. In fact, the same experimental framework can be used for the ψ angle determination by the $H^\alpha_{(i)}–C^\alpha_{(i)}–N_{(i+1)}–H^N_{(i+1)}$ correlation [184].

The molecular structure of the amyloid fibrils formed by fragment 105–115 of transthyretin ($TTR_{105–115}$, YTIAALLSPTS) has been characterized by solid-state NMR. The fibril backbone structure was first established based on the TALOS analysis of the ^{15}N and ^{13}C chemical shifts [89]. Using the correlation experiments of $H^N_{(i)}–N_{(i)}–C^\alpha_{(i)}–H^\alpha_{(i)}$, $H^\alpha_{(i)}–C^\alpha_{(i)}–N_{(i+1)}–H^N_{(i+1)}$, and $N_{(i)}–C^\alpha_{(i)}–C'_{(i)}–N_{(i+1)}$, a total of 41 constraints on 19 backbone torsion angles have been obtained in a

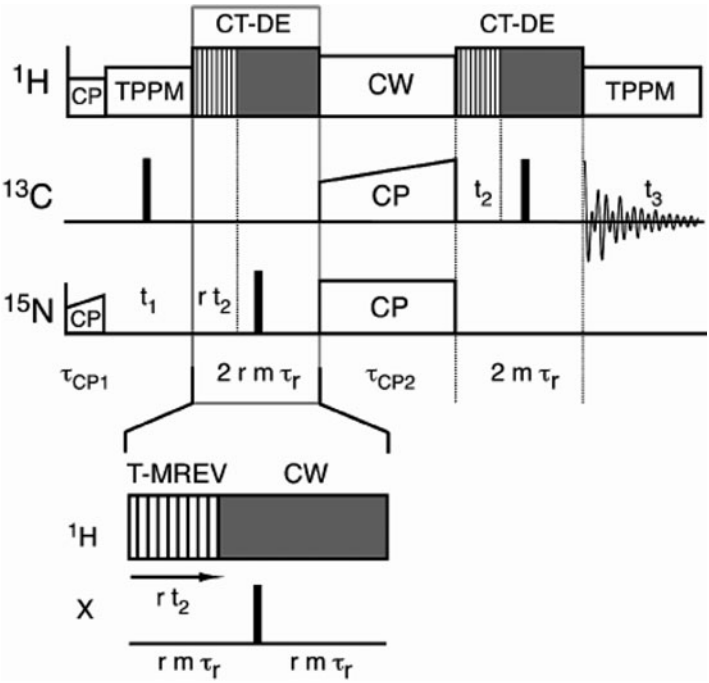

Fig. 13 Pulse sequence for the 3D ^{1}H–^{15}N–^{13}C–^{1}H dipolar chemical shift experiment to constrain backbone and side-chain torsion angles. Polarization was transferred from ^{1}H to ^{15}N via ramped CP, followed by ^{15}N chemical shift evolution during t_1. The period rt_2 was a constant time dipolar recoupling period, composed of an integer number of rotor periods during which T-MREV is applied to the ^{1}H spins. Polarization was subsequently transferred from ^{15}N to ^{13}C by amplitude-ramped SPECIFIC CP, and a second constant time T-MREV recoupling period, t_2, was applied to the transverse ^{13}C coherences. Signal acquisition occurred during the period t_3. The ratio of ^{1}H–^{15}N to ^{1}H–^{13}C dipolar evolution (r) was a fixed integer value, optimally 2. *Narrow* and *wide solid rectangles* represent π/2 and π pulses, respectively. The phase cycling scheme can be found in the original figure and caption. (Figure and caption adapted from [184]. Copyright 2002 American Chemical Society)

subsequent study [104]. In addition, the torsion angles of most side chains have been constrained by the long-range C–N distances obtained by the 3D *z*-filtered TEDOR. Overall, a high-resolution structure of $TTR_{105–115}$ in the fibrillar state has been obtained [104], from which there are two interesting findings. First, the conformations of the backbone and side chains are very close to the regions of minimum intramolecular energy. Apparently, no significant energy barrier is present regarding to the conformational change of the monomer during the fibrillization of $TTR_{105–115}$. Second, the residues P113 and T114 have adopted the β-sheet conformation, although the restricted ϕ angle of proline precludes the formation of regular intermolecular hydrogen bondings at the sites of P113 and T114.

7 Conclusion and Outlook

Thanks to the pioneering works of many research groups, solid-state NMR is now a well established spectroscopy for the study of biological solids, particularly for those with inherent structural disorder such as amyloid fibrils. We have provided an overview of a rather complete set of NMR techniques which have developed for samples prepared by chemical synthesis or protein expression. There are many different ways to present the materials discussed in this review. We hope that the way we have chosen can give a snapshot of some facets of the very exciting discipline of biological solid-state NMR spectroscopy. In spite of the success of solid-state NMR as a tool in biological study, it is not yet a "mature" technique and there is much room for further development. Below we will speculate on a few possibilities from our own perspective.

To maximize the information content for each sample, the isotopic labeling scheme is preferred to be the uniform one. Because long-range contacts are the most important structural constraints, which can only be probed by dipolar-based techniques, further development in the suppression of the dipolar truncation effect and frequency-selective techniques is highly desirable for uniformly labeled samples. Polarization transfer between ^{13}C and ^{15}N is the key step in many pulse sequences. Techniques such as proton assisted insensitive nuclei cross polarization (PAIN-CP) [195] are promising candidates for the design of more efficient heteronuclear correlation experiments. Determination of backbone and side-chain torsion angles is always an important issue in solid-state NMR. Although some very useful techniques have been developed as discussed in this review, it is worthwhile to search for the possibility to characterize uniquely the ϕ and ψ angles in a singly uniformly labeled residue. It can be envisioned that other tensor correlation techniques such as $C^{\alpha}H$–$C'N$ [196] and NH^{N}–NH^{N} [197], which are not covered in this review, may find fruitful applications. A research area which is of great interest is the regime of very fast MAS ($\geq$40 kHz). Recoupling techniques developed for this regime are presumably less susceptible to the higher-order effects. As discussed in the chapter by Nielsen et al. [201] the optimal control theory has opened up a new avenue for the design of pulse sequence. The optimal control software has been implemented in the open-source SIMPSON package [198], which may be used to optimize the performance of many existing recoupling techniques. The importance of ^{14}N is clearly underrepresented in biological NMR. Nevertheless, some promising techniques have been reported in the literature as discussed in the chapter by Fernandez and Pruski [199]. Needless to say, dynamic nuclear polarization (DNP) is an exciting option for signal enhancement in the NMR studies of biological samples [200]. All in all, it can be safely concluded that biological solid-state NMR will remain as a vibrant field for many years to come.

Acknowledgment This work was supported by the National Science Council of Taiwan. I would like to take this opportunity to thank Dr. Robert Tycko (NIH, Bethesda, USA) for introducing me to the field of amyloid fibrils. I also thank my former students Yun Mou, John Chin-Hao Chao, Tim Wen-Tin Tsai, Shin-Wen Lee, Ni-Shian Lin, Fang-Chieh Chou, Hsin-Mei Cheng, Wen-Chi Chu,

Yun-Ju Tang, Huei-Ying Lian, Hsin-Kuan Lee, Tzu-Hsueh Huang, and Yuan-Chi Huang for their many contributions in our own study of amyloid fibrils.

References

1. Dobson CM (2003) Nature 426:884
2. Chiti F, Dobson CM (2006) Annu Rev Biochem 75:333
3. Spencer RGS, Halverson KJ, Auger M, McDermott AE, Griffin RG, Lansbury PT (1991) Biochemistry 30:10382
4. Tycko R (2006) Q Rev Biophys 39:1
5. Heise H (2008) ChemBioChem 9:179
6. Tycko R (2000) Curr Opin Chem Biol 4:500
7. Tycko R (2001) Annu Rev Phys Chem 52:575
8. Tycko R (2003) Biochemistry 42:3151
9. Tycko R (2003) Prog Nucl Magn Reson Spectrosc 42:53
10. Tycko R, Ishii Y (2003) J Am Chem Soc 125:6606
11. Tycko R (2004) Curr Opin Struct Biol 14:96
12. Naito A, Kawamura I (2007) Biochim Biophys Acta 1768:1900
13. Lansbury PT, Costa PR, Griffiths JM, Simon EJ, Auger M, Halverson KJ, Kocisko DA, Hendsch ZS, Ashburn TT, Spencer RGS et al (1995) Nat Struct Biol 2:990
14. Griffiths JM, Ashburn TT, Auger M, Costa PR, Griffin RG, Lansbury PT (1995) J Am Chem Soc 117:3539
15. Costa PR, Kocisko DA, Sun BQ, Lansbury PT, Griffin RG (1997) J Am Chem Soc 119:10487
16. Raleigh DP, Levitt MH, Griffin RG (1988) Chem Phys Lett 146:71
17. Levitt MH, Raleigh DP, Creuzet F, Griffin RG (1990) J Chem Phys 92:6347
18. Gregory DM, Benzinger TLS, Burkoth TS, Miller-Auer H, Lynn DG, Meredith SC, Botto RE (1998) Solid State Nucl Magn Reson 13:149
19. Walsh P, Simonetti K, Sharpel S (2009) Structure 17:417
20. Sawaya MR, Sambashivan S, Nelson R, Ivanova MI, Sievers SA, Apostol MI, Thompson MJ, Balbirnie M, Wiltzius JJW, McFarlane HT et al (2007) Nature 447:453
21. Ramachandran R, Ladizhansky V, Bajaj VS, Griffin RG (2003) J Am Chem Soc 125:15623
22. Costa PR, Sun BQ, Griffin RG (2003) J Magn Reson 164:92
23. Ramachandran R, Lewandowski JR, van der Wel PCA, Griffin RG (2006) J Chem Phys 124:214107
24. van der Wel PCA, Lewandowski JR, Griffin RG (2007) J Am Chem Soc 129:5117
25. van der Wel PCA, Lowandowski JR, Griffin RG (2010) Biochemistry 49:9457
26. Gregory DM, Mitchell DJ, Stringer JA, Kiihne S, Shiels JC, Callahan J, Mehta MA, Drobny GP (1995) Chem Phys Lett 246:654
27. Mehta MA, Gregory DM, Kiihne S, Mitchell DJ, Hatcher ME, Shiels JC, Drobny GP (1996) Solid State Nucl Magn Reson 7:211
28. Benzinger TLS, Gregory DM, Burkoth TS, Miller-Auer H, Lynn DG, Botto RE, Meredith SC (1998) Proc Natl Acad Sci USA 95:13407
29. Caporini MA, Bajaj VS, Veshtort M, Fitzpatrick A, MacPhee CE, Vendruscolo M, Dobson CM, Griffin RG (2010) J Phys Chem B 114:13555
30. Gregory DM, Wolfe GM, Jarvie TP, Sheils JC, Drobny GP (1996) Mol Phys 89:1835
31. Liu P, Ni R, Mehta AK, Childers WS, Lakdawala A, Pingali SV, Thiyagarajan P, Lynn DG (2008) J Am Chem Soc 130:16867
32. Childers WS, Mehta AK, Ni R, Taylor JV, Lynn DG (2010) Angew Chem Int Ed Engl 49:4104

33. Karlsson T, Popham JM, Long JR, Oyler N, Drobny GP (2003) J Am Chem Soc 125:7394
34. Schmedt auf der Gunne J, Eckert H (1998) Chem Eur J 4:1762
35. Gullion T, Vega S (1992) Chem Phys Lett 194:423
36. Bennett AE, Ok JH, Griffin RG, Vega S (1992) J Chem Phys 96:8624
37. Bennett AE, Rienstra CM, Griffiths JM, Zhen WG, Lansbury PT, Griffin RG (1998) J Chem Phys 108:9463
38. Ishii Y (2001) J Chem Phys 114:8473
39. Bennett AE, Weliky DP, Tycko R (1998) J Am Chem Soc 120:4897
40. Waugh JS, Huber LM, Haeberle U (1968) Phys Rev Lett 20:180
41. Ishii Y, Balbach JJ, Tycko R (2001) Chem Phys 266:231
42. Balbach JJ, Petkova AT, Oyler NA, Antzutkin ON, Gordon DJ, Meredith SC, Tycko R (2002) Biophys J 83:1205
43. Petkova AT, Ishii Y, Balbach JJ, Antzutkin ON, Leapman RD, Delaglio F, Tycko R (2002) Proc Natl Acad Sci USA 99:16742
44. Antzutkin ON, Leapman RD, Balbach JJ, Tycko R (2002) Biochemistry 41:15436
45. Chan JCC, Oyler N, Yau WM, Tycko R (2005) Biochemistry 44:10669
46. Shewmaker F, Wickner RB, Tycko R (2006) Proc Natl Acad Sci USA 103:19754
47. Luca S, Yau WM, Leapman R, Tycko R (2007) Biochemistry 46:13505
48. Wickner RB, Dyda F, Tycko R (2008) Proc Natl Acad Sci USA 105:2403
49. Wasmer C, Lange A, Van Melckebeke H, Siemer AB, Riek R, Meier BH (2008) Science 319:1523
50. Lin NS, Chao JCH, Cheng HM, Chou FC, Chang CF, Chen YR, Chang YJ, Huang SJ, Chan JCC (2010) Chem Eur J 16:5492
51. Tycko R, Sciarretta KL, Orgel J, Meredith SC (2009) Biochemistry 48:6072
52. Lee SW, Mou Y, Lin S-Y, Chou F-C, Tseng W-H, Chen C-H, Yu SS-F, Lu C-YD, Chan JCC (2008) J Mol Biol 378:1142
53. Shewmaker F, Kryndushkin D, Chen B, Tycko R, Wickner RB (2009) Biochemistry 48: 5074
54. Tycko R, Savtchenko R, Ostapchenko VG, Makarava N, Baskakov IV (2010) Biochemistry 49:9488
55. Tycko R (2007) J Chem Phys 126:064506
56. Bower PV, Oyler N, Mehta MA, Long JR, Stayton PS, Drobny GP (1999) J Am Chem Soc 121:8373
57. Antzutkin ON, Balbach JJ, Tycko R (2003) Biophys J 84:3326
58. Weitekamp DP (1983) In: Waugh JS (ed) Advances in magnetic resonance. Academic, New York, pp 111
59. Antzutkin ON, Balbach JJ, Leapman RD, Rizzo NW, Reed J, Tycko R (2000) Proc Natl Acad Sci USA 97:13045
60. Oyler NA, Tycko R (2002) J Phys Chem B 106:8382
61. Eden M, Brinkmann A, Luthman H, Eriksson L, Levitt MH (2000) J Magn Reson 144:266
62. Baldus M (2002) Prog Nucl Magn Reson Spectrosc 41:1
63. Schnell I (2004) Prog Nucl Magn Reson Spectrosc 45:145
64. Ramamoorthy A, Fujiwara T, Nagayama K (1993) J Magn Reson A 104:366
65. Baldus M, Meier BH (1996) J Magn Reson A 121:65
66. Baldus M, Iuliucci RJ, Meier BH (1997) J Am Chem Soc 119:1121
67. Lesage A, Auger C, Caldarelli S, Emsley L (1997) J Am Chem Soc 119:7867
68. Verel R, van Beek J, Meier BH (1999) J Magn Reson 140:300
69. Lesage A, Bardet M, Emsley L (1999) J Am Chem Soc 121:10987
70. Heindrichs ASD, Geen H, Giordani C, Titman JJ (2001) Chem Phys Lett 335:89
71. Hardy EH, Verel R, Meier BH (2001) J Magn Reson 148:459
72. Chan JCC, Brunklaus G (2001) Chem Phys Lett 349:104
73. Hardy EH, Detken A, Meier BH (2003) J Magn Reson 165:208
74. Ernst M, Detken A, Bockmann A, Meier BH (2003) J Am Chem Soc 125:15807

75. Mueller LJ, Elliott DW, Leskowitz GM, Struppe J, Olsen RA, Kim K-C, Reed CA (2004) J Magn Reson 168:327
76. Duma L, Lai WC, Carravetta M, Emsley L, Brown SP, Levitt MH (2004) ChemPhysChem 5:815
77. Ishii Y, Ashida J, Terao T (1995) Chem Phys Lett 246:439
78. Yannoni CS, Kendrick RD (1981) J Chem Phys 74:747
79. Hughes CE, Luca S, Baldus M (2004) Chem Phys Lett 385:435
80. Mou Y, Chao JCH, Chan JCC (2006) Solid State Nucl Magn Reson 29:278
81. Mou Y, Chan JCC (2006) Chem Phys Lett 419:144
82. Lee YK, Kurur ND, Helmle M, Johannessen OG, Nielsen NC, Levitt MH (1995) Chem Phys Lett 242:304
83. Hohwy M, Jakobsen HJ, Eden M, Levitt MH, Nielsen NC (1998) J Chem Phys 108:2686
84. Paravastu AK, Tycko R (2006) J Chem Phys 124:194303
85. Hu KN, Tycko R (2009) J Chem Phys 131:045101
86. Gullion T, Schaefer J (1989) J Magn Reson 81:196
87. Gullion T (1998) Concepts Magn Reson 10:277
88. Gullion T, Vega AJ (2005) Prog Nucl Magn Reson Spectrosc 47:123
89. Jaroniec CP, MacPhee CE, Astrof NS, Dobson CM, Griffin RG (2002) Proc Natl Acad Sci USA 99:16748
90. Anderson RC, Gullion T, Joers JM, Shapiro M, Villhauer EB, Weber HP (1995) J Am Chem Soc 117:10546
91. Nelson R, Sawaya MR, Balbirnie M, Madsen AO, Riekel C, Grothe R, Eisenberg D (2005) Nature 435:773
92. Jaroniec CP, Tounge BA, Herzfeld J, Griffin RG (2001) J Am Chem Soc 123:3507
93. Li Y, Wylie BJ, Rienstra CM (2006) J Magn Reson 179:206
94. Perutz MF (1996) Curr Opin Struct Biol 6:848
95. Perutz MF, Staden R, Moens L, Debaere I (1993) Curr Biol 3:249
96. Perutz MF, Pope BJ, Owen D, Wanker EE, Scherzinger E (2002) Proc Natl Acad Sci USA 99:5596
97. Wagner A, Luger P (2001) J Mol Struct 595:39
98. Gullion T, Baker DB, Conradi MS (1990) J Magn Reson 89:479
99. Bennett AE, Rienstra CM, Auger M, Lakshmi KV, Griffin RG (1995) J Chem Phys 103:6951
100. Sorensen OW, Eich GW, Levitt MH, Bodenhausen G, Ernst RR (1983) Prog Nucl Magn Reson Spectrosc 16:163
101. Oyler NA, Tycko R (2007) Magn Reson Chem 45:S101
102. Jaroniec CP, Filip C, Griffin RG (2002) J Am Chem Soc 124:10728
103. Helmus JJ, Surewicz K, Surewicz WK, Jaroniec CP (2010) J Am Chem Soc 132:2393
104. Jaroniec CP, MacPhee CE, Bajaj VS, McMahon MT, Dobson CM, Griffin RG (2004) Proc Natl Acad Sci USA 101:711
105. Bielecki A, Kolbert AC, de Groot HJM, Griffin RG, Levitt MH (1990) Adv Magn Reson 14:111
106. Takegoshi K, Nakamura S, Terao T (1999) Chem Phys Lett 307:295
107. Hohwy M, Jaroniec CP, Reif B, Rienstra CM, Griffin RG (2000) J Am Chem Soc 122:3218
108. Zhao X, Sudmeier JL, Bachovchin WW, Levitt MH (2001) J Am Chem Soc 123:11097
109. Szeverenyi NM, Sullivan MJ, Maciel GE (1982) J Magn Reson 47:462
110. Takegoshi K, Nakamura S, Terao T (2001) Chem Phys Lett 344:631
111. Takegoshi K, Nakamura S, Terao T (2003) J Chem Phys 118:2325
112. Morcombe CR, Gaponenko V, Byrd RA, Zilm KW (2004) J Am Chem Soc 126:7196
113. Verel R, Ernst M, Meier BH (2001) J Magn Reson 150:81
114. Leppert J, Ohlenschlager O, Gorlach M, Ramachandran R (2004) J Biomol NMR 29:167
115. Wasmer C, Soragni A, Sabate R, Lange A, Riek R, Meier BH (2008) Angew Chem Int Ed Engl 47:5839

116. Heise H, Celej MS, Becker S, Riede D, Pelah A, Kumar A, Jovin TM, Baldus M (2008) J Mol Biol 380:444
117. Wasmer C, Benkemoun L, Sabate R, Steinmetz MO, Coulary-Salin B, Wang L, Riek R, Saupe SJ, Meier BH (2009) Angew Chem Int Ed Engl 48:4858
118. Nielsen JT, Bjerring M, Jeppesen MD, Pedersen RO, Pedersen JM, Hein KL, Vosegaard T, Skrydstrup T, Otzen DE, Nielsen NC (2009) Angew Chem Int Ed Engl 48:2118
119. Helmus JJ, Surewicz K, Nadaud PS, Surewicz WK, Jaroniec CP (2008) Proc Natl Acad Sci USA 105:6284
120. Chimon S, Shaibat MA, Jones CR, Calero DC, Aizezi B, Ishii Y (2007) Nat Struct Mol Biol 14:1157
121. Siemer AB, Ritter C, Steinmetz MO, Ernst M, Riek R, Meier BH (2006) J Biomol NMR 34:75
122. Bayro MJ, Ramachandran R, Caporini MA, Eddy MT, Griffin RG (2008) J Chem Phys 128:11
123. De Paepe G, Bayro MJ, Lewandowski J, Griffin RG (2006) J Am Chem Soc 128:1776
124. Bayro MJ, Maly T, Birkett NR, MacPhee CE, Dobson CM, Griffin RG (2010) Biochemistry 49:7474
125. Debelouchina GT, Platt GW, Bayro MJ, Radford SE, Griffin RG (2010) J Am Chem Soc 132:10414
126. Nadaud PS, Helmus JJ, Hofer N, Jaroniec CP (2007) J Am Chem Soc 129:7502
127. Su Y, Mani R, Hong M (2008) J Am Chem Soc 130:8856
128. Nadaud PS, Helmus JJ, Kall SL, Jaroniec CP (2009) J Am Chem Soc 131:8108
129. Wickramasinghe NP, Parthasarathy S, Jones CR, Bhardwaj C, Long F, Kotecha M, Mehboob S, Fung LW, Past J, Samoson A, Ishii Y (2009) Nat Methods 6:215
130. Walsh P, Neudecker P, Sharpe S (2010) J Am Chem Soc 132:7684
131. Baldus M, Petkova AT, Herzfeld J, Griffin RG (1998) Mol Phys 95:1197
132. Petkova AT, Yau WM, Tycko R (2006) Biochemistry 45:498
133. Andronesi OC, Becker S, Seidel K, Heise H, Young HS, Baldus M (2005) J Am Chem Soc 127:12965
134. Heise H, Hoyer W, Becker S, Andronesi OC, Riedel D, Baldus M (2005) Proc Natl Acad Sci USA 102:15871
135. Siemer AB, Arnold AA, Ritter C, Westfeld T, Ernst M, Riek R, Meier BH (2006) J Am Chem Soc 128:13224
136. Lange A, Gattin Z, Van Melckebeke H, Wasmer C, Soragni A, van Gunsteren WF, Meier BH (2009) ChemBioChem 10:1657
137. Tycko R, Hu KN (2010) J Magn Reson 205:304
138. Cornilescu G, Delaglio F, Bax A (1999) J Biomol NMR 13:289
139. Shen Y, Delaglio F, Cornilescu G, Bax A (2009) J Biomol NMR 44:213
140. Lange A, Luca S, Baldus M (2002) J Am Chem Soc 124:9704
141. Seidel K, Etzkorn M, Heise H, Becker S, Baldus M (2005) ChemBioChem 6:1638
142. Castellani F, van Rossum B, Diehl A, Schubert M, Rehbein K, Oschkinat H (2002) Nature 420:98
143. Ahmed M, Davis J, Aucoin D, Sato T, Ahuja S, Aimoto S, Elliott JI, Van Nostrand WE, Smith SO (2010) Nat Struct Mol Biol 17:561
144. Luhrs T, Ritter C, Adrian M, Riek-Loher D, Bohrmann B, Doeli H, Schubert D, Riek R (2005) Proc Natl Acad Sci USA 102:17342
145. Petkova AT, Leapman RD, Guo ZH, Yau WM, Mattson MP, Tycko R (2005) Science 307:262
146. Paravastua AK, Leapman RD, Yau WM, Tycko R (2008) Proc Natl Acad Sci USA 105:18349
147. Bayro Marvin J, Maly T, Birkett Neil R, Dobson Christopher M, Griffin Robert G (2009) Angew Chem Int Ed 48:5708

148. De Paepe G, Lewandowski JR, Loquet A, Bockmann A, Griffin RG (2008) J Chem Phys 129:245101
149. Ladizhansky V (2009) Solid State Nucl Magn Reson 36:119
150. Nieuwkoop AJ, Rienstra CM (2010) J Am Chem Soc 132:7570
151. Debelouchina GT, Platt GW, Bayro MJ, Radford SE, Griffin RG (2010) J Am Chem Soc 132:17077
152. Ritter C, Maddelein ML, Siemer AB, Luhrs T, Ernst M, Meier BH, Saupe SJ, Riek R (2005) Nature 435:844
153. Vilar M, Chou HT, Luhrs T, Maji SK, Riek-Loher D, Verel R, Manning G, Stahlberg H, Riek R (2008) Proc Natl Acad Sci USA 105:8637
154. Kheterpal I, Wetzel R (2006) Acc Chem Res 39:584
155. Hoshino M, Katou H, Yamaguchi K, Goto Y (2007) Biochim Biophys Acta 1768:1886
156. Svane ASP, Jahn K, Deva T, Malmendal A, Otzen DE, Dittmer J, Nielsen NC (2008) Biophys J 95:366
157. Liu SF, Mao JD, Schmidt-Rohr K (2002) J Magn Reson 155:15
158. Chan JCC, Tycko R (2003) J Chem Phys 118:8378
159. Levitt MH (2002) In: Grant DM, Harris RK (eds) Encyclopedia of nuclear magnetic resonance. Wiley, Chichester, pp 165
160. Chan JCC (2001) Chem Phys Lett 335:289
161. Chan JCC, Eckert H (2001) J Chem Phys 115:6095
162. Oldfield E (2002) Annu Rev Phys Chem 53:349
163. Wylie BJ, Rienstra CM (2008) J Chem Phys 128:052207
164. Mou Y, Chen PH, Lee SW, Chan JCC (2007) J Magn Reson 187:352
165. Tycko R, Dabbagh G (1991) J Am Chem Soc 113:9444
166. Robyr P, Meier BH, Fischer P, Ernst RR (1994) J Am Chem Soc 116:5315
167. Feng X, Lee YK, Sandstrom D, Eden M, Maisel H, Sebald A, Levitt MH (1996) Chem Phys Lett 257:314
168. Tycko R, Weliky DP, Berger AE (1996) J Chem Phys 105:7915
169. Weliky DP, Tycko R (1996) J Am Chem Soc 118:8487
170. Gregory DM, Mehta MA, Shiels JC, Drobny GP (1997) J Chem Phys 107:28
171. Blanco FJ, Tycko R (2001) J Magn Reson 149:131
172. Walling AE, Pargas RE, deDios AC (1997) J Phys Chem A 101:7299
173. Oas TG, Hartzell CJ, McMahon TJ, Drobny GP, Dahlquist FW (1987) J Am Chem Soc 109:5956
174. Oas TG, Hartzell CJ, Dahlquist FW, Drobny GP (1987) J Am Chem Soc 109:5962
175. Hartzell CJ, Whitfield M, Oas TG, Drobny GP (1987) J Am Chem Soc 109:5966
176. Teng Q, Iqbal M, Cross TA (1992) J Am Chem Soc 114:5312
177. Asakawa N, Kuroki S, Kurosu H, Ando I, Shoji A, Ozaki T (1992) J Am Chem Soc 114:3261
178. Kameda T, Takeda N, Kuroki S, Kurosu H, Ando S, Ando I, Shoji A, Ozaki T (1996) J Mol Struct 384:17
179. Takeda N, Kuroki S, Kurosu H, Ando I (1999) Biopolymers 50:61
180. Saito H, Ando I, Ramamoorthy A (2010) Prog Nucl Magn Reson Spectrosc 57:181
181. Costa PR, Gross JD, Hong M, Griffin RG (1997) Chem Phys Lett 280:95
182. Feng X, Eden M, Brinkmann A, Luthman H, Eriksson L, Graslund A, Antzutkin ON, Levitt MH (1997) J Am Chem Soc 119:12006
183. Ladizhansky V, Jaroniec CP, Diehl A, Oschkinat H, Griffin RG (2003) J Am Chem Soc 125:6827
184. Rienstra CM, Hohwy M, Mueller LJ, Jaroniec CP, Reif B, Griffin RG (2002) J Am Chem Soc 124:11908
185. Schmidt-Rohr K (1996) J Am Chem Soc 118:7601
186. Ishii Y, Terao T, Kainosho M (1996) Chem Phys Lett 256:133
187. Chan JCC, Tycko R (2003) J Am Chem Soc 125:11828
188. Mou Y, Tsai TWT, Chan JCC (2007) Solid State Nucl Magn Reson 31:72

189. Zhao X, Eden M, Levitt MH (2001) Chem Phys Lett 342:353
190. Lehmann MS, Koetzle TF, Hamilton WC (1972) J Am Chem Soc 94:2657
191. Carroll PJ, Stewart PL, Opella SJ (1990) Acta Crystallogr Sect C Cryst Struct Commun 46:243
192. Hong M, Gross JD, Rienstra CM, Griffin RG, Kumashiro KK, Schmidt-Rohr K (1997) J Magn Reson 129:85
193. Hong M, Gross JD, Griffin RG (1997) J Phys Chem B 101:5869
194. Nielsen NC, Bildsoe H, Jakobsen HJ, Levitt MH (1994) J Chem Phys 101:1805
195. Lewandowski JR, De Paepe G, Griffin RG (2007) J Am Chem Soc 129:728
196. Ladizhansky V, Veshtort M, Griffin RG (2002) J Magn Reson 154:317
197. Reif B, Hohwy M, Jaroniec CP, Rienstra CM, Griffin RG (2000) J Magn Reson 145:132
198. Bak M, Rasmussen JT, Nielsen NC (2000) J Magn Reson 147:296
199. Fernandez C, Pruski M (2011) Probing quadrupolar nuclei by solid-state NMR spectroscopy: recent advances. Top Curr Chem. doi:10.1007/128_2011_141
200. Griffin RG, Prisner TF (2010) Phys Chem Chem Phys 12:5737
201. Nielsen NC, Strassø LA, Nielsen AB (2011) Top Curr Chem DOI: 10.1007/128_2011_129

Top Curr Chem (2012) 306: 89–118
DOI: 10.1007/128_2011_162

Published online: 20 May 2011

Solid-State ^{19}F-NMR of Peptides in Native Membranes

Katja Koch, Sergii Afonin, Marco Ieronimo, Marina Berditsch, and Anne S. Ulrich

Abstract To understand how membrane-active peptides (MAPs) function *in vivo*, it is essential to obtain structural information about them in their membrane-bound state. Most biophysical approaches rely on the use of bilayers prepared from synthetic phospholipids, i.e. artificial model membranes. A particularly successful structural method is solid-state NMR, which makes use of macroscopically oriented lipid bilayers to study selectively isotope-labelled peptides. Native biomembranes, however, have a far more complex lipid composition and a significant non-lipidic content (protein and carbohydrate). Model membranes, therefore, are not really adequate to address questions concerning for example the selectivity of these membranolytic peptides against prokaryotic vs eukaryotic cells, their varying activities against different bacterial strains, or other related biological issues.

Here, we discuss a solid-state ^{19}F-NMR approach that has been developed for structural studies of MAPs in lipid bilayers, and how this can be translated to measurements in native biomembranes. We review the essentials of the methodology and discuss key objectives in the practice of ^{19}F-labelling of peptides. Furthermore, the preparation of macroscopically oriented biomembranes on solid supports is discussed in the context of other membrane models. Two native biomembrane systems are presented as examples: human erythrocyte ghosts as representatives of eukaryotic cell membranes, and protoplasts from *Micrococcus luteus* as membranes

K. Koch, M. Ieronimo, and M. Berditsch
Institute of Organic Chemistry and CFN, Karlsruhe Institute of Technology (KIT), Fritz-Haber-Weg 6, 76131 Karlsruhe, Germany

S. Afonin
Institute of Biological Interfaces (IBG-2), Karlsruhe Institute of Technology (KIT), P.O.B. 3640, 76021 Karlsruhe, Germany

A.S. Ulrich (✉)
Institute of Organic Chemistry and CFN, Karlsruhe Institute of Technology (KIT), Fritz-Haber-Weg 6, 76131 Karlsruhe, Germany
and
Institute of Biological Interfaces (IBG-2), Karlsruhe Institute of Technology (KIT), P.O.B. 3640, 76021 Karlsruhe, Germany
e-mail: anne.ulrich@kit.edu

from Gram-positive bacteria. Based on our latest experimental experience with the antimicrobial peptide gramicidin S, the benefits and some implicit drawbacks of using such supported native membranes in solid-state ^{19}F-NMR analysis are discussed.

Keywords Solid-state NMR structure analysis · 19F-labeling · Membrane-active peptides · Native biomembranes · Oriented membrane models · Antimicrobial peptides

Contents

1 Introduction: Towards *In-Cell* NMR

There are several advantages to studying proteins *in-cell*, instead of analyzing them *in vitro* or in crude lysates. The presence of a natural environment obviously brings about the genuinely relevant structures and it may modulate the molecular interactions and overall behaviour of a protein. For various reasons, it may not be possible to imitate these aspects adequately *in vitro*. Another advantage is the ability to study proteins that are difficult to purify or unstable outside the cellular surrounding. It may even be advantageous to introduce externally prepared proteins into eukaryotic cells. This allows the analysis of complex biological processes, like signalling cascades, protein turnover cycles and stimulus-responsive post-translational modifications, and may even lead to the discovery of new metabolic pathways [1–3]. A recent remarkable example of the power of *in-cell* NMR *in acto* is the 3D structure determination of the putative heavy-metal binding protein TTHA1718 from *Thermus thermophilus* HB8, which was overexpressed in living *Escherichia coli* and solved exclusively on the basis of *in-cell* NMR data [4].

When placed into an NMR spectrometer, a biological sample is examined essentially without perturbations. NMR structures are considered as native, as the method does not interfere with metabolically relevant conformational changes, binding events, post-translational modifications, or dynamic features of the protein [5]. The only potentially perturbing factors in an experiment are the presence of static and oscillating magnetic fields, and sample heating due to radiofrequency-driven or

mechanical rotation [6, 7]. The heating effects can be compensated, and their impact is anyhow significantly lower than the radiation damage associated with crystallography or high-resolution microscopy. As NMR observation is perfectly compatible with living organisms, as in magnetic resonance imaging (MRI), and causes no degradation of macromolecules, this technique is considered as truly non-invasive. Naturally, NMR is the prime candidate to solve detailed 3D molecular structures non-invasively *in-cell*.

In the above-mentioned study of the protein TTHA1718, the authors also reported the problems they faced, namely significant instability of the cell culture, and low NMR signal intensities [4]. The latter illustrates the principal disadvantage of the technique: an intrinsically low sensitivity. Some improvements in the short term are expected, i.e. based on improved hardware (higher magnetic fields, alternative designs of probe-heads), on software advancements (sparse data acquisition, maximum-entropy signal deconvolution), and especially on recent developments in metabolic isotope-labelling strategies, and mediated signal enhancements such as dynamic nuclear polarisation (DNP) [8]. Though highly encouraging, these improvements are not yet able to overcome routinely the sensitivity problem, hence certain manipulations of a sample before the measurement are usually unavoidable. These include the preparation of densely packed cell pellets, the use of deficient growth media for isotope enrichment, or anabolic conditions to overexpress a protein. Such treatments cause some stress on the cells, hence the absolute non-invasiveness of NMR has been questioned [9, 10]. Nevertheless, these effects are comparable to the stresses induced by the mechanical, electric or chemical treatments applied by other methods of observing living cells. Concerning the structure analysis contest between spectroscopic and scattering methods, the latter are mostly challenged by solving structures of weak oligomeric complexes and membrane proteins, which tend to be inaccessible to NMR due to their large size. Notably, with the development of milder crystallization conditions, the traditionally artefact-prone scattering methods are progressively placing the proteins into more biomimetic environments. At the same time, the intrinsically non-invasive NMR methods seemingly move towards more perturbing sample pre-treatments like DNP or ^{19}F-labelling to increase sensitivity [11].

Faced with low sensitivity, the first *in-cell* NMR experiments were logically performed in cells with high native protein concentrations, such as haemoglobin in erythrocytes [12]. Next, *in-cell* NMR was demonstrated on organisms like *E. coli*, which could be readily genetically manipulated overexpress the desired protein [1, 13]. At the same time, isotope-labelled proteins have been introduced into cultured cells using mechanical microsyringe injections, electroporation or carrier-mediated delivery [1–4, 14]. These methods tend to be limited to specific cell types, e.g. microinjection is applicable to large oocytes and carrier-mediated delivery is successful in cells with high constitutive levels of endocytosis, such as immortalized cancer cell lines.

The current state of *in-cell* NMR has been recently reviewed [5, 9], and it appears that genuine non-invasive NMR measurements of any protein of interest in any cell type will be achievable only in the mid-term future. However, the

promise of such experiments as an ultimate scientific goal provides a strong driving force for the immediate progress of biological NMR. One step towards this scientific vision, i.e. the structural characterization of a protein under native conditions, is the subject of this contribution. We will specifically discuss the progress of solid-state NMR (ssNMR) applied to ^{19}F-labelled membrane-active peptides (MAPs) when bound to native biomembranes in macroscopically oriented samples.

2 Solid-State ^{19}F-NMR

The traditional power of liquid-state NMR is the characterization of molecular structures to atomic-resolution, and the simultaneous access to dynamic information on various time-scales. For proteins in solution such a dynamic view is particularly relevant and unique for partially unfolded sequences, as well as for conformational interchanges, e.g. during catalysis. Proteins that are associated with biomembranes, on the other hand, are not readily accessible by liquid-state NMR unless they are relatively small and stably folded in detergent micelles. The only way to study membrane proteins in a quasi-native lipid bilayer is provided by ssNMR. Besides membrane protein structure analysis, ssNMR is particularly powerful in addressing the lipid interactions of MAPs, and characterizing other types of non-crystalline complexes such as amyloid fibrils [15–21]. Given the fluid nature of a liquid crystalline membrane, special attention has to be paid to the dynamic behaviour of membrane-bound peptides and proteins. The following sections will be devoted to their ssNMR analysis in macroscopically oriented membrane samples. Magic-angle-spinning (MAS) NMR methods will not be discussed here, as the samples usually need to be cooled down below the lipid phase transition or frozen to sub-zero temperatures. The significant morphological changes in both the lipidic as well as peptidic components suggest that the resulting structural MAS NMR data are less meaningful in a biological context.

MAPs exhibit a wide range of different biological functions, such as antimicrobial, cell-penetrating and fusogenic. The interested reader is referred to the recent *Special Issue* of the *European Biophysics Journal* [22] in which diverse examples are presented. MAPs are typically short, cationic, and unstructured in aqueous solution. In the membrane-bound state, however, they tend to fold into simple well-defined 3D structures (such as an α-helix) with an overall amphiphilic character. Discrete steps of oligomerization and self-assembly have been reported and seem to reflect the functional mechanism of these peptides, such as pore-formation in the bilayer. Many MAPs are also known to undergo dramatic conformational changes as a response to the environment, i.e. they exhibit a pronounced structural plasticity when converting, e.g. from a monomeric α-helix to a β-pleated aggregate. Hence, although easy to obtain, atomic structures of MAPs as determined by liquid-state NMR or X-ray diffraction tend to have only limited relevance with regard to their biological mode of action. Once the 3D conformation has been established, the critical structural information is related to alignment of the molecule in the

membrane, to its depth of immersion, to its oligomeric state and to its overall dynamic behaviour as a response to changes in the environment (e.g. peptide concentration, temperature, lipid composition, pH, ionic strength, presence of other membrane-bound components, etc.). When studying a MAP in action, at least two situations have to be considered – the unbound state in solution and the membrane-bound structure – which are interrelated by the specific binding affinity under the given conditions. The second situation is technically very challenging because an adequate membrane environment is required. Here, ssNMR appears to be the only method that is capable of revealing the genuine structural behaviour of an MAP at quasi-atomic resolution, even in a native biomembrane and possibly in the context of a living cell [19, 21, 23–25]. For this type of application alone, ssNMR can be expected to be heavily used, since the number of known MAPs is in the thousands, with further hundreds of thousands of sequences predicted and as yet unexplored [26–29].

In ssNMR the problem of low sensitivity prevails and is especially severe, as the spectral lines are much broader and the signal-to-noise levels are orders of magnitude lower than in liquid-state NMR. The use of macroscopically oriented samples alleviates this problem to some extent, but cannot reach the comparatively narrow line-widths of typical MAS spectra. Yet, a fundamentally simple and elegant way to overcome the sensitivity issue is the use of selective ^{19}F-labels [30–32], taking advantage of the high gyromagnetic ratio of the fluorine nucleus. For MAPs in particular, ^{19}F-NMR enables unprecedented sensitivity, in practice about 20-fold higher than for ^{2}H-NMR and 100-fold better than ^{15}N-NMR in comparable samples [33, 34]. Only a fraction of a milligram is needed to record a ^{19}F-NMR spectrum, i.e. 0.25 mg of a selectively labelled 20-amino acid peptide can be typically measured in about 1 h. This remarkable sensitivity gives unique access to ssNMR studies of peptide-to-lipid ratios of down to 1/3000 in model membranes, and in principle even to background-free *in-cell* observation. As the methodological aspects have been reviewed before [35–37], here we will only briefly present the major arguments behind the use of ^{19}F-NMR from a biological point of view, and then focus on the peculiarities of selective ^{19}F-labelling of MAPs.

The fluorine nucleus possesses a very high magnetic moment (81% of ^{1}H), leading to exquisite NMR sensitivity and strong dipolar couplings. A spin of 1/2 keeps the ssNMR spectral lineshapes simple, as there are no quadrupolar contributions. The absence of a natural background in biological samples, together with the 100% natural abundance, advertises ^{19}F for selective labelling – especially under *in-cell* conditions which suffer from an enormous ^{13}C natural abundance background and even considerable intensity from ^{2}H. Owing to the lone pairs of electrons on a fluorine substituent, its isotropic chemical shift (CS) has a much broader range than ^{1}H, and it is rather sensitive to the local environment. Being dependent on temperature, pH, solvent and dielectric environment, the CS can be used to monitor these parameters [32, 34, 38]. However, in the present applications of ^{19}F-NMR to MAPs in oriented membrane samples, we will focus entirely on the anisotropy, i.e. the orientation-dependence of the CS and of the dipolar couplings.

^{19}F-labelling has been explored, amongst other signal-enhancement strategies, for *in-cell* NMR studies as early as 1989 [39] and continues to be used for proof-of-principle demonstrations to date [40]. There are several inherent difficulties associated with the use of this particular nucleus, however. The first type is purely of a technical nature, as the ^{19}F- and ^{1}H-NMR frequencies are close to one another, especially at low magnetic field strength. High-performance rf-filters are therefore required on both NMR channels (^{1}H/^{19}F), which are fortunately now available commercially [41–43]. Likewise, the stringent necessity to use custom-made Teflon-free NMR-probes and electronics has been alleviated by designated commercial hardware, yielding essentially background-free spectra. Another, less obvious, aspect is the considerable risk of introducing a chemical ^{19}F-contamination during sample preparation. Especially when working with synthetic peptides, or even with natural materials that have been purified by HPLC, traces of fluorinated solvents (trifluoroethanol, hexafluoro-2-propanol) or synthetic reagents (trifluoroacetic acid) may remain in the sample and actually dominate the NMR spectrum. In our experience, this problem can only be completely eliminated by designating a "fluoro-solvent-free" zone in the lab, comparable to the typical "protease-free" or "nuclease-free" areas in a bio-lab. Even though the removal of TFA has been reported [44, 45], we rarely found this approach to give satisfactory results.

2.1 NMR of Oriented Membranes

ssNMR structure analysis of MAPs in macroscopically oriented samples is based on the simple principle that all membrane-bound molecules are aligned the same way relative to the bilayer normal. The sample is placed into the spectrometer such that its unique axis is parallel to the static magnetic field. This way, the orientational dependence of the chemical shift anisotropy (CSA) and/or the dipole–dipole interaction (DD) (or the quadrupolar anisotropy in case of ^{2}H) directly reveals the alignment of the NMR label. In the present context a single ^{19}F-substituent or a CF_3-group is observed, but the same principle applies to ^{2}H-NMR (works well for $^{2}H_3$-alanine) and ^{15}N-NMR (works well for uniformly backbone-labelled helices). The most suitable ^{19}F-NMR reporter is in fact the CF_3-group, which is always engaged in fast rotation around the C–CF_3 axis at room temperature. The characteristic feature to be measured is the angle θ between the C–CF_3 axis and the spectrometer magnetic field, which obeys the simple relationship $DD \propto 3\cos^2\theta - 1$ (see Fig. 1a). The splitting DD is taken from the NMR spectrum, which has a triplet lineshape consisting of both the axially symmetric ^{19}F–^{19}F dipolar coupling and an axially symmetric CSA (see Fig. 2c). The CSA of a *mono*-fluoro substituent, on the other hand, is axially non-symmetric and therefore can no longer be described by a unique angle θ. Another advantage of the CF_3-group is the fact that the dipolar splitting can be directly read off a single-pulse 1D spectrum, which needs to be referenced (as has to be done for the CSA). The intrinsically unknown sign of DD can be readily determined from the simultaneous spectral shift associated with the

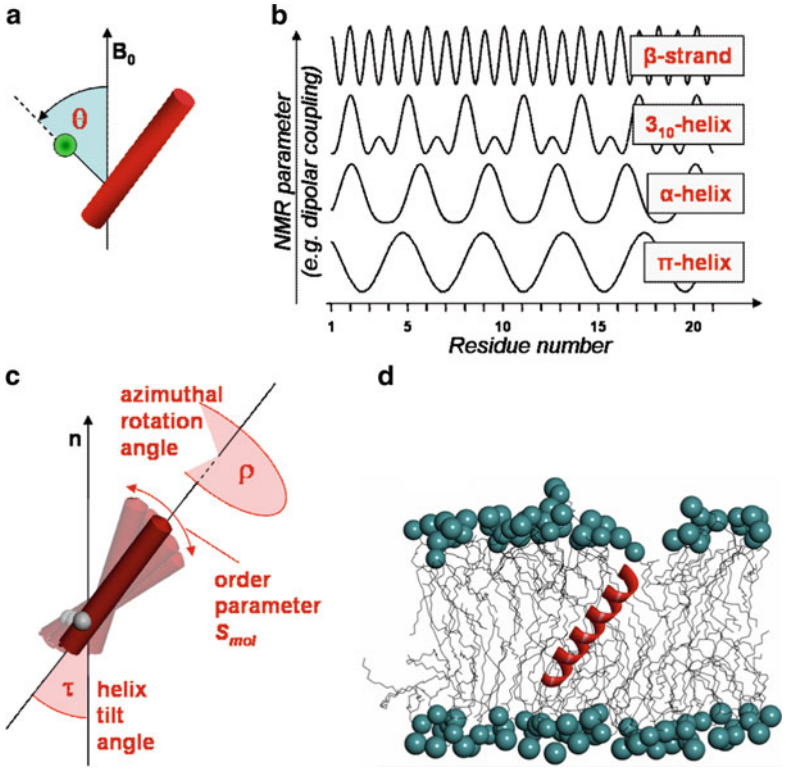

Fig. 1 Solid-state NMR structure analysis relies on the ^{19}F-labelled peptides being uniformly embedded in a macroscopically oriented membrane sample. (**a**) The angle (θ) of the ^{19}F-labelled group (e.g. a CF_3-moiety) on the peptide backbone (shown here as a *cylinder*) relative to the static magnetic field is directly reflected in the NMR parameter measured (e.g. DD, see Fig. 2c). (**b**) The value of the experimental NMR parameter varies along the peptide sequence with a periodicity that is characteristic for distinct peptide conformations. (**c**) From such wave plot the alignment of the peptide with respect to the lipid bilayer normal (n) can then be evaluated in terms of its tilt angle (τ) and azimuthal rotation (ρ). Whole-body wobbling can be described by an order parameter S_{mol}. (**d**) The combined data from several individual ^{19}F-labelled peptide analogues thus yields a 3D structural model of the peptide and how it is oriented in the lipid bilayer

CSA [46]. The local alignment of a peptide segment can thus be described by a C–CF_3 vector that protrudes in a well-defined way from the α carbon on the backbone (see Sect. 2.2 on ^{19}F-labelled amino acids).

Several local labels need to be measured, usually one-by-one in individual samples in the case of ^{19}F-NMR. The combined set of anisotropic NMR parameters then allows one to re-construct the geometry of the entire peptide and to determine its alignment in the membrane, as illustrated in Fig. 1 [35–37, 47, 48]. The only prerequisite is that the ^{19}F-labelled moiety has to be rigidly attached to the peptide backbone, and that the peptide assumes a well-defined secondary structure. Provided that a sufficient number of local orientational constraints can be measured

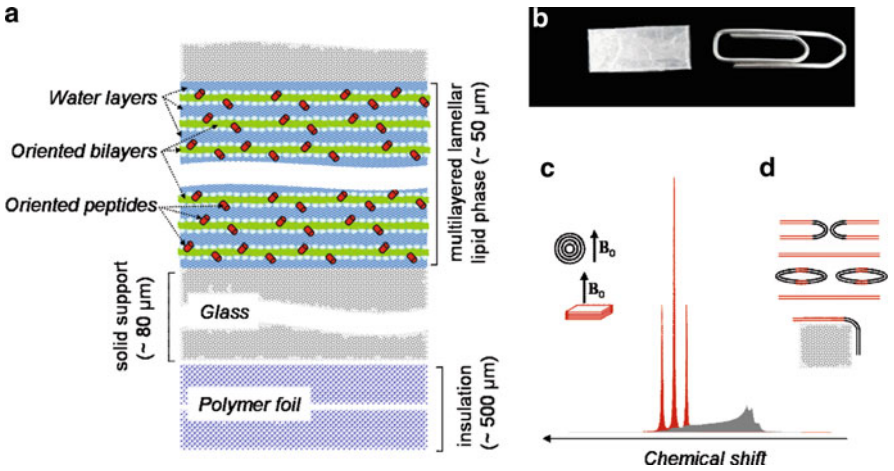

Fig. 2 Mechanically oriented bilayer samples as a membrane model for ssNMR. (**a**) Illustration of the hydrated lipid bilayers with MAPs embedded, the glass supports, and the insulating wrapping. (**b**) A real sample consists of 15 stacked glass slides. (**c**) Schematic solid-state ^{19}F-NMR lineshapes from an oriented CF_3-labelled peptide (*red*), and the corresponding "powder" lineshape from a non-oriented sample (*grey*). (**d**) Illustration of typical orientational defects in real samples – the sources of "powder" contribution in the spectra

(usually ≥ 3), it is possible to calculate not only the tilt-angle (τ) and the azimuthal rotation (ρ) of such a secondary structure element, but also to describe its wobbling in terms of an order parameter S_{mol} ($0 \leq S_{mol} \leq 1$). When four or more independent constraints are available, the whole-body dynamics can in principle be evaluated in terms of an extended dynamical model [49–51]. The least-squares fitting procedure can best be visualized by plotting the experimental NMR data (DD or CSA) against the residue number of the peptide sequence. A wave-like pattern will be obtained with a repetition after 3.6 residues for an α-helix, 3 residues for a 3_{10}-helix, 4 for a π-helix, or 2 for a β-strand (see Fig. 1b). It is thus straightforward to find out which secondary structure is compatible with the experimental data and which conformations can be excluded [35, 48]. The best-fit solution then yields at the same time the values of τ, ρ and S_{mol}, which fully describe the orientation of the peptide with respect to the membrane normal. In this way, the membrane-bound structures of several different types of MAPs have been resolved over recent years [46, 52–54]. Notably, a peptide that does not bind at all and rather diffuses freely in the aqueous layer will produce exclusively isotropic signals. A non-ordered or aggregated peptide, on the other hand, will reveal itself by producing so-called "powder"-lineshapes in an oriented sample.

For the orientation-based structure analysis of MAPs, uniformly oriented lipid bilayers are typically prepared on solid supports as illustrated in Fig. 2 [23, 47, 55]. These mechanically oriented membranes are advantageous for static ssNMR experiments, as they provide a robust way to orient a sample with any desired lipid composition, peptide concentration, and at any desired temperature. The lipids

and the ^{19}F-labelled MAP are usually co-dissolved in an appropriate organic solvent, spread onto a number of glass plates, and stacked after evaporation of the solvent. Oriented bilayers are spontaneously formed when this stack is equilibrated in a humid atmosphere (typically 96% relative humidity over a saturated K_2SO_4 solution), and finally it has to be wrapped in a water-impermeable foil to maintain the hydration level [34, 37, 56, 57]. Alternatively, when working with delicate or aggregation-prone peptides, oriented samples can be formed from aqueous suspensions of liposomes into which the peptide has been reconstituted by detergent dialysis. In this case the suspension is deposited onto the support slide, and excess water is removed by equilibration in a hydration chamber. During this process the vesicles fuse and align on the slide as flat multi-bilayers.

2.2 *^{19}F-Labelling of Peptides*

Compared to conventional NMR isotopes (^{13}C, ^{15}N, ^{2}H), ^{19}F-labels cannot be readily placed into proteins in a versatile manner by any biosynthetic expression strategy. Certain auxotrophic bacterial strains can be used to incorporate *iso*-steric ^{19}F-labelled amino acids (e.g. Fluoro-Phe, Fluoro-Trp, Fluoro-Leu, Fluoro-Ile; see Fig. 3), but yields tend to be low. Many other fluoro-organics are toxic if they get converted into fluoroacetic acid, which blocks the enzyme aconitase in the citric

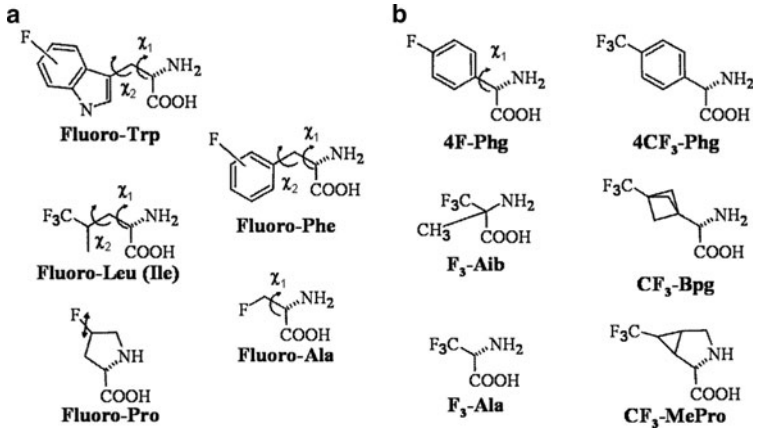

Fig. 3 Important ^{19}F-labelled amino acids. (**a**) Compounds that are *iso*-steric to native amino acids can be incorporated into proteins biosynthetically, but they possess too many degrees of torsional freedom to be useful for ssNMR structure analysis. (**b**) In these artificial amino acids the ^{19}F-reporter group is rigidly attached to the peptide backbone. They can be incorporated by solid-phase peptide synthesis, but some problems can arise due to racemisation (4F-Phg, 4CF_3-Phg), steric hindrance of coupling (F_3-Aib) or HF elimination (fluoro-Ala, F_3-Ala). 4F-Phg is additionally problematic due to an ambiguity of the side-chain rotamer. The preferred ^{19}F-labels for ssNMR structure analysis are CF_3-Bpg and CF_3-Phg (as suitable substitutes for Leu, Ile, Met, Val and Ala), as well as F_3-Aib and CF_3–MePro

acid cycle. Alternative ways of obtaining large ^{19}F-labelled proteins are by means of native chemical ligation, or by cell-free biosynthesis and semi-synthetic approaches based on an extended genetic code [58–60]. Even though the yields are still low, there is hope that methodological progress will favour these alternative routes in the not-too-distant future.

Notably, when aiming to produce short MAPs, their biosynthetic production tends to be particularly difficult anyhow. One reason is that the short mRNA is rapidly degraded, such that recombinant expression is often only possible as a fusion construct together with a large protein. On top of that, many amphiphilic MAPs are intrinsically prone to cause membrane lysis, and organisms like *E. coli* cannot usually cope with such toxic effects. Therefore, when at all possible, a fresh recombinant ^{19}F-labelling of MAPs would only make sense when an *iso*-steric ^{19}F-amino acid is to be incorporated. However, as these are too pliable to be used for the ssNMR approach outlined (see below), chemical peptide synthesis remains the best option. In principle, the covalent addition of a fluorinated moiety to an existing peptide or protein (via SH-, COOH-, or NH_2-groups) could enhance the repertoire of ^{19}F-labels, but these groups, too, are inappropriate for structure analysis.

Solid-phase peptide synthesis is the method of choice to produce polypeptides of up to 50 amino acids, especially in the case of MAPs. Any unnatural amino acid can be introduced, and recent developments in fully automated and microwave-assisted instruments allow even some less reactive or sterically confined compounds to be coupled [35, 61–63]. When selecting or designing a ^{19}F-amino acid as a label for ssNMR, several criteria have to be met. (a) For structure analysis in oriented membranes the ^{19}F-reporter group has to be rigidly attached to the Cα atom of the peptide backbone. This is a fundamental prerequisite to be able to translate the local angle θ of the label into the overall geometry and alignment of the peptide (see Fig. 1). (b) The ^{19}F-labelled amino acid must not compromise the conformation or biological action of the peptide, hence the substitution should maintain the secondary structure propensity, steric size and polarity. (c) The ^{19}F-labelled amino acid should be stable under conditions of peptide synthesis. In view of all these restrictions, it is obvious why only very few out of the many known ^{19}F-labelled amino acids can be used for ssNMR. Adequate substituents have been demonstrated for Leu, Ile, Met, Val, Ala, Aib, and more recently also Pro [53, 61, 64].

Commercially available 4F-Phg was historically the first label used to develop the basic ssNMR approach on the fusogenic peptide B18 and on antimicrobial gramicidin S (GS) (see Fig. 4 for sequences) [52, 65, 66]. From nine individual substitutions, the B18 peptide was shown to assume a "boomerang"-like helix-loop-helix structure in the membrane. In the case of GS, four positions were used, though in principle two are sufficient thanks to the symmetrical cyclic backbone. Given the latent ambiguities of single ^{19}F-substituents, CF_3-Phg were introduced and their advantages demonstrated for the helical antimicrobial peptide PGLa [46]. Four ^{19}F-labelled PGLa analogues were used to determine the molecular conformation and to describe several different alignment states in the membrane. Depending on the sample conditions, this representative α-helical peptide is able to bind flat to the membrane surface, to insert into the bilayer with an oblique tilt angle, and to assume an upright transmembrane

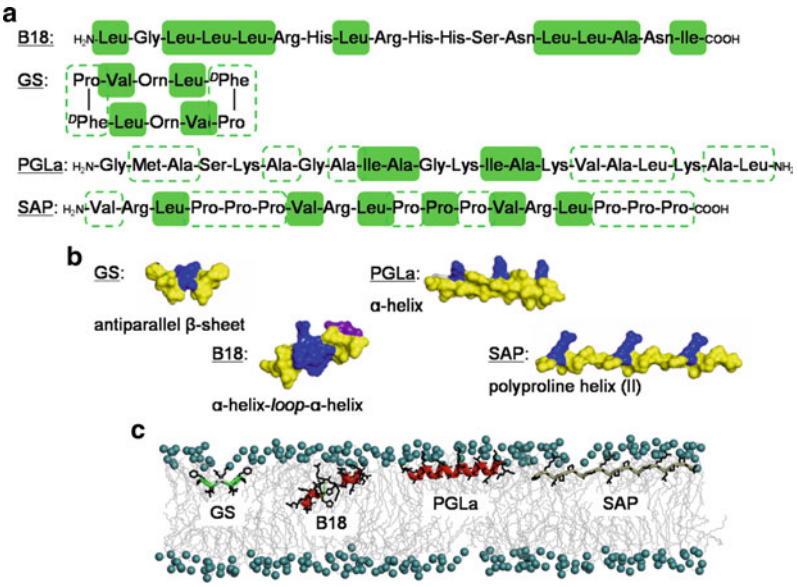

Fig. 4 Representative membrane-active peptides that have been studied by solid-state ^{19}F-NMR. (**a**) The primary sequences show which positions were substituted (*filled green boxes*) or which ones could in principle be substituted (*dotted green lines*). (**b**) Characteristic conformations of the peptides in the membrane-bound state. The space-filling solvent-accessibility models emphasize the amphiphilicity by colouring hydrophobic residues in *yellow* and cationic side-chains in *blue*. (**c**) Observed structures and alignment states of the peptides as determined by ^{19}F-NMR

alignment that is presumably responsible for pore formation. These intriguing ^{19}F-NMR results were found to be in excellent agreement with an independent ^{2}H-NMR analysis based on entirely non-perturbing $^{2}H_3$-Ala substitutions [33].

As a further improvement in the development of ^{19}F-labels, CF_3-Bpg was specifically designed and custom-made for ^{19}F-NMR. Again, PGLa was used to demonstrate the ideal properties of this novel label. This amino acid has since become a "gold standard" for ^{19}F-NMR of MAPs and been applied to several different types of peptides [54, 64, 67–69]. Likewise, F_3-Aib in both *R*- and *S*-configurations has been introduced as an ideal label for peptaibols, with alamethicin as a representative example [70]. Most recently, CF_3–methano-proline with a rigidified ring has been prepared and is currently being explored as a ^{19}F-label in the proline-rich peptide SAP [53].

3 Lipid Model Membranes

To study the structural behaviour of MAPs, an adequate membrane model (see Fig. 5) is essential. Simple organic solvent systems, such as DMSO, MeOH/H_2O or TFE/H_2O mixtures, present a similar dielectric environment as a membrane on

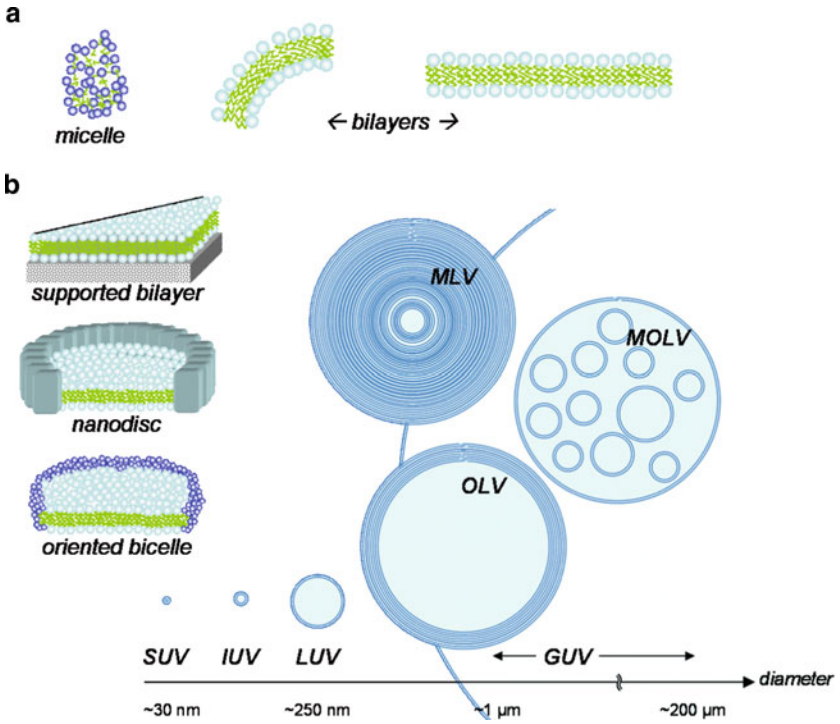

Fig. 5 Membrane models for NMR structure analysis. (**a**) An isotropic detergent micelle (*left*) is compared to the dimensions of lipid bilayers (*right*). (**b**) Macroscopically oriented membrane samples can be prepared on solid support, as nanodiscs, or as magnetically oriented bicelles. (**c**) Nomenclature and variability of liposomes: small (SUV, 20–40 nm), intermediate (IUV, 40–60 nm), large (LUV, 100–400 nm), and giant unilamellar vesicles (GUV, ~1 µm); multilamellar (MLV), oligo-lamellar (OLV) and highly heterogeneous multi-oligo-lamellar vesicles (MOLV)

average, and tend to favour H-bond formation. Though perfectly suitable for many spectroscopic techniques, including liquid-state NMR [71, 72], and even extendable to an ssNMR situation by freezing the solution [73, 74], such models obviously fall a long way short of an anisotropic lipid bilayer environment. Spherical detergent micelles exhibit a diffuse membrane–water interface and a hydrophobic core, hence an overall dielectric gradient is present [75–77]. However, their high radius of curvature makes it difficult to assess the membrane alignment of a peptide, and structural aspects related to higher-order peptide–peptide interactions such as pore-formation cannot be addressed either. The former problem is alleviated by the use of isotropic bicelles [78–80], which are prepared from a mixture of a long-chain lipid and a short chain detergent (such as SDS, DPC, CHAPSO or DHPC) with a molar ratio $q < 1$ and concentrations of ~10–15 wt% [81, 82]. Small isotropic bicelles are increasingly used in liquid-state NMR, empirically providing better

spectra. In most cases when using micelles, however, solubilization is the prime aim, though words of caution have been raised [83]. Isotropic detergent assemblies are often visualized with a definite shape, even as a rigid ball (oblate or prolate at best), in which the peptide or protein is immersed [84, 85]. In reality, though, micelles possess neither well-defined hydrophobic nor stable surface dimensions, as the detergent molecules rather adjust themselves around the hydrophobic part of the protein or peptide. Micelles are therefore perfect solubilizing agents for transmembrane segments, but of limited use in characterizing amphiphilic MAPs.

A different scenario is encountered with large planar bicelles, e.g. of DMPC/DHPC with a typical molar ratio $q > 3$ in suspensions of 15–25 wt%, which are often depicted as pancakes but may also look like a stack of cylindrical micelles or a slice of Swiss cheese [86–88]. These assemblies can orient themselves macroscopically in the strong magnetic field of an NMR spectrometer within a certain temperature window. Due to the magnetic susceptibility of the lipid acyl chains, the bilayer normal will usually be aligned at right angle to the field axis, but they can be flipped parallel by the addition of lanthanide ions [47, 86, 89]. This latter type of membranous sample is particularly well suited to measure anisotropic ssNMR parameters with a structural approach that has been outlined in Sect. 2.1 for the case of mechanically oriented bilayers (see Fig. 5b). Oriented bicelles are perfectly applicable to study transmembrane segments of proteins, though amphiphilic MAPs might interact with the rim and perturb the system in an unforeseen way. Lipidic nanodiscs, finally, fenced in, e.g. by an apolipoprotein belt, can in principle be used in the same way as magnetically oriented bicelles [90].

Lamellar bilayers formed from synthetic lipids are the preferred models that most closely mimic natural cell membranes. Vesicles – or liposomes – with distinct sizes and degrees of lamellarity (see Fig. 5) can be prepared by extrusion, dialysis, sonication, vortexing, freeze-thawing or similar treatments [91, 92]. In vigorously sonicated lipid dispersions [75–77, 93] the overall molecular re-orientation is relatively fast on the NMR time scale due to tumbling of the SUVs and/or lateral diffusion of the lipids around the curved surfaces. Such orientational averaging, however, can be essentially ignored in multilamellar vesicles, which are typically prepared as non-oriented samples for ssNMR with a total water content of about 50 wt%. In these samples the full spherical distribution of molecular orientations makes the above-mentioned anisotropic ssNMR approach theoretically possible though less straightforward in the case of mobile peptides, while being impossible in the case of immobilized peptides.

Compared to the sizes of living cells,[1] IUV and LUV resemble the dimensions of enveloped viruses (ranging from 80 to 400 nm) [94], while GUVs resemble typical bacteria and erythrocytes (1–7 μm). Eukaryotic cells tend to be even larger (10–30 μm in animals, 10–100 μm in plants). These dimensions imply that, except for viruses or specific sub-cellular membranes, flat bilayers are the only relevant membrane models. Hence, macroscopically oriented bilayers on solid supports (see

[1] http://bionumbers.hms.harvard.edu.

Figs. 2a and 5b) are a good choice for ssNMR structure analysis of MAPs [23, 47, 55]. The fact that mechanically aligned multi-bilayer stacks are hydrated close to 100% but do not contain any excess bulk water turns into an important but often overlooked advantage. Since the binding equilibrium of a peptide is driven completely towards the membrane-bound state under these conditions, even when electrostatics are not optimal, MAPs with a low membrane-affinity or in certain cases even transient states can also be trapped and characterized [95–97]. In mechanically supported bilayers the lipid composition can be chosen in a highly flexible way, the peptide concentration can be fully controlled, and it has even been possible to prepare pH-controlled samples recently. The physico-chemical aspects of peptide–lipid interactions are conveniently modelled in binary or ternary mixtures of synthetic phospholipids. For example, systems based on the uncharged 1,2-dimyristoyl-glycero-3-phosphocholine (DMPC, a good bilayer-forming lipid with a chain melting phase transition temperature around 22 °C, which is stable against oxidation, hydrolysis, etc.) can be combined with an anionic species such as 1,2-dimyristoyl-glycero-3-phosphoglycerol (DMPG, which mixes smoothly with DMPC without phase segregation), and/or with cholesterol (which modulates membrane fluidity in animals), and/or with 1-palmitoyl-2-oleoyl-glycero-3-phos phoethanolamine (POPE, which has an intrinsic negative curvature and favours inverted hexagonal phases), etc. Our two representative antimicrobial peptides PGLa and GS (Fig. 2) have been extensively studied by ^{19}F-NMR in supported membranes over a wide range of conditions by systematically varying the lipid composition, membrane charge, peptide concentration, lipid phase state, degree of sample hydration and spontaneous lipid curvature [33, 46, 65–67, 95–99]. These physico-chemical factors have been found to affect the peptide behaviour, as characterized in terms of molecular orientation, re-alignment and self-assembly, in a logical and comprehensive way.

The more biological properties of native membranes with highly complex lipid compositions can be imitated by choosing appropriate mixtures reflecting the major components of a typical prokaryotic or eukaryotic membrane [55, 97, 100, 101]. The lipid acyl chains tend to be partially unsaturated, rendering the bilayers in a liquid crystalline state, though various kinds of gel-like microdomains are known to co-exist. Prokaryotic membranes are conveniently modelled by mixtures of anionic phosphatidylglycerols (PG) and cardiolipins (CL) with zwitterionic phosphatidylethanolamines (PE) [102–104]. Eukaryotic plasma membranes, on the other hand, consist mainly of zwitterionic phosphatidylcholines (PC), sphingomyelines (SM) and PE. They also contain small but significant amounts of PG, phosphatidylserines (PS) and phosphatidylinositols (PI). One of the major differences to *prokaryotes* is the presence of cholesterol, which provides the *eukaryotes* with enhanced membrane stability. However, this is a highly oversimplified view, as there are thousands of lipid species present in every native membrane. The analysis and documentation of all membrane lipids from different types of cells is a project of global dimensions, and one of the main goals of the recent post-genome screening initiatives [105].

Given the overwhelming compositional complexity of biomembranes, a slightly better representation can be achieved when lipid extracts from native sources are used

for bilayer formation (e.g. the total or polar *E. coli* extracts, or preparations from bovine brain, liver or heart, which are all available commercially). The batch-to-batch reproducibility of individual preparations is limited, and a more serious problem is that these "total" extracts are prepared from the whole tissue. Hence they naturally contain some non-lipidic hydrophobic molecules, and in eukaryotic cases they do not originate from a single membrane type but contain all components from all membranous organelles as well. In these samples, due to their comparatively poor compositional characterization, it is difficult to specify a peptide-to-lipid ratio. Instead, weight/weight ratios can be used, or the number of phospholipid molecules can be estimated from phosphate determination, using, e.g. a Bartlett or Stewart assay [91, 106].

4 Native Biomembranes

Intact biological membranes are far more complex systems than even the lipid extracts (see Fig. 6). In hardly any case do the lipid components exceed 50% of the dry weight, as membranes intrinsically contain numerous proteins and various glycoconjugates. This diversity is most pronounced in the plasma membrane (irrespective of the genera) which is effectively amalgamated with the non-lipidic

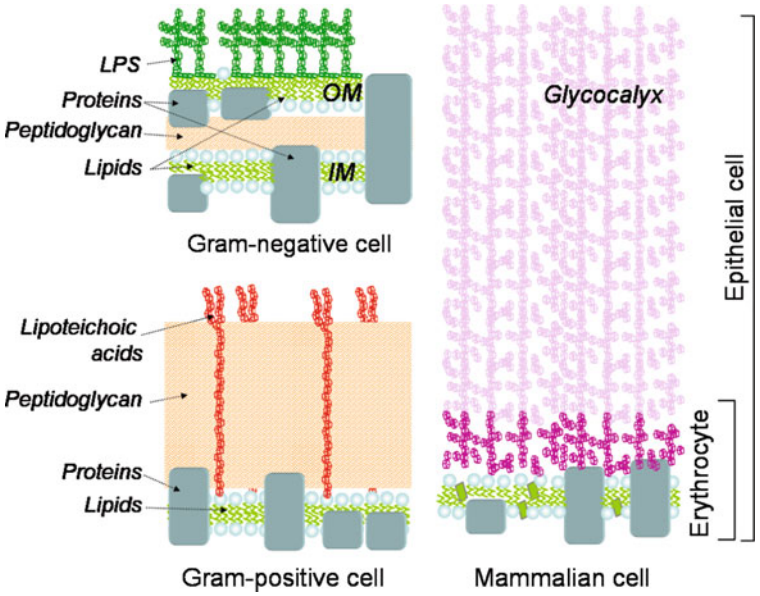

Fig. 6 Illustration of representative cell envelopes from *prokaryotes* and *eukaryotes* that are typically encountered by antimicrobial peptides. The key components of the biomembranes and cell wall or glycocalyx are shown, and the averaged protein content and typical dimensions are drawn to scale

exoskeleton or glycocalyx. Bacteria possess a rigid cell wall outside the cell membrane, which are together referred to as the cell envelope. The cell wall consists of the heteropolymer peptidoglycan, in which linear chains of alternating *N*-acetylglucosamine and *N*-acetylmureic acid are cross-linked by group- and strain specific, often unusual, amino acids [107, 108].

In Gram-positive species the cell wall is assembled from multiple layers to about 25 nm thickness, and it is covered by extracellular anionic polymers which contribute up to 10% of the total weight [109–111]. Typical are teichoic acids (TA), which are phosphorus-containing polymers with 16 to 40 units of ribitol or glycerol that can be adenylated and/or glycosylated. TAs are either covalently bound to the peptidoglycan (wall teichoic acids – WTA) or anchored in the membrane via a glycolipid (lipoteichoic acids – LTA). A few Gram-positive bacteria do not possess conventional LTA and WTA, but instead have functionally analogous polyanions. *Micrococcus luteus*, for instance, possesses lipomannan, a polymer of mannosyl residues being esterified with succinyl groups to approximately 25% [110, 112, 113].

In Gram-negative bacteria the cell wall is only about 3 nm thick, and located in the extended periplasmatic space between the inner membrane (IM) and an additional outer membrane (OM). The lipid monolayer in the outer leaflet of the OM contains about 90% lipopolysaccharides (LPS). LPS consist of Lipid A and an oligosaccharide component, which is highly specific for individual bacterial species and phenotypes [108, 114].

Unlike other *Eukarya*, animal cells lack cell walls, though they tend to be surrounded by a highly developed glycocalyx of up to 140 nm in thickness [108]. This diffuse layer of densely packed oligosaccharides has a heterogeneous composition and is connected to the membrane via lipids or integral proteins. The "boundary" of the cell usually extends beyond the mere lipid bilayer with its embedded proteins, and the extracellular structures provide initial sites of interaction or are themselves targets for MAPs such as antimicrobial peptides [115].

4.1 Erythrocyte Ghosts

Erythrocytes are probably the best-established cell system and the most common model for eukaryotic cell membranes. For instance, in evaluations of MAPs as antibiotics, their cytolytic effect on red blood cells is routinely studied in haemolysis assays as a general measure of toxic side-effects [116, 117]. In human erythrocytes, which do not contain a nucleus or intracellular organelles, the protein-to-lipid ratio is about 1:1 (wt/wt). Of the membrane lipids, 60–80% are phospholipids (SM and PC in the outer monolayer; PE, PS and PI in the inner one), up to 25% cholesterol, and up to 10% glycolipids. The latter are almost entirely (95%) located in the outer leaflet [103, 118, 119]. To prepare erythrocyte membranes as so-called "ghosts", the cells are exposed in extensive washing steps to a hypotonic medium, which causes them to swell and the membrane permeability to increase. The membrane reseals again for larger molecules like haemoglobin, but stays

permeable for smaller compounds like ions [119–121]. By repeated washing/centrifugation cycles the cytoplasm is effectively removed, and upon membrane re-sealing "ready-to-use" ghost suspensions are obtained [122–124]. These are accessible relatively quickly (in a couple of days), in large quantities (several tens of milligrams from a single blood bag) and low in contaminations [122, 125].

Several ssNMR investigations have already been performed on erythrocyte membrane vesicles [126, 127] and even on erythrocyte membranes oriented by an isopotential spin-dry ultracentrifugation technique [128]. However, this latter procedure is rather tedious and not really required, as we recently found that orientation can also be achieved by depositing a ghost suspension onto a glass slide, followed by vapour-phase equilibration against a saturated K_2SO_4 solution (96% humidity [129]) [124]. Representative solid-state ^{31}P-NMR spectra of non-oriented and of macroscopically aligned ghosts prepared this way are shown in Fig. 7. The non-oriented membranes yield classical "powder" lineshapes with the characteristic dimensions (CSA span of ~ 35 ppm) of synthetic phospholipid bilayers [124, 128]. The spectra of the oriented ghost samples are also equivalent to those of model phospholipid bilayers. At the horizontal sample alignment they show a narrow lipid signal (6–7 ppm width), which is scaled by the factor −1/2 after tilting the sample to 90° in the static magnetic field [124]. Notably, no separate signals of individual types of phospholipids in erythrocyte membranes are resolved. A small isotropic component of varying intensity was observed in different freshly prepared samples and can be attributed to residual inorganic phosphorus after washing, or to a small fraction of lipidic non-bilayer phases

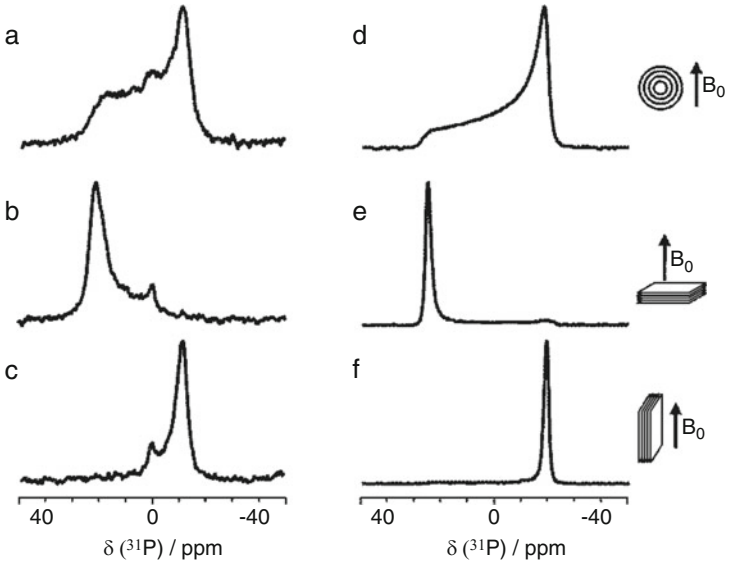

Fig. 7 Comparison of the solid-state ^{31}P-NMR spectra from erythrocyte ghosts (*left column*) and of DMPC model membranes (*right column*). Samples are prepared as a non-oriented suspension in excess water (**a**, **d**), and as macroscopically oriented membranes on glass slides that are aligned either parallel (**b**, **e**) or perpendicular (**c**, **f**) to the static magnetic field

like micelles or a cubic phase. Nevertheless, these isotropic signals were found to be useful as an internal reference and as an indicator on the hydration status. They are sharp in freshly prepared samples, but broaden, decrease or vanish during long NMR measurements or upon heating, due to drying of the sample, since the intensity is restored after rehydration in a humid atmosphere.

When the ^{19}F-labelled antimicrobial peptide PGLa was co-incubated with ghosts in the final washing step, the ^{19}F-NMR signal was fully contained in the pellet after centrifugation, which indicates complete membrane binding [124]. The corresponding ^{31}P-NMR spectra showed no difference between peptide-supplemented and peptide-free preparations up to a peptide-to-lipid ratio of P/L $\approx$ 1:20 (mol/mol) (as estimated by a modified Bartlett phosphorus assay [91]). By analyzing the same four ^{19}F-labelled PGLa analogues as in the model membrane studies cited above, we found that this α-helical peptide assumes a surface-aligned state in ghost membranes. It could thus be demonstrated for the first time that the sensitivity of ^{19}F-NMR and the lack of a natural abundance background indeed permit ssNMR studies of native biomembranes. The lineshapes were broader and less well resolved than in model membranes, and NMR measuring times were up to 36 h (compared to 12 h for the same P/L $\approx$ 1:300 in DMPC/DMPG). Nevertheless, a comparison of the characteristic dipolar splittings provided a unique answer on the dominant alignment state of PGLa in ghost membranes. We did not, however, find evidence for a tilted or membrane-inserted state of the peptide that would correspond to the formation of a transmembrane pore, as had been detected in DMPC model membranes [96, 130]. In contrast to the more uniform situation in synthetic lipids, where unique alignment states could be trapped, it was noted that multiple peptide pools co-exist in the ghost samples. A significant proportion of the spectral intensity corresponded to an immobilized and non-oriented "powder" fraction of peptides. This signal got reduced with increasing temperature and was attributed to peptides bound to the glycocalyx rather than the lipid bilayer [124].

More recently we observed a similar picture for the ^{19}F-labelled antimicrobial peptide gramicidin S in ghost membranes, which is illustrated in Fig. 8 and has not been published before. At low temperature the ^{19}F-NMR signal of ^{19}F-labelled GS is very broad (Fig. 8c) and corresponds to the "powder" lineshape that is known from DMPC/cholesterol model membranes (Fig. 8f). Under these conditions the peptide is immobilized and not bound to the membranes in any well-defined, oriented manner [130]. Upon raising the temperature, a narrow signal successively appears close to −117 ppm (Fig. 8a, d), which can be assigned to surface-aligned peptides [65, 96]. At around 25 °C in DMPC bilayers, an additional broad signal appears transiently near −80 ppm (Fig. 8e), which has been attributed to peptide molecules that have flipped their alignment and inserted into the membrane as a putative oligomeric pore [96, 97, 130]. In ghost membranes, we have carefully analyzed the corresponding region of the spectrum to obtain evidence for such an upright peptide orientation. However, spectral the intensity seen around 35 °C in ghosts (Fig. 8b) is only a remnant of the powder contribution and does not signify an inserted alignment of the peptide as a pore.

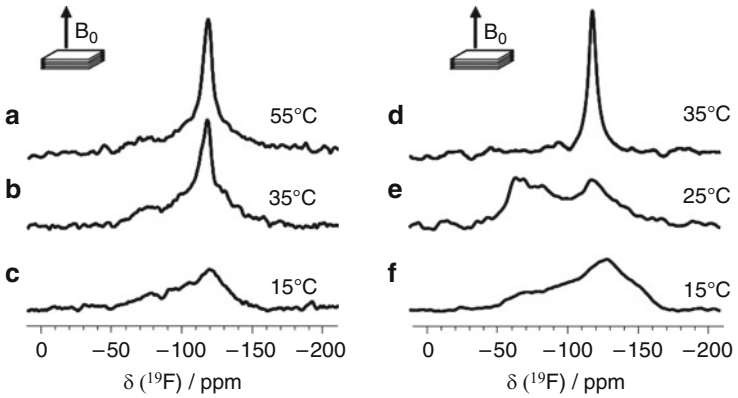

Fig. 8 Representative solid-state ^{19}F-NMR spectra of ^{19}F-labelled gramicidin S (substituted at both Leu positions with 4F-Phg), embedded in macroscopically oriented ghost membranes (*left column*) and DMPC bilayers (*right column*) at a peptide-to-lipid ratio of about 1:40 [in (F) the lipid was 1:1 DMPC/cholesterol]. Depending on temperature, the peptide can assume different alignment states, which are strikingly similar in the native membranes and the model bilayers

In summary, we may thus conclude that PGLa and GS do not form stable, NMR-observable pores in native membrane as readily as they do in model bilayers. The corresponding tilted and/or inserted states of our two representative MAPs could only be comprehensively characterized in DMPC-based samples, where the peptides could be trapped in a uniform state. In living cells, on the other hand, these states would seem to be only of a transient nature, i.e. at the very moment when the antimicrobial peptide attacks the membrane and passes through the lipid barrier along its concentration gradient towards the cytosol.

4.2 Bacterial Protoplasts

As for erythrocyte ghosts and other animal cell membranes, protocols for bacterial membrane isolation have been used for decades by cell microbiologists [131]. Until our pioneering ^{19}F-NMR study on PGLa in native membranes [124], however, such preparations were not employed in ssNMR spectroscopy. Initial attempts to copy the alignment procedure for ghosts with Gram-positive *Bacillus subtilis* protoplasts had failed at the stage of obtaining "clean" ^{31}P-NMR spectra, as they were dominated by an intense isotropic signal. Since this component could not be removed by extensive washing, it was obviously membrane-bound and originated from TA, which are known to be abundant in the envelope of most Gram-positive bacteria including *B. subtilis*. Even bacteria that are devoid of TA often still possess phosphate-containing anionic cell wall components, like lipomannanes [109, 110]. Lipomannan of *Micrococci*, however, is a lucky exception as it completely lacks phosphates [132], and *M. luteus* is a typical example of these microorganisms.

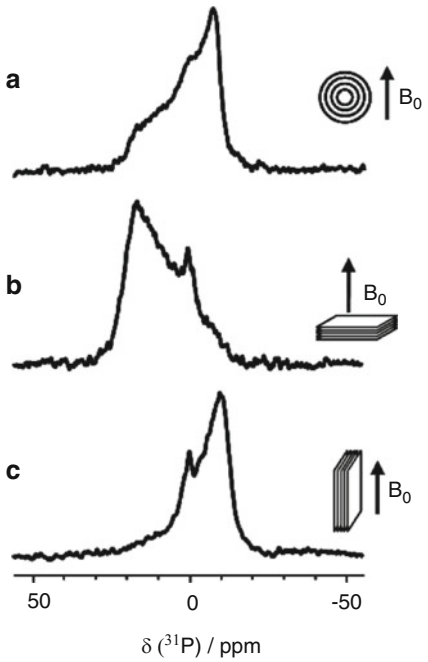

Fig. 9 Representative solid-state ^{31}P-NMR spectra from *M. luteus* protoplasts, prepared as a non-oriented suspension in excess water (**a**), and as macroscopically oriented membranes on glass slides that are aligned either parallel (**b**) or perpendicular (**c**) to the static magnetic field

The ratio of protein to lipid in the cell membrane of *M. luteus* is about 7 to 3 (wt/wt), and the lipids comprise up to 70% negatively charged PG. This lipid is predominantly located in the outer monolayer, and the remaining 30% dimannosyldiacylglycerol (DMDG) are symmetrically distributed between both leaflets [103, 133].

To prepare native membranes from *M. luteus* by osmotic lysis in a similar manner as described for erythrocytes, the thick cell wall first needs to be removed by lysozyme, and the protoplasts can be treated with hypotonic medium [122, 123]. Similar to erythrocyte ghosts, *M. luteus* protoplast preparations can be aligned on glass slides, as seen in Fig. 9. Once again, no separate ^{31}P-NMR signals of individual types of phospholipids are resolved, and isotropic signals with low intensity are present, within a CSA span of about 27 ppm. However, the linewidths of the oriented protoplast membranes are significantly larger than in oriented ghosts. This higher mosaic spread might be a consequence of the higher percentage of proteins in membranes of *M. luteus*. On top of that, the surface area of a flattened bacterial protoplasts ($\leq$ 12 μm^2) is more than an order of magnitude smaller than that of an erythrocyte ($\geq$ 120 μm^2), with a correspondingly higher number of edge defects in an oriented sample (see Fig. 2d). Together with the fast diffusion of lipids around these highly curved defects, this will contribute a broadening of the oriented signals within a narrowed CSA span.

In these protoplast preparations the possibility of solid-state ^{19}F-NMR was also demonstrated using PGLa, and the presence of a surface-bound α-helix was

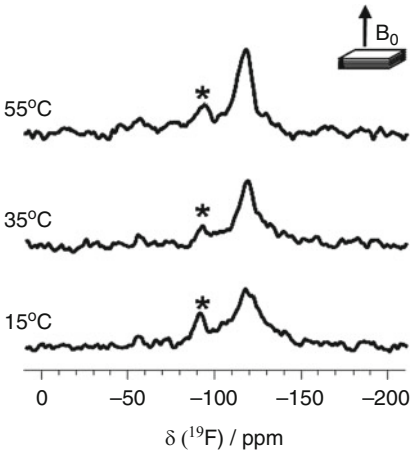

Fig. 10 Representative solid-state ^{19}F-NMR spectra of ^{19}F-labelled gramicidin S (substituted at both Leu positions with 4F-Phg), embedded in macroscopically oriented bacterial protoplasts at a peptide-to-lipid ratio of about 1:40. These membrane samples are intrinsically less well oriented than the ghosts in Fig. 8, and a TFA contamination is marked with an *asterisk*

confirmed [124]. Our more recent spectra of ^{19}F-labelled GS (Fig. 10) support a similar surface-bound state at higher temperature, and a more immobilized fraction at low temperature, similar to the situation seen in ghost membranes (Fig. 8). These data are less clear-cut, however, and also of a lower quality. While it had been noted that the protoplasts of *M. luteus* bind about tenfold more PGLa than erythrocyte ghosts, this could not be confirmed for GS.

4.3 LPS-Containing Membranes

Having established a suitable system to study MAPs in native membranes from Gram-positive bacteria, it would also be very interesting to characterize their interactions with Gram-negative ones. An antimicrobial peptide will at first encounter the LPS-monolayer of the OM, which we have accordingly tried to prepare as an oriented NMR sample. The hope was to use so-called exosomes as intrinsic membrane sources, as these vesicles (MV) are constitutively secreted by almost any cell type [134–136]. In common animal cells there are only a few dozen exosomes per cell and the accessible amount of material precludes mass production, but for bacteria the situation is advantageous [137, 138]. Like many other biofilms producing Gram-negative bacteria, *Pseudomonas aeruginosa*, for instance, is able to produce MVs in milligram quantities per litre. As these MVs have budded off from the OM of the cell envelope, they constitute a genuine, asymmetrical LPS-lipid bilayer. They are 50–100 nm in diameter and provide communication between cells, defence against harmful substances, or mediate toxicity towards the host organism. Following a period of bacterial growth, the MVs can be obtained from

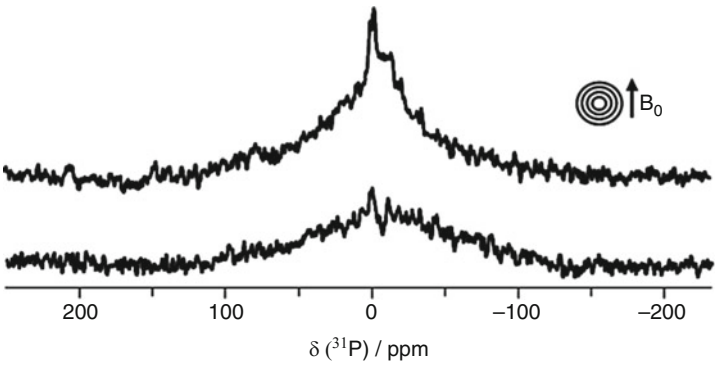

Fig. 11 Representative ^{31}P-ssNMR spectra from exosomes of *P. aeruginosa* prepared as suspensions in water excess. Preparations are from two strains, which differ in their LPS structure: rmlC (*top*) and PAO1 (*bottom*). Spectra are dominated by signals from DNA

a cell-free supernatant by ultracentrifugation [139–141]. In contrast to the erythrocyte ghosts and protoplasts of *M. luteus*, however, we have not found the harvested MVs to be applicable for ssNMR. The ^{31}P-NMR spectra are much broader and dominated by an isotropic component, as illustrated in Fig. 11. Detected significant amounts of DNA in these preparations interfere with the ^{31}P-NMR, which emphasises that the interior of MV should not be ignored. Yet, by optimized washing procedures and with application of nucleases, some control over these might be gained. Furthermore, the very small size of these vesicles makes the prospect of obtaining well-oriented membrane samples rather gloomy, given our experience with the increased abundance of defects in the oriented protoplast samples compared to the ghosts.

5 Limitations and Future Perspectives

On the way towards *in-cell* NMR, the principle feasibility of studying MAPs in native cell membranes by solid-state ^{19}F-NMR has now been demonstrated for two examples: the antimicrobial peptides PGLa and gramicidin S. Further applications can now be envisaged for other MAPs with simple secondary structures like short temporins [142], magainins [143], and designer-made analogues like MSI-103 [144], MAP [145], or BP100 [146], which are currently being characterized in lipid model membranes. In parallel, other types of cell membranes could be explored, from plants, fungi, and even from intracellular organelles. From the methodological perspective, the main restrictions are (a) the absence of ^{31}P-signals other than from phospholipids to allow a characterization of the oriented membranes, and (b) the membrane preparation should yield sufficient material (several milligrams of dry weight per sample).

The solid-state ^{19}F-NMR experiments have become possible by exploiting the high sensitivity of fluorine and its lack of a natural abundance background on the one hand, and by optimizing the preparation of oriented samples from native membranes on the other. These two aspects also represent the critical points for further improvements in moving from native membranes towards living cells. The whole arsenal of signal enhancement approaches could be applied by using novel hardware, DNP, and/or ^{19}F-NMR. Sufficient sensitivity and signal-to-noise would even alleviate the need to prepare macroscopically aligned samples when working with small, rapidly diffusing peptides in fluid membranes.

In these first demonstration studies we have always found the peptides to be in a structurally more heterogeneous situation than in model bilayers, as evident from the multi-component ^{19}F-NMR spectra. There were multiple peptide fractions co-existing in these samples, including not only surface-bound but also immobilized and freely tumbling peptide pools. Their relative proportions varied with temperature, but no conditions could be found where a single species was uniformly present. This finding is not surprising, given that extra-membranous carbohydrate- and protein-rich layers are present in native membranes, with dimensions similar to or larger than the lipid bilayer. Essentially, due to this complexity of biological membranes, the *in-cell* NMR determination of structural parameters for any MAP is *de facto* going to be intrinsically difficult. It has so far not been possible to detect a tilted or membrane-inserted state of a ^{19}F-labelled peptide in a native membrane sample, which has been reported from model membrane studies to represent distinct re-alignment steps into a transmembrane pore. This lack of data may have two reasons: (a) either the experimental conditions have not yet been found to trap these remarkable alignment states, and/or (b) the pore-associated state may occur only transiently and/or only at very low concentration in the heterogeneous environment of a native cell membrane. Nevertheless, having demonstrated here the fundamental similarity of a peptide's alignment in model bilayers and in native membranes, it is straightforward now to screen the structural behaviour and orientational states of MAPs in model membranes before further characterizing a selected few in native biomembranes. Especially the comparison between bacterial protoplasts and eukaryotic ghost membranes, including quantitative binding affinities and stepwise re-alignment thresholds by NMR, should help to shed light on the selectivity of antimicrobial peptides in terms of their molecular mechanisms of membrane perturbation.

Acknowledgements We thank PEPSY-lab at IBG2 for peptide material, and the DFG-Center for Functional Nanostructures (TP E1.2) for supporting the NMR facility.

References

1. Serber Z, Selenko P, Hansel R, Reckel S, Lohr F, Ferrell JE, Wagner G, Dotsch V (2006) Investigating macromolecules inside cultured and injected cells by in-cell NMR spectroscopy. Nat Protoc 1:2701–2709

2. Burz DS, Dutta K, Cowburn D, Shekhtman A (2006) Mapping structural interactions using in-cell NMR spectroscopy (STINT-NMR). Nat Methods 3:91–93
3. Burz DS, Shekhtman A (2008) In-cell biochemistry using NMR spectroscopy. PLoS One 3: e2571
4. Sakakibara D, Sasaki A, Ikeya T, Hamatsu J, Hanashima T, Mishima M, Yoshimasu M, Hayashi N, Mikawa T, Walchli M, Smith BO, Shirakawa M, Guntert P, Ito Y (2009) Protein structure determination in living cells by in-cell NMR spectroscopy. Nature 458:102–105
5. Reckel S, Hansel R, Lohr F, Dotsch V (2007) In-cell NMR spectroscopy. Prog Nucl Magn Reson Spectrosc 51:91–101
6. McNeill SA, Gor'kov PL, Shetty K, Brey WW, Long JR (2009) A low-E magic angle spinning probe for biological solid state NMR at 750 MHz. J Magn Reson 197:135–144
7. Dvinskikh SV, Castro V, Sandstrom D (2004) Heating caused by radiofrequency irradiation and sample rotation in C-13 magic angle spinning NMR studies of lipid membranes. Magn Reson Chem 42:875–881
8. Griffin RG, Prisner TF (2010) High field dynamic nuclear polarization-the renaissance. Phys Chem Chem Phys 12:5737–5740
9. Selenko P, Wagner G (2007) Looking into live cells with in-cell NMR spectroscopy. J Struct Biol 158:244–253
10. Reckel S, Lohr F, Dotsch V (2005) In-cell NMR spectroscopy. ChemBioChem 6:1601–1606
11. Bhattacharya A (2009) Protein structures: structures of desire. Nature 459:24–27
12. Brown FF, Campbell ID, Kuchel PW, Rabenstein DC (1977) Human erythrocyte metabolism studies by H-1 spin-echo NMR. FEBS Lett 82:12–16
13. Pielak GJ, Li CG, Miklos AC, Schlesinger AP, Slade KM, Wang GF, Zigoneanu IG (2009) Protein nuclear magnetic resonance under physiological conditions. Biochemistry-US 48:226, 9170
14. Inomata K, Ohno A, Tochio H, Isogai S, Tenno T, Nakase I, Takeuchi T, Futaki S, Ito Y, Hiroaki H, Shirakawa M (2009) High-resolution multi-dimensional NMR spectroscopy of proteins in human cells. Nature 458:106–109
15. Hu KN, Tycko R (2010) What can solid state NMR contribute to our understanding of protein folding? Biophys Chem 151:10–21
16. Bockmann A, Meier BH (2010) Prions en route from structural models to structures. Prion 4:72–79
17. Brown MF, Salgado GFJ, Struts AV (2010) Retinal dynamics during light activation of rhodopsin revealed by solid-state NMR spectroscopy. BBA-Biomembranes 1798:177–193
18. Tompa P (2009) Structural disorder in amyloid fibrils: its implication in dynamic interactions of proteins. FEBS J 276:5406–5415
19. Ramamoorthy A (2009) Beyond NMR spectra of antimicrobial peptides: dynamical images at atomic resolution and functional insights. Solid State Nucl Mag 35:201–207
20. Baldus M (2007) Magnetic resonance in the solid state: applications to protein folding, amyloid fibrils and membrane proteins. Eur Biophys J 36(Suppl 1):S37–48
21. Opella SJ, Nevzorov A, Mesleb MF, Marassi FM (2002) Structure determination of membrane proteins by NMR spectroscopy. Biochem Cell Biol 80:597–604
22. Afonin S, Juretic D, Separovic F, Ulrich AS (2011) Special issue on membrane-active peptides. Eur Biophys J 40:347–348
23. Naito A (2009) Structure elucidation of membrane-associated peptides and proteins in oriented bilayers by solid-state NMR spectroscopy. Solid State Nucl Mag 36:67–76
24. Hong M (2006) Oligomeric structure, dynamics, and orientation of membrane proteins from solid-state NMR. Structure 14:1731–1740
25. Hong M (2007) Structure, topology, and dynamics of membrane peptides and proteins from solid-state NMR spectroscopy. J Phys Chem B 111:10340–10351
26. Zelezetsky I, Tossi A (2006) Alpha-helical antimicrobial peptides – using a sequence template to guide structure–activity relationship studies. BBA-Biomembranes 1758:1436–1449

27. Scott RW, DeGrado WF, Tew GN (2008) De novo designed synthetic mimics of antimicrobial peptides. Curr Opin Biotechnol 19:620–627
28. Epand RM, Vogel HJ (1999) Diversity of antimicrobial peptides and their mechanisms of action. BBA-Biomembranes 1462:11–28
29. Giuliani A, Pirri G, Bozzi A, Di Giulio A, Aschi M, Rinaldi AC (2008) Antimicrobial peptides: natural templates for synthetic membrane-active compounds. Cell Mol Life Sci 65:2450–2460
30. Danielson MA, Falke JJ (1996) Use of F-19 NMR to probe protein structure and conformational changes. Annu Rev Biophys Biomol Struct 25:163–195
31. Yu JX, Kodibagkar VD, Cui WN, Mason RP (2005) F-19: a versatile reporter for noninvasive physiology and pharmacology using magnetic resonance. Curr Med Chem 12:819–848
32. Ulrich AS (1999) High resolution solid state NMR, 1H, 19F. In: Lindon J, Tranter G, Holmes J (eds) Encyclopedia of spectroscopy and spectrometry. Elsevier, Oxford, pp 813–825
33. Strandberg E, Wadhwani P, Tremouilhac P, Durr UHN, Ulrich AS (2006) Solid-state NMR analysis of the PGLa peptide orientation in DMPC bilayers: structural fidelity of H-2-labels versus high sensitivity of F-19-NMR. Biophys J 90:1676–1686
34. Glaser RW, Ulrich AS (2003) Susceptibility corrections in solid-state NMR experiments with oriented membrane samples. Part I: applications. J Magn Reson 164:104–114
35. Wadhwani P, Strandberg E (2009) Structure analysis of membrane-active peptides using 19F-labeled amino acids and solid-state NMR. In: Ojima I (ed) Fluorine in medicinal chemistry and chemical biology. Wiley, Chichester, pp 463–493
36. Wadhwani P, Tremouilhac P, Strandberg E, Afonin S, Grage S, Ieronimo M, Berditsch M, Ulrich AS (2007) Using fluorinated amino acids for structure analysis of membrane-active peptides by solid-state 19F-NMR. In: Soloshonok V, Mikami K, Yamazaki T, Welch JT, Honek J (eds) Current fluoroorganic chemistry (ACS symposium series). American Chemical Society, Washington, pp 431–446
37. Ulrich AS (2005) Solid state F-19 NMR methods for studying biomembranes. Prog Nucl Magn Reson Spectrosc 46:1–21
38. Mason RP (1999) Transmembrane pH gradients in vivo: measurements using fluorinated vitamin B6 derivatives. Curr Med Chem 6:481–499
39. Brindle K, Williams S-P, Boulton M (1989) 19F NMR detection of a fluorine-labelled enzyme in vivo. FEBS Lett 255:121–124
40. Li CG, Wang GF, Wang YQ, Creager-Allen R, Lutz EA, Scronce H, Slade KM, Ruf RAS, Mehl RA, Pielak GJ (2010) Protein F-19 NMR in *Escherichia coli*. J Am Chem Soc 132:321–327
41. Gor'kov PL, Witter R, Chekmenev EY, Nozirov F, Fu R, Brey WW (2007) Low-E probe for F-19-H-1 NMR of dilute biological solids. J Magn Reson 189:182–189
42. Haase J, Curro NJ, Slichter CP (1998) Double resonance probes for close frequencies. J Magn Reson 135:273–279
43. Graether SP, DeVries JS, McDonald R, Rakovszky ML, Sykes BD (2006) A H-1/F-19 minicoil NMR probe for solid-state NMR: application to 5-fluoroindoles. J Magn Reson 178:65–71
44. Andrushchenko VV, Vogel HJ, Prenner EJ (2007) Optimization of the hydrochloric acid concentration used for trifluoroacetate removal from synthetic peptides. J Pept Sci 13:37–43
45. Valenti LE, Paci MB, De Pauli CP, Giacomelli CE (2011) Infrared study of trifluoroacetic acid unpurified synthetic peptides in aqueous solution: trifluoroacetic acid removal and band assignment. Anal Biochem 410:118–123
46. Glaser RW, Sachse C, Durr UHN, Wadhwani P, Ulrich AS (2004) Orientation of the antimicrobial peptide PGLa in lipid membranes determined from F-19-NMR dipolar couplings of 4-CF3-phenylglycine labels. J Magn Reson 168:153–163
47. Park SH, Das BB, De Angelis AA, Scrima M, Opella SJ (2010) Mechanically, magnetically, and "rotationally aligned" membrane proteins in phospholipid bilayers give equivalent angular constraints for NMR structure determination. J Phys Chem B 114:13995–14003

48. Strandberg E, Ulrich AS (2004) NMR methods for studying membrane-active antimicrobial peptides. Concepts Magn Reson A 23A:89–120
49. Strandberg E, Esteban-Martin S, Salgado J, Ulrich AS (2009) Orientation and dynamics of peptides in membranes calculated from 2H-NMR data. Biophys J 96:3223–3232
50. Esteban-Martin S, Strandberg E, Salgado J, Ulrich AS (2010) Solid state NMR analysis of peptides in membranes: influence of dynamics and labeling scheme. BBA-biomembranes 1798:252–257
51. Esteban-Martin S, Strandberg E, Fuertes G, Ulrich AS, Salgado J (2009) Influence of whole-body dynamics on 15N PISEMA NMR spectra of membrane proteins: a theoretical analysis. Biophys J 96:3233–3241
52. Afonin S, Dur UHN, Glaser RW, Ulrich AS (2004) 'Boomerang'-like insertion of a fusogenic peptide in a lipid membrane revealed by solid-state F-19 NMR. Magn Reson Chem 42:195–203
53. Mykhailiuk PK, Afonin S, Palamarchuk GV, Shishkin OV, Ulrich AS, Komarov IV (2008) Synthesis of trifluoromethyl-substituted proline analogues as F-19 NMR labels for peptides in the polyproline II conformation. Angew Chem Int Edit 47:5765–5767
54. Grasnick D, Sternberg U, Strandberg E, Wadhwani P, Ulrich AS (2011) Irregular structure of the HIV fusion peptide in membranes demonstrated by solid-state NMR and MD simulations Eur Biophys J 40:529–543
55. Auger M (2000) Biological membrane structure by solid-state NMR. Curr Issues Mol Biol 2:119–124
56. Rainey JK, Sykes BD (2005) Optimizing oriented planar-supported lipid samples for solid-state protein NMR. Biophys J 89:2792–2805
57. Aisenbrey C, Bertani P, Bechinger B (2010) Solid-state NMR investigations of membrane-associated antimicrobial peptides. Methods Mol Biol 618:209–233
58. Young TS, Schultz PG (2010) Beyond the canonical 20 amino acids: expanding the genetic lexicon. J Biol Chem 285:11039–11044
59. Jones DH, Cellitti SE, Hao X, Zhang Q, Jahnz M, Summerer D, Schultz PG, Uno T, Geierstanger BH (2010) Site-specific labeling of proteins with NMR-active unnatural amino acids. J Biomol NMR 46:89–100
60. Staunton D, Schlinkert R, Zanetti G, Colebrook SA, Campbell LD (2006) Cell-free expression and selective isotope labelling in protein NMR. Magn Reson Chem 44:S2–9
61. Kubyshkin VS, Komarov IV, Afonin S, Mykhailiuk PK, Grage SL, Ulrich AS (2011) Trifluoromethyl-substituted α-amino acids as solid state 19F-NMR labels for structural studies of membrane-bound peptides. In: Gouverneur V, Müller K (eds) Fluorine in pharmaceutical and medicinal chemistry: from biophysical aspects to clinical applications. Imperial College Press (in press)
62. Wadhwani P, Afonin S, Ieromino M, Buerck J, Ulrich AS (2006) Optimized protocol for synthesis of cyclic gramicidin S: starting amino acid is key to high yield. J Org Chem 71:55–61
63. Fields GB, Noble RL (1990) Solid-phase peptide-synthesis utilizing 9-fluorenylmethoxycarbonyl amino-acids. Int J Pept Prot Res 35:161–214
64. Mikhailiuk PK, Afonin S, Chernega AN, Rusanov EB, Platonov MO, Dubinina GG, Berditsch M, UIrich AS, Komarov IV (2006) Conformationally rigid trifluoromethyl-substituted alpha-amino acid designed for peptide structure analysis by solid-state F-19 NMR spectroscopy. Angew Chem Int Edit 45:5659–5661
65. Salgado J, Grage SL, Kondejewski LH, Hodges RS, McElhaney RN, Ulrich AS (2001) Membrane-bound structure and alignment of the antimicrobial beta-sheet peptide gramicidin S derived from angular and distance constraints by solid state F-19-NMR. J Biomol NMR 21:191–208
66. Afonin S, Glaser RW, Berditchevskaia M, Wadhwani P, Guhrs KH, Mollmann U, Perner A, Ulrich AS (2003) 4-Fluorophenylglycine as a label for F-19 NMR structure analysis of membrane-associated peptides. ChemBioChem 4:1151–1163

67. Afonin S, Mikhailiuk PK, Komarov IV, Ulrich AS (2007) Evaluating the amino acid CF3-bicyclopentylglycine as a new label for solid-state F-19-NMR structure analysis of membrane-bound peptides. J Pept Sci 13:614–623
68. Mink C (2009) Zusammenhänge von Struktur und Funktion unterschiedlicher membranaktiver Peptide. PhD thesis, University of Karlsruhe (KIT)
69. Tiltak D (2009) Strukturelle und funktionelle Untersuchungen der antimikrobiellen Peptide MSI- 103 und Temporin A. PhD thesis, University of Karlsruhe (KIT)
70. Maisch D, Wadhwani P, Afonin S, Bottcher C, Koksch B, Ulrich AS (2009) Chemical labeling strategy with (R)- and (S)-trifluoromethylalanine for solid state 19F NMR analysis of peptaibols in membranes. J Am Chem Soc 131:15596–15597
71. Pervushin KV, Orekhov V, Popov AI, Musina L, Arseniev AS (1994) Three-dimensional structure of (1–71)bacterioopsin solubilized in methanol/chloroform and SDS micelles determined by 15N-1H heteronuclear NMR spectroscopy. Eur J Biochem 219:571–583
72. Tyukhtenko S, Tiburu EK, Deshmukh L, Vinogradova O, Janero DR, Makriyannis A (2009) NMR solution structure of human cannabinoid receptor-1 helix 7/8 peptide: candidate electrostatic interactions and microdomain formation. Biochem Biophys Res Commun 390:441–446
73. Luca S, White JF, Sohal AK, Filippov DV, van Boom JH, Grisshammer R, Baldus M (2003) The conformation of neurotensin bound to its G protein-coupled receptor. Proc Natl Acad Sci USA 100:10706–10711
74. Lopez JJ, Shukla AK, Reinhart C, Schwalbe H, Michel H, Glaubitz C (2008) The structure of the neuropeptide bradykinin bound to the human G-protein coupled receptor bradykinin B2 as determined by solid-state NMR spectroscopy. Angew Chem Int Ed Engl 47:1668–1671
75. Sanders CR, Sonnichsen F (2006) Solution NMR of membrane proteins: practice and challenges. Magn Reson Chem 44 Spec No:S24–40
76. Henry GD, Sykes BD (1994) Methods to study membrane protein structure in solution. Methods Enzymol 239:515–535
77. Fernandez C, Wuthrich K (2003) NMR solution structure determination of membrane proteins reconstituted in detergent micelles. FEBS Lett 555:144–150
78. Sanders CR, Hare BJ, Howard KP, Prestegard JH (1994) Magnetically-oriented phospholipid micelles as a tool for the study of membrane-associated molecules. Prog Nucl Magn Reson Spectrosc 26:421–444
79. Marcotte I, Auger M (2005) Bicelles as model membranes for solid- and solution-state NMR studies of membrane peptides and proteins. Concept Magn Reson A 24A:17–37
80. Matsumori N, Murata M (2010) 3D structures of membrane-associated small molecules as determined in isotropic bicelles. Nat Prod Rep 27:1480–1492
81. Vold RR, Prosser RS, Deese AJ (1997) Isotropic solutions of phospholipid bicelles: a new membrane mimetic for high-resolution NMR studies of polypeptides. J Biomol NMR 9:329–335
82. Canlas CG, Ma D, Tang P, Xu Y (2008) Residual dipolar coupling measurements of transmembrane proteins using aligned low-q bicelles and high-resolution magic angle spinning NMR spectroscopy. J Am Chem Soc 130:13294–13300
83. Cross TA, Sharma M, Yi M, Zhou HX (2011) Influence of solubilizing environments on membrane protein structures. Trends Biochem Sci 36:117–125
84. Wang G (2008) NMR of membrane-associated peptides and proteins. Curr Protein Pept Sci 9:50–69
85. Bader R, Lerch M, Zerbe O (2003) NMR of membrane-associated peptides and proteins. In: Zerbe O (ed) BioNMR in drug research. Wiley-VCH, Weinheim, pp 95–120
86. Diller A, Loudet C, Aussenac F, Raffard G, Fournier S, Laguerre M, Grelard A, Opella SJ, Marassi FM, Dufourc EJ (2009) Bicelles: a natural 'molecular goniometer' for structural, dynamical and topological studies of molecules in membranes. Biochimie 91:744–751
87. Nieh MP, Raghunathan VA, Glinka CJ, Harroun TA, Pabst G, Katsaras J (2004) Magnetically alignable phase of phospholipid "bicelle" mixtures is a chiral nematic made up of wormlike micelles. Langmuir 20:7893–7897

88. van Dam L, Karlsson G, Edwards K (2006) Morphology of magnetically aligning DMPC/DHPC aggregates-perforated sheets, not disks. Langmuir 22:3280–3285
89. Prosser RS, Hwang JS, Vold RR (1998) Magnetically aligned phospholipid bilayers with positive ordering: a new model membrane system. Biophys J 74:2405–2418
90. Borch J, Hamann T (2009) The nanodisc: a novel tool for membrane protein studies. Biol Chem 390:805–814
91. Gregoriadis G (1993) Liposome technology. CRC Press, Boca Raton, FL
92. Storm G, Crommelin DJA (1998) Liposomes: quo vadis? Pharm Sci Technol To 1:19–31
93. Da Costa G, Mouret L, Chevance S, Le Rumeur E, Bondon A (2007) NMR of molecules interacting with lipids in small unilamellar vesicles. Eur Biophys J Biophy 36:933–942
94. Leland DS (1996) Clinical virology. W.B. Saunders, Philadelphia
95. Tremouilhac P, Strandberg E, Wadhwani P, Ulrich AS (2006) Conditions affecting the re-alignment of the antimicrobial peptide PGLa in membranes as monitored by solid state H-2-NMR. BBA-Biomembranes 1758:1330–1342
96. Afonin S, Durr UHN, Wadhwani P, Salgado J, Ulrich AS (2008) Solid state NMR structure analysis of the antimicrobial peptide gramicidin S in lipid membranes: concentration-dependent re-alignment and self-assembly as a beta-barrel. Top Curr Chem 273:139–154
97. Grage SL, Afonin S, Ulrich AS (2010) Dynamic transitions of membrane-active peptides. Methods Mol Biol 618:183–207
98. Afonin S, Grage SL, Ieronimo M, Wadhwani P, Ulrich AS (2008) Temperature-dependent transmembrane insertion of the amphiphilic peptide PGLa in lipid bilayers; observed by solid state F-19 NMR spectroscopy. J Am Chem Soc 130:16512–16514
99. Strandberg E, Tremouilhac P, Wadhwani P, Ulrich AS (2009) Synergistic transmembrane insertion of the heterodimeric PGLa/magainin 2 complex studied by solid-state NMR. BBA-Biomembranes 1788:1667–1679
100. Arora A, Tamm LK (2001) Biophysical approaches to membrane protein structure determination. Curr Opin Struct Biol 11:540–547
101. Kosol S, Zangger K (2010) Dynamics and orientation of a cationic antimicrobial peptide in two membrane-mimetic systems. J Struct Biol 170:172–179
102. Yeaman MR, Yount NY (2003) Mechanisms of antimicrobial peptide action and resistance. Pharmacol Rev 55:27–55
103. Graham JM, Higgins JA (1998) Molekularbiologische Membrananalyse. Spektrum Akademischer Verlag GmbH, Heidelberg
104. Hanke W, Hanke R (1997) Methoden der Membranphysiologie. Spektrum Akademischer, Heidelberg
105. Shevchenko A, Simons K (2010) Lipidomics: coming to grips with lipid diversity. Nat Rev Mol Cell Bio 11:593–598
106. Stewart JC (1980) Colorimetric determination of phospholipids with ammonium ferrothiocyanate. Anal Biochem 104:10–14
107. Madigan MT, Martinko JM, Parker J (2000) Brock biology of microorganisms. Prentice Hall, Upper Saddle River, NJ
108. Voet DJ, Voet JG, Pratt CW (2010) Lehrbuch der Biochemie. Wiley-VCH, Weinheim
109. Neuhaus FC, Baddiley J (2003) A continuum of anionic charge: structures and functions of D-alanyl-teichoic acids in Gram-positive bacteria. Microbiol Mol Biol R 67:686–723
110. Sutcliffe IC, Shaw N (1991) Atypical lipoteichoic acids of Gram-positive bacteria. J Bacteriol 173:7065–7069
111. Kennedy LD (1974) Teichoic-acid synthesis in Bacillus-stearothermophilus. Biochem J 138:525–535
112. Owen P, Salton MRJ (1975) Succinylated mannan in membrane system of Micrococcus-lysodeikticus. Biochem Biophys Res Commun 63:875–880
113. Powell DA, Duckworth M, Baddiley J (1975) Membrane-associated lipomannan in micrococci. Biochem J 151:387–397
114. Schlegel HG (1992) Allgemeine Mikrobiologie. Georg Thieme Verlag, Stuttgart

115. Papo N, Shai Y (2003) Can we predict biological activity of antimicrobial peptides from their interactions with model phospholipid membranes? Peptides 24:1693–1703
116. Kondejewski LH, Farmer SW, Wishart DS, Kay CM, Hancock REW, Hodges RS (1996) Modulation of structure and antibacterial and hemolytic activity by ring size in cyclic gramicidin S analogs. J Biol Chem 271:25261–25268
117. Ruden S, Hilpert K, Berditsch M, Wadhwani P, Ulrich AS (2009) Synergistic interaction between silver nanoparticles and membrane-permeabilizing antimicrobial peptides. Antimicrob Agents Chemother 53:3538–3540
118. Evans WH, Graham JM (1991) Struktur und Funktion biologischer Membranen. Georg Thieme Verlag, Stuttgart
119. Begemann H, Rastatter J (1993) Klinische Hämatologie. Georg Thieme Verlag, Stuttgart
120. Baake M, Gilles A (1994) Hämatologie. Theorie und Praxis für medizinische Assistenzberufe. GIT Verlag GmbH, Darmstadt
121. Schwoch G, Passow H (1973) Preparation and properties of human erythrocyte-ghosts. Mol Cell Biochem 2:197–218
122. Hanahan DJ, Ekholm JE (1974) The preparation of red cell ghosts (membranes). Methods Enzymol 31:168–172
123. Dodge JT, Mitchell C, Hanahan DJ (1963) The preparation and chemical characteristics of hemoglobin-free ghosts of human erythrocytes. Arch Biochem Biophys 100: 119–130
124. Ieronimo M, Afonin S, Koch K, Berditsch M, Wadhwani P, Ulrich AS (2010) 19F NMR analysis of the antimicrobial peptide PGLa bound to native cell membranes from bacterial protoplasts and human erythrocytes. J Am Chem Soc 132:8822–8824
125. Steck TL (1974) The organization of proteins in the human red blood cell membrane. A review J Cell Biol 62:1–19
126. McLaughlin AC, Cullis PR, Hemminga MA, Hoult DI, Radda GK, Ritchie GA, Seeley PJ, Richards RE (1975) Application of 31P NMR to model and biological membrane systems. FEBS Lett 57:213–218
127. Yeagle PL (1982) 31P nuclear magnetic resonance studies of the phospholipid-protein interface in cell membranes. Biophys J 37:227–239
128. Grobner G, Taylor A, Williamson PT, Choi G, Glaubitz C, Watts JA, de Grip WJ, Watts A (1997) Macroscopic orientation of natural and model membranes for structural studies. Anal Biochem 254:132–138
129. Rockland LB (1960) Saturated salt solutions for static control of relative humidity between 5-degrees-C and 40-degrees-C. Anal Chem 32:1375–1376
130. Afonin S (2004) Structural studies on membrane-active peptides in lipid bilayers by solid state 19F-NMR. PhD thesis, University of Jena
131. Martin HH (1963) Bacterial protoplasts – a review. J Theor Biol 5:1–34
132. Pless DD, Schmit AS, Lennarz WJ (1975) The characterization of mannan of Micrococcus lysodeikticus as an acidic lipopolysaccharide. J Biol Chem 250:1319–1327
133. de Bony J, Lopez A, Gilleron M, Welby M, Laneelle G, Rousseau B, Beaucourt JP, Tocanne JF (1989) Transverse and lateral distribution of phospholipids and glycolipids in the membrane of the bacterium *Micrococcus luteus.* Biochemistry-Us 28:3728–3737
134. Hurley JH, Boura E, Carlson LA, Rozycki B (2010) Membrane budding. Cell 143:875–887
135. Mause SF, Weber C (2010) Microparticles: protagonists of a novel communication network for intercellular information exchange. Circ Res 107:1047–1057
136. Simons M, Raposo G (2009) Exosomes–vesicular carriers for intercellular communication. Curr Opin Cell Biol 21:575–581
137. Beveridge TJ (1999) Structures of Gram-negative cell walls and their derived membrane vesicles. J Bacteriol 181:4725–4733
138. Mashburn-Warren L, Mclean RJC, Whiteley M (2008) Gram-negative outer membrane vesicles: beyond the cell surface. Geobiology 6:214–219

139. Schooling SR, Beveridge TJ (2006) Membrane vesicles: an overlooked component of the matrices of biofilms. J Bacteriol 188:5945–5957
140. Renelli M, Matias V, Lo RY, Beveridge TJ (2004) DNA-containing membrane vesicles of *Pseudomonas aeruginosa* PAO1 and their genetic transformation potential. Microbiol-Sgm 150:2161–2169
141. Kadurugamuwa JL, Beveridge TJ (1995) Virulence factors are released from Pseudomonas-aeruginosa in association with membrane-vesicles during normal growth and exposure to gentamicin – a novel mechanism of enzyme-secretion. J Bacteriol 177:3998–4008
142. Mangoni ML, Rinaldi AC, Di Giulio A, Mignogna G, Bozzi A, Barra D, Simmaco M (2000) Structure-function relationships of temporins, small antimicrobial peptides from amphibian skin. Eur J Biochem 267:1447–1454
143. Matsuzaki K, Murase O, Fujii N, Miyajima K (1996) An antimicrobial peptide, magainin 2, induced rapid flip-flop of phospholipids coupled with pore formation and peptide translocation. Biochemistry-Us 35:11361–11368
144. Blazyk J, Wiegand R, Klein J, Hammer J, Epand RM, Epand RF, Maloy WL, Kari UP (2001) A novel linear amphipathic beta-sheet cationic antimicrobial peptide with enhanced selectivity for bacterial lipids. J Biol Chem 276:27899–27906
145. Steiner V, Schar M, Bornsen KO, Mutter M (1991) Retention behaviour of a template-assembled synthetic protein and its amphiphilic building blocks on reversed-phase columns. J Chromatogr 586:43–50
146. Ferre R, Badosa E, Feliu L, Planas M, Montesinos E, Bardaji E (2006) Inhibition of plant-pathogenic bacteria by short synthetic cecropin A-melittin hybrid peptides. Appl Environ Microbiol 72:3302–3308

Top Curr Chem (2012) 306: 119–188
DOI: 10.1007/128_2011_141

Published online: 8 June 2011

Probing Quadrupolar Nuclei by Solid-State NMR Spectroscopy: Recent Advances

Christian Fernandez and Marek Pruski

Abstract Solid-state nuclear magnetic resonance (NMR) of quadrupolar nuclei has recently undergone remarkable development of capabilities for obtaining structural and dynamic information at the molecular level. This review summarizes the key achievements attained during the last couple of decades in solid-state NMR of both integer spin and half-integer spin quadrupolar nuclei. We provide a concise description of the first- and second-order quadrupolar interactions, and their effect on the static and magic angle spinning (MAS) spectra. Methods are explained for efficient excitation of single- and multiple-quantum coherences, and acquisition of spectra under low- and high-resolution conditions. Most of all, we present a coherent, comparative description of the high-resolution methods for half-integer quadrupolar nuclei, including double rotation (DOR), dynamic angle spinning (DAS), multiple-quantum magic angle spinning (MQMAS), and satellite transition magic angle spinning (STMAS). Also highlighted are methods for processing and analysis of the spectra. Finally, we review methods for probing the heteronuclear and homonuclear correlations between the quadrupolar nuclei and their quadrupolar or spin-1/2 neighbors.

Keywords Cross-polarization · Double rotation (DOR) · Dynamic angle spinning (DAS) · Half-integer spin quadrupolar nuclei · Heteronuclear correlation (HETCOR) · High-resolution methods · Homonuclear recoupling · Indirect detection · Integer spin nuclei · *J*-coupling · Multiple-quantum magic angle spinning (MQMAS) · Quadrupolar echo · Quadrupolar interaction · Quadrupolar nuclei ·

C. Fernandez (✉)
Laboratoire Catalyse et Spectrochimie, ENSICAEN, Université de Caen, CNRS, 6 Bd Maréchal Juin, 14050 Caen, France
e-mail: christian.fernandez@ensicaen.fr

M. Pruski (✉)
Ames Laboratory, Iowa State University, Ames, IA 50011-3020, USA
and
Department of Chemistry, Iowa State University, Ames, IA 50011-3020, USA
e-mail: mpruski@iastate.edu

Satellite transition magic angle spinning (STMAS) · Selection of coherences · Sensitivity enhancement · Solid-state NMR

Contents

1 Introduction

Quadrupolar nuclei, i.e., those with a nuclear spin quantum number I greater than or equal to one, outnumber their spin-1/2 counterparts by a factor of roughly 3:1 and are critically important in the study of many solid materials. For example, ^{11}B (spin $I = 3/2$, 80% natural abundance), ^{14}N ($I = 1$, 99.6%), ^{23}Na ($I = 3/2$, 100%), ^{17}O ($I = 5/2$, 0.04%) and ^{27}Al ($I = 5/2$, 100%) comprise some of the most important atomic nuclei in chemistry, materials science, and biology. As is well

known, the solid-state NMR spectra of quadrupolar nuclei are difficult to observe under high resolution compared to the more tractable spin-1/2 nuclei due to the interaction between the non-spherical distribution of electric charge in such nuclei and the electric field created by the surrounding electrons. Low natural abundance and small gyromagnetic ratios often add to the difficulty.

Given the importance of quadrupolar nuclei in solid-state NMR, it is not surprising that extensive research efforts during the last couple of decades aimed at addressing challenges posed by the quadrupolar interaction. The quest to improve resolution has been particularly noteworthy, culminating in the development of multiple-quantum magic-angle spinning (MQMAS) and satellite-transition MAS (STMAS) experiments, which followed earlier approaches utilizing more complex sample rotations (double rotation and dynamic angle spinning). In this chapter, we focus on a number of recent critical developments enhancing the sensitivity and resolution of quadrupolar NMR spectra. Only a brief overview of the necessary theoretical background will be given here, as the features of the quadrupolar interaction in NMR have already been described in detail [1–7]. Several reviews dedicated to specific classes of techniques [8–16], and general overviews of recent advances and their applications [4, 17–20], have been published, as well. Our goal is to present a coherent, comparative description of state-of-the-art methods in solid-state NMR spectroscopy of quadrupolar nuclei, with emphasis on both theoretical and experimental aspects of high-resolution experiments. We will also describe the recent advances in homo- and hetero-nuclear correlation experiments involving quadrupolar nuclei.

2 Solid-State NMR Spectra of Quadrupolar Nuclei

The strength of the quadrupolar interaction is proportional to the quadrupole moment Q of a nucleus and the electric field gradient (EFG) [21–23]. The size of Q depends on the effective shape of the ellipsoid of nuclear charge distribution, and a non-zero value indicates that it is not spherically symmetric (Fig. 1).

The quadrupolar interaction perturbs the $2I + 1$ Zeeman energy levels of a quadrupolar nucleus experiencing a homogeneous external magnetic field B_0 in an orientation-dependent fashion. The resulting anisotropic broadening of the NMR spectra constitutes a mixed blessing for a spectroscopist. On the one hand, it hinders the observation of individual sites, but on the other hand provides a measure of the strength and geometry of the EFG tensors and, consequently, important information about the local chemical and electronic structure of the solid around the observed nuclei.

2.1 The Quadrupolar Interaction

The Hamiltonian describing the quadrupolar interaction in the laboratory frame (L), in the units of radians/s, can be written using the spherical tensor formalism as [1, 6, 24]

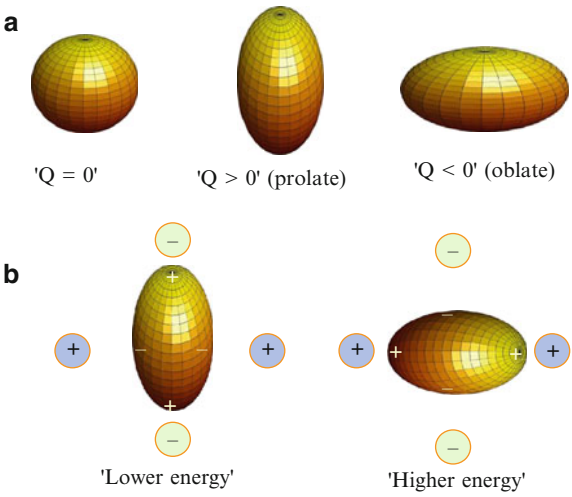

Fig. 1 (**a**) Schematic representation of the spherical and non-spherical charge distribution in a nucleus. The value of electric quadrupole moment Q for the quadrupolar nucleus depends on the isotope under consideration. (**b**) The quadrupolar interaction arises from the interaction of Q with surrounding electric field gradient (EFG)

$$\mathcal{H}_Q = \frac{\omega_Q}{3} \sum_{k=-2}^{2} (-1)^k A^L_{2,-k} T_{2,k}, \tag{1}$$

with [21]

$$\omega_Q = \frac{3e^2qQ}{2I(2I-1)\hbar} = 2\pi \frac{3C_Q}{2I(2I-1)}, \tag{2}$$

where ω_Q and C_Q denote the quadrupolar frequency and the quadrupole coupling constant expressed in radians/s and hertz, respectively. These parameters are typically used to describe the magnitude of the quadrupolar interaction. The spatial tensors, $A^L_{2,k}$, in the L frame are obtained from the corresponding tensors, $A^P_{2,k}$, in the principal axis frame (P) of the EFG tensor using the appropriate Wigner rotation matrices, $D^2_{n,k}(\Theta_{PL})$:

$$A^L_{2,k}(\Theta_{PL}) = \sum_{n=-2}^{2} A^P_{2,n} D^2_{n,k}(\Theta_{PL}), \tag{3}$$

where $\Theta_{PL} = (\alpha_{PL}, \beta_{PL}, \gamma_{PL})$ are the Euler angles defining the orientation of the P frame in the L frame. Note that the principal axis frame, P, should also be oriented with respect to the local molecular (or crystalline) frame, M. In the absence of motion, which is assumed herein, the molecular framework is rigid and thus the M and P frames can be considered as one. The coefficients $A^P_{2,n}$ are given by

$$A^P_{2,0} = \sqrt{\frac{3}{2}}, \quad A^P_{2,\pm1} = 0, \quad A^P_{2,\pm2} = \frac{1}{2}\eta, \tag{4}$$

where the asymmetry parameter η characterizes the deviation of the EFG tensor from axial symmetry. The spin tensor operators, $T_{2,k}$, in (1) are defined by [6]

$$T_{2,0} = \frac{1}{\sqrt{6}}(3I_z^2 - I(I+1)), T_{2,\pm1} = \mp\frac{1}{2}(I_\pm I_z + I_z I_\pm), T_{2,\pm2} = \frac{1}{2}I_\pm^2. \tag{5}$$

In the rotating frame, the quadrupolar interaction is modulated with the Larmor frequency, ω_0:

$$\widetilde{\mathcal{H}_Q(t)} = \frac{\omega_Q}{3}\sum_{k=-2}^{2}(-1)^k A^L_{2,-k}(\Theta_{PL})T_{2,k}\mathrm{e}^{\mathrm{i}k\omega_0 \mathrm{t}}. \tag{6}$$

When the Zeeman interaction is much larger than the quadrupolar frequency ($\omega_0 \gg \omega_Q$), the averaged quadrupolar Hamiltonian over a Larmor period, $T = \dfrac{2\pi}{\omega_0}$, can be expanded as a series [25, 26]:

$$\overline{\widetilde{\mathcal{H}_Q(t)}} = \mathcal{H}_Q^I + \mathcal{H}_Q^{II} + \mathcal{H}_Q^{III}\ldots \tag{7}$$

Generally, it is sufficient to truncate the series after the first- and second-order terms [1, 6]:

$$\begin{aligned}\mathcal{H}_Q^I &= \frac{1}{T}\int_0^{\frac{1}{T}}\widetilde{\mathcal{H}_Q(t)}\,\mathrm{d}t \\ &= \frac{\omega_Q}{3}A^L_{2,0}(\Theta_{PL})T_{2,0} \\ &= \frac{\omega_Q}{3\sqrt{6}}A^L_{2,0}(\Theta_{PL})\left(3I_z^2 - I(I+1)\right)\end{aligned} \tag{8}$$

and

$$\begin{aligned}\mathcal{H}_Q^{II} &= -\frac{i}{2T}\int_0^{\frac{1}{T}}\int_0^t\left[\widetilde{\mathcal{H}_Q(t)}, \widetilde{\mathcal{H}_Q(t')}\right]\mathrm{d}t'\,\mathrm{d}t \\ &= \frac{1}{9}\frac{{\omega_Q}^2}{\omega_0}\sum_{m>0}\frac{1}{m}A^L_{2,m}(\Theta_{PL})A^L_{2,-m}(\Theta_{PL})\left[T_{2,m}, T_{2,-m}\right].\end{aligned} \tag{9}$$

The products of second-rank tensor components, such as $A^L_{2,1}(\Theta_{PL})A^L_{2,-1}(\Theta_{PL})$, can be expressed in coupled form using the Clebsch–Gordan coefficients, yielding tensor terms, $B^L_{l,0}(\Theta_{PL})$, of spatial rank $l = 0$, 2, and 4:

$$\mathcal{H}_Q^{II} = \frac{1}{9}\frac{{\omega_Q}^2}{\omega_0}\left(B^L_{0,0}K_0 + B^L_{2,0}(\Theta_{PL})K_2 + B^L_{4,0}(\Theta_{PL})K_4\right), \tag{10}$$

where

$$\begin{aligned}K_0 &= \frac{1}{\sqrt{5}}I_z\left(3I_z^2 - I(I+1)\right), \quad K_2 = -\frac{1}{2\sqrt{14}}I_z\left(12I_z^2 - 8I(I+1) + 3\right), \\ K_4 &= -\frac{1}{2\sqrt{70}}I_z\left(34I_z^2 - 18I(I+1) + 5\right).\end{aligned} \tag{11}$$

The elements $B^L_{k,0}(\Theta_{PL})$ are expressed in terms of $B^P_{k,n}$ in the principal axis frame of the EFG, as in the case of the $A^L_{2,k}(\Theta_{PL})$ (3):

$$B^L_{k,0}(\Theta_{PL}) = \sum_{n=-k}^{k} B^P_{k,n} D^k_{n,0}(\Theta_{PL}) \tag{12}$$

with the non-vanishing terms given by

$$\begin{aligned} B^P_{0,0} &= \frac{3+\eta^2}{2\sqrt{5}}, \quad B^P_{2,0} = \frac{-3+\eta^2}{\sqrt{14}}, \quad B^P_{2,\pm 2} = \eta\sqrt{\frac{3}{7}}, \\ B^P_{4,0} &= \frac{18+\eta^2}{2\sqrt{70}}, \quad B^P_{4,\pm 2} = \frac{3\eta}{2\sqrt{7}}, \quad B^P_{4,\pm 4} = \frac{\eta^2}{4}. \end{aligned} \tag{13}$$

It follows from (12) that $B^L_{0,0}(\Theta_{PL}) = B^P_{0,0}$ is independent of the sample orientation.

When the sample is spun in a rotor with a spinning frequency ω_R about an axis at angle β_{RL} with respect to B_0, the first-order quadrupolar Hamiltonian can be rewritten as

$$\begin{aligned} \mathcal{H}^I_Q &= \frac{\omega_Q}{3} A^L_{2,0}(\Theta_{PL}) T_{2,0} = \frac{\omega_Q}{3} \left(\sum_{k=-2}^{2} A^R_{2,k}(\Theta_{PR}) D^2_{k,0}(\Theta_{RL}) \right) T_{2,0} \\ &= \frac{\omega_Q}{3} \left(\sum_{k=-2}^{2} A^R_{2,k}(\Theta_{PR}) e^{ik\omega_R t} d^2_{k,0}(\beta_{RL}) \right) T_{2,0}, \end{aligned} \tag{14}$$

where $\Theta_{RL} = (\omega_R t, \beta_{RL}, 0)$ and $\Theta_{PR} = (\alpha_{PR}, \beta_{PR}, \gamma_{PR})$ are the Euler angles defining the orientations of the rotor frame, R, in the L frame, and the P frame in the R frame, respectively. As previously, it is easy to write the $A^R_{2,k}(\Theta_{PR})$ tensors in terms of $A^P_{2,k}$ in the P frame using the Wigner rotation matrix:

$$A^R_{2,k}(\Theta_{PR}) = \sum_{n=-2}^{2} A^P_{2,n} D^2_{n,k}(\Theta_{PR}). \tag{15}$$

In the fast ("infinite") spinning speed regime, $\omega_R \gg \omega_Q$, (14) can be simplified by averaging over a rotor period:

$$\begin{aligned} \overline{\mathcal{H}}^I_Q &= \frac{\omega_Q}{3} \left(\sum_{k=-2}^{2} A^R_{2,k}(\Theta_{PR}) \overline{e^{ik\omega_R t}} d^2_{k,0}(\beta_{RL}) \right) T_{2,0} \\ &= \frac{\omega_Q}{3} A^R_{2,0}(\Theta_{PR}) d^2_{0,0}(\beta_{RL}) T_{2,0}. \end{aligned} \tag{16}$$

The Wigner component $d^2_{0,0}$ is equal to the second-order Legendre polynomial:

$$d^2_{0,0}(\beta_{RL}) = P_2(\cos(\beta_{RL})) = \frac{1}{2}\left(3\cos^2(\beta_{RL}) - 1\right). \tag{17}$$

As is well known, this term vanishes when the sample is spun at the magic angle, i.e., when $\beta_{RL} = \text{acos}\left(1/\sqrt{3}\right) = 54.736°$ (Fig. 2).

For the second-order term in the Hamiltonian, the rotation of the rotor implies similar transformations, which in the fast-spinning case yields an average operator

$$\begin{aligned}\overline{\mathcal{H}^{II}_Q} &= \frac{1}{9}\frac{{\omega_Q}^2}{\omega_0}\left(B^L_{0,0}K_0 + \overline{B^L_{2,0}}(\Theta_{PL})K_2 + \overline{B^L_{4,0}}(\Theta_{PL})K_4\right)\\ &= \frac{1}{9}\frac{{\omega_Q}^2}{\omega_0}\left(\begin{array}{c} B^R_{0,0}K_0 + \left(\sum_{k=-2}^{2} B^R_{2,k}(\Theta_{PR})\overline{e^{ik\omega_R t}}d^2_{k,0}(\Theta_{RL})\right)K_2 \\ + \left(\sum_{k=-4}^{4} B^R_{4,k}(\Theta_{PR})\overline{e^{ik\omega_R t}}d^4_{k,0}(\Theta_{RL})\right)K_4 \end{array}\right)\\ &= \frac{1}{9}\frac{{\omega_Q}^2}{\omega_0}\left(B^R_{0,0}K_0 + B^R_{2,0}(\Theta_{PR})d^2_{0,0}(\beta_{RL})K_2 + B^R_{4,0}(\Theta_{PR})d^4_{0,0}(\beta_{RL})K_4\right),\end{aligned} \tag{18}$$

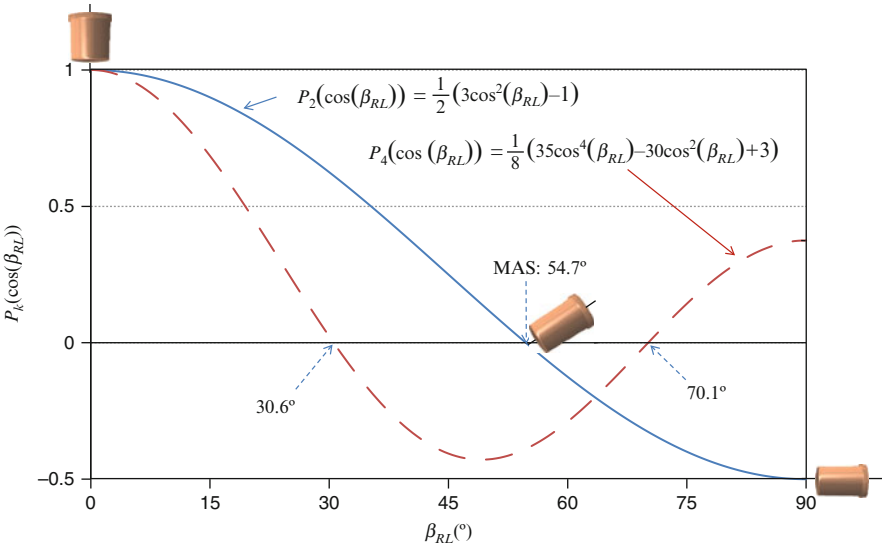

Fig. 2 The values of second-order P_2 and fourth-order P_4 Legendre polynomials as functions of β_{RL}. The two polynomials do not have a common root, i.e., the anisotropic terms in the second-order quadrupolar Hamiltonian cannot both be canceled at once, regardless of the orientation of the rotor axis

which can be written as the sum of the contributions of ranks 0, 2, and 4:

$$\overline{\mathcal{H}_Q^{II}} = \overline{\mathcal{H}_Q^{(0)}} + \overline{\mathcal{H}_Q^{(2)}} + \overline{\mathcal{H}_Q^{(4)}}. \tag{19}$$

The rank 0 term, referred to as the quadrupolar-induced shift (QIS) operator, is independent of the molecular and rotor orientation ($B_{0,0}^R = B_{0,0}^L$). Using (11), (13), and (18), this term can be written

$$\begin{aligned}\overline{\mathcal{H}_Q^{(0)}} &= \frac{1}{9}\frac{{\omega_Q}^2}{\omega_0} B_{0,0}^L K_0 = \frac{(1+\eta^2/3)}{30}\frac{{\omega_Q}^2}{\omega_0} I_z\left(3I_z^2 - I(I+1)\right) \\ &= \frac{1}{30}\frac{{\chi_Q}^2}{\omega_0} I_z\left(3I_z^2 - I(I+1)\right),\end{aligned} \tag{20}$$

where $\chi_Q = \omega_Q\sqrt{1+\eta^2/3}$ is used to simplify the expression.

As previously, the $B_{20}^R(\Theta_{PR})$ and $B_{40}^R(\Theta_{PR})$ tensors can be expressed in terms of B_{kn}^P in P frame using the Wigner rotation matrix:

$$B_{l0}^R(\Theta_{PR}) = \sum_{n=-l}^{l} B_{ln}^P D_{n,0}^l(\Theta_{PR}). \tag{21}$$

When the rotor is spun at the magic angle, the term containing $d_{0,0}^2(\beta_{RL})$vanishes, and (18) reduces to

$$\overline{\mathcal{H}_Q^{II}} = \overline{\mathcal{H}_Q^{(0)}} + \overline{\mathcal{H}_Q^{(4)}} = \frac{1}{9}\frac{{\omega_Q}^2}{\omega_0}\left(B_{0,0}^R K_0 + B_{4,0}^R(\Theta_{PR}) d_{0,0}^4(\beta_{RL}) K_4\right). \tag{22}$$

The fourth rank orientation-dependent term $\overline{\mathcal{H}_Q^{(4)}}$, includes the fourth-order Legendre polynomial:

$$d_{0,0}^4(\beta_{RL}) = P_4(\cos(\beta_{RL})) = \frac{1}{8}\left(35\cos^4(\beta_{RL}) - 30\cos^2(\beta_{RL}) + 3\right) \tag{23}$$

which does not vanish at the magic angle (Fig. 2). Indeed, $\overline{\mathcal{H}_Q^{(2)}}$ and $\overline{\mathcal{H}_Q^{(4)}}$ cannot be simultaneously nullified for any single value of β_{RL}. It is also noted that for $\beta_{RL} = 0$, (18) becomes strictly identical to (10) and thus can be used to describe the Hamiltonian of a static sample.

2.2 Second-Order Cross Terms

The total Hamiltonian that governs the spin system is the sum of contributions arising from the various interactions, including Zeeman interaction, chemical shift

anisotropy (CSA), J-couplings, dipolar couplings, and quadrupolar couplings. As seen in the previous section, the quadrupole coupling is sufficiently strong to warrant analysis of the second-order or higher perturbation terms of the Zeeman interaction. The CSA, J, and dipolar interactions are generally only weak (first-order) perturbations of the dominant Zeeman interaction.

However, in the presence of a strong quadrupolar interaction, the second-order cross-terms between the quadrupolar interaction and the CSA [27, 28] or the heteronuclear dipolar interaction [29, 30] also have to be taken into account. For instance, upon including the CSA in the expression of the time-dependent Hamiltonian in (9), the second-order term becomes

$$\begin{aligned}\left(\mathcal{H}_Q + \mathcal{H}_{\mathrm{CSA}}\right)^{II} &= -\frac{i}{2T}\int_0^T\int_0^t \left[\overbrace{\left(\mathcal{H}_Q(t) + \mathcal{H}_{\mathrm{CSA}}(t)\right)}, \overbrace{\left(\mathcal{H}_Q(t') + \mathcal{H}_{\mathrm{CSA}}(t')\right)}\right] \mathrm{d}t'\,\mathrm{d}t \\ &= -\frac{i}{2T}\int_0^T\int_0^t \left[\widetilde{\mathcal{H}_Q(t)}, \widetilde{\mathcal{H}_Q(t')}\right] \mathrm{d}t'\,\mathrm{d}t \\ &\quad -\frac{i}{2T}\int_0^T\int_0^t \left[\widetilde{\mathcal{H}_{\mathrm{CSA}}(t)}, \widetilde{\mathcal{H}_{\mathrm{CSA}}(t')}\right] \mathrm{d}t'\,\mathrm{d}t \\ &\quad -\frac{i}{2T}\int_0^T\int_0^t \left[\widetilde{\mathcal{H}_Q(t)}, \widetilde{\mathcal{H}_{\mathrm{CSA}}(t')}\right] \mathrm{d}t'\,\mathrm{d}t \\ &= \mathcal{H}_Q^{II} + \mathcal{H}_{\mathrm{CSA}}^{II} + \mathcal{H}_{Q*\mathrm{CSA}}^{II}. \end{aligned} \tag{24}$$

The first term in (24) was already calculated in (9). The second term can be neglected, as the CSA is usually too weak to require the second-order treatment. The last term is the second-order cross-term between the two interactions. A complete review of the second-order cross-terms and their effect on high-resolution solid-state NMR powder spectra of quadrupolar nuclei was recently published by Ashbrook et al. [31].

2.3 *Coherences and Powder Spectra*

2.3.1 Coherence and Satellite Orders

The observable NMR signal $s(t)$, detected in the quadrature mode, is related to the density matrix $\rho(t)$ at time t as follows:

$$s(t) = tr(\rho(t)I^+). \tag{25}$$

Equation (25) implies that the only density matrix components that contribute to the observed signal correspond to transitions between eigenstates $|s\rangle$ and $|r\rangle$ with $p = (r - s) = -1$. For spin $I = 3/2$, these include the central transition (CT) $|1/2\rangle \rightarrow |-1/2\rangle$ and the satellite transitions (STs), e.g., ($|3/2\rangle \rightarrow |1/2\rangle$) or

($|-1/2\rangle \rightarrow |-3/2\rangle$). The quantum number p is known as the coherence order of the transition.

The use of coherence order can be very helpful in understanding the evolution of spin magnetization. Diagrams illustrating the coherence transfer pathways are used to design new pulse sequences and derive phase-cycles (or pulsed field gradient schemes) that select the desired pathways and lead to pure absorptive lineshapes in two-dimensional (2D) spectra [32–34]. The concept of coherence transfer pathways is particularly useful in solid-state NMR of quadrupolar nuclei, and will be utilized extensively in the ensuing sections. We will follow the formalism proposed recently by Antonijevic et al. [35], which distinguishes coherences that have the same order p but different satellite orders $q = (r^2 - s^2)$. The index q can adopt $2I + 1 - |p|$ different integer values corresponding to the number of lines in the pQ spectrum. Using this additional index, the various coherences will be differentiated using single-element operators $I_{p,q}$ [35]. For example, the three observable coherences in spin-3/2 nuclei corresponding to the CT, $|1/2\rangle \rightarrow |-1/2\rangle$, and two STs, $|3/2\rangle \rightarrow |1/2\rangle$ and $|-1/2\rangle \rightarrow |-3/2\rangle$, are denoted $I_{-1,0}$, $I_{-1,-2}$ and $I_{-1,2}$, respectively.

2.3.2 Selection of Coherences

As explained in depth in the next sections, most of the advanced high-resolution experiments on quadrupolar nuclei are based on the selection of specific coherences and on the transfer of these coherences along the selected pathways, which always terminate at the observable SQ coherence $p = -1$. Most of the time, the selection is done using nested phase-cycling of the radiofrequency (rf) pulses included in the pulse sequence [34]. Recently, new methods have been proposed to optimize the nested phase-cycling procedure, including the schemes referred to as cogwheel [36–39] and multiplex [40–42].

2.3.3 Transition Frequencies and Powder Spectra

Let us calculate the frequencies of transitions between Zeeman eigenstates $|s\rangle$ and $|r\rangle$, assuming that the nuclei are only subjected to an isotropic chemical shift and the first- and second-order quadrupolar interaction. As seen in Sect. 2.1, the Hamiltonian that governs the spin system in the frame of the Zeeman interaction (the rotating frame) is

$$\mathcal{H} = \mathcal{H}_{\mathrm{CS}} + \overline{\mathcal{H}_Q^I} + \overline{\mathcal{H}_Q^{II}} = \mathcal{H}_{CS} + \overline{\mathcal{H}_Q^I} + \overline{\mathcal{H}_Q^{(0)}} + \overline{\mathcal{H}_Q^{(2)}} + \overline{\mathcal{H}_Q^{(4)}} \ . \tag{26}$$

In the fast-spinning case $\mathcal{H}_{\mathrm{CS}} = \omega_0 \delta_{\mathrm{CS}} I_z$, where δ_{CS} represents the resonance offset or the isotropic chemical shift and the quadrupolar terms are given by (16) and (18). Thus, we obtain

$$\begin{aligned}\mathcal{H} &= \omega_0\delta_{\mathrm{CS}}I_z + \frac{1}{3}\omega_Q A^R_{2,0}(\Theta_{PR})d^2_{0,0}(\beta_{RL})T_{2,0} \\ &+ \frac{1}{9}\frac{{\omega_Q}^2}{\omega_0}\left(B^R_{0,0}K_0 + B^R_{2,0}(\Theta_{PR})d^2_{0,0}(\beta_{RL})K_2 + B^R_{4,0}(\Theta_{PR})d^4_{0,0}(\beta_{RL})K_4\right).\end{aligned} \tag{27}$$

For a given orientation Θ_{PR} of the molecule, the transition frequency between eigenstates $|s\rangle$ and $|r\rangle$ is given by

$$\omega_{s\to r} = \langle r|\mathcal{H}|r\rangle - \langle s|\mathcal{H}|s\rangle. \tag{28}$$

It is convenient to express these frequencies in term of p (coherence order) and q (satellite order), following the convention described in Sect. 2.3.1:

$$\begin{aligned}\omega_{p,q} &= \omega^{\mathrm{CS}}_{p,q} + \omega^{I}_{p,q} + \omega^{II}_{p,q} = \left(\omega^{\mathrm{CS}}_{p,q} + \omega^{(0)}_{p,q}\right) + \omega^{I}_{p,q} + \left(\omega^{(2)}_{p,q} + \omega^{(4)}_{p,q}\right) \\ &= \omega^{\mathrm{ISO}}_{p,q} + \omega^{I}_{p,q} + \omega^{\mathrm{ANISO}}_{p,q},\end{aligned} \tag{29}$$

where the term $\omega^{\mathrm{ISO}}_{p,q}$ is the orientation-independent isotropic frequency corresponding to the sum of isotropic chemical frequency, $\omega^{\mathrm{CS}}_{p,q}$, and the additional quadrupolar-induced (rank-0) frequency term, $\omega^{(0)}_{p,q}$:

$$\begin{aligned}\omega^{\mathrm{ISO}}_{p,q} &= \omega^{\mathrm{CS}}_{p,q} + \omega^{(0)}_{p,q} = \langle r|\mathcal{H}_{\mathrm{CS}} + \overline{\mathcal{H}^{(0)}}|r\rangle - \langle s|\mathcal{H}_{\mathrm{CS}} + \overline{\mathcal{H}^{(0)}}|s\rangle \\ &= p\omega_0\delta_{\mathrm{CS}} - \frac{1}{30}p\left(I(I+1) - \frac{3}{4}\left(p^2 + \frac{3q^2}{p^2}\right)\right)\frac{{\chi_Q}^2}{\omega_0}.\end{aligned} \tag{30}$$

For the SQ CT ($p = -1$, $q = 0$), (30) yields

$$\omega^{\mathrm{ISO}}_{-1,0} = -\omega_0\delta_{\mathrm{CS}} + \frac{1}{30}\left(I(I+1) - \frac{3}{4}\right)\frac{{\chi_Q}^2}{\omega_0} = -\omega_0(\delta_{\mathrm{CS}} + \delta_{\mathrm{QIS}}), \tag{31}$$

where

$$\delta_{\mathrm{QIS}} = -\frac{1}{30}p\left(I(I+1) - \frac{3}{4}\right)\left(\frac{\chi_Q}{\omega_0}\right)^2 \tag{32}$$

describes the magnitude of the quadrupolar-induced shift. It follows from (31) that the center of gravity of a quadrupolar lineshape is not located at the "true" chemical shift $-\omega_0\delta_{\mathrm{CS}}$, but is shifted from it by $-\omega_0\delta_{\mathrm{QIS}}$.

The second term in (29) is the anisotropic, orientation-dependent frequency shift due to the first-order quadrupolar interaction

$$\omega^{I}_{p,q} = q\frac{\omega_Q}{\sqrt{6}}A^R_{20}(\Theta_{PR})d^2_{00}(\beta_{RL}). \tag{33}$$

This term is independent of the coherence order p. Furthermore, it vanishes for all symmetric transitions ($q = 0$), and thus can be disregarded when describing the SQ CT coherence or the symmetric MQ coherence. Note, however, that this is not the case for the STs ($q \neq 0$), which are therefore strongly affected by the first-order quadrupolar interaction, except when the sample is spun at the magic angle.

The last two terms in (29) are the anisotropic frequency shifts due to the second- and fourth-rank parts of the second-order quadrupolar interaction:

$$\omega_{p,q}^{\mathrm{ANISO}} = \omega_{p,q}^{(2)} + \omega_{p,q}^{(4)}, \tag{34}$$

where

$$\omega_{p,q}^{(2)} = C_2(\Theta_{PR})\left(3\left(p^3 + \frac{3q^2}{p}\right) - p(8I(I+1) - 3)\right)d_{00}^2(\beta_{RL}) \tag{35}$$

and

$$\omega_{p,q}^{(4)} = C_4(\Theta_{PR})\left(\frac{17}{2}\left(p^3 + \frac{3q^2}{p}\right) - p(18I(I+1) - 5)\right)d_{00}^4(\beta_{RL}), \tag{36}$$

with

$$C_2(\Theta_{PR}) = -\frac{1}{9}\frac{{\omega_Q}^2}{\omega_0}\frac{B_{20}^R(\Theta_{PR})}{2\sqrt{14}} \tag{37}$$

and

$$C_4(\Theta_{PR}) = -\frac{1}{9}\frac{{\omega_Q}^2}{\omega_0}\frac{B_{40}^R(\Theta_{PR})}{2\sqrt{70}}. \tag{38}$$

The energy level diagram, which summarizes the above results for a spin-3/2 nucleus, is shown in Fig. 3a. When averaging the signal over the entire set of orientations Θ_{PR} in a powdered sample, both rank-2 and rank-4 anisotropic terms give rise to well-known powder patterns (Fig. 3b) [4, 6, 43, 44]. Equation (33) confirms what has already been suggested in Sect. 2.1, namely that the anisotropic contribution due to the first-order quadrupolar interaction averages out to zero. Since the spectral width is usually higher than the MAS rate ($\omega_Q \gg \omega_R$), numerous spinning sidebands are observed (see Sect. 4.1.2). It is also clear from (35) and (36) that MAS alone cannot fully average out the second-order quadrupolar interaction. Even under infinitely fast MAS, the second-order quadrupolar broadening of the CT in a powder sample is reduced by a factor of ~3 [45, 46].

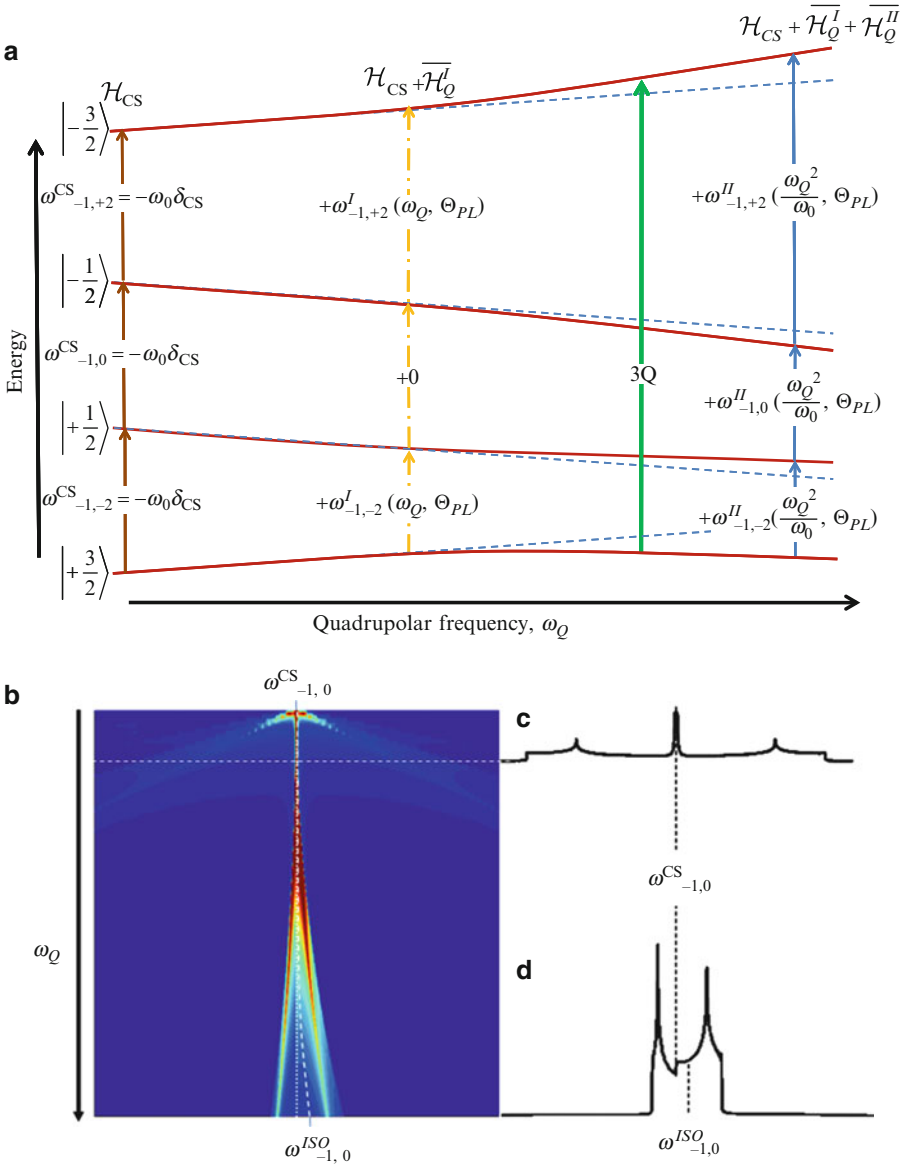

Fig. 3 (**a**) Schematic energy level diagram of a nucleus with spin $I = 3/2$ exposed to a strong homogeneous external magnetic field B_0, featuring $2I + 1$ energy levels, $2I$ single-quantum (SQ) transitions, and a single triple-quantum transition (3Q), as a function of the quadrupolar frequency ω_Q. (**b**) Plot showing the evolution of the main singularities of the corresponding static powder spectra. (**c**) Powder spectrum corresponding to small quadrupolar frequency (first-order perturbation): all transitions are visible; the central transition remains very narrow at the position of the chemical shift. (**d**) Powder spectrum corresponding to strong quadrupolar interaction: only the central transition is easily observed, which exhibits a shift of the center of gravity given by (31)

2.3.4 Excitation of Single- and Multiple-Quantum Coherences Using rf-Pulses

During an rf-field irradiation, the Hamiltonian governing a quadrupolar spin system can be written in the rotating frame as

$$\mathcal{H}_1 = \mathcal{H}_{\mathrm{rf}} + \mathcal{H}_\Delta + \mathcal{H}_Q^I(t) = -\omega_{\mathrm{rf}} I_x + \Delta\omega I_z + \tfrac{1}{2}\Omega_Q\left(3I_z^2 - I(I+1)\right), \tag{39}$$

where $\omega_{\mathrm{rf}} = \gamma B_1$ with B_1 being the amplitude of the oscillating rf magnetic field applied along the x axis, $\Delta\omega$ is the resonance offset (formally equivalent to the isotropic chemical shift), and Ω_Q is the first-order, orientation-dependent quadrupole splitting given by (8). The non-secular part of the Hamiltonian as well as dipolar interactions are neglected in (39), and it is assumed that the Larmor frequency is much larger than the quadrupolar frequency ($\omega_0 \gg \omega_Q$). In the static sample, Ω_Q can be written as follows:

$$\Omega_Q = \sqrt{\frac{2}{3}}\omega_Q A_{2,0}^L(\Theta_{PL}) = \frac{1}{2}\omega_Q\left(3\cos^2\beta_{PL} - 1 + \eta\,\sin^2\beta_{PL}\cos 2\alpha_{PL}\right). \tag{40}$$

Under MAS, the quadrupole splitting is modulated due to the reorientation of the molecular frame [see (14)]:

$$\Omega_Q = \Omega_Q(\omega_R t) = \sqrt{\frac{2}{3}}\omega_Q\left(\sum_{k=-2}^{2} A_{2,k}^R(\Theta_{PR})\,\mathrm{e}^{\mathrm{i}k\omega_R t} d_{k,0}^2(\beta_{RL})\right). \tag{41}$$

The signal detectable after a pulse of duration τ_{pulse}, is given by (25), which for the time-independent Hamiltonian (i.e., under the static condition) yields

$$\rho(\tau_{\mathrm{p}}) = \mathrm{e}^{-\mathrm{i}\mathcal{H}_1\tau_{\mathrm{pulse}}}\rho(0)\mathrm{e}^{\mathrm{i}\mathcal{H}_1\tau_{\mathrm{pulse}}}. \tag{42}$$

The analytic evaluation of the density matrix requires the diagonalization of $\mathcal{H}_1$, which can be easily performed for the two extreme cases, $\omega_{\mathrm{rf}} \ll \left|\Omega_Q\right|$ and $\omega_{\mathrm{rf}} \gg \left|\Omega_Q\right|$. Indeed, in the case of a low rf-field, only off-diagonal terms related to the CT are retained in the $\mathcal{H}_1$ Hamiltonian (39), which thus behaves like a fictitious spin-1/2 operator, affecting only the CT coherences $I_{\pm1,0}$. These coherences are thus selectively excited with the nutation frequency:

$$\omega_{\mathrm{nut}} = \left(I + \frac{1}{2}\right)\omega_{\mathrm{rf}}. \tag{43}$$

Under such conditions, the maximum signal is thus obtained with $\tau_{\mathrm{pulse}} = \dfrac{\pi}{(2I+1)\omega_{\mathrm{rf}}}$.

When $\omega_{\mathrm{rf}} \gg \left|\Omega_Q\right|$, the excitation becomes non-selective and thus all spin states develop coherences. The resulting transverse magnetization nutates with the

frequency $\omega_{\text{nut}} = \omega_{\text{rf}}$, similarly to spin-1/2 nuclei. In a powder, Ω_Q assumes values in a continuous range between ω_Q and $-(1+\eta)\omega_Q$, and the collective behavior of the spin system under the rf-pulse excitation corresponds to an average that depends approximately on the ratio $\omega_Q/\omega_{\text{rf}}$. This complicates the quantitative analysis of spectra, unless they are recorded under one of the above-mentioned extreme conditions [47]. Interestingly, the dependence of the nutation frequency on the spin number I has been exploited to separate the lineshapes of two isotopes, ^{47}Ti ($I = 5/2$) and ^{49}Ti ($I = 7/2$), whose spectra strongly overlapped due to very close Larmor frequencies and similar natural abundance [48].

However, the purely selective or purely non-selective conditions are rarely met, and the intermediate regime, $\omega_{\text{rf}} \sim |\Omega_Q|$, is more realistic. With such intermediate values of Ω_Q, the transverse magnetization exhibits aperiodic behavior as both SQ and MQ coherences of odd order p are being created by the rf irradiation. This phenomenon was used to design the so-called *2D* nutation experiment [49, 50], which provides a unique way to measure quadrupole coupling strength, in the case when $1 < \Omega_Q/\omega_{\text{rf}} < 6$ [51, 52]. The intermediate regime is also critical for the generation of MQ coherences in MQMAS (see Sect. 5.4.1.) [53]. Indeed, it was observed that the nutation spectra of static or spinning samples contain contributions from SQ as well as MQ transitions [52, 54].

2.3.5 Spin Echoes

The detection of broad powder spectra using a single rf-pulse is often unfeasible due to the spectrometer dead-time. In such circumstances, the detection period can be delayed by using the spin echo experiment, thereby permitting acquisition of the entire free induction decay. Since the discovery of spin echoes by E.L. Hahn in 1950 [55], their spin dynamics have also been extensively studied and reviewed in the context of the quadrupolar interaction [3, 56, 57]. However, the principle of refocusing the spin interactions by the spin echo can also be used to design experiments that are more advanced. In particular, most of the high-resolution experiments on half-integer quadrupolar nuclei described in Sect. 5.2 use spin echo refocusing as their founding block.

As a rule, spin echo experiments commence with an initial excitation pulse (or a sequence of pulses), which is followed by the defocusing period, τ_1, during which the coherences $I_{p,q}$ evolve under the effect of all relevant nuclear interactions. This is followed by the second delay, τ_2, during which the selected interactions are refocused. The refocusing requires a change of coherence to $I_{p',q'}$, which is typically achieved by a second rf-pulse (but can also be orchestrated by field gradients or reorientation of the rotation axis, as in DAS [10]). In a perfectly executed refocusing of a given nuclear interaction, the net accumulated evolution phase at the end of the experiment, that is at $\tau = \tau_1 + \tau_2$, should be null for all molecular orientations Θ_{PL} in the powder, i.e.,

$$\Phi(\tau) = \omega_{p,q}\tau_1 + \omega_{p',q'}\tau_2 = \frac{1}{1+k}\left(\omega_{p,q} + k\omega_{p',q'}\right)\tau = 0, \tag{44}$$

where $k = \tau_1/\tau_2$, and the frequencies $\omega_{p,q}$ and $\omega_{p',q'}$ in the first and second evolution periods are given by (29). Of course, even though the signal can be observed at time τ only for $p' = -1$, coherences $p' \neq -1$ can be used when the echo block is included as part of a more complex experiment.

3 Sensitivity Enhancement Techniques by Adiabatic Population Transfer

The existence of multiple energy levels in half-integer quadrupolar nuclei makes it possible to enhance the sensitivity of any chosen transition, in particular the CT $|1/2\rangle \rightarrow |-1/2\rangle$, by appropriately driving the level populations away from thermal equilibrium. In 1991, inspired by the pioneering work of Vega and Naor [58], Kentgens [59] used the frequency sweep scheme to perform adiabatic population transfer across the ST (half-passage). Shortly thereafter, Haase and Conradi achieved signal enhancement in spin-5/2 nuclei by consecutively inverting the populations across symmetric pairs of STs [60]. In the last decade, the same principle was used in several novel protocols, which took advantage of improved instrumentation to optimize sensitivity and adapt these techniques for routine use. An excellent review of these methods has been written by Siegel et al. [61]. Here, we briefly discuss the underlying principles and the most recent approaches involving simultaneous manipulation of STs ($|3/2\rangle \rightarrow |1/2\rangle$) and ($|-1/2\rangle \rightarrow |-3/2\rangle$).

3.1 Double Frequency Sweeps

Significant progress in signal enhancement methods for the central transition has been achieved by the implementation of double frequency sweeps (DFS) [62]. The basic idea of DFS, applicable for both static and MAS experiments, is to invert simultaneously the STs so that the populations of the outer spin levels are transferred to the CT energy levels before they are selectively excited (Fig. 4).

The population inversion between two energy levels can be achieved under the so-called "adiabatic passage," by sweeping a continuous rf-field through the entire spectrum. The high- and low-frequency "sides" of the CT are irradiated simultaneously using waveform generators. A diverging frequency sweep starts at a frequency near the CT and continues toward the outer transition resonances, while a converging frequency sweep starts far from the CT frequency and moves toward it. The DFS waveform has a constant phase and an amplitude modulated according to [63]

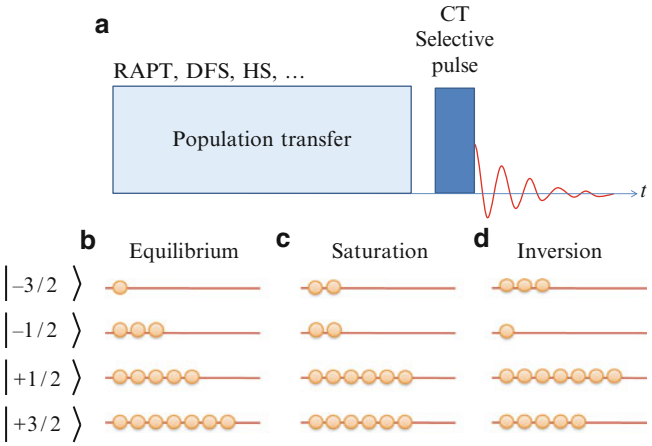

Fig. 4 (**a**) Pulse scheme for signal enhancement of the CT and schematic representations of the population distribution for an ensemble of spin-3/2 nuclei under (**b**) thermal equilibrium, (**c**) satellite saturation, and (**d**) satellite inversion

$$\omega_{\mathrm{rf}}(t) = \omega_{\mathrm{rf}}^{\max} \cos\left(\omega_{\mathrm{s}} t + \frac{\omega_{\mathrm{f}} - \omega_{\mathrm{s}}}{2\tau} t^2\right), \tag{45}$$

where τ is the duration of the sweep, $\omega_{\mathrm{rf}}^{\max}$is the maximum amplitude of the waveform, and ω_{s} and ω_{f} are the start and final offset frequencies, respectively.

The passage is considered adiabatic when the frequency sweep is sufficiently slow to maintain a continuous alignment of the magnetization vector with the effective magnetic field, yet sufficiently fast to avoid significant relaxation. If the sweep rate is too high, i.e., under the condition referred to as "sudden passage," the populations of energy levels cannot be reversed. To maximize the enhancement of the CT, it is necessary to achieve an adiabatic passage through the SQ STs without perturbing the populations of energy levels through the MQ transitions, which thus should undergo a sudden passage. Since each transition has its own adiabaticity factor, these two conditions can be simultaneously achieved. However, the overall signal enhancements are lower than the theoretically expected value of $2I$. Indeed, the adiabaticity factors also depend on the quadrupole frequency ω_Q, and thus vary among the different crystallites in a powder. The spin dynamics becomes even more complex under MAS, which modulates the resonance frequency as well as the frequency sweep. Ideal adiabatic SQ and sudden MQ transitions are thus difficult to achieve simultaneously [63]. For example, Schaefer et al. obtained enhancements of 2.3 for ^{23}Na CT for a static sample of $NaNO_2$ and 1.7 for a sample of Na_2SO_4 under MAS at 5 kHz [64].

3.2 *Rotor-Assisted Population Transfer*

Signal enhancement of the CT can also be obtained using rotor-assisted population transfer (RAPT), introduced in 2000 by Yao et al. [65]. It is based on the same

concept as the fast amplitude modulation (FAM) protocol developed for the MQMAS experiment [66, 67]. Instead of using the frequency sweep, as in DFS, only a constant frequency offset is generated by an $[x, -x]$ rf-pulse modulation. The coherence transfer leading to the population saturation is driven by spinning of the powder sample, which has the effect of sweeping the frequency of the satellite STs through the resonance condition. For spin-3/2 nuclei, an optimum RAPT enhancement of 1.9 was reported for the RAPT modulation frequency equal to $C_Q/4$ [65].

An improved RAPT sequence utilizing frequency-switched Gaussian pulses (FSG-RAPT) was later proposed [68]. This method also allows for the measurement of C_Q values. The dependence of the FSG-RAPT enhancement on offset frequency for nuclei with different C_Qs has been exploited to design pulse schemes for the selective selection of nuclei with large quadrupole couplings [69–71].

Madhu et al. proposed the use of two consecutive RAPT pulse trains to obtain signal enhancement in spin-5/2 nuclei, such as ^{27}Al and ^{17}O [72]. In their scheme, the saturation of population achieved for the outermost ($|\pm 5/2\rangle \rightarrow |\pm 3/2\rangle$) transitions was followed by saturation of the $|\pm 3/2\rangle \rightarrow |\pm 1/2\rangle$ populations before detection of the CT NMR signal. Kwak et al. used similar RAPT pulse trains to obtain significantly improved signal enhancement on ^{27}Al and ^{93}Nb [73].

3.3 *Hyperbolic Secant Inversion Pulses and Wideband Uniform Rate Smooth Truncation*

Siegel et al. showed that enhancement of the CT can also be obtained using hyperbolic secant (HS) pulses to invert selectively the STs [74]. Unlike the DFS waveform, whose frequency sweep is generated by a constant rf-pulse phase while modulating the amplitude, the HS pulse utilizes both amplitude and phase modulation, yielding an enhancement exceeding that obtained by DFS or RAPT [61, 74, 75]. Most recently, the pulse sequence called "wideband uniform-rate smooth truncation" (WURST) [76] was introduced to achieve selective adiabatic inversion using a lower power of the rf-field than that required for the HS pulses [77, 78]. One of its applications involved more efficient detection of insensitive nuclei, such as ^{33}S [79].

4 Wideline Acquisition of Quadrupolar Powder Spectra

Despite the benefits of high resolution, measurements of wideline spectra of quadrupolar nuclei under static or MAS conditions are still commonly used in a variety of applications. For both integer and half-integer spins, simulations of quadrupolar lineshapes can yield full sets of NMR parameters associated with quadrupolar and chemical shift tensors and can be used for studying molecular dynamics.

4.1 Integer Spin Nuclei

There are only eight nuclei with integer spins, yet two of those, ^{2}H and ^{14}N (both with $I = 1$), are of great importance in NMR spectroscopy. Deuterium has a relatively small C_Q, typically around 200 kHz in organic compounds. Since the contributions due to second-order quadrupolar interactions, chemical shifts, and dipolar broadenings are usually negligible, observation of undistorted first-order quadrupolar ^{2}H powder spectra is possible using nonselective rf-pulses. Such spectra are very sensitive to molecular motions on the microsecond timescale and can provide a wealth of information about dynamics in solids. For several decades studies of deuterated samples were performed by measuring the static or MAS quadrupolar echoes and fitting the resulting spectra to determine the type and rate of motion; this work has been reviewed by Batchelder [80] and Duer [81]. Below, we briefly explain the ^{2}H quadrupolar echo experiment and focus on several new approaches to studying motion-induced effects on ^{2}H spectra. Nitrogen is one of the key elements in chemistry and biology, but the first-order quadrupolar broadening makes the detection of ^{14}N nuclei in powdered samples very challenging [82]. Still, in the absence of homogeneous broadening, wideline ^{14}N MAS spectra can be successfully acquired and simulated.

4.1.1 Quadrupolar Echoes

Solid-state NMR spectra of ^{2}H, where the main concern is to refocus the reasonably small first-order broadening, are commonly obtained by measuring the quadrupolar echo on a static sample. In such a case, the $\omega_{p,q}$ frequencies can be approximated as (29)

$$\omega_{p,q} = \omega_{p,q}^{\mathrm{CS}} + \omega_{p,q}^{I}. \tag{46}$$

The accumulated phase cancels out for the observed single-coherence when

$$k = -\omega_{p,q}/\omega_{-1,q'} > 0. \tag{47}$$

Refocusing of the first-order quadrupolar interaction occurs under the condition [35]

$$\omega_{p,q}^{I} = -k\omega_{-1,q'}^{I} = -\frac{q}{q'}\omega_{-1,q'}^{I}, \tag{48}$$

which implies that the satellite order must be inverted between the two evolution periods, i.e., $q = -q'$. For spin-1 nuclei, the only non-zero q values correspond to the SQ coherence ($p = 1$), and thus the double-quantum coherence (DQ) is not refocused (as $q = 0$). In order to refocus the chemical shift interaction and offset, it is required that

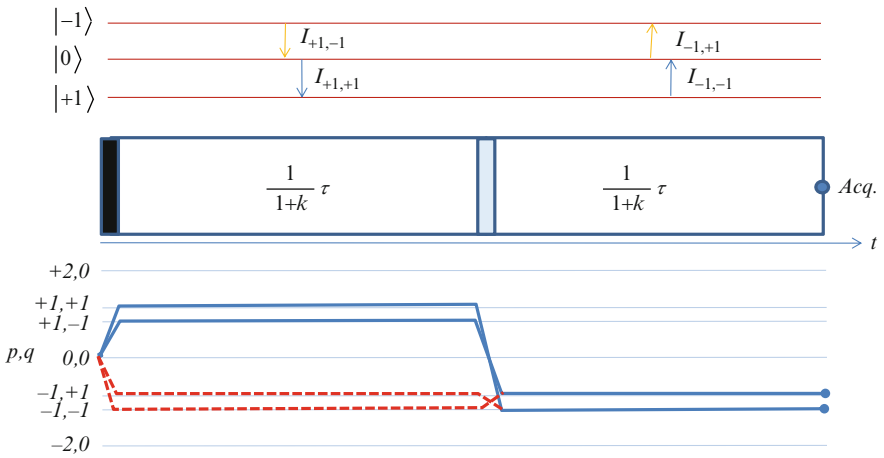

Fig. 5 The quadrupolar echo pulse sequence and coherence transfer pathways for $I = 1$. The pathway marked in *red* is eliminated by the EXORCYCLE but not by the conventional quadrupolar echo

$$\omega_{p,q}^{\mathrm{CS}} = -\omega_{-1,q'}^{\mathrm{CS}}, \tag{49}$$

and thus the coherence order has to be inverted as well; i.e., $p = -p' = +1$. As shown in Fig. 5, the desired coherence and satellite transfer pathways are easy to establish using a $\pi/2$ pulse (to invert the satellite order) and the correct phase-cycling to select the $0 \rightarrow +1 \rightarrow -1$ coherence transfer pathway ("EXORYCLE") [34, 35]. It is obvious that the second-order quadrupolar interactions are also refocused by the exorcycled quadrupolar echo experiment.

It should finally be noted that the first-order quadrupolar interactions (but not the second-order) can also be refocused while using $p = -1$ during the defocusing period. However, in this case the offsets are not refocused, which may lead to signal distortions if they are significant, e.g., in paramagnetic solids [83]. On the other hand, by measuring a series of such echoes while incrementing the echo delays, a 2D spectrum can be obtained in which the spin evolutions due to shift (chemical or paramagnetic) and quadrupolar interactions are separated in the Ω_1 and Ω_2 dimensions, respectively [84].

4.1.2 Wideline MAS Acquisition: Solid-State Dynamics

Static ^{2}H NMR spectra suffer from low sensitivity, as resonances are spread continuously over the ~200 kHz range. In samples with multiple sites, they also lack resolution. However, both shortcomings can be remedied by using MAS. As was shown in Sect. 2.3.3, in a rigid sample MAS averages out the inhomogeneous first-order quadrupolar broadening in the same way as it eliminates the CSA in

spin-1/2 nuclei. The resulting patterns of narrow spinning sidebands follow the static powder spectra for individual sites and have distinct centerbands whose positions are determined by the combinations of isotropic chemical shifts and small second-order quadrupolar shifts (the isotropic first-order shift is null; see Sect. 2.3.3). Given the conservation of the overall integrated spectral intensity, the signal-to-noise ratio (S/N) within the sidebands can be considerably higher, although the lineshape analysis is not necessarily easier due to the reduced number of meaningful data points across the spectrum.

It has recently been demonstrated that the analysis of MAS sidebands patterns can be used to study molecular dynamics in the solid state [85–88]. Indeed, the line narrowing effect of MAS can be partly offset, or completely eliminated, if the ^{2}H quadrupole tensor is reoriented due to motion on a time scale comparable to $(\omega_R)^{-1}$. Since the DQ transition in ^{2}H is not influenced by the first-order quadrupolar broadening, such motion-induced effects should be less evident in the DQMAS spectrum, as has indeed been observed by Wimperis and colleagues in several deuterated solids [87, 88]. For example, the simulation of the SQ spectrum of tetrathionate dihydrate-d_4 yielded the same reorientational rate constant as the previously described quadrupolar echo approach (Fig. 6).

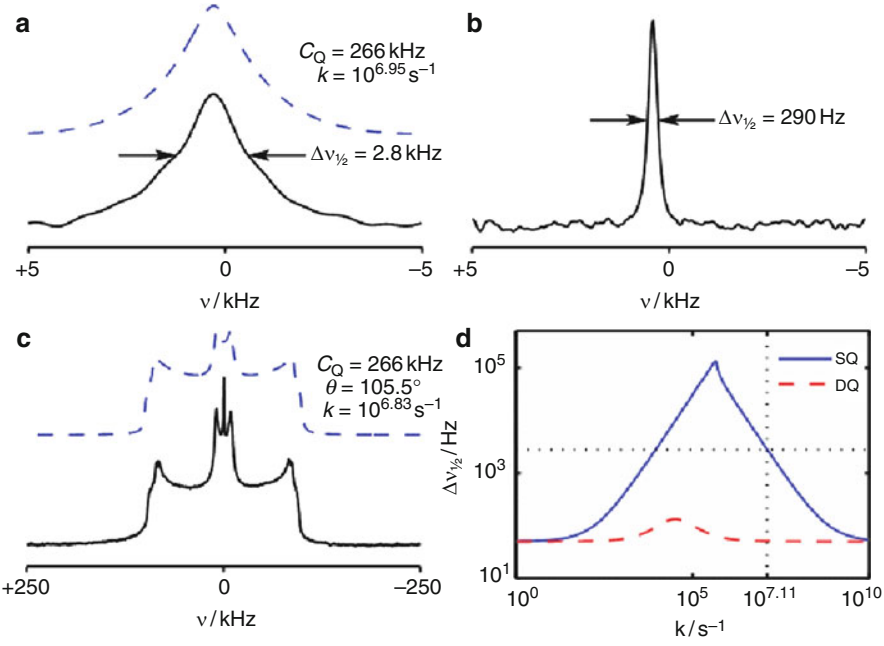

Fig. 6 (**a**) SQ and (**b**) DQ rotor-synchronized ^{2}H MAS NMR spectra of sodium tetrathionate dihydrate-d_4 (*solid lines*). The dashed line in (**a**) represents the exact numerical simulation of the SQ spectrum for random molecular motion with the rate constant k given in the figure. (**c**) The corresponding experimental and simulated static ^{2}H quadrupolar-echo spectra. (**d**) Simulated SQ (*solid line*) and DQ (*dashed line*) linewidths as functions of k. (Reproduced with permission from [88])

4.1.3 Wideline MAS Acquisition of Nitrogen-14

Significant progress has recently been made in applying the MAS technique to the study of ^{14}N nuclei. Despite the high natural abundance (99.6%), the ^{14}N MAS spectra are difficult to obtain due to their large breadth, which is often in excess of 1 MHz [82, 89, 90]. Jakobsen and colleagues showed that the acquisition of such wide spectra is possible using on-resonance single-pulse excitation under carefully controlled experimental conditions, which involve precise setting of the magic angle ($\beta_{RL} = 54.736 \pm 0.003°$), high long-term stability of the spinning frequency (to about 0.1 Hz), control of the effect of the Q factor of the probe on the excitation profile, and the use of proper circuitry (filters, preamplifiers, cable lengths) [89, 91]. Even under optimized conditions the individual sidebands are subject to second-order broadening. This broadening can be considerable (on the order of several hundred Hz), necessitating the acquisition of 10^5 or more scans. Under state-of-the-art conditions, high-quality ^{14}N MAS spectra of several classes of materials, including common amino acids, have been measured. Their numerical analysis yielded precise values of C_Q, η_Q, and δ_{CS}, provided that the second-order cross-term between the quadrupolar and CSA interactions (Sect. 2.2) was included in the average Hamiltonian [82, 92, 93]. Most recently, it has been shown that the first-order broadening can be eliminated by rotor-synchronized indirect detection of ^{14}N spectra, as will be explained in Sect. 7.4.

4.2 Half-Integer Spin Nuclei

In principle, the methods described in Sect. 4.1.2 can also be used to obtain wideline first-order quadrupolar spectra of half-integer spins. However, most of the time, the static and MAS studies of half-integer quadrupolar nuclei focus on studying the CT, because it is not affected by the first-order broadening. As shown in Sect. 2.3.3, in the absence of other line-broadening mechanisms, MAS reduces this broadening by a factor of approximately 3. MAS offers the additional advantage of removing broadenings due to the CSA and dipolar interactions. However, the second-order broadening itself can be significant, on the order of tens of kilohertz in the most commonly studied nuclei (^{11}B, ^{23}Na, ^{17}O, ^{27}Al), necessitating the use of various types of spin echoes and other multiple-pulse sequences. High-resolution protocols aimed at removing the second-order broadening are described in Sect. 5.

4.2.1 High-Field and Multi-Field Experiments

Since the second-order quadrupolar broadening is inversely proportional to the Larmor frequency [(35) and (36)], one obvious means for improving the resolution is to employ the highest available magnetic field strength [94]. The use of several spectrometers operated at different magnetic field strengths can be helpful in

refining NMR parameters, especially in spectra consisting of overlapping lineshapes. The availability of a high magnetic field has also advanced the investigations of low-γ nuclei, including ^{33}S [95], ^{39}K [96], $^{47/49}$Ti [97], ^{59}Co [98], ^{67}Zn [99], ^{73}Ge [100], ^{95}Mo [101], ^{115}In [102], $^{135/137}$Ba [103, 104], and ^{209}Bi [105].

4.2.2 Central Transition Echoes

Acquisition of wide static or MAS spectra of the CT is typically made using a two-pulse echo sequence $\pi/2 - \tau - \pi$ (the Hahn echo [55, 106]). By setting the strength of the rf-field at $\omega_{\mathrm{rf}} = \Delta\omega/(I + 1/2)$, where $\Delta\omega$ is the CT linewidth, these sequences selectively irradiate the CT, while minimizing the contributions from the STs [107, 108]. In such case, the $\omega_{p,q}$ frequencies are given by (29):

$$\omega_{p,0} = \omega_{p,0}^{\mathrm{CS}} + \omega_{p,0}^{(0)} + \omega_{p,0}^{(2)} + \omega_{p,0}^{(4)} = \omega_{p,0}^{\mathrm{ISO}} + \omega_{p,0}^{\mathrm{ANISO}}. \tag{50}$$

It is easy to show that refocusing occurs in the observable time-domain only if the refocusing pulse changes the sign of p; thus, the coherences must follow the pathway $0 \rightarrow +1 \rightarrow -1$. When using MAS, it is practical to synchronize the defocusing and refocusing periods with the rotor period to avoid dephasing of the spinning sidebands. In the case of very fast free induction decay it may be advantageous to record the signal immediately following the second pulse. This so-called whole-echo acquisition yields an increased S/N (by a factor of $\sqrt{2}$) and provides the flexibility of shifting the signal freely during data acquisition or processing without causing rolling baselines.

4.2.3 Quadrupolar Carr–Purcell–Meiboom–Gill

In spin systems with sufficiently long transverse relaxation time T_2', it is often possible to generate a significant number of echoes by applying a Carr–Purcell–Meiboom–Gill (CPMG) [109, 110] train of refocusing π pulses during the signal acquisition. After a Fourier transformation, the spectrum consists of a manifold of narrow spin-echo sidebands, which can be numerically analyzed, i.e., using the approach of Maricq and Waugh [111]. Since the integrated spectral intensity is not affected by this protocol, the apparent S/N ratio for individual spin-echo sidebands can be substantially enhanced compared to the spectra with continuous signal dispersion. The CPMG train of selective π pulses can be applied to quadrupolar nuclei (QCPMG) to increase the CT sensitivity compared to a conventional spin-echo spectrum, in some cases by more than one order of magnitude. The appearance of the Quadrupolar Carr–Purcell–Meiboom–Gill (QCPMG) spectrum is determined by the sampling conditions; smaller separation between the echoes in the time domain increases the S/N ratio in the frequency domain at the expense of

anisotropic information, which is provided by the reduced number of sidebands [112, 113]. The homogeneous homonuclear dipolar couplings affect the lineshapes of individual sidebands, whereas information about the inhomogeneous interactions (CSA and first- or second-order quadrupolar interactions) can be extracted from the envelope of the sideband manifold. QCPMG refocusing is often used in rotor-synchronized MAS experiments (where the sensitivity can be further enhanced by the techniques described in Sect. 3) in various MQMAS schemes (Sect. 5.2.2), and in static measurements of wide spectra (including those of STs), where the limited spectrometer bandwidth can be overcome by frequency stepping or WURST [114–127].

5 High-Resolution Methods

As already explained in Sect. 2, the spatial components of the second-order quadrupolar Hamiltonian involve the second-rank tensors giving rise to complex anisotropies, which cannot be removed merely by spinning the sample around a fixed axis, regardless of the choice of β_{RL}. One of the first strategies for improving the resolution, referred to as "variable-angle sample spinning" (VAS), used a different rotation axis to achieve a more favorable scaling of the anisotropy of the second-order quadrupolar interaction [43, 44, 128–130]. Another method, called "satellite transition spectroscopy" (SATRAS), increased the resolution in spin-5/2 and 9/2 nuclei under MAS using the spinning sidebands of the STs, instead of the CT spectrum [131, 132]. More recently, a two-dimensional one pulse (TOP) processing method was employed to represent MAS data using the spinning sideband manifold in the reconstruction of higher-resolution ST spectra [133].

The pursuit of high resolution has brought about several strategies for the complete removal of second-order broadening, which will be described in the sections below. The first two methods, double rotation (DOR) and dynamic angle spinning (DAS), achieved isotropic resolution by making β_{RL} time-dependent, i.e., by employing mechanical reorientation of the rotation axis during the experiment [134–139]. The most significant advancement was made in 1995 by Frydman et al. [140], who achieved line narrowing in a 2D MQMAS experiment that did not require the mechanical sophistication of DOR and DAS and could be performed using a conventional MAS probehead. A few years later, Gan introduced a related method, referred to as "satellite transition MAS" (STMAS), allowing a similar resolution [141]. These line-narrowing concepts were then exploited in "ultrafast" acquisition of high-resolution spectra using an STMAS-based approach with double-quantum filtering (STARTMAS) [142] or orientational encoding [143]. Finally, high-resolution spectra can be produced from one-dimensional (1D) data acquired at different magnetic fields using a projection-reconstruction technique (CQ-PRODI) [144].

5.1 Double Rotation

In the DOR method, proposed by Llor and Virlet [134], the sample is spun around two different axes simultaneously, such that both anisotropic terms in (18) given by second-order and fourth-order Legendre polynomials (Fig. 2) are simultaneously averaged to zero using a 1D measurement [135, 137, 145]. In practice, the DOR probe requires a very sophisticated spinning module consisting of a small inner rotor, which is spun inside a larger outer rotor. The outer rotor (*OR*) is spun about an axis at angle β_{OL} with respect to B_0, while the inner rotor (*IR*) is oriented at angle β_{IO} with respect to the rotation axis of the outer rotor.

Using the Wigner rotation matrices, as before, it can be shown that if both rotations are assumed to be fast, the Hamiltonian of (27) is transformed as

$$\begin{aligned}\mathcal{H} = {} & \omega_0\delta_{\mathrm{CS}}I_z + \omega_Q A^{IR}_{2,0}(\Theta_{PI})d^2_{0,0}(\beta_{OL})d^2_{0,0}(\beta_{IO})T_{2,0} \\ & + \frac{1}{9}\frac{{\omega_Q}^2}{\omega_0}\begin{pmatrix} B^{IR}_{0,0}K_0 \\ +B^{IR}_{2,0}(\Theta_{PI})d^2_{0,0}(\beta_{OL})d^2_{0,0}(\beta_{IO})K_2 \\ +B^{IR}_{4,0}(\Theta_{PI})d^4_{0,0}(\beta_{OL})d^4_{0,0}(\beta_{IO})K_4 \end{pmatrix},\end{aligned} \tag{51}$$

where K_0, K_2, and K_4 are given by (11). The orientation-dependent coefficients $A^{IR}_{2,0}$, $B^{IR}_{2,0}$, and $B^{IR}_{4,0}$ are now expressed in the frame *IR* of the inner rotor. If β_{OL} is set at the magic angle (54.736°) and β_{IO} is equal to 30.6° or 70.1°, the terms proportional to $d^2_{0,0}(\beta_{OL})$ and $d^4_{0,0}(\beta_{IO})$ vanish, thereby reducing the Hamiltonian to its isotropic part:

$$\mathcal{H} = \omega_0\delta_{\mathrm{CS}}I_z + \frac{1}{9}\frac{{\omega_Q}^2}{\omega_0}B^{IR}_{0,0}K_0 = \omega_0\delta_{\mathrm{CS}}I_z + C_0K_0 \tag{52}$$

with $B^{IR}_{0,0} = B^L_{0,0}$. Therefore, one obtains an isotropic CT spectrum at

$$\begin{aligned}\Omega^{\mathrm{ISO}}_{\mathrm{DOR}} &= \omega^{\mathrm{CS}}_{-1,0} + \omega^{(0)}_{-1,0} \\ &= -\omega_0\delta_{\mathrm{CS}} + \frac{1}{30}\left(I(I+1) - \frac{3}{4}\right)\frac{{\chi_Q}^2}{\omega_0} \\ &= -\omega_0(\delta_{\mathrm{CS}} + \delta_{\mathrm{QIS}}) = \omega^{\mathrm{ISO}}_{-1,0},\end{aligned} \tag{53}$$

as in (31).

The DOR spectra are thus composed of narrow lines, removed from the chemical shift positions by the second-order QIS, and often flanked by numerous spinning sidebands due to limited spinning rates (Fig. 7). Indeed, achieving a fast spinning rate for the outer rotor poses a formidable mechanical challenge. The original design of the DOR spinning module, which consisted of an inner rotor stabilized by needle bearings within an outer rotor, allowed for spinning of the outer rotor at

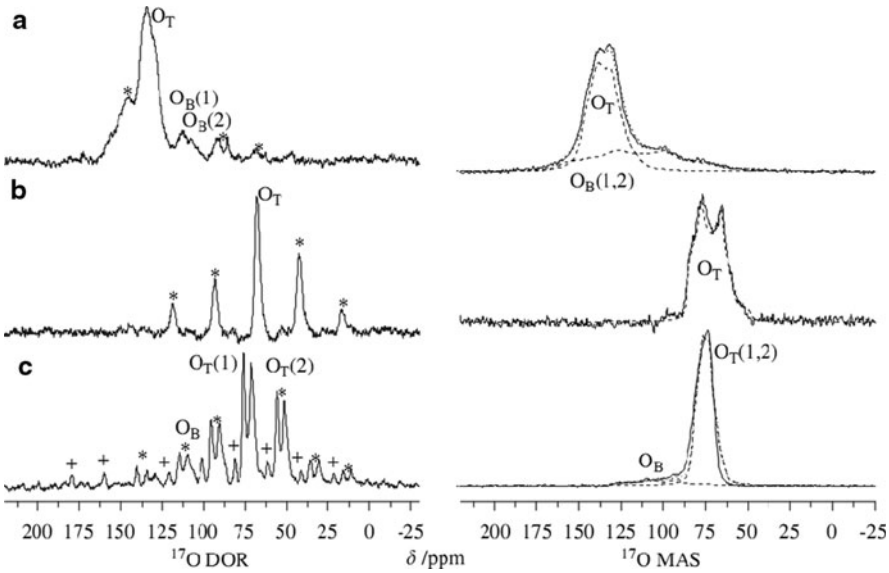

Fig. 7 Comparison of the ^{17}O DOR and MAS NMR (30 kHz) spectra of $Ba_2P_2O_7$ (**a**), $Mg_2P_2O_7$ (**b**), and $Na_4P_2O_7$ (**c**) at $B_0 = 17.4$ T. Spinning sidebands (*asterisks*, *plus symbol*) arise due to the limited spinning speed of the outer rotor (~1,400 Hz). (Reproduced with permission from [146])

about 1,000 Hz and was unreliable during long acquisitions [135, 137]. Samoson and colleagues were able to double this spinning rate by using air-bearings for the inner rotor and a computer-assisted start-up system [147, 148]. Another drawback of DOR is the relatively low filling factor of the receiver coil, leading to poor sensitivity with respect to a conventional MAS probe. However, DOR is compatible with the sensitivity enhancement methods described in Sect. 3, as shown by Kentgens et al. for DFS [148]. Several recent studies have demonstrated the continuing utility of DOR, on its own or in combination with other high-resolution methods, especially in applications involving ^{17}O in inorganic and biological materials [146, 147, 149–152].

5.2 *Refocusing of the Second-Order Quadrupolar Interactions*

In the following section, we explain the basic protocols used for removing the second-order quadrupolar broadening based on the refocusing of the second-order quadrupolar interaction. These protocols rely on mechanical reorientation of the rotor axis (DAS) or use a combination of sample spinning and rf manipulation of the spins' evolution (MQMAS and STMAS). Experimental aspects of these methods, as well as methods for data processing and analysis, are described in Sects. 5.3 and 5.4.

5.2.1 Dynamic Angle Spinning

Concurrently with the development of DOR, Pines and colleagues introduced the DAS method, which removes the second-order dephasing by consecutively spinning the sample about two different axes during a single scan [10, 136, 138, 153]. The experimental scheme and the coherence pathway for the DAS experiment are shown in Fig. 8. The SQ coherence ($p = -1$, $q = 0$) created by selective excitation of the CT evolves during two time intervals, $\tau/(1 + k)$ and $k\tau/(1 + k)$, defined by the direction of the rotor axis, which is rapidly switched between two different orientations, β_{RL1} and β_{RL2}. At the end of the τ period, the phase of the CT coherence is given by

$$\begin{aligned}\Phi(\tau) &= \frac{1}{1+k}\left(\omega_{-1,0}(\beta_{RL1}) + k\omega_{-1,0}(\beta_{RL2})\right)\tau \\ &= \omega^{\mathrm{ISO}}_{-1,0}\tau + \frac{1}{1+k}\left(\omega^{\mathrm{ANISO}}_{-1,0}(\beta_{RL1}) + k\omega^{\mathrm{ANISO}}_{-1,0}(\beta_{RL2})\right)\tau. \end{aligned} \tag{54}$$

The simultaneous cancelation of both anisotropic parts of the second-order quadrupolar interaction occurs if at the end of the evolution period τ the anisotropic component of the phase is null:

$$\left[\omega^{(2)}_{-1,0}(\beta_{RL1}) + \omega^{(4)}_{-1,0}(\beta_{RL1})\right] + k\left[\omega^{(2)}_{-1,0}(\beta_{RL2}) + \omega^{(4)}_{-1,0}(\beta_{RL2})\right] = 0. \tag{55}$$

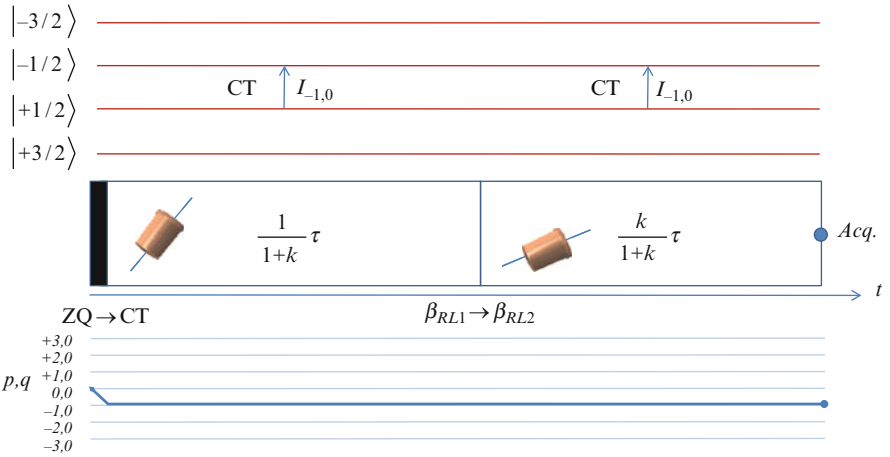

Fig. 8 Schematic representation of the DAS experiment for $I = 3/2$: the second-order broadening is refocused at the end of τ period (see text). In theory, there is no need to use rf-pulses when switching between β_{RL1} and β_{RL2}. In practice, however, reorientation of the rotor takes about 50 ms, which requires storing the magnetization along the z axis to avoid losses due to relaxation

To fulfill the refocusing condition for all crystallites in a powder, the choices of β_{RL1} and β_{RL2} are dictated by

$$\begin{cases} d^2_{0,0}(\beta_{RL1}) = -kd^2_{0,0}(\beta_{RL2}) \\ d^4_{0,0}(\beta_{RL1}) = -kd^4_{0,0}(\beta_{RL2}). \end{cases} \tag{56}$$

One possible solution, obtained for $k = 1$, is $\beta_{RL1} = 37.4°$ and $\beta_{RL2} = 79.2°$. Note that no solution exists for β_{RL1} or $\beta_{RL2} = 54.736°$. When both conditions in (56) are fulfilled, we obtain

$$\Phi(\tau) = \omega^{\mathrm{ISO}}_{-1,0}\tau\,, \tag{57}$$

i.e., the coherence phase evolves under the isotropic terms given in (31). Thus, the signal intensity as a function of τ is given by

$$S(\tau) = S(0)\mathrm{e}^{\mathrm{i}\phi(\tau)} = S(0)\mathrm{e}^{\mathrm{i}\omega^{\mathrm{ISO}}_{-1,0}\tau}, \tag{58}$$

where the relaxation phenomena are neglected. Hence, a Fourier transformation of this signal yields a fully isotropic spectrum similar to that obtained by DOR ($\Omega^{\mathrm{ISO}}_{\mathrm{DAS}} = \Omega^{\mathrm{ISO}}_{\mathrm{DOR}} = \omega^{\mathrm{ISO}}_{-1,0}$). A 2D dataset, $S(t_1, t_2)$, can also be acquired, correlating the evolutions at different orientations, as will be explained in Sect. 5.3.

In practice, it is necessary to apply two $\pi/2$ pulses, i.e., before and after changing the rotor axis angle, as this operation cannot be instantaneous. Consequently, although DAS fully refocuses second-order quadrupolar anisotropy, it cannot refocus homonuclear dipolar couplings [154]. Therefore, the linewidths of DAS resonances often exceed those obtained with the MQMAS method described in the following section [155]. The DAS experiment is less mechanically demanding than DOR, and has been especially useful in the studies of ^{17}O nuclei in glasses [156], and in experiments involving cross-polarization where spinning at $\beta_{RL} = 0°$ offers high efficiency of magnetization transfer [154].

5.2.2 MQMAS

In 1995, Frydman et al. demonstrated that an isotropic spectrum of the CT could be obtained by manipulating both spatial and spin parts of $\mathcal{H}^{II}_Q$, but without changing the orientation of the spinning axis [140]. The unique aspect of this approach is that the refocusing is achieved by transferring the spin system into an unobservable symmetric MQ coherence ($p = 3$, 5, 7, or 9, $q = 0$) during the first part of the experiment, and changing the coherence order to SQ to "undo" the dephasing that occurred at the MQ level. As in DAS, all crystallites in a powdered sample experience refocusing at the same time, yet the experiment avoids the difficulties associated with using the rotor orientation as a variable.

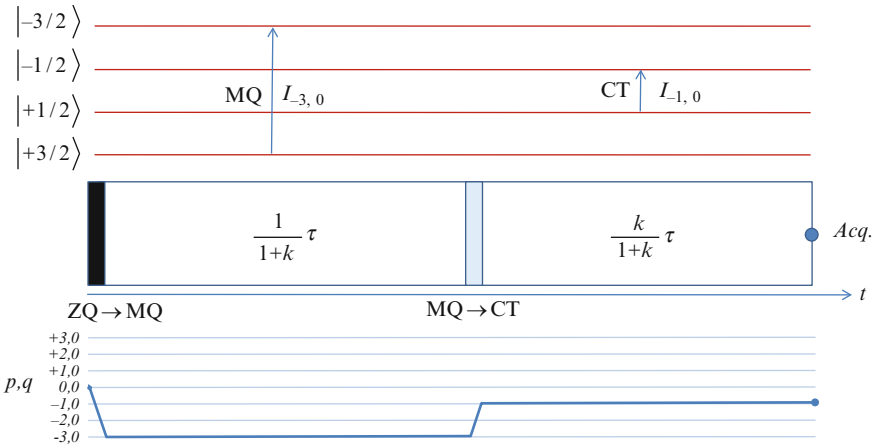

Fig. 9 Schematic representation of the MQMAS experiment for $I = 3/2$. Again, all $\mathcal{H}_Q^{II}$-driven dephasings are refocused at $t = \tau$

As shown in Fig. 9, the symmetric MQ coherence is generated by an initial strong rf-pulse (or a sequence of pulses) and evolves during the first fraction of the τ period, before being converted to the SQ CT coherence at $t = \tau/(1 + k)$ by another strong rf-pulse (or pulses). At $t = \tau$ the coherence phase is given by

$$\begin{aligned}\Phi(\tau) &= \frac{1}{1+k}\left(\omega_{p,0}(\beta_{RL}) + k\omega_{-1,0}(\beta_{RL})\right)\tau \\ &= \frac{1}{1+k}\left(\left(\omega_{p,0}^{\mathrm{ISO}} + k\omega_{-1,0}^{\mathrm{ISO}}\right) + \left(\omega_{p,0}^{\mathrm{ANISO}}(\beta_{RL}) + k\omega_{-1,0}^{\mathrm{ANISO}}(\beta_{RL})\right)\right)\tau. \end{aligned} \tag{59}$$

Since all transitions involved in MQMAS are symmetric ($q = 0$), the first-order quadrupolar broadening does not contribute to the dephasing (33). As in DAS, the refocusing condition at time τ can be written as

$$\omega_{p,0}^{\mathrm{ANISO}}(\beta_{RL}) + k\omega_{-1,0}^{\mathrm{ANISO}}(\beta_{RL}) = 0. \tag{60}$$

For a symmetric MQ transition of order p, (34) yields

$$\begin{aligned}\omega_{p,0}^{\mathrm{ANISO}} &= C_2(\Theta_{PR})\left(3p^3 - p(8I(I+1) - 3)\right)d_{0,0}^2(\beta_{RL}) \\ &+ C_4(\Theta_{PR})\left(\frac{17}{2}p^3 - p(18I(I+1) - 5)\right)d_{0,0}^4(\beta_{RL}).\end{aligned} \tag{61}$$

If the sample is spun at the magic angle ($d_{0,0}^2 = 0$), the refocusing condition (60) is fulfilled when

$$k = -\frac{\omega_{p,0}^{\mathrm{ANISO}}(\beta_{RL})}{\omega_{-1,0}^{\mathrm{ANISO}}(\beta_{RL})} = -\frac{\omega_{p,0}^{(4)}(\beta_{RL})}{\omega_{-1,0}^{(4)}(\beta_{RL})} = \frac{1}{9}\frac{p(-17p^2 + 36I(I+1) - 10)}{4I(I+1) - 3}. \quad (62)$$

Since the sign of $\omega_{p,0}^{\mathrm{ANISO}}(\beta_{RL})$ is reversed when that of p is changed, it is always possible to arrange a coherence pathway that leads to a detectable refocusing echo ($k > 0$). For example, in the 3QMAS experiment with spin-3/2 nuclei ($I = 3/2$), refocusing is obtained for $p = -3$ and $k = 7/9$ [140]. Again, the isotropic chemical shift and QIS are not refocused; hence the intensity $S(\tau)$ of the signal acquired at the end of the evolution period is modulated according to the following frequency, calculated using (30):

$$\begin{aligned}\Omega_{\mathrm{MQMAS}}^{\mathrm{ISO}} &= \frac{1}{1+k}\left(\omega_{p,0}^{\mathrm{ISO}} + k\omega_{-1,0}^{\mathrm{ISO}}\right) \\ &= \frac{p-k}{1+k}\omega_0\delta_{\mathrm{CS}} + \frac{1}{30}\left(\frac{3}{4}\frac{p^3-k}{1+k} - I(I+1)\frac{p-k}{1+k}\right)\frac{{\chi_Q}^2}{\omega_0} \\ &= \frac{17p(p-1)}{27 - 36I(I+1) - 17p(p-1)} \\ &\quad \times \left(-\omega_0\delta_{\mathrm{CS}} - \frac{1}{51}\left(I(I+1) - \frac{3}{4}\right)\frac{{\chi_Q}^2}{\omega_0}\right) \\ &= -\frac{17p(p-1)}{27 - 36I(I+1) - 17p(p-1)}\omega_0\left(\delta_{\mathrm{CS}} - \frac{10}{17}\delta_{\mathrm{QIS}}\right). \end{aligned} \quad (63)$$

The MQMAS experiment is technically straightforward and has truly revolutionized solid-state NMR of half-integer quadrupolar nuclei (see Sects. 5.3, 5.4, 6, and 7).

5.2.3 STMAS

In 2000, Gan proposed the previously mentioned STMAS method, which is similar to MQMAS in that it can be performed on a standard MAS probehead, but uses a different coherence pathway [141]. The STMAS protocol, schematically described in Fig. 10, relies on excitation of the SQ ST coherences of order q (with $q \neq 0$ and $p = -1$), instead of symmetric MQ coherences with $q = 0$. Note that such excitation inevitably involves the CT, as well. The ST coherences are converted to the CT coherence at $t = \tau/(1 + k)$ using suitable rf-pulse pulse(s).

At $t = \tau$, the phase of coherence that followed the ST $\rightarrow$ CT pathway is given by

$$\begin{aligned}\Phi(\tau) &= \frac{1}{1+k}\left(\omega_{-1,q} + k\omega_{-1,0}\right)\tau \\ &= \frac{1}{1+k}\left(\left(\omega_{-1,q}^{\mathrm{ISO}} + k\omega_{-1,0}^{\mathrm{ISO}}\right)\tau + \omega_{-1,q}^{I}\tau + \left(\omega_{-1,q}^{\mathrm{ANISO}} + k\omega_{-1,0}^{\mathrm{ANISO}}\right)\tau\right). \end{aligned} \quad (64)$$

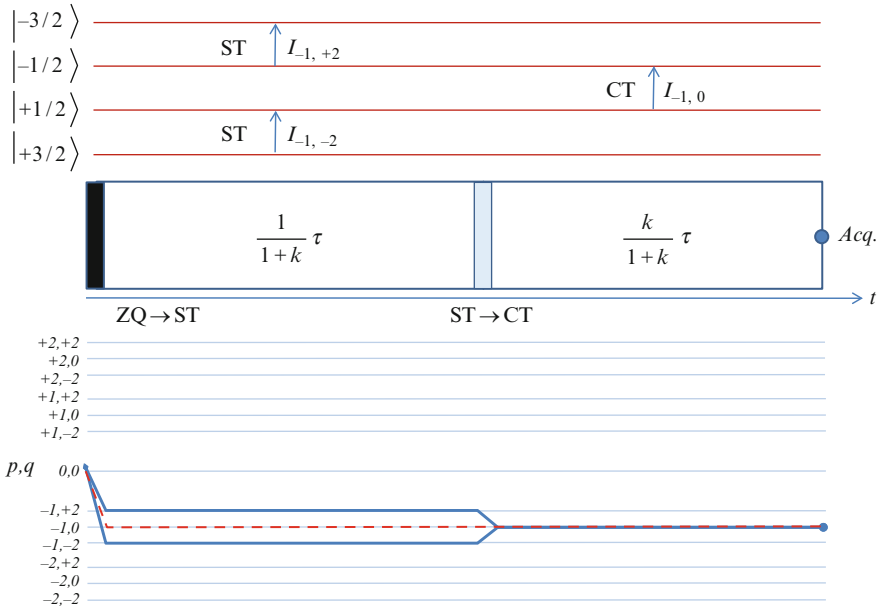

Fig. 10 Schematic representation of the STMAS experiment for $I = 3/2$. The unwanted CT → CT pathway is not eliminated by this simple pulse sequence

As previously, the phase evolution due to anisotropic terms is refocused if

$$\begin{cases} \omega^{I}_{-1,q} = 0 \\ \omega^{\mathrm{ANISO}}_{-1,q} + k\omega^{\mathrm{ANISO}}_{-1,0} = 0. \end{cases} \tag{65}$$

If the sample is spun exactly at $\beta_{RL} = 54.736°$ and at "infinite" spinning speed, the first-order term $\omega^{I}_{-1,q}$ vanishes (33) and the second-order anisotropic term yields

$$\omega^{\mathrm{ANISO}}_{-1,q} = \omega^{(4)}_{-1,q} = C_4(\Theta_{PR})\left[\frac{3}{2}\left(-17q^2 + 12I(I+1) - 9\right)\right] d^4_{0,0}(\beta_{RL}). \tag{66}$$

Therefore, both conditions in (65) are satisfied if

$$k = -\frac{\omega^{(4)}_{-1,q}}{\omega^{(4)}_{-1,0}} = \frac{17}{3}\frac{q^2}{(4I(I+1) - 3)} - 1. \tag{67}$$

For $I = 3/2$, the second-order anisotropy is thus refocused when $k = 8/9$, for both STs corresponding to $q = -2$ and 2 ($|3/2\rangle \rightarrow |1/2\rangle$ and $|-1/2\rangle \rightarrow |-3/2\rangle$). A related scheme, referred to as I-STMAS and utilizing the inverse transfer CT → ST ($|q| = 2$), has also been proposed [157]. The frequency observed in the isotropic spectrum is given by

$$\Omega_{\mathrm{STMAS}}^{\mathrm{ISO}} = \frac{1}{1+k}\left[\omega_{-1,q}^{\mathrm{ISO}} + k\omega_{-1,0}^{\mathrm{ISO}}\right]$$
$$= -\omega_0\delta_{\mathrm{CS}} + \frac{1}{30}\left[I(I+1) - \frac{3}{4}\left(1 + \frac{3q^2}{1+k}\right)\right]\frac{{\chi_Q}^2}{\omega_0}$$
$$= -\omega_0\delta_{\mathrm{CS}} - \frac{1}{51}\left(I(I+1) - \frac{3}{4}\right)\frac{{\chi_Q}^2}{\omega_0} = -\omega_0\left(\delta_{\mathrm{CS}} - \frac{10}{17}\delta_{\mathrm{QIS}}\right). \quad (68)$$

It follows from (63) and (68) that the isotropic frequencies in MQMAS and STMAS spectra are related by

$$\Omega_{\mathrm{MQMAS}}^{\mathrm{ISO}} = -\lambda\Omega_{\mathrm{STMAS}}^{\mathrm{ISO}}, \quad (69)$$

where the scaling factor λ is given by

$$\lambda = \lambda(I,p) = -\frac{17p(p-1)}{27 - 36I(I+1) - 17p(p-1)}. \quad (70)$$

In addition to unwanted contributions from the CT → CT pathway (see Sect. 5.2.4), the STMAS spectra may suffer from first-order quadrupolar effects. Indeed, unless the rotor axis is set precisely at 54.736°, the ω_Q-dependent term given by (33) may introduce unacceptable broadening to the STMAS spectrum. Furthermore, (33) is valid for the "infinite" MAS rate, or more precisely, for $\omega_R > \omega_{\mathrm{Q}}$. This condition is not met in practical applications of STMAS. Since the first-order dephasing is averaged over each rotor period, its effect can be avoided by setting τ (and the increment of τ in 2D data acquisition) at $2n\pi/\omega_R$. Numerous studies have demonstrated that accurate setting of the magic angle and precise rotor synchronization are both essential and challenging [158]. Ashbrook and Wimperis showed that the off-magic-angle evolution can be compensated by inverting the satellite order q at $t = \tau/2(1 + k)$ via an rf-pulse, in the experiment referred to as "self-compensated for angle missets" (SCAM) [159]. A sensor utilizing the Hall effect can be affixed to the MAS module allowing angle setting to within 0.01° accuracy, as recently proposed by Levitt et al. [160].

5.2.4 DQF-STMAS

The basic implementation of the STMAS experiment, shown in Fig. 10, does not allow for rejecting the undesired CT → CT transfer through phase-cycling. Gan proposed that using a DQ filter (DQF) can provide an elegant solution to this problem (Fig. 11) [161]. Indeed, inserting a selective 180° pulse directly before the ST → CT conversion pulse has the effect of creating a DQ coherence ($p = -2$) from the ST coherence ($p = -1$), while keeping the same satellite order q. Meanwhile, the CT coherence order changes its sign from $p = -1$ to $p = +1$, and thus

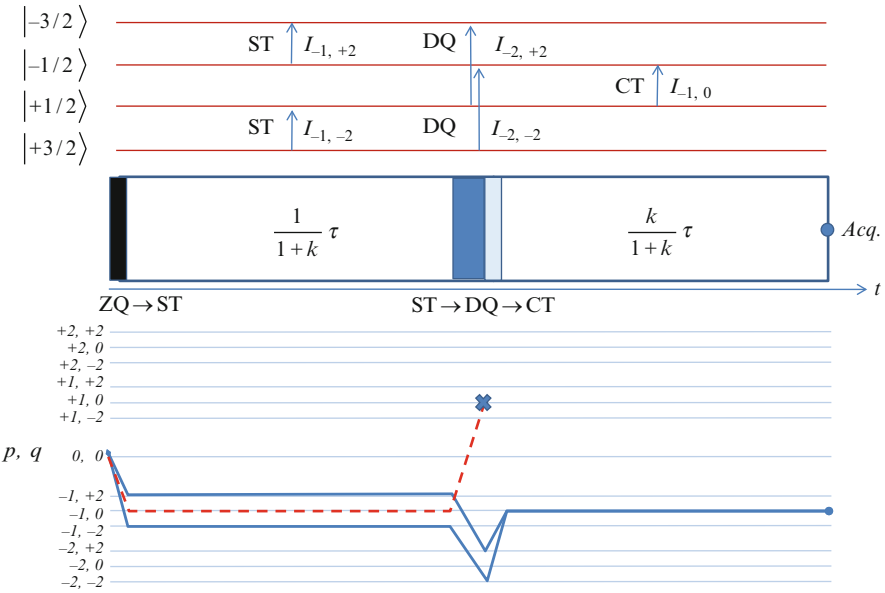

Fig. 11 Schematic representation of the DQF STMAS experiment for $I = 3/2$

can be eliminated by phase-cycling to provide a "clean" STMAS spectrum without contribution from the CT → CT transfer. Additionally, for spin $I > 3/2$, contributions from the outer STs are also perfectly canceled.

5.2.5 Third-Order Quadrupolar Contributions in STMAS

The quadrupolar effects of order higher than two (7) are usually assumed to be negligible, especially at high magnetic fields. However, once the first- and second-order effects are removed, the measurement of third-order contributions becomes realistic. It can be easily shown that, similar to the first-order case, the CT and all symmetric MQ transitions ($q = 0$) are free of the third-order contribution, which thus can be safely ignored in DAS, DOR, and MQMAS experiments [161, 162]. This is not the case for transitions between non-symmetric spin states, such as the STs. Indeed, numerical simulations of the third-order effect have explained the spectral features that have been observed in ^{27}Al STMAS spectra of andalusite mineral [161].

5.3 *Isotropic and Second-Order Anisotropic Powder Spectra Correlations*

The high-resolution experiments presented in Sect. 5.2 can refocus the anisotropic contributions of the second and fourth ranks using complex mechanical reorientation

(DAS), or those of the fourth rank using MAS (MQMAS, STMAS, DQF-STMAS). Until now, all these sequences have been presented in their 1D versions, which entails the recording for increasing τ values of a series of data points having a phase $\Phi(\tau) = \Omega\tau$; where in its general form [see (54), (59), and (64)]

$$\Omega = \frac{1}{1+k}\left[\left(\omega_{p,q}^{\mathrm{ISO}} + k\omega_{-1,0}^{\mathrm{ISO}}\right) + \left(\omega_{p,q}^{\mathrm{ANISO}}(\beta_{RL}) + k\omega_{-1,0}^{\mathrm{ANISO}}(\beta_{RL})\right)\right]\tau. \tag{71}$$

This process yields an interferogram

$$S(\tau) = S(0)\mathrm{e}^{\mathrm{i}\Phi(\tau)} = S(0)\mathrm{e}^{\mathrm{i}\Omega\tau} \tag{72}$$

that can be subsequently Fourier-transformed with respect to τ, giving resonance lines at frequency Ω. However, in all these methods the acquisition process is usually extended to two time domains, such that the isotropic and anisotropic spectra appear in separate dimensions [139–141, 163–167].

5.3.1 Pure-Absorption 2D Spectra

In the most basic implementation of 2D acquisition, a series of free induction decays are recorded as a function of the first evolution period (t_1 time domain), starting at the beginning of the second evolution period (t_2 time domain), instead of at the top of the isotropic echoes. The phase of the signal is

$$\Phi(t_1, t_2) = \Omega_1 t_1 + \Omega_2 t_2, \tag{73}$$

where $\Omega_1 = \omega_{p,q} = \omega_{p,q}^{\mathrm{ISO}} + \omega_{p,q}^{\mathrm{ANISO}}(\beta_{RL})$ and $\Omega_2 = \omega_{-1,0} = \omega_{-1,0}^{\mathrm{ISO}} + \omega_{-1,0}^{\mathrm{ANISO}}(\beta_{RL})$ are the frequencies corresponding to the t_1 and t_2 evolution periods, respectively. The rectangular matrix of the time-domain signal is thus given by

$$S(t_1, t_2) = S(0,0)\mathrm{e}^{\mathrm{i}\Phi(t_1,t_2)} = S(0,0)\mathrm{e}^{\mathrm{i}\Omega_1 t_1}\mathrm{e}^{\mathrm{i}\Omega_2 t_2} = S_p(0,0)\mathrm{e}^{\mathrm{i}\omega_{p,q}t_1}\mathrm{e}^{\mathrm{i}\omega_{-1,0}t_2}, \tag{74}$$

where relaxation effects are neglected. When q is different from zero (e.g., in STMAS) and since $\omega_{p,q}$ does not depend on the sign of q for the second-order quadrupolar interaction, the amplitude $S_p(0,0)$ always includes the contributions from both q and $-q$. Using this method, refocused echoes appear in the t_2 time-domain at the time

$$t_2^{\mathrm{echo}} = kt_1, \tag{75}$$

where $k = -\omega_{p,q}^{\mathrm{ANISO}} \Big/ \omega_{-1,0}^{\mathrm{ANISO}}$ is the refocusing factor detailed in the previous sections for the various high-resolution methods [see (56), (62), and (67)]. A double

complex Fourier transformation of this phase-modulated signal yields a spectrum with two dimensions, Ω_1 and Ω_2, corresponding to the indirect t_1 and direct t_2 time domains, respectively. Unfortunately, such a Fourier transformation leads to spectra with phase-twisted lineshapes [34]. To avoid this problem, one alternative is to modify the experiment in such a way that the signal is amplitude-modulated as a function of t_1. This can be done by selecting both $+p$ and $-p$ coherences during the t_1 evolution. The pathway for which k has a positive value (e.g., in MQMAS, the $-3 \rightarrow -1$ pathway when $I = 3/2$ or $+3 \rightarrow -1$ when $I = 5/2$) is called the echo pathway. For the antiecho pathway, the refocusing occurs for negative t_2 values:

$$t_2^{\text{antiecho}} = -kt_1. \tag{76}$$

If the two symmetric coherence transfer pathways are designed to have the same efficiency and thus yield signals with the same amplitude (e.g., by using the popular z-filter method (Fig. 12a) [168]), the resulting signal can be written as

$$\begin{aligned} S_+(t_1,t_2) &= \left(S_p(0,0)\mathrm{e}^{\mathrm{i}\omega_{p,q}t_1} + S_{-p}(0,0)\mathrm{e}^{\mathrm{i}\omega_{-p,q}t_1}\right)\mathrm{e}^{\mathrm{i}\omega_{-1,0}t_2} \\ &= 2S_p(0,0)\cos\left(\omega_{p,q}t_1\right)\mathrm{e}^{\mathrm{i}\omega_{-1,0}t_2}, \end{aligned} \tag{77}$$

recognizing that $\omega_{p,q} = -\omega_{-p,q}$ and $S_p = S_{-p}$. For each time increment in t_1, a second signal can be measured by properly incrementing the phase of the preparation pulse sequence to yield

$$\begin{aligned} S_-(t_1,t_2) &= \left(S_p(0,0)\mathrm{e}^{\mathrm{i}\omega_{p,q}t_1} - S_{-p}(0,0)\mathrm{e}^{\mathrm{i}\omega_{-p}t_1}\right)\mathrm{e}^{\mathrm{i}\omega_{-1,0}t_2} \\ &= 2iS_p(0,0)\sin\left(\omega_{p,q}t_1\right)\mathrm{e}^{\mathrm{i}\omega_{-1,0}t_2}. \end{aligned} \tag{78}$$

The signals S_+ and S_- are now amplitude-modulated as a function of t_1; therefore, a double hypercomplex Fourier transformation of these data, following for instance the States–Haberkorn–Ruben procedure, yields a pure-absorption 2D spectrum with sign discrimination in the Ω_1 dimension [169].

A second solution is offered by the whole shifted-echo method, whereby a selective π pulse is added after a time delay δ at the end of the refocusing block to create an additional spin echo on the CT (Fig. 12b) [139, 164, 167]. In this case, the echo and antiecho signals are delayed by

$$t_2^{\text{echo}} = \delta + kt_1\,; \quad t_2^{\text{antiecho}} = \delta - kt_1, \tag{79}$$

where the delay δ has to be long enough to avoid truncation of the full-echo signal in the t_2 domain. Indeed, the complex Fourier transformation of a function whose real and imaginary parts are respectively symmetric and anti-symmetric yields a purely absorptive spectrum. Therefore, the two-dimensional Fourier transformation

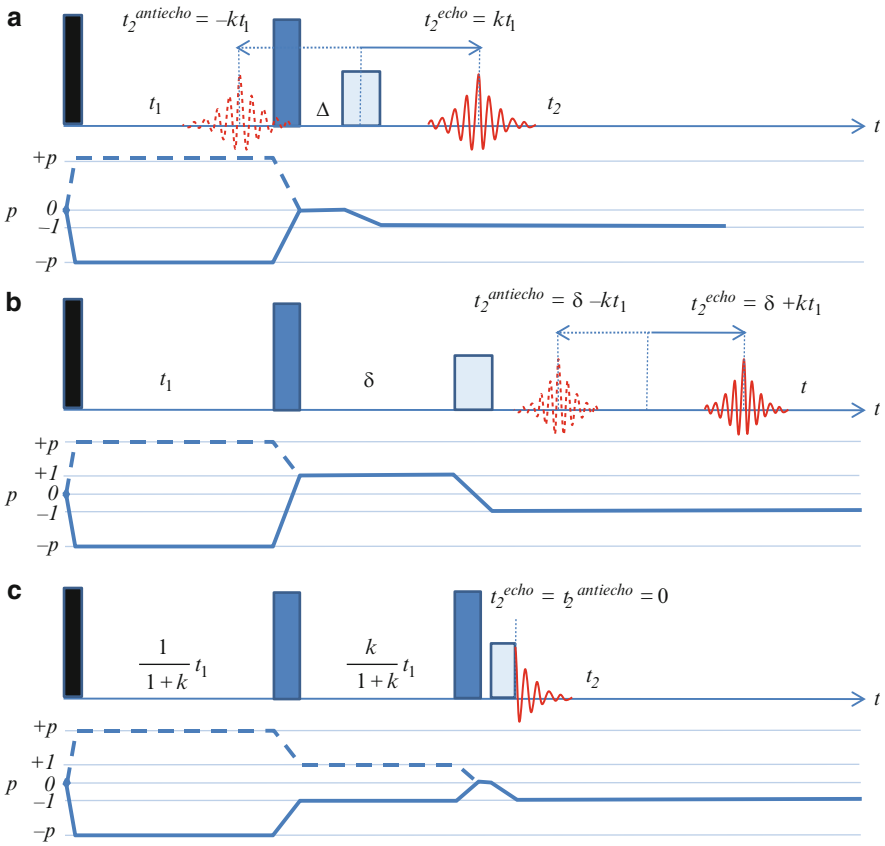

Fig. 12 Most commonly used two-dimensional schemes: (**a**) *z*-filter, (**b**) whole shifted echo, and (**c**) split-t_1

of a 2D dataset acquired with the whole shifted-echo pulse sequence produces a pure-absorption 2D spectrum. Two options are possible in this experiment: either to use only one pathway or, if transverse relaxation permits, both the echo and antiecho pathways simultaneously.

5.3.2 Shearing

One feature of the 2D high-resolution spectra acquired using the *z*-filter or shifted-echo methods is that the quadrupolar broadening is spread out along a ridge with a slope direction given by the *k* ratio. Spectra displaying only isotropic shifts in the Ω_1' dimension and anisotropic lineshapes along the Ω_2 dimension can be obtained by performing a shearing transformation along the indirect dimension [34]:

$$\begin{pmatrix}\Omega_1'\\ \Omega_2'\end{pmatrix}=\begin{pmatrix}\dfrac{1}{1+R} & \dfrac{R}{1+R}\\ 0 & 1\end{pmatrix}\begin{pmatrix}\Omega_1\\ \Omega_2\end{pmatrix}=\begin{pmatrix}\dfrac{1}{1+R}\left(\omega_{p,q}+R\omega_{-1,0}\right)\\ \omega_{-1,0}\end{pmatrix}, \tag{80}$$

where R is the shearing ratio. It is clear that, for $R = k$, Ω_1' becomes equal to a linear combination of the isotropic chemical and quadrupolar-induced shifts only:

$$\Omega_1' = \Omega_{\mathrm{ISO}} = \frac{1}{1+k}\left(\omega_{p,q}^{\mathrm{ISO}} + k\omega_{-1,0}^{\mathrm{ISO}}\right) = \omega_0\lambda\left(\delta_{\mathrm{CS}} - \frac{10}{17}\delta_{\mathrm{QIS}}\right), \tag{81}$$

where λ is given by (70) for MQMAS and is equal to -1 for STMAS.

The resulting 2D spectrum projects the desired isotropic-anisotropic correlation spectra onto two orthogonal axes (Fig. 13). Note that, recently, a generalized biaxial shearing procedure was proposed which provides in some cases a more efficient use of the spectral area and which may thus be particularly useful at high magnetic fields, but to the detriment of clear separation of the isotropic and quadrupolar anisotropy [170, 171]. Additionally, Wimperis et al. have also proposed an alternative method, called split-t_1, which avoids the use of a shearing transformation by initiating the t_2 domain at the end of the refocusing sequence [163, 164]. Both echo and antiecho pathways are retained in this method and added as shown in Fig. 12c, leading to a pure-phase spectrum. More details on all these methods and their variants can be found in several review articles discussing their respective advantages and drawbacks [4, 8–13, 17, 18, 172–175].

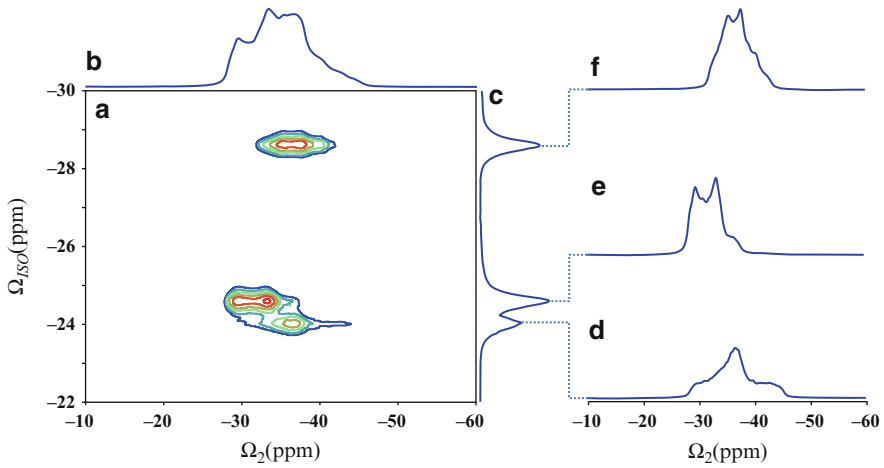

Fig. 13 ^{87}Rb NMR spectra of polycrystalline $RbNO_3$: (**a**) sheared z-filter 2D triple-quantum MQMAS spectrum, (**b**) MAS spectrum, (**c**) MQMAS isotropic projection, and (**d**-**f**) cross-sections of the 2D spectrum showing the three different crystallographic sites

5.3.3 Scaling

The final 2D spectra obtained by shearing or by using the split-t_1 pulse sequence can benefit from a proper scaling of the isotropic and anisotropic dimensions in order to facilitate comparisons between various experiments [171, 176–179]. In our opinion, the most convenient way to reference such 2D spectra is to define a ppm scale using, in the isotropic dimension, an apparent Larmor frequency depending on the given experiment and defined as

$$\omega_{\text{apparent}} = \lambda\omega_0. \tag{82}$$

Again, the value of λ for MQMAS is given in (70), and $\lambda = -1$ for STMAS (as for the anisotropic dimension Ω_2). Using this convention, the apparent shifts of the quadrupolar resonances expressed in ppm are given by

$$\delta_{\text{ISO}} = \delta_{\text{CS}} - \frac{10}{17}\delta_{\text{QIS}} \quad \text{and} \quad \delta_2 = \delta_{\text{CS}} + \delta_{\text{QIS}} \tag{83}$$

in the isotropic and anisotropic dimensions, respectively.

5.3.4 Determination of δ_{CS} and δ_{QIS}

Measuring the position of the resonance (center of gravity) in the spectrum scaled as shown above provides a very straightforward means of determining the true chemical shift (δ_{CS}) and the quadrupole-induced shift (δ_{QIS}), and thus the magnitude of quadrupole coupling. Indeed, these parameters can be directly extracted using (83):

$$\begin{aligned} \delta_{\text{CS}} &= \frac{17}{27}\delta_{\text{ISO}} + \frac{10}{27}\delta_2 \\ \delta_{\text{QIS}} &= \frac{17}{27}(\delta_2 - \delta_{\text{ISO}}). \end{aligned} \tag{84}$$

The chemical shift and quadrupolar parameters can also be easily extracted from the unsheared spectrum [8].

5.4 Improving the Sensitivity of High-Resolution 2D Techniques

All the aforementioned high-resolution experiments (except DOR) are two-dimensional and thus require long acquisition times. Moreover, experiments involving excitation of MQ coherences and their transfer to an observable signal suffer from the intrinsically low efficiency of these processes. The sensitivity can worsen

further when these methods are combined with homonuclear or heteronuclear correlation schemes (Sects. 7 and 8). However, numerous strategies have been developed to improve the sensitivity in all basic phases of these experiments: preparation (excitation of MQ coherences), evolution, mixing (conversion to observable signal), and detection. Given below is a very short overview of these efforts, with emphasis on MQMAS.

5.4.1 Excitation

Enhancement techniques for improving the excitation have received moderate attention up to now since the overall efficiency of MQMAS is mainly controlled by the conversion step. It has been shown in the early studies that, under typical conditions, increased MQ intensity can be obtained using fast MAS and a single-pulse excitation with the highest available rf-field [53, 176, 180, 181]. A different excitation mechanism is used in rotationally induced adiabatic coherence transfer (RIACT), which exploits the redistribution of coherences in the presence of an rf-field and MAS-induced oscillations of the quadrupolar frequency, and combines good efficiency with low sensitivity to the magnitude of C_Q [182]. Later modifications of RIACT included preceding the excitation pulse by a RAPT block lasting for a rotor period and, most recently, using shaped RIACT pulses for both coherence excitation and conversion [183, 184].

While most of the approaches used for the excitation of MQ coherences utilize strong rf-pulses, Vosegaard et al. have shown that very efficient excitation may also be achieved in the regime of weak rf and long pulses, using rotational resonance conditions in a method called "fast spinning transfer enhancement at rotary resonance" (FASTER) [185]. One drawback of FASTER is that it is very sensitive to rf inhomogeneity. However, recently, a new approach called ^{OC}FASTER has been claimed to yield 50% higher sensitivity by using optimal control theory for the numerical computation of the FASTER pulse [186].

5.4.2 Evolution

An increase in the sensitivity of the MQMAS method can be obtained by synchronizing the sampling of the evolution period to a sub-multiple of the spinning frequency, in order to alias all spinning sidebands on the center resonance [187]. Another interesting approach, proposed in 2003 by Rovnyak et al., consists of the use of nonlinear sampling in the indirect dimension of MQMAS experiments to reduce the total acquisition time and hence to improve sensitivity and resolution. Since nonlinear sampling prevents the use of Fourier transformation, the maximum entropy (MaxEnt) reconstruction method was used instead to obtain accurate MQMAS spectra with time savings of 2–4 [188].

Finally, it is important for optimal resolution and thus sensitivity to use a proper decoupling sequence when necessary, during both the evolution and detection

periods. For proton-containing systems, the application of proton decoupling using techniques such as TPPM, SPINAL, or SW_f-TPPM during the evolution period of a MQMAS experiment significantly improves the resolution in the indirect dimension of the spectrum [189–193].

5.4.3 Conversion

Enhancing the efficiency of the conversion period in a 2D pulse sequence has attracted the lion's share of the research in this field. This is due to the fact that the conversion of the coherences that have evolved during t_1 into SQ CT to be observed in t_2 is the least efficient part in all high-resolution methods, especially MQMAS. Numerous alternative pulse schemes have been proposed to replace the strong rf-pulse used in the original experiment for this conversion, including the above-mentioned double frequency sweeps (DFS) [62, 63], RIACT [182, 183], hyperbolic secant pulses (HS) [194], fast-amplitude modulation (FAM/RAPT) [12, 66, 172, 195], and soft-pulse-added mixing (SPAM) for the final step to combine the $\pm 1,0 \rightarrow -1$ pathways [196, 197]. The merits of these approaches have been compared in several dedicated studies and reviewed extensively [8, 17, 18, 198–200]. In general, DFS, HS, and FAM yield the highest conversion efficiency and are least sensitive to the C_Q value, whereas the usefulness of SPAM relies on its robustness and compatibility with heteronuclear correlation experiments (Sect. 7). Nonetheless, the simple z-filter conversion scheme continues to be by far the most frequently used in MQMAS and STMAS experiments, because it is very easy to optimize and yields relatively undistorted 2D absorption spectra.

5.4.4 Detection

Improvement in sensitivity during the detection period can be obtained by using the QCPMG method already described in Sect. 4.2.3, which is easy to implement in all 2D schemes. The QCPMG refocusing can lead to substantial S/N gain providing that the transverse relaxation time T_2' is considerably longer than the free induction decay (often described by time constant T_2^*) but much shorter than T_1 [112, 115, 201].

5.5 "Ultrafast" Acquisition of 2D STMAS Spectra

Among the high-resolution techniques for quadrupolar nuclei, DOR has the advantage of providing isotropic 1D spectra in real time; however, it requires a sophisticated probe. A couple of interesting alternative protocols for speeding up the acquisition of high-resolution spectra of quadrupolar nuclei using standard MAS probes have recently been described.

5.5.1 STARTMAS

In 2006 Wimperis et al. proposed a method called "satellite transitions acquired in real time by MAS" (STARTMAS) [142, 202], which allows for the real-time acquisition of high-resolution NMR spectra of spin-3/2 nuclei under MAS. This method combines a train of pulses, similar to CPMG [109, 110], with sample rotation at the magic angle to refocus the quadrupolar broadening in a series of echoes, while allowing the isotropic quadrupolar shift and chemical shift to evolve.

In STARTMAS, SQ STs of order q (with $q = \pm 2$ and $p = -1$) are initially excited as in STMAS (Fig. 14). The ST coherences then evolve during the first time period $\tau/[2(1 + k)]$, before being converted to a DQ transition by a selective π inversion pulse on the CT (as in DQF-STMAS [161]) and allowed to evolve during $k\tau/(1 + k)$. A second selective π pulse brings the system back to an SQ transition for the last part of the ST evolution. At time $t = \tau$, the phase of the detected SQ ST coherence is thus

$$\begin{aligned}\Phi(t_1) &= \frac{1}{1+k}\left(\frac{1}{2}\omega_{-1,q} + k\omega_{-2,q} + \frac{1}{2}\omega_{-1,q}\right)\tau \\ &= \frac{1}{1+k}\left(\left(\omega^{\mathrm{ISO}}_{-1,q} + k\omega^{\mathrm{ISO}}_{-2,q}\right) + \left(\omega^{I}_{-1,q} + k\omega^{I}_{-2,q}\right) + \left(\omega^{(4)}_{-1,q} + k\omega^{(4)}_{-2,q}\right)\right)\tau. \quad (85)\end{aligned}$$

Again, a refocusing of the anisotropic part of the quadrupolar interaction can be obtained if the anisotropic component of the phase is zero at the end of the evolution period t_1:

$$\begin{cases} \omega^{I}_{-1,q} + k\omega^{I}_{-2,q} = 0 \\ \omega^{(4)}_{-1,q} + k\omega^{(4)}_{-2,q} = 0. \end{cases} \quad (86)$$

If β_{RL} is exactly the magic angle and "infinite" spinning speed is assumed, the first-order anisotropic terms are zero for both single and DQ coherence (33). This does not hold true for finite spinning speed, but a complete averaging of the first-order effect occurs at the exact rotor cycles. Therefore, the τ evolution time has to match exactly a multiple of the rotor period. The second-order anisotropy refocusing occurs for

$$k = -\frac{\omega^{(4)}_{-1,q}}{\omega^{(4)}_{-2,q}} = \frac{-34q^2 + 24I(I+1) - 18}{17q^2 - 48I(I+1) + 104}. \quad (87)$$

For spin 3/2 and thus $q = \pm 2$ corresponding to the two symmetric ST and DQ transitions (Fig. 14), it follows that $k = 8$, meaning that the time evolution on the DQ coherences has to be set to $8\tau/9$. Several protocols for the acquisition and processing of STARTMAS data have been described [202]. The simplest method is to use only the data points acquired stroboscopically at times $t = n\tau$, which can be

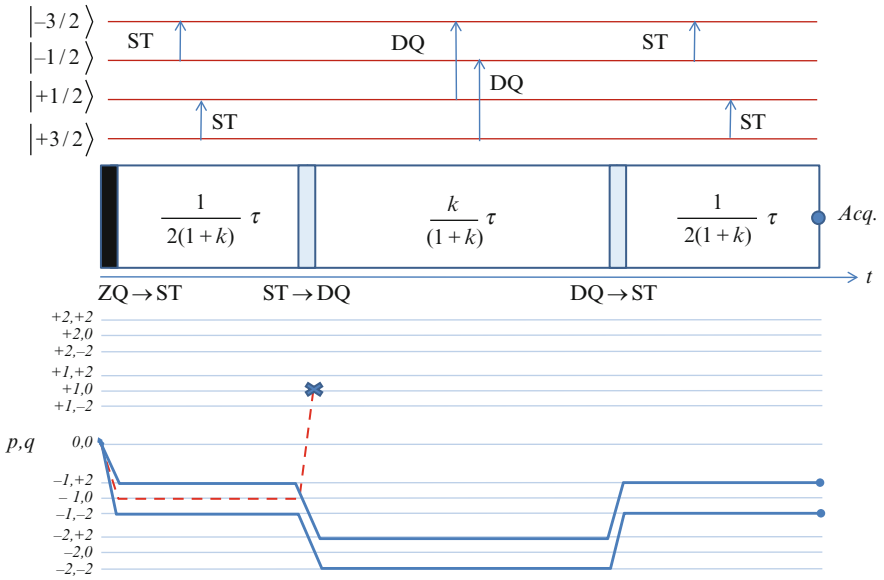

Fig. 14 Schematic representation of the STARTMAS experiment. The CT coherence excited by the initial pulse is suppressed by phase-cycling

Fourier transformed to yield a 1D isotropic spectrum. Alternatively, the isotropic echoes can be extracted and arranged in 1D or 2D arrays, leading to 1D DOR-like or 2D isotropic-anisotropic correlation spectra. The STARTMAS method is, however, quite sensitive to pulse imperfections and misadjustments, and unfortunately does not apply to spin $I > 3/2$ because the k ratio is negative in that case [202].

5.5.2 Orientational Encoding

Bhattacharyya and Frydman proposed a different method to perform ultrafast acquisition of STMAS spectra [143]. The method was inspired by earlier technical developments enabling the acquisition of arbitrary 2D NMR spectra within a single scan [203]. Ultrafast NMR replaces $S(t_1,t_2)$, the rectangular matrix of data used in traditional 2D spectroscopy (74), by a single-scan encoding of the indirect-domain interactions Ω_1, which is broadened by an additional inhomogeneous interaction ω_{inh}. In general, this is implemented using a pulsed magnetic field gradient along z such as $\omega_{\text{inh}}(z) = \gamma G_z$ in combination with a frequency-incremented train of selective rf-pulses sweeping the range $\omega_{\text{inh}}^{\text{MAX}}$during time t_1^{MAX}, and thus giving the signal

$$S(z,t_2) = \Omega_1 \frac{\omega_{\text{inh}}(z)}{\omega_{\text{inh}}^{\text{MAX}}} t_1^{\text{MAX}} + \Omega_2 t_2. \tag{88}$$

This encoding provides a series of echoes in conventional acquisition in t_2, from which a 2D spectrum can be reconstructed. Unfortunately, this method is hardly useful in solid-state MAS NMR, due to the interference of gradients with the sample rotation. In the case of quadrupolar nuclei, however, it is possible to replace the inhomogeneity produced by the gradients with broadening due to the anisotropy of the quadrupolar interaction $\omega_{\mathrm{inh}}(\Theta_{PR})$; again, using a train of rotor-synchronized selective rf-pulses, a series of echoes can be generated to reconstruct the 2D STMAS spectrum:

$$S(\Theta_{PR}, t_2) = \Omega_1 \frac{\omega_{\mathrm{inh}}(\Theta_{PR})}{\omega_{\mathrm{inh}}^{\mathrm{MAX}}} t_1^{\mathrm{MAX}} + \Omega_2 t_2. \tag{89}$$

Up to now, neither this method nor STARTMAS has been used by researchers other than their authors, especially because they are subjected to many imperfections of the pulse sequence. Still, it may be anticipated that they will open up new possibilities in a variety of applications, including studies on unstable systems, in-situ high-temperature experiments, hyperpolarized solids, or measurements on very slowly relaxing spins.

5.6 *Building High-Resolution Spectra Using Projection-Reconstruction Techniques*

Vosegaard and Massiot [144] showed that it is possible to create a high-resolution 2D spectrum correlating the chemical shifts with the second-order quadrupolar lineshapes from several spectra recorded at different magnetic field strengths using a projection-reconstruction method called "chemical shift-quadrupolar projection-reconstruction of one-dimensional spectra" (CQ-PRODI).

The technique can be applied to both spinning and static samples, taking advantage of the fact that chemical shifts are proportional to the Larmor frequency while second-order quadrupole couplings are inversely proportional to the Larmor frequency (9). Thus, the spectrum of the CT can be seen as the projection along a specific angle α of a 2D chemical shift/second-order quadrupolar correlation spectrum. The angle α for a spectrum acquired at ω_0 is defined as

$$\alpha(\omega_0) = \arctan\left((\omega_0/\omega_0^{\mathrm{ref}})^2\right), \tag{90}$$

where ω_0^{ref} is the Larmor frequency for one of the spectra chosen as a reference. When several of these projections are combined, it becomes possible to generate the full 2D spectrum using the projection-reconstruction techniques introduced to reduce the dimensionality of liquid-state experiments, as shown in Fig. 15.

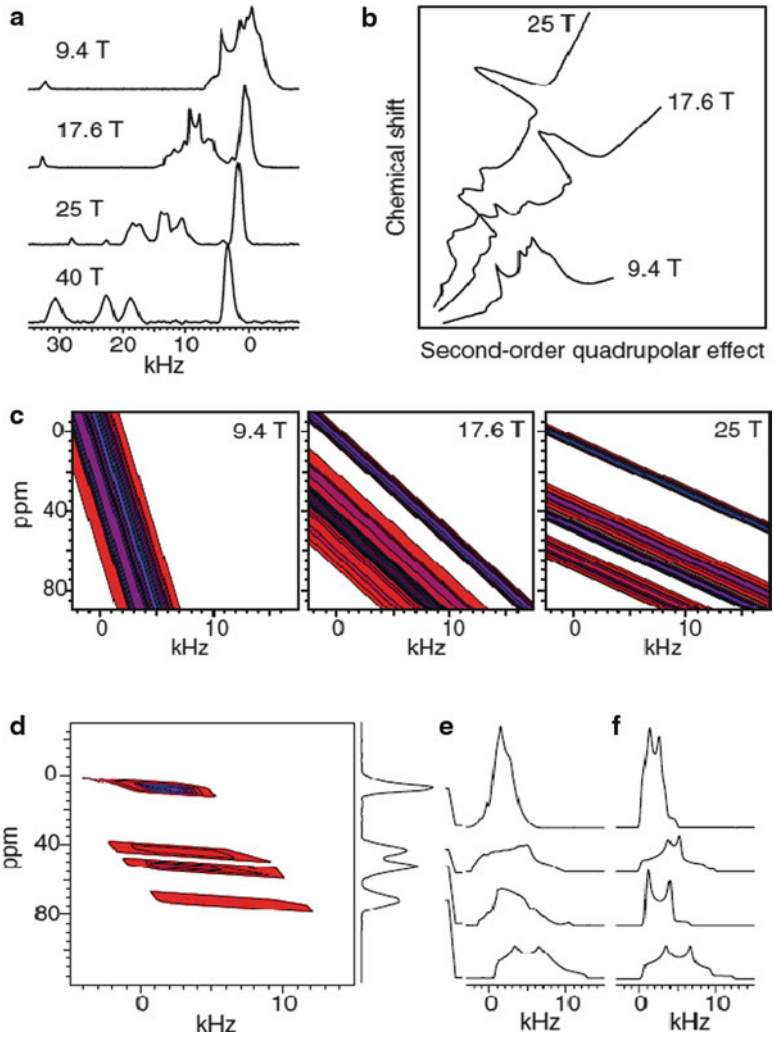

Fig. 15 (**a**) ^{27}Al MAS spectra of aluminoborate $9Al_2O_3{\cdot}2B_2O_3$ recorded at various external magnetic fields, (**b**) schematic representation of a 2D chemical shift/quadrupolar correlation spectrum showing ^{27}Al spectra with orientations according to their magnetic field strengths relative to the reference arbitrarily taken at 17.6 T, and (**c**) contour plots of the corresponding 2D projections. (**d**) 2D CQ-PRODI spectrum achieved from projections of spectra displayed in (**a**), (**e**) experimental traces through the four resonances in the chemical shift dimension, and (**f**) simulated second-order lineshapes based on previously reported parameters. (Reproduced with permission from [144])

6 Separation of the Quadrupolar Couplings from Other Interactions

6.1 Isotropic Chemical Shift and Second-Order Quadrupolar Induced Shift Correlations: The MQDOR Method

The combination of MQMAS and DOR into a single scheme led to the development of the MQDOR method [204, 205]. In MQDOR a full averaging of the second-order interaction is achieved in the t_1 (MQ evolution under DOR condition) and t_2 domains (DOR), yielding truly isotropic spectra in both dimensions, where the positions of the lines are given by (75).

It was shown recently by Hung et al. [150] that the experiment also provides a straightforward way to separate completely δ_{CS} and δ_{QIS} in the 2D graph, using a biaxial shearing transformation starting from the spectra processed previously in the conventional manner (80):

$$\underbrace{\begin{pmatrix} 1 & 0 \\ -1 & 1 \end{pmatrix}}_{\text{Shearing in } \delta_2} \underbrace{\begin{pmatrix} -\frac{17}{27} & 0 \\ 0 & 1 \end{pmatrix}}_{\text{Scaling in } \delta_1} \underbrace{\begin{pmatrix} 1 & -1 \\ 0 & 1 \end{pmatrix}}_{\text{Shearing in } \delta_1} \begin{pmatrix} \delta_{CS} - \frac{10}{17}\delta_{QIS} \\ \delta_{CS} + \delta_{QIS} \end{pmatrix} = \begin{pmatrix} \delta_{QIS} \\ \delta_{CS} \end{pmatrix}, \qquad (91)$$

where the matrix multiplications correspond, from right to left, to shearing with ratio -1 along the δ_1 dimension, scaling of the indirect dimension with ratio 17/27, and shearing along the δ_2 dimension (Fig. 16). Several studies have demonstrated the utility of this method to measure the distribution of chemical shifts and quadrupole couplings in glasses [150, 151].

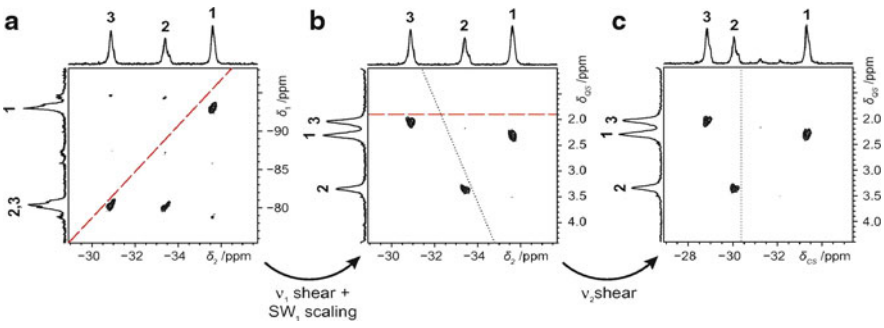

Fig. 16 ^{87}Rb (196.3 MHz) 3QDOR spectra of $RbNO_3$ (**a**) before and (**b**) after shearing and scaling of the ν_1 dimension. (**c**) ^{87}Rb 3QDOR spectrum of $RbNO_3$ after shearing and scaling of ν_1 and ν_2. Note that the scaling convention used in these graphs is different from that proposed in the present paper. (Reproduced with permission from [150])

6.2 Separation of Chemical Shift and Quadrupolar Anisotropies

Several methods have been developed to determine the chemical shift anisotropies in the presence of small and large quadrupolar broadenings, including lineshape analysis of CT or CT plus ST spectra measured under static, MAS, or high-resolution conditions [206–210]. These methods allow for determination of the quadrupolar parameters (C_Q, η_Q) and chemical shift parameters (δ_{CS}, η_{CS}, δ_σ), as well as the relative orientation of the quadrupolar and chemical shift tensors. In this context, the MQMAS experiment can be useful, as it scales the CSA by a factor of p in the isotropic dimension, allowing for determination of chemical shift parameters from the spinning sideband manifold [211].

It has also been shown that the technique referred to as "multiple-quantum variable angle spinning" (MQVAS) can be used for the purpose of separating the CSA and quadrupolar lineshapes [155]. In this experiment, a judicious choice of the rotor orientation is $\beta_{RL} = 70.12°$, which leads to cancelation of the fourth-rank term of the second-order interaction (Fig. 2). Thus, the refocusing ratio k for the quadrupolar interaction depends on the ratio of the second-rank terms

$$k = -\frac{\omega_{p,0}^{\mathrm{ANISO}}(\beta_{RL})}{\omega_{-1,0}^{\mathrm{ANISO}}(\beta_{RL})} = -\frac{\omega_{p,0}^{(2)}(\beta_{RL})}{\omega_{-1,0}^{(2)}(\beta_{RL})} = \frac{3p^3 - p(8I(I+1)-3)}{8I(I+1)-9}, \qquad (92)$$

while the chemical shift is refocused for a different ratio $k_{CS} = -p$. A procedure similar to the biaxial shearing used in the MQDOR experiment (referred as the COASTER method [212]) can be used to project the chemical shift and quadrupolar contributions onto two orthogonal axes. The resulting lineshapes permit an accurate determination of quadrupolar and chemical shift parameters, while the relative orientation of the quadrupolar and chemical shift tensors can be obtained from the shape of the 2D pattern.

6.3 Relaxation-Assisted Separation of Chemical Sites

The high-resolution methods described in the previous sections cannot in general offer improved resolution in the presence of very strong quadrupolar couplings ($\omega_Q \gg \omega_{rf}$). To help resolve broad overlapping powder lineshapes, Frydman et al. proposed a 2D experiment dubbed relaxation-assisted separation (2D-RAS) that can discriminate individual sites based on their relaxation properties rather than the isotropic shifts. The method can be applied to static or spinning samples, in which nuclei exhibit sufficiently heterogeneous relaxation behavior resulting from different coordinations or dynamic environments [213]. The separation of sites is achieved using an approach similar to that introduced in DOSY experiments [214], which here relies on measuring the set of NMR spectra as a function of a parameter

encoding the relaxation behavior of different sites. A reasonably stable numerical algorithm for extracting the two-dimensional distribution $I(\nu, R)$ separating the quadrupolar lineshapes present in the sample according to their relaxation rates was proposed and tested on a variety of model compounds containing ^{23}Na, ^{35}Cl and ^{25}Mg nuclei [213].

7 Probing Internuclear Correlations

The analytical capabilities of high-resolution techniques for quadrupolar nuclei described in Sect. 5 have been significantly improved by the development of methods that utilize through-space dipolar couplings (hetero- and homonuclear) and through-bond heteronuclear scalar (J) couplings between these nuclei and their spin-1/2 or quadrupolar neighbors. The wealth of such methods has been scrutinized in several recent reviews dedicated to this topic [8, 14–16, 19]. Many of these techniques can afford better resolution by "stretching" the resonances along a second dimension, and provide detailed structural information about complex spin systems. Here, we briefly describe the methods for polarization transfer using dipolar and scalar interactions, and review the most recent advances in hetero- and homonuclear correlation methodology and applications under MAS and high-resolution conditions.

7.1 Polarization Transfer via Dipolar Coupling

The majority of double-resonance solid-state NMR experiments involving spin-1/2 nuclei use transfer of nuclear polarization via dipolar cross polarization (CP) to enhance polarization of the diluted spins S with small gyromagnetic ratio γ_S and significant longitudinal relaxation time T_1^I at the expense of abundant spins I with large γ_I and short T_1^S [215]. Typically, CP is used in combination with MAS, to eliminate the line broadening due to CSA, as well as with heteronuclear decoupling. To achieve the $I \rightarrow S$ CP transfer, a $(\pi/2)_y$ pulse is applied at the I spin frequency, followed by a period τ of simultaneous irradiation along the x axes of the rotating frames of both spins I and S, with rf magnetic fields, B_1^I and B_1^S, respectively, and using constant amplitude [216], ramped amplitude [217], pulsed [218], and adiabatic passage [219] methods. The rf-field strengths must be such that

$$\omega_{\mathrm{rf}}^I = \gamma_I B_1^I, \quad \omega_{\mathrm{rf}}^S = \gamma_S B_1^S \gg |\mathcal{H}_{II}|, |\mathcal{H}_{SS}|, \tag{93}$$

where $|\mathcal{H}_{II}|$ and $|\mathcal{H}_{SS}|$ are the magnitudes of homonuclear dipolar interactions. The transfer of polarization between spin-1/2 nuclei is efficient, experimentally straightforward, and well understood [1, 220]. In short, the spin-locked I spin magnetization

can be transferred to S spins through mutual flips within dipolar-coupled pairs, provided that the nutation frequencies of spins I and S are equal in their rf rotating frames (Hartmann–Hahn condition) [221]:

$$\omega_{\mathrm{rf}}^{I} \pm \omega_{\mathrm{rf}}^{S} = n\omega_R, \tag{94}$$

where $n = \pm 1$ or ± 2. The maximum enhancement of S spin magnetization is given by

$$\frac{M_S(\tau = \infty)}{M_S^{\mathrm{eq}}} = \frac{\gamma_I N_I}{\gamma_S (N_I + 1)}, \tag{95}$$

where M_S denotes the magnetization of the polarized spin in the interaction frame (i.e., transverse in the laboratory frame), M_S^{eq} is the Boltzmann equilibrium value, and N_I is the number of strongly coupled I spins surrounding each diluted spin S.

In contrast to the spin-1/2 → spin-1/2 polarization case, the transfer of polarization between spin-1/2 and quadrupolar nuclei presents a considerable challenge due to the very complex spin dynamics involved in the CP process and the spin-locking of quadrupolar nuclei under MAS. The overall sensitivity is rarely enhanced with respect to the direct polarization method, even if T_1^I is much shorter than T_1^S. The usefulness of the CP experiment relies mainly on its ability to probe the interactions between the neighboring nuclei in 1D or 2D schemes under MAS or isotropic resolution. The theoretical and practical aspects of spin-locking and CP transfer between spin-1/2 and the SQ or MQ coherences of the quadrupolar nuclei (SQ-CP or MQ-CP) have been thoroughly studied and reviewed [20, 221–227]. Some of the challenges involved in such experiments are summarized below.

7.1.1 Single-Quantum Cross-Polarization

The spin-locking and CP behavior of the most commonly used SQ coherence (CT) in quadrupolar nuclei under static and MAS conditions has been described in detail by Vega using the fictitious spin-1/2 approximation [223]. In a static sample, the Hartmann–Hahn matching condition requires that $\omega_{\mathrm{rf}}^{I} = \omega_{\mathrm{nut}}^{S}$, where $\omega_{\mathrm{nut}}^{S}$ is one of the nutation frequencies associated with the SQ coherence of the quadrupolar S spin (see Sect. 2.3.4). In the simple case of on-resonance SQ-CP this translates to [224]

$$\omega_{\mathrm{rf}}^{I} = \omega_{\mathrm{rf}}^{S} \quad \left(\left| \Omega_Q^S \right| \ll \omega_{\mathrm{rf}}^{S} \right) \tag{96}$$

and

$$\omega_{\mathrm{rf}}^{I} = (S + 1/2)\omega_{\mathrm{rf}}^{S} \quad \left(\left| \Omega_Q^S \right| \gg \omega_{\mathrm{rf}}^{S} \right) \tag{97}$$

with the quadrupolar splitting Ω_Q^S as given in (40). In the range $\left|\Omega_Q^S\right| \cong \omega_{\mathrm{rf}}^S$ the behavior of the spins cannot be described by a simple Hartmann–Hahn formula [222, 224].

Under MAS the quadrupole splitting becomes time dependent, $\Omega_Q^S = \Omega_Q^S(t)$ (see Sect. 2.3.4). This influences both the spin-locking behavior [223] and the polarization transfer [224], with the latter being further affected by the periodic modulation of the *I*-*S* dipolar interaction. The effect of MAS on spin-locking of the *S* magnetization depends on the magnitude of the so-called adiabaticity parameter:

$$\alpha = \frac{\left(\omega_{\mathrm{rf}}^S\right)^2}{\omega_Q^S \omega_R}, \tag{98}$$

where ω_Q^S is the quadrupole frequency defined in (2). This adiabaticity parameter is related to the rate at which Ω_Q crosses zero as it oscillates under MAS between positive and negative values. The modulation of the quadrupole splitting further implies that most crystallites will experience $\left|\Omega_Q^S\right| > \omega_{\mathrm{rf}}^S$ and $\left|\Omega_Q^S\right| < \omega_{\mathrm{rf}}^S$ during different parts of the rotor cycle, which in turn affects the eigenstates and eigenvalues of the Hamiltonian and the spin-locking behavior of the spins [223]. The spin-locking is reasonably efficient in the extreme cases of $\alpha << 1$ (the so-called "sudden" or "fast" passage) or $\alpha >> 1$ ("adiabatic" or "slow" passage). When $\alpha << 1$, i.e., when the applied nutation frequency is low, the zero crossings are too sudden for the eigenstates to follow the changes of the Hamiltonian. Thus, the CT coherence remains unaffected by MAS and retains its spin-locked state. In the opposite extreme of $\alpha >> 1$, the eigenstates and the level populations of *S* spins adiabatically follow the Hamiltonian, which in spin $S = 3/2$ results in rotor-synchronized interconversion of CT SQ and 3Q coherences [223]. This phenomenon, referred to as rotation-induced adiabatic coherence transfer (RIACT), can be used for the conversion of SQ to 3Q coherences in some of the MQMAS schemes, as noted earlier in Sect. 5 [182]. The intermediate case $\alpha \cong 1$ results in a loss of the spin-locked state. Due to the orientational dependence of Ω_Q^S, a distinction between sudden and adiabatic cases is often ambiguous in practical applications, as significant fractions of crystallites undergo adiabatic and sudden passages in the same sample. Still, the SQ-CP transfers are mostly carried out in the sudden-passage regime because (1) the ω_Q^S values are typically in megahertz range, (2) fast MAS is preferred to remove the CSA and dipolar terms, and is also beneficial in experiments involving MQMAS [180, 181], (3) the practically achievable rf-fields are in the range of a couple of hundred kilohertz, and (4) the negative effects of the second-order quadrupolar interaction on the spin-locking efficiency are notably diminished for very low values of α [225, 226].

The CP dynamics is affected both by the periodic modulation of Ω_Q^S and by the periodic modulation of the *I*-*S* dipolar interaction [216, 224]. Assuming that the

sudden-passage regime is indeed preferred in SQ-CP experiments, we consider only the use of a weak rf-field ω_{rf}^{S}. In such a case, only the CT is selectively affected, and the Hartmann–Hahn condition for on-resonance CP transfer in isolated spin pairs is similar to that given earlier for $I = S = 1/2$ (94):

$$(S + 1/2)\omega_{\mathrm{rf}}^{S} + \varepsilon\omega_{\mathrm{rf}}^{I} = n\omega_R, (\varepsilon = \pm 1,\ n = \pm 1, \pm 2) \tag{99}$$

with the signal intensity being reduced due to the inefficiency of the spin-locking. The overall CP efficiency is strongly anisotropic with respect to crystallite orientation and depends on the relative size of the rf-field amplitudes ω_{rf}^{I} and ω_{rf}^{S}, the spinning speed ω_R, the resonance offsets $\Delta\omega_0^I$ and $\Delta\omega_0^S$, as well as the first-order quadrupole splitting Ω_Q^S [225, 226]. These effects have been reviewed in [227] and are not further discussed here, except to point out that the optimization of the Hartmann–Hahn match can be complex and site-dependent. Thus, the absence of a resonance in the CP spectrum should not be used as evidence for the lack of $I \leftrightarrow S$ connectivity without careful experimentation. This complexity is demonstrated in Fig. 17, where several matches are observed at frequencies following the rule given by (99).

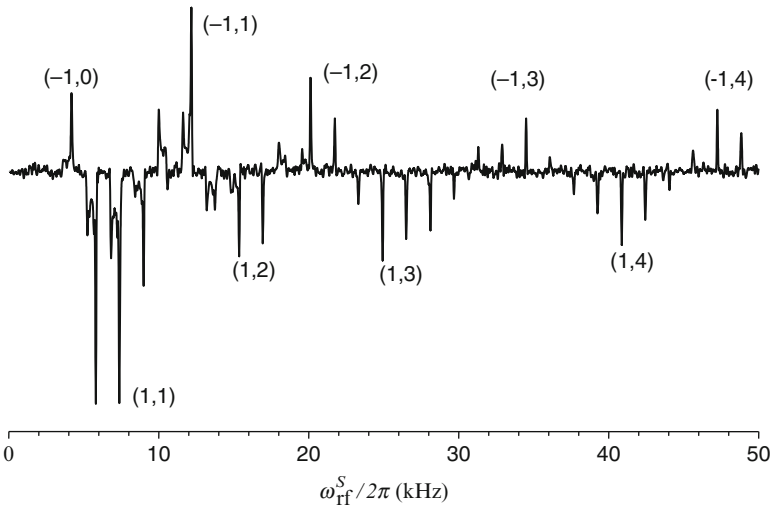

Fig. 17 Efficiency of $^{1}\mathrm{H} \rightarrow {}^{11}\mathrm{B}$ CPMAS in borax measured as a function of ω_{rf}^{S} (Hartmann–Hahn matching curve). The spectra were measured on-resonance at 9.4 T using $\omega_{\mathrm{rf}}^{I}/2\pi = 6$ kHz, $\tau_{\mathrm{CP}} = 300$ μs, and $\omega_R/2\pi = 20$ kHz. The numbers in parentheses correspond to (ε, n) values from (99). The transfers observed for $n = 0$, 3 and 4 are due to the presence of residual dipolar terms ($\mathcal{H}_{II}$ and $\mathcal{H}_{SS}$) and the fact that each ^{11}B nucleus interacts with more than one proton

7.1.2 Multiple-Quantum Cross-Polarization

The CP can also be used for polarization transfer to MQ coherences of half-integer quadrupolar nuclei [222, 223, 228–231]. This type of transfer is mainly used in the context of MQMAS [228, 229, 231], although the spin-locking of MQ coherences is also featured in experiments involving homonuclear dipolar recoupling experiments [232].

The spin-locking behavior of SQ and MQ coherences in spin $I = 3/2$ and $I = 5/2$ nuclei has recently been scrutinized by Ashbrook and Wimperis [20], taking into account the nature of the initial pulse used to prepare the spin-locked state and its further evolution under full quadrupolar Hamiltonian (first and second order), the resonance offset, and the time dependence introduced by MAS. In the adiabatic approximation, the above-mentioned interconversion between SQ and 3Q coherences takes place in spin-3/2 nuclei with the maximum efficiency expected when the spin-locking field is on resonance with the with 3Q coherence in the 3Q frame, with high sensitivity to offset. In the sudden regime, the amplitude of 3Q coherences generated from the initial state $\rho(0) = I_x^{\{3/2,-3/2\}}$, i.e., a central 3Q transition coherence, also exhibits oscillatory behavior, which in this case does not follow the rotor period. Due to the low ω_{rf}^S field strength used in this regime, the 3Q coherence is very sensitive to offset, which again can be controlled by staying on-resonance with the isotropic frequency of the 3Q coherence. Efficient 3Q spin-locking efficiency can be achieved in the sudden regime provided that a ω_{rf}^S value can be found which satisfies the requirement $\alpha \ll 1$ yet is sufficiently strong to minimize the offset effects. Additionally, a loss of spin-locking can occur at the rotary resonance condition

$$\omega_{\mathrm{rf}}^S = \frac{m}{S + 1/2}\omega_R, \tag{100}$$

where $m = 0, 1, 2, \ldots$, if first- and second-order quadrupolar interactions are present [20].

The Hartmann–Hahn MQ-CP transfer can be achieved when the rf frequency of spin I in the rotating frame is sufficiently close to one of the SQ or MQ nutation frequencies of spin S, $\omega_{\mathrm{nut}}^S \cong \omega_{\mathrm{rf}}^I$. In the case $\left|\Omega_Q^S\right| > \omega_{\mathrm{rf}}^S$, the nutation frequency for a symmetric MQ coherence of order p is given by [222, 229]

$$\omega_{\mathrm{nut}}^S = K(S,p)\frac{\left(\omega_{\mathrm{rf}}^S\right)^p}{\left(\Omega_Q^S\right)^{p-1}} \tag{101}$$

with

$$K(S,p) = \frac{(S + p/2)!}{(p-1)!^2(S - p/2)!}. \tag{102}$$

Under MAS, the Hartmann–Hahn condition for 3Q-CPMAS of spin-3/2 nuclei can be written as

$$\omega_{\text{nut}}^{S} = \omega_{\text{rf}}^{I} \pm n\omega_{R}, \tag{103}$$

where $\omega_{\text{nut}}^{S} = \dfrac{3\left(\omega_{\text{rf}}^{S}\right)^{3}}{2\left(\Omega_{Q}^{S}\right)^{2}}$, with higher-order sidebands and a centerband (i.e., $n = 0$, $\pm 1, \pm 2, \pm 3, \ldots$) being operable. The dependence of the Hartmann–Hahn condition on molecular orientation implies that for different crystallites the maximum 3Q-CPMAS efficiency may occur for different values of n. An extensive theoretical and experimental study of 3Q-CP between ^{19}F and ^{23}Na nuclei in a powdered sample under static and MAS conditions was reported by Lim and Grey [231]. While a reasonable SQ-CP efficiency could be reached in the sudden regime ($\alpha \ll 1$, i.e., weak rf-field and fast spinning speed), 3Q-CP was ineffective in such a condition: it requires a slow regime ($\alpha > 1$). The calculated and observed matching curves are very different from that depicted in Fig. 17. Since the matching patterns depend on the orientation of the individual crystallites, only a broad and relatively featureless matching profile is observed in a powdered sample under a wide range of experimental conditions, which may reduce the CP efficiency. However, this reduction can be neutralized by ramping the amplitude of the rf-field. For example, by ramping the amplitude of the ω_{rf}^{I} field [217], the efficiency of the 3Q-CPMAS transfer between ^{19}F and ^{23}Na in $NaMoO_3F$ was shown almost to double [231]. The timescale of the 3Q-CPMAS transfer is roughly proportional to $(p)^{-1}$; i.e., it is considerably faster than in the case of 1Q-CPMAS.

To sum up, optimization of the MQ-CPMAS experiment is not straightforward, as the best conditions for spin-locking and the CP are not generally compatible. For the reasons described above, the most efficient MQ-CP process will be typically achieved using the considerable rf-field strengths. Under slow MAS, these conditions would correspond to the adiabatic regime for spin-locking ($\alpha > 1$). However, when fast MAS is required, as is the case of MQMAS (see below), a significant loss of spin-locked magnetization may occur, especially in transfers requiring long τ_{CP} times. A scheme in which slow CP transfer to the CT under the sudden condition (low spin-locking field, $\tau_{\text{CP}} \sim 1/D$, where D denotes the dipolar coupling) is followed by a faster RIACT-type transfer (high spin-locking field, $\tau_{\text{CP}} \sim T_{\text{R}}/4$, where T_{R} is the rotor period) can also be envisioned.

7.2 *Polarization Transfer via J* Coupling

Scalar (J) interactions between nuclei are transmitted indirectly through the electrons of the bonds. In the solid state, the effects of J couplings are usually obscured by the dipolar, chemical shift, and quadrupolar contributions to the linewidth. Nevertheless, the measurement and utilization of J couplings are possible even if

J splittings cannot be directly resolved. In addition to the obvious advantage of providing a map of chemical bonds between the spins, *J*-based transfers do not require spin-locking and are not disturbed by molecular motions. The major drawback of polarization transfer through *J* coupling is that the delays involved in the pulse sequences, such as "insensitive nuclei enhanced by polarization transfer" (INEPT) [233] or "heteronuclear multiple-quantum coherence" (HMQC) [234], are inversely proportional to the strength of the J_{IS} constant between spins *I* and *S*. The non-refocusable transverse relaxation processes typically force shortening of these delays, which results in a substantial loss of efficiency. The performance of refocused INEPT (R-INEPT) and HMQC experiments was recently scrutinized theoretically and experimentally in the case of multi-spin systems I_nS ($n \leq 4$), where both *I* and *S* spins can be spin-1/2 or half-integer quadrupolar nuclei [235]. The details of this analysis, which is a generalization of a previous formalism for $n = 1$ [236], are beyond the scope of this review. Overall, the efficiency of R-INEPT and HMQC experiments has been found to be comparable, at least in applications involving ^{31}P and ^{27}Al. A major advantage of R-INEPT is that it can be combined with MQMAS or STMAS into a simple 2D heteronuclear correlation experiment, MQ/ST-J-HETCOR (Sect. 7.3).

7.3 HETCOR NMR of Half-Integer Quadrupolar Nuclei

Early studies of heteronuclear interactions involving quadrupolar nuclei relied on dipolar cross-polarization transfer in simple 1D schemes. Later developments utilized MAS-based methods for spectral editing or measurement of dipolar interactions, including rotational echo double resonance (REDOR) [237, 238], transferred echo double resonance (TEDOR) [218, 238], transfer of populations in double resonance (TRAPDOR) [239, 240], and rotational echo adiabatic passage double resonance (REAPDOR) [241, 242]. Some of the early exploits of *J* spectroscopy in solids involved polarization transfers in spin pairs involving half-integer quadrupolar nuclei, in spite of the challenges posed by the quadrupolar interaction. These include observation of 1D INEPT transfers in ^{27}Al-^{29}Si, ^{23}Na-^{29}Si, and ^{27}Al-^{31}P spin pairs [236, 243], as well as 2D HETCOR spectra [244].

The developments described in Sect. 5 stimulated rapid expansion of double resonance techniques, which hitherto suffered from the second-order quadrupolar broadening, to the realm of high-resolution. It has been shown by several groups that cross-polarization can be coupled with the MQMAS experiment by transferring magnetization of spin-1/2 nuclei (*I*) to the single-quantum or multiple-quantum symmetric transitions of the quadrupolar nuclei (*S*). The pulse sequences and coherence transfer pathways used in these experiments, referred to as SQ-CP-MQMAS and MQ-CP-MQMAS, are shown in Fig. 18a, b, respectively. In the initially proposed SQ-CP-MQMAS method by Pruski et al. [245] and Fernandez et al. [246], the magnetization is first transferred to the SQ CT of *S* spins, then converted into a population inversion between the Zeeman eigenstates $m = \pm 1/2$,

only to be further used in a standard *z*-filtered MQMAS scheme. Other versions of this experiment were later developed by Ashbrook and Wimperis [247], in which the number of coherence transfers is reduced by converting the CP-derived SQ coherences directly to MQ coherences, in amplitude-modulated or phase-modulated schemes. The MQ-CP-MQMAS approach was also introduced in amplitude-modulated (using the *z*-filter, as shown in Fig. 18b) and phase-modulated (split-t_1) version [228, 229]. Although few studies have directly compared the sensitivities of SQ-CP and MQ-CP approaches, both methods can yield similar S/N, as demonstrated by Lim and Grey in $^{19}F \rightarrow {}^{23}Na$ CP-MQMAS of $NaMoO_3F$ [231]. Whereas the SQ version is best carried out under the sudden condition, MQ-CPMAS appears to work better when using considerable rf-field strengths, as discussed in Sect. 7.1. The previously described RIACT mechanism can directly transfer the spin-1/2 polarization to MQ coherences, as shown by Griffin and coworkers [248]. In this case, the 3Q-CP process also requires the use of a high rf-field and can be viewed as dipolar SQ-CP transfer followed by MAS-driven SQ→3Q RIACT.

As in the case of CPMAS, the CP-MQMAS transfers are incapable of enhancing the sensitivity, but can provide dipolar filtering of high-resolution spectra of quadrupolar nuclei and, most importantly, serve as a method for obtaining the HETCOR

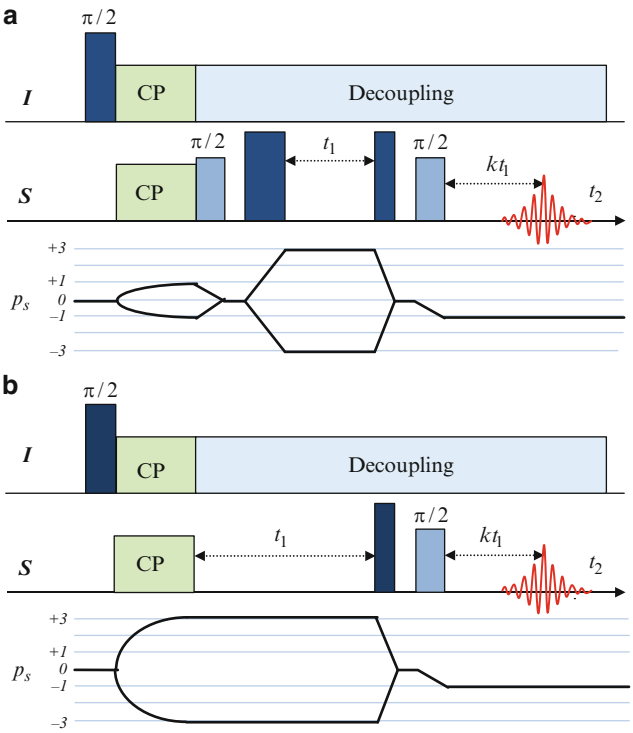

Fig. 18 (**a**, **b**) Pulse sequences and coherence transfer pathways for SQ-CP-3QMAS with *z*-filter and MQ-CP-3QMAS with *z*-filter

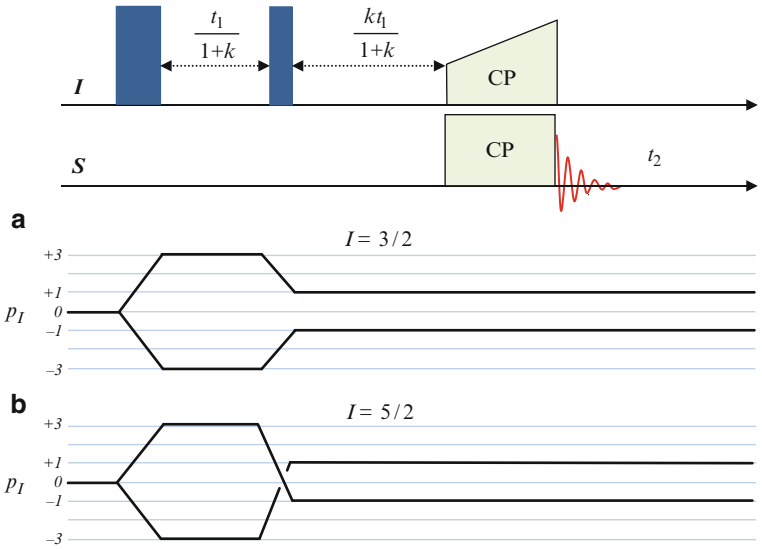

Fig. 19 Pulse sequences and coherence transfer pathways used in MQMAS-*D*-HETCOR experiments. In MQMAS-*J*-HETCOR, CP is replaced by *J*-based transfer

spectra displaying high resolution in both dimensions. In this case, however, it is advantageous to transfer polarization from the fast relaxing quadrupolar nuclei to spin-1/2 nuclei, as it also preserves the two-dimensional structure of the experiment. The first such method, reported by Jarvie et al., used DAS to remove the second-order quadrupolar broadening in the t_1 domain [249]. The MQMAS-based 2D HETCOR protocols follow the general scheme introduced by Wang et al. (Fig. 19a, b), where the magnetization involved in the isotropic echo, formed under the conditions discussed in Sect. 5 is spin-locked and subsequently used to polarize the spin-1/2 nuclei, which are observed in the t_2 domain [250]. This method was used to obtain high-resolution CP-based HETCOR spectra involving spin-3/2 nuclei (^{23}Na→^{31}P 3QMAS-*D*-HETCOR of $Na_3P_3O_9$ [250], where "*D*" denotes "dipolar") and spin-5/2 nuclei (^{27}Al→^{31}P 3QMAS- and 5QMAS-*D*-HETCOR spectra of microporous aluminophosphate VPI-5 [251]). Subsequently, Wiench and Pruski introduced an MQMAS-*J*-HETCOR experiment, which yields high-resolution through-bond correlations, by using INEPT instead of CP for polarization transfer [252]. The sensitivity of the MQMAS-*D*-HETCOR and MQMAS-*J*-HETCOR methods was later enhanced by using the SPAM mixing scheme to take advantage of previously unexploited coherence pathways. This improvement was instrumental in recording the first high-resolution correlation spectrum between ^{27}Al and ^{29}Si [253].

The capabilities of some of these schemes are shown in Fig. 20, featuring a series of 2D ^{27}Al-^{31}P HETCOR spectra of $AlPO_4$-14, including ^{27}Al→^{31}P R-INEPT (MAS-based, acquired at 9.4 T and 18.8 T), {^{31}P}^{27}Al HMQC (following the approach of Massiot et al. [254], also acquired at 9.4 T and 18.8 T), as well as

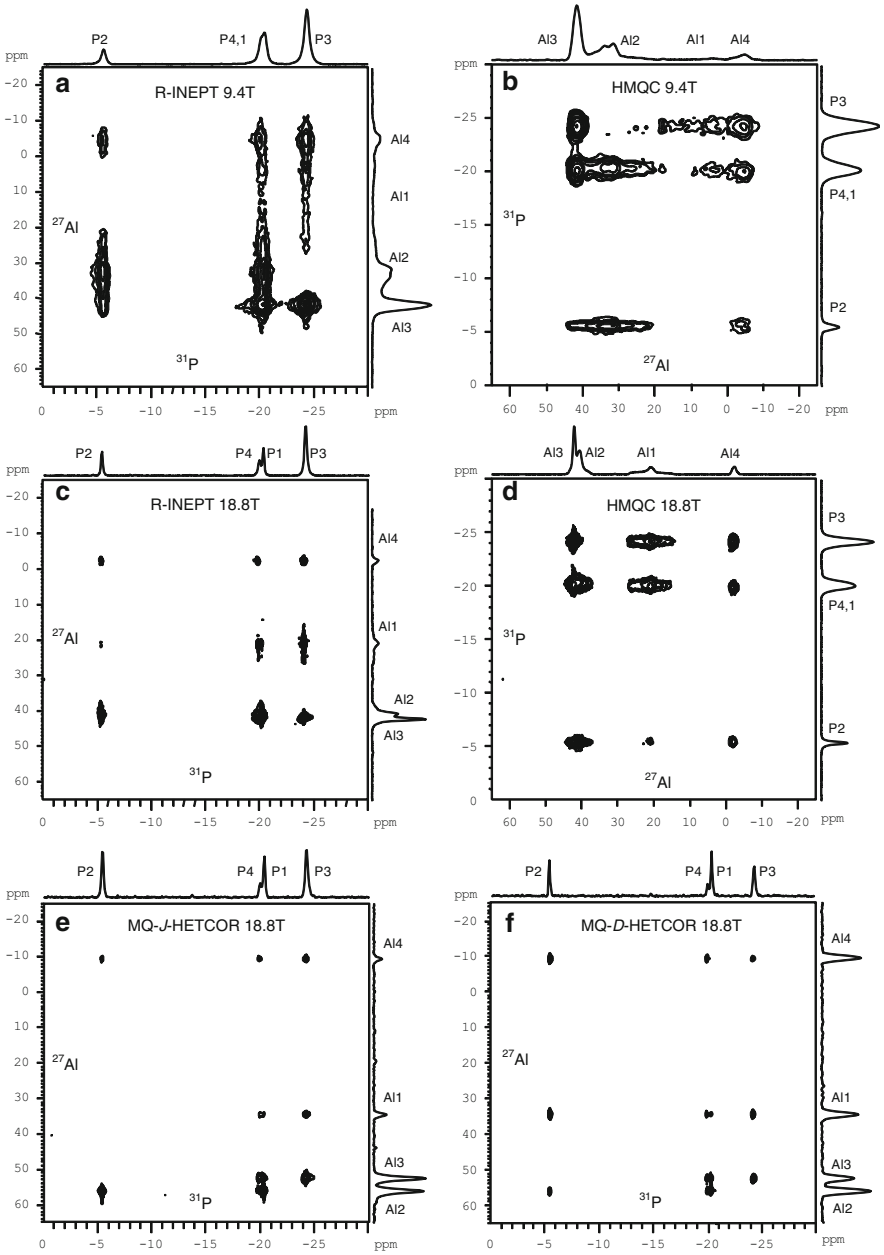

Fig. 20 2D HETCOR spectra of $AlPO_4$-14: (**a**) $^{27}Al \rightarrow {}^{31}P$ R-INEPT at 9.4 T, (**b**) $^{27}Al\{^{31}P\}$ HMQC at 9.4 T, (**c**) $^{27}Al \rightarrow {}^{31}P$ R-INEPT at 18.8 T, (**d**) $^{27}Al\{^{31}P\}$ HMQC at 18.8 T, (**e**) $^{27}Al \rightarrow {}^{31}P$ SPAM-MQ-*J*-HETCOR with R-INEPT at 18.8 T, and (**f**) $^{27}Al \rightarrow {}^{31}P$ SPAM-MQ-*D*-HETCOR obtained using cross-polarization at 18.8 T. The total experimental times were 5 h (**a**), 5 h (**b**), 2 h (**c**), 2 h (**d**), 10 h (**e**) and 7 h (**f**). (Reproduced with permission from [235])

$^{27}Al \rightarrow {}^{31}P$ MQMAS-*J*-HETCOR and $^{27}Al \rightarrow {}^{31}P$ MQMAS-*D*-HETCOR spectra taken at 18.8 T [235]. The experimental procedures and interpretation of these spectra are detailed elsewhere [252, 253]; herein we focus on methodological aspects. First, owing to the long T_1 relaxation of ^{31}P nuclei, all experiments must rely on T_1 of ^{27}Al, i.e., correspond to $I = {}^{27}Al$ and $S = {}^{31}P$ in R-INEPT, and to $I = {}^{31}P$ and $S = {}^{27}Al$ in HMQC. The resolution in the ^{31}P dimension of the HMQC spectra (Fig. 20b, d) is adversely affected by the dephasing due to $J_{Al\text{-}P}$ scalar interactions associated with the satellite transitions. The resolution in the ^{27}Al dimension of MAS-based spectra taken at 18.8 T is considerably better than at 9.4 T [compare spectra (a) and (b) with (c) and (d) in Fig. 20], and rivals that of the MQMAS-based HETCOR spectra taken at 9.4 T (not shown). These observations underscore the remarkable benefits of investing in high-field spectrometers for such studies.

A number of other methods for studying the heteronuclear correlations have been developed, which cannot be comprehensively described in a short review. For example, a *D*-HMQC HETCOR experiment based on split-t_1 STMAS scheme has been proposed and used to measure high-resolution $^{23}Na\{^{31}P\}$ spectrum of Na_2HPO_4 [14, 173]. The 2D *J*-HMQC experiment was performed utilizing *J* couplings to provide the connectivities between two half-integer quadrupolar nuclei (^{27}Al and ^{17}O) in ^{17}O-enriched crystalline grossite ($CaAl_2O_4$) [255]. Another method, referred to as MQ-REDOR [256, 257], has been developed that allows for precise determination of heteronuclear dipolar couplings (and thus internuclear distances) without the limitations in sensitivity imposed by CP and with the full use of the resolving power of MQMAS [253, 256].

7.4 Indirect Detection of Nitrogen-14

Nitrogen-14, with its natural abundance of 99.6%, is one of the most ubiquitous and, until recently, least studied NMR-active nuclei. Due to the integer spin number ($I = 1$), its single-quantum transitions are affected by first-order quadrupolar broadening, which in most materials is on the order of a few megahertz. A new class of 2D HETCOR protocols has been recently developed, which makes it possible to indirectly observe well-resolved ^{14}N sites via their spin-1/2 neighbors and obtain the related parameters of the quadrupolar tensors.

The first such experiment (Fig. 21a), introduced independently by Gan [258] and Bodenhausen et al. [259], used ^{13}C as the so-called "spy" nuclei in a 2D experiment similar to the HMQC scheme used in solution NMR [260]. The transfer of magnetization occurred by a combination of weak $^1J^{CN}$ (through-bond) couplings and second-order quadrupolar-dipolar (through-space) cross-terms between ^{14}N and ^{13}C, which contain the isotropic and anisotropic terms $l = 0$, 2, and 4 and are referred to as residual dipolar splittings (RDS) [261–263]. Under MAS, the $l = 0$ term results in isotropic coupling, which for NH_3 groups is expected to be

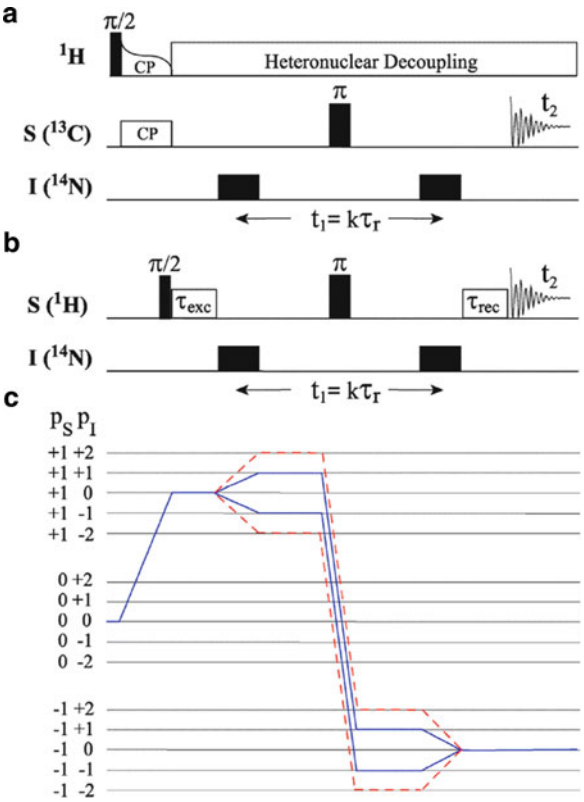

Fig. 21 HMQC pulse sequences for (**a**) ^{14}N-^{13}C and (**b**) ^{14}N-^{1}H correlations under rotor-synchronized MAS. In (**b**), dipolar recoupling is usually applied during time intervals τ_{exc} and τ_{rec}. (**c**) Coherence transfer pathways for the observation of SQ (*solid lines*) and DQ (*dashed lines*) in the ^{14}N dimension

$D_{\mathrm{RDS}}(CN) \cong 30$ Hz (at 14.1 T), i.e., exceeds the typical value of $^1J^{CN}$(a few hertz). Indeed, the MAS spectra of spin-1/2 nuclei (^{13}C or ^{1}H) coupled to ^{14}N often exhibit characteristic measurable 2:1 doublets corresponding to the $m_I = \pm 1$ and $m_I = 0$ states of ^{14}N nuclei. Both components are anisotropically broadened due to scaled terms with $l = 4$, and their centers of mass are separated by D_{RDS}. Following the initial excitation of the ^{13}C SQ coherence by ^{1}H-^{13}C cross-polarization, the anti-phase $S_x I_z^2$ coherence is created during the excitation time $\tau_{exc} \cong (2D_{\mathrm{RDS}})^{-1}$, which can be subsequently converted into heteronuclear DQ coherence by the rf-pulse at the ^{14}N frequency. During the evolution time, the first-order quadrupolar broadening is averaged to zero, provided that t_1 is advanced in a rotor-synchronized fashion and the sample is rotated precisely at the magic angle. The ^{14}N coherences evolve under the isotropic chemical shift and a second-order quadrupolar shift (32) on the order of several hundred ppm. Consequently, the ^{14}N resonances are widely spread in the indirect dimension, exhibiting relatively small anisotropic broadening due to

scaled-down second- and third-order quadrupolar interaction. We note that, by using appropriate phase-cycling, the HMQC experiment can provide SQ and/or DQ spectra of ^{14}N nuclei (Fig. 21c) [259, 264]. The DQ transition is not influenced by the first- and third-order quadrupolar interactions, which eliminates the constraints of very precise setting of the magic angle (to within 0.005° in the SQ case) and stable spinning. However, the DQ version of the experiment is less efficient and results in a narrower spectral window in Ω_1. The π pulse applied in the middle of the evolution period refocuses the chemical shift and other inhomogeneous contributions to the decay of ^{13}C magnetization, which is detected following the reconversion to S_x coherence by the second ^{14}N pulse.

The resulting 2D HMQC spectra, such as that shown in Fig. 22a for a natural abundance sample of tripeptide AGG, feature highly resolved cross-peaks representing the neighboring ^{14}N-^{13}C pairs [258]. The above-mentioned splittings due to $D_{\mathrm{RDS}}(CN)$ are usually obscured in such spectra by inhomogeneous broadening due to structural disorder, dipolar interactions, misadjustment of the magic angle, etc.

The value of δ_{QIS} can be determined from the ^{14}N-^{13}C HMQC experiment by comparing the observed shifts with the separately measured ^{15}N shifts, and further used to estimate the value of the parameter χ_Q representing the magnitude of the

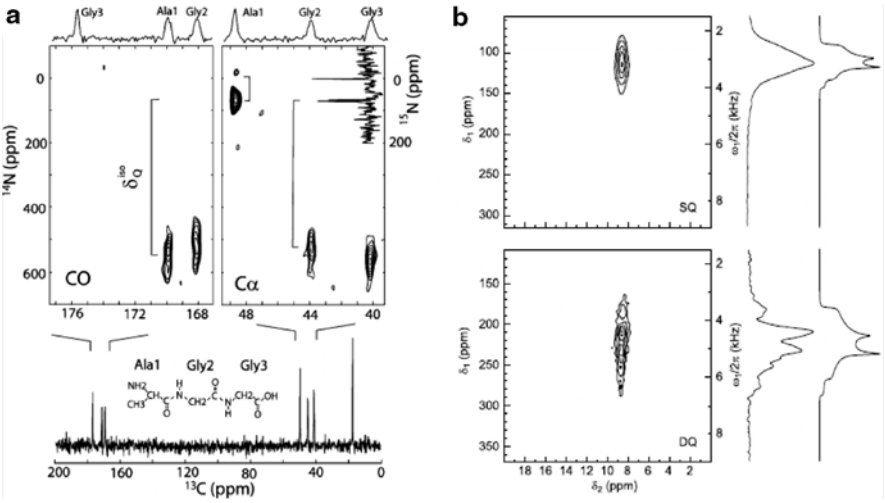

Fig. 22 (**a**) ^{14}N-^{13}C SQ-HMQC spectrum of Ala·Gly·Gly tripeptide with natural abundance of ^{13}C, taken at 14.1 T under 25 kHz MAS. The corresponding ^{15}N MAS spectrum is shown in the top right corner. (Reproduced with permission from reference [258].) (**b**) ^{14}N-^{1}H SQ-HMQC and DQ-HMQC spectra of partly deuterated glycine-d2 $NH_3^+CD_2COO$, taken at 9.4 T under 30 kHz MAS. The ^{14}N projections were simulated using second-order quadrupolar powder patterns with $C_Q = 1.18$ MHz and $\eta_Q = 0.5$, assuming uniform excitation of all crystallite orientations. (Reproduced with permission from [264])

quadrupolar coupling tensor [$\chi_Q = \omega_Q \sqrt{1 + \frac{\eta^2}{3}}$; see (20)]. Additional information about the quadrupolar interaction can be obtained by fitting the projections of ^{14}N line shapes (Fig. 22b). The overall efficiencies of SQ and DQ versions of ^{14}N-^{13}C HMQC tend to be relatively low (e.g., 16% and 8%, respectively, were reported for L-alanine [259]), primarily due to the excitation bandwidth associated with typical ω_{rf}^{N} values (~100 kHz in fast MAS probes) being much smaller than typical offsets encountered in ^{14}N NMR. Additional losses are associated with ^{13}C T_2' relaxation during the long mixing time required for the buildup of two-spin coherences.

The sensitivity of ^{14}N detection can be greatly improved by using ^{1}H instead of ^{13}C as the spy nuclei [7, 8]. First, protons possess a high gyromagnetic ratio and are 100 % abundant. Second, the values of $^{1}J^{NH}$ and $D_{\mathrm{RDS}}(NH)$ are considerably larger than those of $^{1}J^{NC}$ and $D_{\mathrm{RDS}}(CN)$ given above. Indeed, the SQ and DQ versions of ^{14}N-^{1}H spectra were obtained within minutes (Fig. 22b) by using the basic HMQC sequence with properly optimized time intervals $\tau_{\mathrm{exc}} = \tau_{\mathrm{rec}}$ (Fig. 21b) [264]. However, the use of ^{1}H detection has its shortcomings. Because of the strong ^{1}H-^{1}H homonuclear dipolar interactions and small chemical shift range, the spectra are poorly resolved in the Ω_2 dimension. Furthermore, the T_2' relaxation of ^{1}H nuclei is fast compared to $(^{1}J^{NH})^{-1}$ or $(D_{\mathrm{RDS}}(NH))^{-1}$, which attenuates the coherence transfers. SQ and DQ experiments performed on partly deuterated glycine had respective efficiencies of 2% and 0.4% compared to a ^{1}H spin-echo experiment without the ^{14}N rf-pulses. However, the transfer efficiency can be significantly improved by manipulating the homo- and heteronuclear dipolar couplings during τ_{exc} and τ_{rec} with appropriately chosen rf irradiation (Fig. 21b). For example, by irradiating the ^{1}H nuclei at $\omega_{\mathrm{rf}}^{H} = 2\omega_R$ (the so-called rotary resonance) the ^{14}N-^{1}H dipolar interactions can be efficiently reintroduced, which enables their use for the coherence transfer instead of much weaker $^{1}J^{NH}$ and D_{RDS} couplings [265]. Concomitantly, such irradiation assists MAS in ^{1}H-^{1}H homonuclear decoupling, thereby reducing the losses due to T_2' relaxation. Indeed, the efficiency of the SQ version of the ^{14}N-^{1}H HMQC experiment in glycine increased to 5–7% using rf-assisted heteronuclear recoupling/homonuclear decoupling [265, 266], with incomplete irradiation of the ^{14}N nuclei being the main limiting factor.

Several additional modifications have been proposed to expand the capabilities of indirectly detected ^{14}N NMR spectroscopy. The ^{14}N resolution in SQ and DQ versions of ^{1}H-detected spectra was improved by suppressing the ^{1}H-^{1}H dipolar interactions during the evolution time t_1 via PMLG or rotor-synchronized symmetry-based sequences [267]. The single-quantum heteronuclear correlation scheme, known in solution NMR as HSQC, has been adapted to make the Ω_1 dimension immune to broadening due to the T_2' decay of the directly observed nuclei [268]. Most recently, it has been shown that very fast MAS (at rates up to 80 kHz) and high rf-field strengths available in state-of-the-art modern probes serve to enhance further the sensitivity and resolution in ^{14}N-^{1}H HMQC experiments. Despite limited sample volumes (0.8 μL), high-quality HMQC spectra of glycine and alanine were obtained at 11.7 T by collecting two scans per rotor-synchronized t_1 point [266].

7.5 *Homonuclear Dipolar Recoupling Involving Quadrupolar Nuclei*

Homonuclear correlation NMR spectroscopy of quadrupolar nuclei is less explored than the HETCOR methodology due to a number of contributing factors, as pointed out in the excellent recent review by Eden [15]. First, the strong quadrupolar broadening controls resolution in both dimensions, which necessitates the use of selective manipulation of the CTs by weak rf-fields. Second, the nearest quadrupolar neighbors are rarely located in close spatial proximity (even if 100% abundant), and thus the recoupling of dipolar interactions is inevitably carried out in the simultaneous presence of several dominant interactions which, in addition to the quadrupolar coupling, include chemical shifts and resonance offsets. Another difficulty stems from the multi-basis nature of the Zeeman product states for a pair of quadrupolar spins. This complicates the experiments targeting the DQ coherences between the CTs of two different spins (DQ_{CT}) rather than the DQ coherences involving the Zeeman states of the same spin. Again, this can be circumvented by isolating the CTs of each spin from other transitions by using weak rf-fields, or by using the recoupling strategies that do not involve the rf irradiation.

Several basic 2D schemes have been applied in these experiments, based on (1) the use of the SQ evolutions during t_1 and t_2, in analogy to the NOESY experiment, (2) the MQ-SQ experiment, in which the evolutions of MQ coherences during t_1 are correlated with the CTs of recoupled spins to enhance the resolution in analogy to MQMAS, and (3) the DQ_{CT}-SQ protocol similar to that used in DQMAS NMR of spin-1/2 nuclei.

Most of the strategies used for mixing rely on the recoupling of homonuclear dipolar interactions between the neighboring spins. The averaging of dipolar interactions under MAS can be prevented by spinning the sample away from the magic angle during the mixing period, which requires a probe with the DAS capabilities [269–271]. The dipolar interactions can also be reactivated at the magic angle by using the MAS- or rf-assisted recoupling tools, similar to those developed for spin-1/2 nuclei. For example, the MAS-driven rotational resonance (R^2) recoupling can be achieved by matching ω_R with the sub-multiple of the difference between the resonance frequencies of the interacting spins [272, 273]. The frequency-selective nature of this approach is a major limitation, especially in the presence of distributed anisotropic lineshapes. The MAS-driven schemes can also exploit the so-called "spontaneous recoupling" through the interference between homonuclear couplings and heteronuclear couplings or quadrupolar interactions [274]. The rf recoupling was first achieved by the CT-selective transverse or longitudinal mixing under the HORROR-type conditions [275, 276], and later using the longitudinal mixing by multiple pulse sequences in SQ-SQ and MQ-SQ schemes [277].

The DQMAS-type experiments have the distinct advantage over the SQ-SQ spectra in that they are not dominated by the diagonal signals representing the non-exchanged magnetization. The first demonstrations of such spectra reported by

Painter and Duer featured the DQ_{CT}-SQ ^{23}Na-^{23}Na correlations in sodium sulfate and sodium zirconate [278]. A CT-selective scheme with improved suppression of the single-spin DQ coherences was later proposed by Mali et al., who used HORROR$y\bar{y}$ sequence to generate ^{27}Al-^{27}Al correlations in crystalline $AlPO_4$-14 [279]. The recoupling efficiency was further improved by Eden et al. using the symmetry-based pulse sequences, which proved useful in studying the disordered materials [280, 281].

Several methods which recover homonuclear interactions under high-resolution conditions have been proposed as well. Pines and coworkers presented a 3D MQMAS scheme in which the MQ and SQ evolution periods are interleaved with the R^2 recoupling period of variable length to enable the observation of dipolar coupling and CSA interactions [276]. Another MQMAS-based method, proposed by Mali and Kaucic [282], uses the (DQ_{CT}-6Q)-SQ protocol to yield homonuclear ^{23}Na-^{23}Na correlations with highly resolved indirect dimension. A DOR-based DQMAS-type experiment by Brinkmann et al. [283], uses symmetry-based recoupling sequence and provides an isotropic resolution in both DQ and SQ dimensions.

Finally, Deschamps et al. reported for the first time a homonuclear connectivity map between the quadrupolar nuclei based on *J* couplings [284]. The experiment uses a relayed heteronuclear transfer via spin-1/2 nuclei to a second quadrupolar spin via four chemical bonds (in this case $^2J^{AlP}$-mediated ^{27}Al-O-^{31}P-O-^{27}Al transfer), in a scheme equivalent to the heteronuclear SQ correlation (HSQC) experiment.

8 Conclusions

Advances in methodology and hardware made over the last two decades have fundamentally improved the ability of solid-state NMR to probe the local environment of quadrupolar nuclei. New methods were developed for increasing the population of excitable transitions and significant progress has been made in the detection and analysis of wideline spectra. However, the development of high-resolution methods, DOR, DAS, MQMAS, and STMAS, had the largest impact on the structural studies of both crystalline and amorphous materials. Owing to its simplicity and robustness, the *z*-filtered version of MQMAS experiment has become available for routine use in most laboratories. Other high-resolution protocols will undoubtedly become more accessible on commercial spectrometers, as they often provide complementary information and, in some cases, improved sensitivity or resolution.

Intense research following the discovery of high-resolution methods brought about further advances in high-resolution methodology and led to new opportunities for studying increasingly complex structural properties. In well-ordered materials, the state-of-the-art internuclear correlation experiments can now provide high-quality spectra that resemble those encountered in liquid-state NMR. However,

in spite of recent progress such results cannot be achieved in "less friendly" spin systems. The low gyromagnetic ratio or concentration of studied nuclei, inefficient excitation or polarization transfer, structural disorder, and large quadrupolar coupling pose challenges in terms of sensitivity, resolution, and quantitative accuracy that are yet to be overcome. The quest to meet these challenges will undoubtedly involve further development of NMR instrumentation and improved pulse sequences. The availability of high magnetic fields is essential for the studies of quadrupolar nuclei, as it offers resolution improvement and time saving factors far greater than in the case of spin-1/2 nuclei. More advanced probe technologies are needed as well. For example, better control of the rotor orientation and improved stability of the MAS rate can help to meet the demands of methods contending with first-order quadrupolar broadening, such as STMAS or indirectly detected ^{14}N NMR. The benefits of using ultrafast MAS in these studies are also becoming apparent.

Finally, the computational methods, which are outside of the scope of this review, have become an essential component of solid-state NMR research. The increasingly efficient programs for numerical simulation of spin dynamics, such as SIMPSON [285, 286] or SPINEVOLUTION [287], can provide better understanding of the experimental results and will drive progress in designing the new pulse sequences for the quadrupolar nuclei. The development and use of ab initio calculations offers assistance in spectral assignment and plays an increasingly important role in studying the relationships between the NMR parameters and the physicochemical properties of complex materials, including those which are disordered and/or exhibit molecular dynamics.

Acknowledgment This research was supported, in part, at the Ames Laboratory by the U.S. Department of Energy, Office of Basic Energy Sciences, under Contract No. DE-AC02-07CH11358.

References

1. Mehring M (1983) Principles of high resolution NMR in solids. Springer, Berlin
2. Slichter CP (1990) Principles of magnetic resonance. Springer series in solid-state sciences. Springer, Berlin
3. Freude D, Haase J (1993) In: Diehl P, Fluck E, Gunter H, Kosfeld R, Seelig J (eds) NMR basic principles and progress, vol 29. Springer, Berlin, p 1
4. Smith ME, van Eck ERH (1999) Prog Nucl Magn Reson Spectrosc 34:159
5. Vega AJ (2002) In: Grant DM, Harris R (eds) Encyclopedia of nuclear magnetic resonance, vol 6. Wiley, Chichester, UK, p 3869
6. Jerschow A (2005) Prog Nucl Magn Reson Spectrosc 46:63
7. Ashbrook SE (2009) Phys Chem Chem Phys 11:6892
8. Amoureux JP, Pruski M (2002) Encyclopedia of nuclear magnetic resonance, vol 9. Wiley, Chichester, UK, p 226
9. Frydman L (2002) In: Grant DM, Harris RK (eds) Encyclopedia of nuclear magnetic resonance, vol 9. Wiley, Chichester, UK, p 262

10. Grandinetti P (2002) In: Grant DM, Harris R (eds) Encyclopedia of nuclear magnetic resonance, vol 3. Wiley, Chichester, UK, p 1768
11. Ashbrook SE, Wimperis S (2004) Prog Nucl Magn Reson Spectrosc 45:53
12. Goldbourt A, Madhu PK (2004) Annu Rep NMR Spectrosc 54:81
13. Wimperis S (2006) In: Webb GA (ed) Modern magnetic resonance. Springer, Dordrecht, p 1487
14. Amoureux JP, Trebosc J, Delevoye L, Lafon O, Hu B, Wang Q (2009) Solid State Nucl Magn Reson 35:12
15. Eden M (2009) Solid State Nucl Magn Reson 36:1
16. Cavadini S (2010) Prog Nucl Magn Reson Spectrosc 56:46
17. Rocha J, Morais CM, Fernandez C (2003) Clay Miner 38:259
18. Rocha J, Morais CM, Fernandez C (2004) Top Curr Chem 246:141
19. Ashbrook SE, Duer MJ (2006) Conc Magn Reson A 28:183
20. Ashbrook SE, Wimperis S (2009) J Chem Phys 131:194509
21. Abragam A (1994) The principles of nuclear magnetism. Clarendon Press, Oxford, UK
22. Pyykkö P (2001) Mol Phys 99:1617
23. Pyykkö P (2008) Mol Phys 106:1965
24. Mehring M, Waugh J (1972) Phys Rev B 5:3459
25. Llor A (1992) Chem Phys Lett 199:383
26. Goldman M, Grandinetti PJ, Llor A, Olejniczak Z, Sachleben JR, Zwanziger JW (1992) J Chem Phys 97:8947
27. Wi S, Frydman L (2002) J Chem Phys 116:1551
28. Wi S, Ashbrook SE, Wimperis S, Frydman L (2003) J Chem Phys 118:3131
29. Alarcón SH, Olivieri AC, Harris RK (1993) Solid State Nucl Magn Reson 2:325
30. Wi S, Frydman V, Frydman L (2001) J Chem Phys 114:8511
31. Ashbrook SE, McManus J, Thrippleton MJ, Wimperis S (2009) Prog Nucl Magn Reson Spectrosc 55:160
32. Bain AD (1984) J Magn Reson 56:418
33. Bodenhausen G, Kogler H, Ernst RR (1984) J Magn Reson 58:370
34. Ernst RR, Bodenhausen G, Wokaun A (1990) Principles of nuclear magnetic resonance in one and two dimensions. Clarendon Press, Oxford
35. Antonijevic S, Bodenhausen G (2006) J Magn Reson 180:297
36. Levitt MH, Maduh PK, Hughes CE (2002) J Magn Reson 155:300
37. Jerschow A, Kumar R (2003) J Magn Reson 160:59
38. Hughes CE, Carravetta M, Levitt MH (2004) J Magn Reson 167:259
39. Millot Y, Hajjar R, Man PP (2009) Solid State Nucl Magn Reson 35:223
40. Ivchenko N, Hughes CE, Levitt MH (2003) J Magn Reson 160:52
41. Malicki N, Mafra L, Quoineaud A-A, Rocha J, Thibault-Starzyk F, Fernandez C (2005) Solid State Nucl Magn Reson 28:13
42. Hajjar R, Millot Y, Man PP (2008) C R Chim 11:380
43. Lefebvre F, Amoureux JP, Fernandez C, Derouane EG (1987) J Chem Phys 86:6070
44. Amoureux JP, Fernandez C, Lefebvre F (1990) Magn Reson Chem 28:5
45. Kundla E, Samoson A, Lippmaa E (1981) Chem Phys Lett 83:229
46. Samoson A, Kundla E, Lippmaa E (1982) J Magn Reson 49:350
47. Massiot D, Bessada C, Coutures JP, Taulelle F (1990) J Magn Reson 90:231
48. Larsen FH, Farnan I, Lipton AS (2006) J Magn Reson 178:228
49. Samoson A, Lippmaa E (1983) Chem Phys Lett 100:205
50. Samoson A, Lippmaa E (1983) Phys Rev B 28:6567
51. Kentgens APM, Lemmens JJM, Geurts FMM, Veeman WS (1987) J Magn Reson 71:62
52. Samoson A, Lippmaa E (1988) J Magn Reson 79:255
53. Amoureux JP, Fernandez C, Frydman L (1996) Chem Phys Lett 259:347
54. Nielsen NC, Bildsře H, Jakobsen HJ (1992) J Magn Reson 97:149
55. Hahn EL (1950) Phys Rev 80:580
56. Chan JCC (1999) Conc Magn Reson 11:363

57. Man PP (2000) In: Meyers RA (ed) Encyclopedia of analytical chemistry. Wiley, Chichester, p 12224
58. Vega S, Naor Y (1981) J Chem Phys 75:75
59. Kentgens APM (1991) J Magn Reson 95:619
60. Haase J, Conradi MS (1993) Chem Phys Lett 209:287
61. Siegel R, Nakashima TT, Wasylishen RE (2005) Conc Magn Reson A 26A:47
62. Kentgens APM, Verhagen R (1999) Chem Phys Lett 300:435
63. Iuga D, Schafer H, Verhagen R, Kentgens APM (2000) J Magn Reson 147:192
64. Schaefer H, Iuga D, Verhagen R, Kentgens APM (2001) J Chem Phys 114:3073
65. Yao Z, Kwak HT, Sakellariou D, Emsley L, Grandinetti PJ (2000) Chem Phys Lett 327:85
66. Madhu PK, Goldbourt A, Frydman L, Vega S (1999) Chem Phys Lett 307:41
67. Madhu PK, Goldbourt A, Frydman L, Vega S (2000) J Chem Phys 112:2377
68. Prasad S, Kwak HT, Clark T, Grandinetti PJ (2002) J Am Chem Soc 124:4964
69. Kwak HT, Prasad S, Clark T, Grandinetti PJ (2003) J Magn Reson 160:107
70. Prasad S, Clark TM, Sefzik TH, Kwak HT, Gan ZH, Grandinetti PJ (2006) J Non-Cryst Solids 352:2834
71. Smith LJ, Seith C (2006) J Magn Reson 179:164
72. Madhu PK, Pike KJ, Dupree R, Levitt MH, Smith ME (2003) Chem Phys Lett 367:150
73. Kwak HT, Prasad S, Clark T, Grandinetti PJ (2003) Solid State Nucl Magn Reson 24:71
74. Siegel R, Nakashima TT, Wasylishen RE (2004) Chem Phys Lett 388:441
75. Siegel R, Nakashima TT, Wasylishen RE (2006) Chem Phys Lett 421:529
76. Kupce E, Freeman R (1995) J Magn Reson 115:273
77. Bhattacharyya R, Frydman L (2007) J Chem Phys 127:194503
78. Dey KK, Prasad S, Ash JT, Deschamps M, Grandinetti PJ (2007) J Magn Reson 185:326
79. Hansen MR, Brorson M, Bildsøe H, Skibsted J, Jakobsen HJ (2008) J Magn Reson 190:316
80. Batchelder LS (2002) In: Grant DM, Harris RK (eds) Encyclopedia of nuclear magnetic resonance, vol 3. Wiley, Chichester, UK, p 1574
81. Duer MJ (2002) In: Duer MJ (ed) Solid-state NMR spectroscopy: principles and applications. Wiley-Blackwell, Oxford, p 239
82. Giavani T, Bildsoe H, Skibsted J, Jakobsen HJ (2004) J Magn Reson 166:262
83. Antonijevic S, Wimperis S (2003) J Magn Reson 164:343
84. Antonijevic S, Wimperis S (2005) J Chem Phys 122:044312
85. Kristensen JH, Bildsoe H, Jakobsen HJ, Nielsen NC (1999) J Magn Reson 139:314
86. Kristensen JH, Hoatson GL, Vold RL (1999) J Chem Phys 110:4533
87. Cutajar M, Ashbrook SE, Wimperis S (2006) Chem Phys Lett 423:276
88. Thrippleton MJ, Cutajar M, Wimperis S (2008) Chem Phys Lett 452:233
89. Jakobsen HJ, Bildsoe H, Skibsted J, Giavani T (2001) J Am Chem Soc 123:5098
90. Giavani T, Johannsen K, Jacobsen CJH, Blom N, Bildsoe H, Skibsted J, Jakobsen HJ (2003) Solid State Nucl Magn Reson 24:218
91. Jakobsen HJ, Hove AR, Bildsoe H, Skibsted J, Brorson M (2007) J Magn Reson 185:159
92. Giavani T, Bildsoe H, Skibsted J, Jakobsen HJ (2002) J Phys Chem B 106:3026
93. Zhou B, Giavani T, Bildsoe H, Skibsted J, Jakobsen HJ (2005) Chem Phys Lett 402:133
94. Gan ZH, Gor'kov P, Cross TA, Samoson A, Massiot D (2002) J Am Chem Soc 124:5634
95. Sutrisno A, Terskikh VV, Huang Y (2009) Chem Commun 186
96. Lee PK, Chapman RP, Zhang L, Hu J, Barbour LJ, Elliott EK, Gokel GW, Bryce DL (2007) J Phys Chem A 111:12859
97. Zhu J, Trefiak N, Woo TK, Huang Y (2009) J Phys Chem C 113:10029
98. Ooms KJ, Terskikh VV, Wasylishen RE (2007) J Am Chem Soc 129:6704
99. Mroué KH, Power WP (2010) J Phys Chem A 114:324
100. Sutrisno A, Hanson MA, Rupar PA, Terskikh VV, Baines KM, Huang YN (2010) Chem Commun 46:2817

101. Hu JZ, Kwak JH, Wang Y, Peden CHF, Zheng H, Ma D, Bao X (2009) J Phys Chem C 113:2936
102. Chen F, Ma GB, Bernard GM, Cavell RG, McDonald R, Ferguson MJ, Wasylishen RE (2010) J Am Chem Soc 132:5479
103. Sutrisno A, Lu C, Lipson RH, Huang Y (2009) J Phys Chem C 113:21196
104. Hamaed H, Ye E, Udachin K, Schurko RW (2010) J Phys Chem B 114:6014
105. Hamaed H, Laschuk MW, Terskikh VV, Schurko RW (2009) J Am Chem Soc 131:8271
106. Solomon I (1958) Phys Rev 110:61
107. Dumazy Y, Amoureux JP, Fernandez C (1997) Mol Phys 90:959
108. Bodart PR, Amoureux JP, Dumazy Y, Lefort R (2000) Mol Phys 98:1545
109. Carr HY, Purcell EM (1954) Phys Rev 94:630
110. Meiboom S, Gill D (1958) Rev Sci Instrum 29:688
111. Maricq MM, Waugh JS (1979) J Chem Phys 70:3300
112. Lefort R, Wiench JW, Pruski M, Amoureux JP (2002) J Chem Phys 116:2493
113. Hung I, Gan ZH (2010) J Magn Reson 204:256
114. Larsen FH, Jakobsen HJ, Ellis PD, Nielsen NC (1998) Mol Phys 95:1185
115. Larsen FH, Nielsen NC (1999) J Phys Chem A 103:10825
116. Lipton AS, Sears JA, Ellis PD (2001) J Magn Reson 151:48
117. Larsen FH, Farnan I (2002) Chem Phys Lett 357:403
118. Hung I, Schurko RW (2003) Solid State Nucl Magn Reson 24:78
119. Schurko RW, Hung I, Widdifield CM (2003) Chem Phys Lett 379:1
120. Hung I, Schurko RW (2004) J Phys Chem B 108:9060
121. Hung I, Rossini AJ, Schurko RW (2004) J Phys Chem A 108:7112
122. Widdifield CM, Schurko RW (2005) J Phys Chem A 109:6865
123. Tang JA, Masuda JD, Boyle TJ, Schurko RW (2006) ChemPhysChem 7:117
124. Tang JA, Ellis BD, Warren TH, Hanna JV, Macdonald CLB, Schurko RW (2007) J Am Chem Soc 129:13049
125. O'Dell LA, Schurko RW (2008) Chem Phys Lett 464:97
126. Forgeron MAM, Wasylishen RE (2008) Magn Reson Chem 46:206
127. O'Dell LA, Klimm K, Freitas JCC, Kohn SC, Smith ME (2009) Appl Magn Reson 35:247
128. Ganapathy S, Schramm S, Oldfield E (1982) J Chem Phys 77:4360
129. Oldfield E, Kinsey RA, Montez B, Ray T, Smith KA (1982) J Chem Soc Chem Commun 254
130. Oldfield E, Ganapathy S, Schramm S, Kinsey RA, Smith KA, Meadows MD (1983) ACS Symp Ser 211:545
131. Jaeger C (1994) In: Blumich B, Kosfeld R (eds) NMR basic principles and progress, vol 31. Springer, Berlin, p 134
132. Samoson A (1985) Chem Phys Lett 119:29
133. Massiot D, Hiet J, Pellerin N, Fayon F, Deschamps M, Steuernagel S, Grandinetti PJ (2006) J Magn Reson 181:310
134. Llor A, Virlet J (1988) Chem Phys Lett 152:248
135. Samoson A, Lippmaa E, Pines A (1988) Mol Phys 65:1013
136. Chmelka BF, Mueller KT, Pines A, Stebbins J, Wu Y, Zwanziger JW (1989) Nature 339:42
137. Samoson A, Lippmaa E (1989) J Magn Reson 84:410
138. Mueller KT, Sun BQ, Chingas GC, Zwanziger JW, Terao T, Pines A (1990) J Magn Reson 86:470
139. Mueller KT, Wooten EW, Pines A (1991) J Magn Reson 92:620
140. Medek A, Harwood JS, Frydman L (1995) J Am Chem Soc 117:12779
141. Gan ZH (2000) J Am Chem Soc 122:3242
142. Thrippleton MJ, Ball TJ, Steuernagel S, Ashbrook SE, Wimperis S (2006) Chem Phys Lett 431:390
143. Bhattacharyya R, Frydman L (2006) J Am Chem Soc 128:16014
144. Vosegaard T, Massiot D (2007) Chem Phys Lett 437:120

145. Wu Y (2002) In: Grant DM, Harris R (eds) Encyclopedia of nuclear magnetic resonance, vol 3. Wiley, Chichester, UK, p 1749
146. Prochnow D, Grimmer AR, Freude D (2006) Solid State Nucl Magn Reson 30:69
147. Howes AP, Anupõld T, Lemaitre V, Kukol A, Watts A, Samoson A, Smith ME, Dupree R (2006) Chem Phys Lett 421:42
148. Kentgens APM, van Eck ERH, Ajithkumar TG, Anupold T, Past J, Reinhold A, Samoson A (2006) J Magn Reson 178:212
149. Pike KJ, Lemaitre V, Kukol A, Anupõld T, Samoson A, Howes AP, Watts A, Smith ME, Dupree R (2004) J Phys Chem B 108:9256
150. Hung I, Wong A, Howes AP, Anupold T, Samoson A, Smith ME, Holland D, Brown SP, Dupree R (2009) J Magn Reson 197:229
151. Hung I, Howes AP, Parkinson BG, Anupõld T, Samoson A, Brown SP, Harrison PF, Holland D, Dupree R (2009) J Solid State Chem 182:2402
152. Wong A, Howes AP, Parkinson B, Anupõld T, Samoson A, Holland D, Dupree R (2009) Phys Chem Chem Phys 11:7061
153. Mueller KT, Chingas GC, Pines A (1991) Rev Sci Instrum 62:1445
154. Baltisberger JH, Gann SL, Grandinetti PJ, Pines A (1994) Mol Phys 81:1109
155. Wang SH, Xu Z, Baltisberger JH, Bull LM, Stebbins JF, Pines A (1997) Solid State Nucl Magn Reson 8:1
156. Clark TM, Grandinetti PJ, Florian P, Stebbins JF (2004) Phys Rev B 70:064202
157. Amoureux JP, Morais C, Trebosc J, Rocha J, Fernandez C (2003) Solid State Nucl Magn Reson 23:213
158. Huguenard C, Taulelle F, Knott B, Gan Z (2002) J Magn Reson 156:131
159. Ashbrook SE, Wimperis S (2003) J Magn Reson 162:402
160. Mamone S, Dorsch A, Johannessen OG, Naik MV, Madhu PK, Levitt MH (2008) J Magn Reson 190:135
161. Kwak HT, Gan ZH (2003) J Magn Reson 164:369
162. Bain AD (2006) J Magn Reson 179:308
163. Brown SP, Heyes SJ, Wimperis S (1996) J Magn Reson 119:280
164. Brown SP, Wimperis S (1997) J Magn Reson 128:42
165. Fernandez C, Amoureux JP (1996) Solid State Nucl Magn Reson 5:315
166. Grandinetti PJ, Baltisberger JH, Llor A, Lee YK, Werner U, Eastman MA, Pines A (1993) J Magn Reson 103:72
167. Massiot D, Touzo B, Trumeau D, Coutures JP, Virlet J, Florian P, Grandinetti PJ (1996) Solid State Nucl Magn Reson 6:73
168. Amoureux J-P, Fernandez C, Steuernagel S (1996) J Magn Reson 123:116
169. States DJ, Haberkorn RA, Ruben DJ (1982) J Magn Reson 48:286
170. Gehman JD, Provis JL (2009) J Magn Reson 200:167
171. Hung I, Trebosc J, Hoatson GL, Vold RL, Amoureux JP, Gan ZH (2009) J Magn Reson 201:81
172. Goldbourt A, Madhu PK (2002) Monatsh Chem 133:1497
173. Trebosc J, Amoureux JP, Gan Z (2007) Solid State Nucl Magn Reson 31:1
174. Takahashi T, Kanehashi K, Shimoikeda Y, Nemoto T, Saito K (2009) J Magn Reson 198:228
175. Hajjar R, Millot Y, Man PP (2010) Prog Nucl Magn Reson Spectrosc 57:306
176. Amoureux JP, Fernandez C (1998) Solid State Nucl Magn Reson 10:211
177. Man PP (1998) Phys Rev B 58:2764
178. Amoureux JP, Fernandez C (2000) Solid State Nucl Magn Reson 16:339
179. Amoureux JP, Huguenard C, Engelke F, Taulelle F (2002) Chem Phys Lett 356:497
180. Marinelli L, Frydman L (1997) Chem Phys Lett 275:188
181. Amoureux JP, Pruski M, Lang DP, Fernandez C (1998) J Magn Reson 131:170
182. Wu G, Rovnyak D, Griffin RG (1996) J Am Chem Soc 118:9326
183. Kwak HT, Prasad S, Yao Z, Grandinetti PJ, Sachleben JR, Emsley L (2001) J Magn Reson 150:71

184. Rovnyak D, Kennedy PE (2009) J Magn Reson 196:191
185. Vosegaard T, Florian P, Massiot D, Grandinetti PJ (2001) J Chem Phys 114:4618
186. Vosegaard T, Kehlet C, Khaneja N, Glaser SJ, Nielsen NC (2005) J Am Chem Soc 127:13768
187. Massiot D (1996) J Magn Reson 122:240
188. Rovnyak D, Filip C, Itin B, Stern AS, Wagner G, Griffin RG, Hoch JC (2003) J Magn Reson 161:43
189. Duer MJ (1997) Chem Phys Lett 277:167
190. Hanaya M, Harris RK (1997) Solid State Nucl Magn Reson 8:147
191. Lacassagne V, Florian P, Montouillout V, Gervais C, Babonneau F, Massiot D (1998) Magn Reson Chem 36:956
192. Ganapathy S, Delevoye L, Amoureux JP, Madhu PK (2008) Magn Reson Chem 46:948
193. Thakur RS, Kurur ND, Madhu PK (2008) Magn Reson Chem 46:166
194. Siegel R, Nakashima TT, Wasylishen RE (2005) Chem Phys Lett 403:353
195. Morais CM, Lopes M, Fernandez C, Rocha J (2003) Magn Reson Chem 41:679
196. Gan ZH, Kwak HT (2004) J Magn Reson 168:346
197. Amoureux JP, Delevoye L, Steuernagel S, Gan Z, Ganapathy S, Montagne L (2005) J Magn Reson 172:268
198. Kanellopoulos J, Freude D, Kentgens A (2007) Solid State Nucl Magn Reson 32:99
199. Pruski M, Wiench JW, Amoureux JP (2000) J Magn Reson 147:286
200. Ball TJ, Wimperis S (2007) J Magn Reson 187:343
201. Vosegaard T, Larsen FH, Jakobsen HJ, Ellis PD, Nielsen NC (1997) J Am Chem Soc 119:9055
202. Thrippleton MJ, Ball TJ, Wimperis S (2008) J Chem Phys 128:034507
203. Frydman L, Scherf T, Lupulescu A (2002) Proc Natl Acad Sci USA 99:15858
204. Samoson A (1996) J Magn Reson 121:209
205. Samoson A, Anupõld T (2000) Solid State Nucl Magn Reson 15:217
206. Skibsted J, Nielsen NC, Bildsøe H, Jakobsen HJ (1992) Chem Phys Lett 188:405
207. Fernandez C, Bodart P, Amoureux JP (1994) Solid State Nucl Magn Reson 3:79
208. Fernandez C, Amoureux JP, Bodart P (1995) J Magn Reson 113:205
209. Koons JM, Hughes E, Cho HM, Ellis PD (1995) J Magn Reson 114:12
210. Vosegaard T, Skibsted J, Jakobsen HJ (1999) J Phys Chem A 103:9144
211. Nielsen UG, Jakobsen HJ, Skibsted J (2001) Solid State Nucl Magn Reson 20:23
212. Ash JT, Trease NM, Grandinetti PJ (2008) J Am Chem Soc 130:10858
213. Lupulescu A, Kotecha M, Frydman L (2003) J Am Chem Soc 125:3376
214. Johnson CS (1999) Prog Nucl Magn Reson Spectrosc 34:203
215. Pines A, Gibby MG, Waugh JS (1972) J Chem Phys 56:1776
216. Stejskal EO, Schaefer J, Waugh JS (1977) J Magn Reson 28:105
217. Metz G, Wu XL, Smith SO (1994) J Magn Reson 110:219
218. Hing AW, Vega S, Schaefer J (1992) J Magn Reson 96:205
219. Hediger S, Meier BH, Kurur ND, Bodenhausen G, Ernst RR (1994) Chem Phys Lett 223:283
220. Michel D, Engelke F (1994) NMR basic principles and progress, vol 29. Springer, Berlin, p 1
221. Hartmann SR, Hahn EL (1962) Phys Rev 128:2042
222. Vega S (1981) Phys Rev A 23:3152
223. Vega AJ (1992) J Magn Reson 96:50
224. Vega AJ (1992) Solid State Nucl Magn Reson 1:17
225. Sun W, Stephen JT, Potter LD, Wu Y (1995) J Magn Reson 116:181
226. De Paul SM, Ernst M, Shore JS, Stebbins JF, Pines A (1997) J Phys Chem B 101:3240
227. Amoureux JP, Pruski M (2002) Mol Phys 100:1595
228. Ashbrook SE, Brown SP, Wimperis S (1998) Chem Phys Lett 288:509
229. Ashbrook SE, Wimperis S (2000) J Magn Reson 147:238
230. Ashbrook SE, Wimperis S (2000) Mol Phys 98:1
231. Lim KH, Grey CP (2000) J Chem Phys 112:7490

232. Mali G (2007) J Magn Reson 185:318
233. Morris GA, Freeman R (1979) J Am Chem Soc 101:760
234. Mueller L (1979) J Am Chem Soc 101:4481
235. Amoureux JP, Trebosc J, Wiench J, Pruski M (2007) J Magn Reson 184:1
236. Kao HM, Grey GP (1998) J Magn Reson 133:313
237. Gullion T, Schaefer J (1989) J Magn Reson 81:196
238. Fyfe CA, Mueller KT, Grodney H, Wong-Moon KC (1992) Chem Commun 199:198
239. van Eck ERH, Jansen R, Maas WEJR, Veeman WS (1990) Chem Commun 174:428
240. Grey CP, Vega AJ (1995) J Am Chem Soc 117:8232
241. Gullion T (1995) Chem Commun 246:325
242. Ba Y, Kao HM, Grey CP, Chopin L, Gullion T (1998) J Magn Reson 133:104
243. Fyfe CA, Wong-Moon KC, Huang Y, Grondey H (1995) J Am Chem Soc 117:10397
244. Fyfe CA, Altenschildesche HMZ, Wong-Moon KC, Grondey H, Chezeau JM (1997) Solid State Nucl Magn Reson 9:97
245. Pruski M, Lang DP, Fernandez C, Amoureux JP (1997) Solid State Nucl Magn Reson 7:327
246. Fernandez C, Delevoye L, Amoureux JP, Lang DP, Pruski M (1997) J Am Chem Soc 119:6858
247. Ashbrook SE, Wimperis S (2001) Chem Commun 340:500
248. Rovnyak D, Baldus M, Griffin RG (2000) J Magn Reson 142:145
249. Jarvie TP, Wenslow RM, Mueller KT (1995) J Am Chem Soc 117:570
250. Wang SH, De Paul SM, Bull LM (1997) J Magn Reson 125:364
251. Fernandez C, Morais C, Rocha J, Pruski M (2002) Solid State Nucl Magn Reson 21:61
252. Wiench JW, Pruski M (2004) Solid State Nucl Magn Reson 26:51
253. Wiench JW, Tricot G, Delevoye L, Trebosc J, Frye J, Montagne L, Amoureux JP, Pruski M (2006) Phys Chem Chem Phys 8:144
254. Massiot D, Fayon F, Alonso B, Trebosc J, Amoureux JP (2003) J Magn Reson 164:160
255. Iuga D, Morais C, Gan Z, Neuville DR, Cormier L, Massiot D (2005) J Am Chem Soc 127:11540
256. Fernandez C, Lang DP, Amoureux JP, Pruski M (1998) J Am Chem Soc 120:2672
257. Pruski M, Bailly A, Lang DP, Amoureux JP, Fernandez C (1999) Chem Phys Lett 307:35
258. Gan Z (2006) J Am Chem Soc 128:6040
259. Cavadini S, Lupulescu A, Antonijevic S, Bodenhausen G (2006) J Am Chem Soc 128:7706
260. Muller L (1979) J Am Chem Soc 101:4481
261. Hexem JG, Frey MH, Opella SJ (1981) J Am Chem Soc 103:224
262. Naito A, Ganapathy S, McDowell CA (1981) J Chem Phys 74:5393
263. Harris RK, Olivieri AC (1992) Prog Nucl Magn Reson Spectrosc 24:435
264. Cavadini S, Antonijevic S, Lupulescu A, Bodenhausen G (2006) J Magn Reson 182:168
265. Gan Z, Amoureux JP, Trebosc J (2007) Chem Phys Lett 435:163
266. Nishiyama Y, Endo Y, Nemoto T, Utsumi H, Yamauchi K, Hioka K, Asakura T (2011) J Magn Reson 208:44
267. Cavadini S, Vitzthum V, Ulzeda S, Abraham A, Bodenhausen G (2010) J Magn Reson 201:57
268. Cavadini S, Abraham A, Bodenhausen G (2008) J Magn Reson 190:160
269. Hartmann P, Jager C, Zwanziger JW (1999) Solid State Nucl Magn Reson 13:245
270. Ajithkumar TG, van Eck ERH, Kentgens APM (2004) Solid State Nucl Magn Reson 26:180
271. Tomaselli M, Meier BH, Baldus M, Eisenegger J, Ernst RR (1994) Chem Commun 225:131
272. Levitt MH, Raleigh DP, Creuzet F, Griffin RG (1990) J Chem Phys 90:6347
273. Nijman M, Ernst M, Kentgens APM, Meier BH (2000) Mol Phys 98:161
274. Eden M, Frydman L (2003) J Phys Chem B 107:14598
275. Baldus M, Rovnyak D, Griffin RG (2000) J Chem Phys 112:5902
276. Wi S, Heise H, Pines A (2002) J Am Chem Soc 124:10652
277. Eden M, Annersten H, Zazzi A (2005) Chem Commun 410:24
278. Painter AJ, Duer MJ (2002) J Chem Phys 116:710
279. Mali G, Fink G, Taulelle F (2004) J Chem Phys 120:2835

280. Eden M, Zhou D, Yu J (2006) Chem Commun 431:397
281. Lo AYH, Eden M (2008) Phys Chem Chem Phys 10:6635
282. Mali G, Kaucic V (2004) J Magn Reson 171:48
283. Brinkmann A, Kentgens APM, Anupold T, Samoson A (2008) J Chem Phys 129:174507
284. Deschamps M, Fayon F, Montouillout V, Massiot D (2006) Chem Commun 18:1924
285. Bak M, Rasmussen JT, Nielsen NC (2000) J Magn Reson 147:296
286. Vosegaard T, Tosner Z, Nielsen NC (2010) Solid state NMR studies of biopolymers. John Wiley & Sons, Chichester, UK, p 377
287. Veshtort M, Griffin RG (2006) J Magn Reson 178:248

Top Curr Chem (2012) 306: 189–228
DOI: 10.1007/128_2011_123

Published online: 31 March 2011

Solid State NMR of Porous Materials

Zeolites and Related Materials

Hubert Koller and Mark Weiß

Abstract Solid state NMR spectroscopy applied to the science of crystalline micro- and mesoporous silica materials over the past 10 years is reviewed. A survey is provided of framework structure and connectivity analyses from chemical shift effects of various elements in zeolites including heteroatom substitutions, framework defects and pentacoordinated silicon for zeolites containing fluoride ions. New developments in the field of NMR crystallography are included. Spatial host–guest ordering and confinement effects of zeolite–sorbate complexes are outlined, with special emphasis on NMR applications utilizing the heteronuclear dipolar interaction. The characterization of zeolite acid sites and in situ NMR on catalytic conversions is also included. Finally, the motion of extra-framework cations is investigated in two tutorial cases of sodium hopping in sodalite and cancrinite.

Keywords Catalysis · Mesoporous materials · Solid state NMR · Zeolites · ^{27}Al · ^{11}B · ^{19}F · ^{1}H · ^{23}Na · ^{17}O · ^{29}Si

Contents

H. Koller (✉) and M. Weiß
Institute of Physical Chemistry, University of Münster, Corrensstr. 28/30, 48149 Münster, Germany
e-mail: hubert.koller@uni-muenster.de

1 Introduction

Zeolites and related materials began to emerge decades ago to become one of the most important families of materials in applications such as heterogeneous catalysis, molecular sieving, adsorption, separation technology and ion exchange [1–6]. To date, the term "zeolites" is used for a diverse range of materials which is not limited to crystalline, porous aluminosilicates as in the early years. Other framework compositions, such as titanosilicates, zincosilicates or borosilicates are called zeolites, and also materials devoid of silica belong to this class of materials, e.g., aluminophosphates. More recently, porous coordination polymers, also named – somewhat inaccurately – metal organic frameworks (MOFs), have entered the zeolite scene. MOFs are very versatile in their chemical compositions, and, for this reason, they have generated a quite diffuse literature which makes it hard to provide a meaningful summary here. Therefore, we just wish to point out that various NMR nuclei (apart from ^{1}H and ^{13}C) have been investigated recently, such as ^{2}H [7, 8], ^{11}B [9], ^{15}N [10, 11], ^{31}P [12], ^{17}O [12, 13], ^{27}Al [14, 15], and ^{71}Ga [16].

The official acknowledgement of a material as belonging to the zeolite structure family is decided by the Structure Commission of the International Zeolite Association [17]. All the materials listed in the Atlas of Zeolite Framework Types have in common the fact that they are microporous materials with pore diameters of up to 2 nm. Other related materials with larger pores are ordered mesoporous materials which have an amorphous framework structure but periodic pore ordering [18–20]. Although a wealth of interesting publications covering solid state NMR involving aluminophosphate and other materials exists, this review will be limited to silica-based micro- and mesoporous materials.

High-resolution solid state NMR began to evolve into an important method for structural characterization of zeolites in the early 1980s, and the achievements from this period have been compiled in the book of Engelhardt and Michel [21]. An appreciative personal essay conveying the excitement of those early days was recently published by Thomas [22]. A number of review articles have been published since 1987 [23–30]. This contribution attempts to provide an overview of some important developments of the last 10 years. Nearly 3,000 references were found between 2000 and 2010 with the terms "NMR" and "zeolite" in the Chemical Abstracts Service, and it is clear that a further selection has to be made for a useful contribution to this chapter. The aim of this chapter is to provide an overview of state-of-the-art tools provided by solid state NMR spectroscopy for the study of structural properties of zeolites and related materials. We will not focus on methodological or technical strengths of the method. Rather, we would like to highlight the power of solid state NMR to gain information on zeolitic materials in various areas.

Numerous new developments and applications of solid state NMR techniques have emerged. Multidimensional NMR methods are able to probe connectivity patterns of zeolite framework structures and solve ambiguities in line assignments [27], high-resolution techniques for quadrupolar nuclei have been developed [31–34], and powerful double-resonance methods permit the study of spatial

neighborhoods and interatomic distances [35–38]. New in situ techniques allow the observation of catalytic systems under close to realistic working conditions [39, 40].

All available NMR methods are aimed at the exploitation of the important "NMR interactions" which contain structural information. The most important interactions are as follows:

(a) The *chemical shift* interaction (chemical shift, δ_{iso}) is still the most popular NMR parameter used. The isotropic chemical shift provides insight into the chemical surrounding of a nucleus, e.g., bonding partners, coordination number, and bond angles. If the chemical surroundings are anisotropic, then the chemical shift interaction is anisotropic. The major chemical shift effects and some analytical value of the chemical shift anisotropy (CSA) will be discussed in Sect. 2.1.1. The CSA is a second-rank tensor with principal components, δ_{11}, δ_{22}, δ_{33}. The isotropic chemical shift is the average, $\delta_{iso} = 1/3(\delta_{11} + \delta_{22} + \delta_{33})$, the asymmetry parameter is $\eta = (\delta_{22} - \delta_{11})/(\delta_{33} - \delta_{iso})$, and the span is $\Omega = \delta_{11} - \delta_{33}$.

(b) The *dipolar interaction* is a magnetic interaction between two or more nuclei. This effect is transmitted through space which means that it is not restricted to chemical bond connectivities. The strength of the dipolar interaction is a function of the interatomic distances, and the dipole coupling constant, D, contains direct distance information. For an isolated two-spin system, D is related to the distance, r, by $D = \mu_0\gamma_I\gamma_S\hbar/(8\pi^2r^3)$. γ_I and γ_S are the gyromagnetic ratios of the two interacting nuclei, I and S, and the other parameters have the usual meanings. Various applications using this interaction are outlined throughout this chapter.

(c) The *quadrupolar interaction* is an interaction between the nuclear quadrupole moment, Q, of nuclei with a spin quantum number of $I > 1/2$ and the local electric field gradient (EFG). The EFG is a traceless, second-rank tensor with principal components, V_{xx}, V_{yy}, and V_{zz}. The quadrupolar interaction contains information about the local charge-distribution. With the quadrupole coupling constant, $C_q = e^2qQ/h$ (with $V_{zz} = e.q$, e is the electric charge), and the asymmetry parameter, $\eta = (V_{yy} - V_{xx})/V_{zz}$, information can be obtained on the local symmetry. For ideal cubic, octahedral or tetrahedral coordination (high symmetry), C_q is zero. The quadrupole interaction conveys enormous structural information in the NMR characterization of zeolites, for example for the investigation of acid sites, or the local structure of extraframework cations.

(d) The *indirect spin–spin coupling* is a magnetic interaction between at least two NMR nuclei which is transmitted by bonding electrons. This interaction – sometimes also called J coupling or scalar coupling – is only effective when there is chemical bond connectivity. This interaction is of less importance in solids because the effect is usually too small to be resolved by simple standard techniques. However, more advanced methods based on double-quantum coherences observed by two-dimensional spectroscopy are able to probe the indirect spin–spin coupling. Such tools have proved to be very useful for the analysis of zeolite framework connectivities.

2 Framework Structure

2.1 High-Resolution Solid State NMR of Framework Elements

2.1.1 ^{29}Si and ^{27}Al NMR of Zeolite Framework Structures

Silicon-29 has a spin quantum number of $I = 1/2$, and its sensitivity suffers from the low natural abundance of 4.7%. Nevertheless, an enormous diagnostic value has been established for this nucleus. The most information on silicates and zeolites can be obtained from ^{29}Si isotropic chemical shifts, δ_{iso}, of tetrahedrally coordinated silicon atoms (see [21, 23, 24, 41] and references therein). The chemical shift, δ_{iso}, decreases (high-field shift) by approximately 10 ppm, when the connectivity, n, of a tetrahedral $SiO_{4-n}(OSi)_n$ group increases by one unit. The different connectivity building units are called Q^n groups. When tetrahedrally coordinated silicon in framework silicates is substituted by other T elements, such as Al, Ga, Zn, or Ti, then downfield shifts of neighboring ^{29}Si nuclei are observed. The magnitude of the shift change depends on the number of T neighbors, that is, Si(4Si), Si(3Si,1T), Si (2Si,2T), Si(3Si,1T), Si(4T) have increasing chemical shifts. Further details for various neighbors are discussed below.

Linear correlations have been established between δ_{iso} and the mean SiOT angles, α, nonbonded Si–Si distances, d_{SiSi}, SiO bond lengths, d_{SiO}, and lattice constants, a_0, of cubic structures. Bond angle and bond distance dependences of ^{29}Si chemical shifts can, for example, be utilized to gain detailed insights in the frequently observed negative thermal expansion behavior of framework silicates [42]. Decreasing δ_{iso} values (negative shifts to high field) are observed in such correlations for decreasing d_{SiO} and increasing α, d_{SiSi}, and a_0. A theoretical model was proposed which predicts a decreasing δ_{iso} with increasing positive charge at the silicon atom which in turn depends on the number and type of T atoms in the Q^n environment, $SiO_{4-n}(OT)_n$, and on the s-hybridization, ρ, of the oxygen atoms coordinated to silicon. ρ and α are related by $\rho = \cos\alpha/(\cos\alpha - 1)$, and ρ is reciprocal to d_{SiO}, which accounts for the experimental observations of chemical shift trends. The chemical shift has a diamagnetic and a paramagnetic term. ^{29}Si chemical shifts are dominated by the paramagnetic shielding term [21]. The dependence of ^{29}Si chemical shielding on the charge, q, shows a parabolic behavior with a maximum at $q = 0.4$. Low-field shifts exist for $q < 0.4$ and high-field shifts are observed for $q > 0.4$, when the charge is increased. Silicates have net charges larger than 0.4 for Si. The net charge of sulfides is close to 0.4, and $q < 0.4$ for selenides. Therefore, silicates and selenides show opposite trends of chemical shifts with charge, and sulfides show a very small chemical shift dependence when charges change [43]. The parabola maximum for ^{13}C is at $q = 0.53$, but most organic compounds have smaller charges, which leads to opposite dependence of ^{13}C chemical shift on net charge than observed in ^{29}Si NMR of silicates.

We will now proceed to provide an overview of chemical shift effects of ^{29}Si when framework elements other than silicon and oxygen are present in zeolites.

A variety of tetrahedral framework elements induce only a minor shift effect in ^{29}Si NMR spectra, but they typically lead to line broadening accompanied by a loss of resolution compared to the purely siliceous materials. For example, a possible effect of boron substituted for silicon in a neighboring position in ^{29}Si NMR is often blurred by line broadening [44, 45]. Similarly, germanium substitution does not cause appreciable chemical shift changes in ^{29}Si NMR.

However, removal of boron from the framework by leaching with acetic acid drastically increases the resolution in ^{29}Si MAS NMR spectra, and peaks from different crystallographic silicon sites are becoming visible [46]. This leaching reaction initially creates vacant positions (T vacancies) which would exhibit four Q^3 groups in the ^{29}Si MAS NMR spectra. The T vacancies are obviously refilled by migration of silicon which heals the zeolite framework defects and increases the resolution in the ^{29}Si MAS NMR spectra [46].

The titanosilicate zeolite, ETS-10, shows three ^{29}Si MAS NMR signals for Si (3Si, 1Ti) at chemical shifts from −94 to −97 ppm, and one line at −103.7 ppm for Si(4Si, 0Ti) [47]. Interestingly, an additional resonance at −99 ppm is observed and all lines broaden considerably when boron is incorporated in the framework. Although the authors were hesitant in making a firm assignment, it was assumed that this line at −99 ppm is due to an Si–O–B environment, although no suggestion was made as to whether it is due to Si(3Si, 1B), Si(2Si, 1B, 1Ti), or defect sites.

For other framework substitutions (T = Al, Ga, Ti, Zn...), the chemical shift effects vary. A tetrahedral $AlO_{4/2}^-$ substituted for $SiO_{4/2}$ causes a shift of 5−6 ppm to positive chemical shift values [21]. Substituting a neighboring tetrahedral framework Si position with gallium leads to a downfield shift of 6−8 ppm, a titanium atom causes 3−7 ppm, and zinc shows a comparatively large shift of 14−16 ppm. A schematic diagram for individual substitution effects and chemical shift ranges for these framework substitutions is shown in Fig. 1. Further information on mixed tetrahedral–octahedral substitutions may be obtained in [67].

In addition to the influence of neighbors on ^{29}Si chemical shifts, the geometrical effects (such as Si–O–T angles) already described above are also evident of mixed frameworks with elements other than Si on tetrahedral positions. This is reflected by the broadness of the bars shown in Fig. 1. Multinuclear NMR investigations on a large set of sodalite structures with various framework compositions show that T–O–T bond angle (T = Si, Al, Ga) and d_{TT} distance chemical shift dependences exist, and mutual correlations between chemical shift of these NMR nuclei can be observed [68].

When different Si(nM) sites (n = 0−4) can be resolved in the ^{29}Si solid state NMR spectra of tetrahedral framework silicates, then the Si/M ratio can be determined by the equation [21]

$$\mathrm{Si/M} = \sum_{n=0}^{4} I_{\mathrm{Si(nM)}} \Big/ \sum_{n=0}^{4} \frac{n}{4} I_{\mathrm{Si(nM)}}. \quad (1)$$

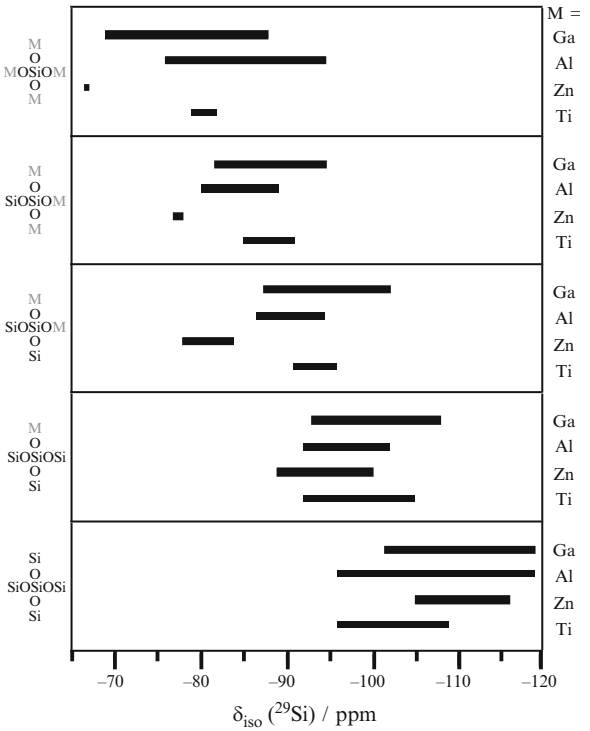

Fig. 1 ^{29}Si chemical shift scales for tetrahedral Si(nM) units in zeolites; data for Al were adapted from [24] for a large variety of zeolites, data for other substitutions are taken from: *Ga*: zeolites A, X, Y, L, sodalite, offretite, mazzite, ZSM-5 [21], TNU-1, TNU-4, sodalite, ZSM-5 [48], beta [49–52], paulingite [53], and natrolite [54]; *Zn*: VPI-7, VPI-9, Na_2ZnSiO_4, ckalovite, $K_2ZnSi_4O_{10}$ [55], sodalite [56], RUB-17, VPI-7 [57, 58]; *Ti*: ETS-4, natisite, sphene, lorenzenite, $Na_2TiSi_2O_7$, $Ba_2TiSi_2O_8$ (fresnoite), benitoite, $K_2TiSi_3O_9$, narsarsukite, $Cs_2TiSi_6O_{15}$, $CsTiSi_2O_{6.5}$ [59], ETS-10 [60, 61], AV-11 [62], AM-18 [63], JLU-1 [64], penkvelkisite [65], nenadkevichite [66]

This equation is based on the assumption that homologous M–O–M (M = Al, Ga…) pairs do not exist. For aluminosilicates this is known as the Al–O–Al avoidance rule introduced by Loewenstein (Loewenstein rule) [69].

Recently, Grey and coworkers have reported on the isoelectronic replacement of bridging oxygen atoms by NH groups by treating Y zeolites under dry conditions with NH_3 [70–72]. A remarkable degree of oxygen replacement (~20%) can be achieved by this method, and large chemical shift effects are observed in the ^{29}Si NMR spectra: lines at −86, −66, −53, and −43 ppm are reported for increasing numbers of nitrogen substitution in the framework, and these resonances were assigned to $Si(NHSi)_x(OSi)_{4-x}$ with $x = 1$, 2, 3, and 4, respectively. This trend is consistent with the chemical shift scale of oxynitride ceramics [24], and with some recent experimental data on ordered crystalline (oxo)nitridosilicates, where chemical shifts of −48 ppm [73] and −54.3 ppm [74] for SiN_4, −56.2 ppm [75] and −52.8 ppm [76] for $SiON_3$, and −64.1/−66.0 ppm [77] and −68.2 ppm [78] for

SiO_2N_2 were clearly assigned. Since NH substitution for O in zeolite Y occurs preferably near Al [70–72], a substitution mechanism may be surmised which involves Lewis acidic framework aluminum which reacts with the Lewis base NH_3.

Apart from the isotropic chemical shift, the components of anisotropic chemical shielding tensors have been measured recently by a CSA recoupling sequence, and the obtained data are compared with Hartree–Fock (HF) computational methods [79]. Different crystallographic positions are observed in high-resolution MAS NMR spectra of high-silica zeolites. A two-dimensional CSA recoupling pulse sequence allows the observation of static powder lineshapes for MAS NMR spectra with a large number of components. The CSA of the resolved NMR lines is determined with the 2D CSA recoupling sequence and the line assignment to crystallographic positions may be achieved by the aforementioned correlation between isotropic chemical shifts and structural parameters. Alternatively, line assignments may also be obtained with two-dimensional correlation experiments which will be discussed in Sect. 2.2. A variety of zeolites, including the 24 T-site monoclinic structure of ZSM-5, has been investigated. A simple structural model for the chemical shift tensor parameters was not suggested, but the HF calculated parameters are in good agreement with experimental data.

Figure 2 shows ^{29}Si solid state NMR data of high-silica ZSM-5 with 24 crystallographic Si positions, 15 of which are well enough resolved in the MAS NMR spectrum to be assigned to crystallographic positions. The CSA parameters are determined by simulation of the lineshapes of the powder pattern as obtained from the 2D experiment.

The CSA is sensitive to structural properties, and they may be used for structure refinement based on NMR data, as will be further discussed in Sect. 2.2.2.

^{27}Al solid state NMR is most often used to distinguish between tetrahedral Al in the zeolite framework and extraframework penta- or hexacoordinated aluminum. For further information, the reader is referred to [21].

2.1.2 ^{29}Si and ^{27}Al NMR on Al Distribution

The distribution of aluminum in the zeolite framework is of relevance to catalytic activity. Therefore, quite a number of studies on Si/Al ordering have been carried out. Most of them are using ^{29}Si MAS NMR to resolve different Si(nAl) sites and the experimental intensities are compared with those predicted for Si/Al distribution models. Typically, these models take into account that the Loewenstein rule is obeyed, and often the so-called Dempsey rule [80] (minimization of Al–O–Si–O–Al connectivities) is considered as an additional constraint for electrostatic grounds. The validity of the suggested model is then judged on the basis of the agreement between predicted and experimental line intensities. However, one should keep in mind that experimental populations could also comply with alternative models which are not under consideration in the study as possible solutions [21]. Almost all of the investigations of Si/Al ordering assume that uniform Al dispersion across the zeolite crystals exist, although a zoned Al distribution may be

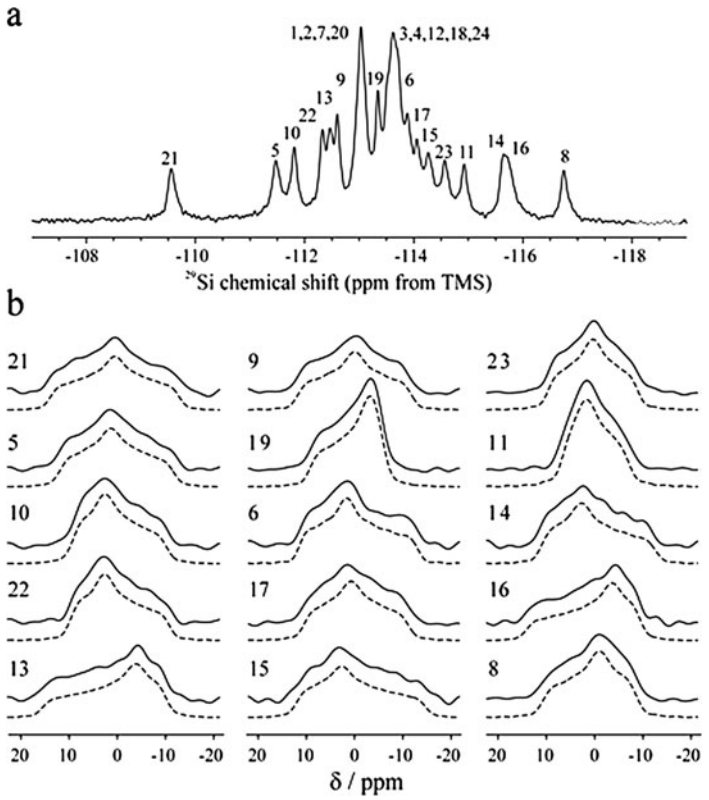

Fig. 2 Experimental analysis of the chemical shift anisotropy of high-silica ZSM-5 zeolite, (**a**) ^{29}Si MAS NMR and (**b**) extracted CSA lineshapes from a two-dimensional CSA recoupling sequence; *dashed lines* are simulated lineshapes. Adapted with permission from [79]. Copyright 2008 American Chemical Society

a more realistic scenario in some cases [81]. With these uncertainties in mind, a careful analysis for each zeolite topology is one of the important prerequisites for a serious application of such an analysis. One of the first zeolites which have been investigated was faujasite [21]. Some of the more recent reports on Si/Al ordering were published for chabazite [82], FAU and EMT crystallized in the presence of crown ethers [83], analcime [84], mordenite and beta [85, 86], faujasite [87], and ferrierite [88]. All studies are in accordance with the Loewenstein rule, but compliance with Dempsey's rule seems to depend on the particular system under investigation. Different Si/Al distribution models are possible for a zeolite structure. For example, the presence of a crown ether in the synthesis of FAU and EMT is reported to have an influence on the Si/Al distribution [83].

An interesting new approach has been made possible by multiple quantum ^{27}Al MAS (MQMAS) NMR investigations of zeolites. Due to its nuclear electric quadrupole moment, ^{27}Al exhibits broad lineshapes in distorted structural environments.

Narrow lines are only observed for ideal tetrahedral or octahedral coordination. With MQMAS NMR it is now feasible to achieve a higher resolution in the spectra than with classical experiments using a single-pulse excitation. Further information about the powerful MQMAS technique may be obtained from the article by Fernandez and Pruski in this book. Sklenak and coauthors have applied it in combination with computational methods to identify 10 distinct ^{27}Al NMR resonances in a set of 11 differently synthesized ZSM-5 zeolites, stretching over a chemical shift range of 13.6 ppm [89], and some of the sufficiently separated lines could be assigned to distinct framework positions. Pairing of aluminum in Al–O–Si–O–Al or Al–O–Si–O–Si–O–Al chains is reported to have an influence on the ^{27}Al NMR chemical shift. However, a prediction of the shift is not possible, not even on its sign, without detailed DFT calculations [90, 91]. Three Al positions have been observed in zeolite MCM-22, and one line (50.5 ppm) disappears upon dealumination with oxalic acid [92]. Hence, this species was assigned to tetrahedral positions near large cavities or the external surface.

Additional information can be obtained by employing double resonance methods which probe the dipolar interaction of ^{29}Si and ^{27}Al within the zeolite framework [93, 94]. The underlying NMR methods will be considered in more detail in Sects. 3 and 4 of this chapter.

2.1.3 ^{11}B NMR

Due to its quadrupolar moment, ^{11}B NMR is very sensitive to its coordination geometry. Trigonal and tetrahedral boron exist in zeolites. Trigonal boron has a large EFG at the ^{11}B nucleus, and a typical powder lineshape for quadrupolar interaction is observed in MAS NMR spectra. On the other hand, tetrahedrally coordinated boron yields narrow lines. The coordination number of boron in zeolite frameworks depends on the counterion [95–99]. Tetrahedral boron, $BO_{4/2}^{-}$, is observed near soft cations (compared to protons), such as Na^+, H_3O^+, or quaternary ammonium cations. Trigonal boron is observed for protonated oxygen sites, and it is easily extracted from the zeolite framework. Partially extracted intermediates, $B(OSi)_x(OH)_{3-x}$, have distinct chemical shifts of ~10 ppm ($x = 3$), ~12 ppm ($x = 2$), ~15 ppm ($x = 1$), and ~18 ppm ($x = 0$) [100, 101]. The calculated ^{11}B chemical shifts of $B(OSi)_3$ framework boron agrees well with the suggested experimental assignments [102].

2.1.4 ^{17}O NMR

A tutorial review of ^{17}O solid state NMR has recently been published by Ashbrook and Smith [103]. Although it has been early envisaged that ^{17}O solid state NMR can provide useful information on the zeolite framework structure [104, 105], the number of publications employing this nucleus has remained scarce compared to ^{27}Al or ^{29}Si which is at least in part due to the need for

isotopic enrichment. In addition, the analysis of ^{17}O NMR of zeolites remains a challenge to date which is due to the large number of oxygen positions in many zeolite structures. Additionally, extraframework species usually interact with framework oxygens, making interpretation difficult. For zeolites with disordered Al distribution, two distinct resonances can usually be resolved for SiOSi and SiOAl by high-resolution ^{17}O NMR techniques [104, 106]. Resolution of different crystallographic oxygens is possible for Si/Al = 1 (ordered Si/Al distributions) [107–110] or Si/Al = ∞ [111, 112]. SiOSi sites in high-silica zeolites are characterized by isotropic ^{17}O chemical shifts, δ_{iso}, between 28 and 48 ppm, quadrupolar coupling constants, C_q, between 5 and 6 MHz, and asymmetry parameters, η, of 0.1−0.3 [111, 112]. SiOAl sites are characterized by ^{17}O chemical shifts between 31 and 76 ppm, C_q between 2.9 and 4.3 MHz, and η between 0.05 and 0.3 [107–110]. While the chemical shift ranges of SiOSi and SiOAl partially overlap, their quadrupolar coupling constants are well separated, which is due to the smaller EFG at the more ionic SiOAl sites [104]. AlOAl sites have been observed at δ_{iso} = 21 ppm in a sample of natural stilbite with a high concentration of Ca^{2+} ions [113], and at δ_{iso} = 26 ppm in analcime [114]. Apparently, such violations of the AlOAl avoidance rule are particularly well detected by ^{17}O MQMAS high-resolution methods, whereas they are more difficult to characterize by ^{27}Al or ^{29}Si NMR.

While some earlier reports have proposed a correlation between ^{17}O isotropic chemical shifts and framework structural parameters [107, 108], more detailed investigations show that no such correlation exists that can be generalized for a broader range of materials [109, 112]. Clearly, extraframework cations and water interacting with framework oxygens have an influence on the ^{17}O isotropic chemical shift which is not yet fully understood [108, 115, 116]. Apparently, the ^{17}O chemical shifts increase with the size of the extraframework counterion [108, 115]. Even the loading of N_2 or O_2 molecules causes changes in ^{17}O NMR of zeolite Li-X [117]. Particularly large chemical shift values at approximately 70 ppm have been detected in zeolites A and X with divalent extraframework cations [117, 118]. These signals have been assigned to "bare" oxygen atoms which have no interaction to extraframework cations or water.

The detection of Brønsted acid sites, SiO(H)Al, is the most recent achievement of ^{17}O NMR of zeolites [119–121]. High magnetic fields and double resonance techniques have allowed the observation of this important species in zeolite HY [120]. Chemical shifts of 21 and 24 ppm have been reported for zeolite HY for the Brønsted sites in the supercage and sodalite cage, respectively [119]. Quadrupole interaction parameters are C_q = 6.0 and 6.2 MHz and η = 1.0 and 0.9, respectively. Signal enhancement by ^{1}H–^{17}O cross-polarization has also permitted the detection of the acid sites in zeolite ZSM-5 [119], where they exist with lower abundance than in HY.

Figure 3 illustrates the resolution of two oxygen sites connected with Brønsted protons [119] in HY zeolite. The separation of these sites from other, non-protonated positions in the zeolite framework was possible by a two-dimensional ^{1}H–^{17}O HETCOR (heteronuclear correlation) NMR experiment which was acquired at

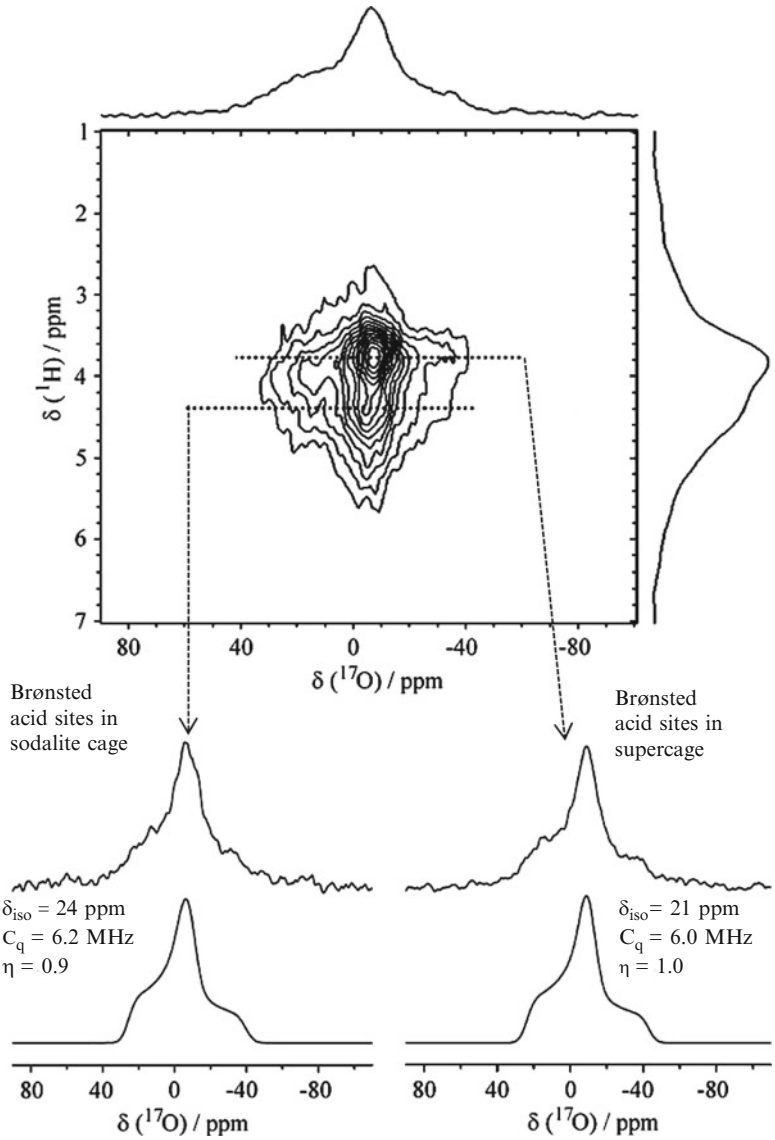

Fig. 3 ^{1}H–^{17}O HETCOR NMR experiment on zeolite HY. Adapted with permission from [119]. Copyright 2007 American Chemical Society

17.6 T. The ^{17}O NMR signals that are due to acid sites in supercages and sodalite cages can be resolved in the two-dimensional plot, and their MAS NMR lineshapes for fitting are obtained by extracting two slices at the corresponding chemical shifts of the proton NMR dimension.

2.2 Framework Connectivities and Structure Refinement

2.2.1 Tetrahedral Site Connectivities from Two-Dimensional NMR

Since the early 1990s, powerful two-dimensional solid state NMR techniques have been applied to monitor the framework connectivities among ^{29}Si nuclei [24, 27, 28]. The most often applied technique so far has been the INADEQUATE pulse sequence that correlates single-quantum with double-quantum coherences in a two-dimensional experiment based on scalar coupling in ^{29}Si–O–^{29}Si linkages. Correlation peaks between two signals are observed in such two-dimensional experiments, when the two corresponding sites are connected.

For investigations with nuclei with low natural abundance, such as ^{29}Si (4.7%), isotopic enrichment is often applied. This is accompanied with difficulties in the analysis of connectivities between selected pairs, because multiple site interactions become more pronounced. Cadars et al. have suggested incorporation of a z-filter that results in a robust method to select local site connectivities and remove complications from multiple site interactions [122].

A novel tool is a symmetry-based ^{29}Si dipolar recoupling method ($SR26_4^{11}$) [123] for small dipolar interactions that has been initially applied in zeolite structural studies by Brouwer et al. [124]. One of the advantages of the new method over INADEQUATE is that the latter misses auto-correlations of symmetry-related double-quantum coherences. The $SR26_4^{11}$ method provides such information on auto-correlation which allows to identification of all four connectivities of a tetrahedral Si position.

Recently, a detailed study was reported for a molecularly ordered layered silicate surfactant mesophase [125, 126]. A subtle change in the surfactant which is used for the synthesis of such mesophases appears to induce dramatic modifications in the silica ordering. When cetyltrimethylammonium ($C_{16}NMe_3^+$) cations are employed, then only two ^{29}Si NMR resonances at −102 ppm (Q^3) and −112 ppm (Q^4) exist. The use of the surfactant $C_{16}NMe_2Et^+$ instead leads to a silica framework structure with distinct peaks for Q^3 at −97.0 and −101.0 ppm or for Q^4 at −103.7, −109.1, and −114.7 ppm. A similar set of five peaks with slightly different chemical shifts (−97.4, −99.4, −106.0, −110.2, and −116.5 ppm) is observed when $C_{16}NMeEt_2^+$ surfactant cations are employed for the synthesis of the material. All three materials exhibit high local ordering which is manifested in narrow ^{29}Si NMR resonance lines, but they are structurally disordered in long-range scale, at least in the two dimensions of the silica layers. However, the INADEQUATE technique reveals significant changes in the connectivity pattern of the two latter materials with five ^{29}Si NMR peaks. This interesting report illustrates that NMR has revealed important insights into the rigorous influence of surface templating of silica materials, depending on the surfactant headgroup charge density.

2.2.2 Structure Refinement: NMR Crystallography

In a follow-up of this study described in Sect. 2.2.1, the ^{29}Si–^{29}Si homonuclear dipole coupling has been recorded for such layered mesophases from spinning sideband analysis of double-quantum coherences by applying the BABA technique [127]. The combination of these data with X-ray diffraction methods and quantum-chemical and empirical force-field modeling has enabled the authors to propose a structural model with atomic coordinates. The computational modeling of three-dimensional structures with experimental NMR data as refinement constraints is called "NMR crystallography" by some authors. The principal workflow is similar to the structure refinement based on X-ray diffraction data. A structural model is adjusted to match with experimental information until the difference between observed and calculated properties falls below a certain threshold. For NMR crystallography, the relevant properties may be the dipole–dipole coupling constants, the isotropic chemical shift, chemical shift anisotropies, or scalar coupling constants. These parameters are theoretically predicted based on a structural model. The model is then repeatedly adjusted until the differences between predicted and experimental NMR parameters are below a threshold which may be defined based on experimental accuracy and least square deviations. The example with layered mesophases discussed above demonstrates that modern solid state NMR methods offer opportunities to solve structural problems ab initio in the absence of long-range ordering which precludes one from solving the structure by diffraction methods. More detailed structural refinement is, for example, possible with the combination of experimental CSA parameters and computational methods. Such CSA parameters may be obtained as discussed in Sect. 2.1.1 [128, 129]. The set of experimentally accessible chemical shift tensor parameters of a complex zeolite structure is, in principle, rich in structural information [128, 129]. Zeolite NMR crystallography may be a possibility to refine crystal structures in the future. Cadars, Brouwer, and Chmelka have suggested that structural refinement based on ^{29}Si–O–^{29}Si scalar couplings offers some potential for even higher accuracy than with CSA parameters [130].

2.3 Negative Charge Centers in High-Silica Frameworks

2.3.1 Defect Sites in As-Made Zeolites

The syntheses of high-silica zeolites commonly require an additive, the so-called structure directing agent (SDA), which is typically an organic quaternary ammonium compound. Since a pure SiO_2 framework structure consisting of fully interconnected tetrahedral $SiO_{4/2}$ building units has no charge, these materials exhibit a large number of Q^3 defect sites, that is, Si–O^- (siloxy) for charge compensation and SiOH (silanol) groups [131]. Three silanol groups form hydrogen bonds

to one siloxy group [132], and they show a characteristic ^{1}H chemical shift of 10.2 ppm. Multiple-quantum ^{1}H MAS NMR data of such defect clusters in zeolite ZSM-12 unequivocally show that three SiOH groups in a cluster contribute to the same ^{1}H MAS NMR signal at 10.2 ppm [132]. Calcination of the quaternary ammonium compound removes the organics from the zeolite pores, but a proton has to remain for charge reasons. The number of Q^3 defect sites is then considerably reduced. A reasonable mechanism is the protonation of the siloxy group to form an SiOH group and subsequent condensation of the four silanol groups in the defect cluster to a fully connected framework. When other charge centers are in the zeolite framework, for example by $BO_{4/2}^-$ or $AlO_{4/2}^-$ heterosubstitutions, then these hydrogen bonds are reduced or not observed [131]. Also, the substitution by Ti leads to a decrease of these hydrogen-bonded protons which was explained by incorporation of pentacoordinated titanium, $[Ti(OSi)_4(OH)]^-$ [133] which balances the charge of the SDA.

Other hydrogen bonds have been observed with proton chemical shifts between 14.0 and 16.6 ppm [134–140] for hydrous layer silicates or alkali layer silicates. Hydrogen-bonded SiOH groups in some alkaline earth silicates have shown proton chemical shifts from 6.7 to 14.9 ppm [141], and silicate minerals, most of which contain additional framework elements such as B or Al, were reported to yield chemical shifts of hydroxyl groups from 0.7 to 15.8 ppm [142]. The proton exchange between a hydrogen-bonded SiOH group and H_2O (coordinated to Na^+) was investigated in detail [136], and an activation energy of 33 ± 2 kJ/mol was reported.

The large range of proton chemical shifts of hydrogen-bonded SiOH raises the question of what is special about silanol groups in zeolitic defect clusters to yield a constant chemical shift of ~10 ppm for a large set of materials. We believe that the special geometric and chemical nature of defect sites in as-made high-silica zeolites can be rationalized by the oxygen valence of the siloxy group (Fig. 4). Formally, the valence of an oxygen atom is 2. This can for example be achieved by two Si–O linkages in an Si–O–Si bridge, when both bonds have the standard bond length of 1.62 Å. However, an SiO^- defect group contributes to the oxygen valence with only one bond. As the Si–O bond valence depends on the bond distance [143], the bond valence may be slightly larger than unity, since Si–O^- bonds are usually shorter than the standard distance of 1.62 Å. For a reasonably short Si–O distance of 1.59 Å, the bond valence would be 1.1. Since this does not complete the valence of 2 for oxygen, additional interactions are necessary for oxygen valence satisfaction. The $SiO^-\cdots$HOSi hydrogen bonds in the zeolitic defect clusters contribute to this valence. This situation is sketched in Fig. 4.

The bond valence of a hydrogen bond depends on the H···O donor–acceptor distance [144, 145] which in turn also correlates with the proton chemical shift [146]. A combination of Eq. (1) in [144] and Eq. (54) of [146] yields an empirical correlation between a hydrogen bond valence, $s_{O\ldots H}$, and proton chemical shifts:

$$s_{O\cdots H} = \left(\frac{54.07}{\delta_H/\mathrm{ppm} + 17.4}\right)^{-2.17}. \tag{2}$$

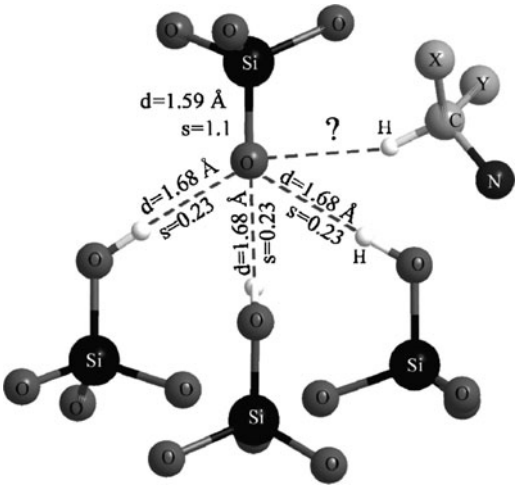

Fig. 4 Proposed defect cluster model in as-made zeolites with quaternary ammonium cations as structure directing agents (SDAs); hydrogen bond distances of 1.68 Å are determined experimentally from the ^{1}H NMR chemical shift of 10.2 ppm; X and Y are atoms not further specified in the SDA; the interaction between the SDA and the SiO^{-} group is assumed based on bond valence arguments (see text)

A similar correlation was previously suggested for vibrational frequencies instead of proton chemical shifts [145]. Each of the three hydrogen bonds in the zeolite defect clusters ($\delta_H = 10.2$ ppm, $d = 1.68$ Å) adds a valence of 0.23. When combined with the estimated Si–O bond valence of 1.1, this results in a total oxygen valence of 1.79. This value is still smaller than 2, but we have now arrived at a number which may be supplemented to valence satisfaction by additional interactions between the oxygen atoms and the organic SDA via C–H···O hydrogen bonds, or interaction(s) between the siloxy group and water. Completion of the oxygen valence by additional interactions requires a total of 0.21 which can for example be provided by a short C–H···O hydrogen bond of 1.46 Å, or two such interactions with a distance of 1.72 Å [143].

When fewer than three hydrogen bonds exist to satisfy the oxygen valence of a siloxy group, as for example in some hydrous layer silicates mentioned above, then they need to be stronger (yielding a low-field shift in proton NMR) and/or additional interaction partners should be present.

A special situation was reported for zeolite SSZ-74 which shows ordered silicon vacancies with two siloxy and two silanol groups [147]. The zeolite framework has a vacant site in between these Q^3 groups. This zeolite also exhibits a proton chemical shift of 10 ppm for defect silanol groups, but it is different in several aspects from the defect clusters in [131]. The geometry of the vacancy in SSZ-74 does not easily allow the accommodation of a tetrahedral $SiO_{4/2}$ group [147], and calcination does not reduce the number of Q^3 groups in SSZ-74. This is untypical of the other high-silica zeolites investigated in [131]. In addition, the clustering of two siloxy with two silanol groups apparently does not follow the bond valence arguments raised above, since only one SiOH group is available per siloxy group for hydrogen bond formation. This point was also discussed in a theoretical study of the defect site in SSZ-74 [148], and it was concluded that one water molecule per siloxy group must be present to interact with two hydrogen bonds in order to achieve

a stable structure in the computational simulation. In total, there are again three hydrogen bonds to a siloxy group, one from a silanol group and two from water, which is the same situation as in the defect clusters with three SiOH per siloxy group shown in Fig. 4 [131, 132]. We suggest that proton chemical shifts in hydrogen bonds reflect the bond valence situation of the accepting oxygen atom. However, future detailed investigations of a variety of structural situations with accurate crystal structures are necessary to prove this hypothesis further.

2.3.2 Fluoride Ions and Pentacoordinated Silicon

Fluoride ions are used as mineralizing agent for the synthesis of zeolites with few framework defects. They are responsible for mobilizing the silica starting material by dissolving small molecules during hydrothermal synthesis. Fluoride is found in the as-made zeolites to balance the charge of the quaternary ammonium cation which serves as SDA. The fluoride ions undergo strong interactions with the zeolite framework, typically in an Si–F bond in pentacoordinated silicates species, $SiO_{4/2}F^-$. Their ^{29}Si chemical shifts appear at about −150 ppm [149, 150]. Fyfe et al. have measured Si–F distances of such sites, using $^{29}Si\{^{19}F\}$ cross-polarization or REDOR [151, 152]. The ^{19}F chemical shift of fluoride ions in zeolite structures is sensitive to the local environment. Generally, the size of the cage correlates with the chemical shift. An overview of data in the literature, including some germanium silicate zeolites, is given in Table 1.

Table 1 ^{19}F chemical shifts and fluoride location in high-silica zeolites; cages are indicated by the n^m nomenclature (number, m, of n-rings)

F^- location known by XRD	^{19}F MAS NMR δ_{iso}/ppm	Material	References
D4R [4^6]	−38, −39	Octadecasil, beta, ITQ-7, ITQ-13, ITQ-21	[153–158]
[$4^3 5^4$]	−68 to −70; −56 to −59	ITQ-4, SSZ-23, beta	[153, 158]
[$4^1 5^2 6^2$]	−64 to −67	ZSM-5, ITQ-13	[153, 155]
[$4^1 5^4 6^2$]	−76	Nonasil	[153]
[5^4]	−56	Ferrierite	[159]
D6R [$4^6 6^2$]	−64	Chabazite	[159]
Cage-like nesting near pore	−74	ZSM-23	[160]
[$4^4 5^4$](proposed)	−69	ITQ-3	[150]
Unknown	−78, −84	ZSM-12, sigma-2	[150, 160]
[4^6] (1Ge)	−20	Octadecasil, beta, ITQ-7, ITQ-21	[154, 156–158, 161]
[4^6] (>1Ge)	−7; −8	Octadecasil, beta, ITQ-7, ITQ-21	[154, 156–158, 161]
[4^6] (8Ge)	−14; −15	Octadecasil, ITQ-21	[154, 157]
[$4^3 5^4$] (≥1Ge)	−46	Beta	[158]

For rigid Si–F bonds, the ^{19}F CSA is characterized by a span, $\Omega = \delta_{11} - \delta_{33}$, of about 80 ppm [150]. This parameter describes the total static linewidth of ^{19}F NMR of rigid Si–F bonds in zeolites. Line narrowing (reduced span values) is observed, when the fluoride ion carries out motional jumps between two or more Si sites.

3 Molecular Ordering and Confinement in Pores

In this chapter we will focus on molecular ordering and confinement effects in pores. Diffusion experiments with the pulse-field gradient method ([162–165] and references therein) and characterization of the surface properties using NMR of noble gases such as ^{129}Xe ([166–171] and references therein), or ^{83}Kr [172], will be omitted due to excellent reviews that have appeared quite recently in these areas.

3.1 Dipolar Interactions and Intermolecular Ordering

3.1.1 Overview of Methods Applied to Zeolites

The dipole interaction is one of the most important NMR interactions that provide detailed information on intermolecular interactions. For isolated two-spin pairs, the dipole–dipole coupling constant is analytically connected to the internuclear distance. Cross-polarization (CP) is the classical method to probe dipole interactions (see for instance [173, 174] and references therein). The typical experiment begins with an excitation (90°) pulse on abundant spins, I, such as ^{1}H or ^{19}F, followed by a contact pulse on both nuclei, that is, the abundant spin and an interacting spin, S (for example ^{13}C or ^{29}Si). The power on both channels is adjusted under consideration of the Hartmann–Hahn condition, $\omega_{rf}(I) = \omega_{rf}(S)$, where ω_{rf} are the nutation frequencies in the rotating frame which is relevant under such spin-lock conditions. When both nuclei have the same ω_{rf}, then they can exchange polarization in the rotating frame which leads to energy transfer from I to S with the kinetic rate constant, T_{cp}. The total magnetization decays by the relaxation times in the rotating frame, $T_{1\rho}(I)$ and $T_{1\rho}(S)$, whereby $T_{1\rho}(I)$ is typically dominant and $T_{1\rho}(S)$ is neglected. The usual assumption that the cross-polarization behavior is governed by the build-up contribution from fast polarization transfer, T_{cp}, and the decay from $T_{1\rho}(^{1}H)$ relaxation is not always valid [175]. When $T_{1\rho}$ relaxation is fast compared to the polarization transfer rate, then the analysis becomes more difficult and $T_{1\rho}$ of both nuclei, I and S, may become important.

Also, the common assumption that CP can be described by two spin reservoirs, I and S, is in some cases not sufficient. Kolodziejski and Klinowski have described the treatment of a system in which I* spins in close contact to S interact with a more remote I spin reservoir (I-I*-S model) [173].

In 1989 rotational echo double resonance (REDOR) was introduced by Gullion and Schaefer [35], and it became a prominent tool to investigate heteronuclear dipole interactions in solids from which model-free and quantitative distance information is available under high-resolution conditions. The REDOR experiment consists of two individual measurements: first, the detection of the MAS NMR intensity in a spin echo experiment, S_0, of the observed spin, X, and second the measurement of the intensity, S, of the echo of X under 90° pulses on the coupled spin, Y, during the echo period. These pulses reintroduce the heteronuclear X–Y dipole interaction in the evolution time of the echo period, leading to a damped echo intensity corresponding to the strength of the dipole interaction. The normalized intensity difference between the two experiments, $\Delta S/S_0$, is then analyzed as a function of echo time, yielding the REDOR evolution curve.

The most challenging limitation of the REDOR method is that it can only be analytically analyzed, when small spin systems, ideally isolated two-spin-1/2 pairs, are involved. For larger spin systems, the geometry between the spins is important, and, since this is often unknown, accurate distance determinations are precluded for complex materials [176]. Bertmer and Eckert have proposed that larger spin systems can still be described, at least semi-quantitatively, by REDOR data in terms of second moment analysis [177].

Additional problems are encountered when quadrupolar nuclei, Y, exist, because different spin states of the coupled quadrupolar spin cause different dipolar interaction strengths. For large quadrupole coupling constants, the satellite transitions, for example $|+1/2> \leftrightarrow |-3/2>$ or $|+3/2> \leftrightarrow |+5/2>$ transitions, do not contribute to the REDOR effect, since they are outside the excitation window of 90° pulses. For such cases, the TRAPDOR [36, 178] and REAPDOR [37] techniques have been developed, and they are also measured with a set of two experiments as the REDOR technique. Both methods, TRAPDOR and REAPDOR, utilize the time dependence of the resonance frequencies of NMR transitions under magic angle spinning conditions to make the satellite transitions effective for analyzing dipolar couplings. The results of their evolution curves can be quantitatively analyzed, at least for two-spin systems, when the coupled nucleus is influenced by the electric quadrupole interaction.

Table 2 lists a number of publications of recent years on investigations of spatial orderings, interactions, and local structures, most of which have employed methods based on heteronuclear dipolar interactions.

Structure refinement using information on dipolar interactions of zeolite–sorbate complexes has been applied by Fyfe and Brouwer [193]. First, the high-resolution ^{29}Si MAS NMR spectrum of high-silica ZSM-5 loaded with *p*-dichlorobenzene was assigned to crystallographic positions by two-dimensional ^{29}Si INADEQUATE. Then, cross-polarization parameters between the sorbate molecules and the zeolite framework were measured for the different ^{29}Si NMR lines. The experimental rates of cross-polarization, T_{cp}, were then correlated with the predicted second moments of heteronuclear dipolar interaction, as calculated from ^{29}Si–^{1}H distances, using the standard model of Van Vleck. To this end, the zeolite–sorbate structure was varied until the predicted second moment was in agreement with the experimental cross-polarization rates.

Table 2 Zeolite surface interactions investigated by dipolar NMR methods

Subject studied	Method	References
SDA/framework defect sites (nonasil, SSZ-23, ZSM-12)	$^{2}H\{^{1}H\}$ CPMAS, HETCOR	[179, 180]
SDA/aluminum in framework (ZSM-12)	$^{29}Si\{^{1}H\}$ REDOR, CPMAS	[181]
SDA/boron in framework (CIT-1, SSZ-24)	$^{13}C\{^{11}B\}$ REDOR	[182]
p-Nitroaniline/Si in framework (ZSM-5)	^{29}Si MAS, $^{15}N\{^{1}H\}$ CPMAS	[183]
Hydrofluorocarbons/extraframework cations and AlO framework atoms (NaX, NaY)	$^{23}Na\{^{19}F\}$, $^{27}Al\{^{1}H\}$, $^{17}O\{^{1}H\}$ CPMAS	[184]
n-Hexane/Si in framework (ZSM-5)	^{29}Si MAS	[185]
p-Xylene/Si in framework (ZSM-5)	^{29}Si-$^{13}C\{^{1}H\}$ TEDOR	[186]
p-Xylene/Si in framework (ZSM-5)	$^{29}Si\{^{1}H\}$ CPMAS	[187]
p-Dichlorobenzene/Si in framework, slow CP regime (ZSM-5)	$^{29}Si\{^{1}H\}$ CPMAS	[175]
Oxygen, *p*-dibromobenzene/Si in framework	^{29}Si MAS, linewidths	[188]
SDA/Si,Al in framework, nucleation (ZSM-5)	$^{29}Si\{^{1}H\}$, $^{27}Al\{^{1}H\}$ REDOR	[189]
NH_3/extraframework Na, framework Al (zeolite A)	$^{15}N\{^{23}Na\}$, $^{15}N\{^{23}Na\}$ TRAPDOR, REAPDOR	[190, 191]
Naphthalene/Si in framework, (ZSM-5)	$^{29}Si\{^{1}H\}$ CPMAS	[192]
p-Dichlorobenzene/Si in framework (ZSM-5), structure refinement using NMR data	$^{29}Si\{^{1}H\}$ CPMAS, second moment refinement	[193]
Toluene/extraframework Li, Na (zeolites Y, L)	$^{23}Na\{^{7}Li\}$, $^{7}Li\{^{1}H\}$, $^{23}Na\{^{1}H\}$ REDOR	[194–196]
Tetrapropylammonium/Si, nucleation (ZSM-5)	$^{29}Si\{^{2}H\}$ REDOR	[197]
C_1–C_6 alkanes/interactions among guest molecules	^{1}H MAS NMR linewidths (effect of molecular motion on MAS line narrowing)	[198]
o-Xylene/Si in framework (ZSM-5)	$^{29}Si\{^{1}H\}$ CPMAS, second moment refinement	[199]
Surfactant/Si in framework (organic–inorganic mesophases)	$^{29}Si\{^{1}H\}$ and $^{13}C\{^{1}H\}$ HETCOR	[200]
Tetrapropylammonium/Al in framework (ZSM-5)	$^{27}Al\{^{14}N\}$, $^{13}C\{^{27}Al\}$ TRAPDOR	[201]
Tetrapropylammonium, phenylaminopro pyltrimethoxysilane (as silanization agent)/Si in framework (ZSM-5)	$^{29}Si\{^{1}H\}$ HETCOR	[202]

SDA structure directing agent

3.1.2 Spatial Ordering of SDAs

The location of boron or aluminum sites in zeolites is of utmost importance to an understanding of the catalytic properties. Due to the inherent long-range disorder of the distribution of these sites in most zeolites, it is difficult to locate them by diffraction methods. The aforementioned methods to measure heteronuclear dipolar interactions can be utilized to determine the orientation between the organic SDA and Al or B in the framework. The SDA location may be obtained by structure refinement or computational modeling. For catalytic reactions, the SDA must be removed from the pores system by calcination.

$^{13}C\{^{1}H\}\{^{27}Al\}$ or $^{13}C\{^{1}H\}\{^{11}B\}$ triple resonance as well as $^{1}H\{^{27}Al\}$ double resonance methods have been employed to measure the local neighborhood between ^{11}B or ^{27}Al nuclei in the zeolite framework and the ^{13}C (or ^{1}H) nuclei in the SDA [203]. A set of various boro- or aluminosilicates has been investigated, and Fig. 5 illustrates one of the examples.

The $^{13}C\{^{27}Al\}$ REAPDOR evolution reflects the strength of the heteronuclear dipolar interaction. Stronger interactions yield steeper curves in Fig. 5. It is striking that the ^{13}C nuclei located near the charge center of the SDA exhibit a stronger REAPDOR evolution effect than the carbons which are more distant to the nitrogen atom. The ITQ-3 sample has an Si/Al ratio of 11.4 (chemical analysis) which means that a high amount aluminum is in the framework, and multiple spin interactions are expected, which precludes quantitative distance analyses. The observation that the charged part of the organic molecule shows a larger dipole coupling is even more striking, as these multiple spin interactions are expected to cause a ^{27}Al lattice background with dipolar coupling to the entire SDA. In addition, this SDA has no mobile fragments for which local mobilities could alter the dipolar interaction. For the other examples in [203], additional experiments to investigate molecular motion were carried out to rule out the possibility that motional effects would cause erroneous conclusions. The overall conclusion of dipolar interaction analyses between SDAs and ^{11}B or ^{27}Al nuclei is a preferred orientation of the SDAs with their molecular dipole moments in the directions of negative charge centers in the zeolite frameworks. When the molecular dipole moment is small, because of the presence of two charge centers which cancel out each other's dipole moment, no preferred molecular orientation was found.

3.2 Confinement Effects of Adsorbed Probe Molecules

The physical properties of probe molecules adsorbed in the confined space of porous materials are known to vary in dependence of structural constraints on molecular motion. Detailed investigations of adsorption geometries are possible, when well-defined sites and loadings exist. This was the case for the adsorption of strongly interacting probe molecules, such as pyridine, on SiOH groups in the

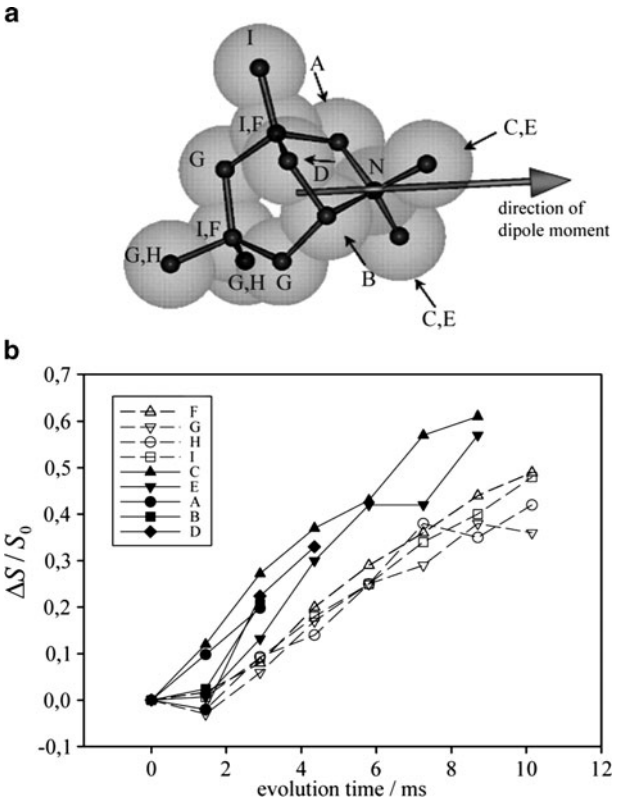

Fig. 5 (**a**) Structure directing agent (SDA) in the synthesis of zeolite ITQ-3; *N*: quaternary nitrogen; *A-I*: carbon atoms of SDA, 1,3,3,6,6-pentamethyl-6-azonium-bicyclo[3.2.1]octane; some ^{13}C line assignments were not unequivocally possible, so these are left open; the orientation of the dipole moment was calculated with a semiempirical AM-1 simulation with the origin at the center of gravity of the molecular cation; (**b**) $^{13}C\{^{1}H\}\{^{27}Al\}$ REAPDOR experiment on synthetic zeolite ITQ-3. Adapted from [204]

mesoporous material, MCM-41, or acetone and acetonitrile on acid sites in ZSM-5 zeolite. These systems were studied to determine the angle of motion of the adsorbed molecule near the adsorption sites [205, 206].

For high loadings of probe molecules, experimental properties are compared to the pure liquid or solid phase of the adsorbed species. For example, water can be stable in the liquid state in nanopores well below its bulk freezing point [207]. Obviously, the surface interactions of water in nanopores hinder crystallization. Grünberg et al. have investigated in detail by ^{1}H NMR various water loadings confined in the two mesoporous silicate materials MCM-41 and SBA-15 [208]. While MCM-41 shows a bimodal line distribution with two chemical shifts, whose line positions and intensities change with loading, only a single line is observed in

SBA-15 that shifts continuously to low field as the loading is increased. Different pore filling mechanisms were held responsible for the difference of the two materials. MCM-41 has a relatively small pore diameter (3.3 nm), and axial pore filling takes place at low relative water pressures. The two observed components were assigned to bulk water at the inner core of the filled pore and to water molecules that are in fast exchange with surface SiOH groups. In contrast, a gradual increase in the layer thickness of adsorbed water takes place in SBA-15, owing to its larger pore diameter (8 nm). The exchange between surface-bound water and free water in the adsorption layer shifts continuously as the loading increases. This radial pore filling mechanism leads to continuous change in ^{1}H chemical shifts until pore condensation occurs at higher fillings. A more detailed analysis of MCM-41 samples with different pore diameters using spin echo NMR shows that a transition between low and high mobility takes place as the temperature is increased [209]. Interestingly, this transition observed by NMR takes place at higher temperatures than in calorimetric DSC measurements, and the discrepancy of the two methods grows with smaller pore diameters. The authors have ascribed this effect to the larger fraction of less mobile water molecules on the first adsorption layers, as the pores become smaller.

Benzene is a probe molecule with weak surface interactions, and it may be employed to pronounce spatial confinement effects in favor of stronger surface interactions [205]. Typically, the motional properties are studied by static ^{2}H NMR. Bulk benzene has two solid phases: while phase I is characterized by a fast rotational jump diffusion of the molecule about its sixfold axis, phase II is static on the NMR time scale. The transition between both phases takes place between 88 and 206 K, and the ^{2}H NMR lineshapes at intermediate temperatures are heavily distorted as is typical for intermediate motional regimes. Such deviations from classical Pake lineshapes occur when rotational correlation times are comparable to quadrupolar frequencies. In contrast to bulk benzene crystals, the molecule shows a completely different motional behavior when it is adsorbed in the 8-nm pores of SBA-15. Here, the temperature-dependent experimental spectra were easily described by a superposition of the three phases, i.e., liquid, solid-I, and solid-II. No intermediate motional properties have been observed in SBA-15. When the same analysis is carried out on benzene in a porous glass with much wider pore diameters (30 nm), then the situation changes again. A complex superposition of various lineshapes, including distorted lines from intermediate motional regimes, as is typical for bulk benzene, describes the experimental data satisfactorily. These observations illustrate the confinement effects on molecular motion for which benzene is a useful probe molecule. Another example for its application in porous materials is a detailed study on zeolite NaY [210]. Tetrahedral jumps in the supercage of NaY have been identified, and the diffusion coefficients have been determined by one- and two-dimensional ^{2}H and ^{13}C NMR.

Confinement effects may also be employed to characterize the nucleation and growth of porous materials [211]. The underlying mechanisms of self-assembly and crystallization of these complex heterogeneous systems may be traced by solid state NMR methods well before their detection by diffraction methods.

4 Catalytic Sites and Catalysis

4.1 Characterization of Acid Sites

4.1.1 Brief Overview of ^{1}H NMR

One of the most important properties of zeolites is their ability to form strong Brønsted acid sites for heterogeneous catalysis. The Brønsted sites are bridging hydroxyl groups, SiO(H)Al, with a highly active threefold coordination of the oxygen atom. This protonation of a bridging oxygen atom weakens all local bonds, which is immediately reflected in spectroscopic properties. All NMR nuclei involved in this structure have been studied. While ^{1}H and ^{29}Si solid state NMR have been applied quite early, ^{27}Al and especially ^{17}O NMR data have become available more recently after the advancement of high-resolution MAS NMR methods of quadrupolar nuclei. Apart from the spectroscopic features of bare acid sites, their behaviors upon adsorption of probe molecules have also been reported in various publications. Since some excellent recent reviews are available [30, 212, 213], we will concentrate in this part on the more recent achievements in the field and limit this work to reporting on some selected NMR properties of acid sites. It should be mentioned that basic catalysis is also possible by zeolites due to Lewis basicity of framework oxygen atoms which is often enhanced by synthetic modifications (e.g., Cs^{+} ion exchange and/or metal supports). Some NMR aspects for their characterization using probe molecules have been published recently [212, 214].

The ^{1}H NMR chemical shift scale of zeolites in their acidic forms [212] exhibits resonance lines for nonhydrogen-bonded metal OH groups (−0.5 to 0.5 ppm), free SiOH groups (1.2–2.2 ppm), AlOH of extraframework Al with hydrogen bonding (2.4–3.6 ppm), CaOH, AlOH, LaOH in small cages or channels with hydrogen bonding (2.8–6.2 ppm), SiOHAl in large cavities (3.6–4.3 ppm), SiOHAl in confined environments (4.6–5.2 ppm) and SiOHAl with hydrogen bonding (5.2–8.0 ppm). Medium strong hydrogen bonds of internal SiOH groups have only been observed in nonacidic, as-made zeolites which contain a quaternary ammonium cation as SDA, and their chemical shifts have been discussed above in more detail in Sect. 2.3.1. Proton chemical shifts of Si–OH–B acid sites in boron zeolites have been assigned at 2.0–2.3 ppm in zeolite beta [100] which is close to the position of free SiOH groups. The discrimination between Si–OH–B and SiOH was possible by measuring ^{1}H–^{11}B dipolar interactions using the REDOR method.

Motion of Brønsted protons has also been addressed by several researchers. Such investigations require very careful dehydration procedures, since vehicle hopping with trace amounts of water may hamper the correct interpretation of the experimental data. A recent paper by Grey and coworkers [215] using H-ZSM-5 shows that the drying procedure has a significant influence. The often used drying process of zeolites in a dry helium gas flow is reported to be less reliable for obtaining a really dry sample than evacuation combined with a careful temperature ramp

protocol. This difference between helium and vacuum drying was earlier observed in ^{23}Na MAS NMR spectra of dehydrated NaY zeolites [216]. The observation of fast motion by NMR spectroscopy does not necessarily mean that conductivity, for example measured by impedance spectroscopy, exists. DC conductivity requires long-range transport, while dynamic averaging in NMR data can also result from local hopping mechanisms which do not contribute to long-range transport. Impedance measurements of zeolite ZSM-5 by Franke et al. with various hydration levels have revealed that conductivity is low until the water loading is sufficiently high to allow the conduction via the Grotthus mechanism at low temperatures, or a vehicle mechanism at elevated temperatures [217]. Notably, the work of Franke et al. implies that trace amounts of water have no significant influence on proton conductivity, although local mobilization may immediately be reflected in NMR analyses.

The successful application of ^{17}O NMR of zeolite acid sites has been discussed in Sect. 2.1.4 in the context of the ^{17}O chemical shift scale.

4.1.2 Phosphine Probe Molecules

Another possibility for characterizing zeolite acid sites is the adsorption of basic probe molecules and subsequent spectroscopic investigation of the adsorbed species. Phosphines or phosphine oxides have been quite attractive candidates due to the high chemical shift sensitivity of ^{31}P, when surface interactions take place [218–222]. This allows one to obtain information on the intrinsic accessibility and acidity behavior, as well as the existence of different sites in zeolite catalysts.

A remarkable application of phosphines by Grey and coworkers for acid site characterization is the use of diphosphines with alkyl chain spacers of different length between the phosphine moieties. Based on careful NMR analysis and appropriate loading levels with diphosphines, the Al distribution can be determined [223, 224]. The idea behind this tool is that the phosphine groups will be protonated, when they are close to an acid site in the zeolite structure. Protonation of both phosphine groups in one probe molecule will only occur, when the distance between the two acid sites is compatible with the molecular dimension of the diphosphine.

4.1.3 ^{27}Al and ^{11}B NMR

^{27}Al NMR of acid sites in the nonhydrated, activated state has long been hampered by the lack of suitable NMR techniques to measure lines with extremely large quadrupole coupling constants with high-resolution methods (invisible aluminum). The quadrupole coupling constants of acidic zeolites are extremely large for a "tetrahedral" Al coordination (C_q values of ~11–18 MHz are reported) [225]. The development of advanced MQMAS NMR techniques has led to a breakthrough in the characterization of ^{27}Al NMR parameters of acid sites [226–228]. Newer studies employ samples which are more realistic representatives for an acid catalyst

as used in catalytic reactions. Extraframework Al is generated either by ion exchange or steaming [228–230], and separated from framework Al by high-resolution ^{27}Al NMR methods. Even more challenging, due to more severe line overlapping, is the study of real samples taken from an industrial catalytic plant after use [231].

The effect of probe molecules on the ^{27}Al NMR has attracted some attention recently. In particular, the determination of the quadrupole coupling constant, C_q, is a sensitive means to learn more about the bonding situation at the aluminum in acid sites, and how it reflects the interaction with basic probe molecules. If one of the four oxygen atoms in an AlO_4 tetrahedral coordination is protonated, as in a zeolitic acid site, the coordination is somewhat in between a trigonal and a tetrahedral Al environment [232]. The protonated oxygen decreases its bond order to Al to approximately half of its size compared to an unprotonated zeolite.

A hydrogen bond acceptor molecule interacts with the acid proton in the bridging hydroxyl group which causes a weakening of the O–H bond of the hydroxyl group. Immediately, the Al–O bond of the same oxygen atom becomes stronger to maintain the valence of the oxygen. The symmetry of all four Al–O bonds increases, associated with a decrease of the C_q value.

This reduction in quadrupole coupling constants has been studied experimentally and theoretically by using DFT calculations. Recently, the groups of Hunger and Haw have proposed dependences between the quadrupole coupling constants and the proton affinities of probe molecules [233, 234]. While the Haw group quantifies C_q by employing theoretical calculations (such as DFT and Hartree–Fock methods), Hunger and coworkers report experimental data, combining high magnetic fields and a special MQMAS NMR method which is suitable for large quadrupole couplings [34]. Upon physical adsorption of weakly interacting molecules (e.g., N_2) the quadrupole coupling constant remains large. It is significantly reduced, when hydrogen bond acceptors (and donor acceptors such as methanol) are adsorbed, and a stronger decrease of the quadrupole coupling is observed for strong bases which induce proton transfer to the probe molecule. Upon proton transfer, the ^{27}Al quadrupole coupling constant is reduced to 19–36% of the value of the unloaded acidic zeolite. Interestingly, the behavior is somewhat different for B-ZSM-5, where the trigonal boron exhibits an unchanged quadrupole coupling unless proton transfer takes place. Upon proton transfer, a sudden collapse of the quadrupole coupling constant to about 30% of its original value is observed (a decrease from 2.65–2.70 MHz to 0.85 MHz).

We have unified experimental and theoretical DFT data to illustrate the significance of this difference between boron and aluminum, and to show the consistency of data from different laboratories and different methods. The results are shown in Fig. 6. For B-ZSM-5, proton transfer takes place at proton affinities of the probe molecule of at least 854 kJ/mol, which is somewhat higher than that reported for Al zeolites (821 kJ/mol) [235].

The data points in Fig. 6 show a slow decrease of C_q for aluminosilicate zeolites with increasing proton affinity of the probe molecule. Experimental data of methanol were not included in the illustration because of possible proton hopping which

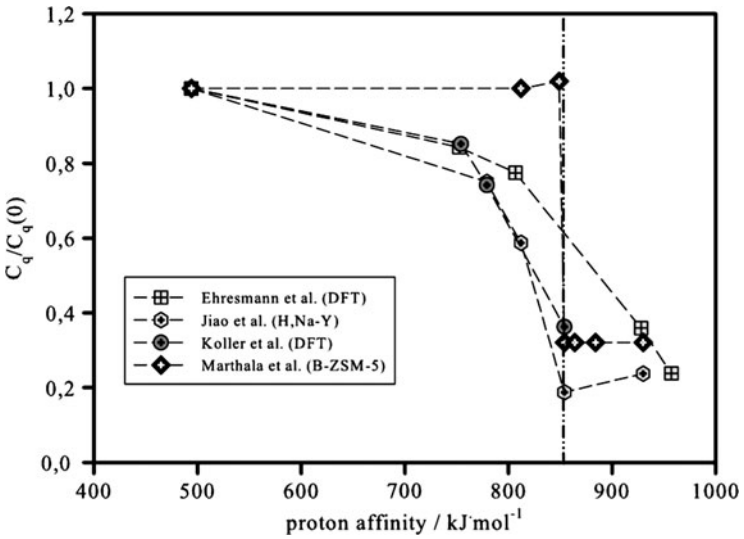

Fig. 6 Normalized quadrupole coupling constants, $C_q/C_q(0)$ as a function of proton affinity of adsorbed probe molecules. $C_q(0)$ is the quadrupole coupling constant of the unloaded acidic zeolite (assumed to be loaded with N_2 molecules, proton affinity of 494 kJ/mol). Data are taken from DFT calculations of Ehresmann [234] and Koller [232], and NMR measurements of Jiao [233], and Marthala [235]

is promoted by a vehicle mechanism induced by methanol between neighboring oxygen atoms in the zeolite framework [225]. The difference observed for boron compared to aluminum reflects the different hardness of the two elements. The boron–oxygen bonds are quite rigid towards bond distance variation, and the softer Al–O bonds are quite flexible under the influence of interacting guest molecules. These properties are relevant to the understanding of zeolite acidity. The catalytic activity of zeolites is a function of the deprotonation energy of the catalyst, but also of the adsorption energy of the protonated base. The latter is expected to depend on the surface bond variations when molecular interactions with guest species occur. Thus, bond variations in the zeolite framework might be of fundamental interest for a more detailed understanding of zeolite acidity. The data collected in Fig. 6 show that the quadrupole coupling constants offer an experimental approach to study such bonding variations.

4.1.4 Dipolar Interactions

The analysis of the structural properties of zeolitic acid sites based on dipolar interactions has further improved the understanding of acidity. Grey and Vega were the first to apply the $^1H\{^{27}Al\}$ TRAPDOR technique [36]. The REAPDOR method was first applied by Kalwei and coauthors [236–238] on bare acid sites and also on zeolites loaded with probe molecules. These methods allow one to distinguish

protons in acid sites from other, nonacidic groups. This is due to the strong ^{1}H–^{27}Al dipolar interaction which is typical for the Brønsted acid sites. In addition, the large quadrupolar coupling constant of ^{27}Al in these sites is also characteristic, as long as the structure is rigid and no motional averaging needs to be taken into account. The advantage of REAPDOR over TRAPDOR is that the former is independent of polar angles between the dipolar and quadrupolar interactions, whereas the latter shows a substantial dependence on these (typically unknown) orientations between the two interactions [236].

Figure 7 shows the $^{1}H\{^{27}Al\}$ REAPDOR analysis of zeolite H-ZSM-5 at 200 K. The two lines at 6.4 and 4.0 ppm are assigned to acid sites, and the small signal at 1.8 ppm is caused by silanol groups. Figure 7b shows that the two signals from acid sites exhibit quite similar REAPDOR evolution. The solid line is a numerical fit to the experimental data. The dipolar coupling constant for the best fit is in the range of 1,750–2,050 Hz corresponding to an H–Al distance of 2.48–2.62 Å. DFT calculations revealed a distance of 2.48 Å [232]. Earlier experimental reports by ^{1}H NMR spinning sideband analysis [239] or $^{27}Al\{^{1}H\}$SEDOR [240] gave H–Al distances of 2.50 and 2.43 Å, respectively. A similar analysis at T = 200 K on the zeolite adsorption complex with one methanol molecule per acid site yields two ^{1}H MAS NMR lines at 14.7 and 4.0 ppm for the two hydrogen-bonded protons, H1 and H2, in Fig. 7c. The fit of the $^{1}H\{^{27}Al\}$ REAPDOR data (Fig. 7d) yields the two Al–H distances indicated in Fig. 7c. At least the Al–H1 distance is in good agreement with DFT calculations [232], but the experimental Al–H2 distance is too large. This was ascribed to a selective mobility of H2, since its hydrogen bond strength is much weaker than that with H1.

The REAPDOR method has also been applied to zeolite mordenite [241]. A relatively weak ^{1}H–^{27}Al dipolar interaction was reported which translates into

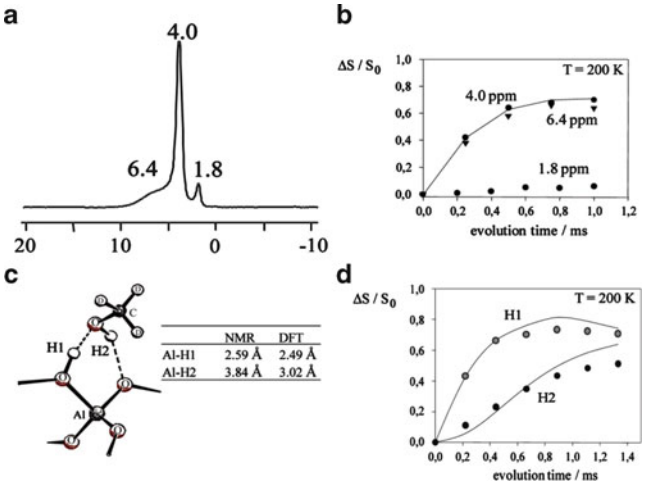

Fig. 7 $^{1}H\{^{27}Al\}$ REAPDOR analyses of bare zeolite H-ZSM-5 (**a**, **b**) and a 1:1 methanol loaded H-ZSM-5 (**c**, **d**). Adapted from [238] and [236] with permission from Elsevier

an H–Al distance of 5.25 Å. This too large distance was attributed to the mobility of the Brønsted proton.

4.2 *In Situ Solid State NMR of Catalytic Reactions*

In situ solid state NMR of catalytic conversion has matured into an important method for the study of reaction mechanisms. In the main, two technical approaches are possible: batch reactions carried out in sealed vessels under magic angle spinning conditions and continuous flow (CF) conditions in which the reactants are fed into a spinning rotor. While batch reactions are technically versatile to employ, as for example demonstrated for water adsorption on ZSM-5 using a breakable glass capillary as adsorbate storage container [242], the CF method is able to mimic industrial processes more realistically, although the latter is more demanding on the design of special equipment. Isotopic labeling and scrambling in the product mixture or in situ observation of intermediates are typical experimental strategies to investigate catalytic reaction mechanisms. A number of review articles have appeared to which the reader is referred for more detailed information on technical setups and for an overview of reactions studied [40, 243–248]. Apart from an overview of chemical reactions studied by in situ NMR experiments, Hunger and Wang also highlight different experimental designs of in situ NMR equipment and special aspects of high-temperature experiments [40]. The same group has also constructed an impressive MAS NMR probehead that allows one to run UV/VIS spectra simultaneously [249] through glass fiber optics.

With the natural fossil fuel resources in mind, it is not surprising that the catalytic conversion of low molecular weight reactants, such as methanol/ethanol [238, 250–264] or light alkanes [265–271], to higher hydrocarbons is the most popular family of reactions investigated by in situ NMR methods. Such catalytic reactions may contribute to the future supply of liquid fuels, or they are important for the manufacturing of intermediates in chemical industry. One of the most intriguing questions is the mechanism of hydrocarbon formation from methanol, since the formation of C–C bonds is still a matter of debate. Nevertheless, solid state NMR experiments have shed some light in possible reaction pathways, involving a "hydrocarbon pool" mechanism. In this model, impurities such as benzene derivatives or cyclopentyl cations are expected to play an important role in hydrocarbon bond formation. Also, surface methoxy groups which can be observed after reaction of methanol with zeolite acid sites are suggested to participate in catalytic reactions (see [40, 238, 264, 272, 273] and references therein). The assignment of ^{13}C NMR lines to surface methoxy groups is sometimes ambiguous due to the existence of several signals. The chemical shift of surface methoxy species varies with the zeolite framework basicity [274]. The ^{27}Al quadrupole coupling constant, C_q, in zeolite Y near surface methoxy groups (12.8 MHz) is about 2 MHz smaller than in acid sites before methoxylation (14.8 MHz), as reported experimentally [275] and by DFT calculations [232]. Van Wüllen and coauthors have used the ^{13}C{^{27}Al}

REAPDOR method to measure the C–Al distances by numerical simulations of the time-dependence of the REAPDOR evolution effect. An internuclear C–Al distance of 3.1 Å was determined for a signal at 57.3 ppm in ZSM-5, which is in excellent agreement with quantum chemical calculations of surface methoxy species [232]. Larger C–Al distances (>4 Å) were determined for nearby signals at 60.0 and 61.7 ppm.

Based on in situ ^{13}C NMR data, surface methoxy groups are reported to form hydrocarbons at temperatures of 523 K and above [273]. The authors have suggested that these hydrocarbons may contribute to the "hydrocarbon pool" that is established to participate in the catalytic reaction mechanism to form higher hydrocarbons from methanol. Other reactions with amines or halides have also been published [276].

Of course, other reaction types have been also investigated more recently, such as the Beckmann rearrangement [247, 277, 278] or ethylbenzene disproportionation [279, 280], just to name a couple. In situ NMR methods are expected to play a vital role in the future science of heterogeneous catalysis.

5 Mobilities of Sodium Cations in Sodalite and Cancrinite

Extraframework cations are needed in anionic zeolites for charge balance, and for several zeolite topologies their locations are well investigated [281, 282]. Different cations have been investigated by solid state NMR in the past with different NMR properties and different project targets. We restrict this section to a tutorial example on sodium cation motion in sodalite and cancrinite structures [283–285]. ^{23}Na has a nuclear electric quadrupole moment, and quadrupolar interaction is useful to investigate jump processes, especially when they are well defined.

The investigation of dynamics by NMR methods usually requires a model with an underlying analytical theory to simulate experimental data. The rationalization of the model and the discrimination of alternatives demand a critical check of the case under investigation.

Numerous examples for polymers exist using ^{2}H solid state NMR, and the underlying theory can be found in detail in the monograph of Schmidt-Rohr and Spiess [286]. The basic principle for jump analysis using ^{23}Na NMR lineshape analysis is the same as for ^{2}H, when the motional exchange rate is considerably faster than the static linewidth of the rigid structure (fast motional limit). For an exchange rate which is much slower than the static linewidth, no lineshape effects are observed in the NMR spectra. In such cases, two-dimensional exchange techniques are able to extend the time scale of NMR to slower processes, and the limit is usually set by the T_2 relaxation time. In the intermediate motional regime, that is when the exchange rate is on the same time scale as the static linewidth, complicated lineshape distortions are observed, and more advanced analytical machinery is necessary for the theoretical description of the spectra. We show here an illustrative example of the simplest case of two-site jump processes of sodium cations in the fast

motional limit. Further information on sophisticated NMR analysis of dynamic processes in solids may be found in [286, 287]. Additional examples of NMR on extraframework cations and their mobilities in zeolites may be found in [288–292].

The quadrupolar interaction is an interaction between the nuclear electric quadrupole moment, Q, of the nucleus under investigation and a local EFG, $e \cdot q = V_{zz}$. The EFG is a second-rank tensor with the principal components, V_{xx}, V_{yy}, V_{zz}. The quadrupole coupling constant is given by:

$$C_q = \frac{e^2 qQ}{h}, \tag{3}$$

where e is the electric charge and h the Planck constant. The asymmetry parameter is

$$\eta = \frac{V_{yy} - V_{xx}}{V_{zz}}, \ (V_{xx} \leq V_{yy} \leq V_{zz}). \tag{4}$$

When a sodium cation jumps between two sites with the same EFG tensor components and the same residence times on both positions, but different orientations, then the two-site exchange process can be described by tensor averaging of the two positions. Depending on the jump angle of the tensor, the motionally averaged principal components, V_{xx}', V_{yy}', and V_{zz}', may eventually have to be redefined in ordering to fulfill the requirement in parenthesis in (4).

Figure 8a shows the motionally averaged quadrupole coupling constant, $\langle C_q \rangle / C_q$, and asymmetry parameter, $\langle n \rangle$, for a two-site jump between axially symmetric equivalent sites. At jump angles of 70° and 109° the principal components (V_{xx}, V_{yy}, V_{zz}) have to be rearranged in order, which leads to the discontinuities in the curve shapes of Fig. 8a.

A tetrahedral jump (109°) for example reduces $\langle C_q \rangle$ to half of its original value, C_q, and $\langle n \rangle = 1$. This can be observed for cation hopping in the cages of anhydrous sodalite which is an aluminosilicate (Si/Al = 1) with a space-filling packing of sodalite cages (Fig. 8b). The sodalite cage has six four-ring and eight six-ring windows, and four of the six-rings in tetrahedral orientation can be occupied by cations within the cage. The other four windows may be occupied in neighboring cages. Double occupancy on both sides of a window is not possible due to charge repulsion. The specific sodalite sample used for this study has three Na^+ cations in the cage, and one window is left empty. The unit cell contains two such cages which is reflected in the formula, $|Na_6\square_2|[Si_6Al_6O_{12}]$-SOD.

Due to the tetrahedral arrangement of the windows within the cage, tetrahedral jumps of the cations are feasible. This jump model is confirmed by the averaged parameters obtained by lineshape simulations of the broad lines at 295 and 813 K. C_q is reduced at 813 K to about half of its original value at 295 K, and the averaged asymmetry parameter, $\langle \eta \rangle$, is 1. Especially $\langle \eta \rangle$ is a very sensitive parameter on jump angle due to the steepness of the curve in Fig. 8a.

It should be mentioned that a jump by another angle rather than the tetrahedral angle (109°) also leads to $\langle \eta \rangle = 1$, that is a 70° jump. Actually, this hopping would

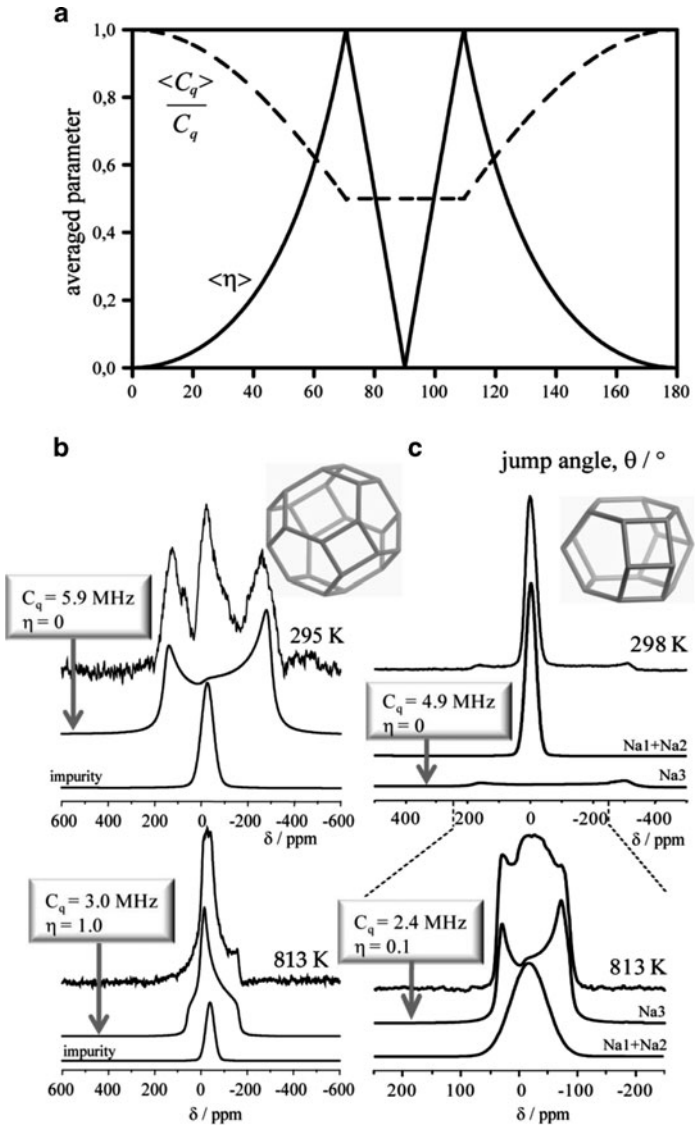

Fig. 8 (**a**) Motionally averaged quadrupole coupling constant (C_q) and asymmetry parameter (η) for a two-site jump between axially symmetric equivalent sites; (**b**) static ^{23}Na NMR spectra (spin echo) of sodalite at 295 and 813 K, the *narrow line* is an impurity with hydrated sodalite, the structure shows the sodalite cage with alternating Si or Al at the corners and oxygen bridges (not shown) along the *connecting lines*; (**c**) static ^{23}Na NMR spectra (spin echo) of chromate cancrinite at 298 and 813 K, the *broad line* is assigned to a cation within the cancrinite cage, the *narrow line* is due to two unresolved positions in large 12-ring channels, where also the chromate anions are located

also be feasible when a cation from a window position of a neighboring cage penetrates into the cage and then jumps on the vacant site within this cage. Lineshape analysis cannot distinguish between these two possibilities, intracage (109°) and intercage (70°) hopping.

A quite different situation exists in cancrinite. Figure 8c shows the data for chromate cancrinite, $|Na_4CrO_4||Na_2|[Si_6Al_6O_{12}]$-CAN. Here, two cancrinite cages (Fig. 8c) per unit cell contain one sodium cation each. The CAN structure also has large 12-ring channels, in which additional sodium cations and chromate anions are located. The broad line in Fig. 8c is assigned to the sodium cations in the small cancrinite cages which have two six-rings at the bottom and top of the cage, and three six-rings on the side walls. The sodium cations carry out hopping processes between the six-rings at the bottom and/or top and the side walls corresponding to a jump angle of 90°. This is reflected by the averaged $\langle C_q \rangle$ to half of its original value and an averaged asymmetry parameter close to 0. The simulated $\langle \eta \rangle$ of 0.1 allows slight deviations of the jump angle from 90°.

The hopping process in the cancrinite cage is only of local nature, and long-range conductivity has been observed only for the sodium cations in the one-dimensional 12-ring channels, where the chromate ions are also located [283].

References

1. Schüth F, Sing KSW, Weitkamp J (2002) Handbook of porous solids. Wiley VCH, Weinheim
2. Van Bekkum H, Flanigen EM, Jacobs P, Jansen JC (2001) Introduction to zeolite science and practice. Elsevier, Amsterdam
3. Vermeiren W, Gilson JP (2009) Top Catal 52:1131
4. Jiang JX, Yu JH, Corma A (2010) Angew Chem Int Ed 49:3120
5. Davis ME (2002) Nature 417:813
6. Corma A (1997) Chem Rev 97:2373
7. Gonzalez J, Devi RN, Tunstall DP, Cox PA, Wright PA (2005) Microporous Mesopor Mater 84:97
8. Gould SL, Tranchemontagne D, Yaghi OM, Garcia-Garibay MA (2008) J Am Chem Soc 130:3246
9. Jiang YJ, Huang J, Kasumaj B, Jeschke G, Hunger M, Mallat T, Baiker A (2009) J Am Chem Soc 131:2058
10. Friščić T, Reid DG, Halasz I, Stein RS, Dinnebier RE, Duer MJ (2010) Angew Chem Int Ed 49:712
11. Li QW, Zhang WY, Miljanic OS, Sue CH, Zhao YL, Liu LH, Knobler CB, Stoddart JF, Yaghi OM (2009) Science 325:855
12. Bajpe SR, Kirschhock CEA, Aerts A, Breynaert E, Absillis G, Parac-Vogt TN, Giebeler L, Martens JA (2010) Chem Eur J 16:3926
13. Müller M, Hermes S, Kähler K, van den Berg MWE, Muhler M, Fischer RA (2008) Chem Mater 20:4576
14. Volkringer C, Loiseau T, Haouas M, Taulelle F, Popov D, Burghammer M, Riekel C, Zlotea C, Cuevas F, Latroche M, Phanon D, Knöfelv C, Llewellyn PL, Férey G (2009) Chem Mater 21:5783
15. Volkringer C, Loiseau T, Guillou N, Férey G, Haouas M, Taulelle F, Audebrand N, Margiolaki I, Popov D, Burghammer M, Riekel C (2009) Cryst Growth Des 9:2927

16. Volkringer C, Loiseau T, Férey G, Morais CM, Taulelle F, Montouillout V, Massiot D (2007) Microporous Mesopor Mater 105:111
17. Baerlocher C, McCusker LB. International Zeolite Association; Database of Zeolite Structures, http://www.iza-online.org/
18. Kresge CT, Leonowicz ME, Roth WJ, Vartuli JC, Beck JS (1992) Nature 359:710
19. Di Renzo F, Galarneau A, Trens P, Fajula F (2002) In: Schüth F, Sing KSW, Weitkamp J (eds) Handbook of porous solids, vol 3. Wiley-VCH, Weinheim, p 1311
20. Meynen V, Cool P, Vansant EF (2009) Microporous Mesopor Mater 125:170
21. Engelhardt G, Michel D (1987) High-resolution solid-state NMR of silicates and zeolites. Wiley, Chichester
22. Thomas JM (2007) Microporous Mesopor Mater 104:5
23. Engelhardt G (2001) In: van Bekkum H, Flanigen EM, Jacobs PA (eds) Studies in surface science and catalysis, vol 137. Elsevier, Amsterdam, p 387
24. Engelhardt G, Koller H (1994) In: Diehl P, Fluck E, Günther H, Kosfeld R, Seelig J (eds) Solid-state NMR II: inorganic matter (NMR basic principles and progress), vol 31. Springer, Berlin, p 1
25. Gédéon A, Fernandez C (2007) In: Čejka J, van Bekkum H, Corma A, Schüth F (eds) Introduction to zeolite science and practice. Elsevier, Amsterdam
26. Parker WO (2000) Comments Inorg Chem 22:31
27. Fyfe CA, Feng Y, Grondey H, Kokotailo GT, Gies H (1991) Chem Rev 91:1525
28. Klinowski J (1991) Chem Rev 91:1459
29. Geppi M, Borsacchi S, Mollica G, Veracini CA (2009) Appl Spectr Rev 44:1
30. Hunger M, Brunner E (2004) In: Karge HG, Weitkamp J (eds) Molecular sieves – science and technology, vol 4. Springer, Berlin, p 2733
31. Frydman L, Harwood JS (1995) J Am Chem Soc 117:5367
32. Alemany LB, Steuernagel S, Amoureux JP, Callender RL, Barron AR (1999) Solid State Nucl Magn Reson 14:1
33. Kentgens APM, Verhagen R (1999) Chem Phys Lett 300:435
34. Iuga D, Schäfer H, Verhagen R, Kentgens APM (2000) J Magn Reson 147:192
35. Gullion T, Schaefer J (1989) J Magn Reson 81:196
36. Grey CP, Vega AJ (1995) J Am Chem Soc 117:8232
37. Chopin L, Vega S, Gullion T (1998) J Am Chem Soc 120:4406
38. Ba Y, Kao HM, Grey GP, Chopin L, Gullion T (1998) J Magn Reson 133:104
39. Hunger M, Weitkamp J (2001) Angew Chem Int Ed 40:2954
40. Hunger M, Wang W (2006) Adv Catal 50:149
41. Hochgräfe M, Gies H, Fyfe CA, Feng Y, Grondey H (2000) Chem Mater 12:336
42. Bull I, Lightfoot P, Villaescusa LA, Bull LM, Gover RKB, Evans JSO, Morris RE (2003) J Am Chem Soc 125:4342
43. Pradel A, Taillades G, Ribes M, Eckert H (1995) J NonCryst Solids 188:75
44. Dong WY, Qiu XP, Ren Y, Long YC (2002) Chem Lett 374
45. De Luca P, Violante D, Vuono D, Catanzaro L, Nagy JB, Nastro A (2004) Microporous Mesopor Mater 71:39
46. Jones CW, Hwang SJ, Okubo T, Davis ME (2001) Chem Mater 13:1041
47. Rocha J, Brãndao P, Anderson MW, Ohsuna T, Terasaki O (1998) Chem Commun 667
48. Cho HH, Kim SH, Kim YG, Kim YC, Koller H, Camblor MA, Hong SB (2000) Chem Mater 12:2292
49. Chao KJ, Sheu SP, Lin LH, Genet MJ, Feng MH (1997) Zeolites 18:18
50. Occelli ML, Eckert H, Wölker A, Auroux A (1999) Microporous Mesopor Mater 30:219
51. Hazm JE, Caullet P, Paillaud JL, Soulard M, Delmotte L (2001) Microporous Mesopor Mater 43:11
52. Ogura M, Nakata S, Kikuchi E, Matsukata M (2001) J Catal 199:41
53. Kim SJ, Jung KD, Joo OS (2004) J Porous Mater 11:211
54. Hong SB, Lee SH, Shin CH, Woo AJ, Alvarez LJ, Zicovich-Wilson CM, Camblor MA (2004) J Am Chem Soc 126:13742

55. Camblor MA, Davis ME (1994) J Phys Chem 98:13151
56. Camblor MA, Lobo RF, Koller H, Davis ME (1994) Chem Mater 6:2193
57. Röhrig C, Dierdorf I, Gies H (1995) J Phys Chem Solids 56:1369
58. Röhrig C, Gies H (1995) Angew Chem Int Ed Engl 34:63
59. Balmer ML, Bunker BC, Wang LQ, Peden CHF, Su YL (1997) J Phys Chem B 101:9170
60. Brãndao P, Philippou A, Valente A, Rocha J, Anderson M (2001) Phys Chem Chem Phys 3:1773
61. Goa Y, Wu P, Tatsumi T (2004) J Catal 224:107
62. Lin Z, Ferreira A, Rocha J (2003) J Solid State Chem 175:258
63. Brãndao P, Valente A, Philippou A, Ferreira A, Anderson MW, Rocha J (2002) J Mater Chem 12:3819
64. Liu YL, Du HB, Xiao FS, Zhu GS, Pang WQ (2000) Chem Mater 12:665
65. Liu YL, Du HB, Xu YH, Ding H, Pang WQ, Yue Y (1999) Microporous Mesopor Mater 28:511
66. Rocha J, Brãndao P, Lin Z, Esculcas AP, Ferreira A, Anderson MW (1996) J Phys Chem 100:14978
67. Rocha J, Anderson MW (2000) Eur J Inorg Chem 801
68. Johnson GM, Mead PJ, Dann SE, Weller MT (2000) J Phys Chem B 104:1454
69. Loewenstein W (1954) Am Mineral 39:92
70. Hammond KD, Dogan F, Tompsett GA, Agarwal V, Conner WC, Grey CP, Auerbach SM (2008) J Am Chem Soc 130:14912
71. Dogan F, Hammond KD, Tompsett GA, Huo H, Conner WC, Auerbach SM, Grey CP (2009) J Am Chem Soc 131:11062
72. Hammond KD, Gharibeh M, Tompsett GA, Dogan F, Brown AV, Grey CP, Auerbach SM, Conner WC (2010) Chem Mater 22:130
73. Kempgens P, Harris RK, Yu ZB, Thompson DP (2001) J Mater Chem 11:2507
74. Stadler F, Schnick W (2007) Z Anorg Allg Chem 633:589
75. Kechele JA, Schmolke C, Lupart S, Schnick W (2010) Z Anorg Allg Chem 636:176
76. Kechele JA, Oeckler O, Stadler F, Schnick W (2009) Solid State Sci 11:537
77. Stadler F, Schnick W (2006) Z Anorg Allg Chem 632:949
78. Koroglu A, Thompson DP, Apperley DC, Harris RK (2004) J Solid State Chem 177:2530
79. Brouwer DH, Enright GD (2008) J Am Chem Soc 130:3095
80. Dempsey E (1968) Molecular sieves. Society of Chemical Industry, London, 293
81. von Ballmoos R, Meier WM (1981) Nature 289:782
82. Akporiaye DE, Dahl IM, Mostad HB, Wendelbo R (1996) J Phys Chem 100:4148
83. Feijen EJP, Lievens JL, Martens JA, Grobet PJ, Jacobs PA (1996) J Phys Chem 100:4970
84. Kato M, Hattori T (1998) Phys Chem Miner 25:556
85. Korányi TI, Nagy JB (2005) J Phys Chem B 109:15791
86. Korányi TI, Nagy JB (2006) J Phys Chem B 110:14728
87. Korányi TI, Nagy JB (2007) J Phys Chem C 111:2520
88. Korányi TI, Nagy JB (2009) J Phys Chem C 113:907
89. Sklenak S, Dědeček J, Li CB, Wichterlová B, Gábová V, Sierka M, Sauer J (2007) Angew Chem Int Ed 46:7286
90. Dědeček J, Sklenak S, Li C, Wichterlová B, Gábová V, Brus J, Sierka M, Sauer J (2009) J Phys Chem C 113:1447
91. Dědeček J, Sklenak S, Li CB, Gao F, Brus J, Zhu QJ, Tatsumi T (2009) J Phys Chem C 113:14454
92. Mériaudeau P, Tuel A, Vu TTH (1999) Catal Lett 61:89
93. Fyfe CA, Wongmoon KC, Huang Y, Grondey H, Mueller KT (1995) J Phys Chem 99:8707
94. Ganapathy S, Kumar R, Montouillout V, Fernandez C, Amoureux JP (2004) Chem Phys Lett 390:79
95. Scholle KFMGJ, Veeman WS (1985) Zeolites 5:118
96. Fild C, Eckert H, Koller H (1998) Angew Chem Int Ed 37:2505

97. Fild C, Shantz DF, Lobo RF, Koller H (2000) Phys Chem Chem Phys 2:3091
98. Axon SA, Klinowski J (1994) J Phys Chem 98:1929
99. de Ruiter R, Kentgens APM, Grootendorst J, Jansen JC, van Bekkum H (1993) Zeolites 13:128
100. Koller H, Fild C, Lobo RF (2005) Microporous Mesopor Mater 79:215
101. Koller H (2004) In: Occelli M (ed) Studies in surface science and catalysis, vol 149. Elsevier, Amsterdam, p 105
102. Goursot A, Berthomieu D (2004) Magn Reson Chem 42:S180
103. Ashbrook SE, Smith ME (2006) Chem Soc Rev 35:718
104. Timken HKC, Turner GL, Gilson JP, Welsh LB, Oldfield E (1986) J Am Chem Soc 108:7231
105. Timken HKC, Janes N, Turner GL, Lambert SL, Welsh LB, Oldfield E (1986) J Am Chem Soc 108:7236
106. Amoureux JP, Bauer F, Ernst H, Fernandez C, Freude D, Michel D, Pingel UT (1998) Chem Phys Lett 285:10
107. Pingel UT, Amoureux JP, Anupold T, Bauer F, Ernst H, Fernandez C, Freude D, Samoson A (1998) Chem Phys Lett 294:345
108. Freude D, Loeser T, Michel D, Pingel U, Prochnow D (2001) Solid State Nucl Magn Reson 20:46
109. Loeser T, Freude D, Mabande GTP, Schwieger W (2003) Chem Phys Lett 370:32
110. Zhao P, Neuhoff PS, Stebbins JF (2001) Chem Phys Lett 344:325
111. Bull LM, Cheetham AK, Anupold T, Reinhold A, Samoson A, Sauer J, Bussemer B, Lee Y, Gann S, Shore J, Pines A, Dupree R (1998) J Am Chem Soc 120:3510
112. Bull LM, Bussemer B, Anupold T, Reinhold A, Samoson A, Sauer J, Cheetham AK, Dupree R (2000) J Am Chem Soc 122:4948
113. Stebbins JF, Zhao PD, Lee SK, Cheng X (1999) Am Mineral 84:1680
114. Cheng X, Zhao PD, Stebbins JF (2000) Am Mineral 85:1030
115. Neuhoff PS, Shao P, Stebbins JF (2002) Microporous Mesopor Mater 55:239
116. Schneider D, Toufar H, Samoson A, Freude D (2009) Solid State Nucl Magn Reson 35:87
117. Readman JE, Grey CP, Ziliox M, Bull LM, Samoson A (2004) Solid State Nucl Magn Reson 26:153
118. Readman JE, Kim N, Ziliox M, Grey CP (2002) Chem Commun 2808
119. Peng L, Huo H, Liu Y, Grey CP (2007) J Am Chem Soc 129:335
120. Peng LM, Liu Y, Kim NJ, Readman JE, Grey CP (2005) Nat Mater 4:216
121. Peng L, Huo H, Gan Z, Grey CP (2008) Microporous Mesopor Mater 109:156
122. Cadars S, Lesage A, Hedin N, Chmelka BF, Emsley L (2006) J Phys Chem B 110:16982
123. Kristiansen PE, Carravetta M, Lai WC, Levitt MH (2004) Chem Phys Lett 390:1
124. Brouwer DH, Kristiansen PE, Fyfe CA, Levitt MH (2005) J Am Chem Soc 127:542
125. Christiansen SC, Zhao DY, Janicke MT, Landry CC, Stucky GD, Chmelka BF (2001) J Am Chem Soc 123:4519
126. Cadars S, Mifsud N, Lesage A, Epping JD, Hedin N, Chmelka BF, Emsley L (2008) J Phys Chem C 112:9145
127. Hedin N, Graf R, Christiansen SC, Gervais C, Hayward RC, Eckert J, Chmelka BF (2004) J Am Chem Soc 126:9425
128. Brouwer DH (2008) J Magn Reson 194:136
129. Brouwer DH (2008) J Am Chem Soc 130:6306
130. Cadars S, Brouwer DH, Chmelka BF (2009) Phys Chem Chem Phys 11:1825
131. Koller H, Lobo RF, Burkett SL, Davis ME (1995) J Phys Chem 99:12588
132. Shantz DF, Schmedt auf der Günne J, Koller H, Lobo RF (2000) J Am Chem Soc 122:6659
133. Parker WO, Millini R (2006) J Am Chem Soc 128:1450
134. Wang YX, Gies H, Lin JH (2007) Chem Mater 19:4181
135. Gardiennet C, Tekely P (2002) J Phys Chem B 106:8928
136. Wolf I, Gies H, Fyfe CA (1999) J Phys Chem B 103:5933
137. Borowski M, Wolf I, Gies H (2002) Chem Mater 14:38

138. Apperley DC, Hudson MJ, Keene MTJ, Knowles JA (1995) J Mater Chem 5:577
139. Burton A, Accardi RJ, Lobo RF, Falcioni M, Deem MW (2000) Chem Mater 12:2936
140. Ai XJ, Deng F, Dong JX, Chen L, Ye CH (2002) J Phys Chem B 106:9237
141. Heidemann D (1994) In: Colombet P, Grimmer AR (eds) Application of NMR spectroscopy to cement science. Gordon and Breach Science, Reading, p 77
142. Yesinowski JP, Eckert H, Rossman GR (1988) J Am Chem Soc 110:1367
143. Brown ID, Altermatt D (1985) Acta Crystallogr, Sect B: Struct Sci 41:244
144. Brown ID (1976) Acta Crystallogr A 32:24
145. Lutz HD, Jung C, Trömel M, Lösel J (1995) J Mol Struct 351:205
146. Brunner E, Sternberg U (1998) Progr Nucl Magn Reson Spectr 32:21
147. Baerlocher C, Xie D, McCusker LB, Hwang SJ, Chan IY, Ong K, Burton AW, Zones SI (2008) Nat Mater 7:631
148. Bushuev YG, Sastre G (2009) J Phys Chem C 113:10877
149. Koller H, Wölker A, Eckert H, Panz C, Behrens P (1997) Angew Chem Int Ed 36:2823
150. Koller H, Wölker A, Villaescusa LA, Díaz-Cabañas MJ, Valencia S, Camblor MA (1999) J Am Chem Soc 121:3368
151. Fyfe CA, Brouwer DH, Lewis AR, Villaescusa LA, Morris RE (2002) J Am Chem Soc 124:7770
152. Fyfe CA, Brouwer DH, Lewis AR, Chézeau JM (2001) J Am Chem Soc 123:6882
153. Camblor MA, Barrett PA, Díaz-Cabañas MJ, Villaescusa LA, Puche M, Boix T, Pérez E, Koller H (2001) Microporous Mesopor Mater 48:11
154. Wang YX, Song JQ, Gies H (2003) Solid State Sci 5:1421
155. Vidal-Moya JA, Blasco T, Rey F, Corma A, Puche M (2003) Chem Mater 15:3961
156. Blasco T, Corma A, Díaz-Cabañas MJ, Rey F, Vidal-Moya JA, Zicovich-Wilson CM (2002) J Phys Chem B 106:2634
157. Blasco T, Corma A, Díaz-Cabañas MJ, Rey F, Rius J, Sastre G, Vidal-Moya JA (2004) J Am Chem Soc 126:13414
158. Vidal-Moya JA, Blasco T, Corma A, Navarro MT, Rey F (2004) In: van Steen E, Claeys M, Callanan LH (eds) Studies in surface science and catalysis, vol 154, part 2. Elsevier, Amsterdam, p 1289
159. Villaescusa LA, Bull I, Wheatley PS, Lightfoot P, Morris RE (2003) J Mater Chem 13:1978
160. Zones SI, Darton RJ, Morris R, Hwang SJ (2005) J Phys Chem B 109:652
161. Sastre G, Vidal-Moya JA, Blasco T, Rius J, Jorda JL, Navarro MT, Rey F, Corma A (2002) Angew Chem Int Ed 41:4722
162. Valiullin R, Kärger J, Gläser R (2009) Phys Chem Chem Phys 11:2833
163. Ulrich K, Freude D, Galvosas P, Krause C, Kärger J, Caro J, Poladli P, Papp H (2009) Microporous Mesopor Mater 120:98
164. Gratz M, Wehring M, Galvosas P, Stallmach F (2009) Microporous Mesopor Mater 125:30
165. Feldhoff A, Caro J, Jobic H, Ollivier J, Krause CB, Galvosas P, Kärger J (2009) Chemphyschem 10:2429
166. Romanenko KV (2010) Ann Rep NMR Spectr 69:1
167. Bonardet JL, Fraissard J, Gédéon A, Springuel-Huet MA (1999) Catal Rev Sci Eng 41:115
168. Fraissard J (2007) In: Xu R, Gao Z, Chen J, Yan W (eds) From zeolites to porous MOF materials – the 40th anniversary of International Zeolite Conference. Elsevier, Amsterdam, p 707
169. Habib S, Launay F, Springuel-Huet MA, Guenneau F, Mazaj M, Tusar NN, Gédéon A (2009) J Porous Mater 16:349
170. Breeze SR, Lang SJ, Nosov AV, Sanchez A, Moudrakovski IL, Ratcliffe CI, Ripmeester JA (2000) In: Sayari A (ed) Studies in surface science and catalysis, vol 129. Elsevier, Amsterdam, p 491
171. Springuel-Huet MA, Bonardet JL, Gédéon A, Fraissard J (1999) Magn Reson Chem 37:S1
172. Cleveland ZI, Meersmann T (2007) Magn Reson Chem 45:S12
173. Kolodziejski W, Klinowski J (2002) Chem Rev 102:613

174. Christiansen SC, Hedin N, Epping JD, Janicke MT, del Amo Y, Demarest M, Brzezinski M, Chmelka BF (2006) Solid State Nucl Magn Reson 29:170
175. Fyfe CA, Brouwer DH, Tekely P (2005) J Phys Chem A 109:6187
176. Fyfe CA, Lewis AR (2000) J Phys Chem B 104:48
177. Bertmer M, Eckert H (1999) Solid State Nucl Magn Reson 15:139
178. Van Eck ERH, Janssen R, Maas WEJR, Veeman WS (1990) Chem Phys Lett 174:428
179. Shantz DF, Lobo RF (1998) J Am Chem Soc 120:2482
180. Shantz DF, Lobo RF (1998) Chem Mater 10:4015
181. Shantz DF, Lobo RF, Fild C, Koller H (2000) In: Corma A, Melo FV, Mendioroz S, Fierro JLG (eds) Studies in surface science and catalysis, vol 130. Elsevier, Amsterdam, p 845
182. Fild C, Eckert H, Koller H (2000) J Am Chem Soc 122:12590
183. Fyfe CA, Brouwer DH (2000) Micropor Mesopor Mater 39:291
184. Lim KH, Jousse F, Auerbach SM, Grey CP (2001) J Phys Chem B 105:9918
185. Morell H, Angermund K, Lewis AR, Brouwer DH, Fyfe CA, Gies H (2002) Chem Mater 14:2192
186. Fyfe CA, Diaz AC (2002) J Phys Chem B 106:2261
187. Fyfe CA, Diaz AC, Grondey H, Lewis AR, Förster H (2005) J Am Chem Soc 127:7543
188. Fyfe CA, Brouwer DH (2004) J Am Chem Soc 126:1306
189. Magusin PCMM, Zorin VE, Aerts A, Houssin CJY, Yakovlev AL, Kirschhock CEA, Martens JA, van Santen RA (2005) J Phys Chem B 109:22767
190. Holland GP, Cherry BR, Alam TM (2004) J Phys Chem B 108:16420
191. Holland GP, Alam TM (2005) Phys Chem Chem Phys 7:1739
192. Fyfe CA, Brouwer DH (2006) Can J Chem 84:345
193. Fyfe CA, Brouwer DH (2006) J Am Chem Soc 128:11860
194. Zhu JF, Mosey N, Woo T, Huang YN (2007) J Phys Chem C 111:13427
195. Zhu JF, Trefiak N, Woo T, Huang YN (2008) Microporous Mesopor Mater 114:474
196. Zhu JF, Huang YN (2008) J Phys Chem C 112:14241
197. Fyfe CA, Darton RJ, Schneider C, Scheffler F (2008) J Phys Chem C 112:80
198. Romanova EE, Krause CB, Stepanov AG, Wilczoke U, Schmidt W, van Baten JM, Krishna R, Pampel A, Kärger J, Freude D (2008) Solid State Nucl Magn Reson 33:65
199. Fyfe CA, Lee JSJ (2008) J Phys Chem C 112:500
200. Kirmayer S, Dovgolevsky E, Kalina M, Lakin E, Cadars S, Epping JD, Fernandez-Arteaga A, Rodriguez-Abreu C, Chmelka BF, Frey GL (2008) Chem Mater 20:3745
201. Abraham A, Prins R, van Bokhoven JA, van Eck ERH, Kentgens APM (2009) Solid State Nucl Magn Reson 35:61
202. Serrano DP, Aguado J, Morales G, Rodriguez JM, Peral A, Thommes M, Epping JD, Chmelka BF (2009) Chem Mater 21:641
203. Koller H, Kalwei M, Fild C, Lobo RF, Camblor MA, Villaescusa LA, van Wüllen L (2001) Studies in surface science and catalysis 135 (CDROM)
204. Kalwei M (2001) Dissertation, University of Münster
205. Buntkowsky G, Breitzke H, Adamezyk A, Roelofs F, Emmler T, Gedat E, Grünberg B, Xu Y, Limbach HH, Shenderovich J, Vyalikh A, Findenegg G (2007) Phys Chem Chem Phys 9:4843
206. Gorte RJ, White D (2000) Microporous Mesopor Mater 35–6:447
207. Findenegg GH, Jahnert S, Akcakayiran D, Schreiber A (2008) Chemphyschem 9:2651
208. Grünberg B, Emmler T, Gedat E, Shenderovich J, Findenegg GH, Limbach HH, Buntkowsky G (2004) Chem Eur J 10:5689
209. Jähnert S, Chavez FV, Schaumann GE, Schreiber A, Schönhoff M, Findenegg GH (2008) Phys Chem Chem Phys 10:6039
210. Geil B, Isfort O, Boddenberg B, Favre DE, Chmelka BF, Fujara F (2002) J Chem Phys 116:2184
211. Epping JD, Chmelka BF (2006) Curr Opin Colloid Interface Sci 11:81

212. Hunger M (2008) In: Ertl G, Knözinger H, Schüth F, Weitkamp J (eds) Handbook of heterogeneous catalysis. Wiley-VCH, Weinheim, p 1163
213. Haw JF, Nicholas JB, Xu T, Beck LW, Ferguson DB (1996) Acc Chem Res 29:259
214. Sanchez-Sanchez M, Blasco T (2009) Catal Today 143:293
215. Huo H, Peng LM, Grey CP (2009) J Phys Chem C 113:8211
216. Koller H, Overweg AR, van Santen RA, de Haan JW (1997) J Phys Chem B 101:1754
217. Franke ME, Simon U (2004) Chemphyschem 5:465
218. Kao HM, Liu HM, Jiang JC, Lin SH, Grey CP (2000) J Phys Chem B 104:4923
219. Luo Q, Deng F, Yuan ZY, Yang J, Zhang MJ, Yue Y, Ye CH (2003) J Phys Chem B 107:2435
220. Kao HM, Chang PC, Liao YW, Lee LP, Chien CH (2008) Microporous Mesopor Mater 114:352
221. Guan J, Li XJ, Yang G, Zhang WP, Liu XC, Han XW, Bao XH (2009) J Mol Catal A 310:113
222. Karra MD, Sutovich KJ, Mueller KT (2002) J Am Chem Soc 124:902
223. Peng LM, Chupas PJ, Grey CP (2004) J Am Chem Soc 126:12254
224. Peng LM, Grey CP (2008) Micropor Mesopor Mater 116:277
225. Koller H, Engelhardt G, van Santen RA (1999) Top Catal 9:163
226. Kentgens APM, Iuga D, Kalwei M, Koller H (2001) J Am Chem Soc 123:2925
227. Fyfe CA, Bretherton JL, Lam LY (2000) Chem Commun 1575
228. Fyfe CA, Bretherton JL, Lam LY (2001) J Am Chem Soc 123:5285
229. Huang J, Jiang Y, Marthala VRR, Thomas B, Romanova E, Hunger M (2008) J Phys Chem C 112:3811
230. Jiao J, Kanellopoulos J, Wang W, Ray SS, Foerster H, Freude D, Hunger M (2005) Phys Chem Chem Phys 7:3221
231. Behera B, Ray SS (2009) Catal Today 141:195
232. Koller H, Meijer EL, van Santen RA (1997) Solid State Nucl Magn Reson 9:165
233. Jiao J, Kanellopoulos J, Behera B, Jiang YJ, Huang J, Marthala VRR, Ray SS, Wang W, Hunger M (2006) J Phys Chem B 110:13812
234. Ehresmann JO, Wang W, Herreros B, Luigi DP, Venkatraman TN, Song WG, Nicholas JB, Haw JF (2002) J Am Chem Soc 124:10868
235. Marthala VRR, Wang W, Jiao J, Jiang YJ, Huang J, Hunger M (2007) Microporous Mesopor Mater 99:91
236. Kalwei M, Koller H (2002) Solid State Nucl Magn Reson 21:145
237. Villaescusa LA, Barrett PA, Kalwei M, Koller H, Camblor MA (2001) Chem Mater 13:2332
238. van Wüllen L, Koller H, Kalwei M (2002) Phys Chem Chem Phys 4:1665
239. Hunger M, Freude D, Fenzke D, Pfeifer H (1992) Chem Phys Lett 191:391
240. Kenaston NP, Bell AT, Reimer JA (1994) J Phys Chem 98:894
241. Ganapathy S, Kumar R, Delevoye L, Amoureux JP (2003) Chem Commun 2076
242. Xu MC, Harris KDM, Thomas JM (2009) Solid State Nucl Magn Reson 35:93
243. Haw JF (2002) Phys Chem Chem Phys 4:5431
244. Hunger M (2004) Catal Today 97:3
245. Hunger M (2005) Microporous Mesopor Mater 82:241
246. Ivanova II, Nesterenko NS, Fernandez C (2006) Catal Today 113:115
247. Lezcano-Gonzalez I, Boronat M, Blasco T (2009) Solid State Nucl Magn Reson 35:120
248. Hunger M (2008) Progr Nucl Magn Reson Spectr 53:105
249. Hunger M, Wang W (2004) Chem Commun 584
250. Song WG, Haw JF, Nicholas JB, Heneghan CS (2000) J Am Chem Soc 122:10726
251. Haw JF, Nicholas JB, Song WG, Deng F, Wang ZK, Xu T, Heneghan CS (2000) J Am Chem Soc 122:4763
252. Hunger M, Schenk U, Seiler M, Weitkamp J (2000) J Mol Catal A 156:153
253. Song WG, Fu H, Haw JF (2001) J Am Chem Soc 123:4749
254. Song WG, Nicholas JB, Haw JF (2001) J Phys Chem B 105:4317
255. Song WG, Nicholas JB, Haw JF (2001) J Am Chem Soc 123:121
256. Song WG, Nicholas JB, Sassi A, Haw JF (2002) Catal Lett 81:49

257. Marcus DM, Song WG, Ng LL, Haw JF (2002) Langmuir 18:8386
258. Song WG, Marcus DM, Fu H, Ehresmann JO, Haw JF (2002) J Am Chem Soc 124:3844
259. Wang W, Jiao J, Jiang YJ, Ray SS, Hunger M (2005) Chemphyschem 6:1467
260. Abubakar SM, Marcus DM, Lee JC, Ehresmann JO, Chen CY, Kletnieks PW, Guenther DR, Hayman MJ, Pavlova M, Nicholas JB, Haw JF (2006) Langmuir 22:4846
261. Wang W, Jiang YJ, Hunger M (2006) Catal Today 113:102
262. Jiang YJ, Wang W, Marthala VRR, Huang J, Sulikowski B, Hunger M (2006) J Catal 238:21
263. Jiang Y, Huang J, Weitkamp J, Hunger M (2007) In: Xu R, Gao Z, Chen J, Yan W (eds) International Zeolite Conference. Elsevier, Amsterdam
264. Wang W, Buchholz A, Seiler M, Hunger M (2003) J Am Chem Soc 125:15260
265. Stepanov AG, Arzumanov SS, Parmon VN, Kolyagin YG, Ivanova II, Freude D (2007) Catal Lett 114:85
266. Kolyagin YG, Ivanova II, Ordomsky VV, Gédéon A, Pirogov YA (2008) J Phys Chem C 112:20065
267. Luzgin MV, Rogov VA, Arzumanov SS, Toktarev AV, Stepanov AG, Parmon VN (2008) Angew Chem Int Ed 47:4559
268. Stepanov AG, Arzumanov SS, Gabrienko AA, Parmon VN, Ivanova II, Freude D (2008) Chemphyschem 9:2559
269. Arzumanov SS, Gabrienko AA, Freude D, Stepanov AG (2009) Solid State Nucl Magn Reson 35:113
270. Kolyagin YG, Ivanova II, Pirogov YA (2009) Solid State Nucl Magn Reson 35:104
271. Ivanova II, Kolyagin YG, Ordomsky VV, Asachenko EV, Pasynkova EM, Pirogov YA (2009) J Mol Catal A 305:47
272. Wang W, Hunger M (2008) Acc Chem Res 41:895
273. Wang W, Seiler M, Hunger M (2001) J Phys Chem B 105:12553
274. Bosáček V (1993) J Phys Chem 97:10732
275. Wang W, Buchholz A, Arnold A, Xu MC, Hunger M (2003) Chem Phys Lett 370:88
276. Jiang YJ, Hunger M, Wang W (2006) J Am Chem Soc 128:11679
277. Marthala VRR, Frey J, Hunger M (2010) Catal Lett 135:91
278. Marthala VRR, Rabl S, Huang J, Rezai SAS, Thomas B, Hunger M (2008) J Catal 257:134
279. Huang J, Jiang YJ, Marthala VRR, Bressel A, Frey J, Hunger M (2009) J Catal 263:277
280. Huang J, Jiang Y, Marthala VRR, Hunger M (2008) J Am Chem Soc 130:12642
281. Frising T, Leflaive P (2008) Microporous Mesopor Mater 114:27
282. Kaduk JA (2005) Crystallogr Rev 11:1
283. Jordan E, Wilmer D, Koller H (2007) Angew Chem Int Ed 46:3359
284. Jordan E, Bell RG, Wilmer D, Koller H (2006) J Am Chem Soc 128:558
285. Jordan E (2006) Thesis, University of Muenster
286. Schmidt-Rohr K, Spiess HW (1994) Multidimensional solid-state NMR and polymers. Academic, London
287. Böhmer R, Jeffrey KR, Vogel M (2007) Progr Nucl Magn Reson Spectr 50:87
288. Hunger M, Schenk U, Buchholz A (2000) J Phys Chem B 104:12230
289. Hunger M, Buchholz A, Schenk U (2001) In: Galarneau A, Di Renzo F, Fajula F, Vedrine P (eds) Zeolites and mesoporous materials at the dawn of the 21st century, Studies in surface science and catalysis, vol 135. Elsevier, Amsterdam, p 14
290. Lim KH, Grey CP (2000) J Am Chem Soc 122:9768
291. Liu HM, Grey CP (2002) Micropor Mesopor Mater 53:109
292. Park SH, Kleinsorge M, Grey CP, Parise JB (2002) J Solid State Chem 167:310

Top Curr Chem (2012) 306: 229–312
DOI: 10.1007/128_2011_208

Published online: 7 September 2011

Solid-State NMR of Inorganic Semiconductors

James P. Yesinowski

Abstract Studies of inorganic semiconductors by solid-state NMR vary widely in terms of the nature of the samples investigated, the techniques employed to observe the NMR signal, and the types of information obtained. Compared with the NMR of diamagnetic non-semiconducting substances, important differences often result from the presence of electron or hole carriers that are the hallmark of semiconductors, and whose theoretical interpretation can be involved. This review aims to provide a broad perspective on the topic for the non-expert by providing: (1) a basic introduction to semiconductor physical concepts relevant to NMR, including common crystal structures and the various methods of making samples; (2) discussions of the NMR spin Hamiltonian, details of some of the NMR techniques and strategies used to make measurements and theoretically predict NMR parameters, and examples of how each of the terms in the Hamiltonian has provided useful information in bulk semiconductors; (3) a discussion of the additional considerations needed to interpret the NMR of nanoscale semiconductors, with selected examples. The area of semiconductor NMR is being revitalized by this interest in nanoscale semiconductors, the great improvements in NMR detection sensitivity and resolution that have occurred, and the current interest in optical pumping and spintronics-related studies. Promising directions for future research will be noted throughout.

Keywords Dopants · Knight shifts · Nanoparticles · NMR · Semiconductors

J.P. Yesinowski
Chemistry Division, Naval Research Laboratory, 4555 Overlook Ave. S.W., Washington, DC 20375-5342, USA
e-mail: yesinowski@nrl.navy.mil

Contents

Abbreviations

BOM	Bond orbital model
CB	Conduction band
CP	Cross-polarization
CSA	Chemical shift anisotropy
CT	Central transition
CVD	Chemical vapor deposition
DFT	Density functional theory
DMS	Diluted magnetic semiconductors
DNP	Dynamic nuclear polarization
DOS	Density of states
EFG	Electric field gradient
ENDOR	Electron-nuclear double resonance
EPR	Electron paramagnetic resonance
ESR	Electron spin resonance
FID	Free induction decay
FMR	Ferromagnetic magnetic resonance
HETCOR	Heteronuclear correlation
HVPE	Hydride vapor-phase epitaxy
LD	Laser diode
LED	Light-emitting diode
MAS	Magic-angle spinning
MAT	Magic-angle turning
MBE	Molecular beam epitaxy

MCDA	Magnetic circular dichroism absorption
MOCVD	Metal-organic chemical vapor deposition
MQ	Multiple-quantum
MRFM	Magnetic resonance force microscopy
MSN	Magic-sized nanocrystals
NAR	Nuclear acoustic resonance
NC	Nanocrystal
NMR	Nuclear magnetic resonance
NNN	Next nearest neighbors
NQCC	Nuclear quadrupole coupling constant
NQR	Nuclear quadrupole resonance
NW	Nanowires
ODMR	Optically-detected magnetic resonance
OMVPE	Organometallic vapor-phase epitaxy
OPNMR	Optically pumped NMR
POWER	Perturbations observed with enhanced resolution (NMR)
QD	Quantum dot
QIP	Quantum information processing
SEDOR	Spin-echo double resonance
SI	Semi-insulating
ST	Satellite transition
TCO	Transparent conducting oxides
TEM	Transmission electron microscopy
TOPO	Trioctylphosphine oxide
VB	Valence band
WZ	Wurtzite
XRPD	X-ray powder diffraction
ZB	Zincblende

1 Introduction

Semiconductors are electronic conductors having typical room-temperature resistivity values of 10^{-2} to 10^{9} ohm-cm, and are thus intermediate between good conductors (10^{-6} ohm-cm) and insulators (10^{14} to 10^{22} ohm-cm) [1]. The history of semiconductor research dates back to 1833, with Michael Faraday's report on a property peculiar to semiconductors, the negative temperature coefficient of resistance in silver sulfide. Despite some subsequent limited device applications after the 1870s [2], recognition of semiconductors as a class of materials separate from both electrical conductors (metals) and non-conductors (insulators) came about only in the 1930s, as a result of the fundamental scientific understanding afforded by the rise of quantum mechanics. The latter half of the twentieth century witnessed an ever-deeper and more detailed scientific understanding of semiconductor properties, aided by the ability to produce materials with extraordinary degrees of

purity and controlled amounts of dopants. These factors allowed ever more advanced devices to be fabricated, beginning with electrical devices such as the transistor in 1947, and optoelectronic devices such as the light-emitting diode (LED) and laser diode (LD) in the 1960s. The ability to produce so-called heterojunction devices with extreme control that can form quantum well structures is well-developed.

The past few decades have witnessed an enormous expansion in the synthesis of nanomaterials based upon semiconductors such as quantum dots (QD), although actual applications to date have been limited compared to more traditional devices. The physics of low-dimensional bulk semiconductors involving 1D chains or 2D layers is also a new area of fundamental theoretical interest [3]. The recent area of spintronics [4], based upon the notion that the spin rather than the charge of the electron will provide a better means of controlling information in semiconductor nanostructures, offers an even more direct connection to the techniques of magnetic resonance to be discussed [5, 6]. The many aspects of electron spin dynamics in semiconductors have recently received an exhaustive review [7], and constitute an area of intense current research in connection with spintronics. Here the role of nuclear spins is a secondary but potentially very significant one, due to the existence of hyperfine couplings between electron and nuclear spins. Although semiconductor technology now and for the near future is dominated by the electronic applications of silicon, many optoelectronic applications make use of compound semiconductors such as GaAs and GaN. All three semiconductors have been the subject of numerous solid-state NMR investigations, and thus will feature heavily in this review. In particular, the Group III nitrides are likely to provide the most significant semiconductor technology base after silicon.

To understand the often subtle differences between semiconductors synthesized under different conditions, and the results such differences may have upon the intended applications, a wide array of techniques including magnetic resonance has been employed. These techniques have also been used in a more fundamental way to probe the electronic structure of semiconductors and its modification by dopants and defects in terms of the band theory of solids. There is thus an interplay between the former more engineering-oriented goals, and the latter more purely scientific goals. Because of the important role of the unpaired electron (or hole) in semiconductor behavior, electron paramagnetic resonance (EPR, or ESR, for electron spin resonance) has proven very useful for identifying defects and dopants in a wide variety of semiconductors. The much higher detection sensitivity of EPR relative to NMR is an important factor in these applications. Optical detection of EPR (optically-detected magnetic resonance, or ODMR) has provided even higher detection sensitivity.

This review will deal only with NMR of crystalline inorganic semiconductors, excluding the limited number of studies of amorphous or even liquid semiconductors. Unlike NMR in metals, which has been the subject of extensive reviews [8, 9] and even books [10], no broad review of the NMR of semiconductors exists, although there are more specialized reviews in narrower areas [5, 6, 11–13]. Part of the reason may have to do with something of a bifurcation in experimental

approaches. Physicists, particularly in the earlier years where much work was done, have tended to carry out static (low-resolution) NMR at lower magnetic field strengths and low temperatures in the liquid helium range. By contrast, chemists have typically used techniques such as magic-angle spinning (MAS) NMR to obtain high resolution spectra at higher magnetic field strengths, and at ambient temperature. The type of information sought, and the level of theoretical interpretation, is also quite different in the two cases. The fact that semiconductors have been studied by NMR generally on an individual case-by-case basis has also tended to obscure certain commonalities and themes.

This review will include both types of studies, but will not discuss in any detail optically pumped NMR of semiconductors, which has been well-reviewed [5, 11, 12, 14], or other unconventional techniques for detection of NMR signals. Physics-related NMR studies of more complicated semiconductor behavior such as Kondo insulators or semiconductors and other "unusual" semiconducting phases, and semiconducting phases of high-T_c superconductors, while very important in physics, will be neglected here. I have deemed it of some value to provide rather extensive citation of the older as well as of the more recent literature, since many of the key concepts and approaches relevant to current studies (e.g., of nanoparticle semiconductors) can be found in the older, often lesser-known, literature. *My overall aim is to provide a necessarily individual perspective on experimental and theoretical approaches to the study of semiconductors by NMR techniques that will prove useful to chemists and other scientists.*

The semiconductors that have been the subject of numerous investigations in bulk, alloyed, or nanocrystalline form include Si, Ge, doped diamond, SiC, (B, Al, Ga, In)(N, P, As, Sb), and (Zn, Cd, Hg, Pb)(O, S, Se, Te). Nature has been exceptionally benign in providing NMR-active isotopes at natural abundances exceeding 4% for all of the preceding elements except in the cases of ^{13}C, ^{33}S, and ^{17}O, and enrichment with isotopic-labels has become more common.

Since this review is oriented towards chemists who may have very little familiarity with semiconductors, Sect. 2 attempts to provide some brief useful background not otherwise readily found in one place (much more detailed exposition can be found in textbooks such as the excellent one by Yu and Cardona [15]). It begins in Sect. 2.1 with a concise introduction to some basics aspects of semiconductors relevant to understanding terminology encountered in the literature on NMR of semiconductors. The four crystal structures adopted by the majority of important semiconductors will be summarized in Sect. 2.2, and the various methods of making semiconductors will be outlined in Sect. 2.3.

Section 3, the main section of this paper, deals with the NMR of bulk semiconductors. Section 3.1 lists the various relevant terms in the NMR spin Hamiltonian. The NMR techniques and strategies that can be employed to obtain the individual NMR parameters of the spin Hamiltonian and theoretical calculations of NMR parameters will be discussed in Sect. 3.2. The remaining subsections will provide examples from the important classes of semiconductors that illustrate the measurement and interpretation of each of the spin Hamiltonian parameters, with an emphasis on what information about semiconductors the parameters convey.

The preceding treatment of the spin Hamiltonian terms in bulk semiconductors, where they are relatively-well understood, will provide a basis for the discussion of the NMR of nanocrystalline semiconductors in Sect. 4, since as a group they present special considerations and many unanswered questions remain. Section 5 will provide some general conclusions and suggest future promising avenues of NMR research in semiconductors.

2 Background on Semiconductors

2.1 Basic Terms

Figure 1a shows schematically that the defining characteristic of an ideal semiconductor at 0 K in terms of the electronic energy levels is the existence of an unoccupied energy gap between the fully occupied levels of the *valence band (VB)* and the unoccupied levels of the *conduction band (CB)*. The *band gap* is defined as the difference in energy between the lowest point of the CB, the *conduction band edge*, and the highest point in the VB, the *valence band edge*. Such a diagram is a simplification of the result of a fully quantum-mechanical calculation of the *band structure* of an infinitely extended solid with a repeating unit cell, which yields a multitude of closely spaced energy levels forming a near continuum in both the VB and the CB. The number of such levels within a (small) unit width of energy is referred to as the *density of states (DOS)*, and plays a role in the interpretation of the hyperfine shifts between the electron or hole spin and the nucleus that produce the Knight shift, as we shall see.

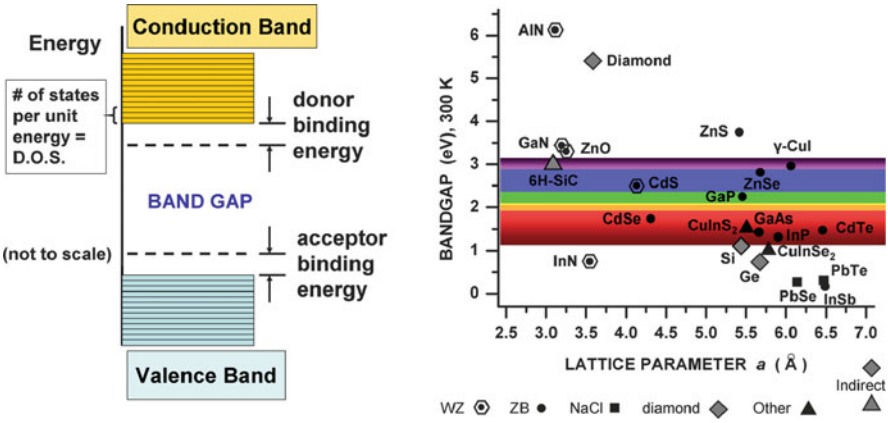

Fig. 1 *Left*: Schematic energy levels in a semiconductor. *Right*: Bandgap energy vs lattice constant for some technologically important semiconductors

The band-structure calculation mentioned above, whether obtained by pseudopotential methods, tight-binding, or **k·p** methods [15], yields energies in terms of the wave-vector *k* characterizing the momentum. If the minimum in the CB and the maximum in the VB have the same wave-vector *k*, then optical excitation is permitted across the bandgap because momentum is conserved, and the semiconductor has a *direct gap*. If not, the optical absorption involves a simultaneous absorption or emission of a *phonon* (lattice vibration) to conserve momentum and the semiconductor is known as an *indirect gap* material. In this case, light absorption (and emission) is much more difficult, silicon being the best-known example. The absorption of light creates an *exciton* (a short-lived electron-hole pair), which can exist as singlet or triplet states depending upon the spin states of the electron and hole. Screening by the high dielectric constants found in semiconductors results in *Wannier excitons*, which have hydrogenic wavefunctions with radii greater than the lattice spacing.

The size of the bandgap can vary from a fraction of an eV (in the IR region of the spectrum) to ca. 4 eV or more (*wide-bandgap semiconductors*). The upper limit is somewhat arbitrary: a substance commonly thought of as an insulator such as diamond has a large bandgap of 5.5 eV, but it can nevertheless be *doped* with elements such as B, N, or P to become an electrically-conducting semiconductor.

For an ideal undoped defect-free semiconductor at temperatures above 0 K, the electrical properties are governed largely by the bandgap. In this *intrinsic regime*, increased electrical conductivity at higher temperatures results from electrons in the VB being thermally promoted into the CB to form *electron carriers* in the C*B*. The absence of an electron in the VB forms a *hole carrier*, which can be treated formally as an entity having spin, just like the electron, but opposite charge and different physical properties such as relaxation times and mobilities.

For semiconductors in the *extrinsic regime*, the electrical properties are governed by *electrically-active* species, both *dopants* and *defects* [16]. Dopants, which can be *unintentional* as well as *intentional*, are elements that can occupy a lattice site (if they are *substitutional*) and provide carriers. For example, doping silicon with P results in the extra electron the P atom has compared to Si being donated into the CB at room temperature, forming an *n-type* semiconductor. Because the energy level of the P atom in Si is only slightly below the CB, it is known as a *shallow donor*. Doping silicon with B, which has one less valence electron than Si, results in the donation of an electron from the VB into the energy level of the B, which resides just slightly above the VB. The resulting hole carrier is characteristic of a *p-type* semiconductor, produced by the dopant B atom acting as a *shallow acceptor* (of an electron). It is perhaps a surprising fact to the newcomer that the replacement of one element in a semiconductor by another can so often lead to energy levels that are close to either the VB or CB, independent of the bandgap itself. Theoretically-based practical doping principles for wide bandgap materials have been described [17]. Typical energy differences of shallow donors or acceptors from the CB minimum or VB maximum respectively are comparable to kT at 300 K, which is 0.0256 eV (2.48 kJ/mol, or 0.593 kcal/mol). In some cases, however, dopants can form *deep-levels* within the bandgap that do not produce

carriers, but which nevertheless can influence other properties including optical properties. The *free carrier concentration* refers to the number of carriers (electrons in the CB, or holes in the VB) present per unit volume; typical levels for low levels of doping (or unintentional doping) might be 10^{14}–10^{16} cm^{-3}, and for high levels of doping above 10^{18} cm^{-3}. Comparing such concentrations to, for example, the concentration of Ga or N atoms in GaN, which is 4.4×10^{22} cm^{-3}, reveals how low a mole fraction of the sample dopants typically represent, and suggests the difficulties encountered when trying to use NMR to study them. The typically low concentration of dopants present in semiconductors also means that, although their effects can often be observed by sensitive techniques, their chemical identity is often a matter of dispute. This is so because unintentional dopants can also be present, and direct chemical or spectroscopic analysis at such low concentrations is usually very difficult or impossible.

With increasing dopant concentration a semiconductor can undergo a *Mott transition* from *semiconductor to metal* over a range of critical concentrations [18]. The electrical conductivity in the *metallic regime* is many orders of magnitude below that of a good metal conductor, but the electrons (for n-type doping) form a degenerate electron gas just as in metals, with electrons occupying the CB up to the *Fermi level*. The Fermi level, or chemical potential, can be defined as the energy at which the probability that an electron orbital is occupied (given by the Fermi-Dirac distribution function) is exactly 1/2.

When both donors and acceptors are present, *compensation* results, whereby the electrons supplied by the donor are given to the acceptor. Thus, the free carrier concentration can be considerably reduced below that expected from introducing a known donor or acceptor if the opposite type of dopant is unintentional. For example, *semi-insulating (SI)* InP (used as a substrate for epitaxial growth) can be made by incorporating low levels of Fe^{3+} as a deep acceptor (reduced to Fe^{2+}) to compensate for unintentional n-type doping in the sample [19].

There are many other species capable of producing free carriers in semiconductors other than dopants of the substitutional type. The dopant may occupy an *interstitial* site in the lattice. There may be *native defects*, in which a stoichiometric deficiency of one component produces a vacancy in a *deficit semiconductor*, or in which one type of atom (e.g., As) occupies the site of another different atom (e.g., Ga), forming what is known as the *antisite defect* in GaAs [20]. This particular antisite defect can be intentionally created by electron irradiation and investigated by EPR and electron-nuclear double-resonance (ENDOR) detected by magnetic circular dichroism absorption (MCDA) [20]. Different types of defects can form *complexes*, such as the As antisite As vacancy complex in GaAs studied by the MCDA technique [20]. Although dopants are often referred to as *point defects*, there can also be *extended defects* such as *line defects* formed by dislocations in the lattice. In addition, *surface defects* are another type that can affect electrical, optical, and magnetic resonance properties. Thus, it is clear that, while NMR spectroscopy may be sensitive to the effects of defects, it is a far greater challenge to identify the specific type of defect responsible, and especially so since more than one type may exist in a given sample.

One other important characteristic of shallow donors and acceptors very relevant to magnetic resonance studies is the temperature-dependence of their donor (or acceptor) abilities. At very low temperatures (say 4 K) shallow donors are said to be *unionized* or *neutral* (a typical ionization energy, to the CB, is 40 meV). The extra electron they would otherwise donate to the CB is weakly bound to the excess positive charge of the shallow donor, and for distances greater than lattice spacings can be assumed to be screened by the uniform dielectric characteristic of the particular semiconductor. The electron thus resides in an extended hydrogenic s-orbital having a *Bohr radius* that depends upon the dielectric constant ε of the semiconductor (typical values of ε are >10) as well as the *effective mass* of the electron. (The latter is a formal quantity in the band-theory of semiconductors that is usually expressed as some small fraction of the actual electron mass; a corresponding parameter exists for holes.) Bohr radii have a typical range of 3–30 nm, the smaller radii generally being associated with higher bandgap materials. This partially-localized electron will obviously have effects in magnetic resonance experiments that are quite distinct from those of localized electrons of paramagnetic centers on the one hand, and delocalized electrons in the CB on the other. The effect of increasing temperature on creating more *ionized* shallow donors and hence more electron carriers in the CB involves both the depth of the shallow donor energy level and the statistics of fermionic particles, and is described in a number of texts [21]. One consequence of the large Bohr radii of shallow donors (or acceptors) is that at high defect concentrations the wavefunctions can overlap and form an *impurity band*, which at even higher concentrations can move into the CB and thus produce the metallic regime above the Mott transition.

As a final comment on terminology, we note that *elemental semiconductors* are formed from a single element, e.g., Si or Ge, whereas *compound semiconductors* are formed from two (*binary*), three (*ternary*), four (*quaternary*), or, rarely, more elements. *Semiconductor alloys* refer to solid solutions where either one anion or one cation can substitute for another, or possibly two or more such substitutions can occur; for a binary semiconductor AB a simple alloy with C would be represented as $A_{1-x}C_xB$. Semiconductors are often classified by the group numbers in the periodic table. Thus, for example, I–VII semiconductors include CuI and AgBr, II–VI semiconductors include ZnS, CdTe, and HgTe, III–V semiconductors include GaAs, GaN, InP, and InSb, and IV_x–VI_y semiconductors include PbSe and SnO_2. Fundamental physical properties are compiled in a recent handbook [22].

2.2 Crystal Structural Forms of Common Semiconductors

Four simple crystal structural types encompass the majority of elemental or binary semiconductors. The high symmetry of the structures has important consequences for the NMR spectra in several respects:

1. Except when alloys or highly doped samples are being considered, it leads to a lack of multiplicity in the NMR peaks, even for inherently oriented single crystals, because of the presence of one unique atom of each element in the unit cell.
2. Because the atoms occupy highly symmetric lattice positions, anisotropic parameters such as chemical shift anisotropy (CSA) or nuclear quadrupole coupling constants (NQCC) are either zero or fairly small.
3. It greatly simplifies the spectroscopist's task in understanding structural aspects and making comparisons between different semiconductors.

The familiar *diamond structure*, with each atom covalently bonded in a perfect tetrahedral fashion to its four neighbors, is adopted not only by C but also by Si and Ge. Silicon can also adopt a wurtzite structure (see below), an example of a *polytype* (one of several crystal structures possible for a substance having an identical chemical composition but differing in the stacking of layers, and which may exist in a metastable state after its formation at some different temperature or pressure).

The *zincblende (ZB)*, or *sphalerite*, structure is named after the mineral (Zn,Fe)S, and is related to the diamond structure in consisting entirely of tetrahedrally-bonded atoms. The sole difference is that, unlike diamond, the atoms each bond to four unlike atoms, with the result that the structure lacks an inversion center. This lack of an inversion center, also characteristic of the wurtzite structure (see below), means that the material may be *piezoelectric*, which can lead to spurious "ringing" in the free-induction decay (FID) when the electric fields from the rf coil excite mechanical resonances in the sample. (Such false signals can be identified by their strong temperature dependence due to thermal expansion effects, and by their lack of dependence on magnetic field strength).

The *wurtzite (WZ)* structure, named after a less common form of the mineral (Zn, Fe)S, also has entirely tetrahedrally-bonded atoms. However, it is a hexagonal crystal form, unlike the cubic form of the ZB lattice (sometimes in discussing semiconductors, these two forms are referred to simply as *hexagonal*, or *cubic*, with *h*- or *c*- preceding the chemical formula). The WZ structure has the hexagonal-close-packed (hcp) ABAB... layer sequence, whereas the ZB structure has an ABCABC... stacking. In the more local terms that NMR is most sensitive to, the difference is reflected in the arrangement of atoms surrounding a Zn–S bond, as shown in Fig. 2. For the Zn–S bond along the hexagonal symmetry axis (c-axis) of the WZ structure, three of the S atoms that are bonded to a Zn are in an eclipsed conformation with respect to three of the Zn atoms bonded to the remaining S atom. In contrast, for the Zn–S bond along the [1,1,1] axis of the ZB structure, the corresponding conformation is staggered. We note that more complicated repeated stacking sequences exist that, for example, give rise to the large number of different polytypes seen for SiC.

The ZB and WZ crystal structures are the most common types for binary octet semiconductors [23], and for III–V semiconductors they constitute practically the only ones known to occur. The energy differences between the two forms have been

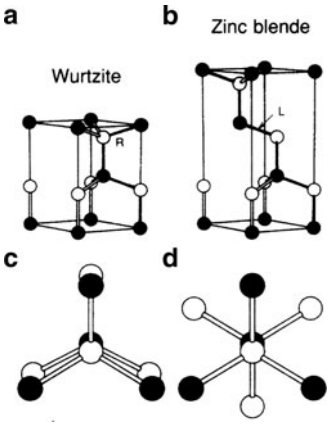

Fig. 2 Differences between wurtzite (WZ) and zincblende (ZB) forms. (**a**, **b**) Handedness of the fourth interatomic bond along the right (R) for WZ and left (L) for ZB. (**c**, **d**) Eclipsed (WZ) and staggered (ZB) conformation of atoms. Reprinted with permission from [23]. Copyright 1992 by the American Physical Society

calculated to be rather small (<20 meV/atom) [23], and the two forms can exist for the same compound depending upon growth conditions. One potential application of NMR is the quantitative identification of polytypes in bulk semiconductors at levels below the detection sensitivity of X-ray powder diffraction (XRPD) techniques, or in semiconductor nanoparticles that exhibit broadened XRPD peaks.

The fourth and final crystal structure type common in binary semiconductors is the *rock salt structure*, named after NaCl but occurring in many divalent metal oxides, sulfides, selenides, and tellurides. It consists of two atom types forming separate face-centered cubic lattices. The trend from WZ or ZB structures to the rock salt structure takes place as covalent bonds become increasingly ionic [24].

2.3 Preparation and Characterization Methods

The way in which a semiconductor material is made has significant implications for NMR spectroscopy in several ways: it governs the amount of sample available for analysis, it determines whether the material will be single-crystal or polycrystalline (or even amorphous), and it controls the nature and amounts of dopants, intentional or otherwise, and defects. In categories most relevant to the NMR spectroscopist, the ways in which most semiconductors are made can be classified as follows:

1. *MBE (molecular beam epitaxy)*, which involves epitaxial growth of thin films on either the same material as substrate (homoepitaxial) or a lattice-matched substrate (heteroepitaxial); the heated substrate reacts with a molecular beam of compounds containing the constituent elements of the semiconductor as well as any dopants; the resultant film is essentially a single crystal; slow growth rates produce films from a few nanometers thick to at most several hundred nanometers that have very high purity and controlled levels of dopants.
2. *MOCVD (metal-organic chemical vapor deposition), OMVPE (organometallic vapor-phase epitaxy),* and *HVPE (hydride vapor-phase epitaxy)* have some

similarities to MBE, but higher gas pressures and chemical precursors are used; HVPE can produce GaN single-crystal films 300 μm thick, whereas MOCVD yields GaN single-crystal films up to a few micrometers thick.
3. *Czochralski* seeded single-crystal growth from semiconductors stable as melts, which yields the meters-large single crystals of ultra-high purity silicon used in nearly all technological applications.
4. *High-Pressure High-Temperature (HP-HT)* synthesis, requiring specialized equipment, and capable of producing high-quality single crystals of, e.g., GaN.
5. *Solvothermal growth* of single crystals or polycrystalline aggregates from hydrothermal or ammonothermal solution.
6. *Flux growth* of polycrystalline aggregates using molten salts or molten metals as solvents.
7. *Chemical synthesis* of polycrystalline aggregates by room-temperature precipitation or sol-gel processes or reaction of elements in tube furnaces.
8. *Nanoparticle "arrested precipitation"* from organic solvents at elevated temperatures containing compounds with constituent elements plus ligands serving as capping groups to prevent aggregation.

The MBE, MOCVD, and HVPE techniques typically employ relatively thick epitaxially-matched substrates such as single-crystal sapphire (Al_2O_3), Si, or SiC. Unless the sample can be successfully removed from the substrate by polishing or etching, problems of unwanted background signals and decreased sample filling factors may result when doing NMR. The limited quantities supplied by MOCVD and especially MBE growth challenge NMR capabilities; approaches to improving detection sensitivity will be discussed. These three growth methods yield samples that can be round wafers (e.g., 2–6 inches in diameter) or square wafers (e.g., 10–15 mm on a side).

One problem with methods that produce polycrystalline or nanocrystalline material is that it is not feasible to characterize electrically dopants in such materials by the traditional four-point-probe contacts needed for Hall measurements. Other characterization methods such as optical absorption, photoluminescence (PL), Raman, X-ray and electron diffraction, X-ray rocking-curve widths to assess crystalline quality, secondary ion mass spectrometry (SIMS), scanning or transmission electron microscopy (SEM and TEM), cathodoluminescence (CL), and wet-chemical etching provide valuable information, but do not directly yield carrier concentrations.

Some of the major questions that semiconductor characterization techniques aim to address are the concentration and mobility of carriers and their level of compensation, the chemical nature and local structure of electrically-active dopants and their energy separations from the VB or CB, the existence of polytypes, the overall crystalline quality or perfection, the existence of stacking faults or dislocations, and the effects of annealing upon *activation* of electrically-active dopants. For semiconductor alloys, that are extensively used to tailor optoelectronic properties such as the wavelength of light emission, the question of whether the solid-solutions are ideal or exhibit preferential clustering of component atoms is important. The next

section will demonstrate how some, if not all, of these questions are addressable by NMR.

3 NMR of Bulk Semiconductors

3.1 Total NMR Spin Hamiltonian in Semiconductors

The starting point for describing the behavior of an ensemble of possibly different nuclear spins in a semiconductor is the spin Hamiltonian $\mathcal{H}$:

$$\mathcal{H}_{\text{total}} = \mathcal{H}_{\text{Zeeman}} + \mathcal{H}_{\text{magnetic shielding}_{(\text{chemical shift})}} \tag{1a}$$

$$+ \mathcal{H}_{\text{magnetic shielding}_{(\text{Knight shift})}} + \mathcal{H}_{\text{electron hyperfine}} + \mathcal{H}_{\text{orbital}} \tag{1b}$$

$$+ \mathcal{H}_{\text{exchange}_{(\text{indirect})}} + \mathcal{H}_{\text{nuclear dipolar}} \tag{1c}$$

$$+ \mathcal{H}_{\text{quadrupolar}} \tag{1d}$$

We do not write out explicitly the spin and spatial (distance and angle) dependences of these terms, since they are readily available in standard references [25, 26] and we do not make direct use of them here. The terms have been grouped to show some common features within each group. Thus, terms in (1a) are linearly dependent on the external magnetic field strength, when the chemical shift is expressed in frequency units (e.g., Hz) rather than the dimensionless *ppm* unit that is employed for convenience in comparing results at different field strengths. We will restrict ourselves to cases where the Zeeman term, which determines the fundamental NMR frequency of Larmor precession, dominates all the other terms. The effects of these other terms can then be treated by first-order perturbation theory or, in the case of larger quadrupolar terms, second-order theory. The Knight shift term in (1b) is also field-dependent in the same way as chemical shift, it is similarly expressed in dimensionless units of ppm, and indeed it is only capable of being distinguished from the chemical shift term by some sort of additional interpretation involving other measurements (e.g., of T_1 relaxation, see Sect. 3.2.4), rather than by any single NMR experiment or pulse sequence. Both the Knight shift and the chemical shift can be anisotropic, being then described by three principal values of a second-rank tensor.

Despite this similarity with chemical shift, the Knight shift is grouped with the electron hyperfine term in (1b) to reflect the fact that both terms arise from the influence of the spin or orbital angular momentum of unpaired electrons. The distinction between the two is that for the electron hyperfine term the electron spin (or hole, as the absence of an electron can be described, e.g., in the case of d^9 Cu^{++}) is *localized* on a paramagnetic defect such as a deep-level transition metal ion.

In the case of the Knight shift the electron or hole spin from a carrier in the CB or VB respectively is delocalized over the entire sample region. It should be noted that the Knight shift is itself a type of electron hyperfine interaction. This is especially so at low temperatures, where carriers at non-degenerate levels of doping are "frozen out" and reside in hydrogenic-orbitals centered on shallow donors or acceptors. In this case, a spatially-varying "Knight shift" results from the Fermi contact interaction that can also be described as an electron-hyperfine interaction. A new optically-detected NMR technique called POWER (perturbations observed with enhanced resolution) has been used to "image" this spatial variation [27], which has also been obtained from ENDOR studies of donors and acceptors in SiC [28–30] as well as ZnO nanoparticles [31].

A third term in the spin Hamiltonian of (1b), $\mathcal{H}_{\mathrm{orb}}$, describes the coupling of the nuclear spin to the *orbital* angular momentum of the electron, and is also linear in the nuclear spin [6]. This term is important for describing interactions of nuclei with holes in the p-type valence bands of semiconductors, which have nonzero angular momentum. The examples we discuss will not involve this omitted term explicitly, although a localized orbital hyperfine interaction can make significant contributions to the Knight shifts in heavier atoms, such as ^{207}Pb and ^{125}Te in PbTe [32].

The electron hyperfine term (sometimes referred to as the transferred hyperfine interaction, and typically expressed either in units of kHz or some other energy equivalent) has an isotropic component due to the Fermi contact interaction (the electron spin in s-orbitals overlapping directly with the nucleus), as well as an anisotropic component due to the through-space dipolar interaction. Both components are derived from the classical electromagnetics expression for a dipolar coupling between two magnetic moments. However, the anisotropic component alone is sometimes referred to as the *pseudodipolar* term because the interaction between the electron and the nuclear spin has an angular and distance dependence identical to the nuclear dipole–dipole interaction (see below). Note that the term "pseudodipolar" is also sometimes used to describe the anisotropic portion of the exchange coupling between two nuclear spins (see below).

The terms in (1a) and (1b) both involve sums of single nuclear spin operators I_z. In contrast, the terms in (1c) involve pairwise sums over the products of the nuclear spin operators of two different nuclei, and are thus *bilinear* in nuclear spin. If the two different nuclei are still of the same isotope and have the same NMR resonant frequency, then the interactions are *homonuclear*; if not, then *heteronuclear*. The requirements of the former case may not be met if the two nuclei of the same isotope have different frequencies due to different chemical or Knight shifts or different anisotropic interactions, and the resulting frequency difference exceeds the strength of the terms in (1c). In this case, the interactions behave as if they were heteronuclear. The dipolar interaction is proportional to $1/r^3$, where r is the distance between the two nuclei. Its angular dependence is described below, after discussing the quadrupolar term.

The quadrupolar interaction in term (1d) applies to nuclei having nuclear spin $I > 1/2$, the so-called *quadrupolar nuclei*. Such nuclei have a nonspherical distribution of positive electric charge that can be expanded in terms of moments, with

the *nuclear electric quadrupole moment* (represented as Q) being the only important one. This asymmetric distribution of electric charge has quantized energy levels in the presence of any gradient of the electric field from surrounding charges (electrons and nucleons) in the lattice. The *electric field gradient* (*EFG*, represented as eq) is different in different directions, and thus is described by a symmetric second-rank and traceless tensor. The three principal components are V_{xx}, V_{yy}, and V_{zz}, where $V_{zz} = eq$ and e is the electric charge and V represents the electric potential, whose second derivative with respect to an axis is the gradient of the electric field along that axis. The product of the EFG and the nuclear quadrupole moment yields the *Nuclear Quadrupole Coupling Constant* $C_q = e^2qQ/h$, with an asymmetry parameter $\eta = (V_{yy} - V_{xx})/V_{zz}$ defining the departure of the tensor from axial symmetry. To specify completely the quadrupole coupling tensor, in addition to these two parameters there are three Euler angles required to relate the principal axis frame to the crystallographic frame. These angles can be deduced on the basis of symmetry arguments for an axially symmetric tensor, but otherwise will require NMR observations as a function of the orientation of a single crystal in the magnetic field.

It turns out that almost all quadrupolar NMR nuclei found in semiconductors have so-called *half-integer spin* ($I = 3/2, 5/2, 7/2$, or $9/2$). The NMR characteristics of such spins, which have a *central-transition (CT)* between the $+1/2$ and $-1/2$ levels, and *satellite-transition (ST)* between the remaining adjacent levels, have been well described [33], as have newer NMR techniques for studying such half-integer quadrupolar nuclei [34–39]. An encyclopedia article on quadrupolar nuclei in semiconductors discusses some examples [13]. The only two integer spin nuclei found in semiconductors (ignoring the ^{2}H isotope) are ^{10}B ($I = 3$) and ^{14}N ($I = 1$). Since the latter is present along with the half-integer ^{69,71}Ga isotopes ($I = 3/2$) in GaN, the next section will give NMR results on this compound that illustrate the characteristic NMR features.

For nuclei that have perfect cubic site symmetry (e.g., those in an ideal rock salt, diamond, or ZB lattice) the EFG is zero by symmetry. However, defects, either charged or uncharged, can lead to non-zero EFG values in nominally cubic lattices. The gradient resulting from a defect having a point charge (e.g., a substitutional defect not isovalent with the host lattice) is not simply the quantity calculated from simple electrostatics, however. It is effectively "amplified" by factors up to 100 or more by the *Sternheimer antishielding factor* [25].

In addition, in crystals lacking a center of inversion (a common situation in semiconductors), the *electric field* produced by a charged defect gives rise to an NMR Stark effect by distorting the electronic environment around a remote nucleus and slightly altering the nuclear positions, both of which contribute to the observed EFG [40]. If an *external* electric field is applied, then the NQCC in the quadrupolar term in the spin Hamiltonian becomes dependent upon the electric field strength and direction (and any time dependence if the field is AC rather than DC) [41–43]. Measurements of this NMR Stark effect upon the NQCC have been reported for ^{69,71}Ga and ^{75}As ($I = 3/2$) in ZB GaAs [41–44] and for ^{9}Be ($I = 3/2$) in WZ BeO [45]. A photoinduced electric field producing a Stark effect on ^{71}Ga in a nanoscale

heterojunction has been observed by the optically-detected POWER NMR technique mentioned above [27]. A mapping of internal electric fields in a multiple quantum well sample has been accomplished by optically-detected NMR of the Stark splitting of ^{75}As [46].

Although calibrated Stark effects can provide a valuable new way of probing internal electric fields in semiconductors and devices, the theoretical calculation and prediction of these Stark coefficients is as yet at an inadequate stage. Also, while NMR Stark effects upon chemical shifts and exchange (J) couplings have been studied in high-resolution solution NMR, they have not yet been observed in the NMR of semiconductors.

As already mentioned, all of the terms in the spin Hamiltonian except the Zeeman term can have *angular dependences*. While it is unnecessary to give the detailed formulae for the most general cases, since they are readily available [25, 26], the angular dependence of so-called *axially-symmetric* NMR tensors is particularly simple: it is $(3\cos^2\theta - 1)$, where θ is the angle between the principal axis of the largest component (the symmetry axis) and the external magnetic field B_0. The direct dipole interaction between two nuclei is necessarily axially-symmetric. The chemical shift tensor and the electric quadrupole tensor *may* be axially symmetric, depending upon the site symmetry. The two terms described as "pseudodipolar" and mentioned above are generally assumed to be axially-symmetric, although this is not necessarily true in all cases. For non-axially-symmetric tensors, one (for electric quadrupole) or two (for chemical shift) additional parameters are used to characterize the angular dependence in slightly more complicated expressions.

The so-called *internal spin Hamiltonian* (all relevant terms except the Zeeman term, which is removed by transforming to the rotating frame) is the starting point in the sense that it determines the appearance of the NMR spectrum. This is true both in cases where many or all interactions are simultaneously present, and in those cases where certain interactions can be removed by the extensive repertoire of *spin-engineering* operations involving application of radiofrequency (rf) fields or mechanical rotation or manipulation of the sample orientation. The motivation for such operations is often to render one interaction, or perhaps a limited number of interactions, dominant. Magic-angle sample spinning and rf decoupling are two examples. Doing so enables the NMR parameters to be more simply and reliably obtained from the resultant spectrum. Double-resonance techniques may serve to correlate resonances from different nuclei, or in the case of cross-polarization (CP) also to enhance the sensitivity of detection of less abundant nuclear spins. Multidimensional NMR techniques can also be used to correlate different interactions along different frequency axes. Numerous books and reviews describe a variety of these techniques, including the references listed earlier for quadrupolar nuclei; the Encyclopedia of Magnetic Resonance [39, 47] is a useful multi-volume compilation of these NMR methods.

The spin Hamiltonian also forms the theoretical basis for describing the temporal response of the spin system to a pulse sequence and/or mechanical manipulations of the sample via calculations of the evolution of the density matrix. Computer

simulations of this evolution and the resulting spectra are today widely used, including the popular, versatile, and freely-available SIMPSON program [48].

The terms in the spin Hamiltonian are in addition responsible for NMR relaxation of various types, including longitudinal relaxation described by the spin-lattice relaxation time T_1. Atomic displacements resulting from phonons in a solid lattice can stochastically modulate terms in the Hamiltonian, thus inducing transitions between the spin energy levels. In the case of NMR spectra exhibiting Knight shifts or hyperfine shifts, the modulation is caused not by atomic displacements but rather by fluctuations of the spin state of the electron spin. Measurements of T_1 in semiconductors can provide important information about carriers and magnetic dopants, as examples below will demonstrate.

3.2 Overview of NMR Techniques and Strategies

3.2.1 Static NMR of Single Crystals and Polycrystalline Powders

Semiconductors have often been studied by *static (i.e., non-spinning)* NMR, either as single crystals or polycrystalline samples. Although all of the anisotropic terms in the spin Hamiltonian discussed above contribute to broadening the NMR signal, and hence lower resolution compared to MAS-NMR, there are some comparative advantages to static NMR. Much lower temperatures (e.g., 4.2 K or lower) can be attained, flat rf coils can be wound around a film to increase the filling factor and sensitivity, and for single crystals anisotropic parameters such as the CSA and NQCC can be accurately measured by following changes in the spectra as a result of changes in the sample orientation with respect to B_0.

Some features of static NMR are illustrated in Fig. 3 (top), which depicts schematically the spectra for the quadrupolar nuclei in GaN, the two isotopes ^{69}Ga and ^{71}Ga with spin $I = 3/2$, and the ^{14}N isotope with $I = 1$. The actual experimental spectra are shown for ^{71}Ga in Fig. 3 (bottom left) and for ^{14}N in Fig. 3 (bottom right). For the case of a single-crystal, Fig. 3 (top) shows that there is a $1/2 \leftrightarrow -1/2$ CT about 4 kHz broad whose frequency changes only slightly with sample orientation, due to small second-order quadrupolar shifts and a small chemical shift anisotropy [49]. There is also a pair of STs, whose broader width is indicative of a distribution of EFGs, as discussed below.

Experimentally, the ^{71}Ga or ^{69}Ga ST splitting is observed to vary as $(3\cos^2\theta - 1)$, as shown by the two spectra in Fig. 3 (bottom left), and as expected it vanishes at the magic-angle orientation of 54.7° [50] (note, this is *not* MAS-NMR). When the ST splitting due to the several megahertz large NQCC is much greater than the rf power (both expressed in kilohertz), all three transitions are not effectively excited simultaneously, although small flip angles as used to acquire the ^{71}Ga spectra shown can mitigate the resultant distortions in relative intensities. In this case, spectra of the CT and one or more ST can be acquired in separate experiments by changing the offset frequency and retuning the probe. Importantly, the pulse lengths that give the

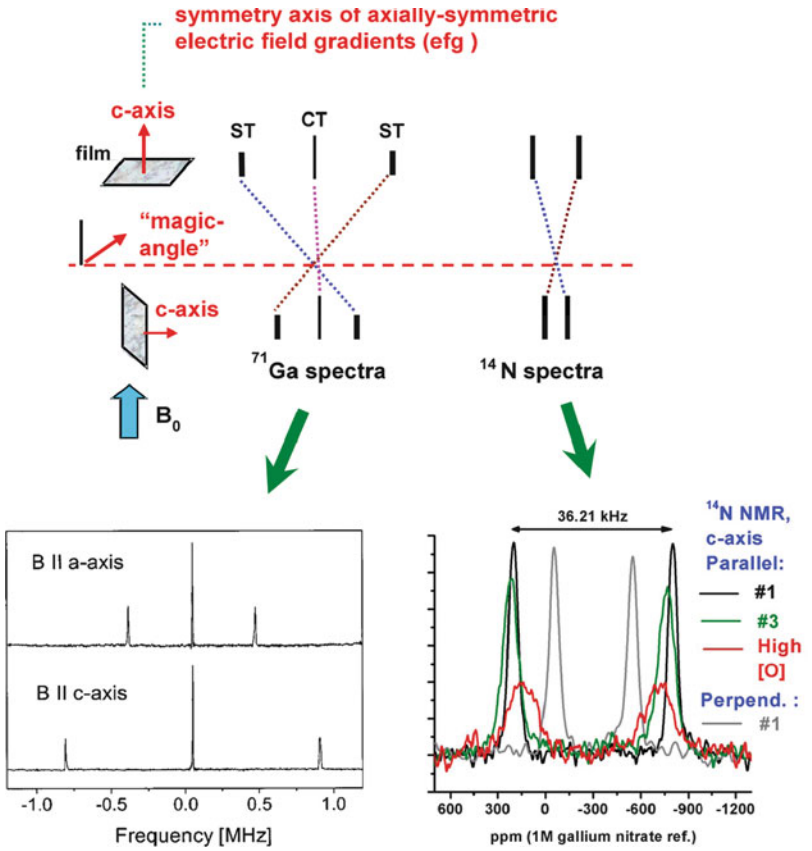

Fig. 3 Quadrupolar NMR of h-GaN (WZ) films. *Top*: Schematic quadrupolar splitting spectra in a single-crystal GaN film of $I = 3/2$ (^{69,71}Ga) and $I = 1$ (^{14}N) nuclei with axially-symmetric EFGs oriented parallel and perpendicular to the magnetic field, showing central-transition (CT) and satellite-transitions (ST) for ^{71}Ga, and doublet (not to scale) for ^{14}N. *Bottom left*: ^{71}Ga NMR spectra of HVPE-grown h-GaN single crystal obtained with small flip angles. Reprinted with permission from [52]. Copyright 2002 by the American Physical Society. *Bottom right*: ^{14}N NMR spectra of highest-quality HVPE h-GaN film (#1) in parallel and perpendicular orientations, of film #3 with poorer crystallinity, and of film doped n-type with high O concentration. Reprinted from [49]

maximal signal for an ST or the CT are reduced by a calculable factor that depends on the nuclear spin I from a simple 90° pulse measured on an isotropic solution standard, where the ST and CT are degenerate [33]. Obtaining the signal vs incremented pulse lengths yields a 2D nutation plot, from which quadrupolar parameters can be deduced [51].

The ^{14}N spectra of single crystals of h-GaN (Fig. 3, bottom right) are doublets, corresponding to the two transitions $-1 \leftrightarrow 0$ and $0 \leftrightarrow +1$, and also show the expected orientation dependence for a C_q of 24.14 kHz [49]. A $90_x - \tau - 90_y - \tau$ quadrupolar-echo pulse sequence was used to eliminate probe ringdown. The spin-

lattice relaxation time T_1 is very long (several minutes), which combined with the low Larmor frequency makes ^{14}N much less sensitive than ^{69,71}Ga in GaN.

The EFGs for both ^{69,71}Ga and ^{14}N have been calculated using the WIEN-97 program, and the results compare more favorably with the experimental results than do those from a simple point charge model including Sternheimer antishielding factors (note that the experimental ^{14}N NQCC value used in the comparison was somewhat larger than the accurate value reported above) [52].

Both the ^{14}N doublet and the ^{71}Ga ST peaks are broader for GaN films of poorer quality, as reflected by X-ray rocking curve linewidths [49]. This is due to the presence of defects that produce a distribution of EFG values (affecting both NQCC parameters C_q and η) about the central ideal value (having $\eta = 0$). The ^{71}Ga ST peaks for a parallel orientation show a Full-Width at Half-Maximum (FWHM) linewidth that increases from 5.8 kHz for the highest quality film to 136 kHz for the poorest quality one (the latter spectrum was obtained by stepping the frequency). The T_2 values for these two ST peaks measured by a $90_x - \tau - 180_y - \tau$ Hahn spin-echo sequence increased from 283 μs to 583 μs, a marked difference attributed to site-to-site variation in the ^{71}Ga frequencies due to the defects that eliminate the otherwise homonuclear character of the ^{71}Ga–^{71}Ga dipolar couplings responsible for T_2 decay.

The ^{71}Ga and ^{14}N spectra of several of these films also showed partially-resolved shoulders shifted to higher frequency and having shorter T_1 relaxation times that were attributed to Knight shifts in more heavily unintentionally doped regions of the film. These Knight shifts were observed in other GaN film samples [53] and will be discussed in more detail in Sects. 3.4.3 and 3.4.4, where MAS-NMR was used to improve the resolution in polycrystalline powders of h-GaN. Section 3.3.2 also shows ^{71}Ga and ^{14}N MAS-NMR spectra of GaN.

However, one significant observation was made that shows how NMR is capable of establishing a correlation between the *spin* and the *charge* effects in semiconductors [49, 53]. In films showing bimodal CT peaks due to a higher frequency Knight-shifted region (a *spin* effect), the ST peaks shifted to higher frequency due to the Knight shifts were more than threefold broader than the ST peaks having no Knight shift. This can be attributed to the fact that whatever defect or dopant is acting as a shallow donor to provide electrons to the CB that affect the ^{71}Ga nuclei by their delocalized *spin* properties (and Knight shift) is also producing a more regional effect via *charge* (and EFG or NQCC). This charge effect need not be a consequence of a net point charge in the lattice; it could simply reflect the altered distribution of electronic charge affecting the EFG a ^{71}Ga nucleus experiences as a result of the presence of the shallow donor. The important point is that, while the *spin* effects of a CB electron (or hole) upon nuclei in the lattice do not depend upon the nature of the ionized shallow donor, the *charge* effects do. Separating the two effects in the manner outlined for intentionally doped semiconductors may thus enable the specific charge effects for a given dopant to be determined, compared with theoretical calculations, and possibly be used as a signature of a given dopant type.

It should be noted that these types of spectra are expected only for quadrupolar nuclei of semiconductors in non-cubic axially-symmetric forms such as the WZ structure; cubic forms such as ZB or rocksalt structures ideally lack any anisotropy, and the ST peaks overlap the CT peak. However, defects in such cubic structures can produce EFGs that have random orientations, and the resulting ST are spread out over a wide range.

Effects of strain upon EFGs produced by subjecting a thin film to uniaxial stress were originally seen for ^{115}In ($I = 9/2$) in InSb [54] and subsequently by nuclear acoustic resonance for many III–V semiconductors [55]. Strain effects have also been measured in GaAs quantum wells by optically-detected NMR [46, 56]. Recently rather small compressive forces applied to a GaP single crystal also revealed strain effects that broadened the ^{69}Ga NMR peak and which could be modeled [57]. The importance of work in this area arises from the ability to monitor not externally applied stress but rather built-in strain in semiconductors as a result of either doping (e.g., In-doped GaAs [58, 59]), alloying, or proximity to epitaxial growth substrate or heterojunction interfaces.

Going from a static single crystal to a static powder generally does not greatly affect the resolution of CT measurements on quadrupolar nuclei if the broadening of the CT by second-order quadrupole [33] or CSA interactions is not large. However, for non-cubic crystal forms such as WZ, it does tremendously weaken the ST intensities due to their dispersal over a wide range of frequencies. While it is possible even in such situations to observe portions of the broad ST pattern that correspond to more intense singularities in order to obtain relevant information (see Sect. 3.8.3) [60], the next section shows how MAS-NMR improves the detection of ST in powder samples.

Static NMR provided ^{77}Se and ^{125}Te chemical shift measurements for many II–VI and IV–VI compounds [61] and for nuclei of some [62] and all elements in all the zinc chalcogenides [63]. Static ^{33}S NMR spectra at natural abundance (0.76%) on the binary sulfide semiconductors ZnS, CdS, CaS, SrS, and PbS were also obtained, and the chemical shifts discussed in terms of bonding models including Harrison's bond orbital model (BOM) [64]. The ^{51}V ($I = 7/2$), ^{93}Nb ($I = 9/2$), ^{181}Ta ($I = 7/2$), and ^{205}Tl chemical shifts in ternary A_3BC_4 semiconductors have been determined by static NMR and interpreted in terms of Harrison's BOM [65].

3.2.2 MAS-NMR of Polycrystalline Powders

The general motivation for doing MAS-NMR rather than static NMR is to obtain increased resolution by effectively removing by averaging the nuclear dipole interactions and CSA that broaden the spectra of both spin-1/2 nuclei and quadrupolar nuclei. Comparison of static and MAS-NMR spectra of ^{27}Al ($I = 5/2$), ^{69,71}Ga, and ^{113,115}In spectra in a survey of a very wide series of III–V semiconductor powder samples demonstrated how MAS removed broadening associated with dipolar, pseudodipolar, and first order quadrupolar terms [66]. The remaining second-order quadrupolar terms and isotropic chemical shift dispersions arising

from sample heterogeneity could be assessed either by measurements at different magnetic field strengths, or by the use of the pair of isotopes ^{69}Ga and ^{71}Ga that have different second-order quadrupolar effects due to the different nuclear quadrupole moments and Larmor frequencies [67]. By assessing these contributions, it was possible to measure the exchange interactions [66]. Many examples of MAS-NMR spectra and conclusions drawn from MAS-NMR studies will be given in the remainder of this review.

We note however that if the range of isotropic chemical or Knight shifts is large, as it can be for the heavier nuclei such as ^{207}Pb or for unintentionally or intentionally heavily-doped samples, then MAS-NMR may offer no significant resolution increase. This occurs when the spinning-sidebands due to the anisotropic dipolar or CSA interactions overlap with the isotropic shift distribution, and can only be solved by going to higher spinning speeds.

3.2.3 Other NMR Techniques

References have already been given in Sect. 3.1 to discussions of NMR techniques, particularly for quadrupolar nuclei, that either have been used in a limited number of studies of semiconductors, or else have potential applications in future studies. They may have the goal of increased sensitivity, as is the case with CP or quadrupolar population-transfer experiments [68–71] the latter type having great potential in semiconductor studies, especially in conjunction with Carr–Purcell–Meiboom–Gill (CPMG) pulse trains on the CT [70, 72]. They may seek to increase resolution, as MAS or decoupling or multiple-quantum (MQ) MAS can accomplish. Or they may seek to establish correlations between different interactions or different peaks, as 2D NMR correlation experiments or various recoupling experiments can achieve.

Optical techniques represent the single most widely applied specialized technique for semiconductor magnetic resonance, both EPR and NMR. Optically-pumped NMR (OPNMR) experiments have been carried out by direct NMR observation [5, 11, 12, 14], mostly in GaAs, but also in InP, CdS, CdTe [73], and originally in the indirect bandgap material silicon. The OPNMR of ^{15}N-labeled ZB c-GaN has been reported [74, 75], but the small (30%) enhancement observed might well arise from a photo-induced decrease in the ^{15}N T_1. The mechanisms by which nuclear polarization is generated by optical-pumping in semiconductors are still not well-understood in detail. Lasers and cryogenic NMR probes capable of operating at around 6 K are generally employed, with single-crystal or thin film samples or heterostructures and quantum wells (QW). There are not only enormous gains in detection sensitivity enabling a small number of nuclei to be observed but also the ability to achieve spatial localization by choosing the irradiation volume. There is also interest in transferring polarization from the InP semiconductor surface to overlying layers of spins in biological or other materials [76–78]. Because as mentioned in the Introduction the topic has been the subject of a number of reviews, it will not be discussed further here.

Other specialized techniques that have been applied to semiconductors but which unfortunately cannot be discussed here because of space limitations include dynamic nuclear polarization (DNP) by microwave saturation of EPR transitions followed by either observation of NMR or of Overhauser shifts in EPR from nuclear polarization [79–88], current-induced DNP [89, 90], ENDOR [28, 30, 31, 91–93] muon spin resonance (μSR) employing muonium as a probe of hydrogen in semiconductors [94, 95], nuclear acoustic resonance (NAR) [55], and optically-pumped β-decay NMR of Li on the Si(111) surface [96]. Also, the very sensitive technique of Optically Detected NMR (ODNMR) has been used to obtain ^{71}Ga and ^{75}As spectra not only in bulk GaAs but also in GaAs QW [97, 98], including higher resolution and higher sensitivity spectra of ^{71}Ga that reflect strain effects by a technique called Larmor Beat Detection [99]. An ODNMR technique based upon the Zeeman-splitting of excitons in a single GaAs QD has shown unprecedented sensitivity for detecting NMR signals from ca. 10^5 nuclei, and has shown different NMR characteristics for individual QDs [100, 101].

However, several cantilever-based techniques deserve slightly more discussion, since they offer a promising approach to the goal of being able to do spatially-resolved NMR on small regions of semiconductor films. One of these techniques is magnetic resonance force microscopy (MRFM) [102–105], where the mechanical forces between nuclear (or electron) spins and magnetic field gradients from permanent magnets are detected by means of a cantilever's deflection. Using a cryogenic MRFM apparatus, and optically pumping a GaAs film to increase sensitivity in this initial demonstration, spatially-resolved ^{71}Ga NMR signals could be obtained, with evidence for a 170-nm slice separation [106]. Although much instrumental development remains before an MRFM instrument can routinely interrogate a semiconductor thin film, the prospect of doing NMR with submicron resolution in semiconductors is enticing. A proposed concept being investigated, Dipolar Field Microscopy [107], uses optically detected NMR of a semiconductor tip very close to a sample containing nuclear spins whose magnetization can be manipulated by rf and thus affect (through the dipolar field) the NMR of the semiconductor tip. Although imaging of proton-rich samples was considered, the principle should extend to NMR-active nuclei in semiconductor films as well.

3.2.4 Measurements of T_1 Spin-Lattice Relaxation Times

Measurements of T_1 in semiconductors, perhaps as a function of either frequency position in the spectrum, temperature or, less commonly, field strength, are important in establishing the existence of Knight shifts, in studying hyperfine interactions to magnetic nuclei, and in understanding the mechanisms of spin-lattice relaxation. Spin-1/2 nuclei present no special problems, and methods such as progressive saturation and inversion-recovery or saturation-recovery can be used. Relaxation is often single-exponential, with a single spin-lattice time constant T_1. In samples relaxed by low levels of paramagnetic impurities and having low-abundance nuclei with low spin-diffusion rates, such as SiC, the magnetization recovery often follows

a *stretched-exponential* form: $M_0\ (1 - \exp(-\tau/T_1')^n)$, where the stretching exponent n is typically 0.5–0.6 and T_1' is the time constant [108, 109].

Detailed interpretation of T_1 values for the quadrupolar nuclei in GaAs, GaSb, InAs, and InSb over a wide temperature range of 4–300 K has shown how "magnetic" mechanisms operating through the nuclear magnetic dipole can be separated from quadrupolar mechanisms of relaxation, and how the relative contributions of acoustic and optical phonons to the latter can be sorted out (optical phonons coupling more strongly to the Group III nuclei) [110]. Many other T_1 relaxation studies of half-integer quadrupolar nuclei ($I = 3/2, 5/2, 7/2, 9/2$) in InSb [111–114], InP [115, 116], GaAs [117, 118], GaN [119], and other semiconductors have been carried out, including one over the very wide temperature range of 300–1425 K in GaAs [120].

However, the situation for such nuclei is more complicated than for spin-1/2 nuclei (see [50] and references within). There are $2I + 1$ Zeeman energy levels. The populations of each of these levels are connected pairwise with other levels by different rate constants, as shown in Fig. 4 for a nuclear spin $I = 3/2$. The quadrupolar relaxation mechanism arises from fluctuations in the EFG due to atomic motions, lattice vibrations in this case, that can induce both single-quantum transitions $\Delta m = \pm 1$ as well as double-quantum transitions $\Delta m = \pm 2$. The two corresponding rate constants W_{Q1} and W_{Q2} are often assumed to be equal, but are not necessarily so, as has been shown for Ga^{71} in a single-crystal of GaN [50]. The two quadrupolar rate constants could be obtained in this case by a strategy of observing the magnetization recovery of the central transition (CT) under two different conditions: when only the CT was selectively saturated, and when both CT and the two satellite transitions ST were saturated by means of frequency jumped irradiation.

When $W_{Q1} \neq W_{Q2}$ the magnetization recovery may appear close to single-exponential, but the time constant thereby obtained is misleading [50]. The measurement of T_1 of quadrupolar nuclei under MAS conditions presents additional complications that have been discussed by comparison to static results in GaN [50]. The quadrupolar (two phonon Raman) relaxation mechanism is strongly temperature dependent, varying as T^7 well below and T^2 well above the Debye temperature [119]. It is also effective even in cases where the static NQCC is zero, as in an ideal ZB lattice, since displacements from equilibrium positions produce finite EFGs.

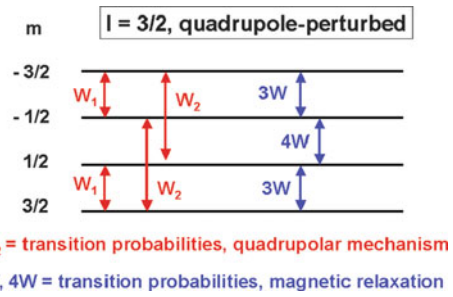

Fig. 4 Relaxation pathways between quadrupole-perturbed Zeeman levels of $I = 3/2$ nuclear spin. Reprinted from [50]

A magnetic relaxation mechanism may also coexist with a quadrupolar mechanism, resulting in single-quantum transitions $\Delta m = \pm 1$ with rate W as shown in Fig. 4. Two sources of fluctuating magnetic interactions are the dipolar or contact interactions with localized paramagnetic moments, and the finite spin density at the nucleus from carriers (electrons or holes) that also gives rise to the Knight shift. The latter contribution can be identified by a characteristic temperature dependence given by the Korringa relationship, which states that K^2T/W is a constant (K is the Knight shift, T is the absolute temperature). Although T_1 ($\equiv W^{-1}$) in this case increases at lower temperatures, it does so much less steeply than for the quadrupolar mechanism described above, and transitions between temperature regimes where each mechanism dominates can be observed, e.g., for ^{71}Ga NMR in GaN [119]. Magnetic relaxation mechanisms can also be distinguished from a quadrupolar one by comparisons of relaxation times for two isotopes of the same atom whose ratio of Larmor frequencies (or magnetogyric ratios) differs from the corresponding ratio of nuclear quadrupole moments, as demonstrated by two studies of the pair ^{69}Ga and ^{71}Ga in GaN [60, 119].

3.2.5 Effects of Electrical Conductivity

It is well known that radiofrequencies typical of NMR experiments only penetrate metals to a certain "skin depth" that depends upon the inverse square root of both the frequency and the conductivity. Using finely powdered samples separated by an inert filler material can overcome such problems. Limited rf penetration can also reduce signal intensity for less conductive materials, and can be avoided by the same technique [121]. Recently very unusual and large spinning-speed dependent ^{63}Cu and ^{127}I MAS-NMR chemical shifts in the semiconductor γ-CuI were shown to arise from dramatic increases in the sample temperature [122]. These increases arise from resistive heating by oscillating electric currents induced by rotating the sample, which is a poorly-conducting p-type semiconductor due to Cu^+ vacancies, in the 11.7 T external magnetic field. At spinning speeds approaching 13 kHz the sample temperature increased by over 200 °C; such effects could be avoided by diluting the sample with an inert filler. The possibility of unexpected temperature increases when doing magic-angle spinning NMR on semiconductor samples at high field strengths and high spinning speeds should always be considered.

3.2.6 Theoretical Calculations of NMR Parameters

The fundamental quantum-mechanical interpretation by Ramsey of the NMR parameters of chemical shift [123, 124] and spin-spin J coupling [125, 126] still forms the basis of our understanding of these terms, as has been recently noted [127]. However, Ramsey neglected relativistic effects, which are very significant for the heavier nuclei such as ^{199}Hg, ^{207}Pb, and ^{203,205}Tl [127]. Derivations and discussion of Ramsey's theoretical results are found in the textbook by Slichter [26]

and the treatise by Abragam [25]. Although the Ramsey theory of chemical shifts, derived by considering the external magnetic field as a perturbation upon the electronic wavefunctions, formed the basis for a qualitative or semi-quantitative understanding of chemical shifts in molecules and solids (including some semiconductors), the difficulty in performing exact calculations meant that it has in some sense been largely supplanted by the DFT methods discussed below. However, these latter methods deliver numerical results without necessarily any of the physical insight that has been obtained using Ramsey's separation of chemical shielding into two terms: a diamagnetic contribution and a "paramagnetic" term. The diamagnetic term can be written [127] as

$$\sigma_{\text{diamagnetic}} = (e^2/3\,\text{mc}^2)\langle 0|1/r|0\rangle, \tag{2}$$

where the symbols pertaining to the electron have their usual meaning, and the ground-state total electronic wave function is $|0\rangle$. Although the diamagnetic term plays an important role in governing ^{1}H chemical shifts, for heavier nuclei it can usually be neglected, not because it is small, but because most of the contribution comes from core electrons that are unchanged in different chemical bonding environments. Therefore, the generally most significant term is the paramagnetic term (note that this name arises from the field-induced mixing of excited states, while the molecule or solid itself remains diamagnetic):

$$\sigma_{zz(\text{paramagnetic})} = 2\Sigma_n[\langle 0|m_z|n\rangle\langle n|m_z/r^3|0\rangle + \text{c.c.}]/(E_0 - E_n). \tag{3}$$

The summation over all the excited states of the molecule or solid having energy E_n and the appropriate finite orbital angular momentum matrix elements represents a hurdle to practical calculation. When fairly low-lying excited states are present and dominant, a "closure approximation" has been invoked in which the inner ket-bra states $|n\rangle\langle n|$ are projected as unity, and the energy difference $E_0 - E_n$ is replaced by an average energy difference slightly larger than E_1, the energy of the first excited state. The success of this approach has been discussed in connection with chemical shifts of d^6 transition metal complexes, where localized d-orbitals are split by ligand fields [128]. It has also been used to rationalize chemical shift trends seen in semiconductor nanocrystals, as discussed in Sect. 4. The limitations of implementing the Ramsey theory in actual numerical calculations, and the calculational approaches taken in more recent times, have been clearly treated by Jameson [129].

In terms deriving from the Ramsey approach, a review of chemical shifts in chalcogenide and pnictide semiconductors in terms of Harrison's BOM and related approaches has been given [130]. The Ramsey approach has also been used to explain chemical shifts in III–V compounds [131], and specifically ^{113}Cd shifts in Cd chalcogenides [132].

Almost all inorganic semiconductors are extended three-dimensional solids. Therefore, the quantum-mechanical calculation methods that have been widely

used in chemistry, such as GAUSSIAN, that are based upon molecular clusters are less useful for semiconductors, although it is possible to terminate a large cluster with hydrogen atoms to simulate an extended solid [133]. In recent decades density functional theory (DFT) has proven very useful in calculating properties of extended solids, including the band structure of semiconductors. For instance, it has been applied to the calculation of the ^{71}Ga and ^{14}N EFG (and resultant) NQCC values in the WZ form of GaN [119]. The effects of conduction band electron carrier concentration upon the EFGs was also calculated and found to be rather small, producing a change of ca. 0.1% for the ^{71}Ga and 1.0% for the ^{14}N NQCC at the high carrier concentration of 4.4×10^{20} cm^{-3}. A molecular cluster approach [134] and the WIEN-97 program [52] have also been used to calculate EFGs in h-GaN. The WIEN-95 program has been used to calculate EFGs in a number of WZ form semiconductors, including h-GaN, and to obtain information about the structural parameter characterizing the distortion from tetrahedrality [135]. A description of the WIEN2k program and an example of the calculation of the Ti EFG in the rutile form of TiO_2 has been given [136].

Very recently the VASP implementation of DFT was used to calculate EFGs for ^{75}As and ^{69}Ga in two alloy samples of $Al_xGa_{1-x}As$ for comparison with experimental NQCC results [137]. Extensive calculations of the *distributions* of EFGs, and comparison with theoretical models for such distributions, were carried out using a large number of different configurations; the calculations were made feasible by the similarity of both the lattice parameters and the dielectric constants of the end members (see also Sect. 3.8.1 for further discussion)..

The recent introduction of the gauge-including projector augmented wave (GIPAW) method into the plane-wave pseudopotential formalism of DFT has enabled the calculation of the NMR parameters of chemical shifts and electric field gradients (yielding NQCC values), both as full tensor quantities related to the crystallographic frame [138]. The accuracy is such that reassignments of small differences in ^{13}C and ^{29}Si chemical shifts were possible in a recent study of SiC polytypes discussed below [133]. The calculation of J-couplings by this approach is also feasible [139], although fewer results have so far been reported.

In these examples of applications of DFT calculations to alloys and polytypes, much of their utility lay in the ability to discriminate longer-range effects beyond the four immediate bonding neighbors. Another situation where longer-range effects are expected to be important is semiconductor nanoparticles, where a surface that may have atoms coordinated to surface ligands represents a discontinuity in the periodic structure that should perturb NMR parameters of nuclei some distance from the surface. Recently such an approach has been demonstrated with DFT calculations of ^{77}Se chemical shifts in ZnSe nanoparticles that were used to help interpret experimental NMR results, as will be described in Sect. 4 [140].

The DFT calculations for both the $Al_xGa_{1-x}As$ alloy and the ZnSe nanoparticles were challenging because of the need to take into account large numbers of unit cells that differed either in composition (for the alloy) or distance from the surface (for the nanoparticle). They indicate that, in addition to calculating NMR parameters of the bulk semiconductors with reasonable accuracy, it is now possible

to consider quantitative approaches to calculating distributions of such parameters. This is a promising area for future progress, particularly if NMR techniques for correlating the different NMR parameters of nearby nuclei can be applied to provide a more stringent test of the calculational results and models.

One point worth noting is that the theoretical calculation of chemical shifts predicts absolute chemical shifts, whereas experimental values are reported with respect to some convenient but otherwise arbitrary reference. Although theoretical chemical shift trends in a series of compounds may be compared with experimental trends, it can be useful to also calculate the chemical shift of a solid reference compound for comparison, while realizing that such a calculation will also be subject to some degree of inaccuracy.

3.3 Chemical Shifts

The isotropic chemical shift, the trace of the chemical shift tensor, is one of the basic NMR parameters often measured for both spin-1/2 and quadrupolar nuclei. The CSA can also be measured in non-cubic environments, such as the ^{113}Cd nuclei experience in the chalcopyrite structure of crystalline $CdGeAs_2$ [141] or $CdGeP_2$ [142], and the ^{31}P nuclei in the latter compound [142]. Although the isotropic chemical shift can be measured from the NMR spectrum of a static powder because the CSA is zero in many cases because of cubic symmetry of the lattice, improved resolution is obtained by using MAS to remove dipolar couplings. Two particular areas where the isotropic chemical shifts have proven very informative will now be discussed, semiconductor alloys and semiconductor polytypes.

3.3.1 Semiconductor Alloys

The introduction of one or more additional components, either cations or anions, into a semiconductor to form solid solutions typically strongly affects the optical and electronic properties. It is one of the mainstays of semiconductor device engineering for creating heterojunctions, quantum wells, selected-wavelength LEDs and LDs, etc. It has long been recognized that the additional components may not form ideal solid solutions with random site distributions, but rather can exhibit short-range or long-range ordering, as theoretical calculations in III–V alloys have shown [143]. The existence of such clustering of one component in alloys can be very significant. For example, the phenomenal success of $In_xGa_{1-x}N$ as a light-emitter in LDs and LEDs, despite the high density of dislocations, has for a long time been attributed to the existence of clustering of In-rich regions. It has been argued that these regions serve to localize the excitons until they emit light, thus avoiding non-radiative recombination at dislocations [144]. More recent evidence showed that the TEM method previously used produced artifactual In clustering due to electron-beam damage, and used other techniques to show that essentially a random solid solution formed

[145]. These difficult experimental controversies show that there is a significant role for NMR, a non-perturbing non-destructive technique that provides structural information about the local atomic environment over several bonds.

Because it is sensitive to the local atomic environment, the isotropic chemical shift can be a valuable parameter with which to monitor the formation of semiconductor alloys. One example is ^{31}P MAS-NMR of the III–V semiconductor alloy $Ga_xIn_{1-x}P$ studied by Tycko and coworkers [146, 147]. Thin OMVPE-grown films of this alloy have been observed by TEM to exist in domains where the Ga and In cations are not randomly distributed, but rather ordered on certain crystallographic planes. Surface thermodynamic and kinetic effects during growth are believed to be responsible for this ordering, which influences electronic and optical properties (e.g., by altering the bandgap). Figure 5a depicts the two extremes, of random "ordering" (actually fully disordered) on the left, and fully ordered (which forms a superlattice) on the right.

Since an earlier static ^{31}P NMR study [148] found no significant shift differences between the end-members GaP and InP and a $Ga_{0.1}In_{0.9}P$ alloy (all having a ZB

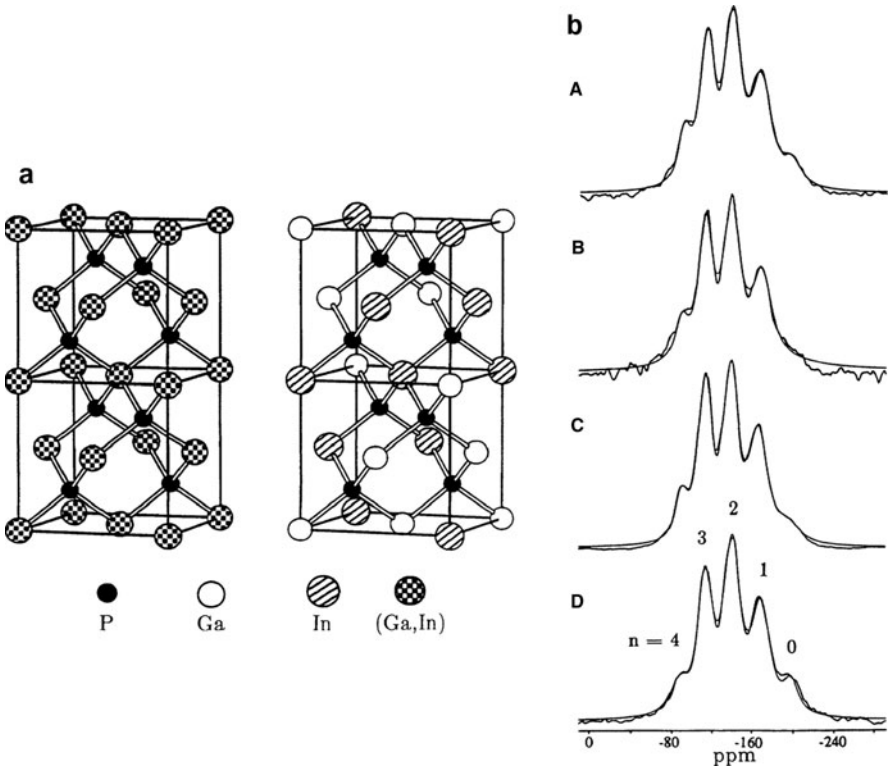

Fig. 5 (**a**) Random (*left*) and fully ordered (*right*) $Ga_{0.5}In_{0.5}P$ structures. (**b**) ^{31}P MAS-NMR spectra of four different $Ga_{0.5}In_{0.5}P$ films A–D and least-squares fit. Reprinted with permission from [146]. Copyright 1992 by the American Physical Society

lattice), the strategy adopted [146] was to eliminate broadening due to heteronuclear and homonuclear dipolar couplings as well as any chemical shift anisotropy in the alloy by using magic-angle spinning. Observing the NMR of the nucleus belonging to the anion (^{31}P) enabled the five different local environments of the P atom in $Ga_nIn_{4-n}P$ clusters to be observed at different chemical shifts, as shown in Fig. 5b for four powdered $Ga_{0.5}In_{0.5}P$ film samples grown under different conditions with the corresponding values for n indicated on the spectrum.

These peaks could be reliably assigned, based on the relative peak intensities observed for a $Ga_{0.14}In_{0.86}P$ bulk sample, by the monotonic nature of the trends of chemical shift vs n, and by trends in transverse relaxation times T_2 as measured by rotor-synchronized spin-echo decays using a $90^\circ-\tau-180^\circ-\tau$ Hahn echo sequence. Interestingly, although the ^{31}P chemical shifts increase by about 30 ppm for each unit increase of n in alloys of different stoichiometry x, the absolute values depend upon the stoichiometry. There are also unresolved significant discrepancies in the ^{31}P chemical shifts reported for GaP and InP by different groups [146, 148–150]. Although possible Knight shifts due to unintentional doping or native defects have been argued to be negligible in this case [151] it is difficult to account for the discrepancies by other effects.

In fact, a ^{31}P MAS-NMR study of doped InP showed that, relative to the sharp peak from the semi-insulating Fe-doped sample, the S-doped n-type sample ($n_c = 6 \times 10^{18}$ cm^{-3}) showed a very broad peak shifted by about 35 ppm to higher frequency, and a Zn-doped p-type sample ($n_c = 5 \times 10^{18}$ cm^{-3}) showed a sevenfold smaller shift in the same direction [152]. Although these were interpreted in terms of the spatial variation of an electron hyperfine interaction in a hydrogenic orbital centered on the shallow donors, at room temperature, where the spectra were obtained, the shallow donors might be expected to be fully ionized. Therefore, the shifts observed would seem instead most likely to be due to Knight shifts from delocalized carriers, either electrons or holes. This supports the suggestion that the discrepancies in reported shifts for InP (and GaP by implication) are due to Knight shifts of varying magnitude from unintentional dopants or defects. That Knight shifts were not a factor in the $Ga_nIn_{4-n}P$ study cited is indicated by the long T_1 values of about 100 s measured for all of the peaks [146].

To describe ordering in such a semiconductor alloy quantitatively, one can introduce an order parameter $S = 2y$ to describe partially ordered crystallographic planes in a sublattice having alternating compositions $Ga_{x+y}In_{1-x-y}$ and $Ga_{x-y}In_{1-x+y}$ such that the average composition is Ga_xIn_{1-x}. For an $x = 0.5$ composition, Fig. 5a (right) shows the extreme (ordered) case of $S = 1$, which consists of equal numbers of only Ga_3InP and $GaIn_3P$ clusters, whereas Fig. 5a (left) represents $S = 0$ (fully disordered). For partially ordered alloys, mathematical expressions for the relative intensities of the five different $Ga_nIn_{1-n}P$ clusters can be obtained as a function of the order parameter S. (Note that despite the correction of a typo in one term of the expression [147], the correct expression was used to analyze the data, so the reanalysis of these data by another group [153] using a different definition of order parameter may be questioned.) By fitting the experimental ^{31}P MAS-NMR spectra of four different $Ga_{0.5}In_{0.5}P$ film samples for varying values of S, Tycko

et al. were able to show that all four samples had a relatively weak degree of ordering ($S \leq 0.6$), despite indications from TEM of a high degree of ordering.

There have been other cases where MAS-NMR of other spin-1/2 nuclei has been used to investigate semiconductor alloys: the II–VI compounds $Hg_{1-x}Cd_xTe$ and $Cd_{1-x}Zn_xTe$ in particular [154–160]. The ^{125}Te MAS-NMR spectra of a wide range of the former alloy exhibited broad peaks over a roughly 600 ppm range, and was initially interpreted in terms of a non-random distribution in the lattice [155]. This conclusion was surprising given that the crystals were grown from a high-temperature melt. A subsequent static NMR study of a single crystal of $Hg_{0.78}Cd_{0.22}Te$ (a composition used as an infrared detector) using the NMR-active nuclei ^{111,113}Cd and ^{199}Hg in addition to ^{125}Te (all isotopes having natural abundances $<17\%$) concluded that the cation distribution was statistical (random) [159].

This study introduced a new strategy for making assignments of peaks in the ^{125}Te spectra, double-resonance between ^{199}Hg and ^{125}Te in a two-dimensional spin-echo double-resonance (SEDOR) experiment. By taking difference spectra (with and without ^{199}Hg pulses), the ^{125}Te signal arising from sites with ^{199}Hg neighbors and moderate to large heteronuclear couplings could be identified. A similar double-resonance strategy between ^{199}Hg and ^{111}Cd, which would be next-nearest neighbors, was less successful because of the small size of the couplings and the relatively low natural abundance.

The ^{199}Hg chemical shifts seemed to depend not on local chemical bonding effects but on some longer range parameter such as the Knight shift. Indeed, the temperature-dependence of ^{199}Hg shifts in a wide range of composition of these alloys has enabled the intrinsic Knight shift to be determined, together with local variations in the Knight shifts [160]. Similarly, Knight shifts of ^{125}Te were inferred from temperature-dependence of shifts and T_1 values, although the interpretation was not straightforward [158]. The possible presence of Knight shifts of unknown magnitude obviously complicates the interpretation of the NMR spectra of semiconductor alloys in terms of neighbor effects upon chemical shifts, as has been done in these examples. One experimental point worth noting is that long T_1 values for the annealed n-type samples made 2D experiments infeasible, whereas uncompensated holes from Hg vacancies in the "as-grown" p-type samples reduced the T_1 values by an order of magnitude, permitting 2D NMR to be carried out in reasonable times.

For the analogous alloy $Cd_{1-x}Zn_xTe$ the ^{125}Te spectra at different compositions x yielded assignments to different Cd_nZn_{4-n} configurations, and the relative peak intensities predicted from a purely statistical distribution agreed fairly well with the experimental spectra [157]. Some evidence for a slight degree of clustering was seen, however. The known decrease in the Cd–Te bond length as Zn is added to the alloy, and the increase in the Zn–Te bond length with increasing Cd concentration was used to rationalize the chemical shift trends, but it also suggests why distributions of chemical shifts might be anticipated. The ^{111}Cd MAS-NMR spectra did not provide any information on possible clustering, since a ^{111}Cd nucleus is always surrounded by four Te atoms, and only the Zn/Cd distribution of the 12 next-nearest neighbors (NNN) should affect the ^{111}Cd chemical shift. This distribution can be calculated for a statistically random occupancy using the Bernoulli function,

and the maximum in the Zn NNN for a given alloy composition can be taken as the most probable number of Zn atoms to be found among the 12 NNN sites; this maximum is linearly dependent upon x, as shown by the dashed-dotted straight line in Fig. 6. This figure also shows that there is an 8.2 ppm change in chemical shift of the ^{111}Cd for each next-nearest neighboring Zn atom. The linewidths also increase at intermediate compositions due to the increasingly large number of different NNN configurations.

The NMR results from the preceding three alloys, $Ga_xIn_{1-x}P$, $Hg_{1-x}Cd_xTe$, and $Cd_{1-x}Zn_xTe$, have been discussed at some length because they illustrate basic strategies dependent upon chemical shifts and heteronuclear couplings (both dipolar and J-couplings) of spin-1/2 nuclei for both the (invariant concentration) anion and the (varying concentration) anions. The same considerations will apply to other binary semiconductor alloys having a ZB or WZ lattice structure. There is a more complicated semiconductor structure known as the chalcopyrite, which forms for ternary II–IV–V_2 compounds, and is derived from the III–V ZB lattice by replacing the group III metal with two different cations and doubling the unit cell [161]. Six such compounds have been studied by ^{29}Si, ^{113}Cd, ^{119}Sn, and ^{31}P MAS-NMR, and in some cases splittings of satellite peaks due to heteronuclear J-couplings to lower-abundant spin-1/2 nuclei could be observed [161]. The ^{31}P MAS-NMR of three of the Zn-containing compounds had been reported earlier [150].

These chalcopyrite semiconductors are of interest for possible optoelectronic and photovoltaic applications. Several such II–IV–V_2 semiconductor alloys have been studied: two where the *anions* are substituted, $CdGeAs_{2-x}P_x$ and $ZnGeAs_{2-x}P_x$ [162], and one where the *cations* are substituted, $Zn_xCd_{1-x}GeP_2$ [163].

Detailed analyses of a combination of ^{113}Cd and ^{31}P MAS-NMR and spin-echo measurements and ^{113}Cd-^{31}P SEDOR experiments led to the conclusions that,

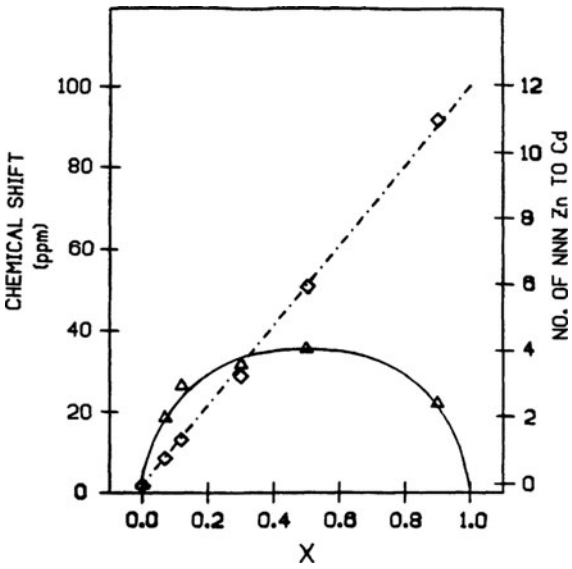

Fig. 6 ^{111}Cd NMR chemical shifts (*diamonds*) and linewidths (*triangles*) of $Cd_{1-x}Zn_xTe$ as a function of x. The *dashed-dotted line* is the most probable number of NNN Zn atoms, and the *solid line* is the width calculated from probability distributions. Reprinted with permission from [157]. Copyright 1987 by the American Physical Society

unlike the previous alloys discussed, chemical shifts could not be used to discriminate between different local nearest neighbor configurations. Instead, ^{31}P-^{31}P and ^{31}P-^{113}Cd dipolar couplings provided the structural information showing a non-random distribution due to both cation and anion sublattices being disordered. For $Zn_xCd_{1-x}GeP_2$ an additional NMR experiment was added to the MAS-NMR and SEDOR experiments: heteronuclear double-quantum filtered (HDQF) NMR [163]. This experiment relies upon the existence of a J-coupling between ^{31}P and a directly-bonded ^{113}Cd nucleus, which is used to create a double-quantum coherence between the pair that is subsequently converted back into observable single-quantum coherence. It is described in detail for the reference compounds $CdSiP_2$, $CdGeP_2$, and Ag_7PSe_6, where heteronuclear J-couplings to ^{31}P were also obtained [164]. Using this sequence, only those ^{31}P nuclei that are bonded to the rare ^{113}Cd nuclei (natural abundance = 12.3%) are observed. By achieving this kind of selectivity for the broad featureless spectra and employing a number of arguments, it was possible to rule out an ordered or completely disordered alloy structure, and to deduce a structure having some bimodal character.

The use of ^{113}Cd-{^{31}P} CP-MAS-NMR for spectral editing in the alloys $CdGeAs_{2-x}P_x$, $CdSiAs_{2-x}P_x$, and $Zn_xCd_{1-x}GeP_2$ has been described [165]. Cross-polarization from ^{31}P to ^{113}Cd or ^{29}Si was also valuable to improve the MAS-NMR sensitivity in the semiconductors $CdSiP_2$ and SiP, using a rotor-synchronized DANTE pulse sequence to obtain a 2D correlation between the six four-coordinate Si sites in the latter compound [166].

In summary, NMR techniques based upon chemical shifts and dipolar or scalar couplings of spin-1/2 nuclei can provide structural information about bonding environments in semiconductor alloys, and more specifically the extent to which substitutions are completely random, partially or fully-ordered, or even bimodal. Semiconductor alloys containing magnetic ions, typically transition metal ions, have also been studied by spin-1/2 NMR; here the often-large frequency shifts are due to the electron hyperfine interaction, and so examples of such studies will be discussed in Sect. 3.5. For alloys containing only quadrupolar nuclei as NMR probes, such as many of the III–V compounds, the nuclear quadrupole interaction will play an important and often dominant role, and can be used to investigate alloy disorder (Sect. 3.8).

3.3.2 Polytypes

Because the cubic ZB and hexagonal WZ crystal structures described in Sect. 2.2 are energetically very similar and differ only in their stacking sequence, in a number of semiconductors either or both forms may be present depending upon growth conditions. Figure 7 shows how MAS-NMR on nuclei of both elements in GaN can clearly distinguish the more stable WZ form from the less common ZB form.

The ^{71}Ga MAS-NMR spectra in Fig. 7a exhibit a difference in the chemical shifts of 24.5 ppm (after correction for a small second-order quadrupolar shift in the CT peak position [60]). The ST peaks for both polytypes shown in the red vertical

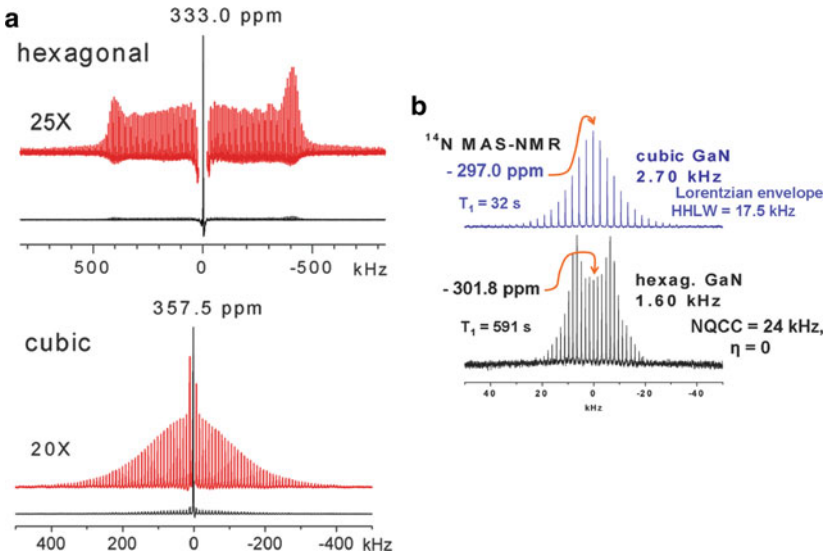

Fig. 7 Identification of cubic ZB and hexagonal WZ polytypes of GaN by chemical shift (indicated) and NQCC differences based upon MAS-NMR of nuclei of both elements. (**a**) ^{71}Ga MAS-NMR, with vertical expansions (*red*) showing ST reflecting NQCCs (reprinted from [60]). (**b**) ^{14}N MAS-NMR at indicated spinning speeds, with measured T_1 values (original spectra, data cited in [60])

expansions are spaced at the spinning speed of 9 kHz, and the envelopes of their intensities reflect the finite NQCCs for both: a $C_q = 1.76$ MHz and $\eta = 0$ for the WZ polytype, and a Gaussian envelope for the ZB polytype having a 297 kHz half-height linewidth and arising solely from the presence of defects in the crystallites.

Many chemically-synthesized GaN samples exhibit a peak from the dominant WZ form, and a much smaller peak from the ZB form. Because of the good resolution, sensitivity, and dynamic range of ^{71}Ga MAS-NMR, polymorphs present at levels below the detection sensitivity of XRPD of ~1% could be identified. Quantitation needs to take into account the differing nutation behavior (mentioned in Sect. 3.2.1 in terms of effective 90° pulse lengths) of the ZB and WZ ^{71}Ga peaks.

The ^{14}N MAS-NMR spectra in Fig. 7b also show a resolvable 4.8 ppm difference between the chemical shifts of the polytypes. Like the ^{71}Ga case, these differences would not be resolved in the static film spectra of Sect. 3.2.1. The very long T_1 values contribute to the low sensitivity of ^{14}N MAS-NMR in GaN in the absence of Korringa relaxation seen for Knight-shifted peaks. The envelope of the spinning-sideband pattern for the WZ polytype approximates the classic powder pattern for an $I = 1$ nucleus (seen mainly for ^{2}H) with $\eta = 0$ and a C_q in this case of 24.14 kHz, as measured in the film samples in Sect. 3.2.1. The envelope for the ZB polytype, which for an ideal sample would have no spinning sidebands, also reflects the effect of defects similarly to the ^{71}Ga spectrum. The much smaller frequency spread for ^{14}N vis-à-vis ^{71}Ga reflects its ca. fivefold smaller nuclear quadrupole moment Q and, for a

point charge model, a smaller Sternheimer antishielding factor, although the EFG values at N and Ga sites are not necessarily equal.

Although it does not relate to polytype identification, we mention a ^{14}N static and MAS-NMR study of WZ AlN, which revealed a fortuitously small $C_q < 10$ kHz [167]. For comparison, the ^{27}Al C_q in the same compound was measured to be 1.913 MHz, and had an unusual positive temperature coefficient that has been seen for other metal nuclei in WZ structures. The ^{14}N MAS-NMR spectrum of BN yielded a C_q of 142 kHz corresponding to an axially-symmetric tensor in the hexagonal ring structure [167].

The ZB and WZ forms of ZnS could be distinguished on the basis of their isotropic ^{67}Zn and ^{33}S static NMR chemical shifts [63]; however, estimates of small CSAs obtained from static ^{33}S NMR of the WZ forms of ZnS and CdS were obtained by ignoring any small second-order quadrupole broadening [65], which may account for discrepancies when NQCCs are assumed to be responsible for the broadenings [65].

Most common semiconductors may exist in the form of one, two, or perhaps three polytypes (especially if high-pressure forms are considered, where the ZB and WZ nitrides can transform into rock-salt structures [168]). Silicon carbide, SiC, a technologically important wide-bandgap semiconductor, is unique in crystallizing in more than 200 different polytypes, all based on a tetrahedral network of alternating Si and C atoms [133]. A useful description of the different possibilities is based on the fact that Si-C six-membered rings can exist in either boat or chair conformations along the c-axis; cubic SiC has only chair forms, whereas other polytypes have different repeating units involving both conformations. The ^{13}C and ^{29}Si MAS-NMR spectra of the polytypes labeled 4 H and 6 H had been previously obtained and, as shown in Fig. 8 (left panel), the different peaks occurring over a small (ca. 10 ppm) chemical shift range were assigned to the four possible local site environments, called A, B, C, and D (not seen here), out to the second-neighbor position (assignments from the two previous studies are labeled 1 and 2 in the figure).

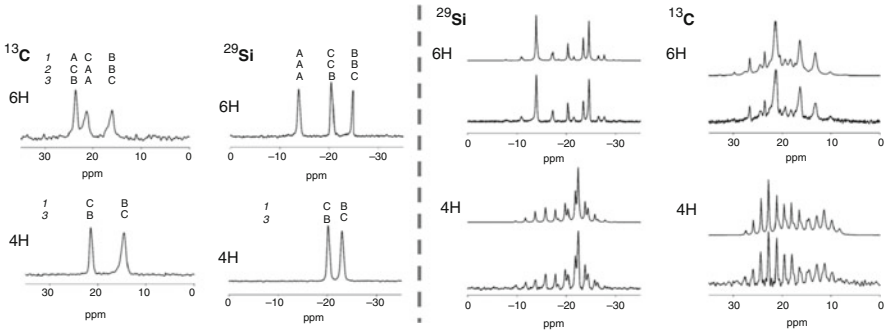

Fig. 8 ^{13}C and ^{29}Si MAS-NMR of two SiC polytypes. *Left panel*: see text for assignments. *Right panel*: Experimental and calculated ultra-slow MAS-NMR spectra at ultra-high field of 21.1 T. Modified and reprinted with permission from [133]. Copyright 2009 by the American Chemical Society

In the most recent study [133] (labeled 3 in Fig. 8, left panel), however, DFT and Gaussian calculation of the chemical shift tensors led to a change in the assignments based on a number of considerations, including measurement of small chemical shift anisotropies by the magic-angle-turning (MAT) method, which eliminates overlapping sidebands from peaks having different chemical shifts. The right panel of Fig. 8 compares the experimental ^{29}Si and ^{13}C MAS-NMR of the two SiC polytypes obtained with slow-spinning (down to 350 Hz) and at a very large magnetic field of 21.1 T (900 MHz ^{1}H frequency) with the spinning side patterns calculated from the theoretically calculated CSA values. The agreement is quite good, indicating that the DFT calculations can give reliable values for the chemical shift tensors in SiC.

Further support for the proposed new assignments came from the ^{13}C to ^{29}Si cross-polarization behavior. Because in the 4 H polytype the type C carbons relax some 70 times faster than the type B due to the Korringa relaxation effect of conduction electrons from the N-doping, saturating both ^{13}C types and allowing only a short recovery delay results in preferential polarization-transfer to ^{29}Si nuclei adjacent to the fast-relaxing ^{13}C nuclei. The observed intensity ratios of peaks supported the assignments given. Overall, this study demonstrates the power of combining theoretical calculations of chemical shift tensors with very high field MAS-NMR of spin-1/2 nuclei and experiments such as CP, MAT, and slow-spinning.

3.4 Knight Shifts

The spin (and possibly orbital) angular momentum of carriers in a semiconductor, either electrons or holes, produces a rapidly fluctuating magnetic field via a contact hyperfine interaction at those nuclear sites having wavefunctions with some s-orbital character for the conduction band or valence band, respectively [25, 26, 169, 170]. The resulting shift in the resonance frequency from what it would be *in the same compound* in the absence of carriers is known as the Knight shift. The fluctuations in the magnetic field also serve to decrease the spin-lattice relaxation time T_1 of the nucleus, a mechanism known as Korringa relaxation. Carrier concentrations even in rather heavily-doped semiconductors are considerably smaller than conduction electron concentrations in metals. As a result Knight shifts in semiconductors are much smaller than in metals, where values of 10,000 ppm (1%) or more are common, and are thus more difficult to identify conclusively. Compared to the vast number of reports of Knight shifts in metals, metal alloys, and small metal particles [8–10], the number of such studies in semiconductors is far smaller, and detailed theoretical explanations taking into account complexities of band structure are few. Among the few studies of Knight shifts in intrinsic semiconductors is a ^{125}Te static NMR study of single-crystal tellurium from room temperature to the melting point of 742 K [171]. The T_1 relaxation behavior yielded the small energy gap as well as revealed atomic self-diffusion above 420 K in the unusual spiral-chain crystal structure. Further relaxation studies of ^{125}Te and ^{77}Se

NMR in single-crystal tellurium and selenium also provided information about atomic diffusion [172, 173] as well as the ^{77}Se CSA [174].

Despite the reasonably large number of different semiconductors that have been studied by NMR techniques, there has been no set of predictions of the magnitude of Knight shifts expected for a given carrier concentration in each compound. In many cases, despite almost certain unintentional doping, no Knight shifts have ever been reported. Such a set of predicted Knight shifts, based on band structure calculations and theoretical considerations of atomic hyperfine constants that yield the magnitude of the contact interaction vs atomic number [175], would be extremely valuable to experimentalists. This is particularly so since in many cases polycrystalline or nanocrystalline samples are studied and carrier concentrations cannot be readily determined; peak shifts or broadening due to Knight shifts when unintentional doping levels are high may go unrecognized.

3.4.1 Knight Shifts and Metal-Insulator Transition in Doped Silicon

Perhaps not surprisingly, the most thorough NMR studies of Knight shifts, Korringa relaxation, metal-insulator transitions, and the NMR of the dopant nuclei themselves have been carried out for doped silicon. Since few semiconductors other than PbTe, which presents a considerably more complicated case, have been studied in such detail, it is worthwhile here to summarize salient points from these studies. They conveniently illustrate a number of points, and can shed light on the behavior to be expected in more contemporary studies of compound semiconductors, which are often hindered by the lack of availability of a suite of samples of known and widely-varying carrier concentrations.

Among the earliest NMR investigations of any semiconductors (InSb and GaSb were studied in 1955 [176]) are reports from 1956 on the ^{29}Si chemical shifts of Si and SiC [177] and on ^{29}Si T_1 relaxation times at 300 K in n-type and p-type Si over a range of concentrations [178]. It was found that T_1^{-1} was proportional to the carrier concentration for the higher carrier concentration samples, but dropped off more rapidly for the purer samples, approaching asymptotic limits. This behavior accorded with theoretical expectations for nuclear relaxation by a Boltzmann distribution of nondegenerate carriers [169]; for a given carrier concentration the T_1^{-1} was eight times faster for the n-type than p-type, due to the large p-orbital character in the hole wave function at the ^{29}Si site [179]. Detailed studies of Knight shifts and relaxation in a semiconductor were carried out by Sundfors and Holcomb [179], who were concerned with understanding the nature of the metal-insulator transition taking place as the electron carrier concentration crossed a region between approximately 4×10^{18} cm^{-3} and 10^{19} cm^{-3}. Holcomb and his coworkers continued detailed studies of n-type (P- or As-doped) and p-type (B-doped) Si over many years [180–185] and summarized early evidence concerning the metal-insulator transition in Si in a review article [23]. He also studied the metal-insulator transition in Si by EPR [186] and in a tungsten bronze by ^{183}W NMR [187]. Warren

and coworkers have also made a detailed study of P- and B-doped Si [188, 189], and other studies of doped Si have been reported [190, 191]. Some of these will be discussed further below.

The temperature dependence of the carrier concentration and the resultant Knight shift in silicon, as in most if not all semiconductors, depends upon the regime one is in. For n-type Si with donor impurity concentrations $n_D < 4 \times 10^{18}$ cm^{-3}, the semiconducting regime, most electrons are bound to the impurities at temperatures below 20 K [179]. At higher temperatures, there is an exponential increase with temperature of the electron carriers. Donor concentrations in the range 4×10^{18} to 10^{19} cm^{-3} result in a transition region where a so-called impurity band just below the conduction band grows in width, and significant conductivity exists at the lowest temperatures and increases slowly with temperature. Finally, for donor concentrations $n_D > 10^{19}$ cm^{-3} the impurity band overlaps the conduction band and a metallic region is reached, and the conductivity (still well below that of a typical metal) is independent of temperature.

The ^{29}Si relaxation rate T_1^{-1} at 1.6 K vs donor concentration n_D shows a sharp decrease between $n_D = 2.5 \times 10^{18}$ cm^{-3} and $n_D = 6 \times 10^{18}$ cm^{-3}. This reflects the fact that in the semiconducting regime (lower donor concentrations), the unionized donors are paramagnetic point sources of relaxation for the ^{29}Si nuclei. Their localized electron spins are more effective in inducing relaxation than the itinerant electrons found in a conduction band at the higher donor concentrations [18].

Let us now consider the metallic regime, following the discussion of [18]. For nuclei coupled to a mobile system of independent electrons by an isotropic exchange interaction of the form $A\mathbf{I} \cdot \mathbf{S}$, where $\mathbf{I}$ is the nuclear spin and $\mathbf{S}$ the electron's spin, the Knight shift can be written as

$$K = (8\pi/3)\chi_s \langle |\Psi(0)|_{k^2} \rangle, \tag{4}$$

where $\langle |\Psi(0)|_{k^2} \rangle$ is the amplitude of the electron wave function at the nuclear site, averaged over the electrons on the Fermi surface, and χ_s is the electronic spin susceptibility. The latter quantity is proportional, for a degenerate system of free electrons, to $n_c^{1/3}$, where n_c is the electron (carrier) density. This proportionality is indeed observed for the ^{29}Si Knight shift for $n_D > 2 \times 10^{19}$ cm^{-3}. An inhomogeneous broadening of the ^{29}Si peaks was ascribed to a distribution of Knight shifts, and a model for such a distribution developed. This model will be discussed later in Sect. 3.4.4. For lower values of n_D, the shift falls away sharply towards a constant value at the beginning of the transition region from the semiconducting state to the impurity band region.

For the metallic regime described above, when the $A\mathbf{I} \cdot \mathbf{S}$ interaction is also responsible for the nuclear relaxation, Korringa [192] showed that the Knight shift and T_1 are related by

$$K^2 T_1 T [(4\pi k_B/\hbar)(\gamma_n/\gamma_e)^2] = 1 \tag{5}$$

where T is the absolute temperature, and the expression in brackets contains standard physical constants. Thus, constancy of the "Korringa product" K^2T_1T over a range of temperatures or Knight shifts is an important indicator of the existence of a degenerate system of electrons of the type described above. The mean electron wave-function density at the ^{29}Si nuclei, $\langle|\Psi(0)|_{k^2}\rangle$, was calculated, from the measured K and by assuming the susceptibility is the Pauli susceptibility and the effective mass is that appropriate to the conduction band, to be the same as that measured for electrons thermally excited into the conduction band at room temperature.

For B-doped p-type samples of Si with an acceptor concentration n_A of 8.5×10^{19} the ^{29}Si NMR also showed a Knight shift of 33 ppm (both n-type and p-type Knight shifts were reported as unsigned, presumably positive, values; see Sect. 3.4.2). Comparison with results for the n-type sample led to the conclusion that there was a nearly equal admixture of s-type wavefunction for the hole wave function near the top of the valence band.

After these and other [193–199] studies on doped Si at temperatures around liquid helium or even as low as 40 mK [200], which included ^{11}B ($I = 3/2$) and ^{31}P Knight shift and T_1 measurements of the dopants at high concentrations, more recent work [188, 189] has sought to explore the intermediate regime of impurity band formation using these dopant nuclei as well as the host ^{29}Si nuclei. Higher magnetic fields of, e.g., 8 T improved sensitivity such that NMR experiments, including T_1 measurements, could be carried out over a wide temperature range between 100 and 500 K. These temperatures are more relevant to the actual operation of semiconductor devices and are also more typical of NMR studies of semiconductors by chemists. For B-doped Si with carrier concentrations from 3.4×10^{18} to 5×10^{19} cm^{-3} both the ^{11}B resonances and the ^{29}Si resonance shifted to higher frequency with decreasing temperature, with both resonances being to high frequency with respect to the reference compound (6N silicon for ^{29}Si) [188]. A high frequency shift relative to the same reference is also reported for n-type P-doped Si [189].

The conclusion of the B-doped Si study [188] was that for the above concentration regime the acceptor impurity band played a significant role in the electronic properties, and that only in the most heavily-doped sample did the behavior approach that expected for delocalized free carriers. An earlier static and MAS ^{11}B NMR study [191] at a higher concentration ([B] $= 2.2 \times 10^{20}$ cm^{-3}) showed Korringa-type relaxation at both 5 K and 300 K, and yielded a mean ^{11}B Knight shift of 68 ppm in the independent electron approximation (the sign of the shift is undetermined by this approach, since it involves K^2). The temperature-dependent ^{11}B resonances reported in the intermediate regime [188] do not provide a value for the Knight shift because the shift reference of $NaBH_4$ cannot be considered a proper "zero" for ^{11}B Knight shift measurements of B in an Si matrix. The ^{11}B MAS-NMR study [191] was also able to show from nutation, spin-counting, and homonuclear dipolar coupling T_{2e} experiments that the NQCC was surprisingly small, ≈12 kHz, in contradiction to several earlier reports. It also showed that all of the ^{11}B was

being observed, that the boron existed in clusters, but that a previous model for such clusters involving a Poisson distribution [179] was incomplete.

The most detailed NMR study of impurity band formation in a semiconductor in the intermediate regime involved ^{31}P and ^{29}Si T_1, linewidth and shift measurements at 8 T from 100–500 K for Si samples doped with P at levels between 4×10^{18} cm^{-3} and 8×10^{19} cm^{-3} [189], and an alternate simplified interpretation of these results in terms of an extended Korringa relation [185]. While the results and interpretation are too involved to discuss here, the important conclusion was that the conventional picture of P-doped Si at 300 K consisting of fully-ionized donors and carriers confined to extended conduction band states is inadequate. Instead, a complex of impurity bands survives in some form to doping levels as high as 10^{19} cm^{-3}. A related example of an impurity NMR study of impurity bands is discussed in Sect. 3.8 for Ga-doped ZnO.

Germanium, directly below silicon in the periodic table, has also been studied by NMR. Impurity band formation in As-doped germanium, where the metal-non-metal transition occurs at a much lower density than in silicon of ~3.5×10^{17} As cm^{-3}, has been studied by measuring ^{73}Ge ($I = 9/2$) T_1 values at 4.2 K in single crystals over a range of dopant densities spanning the transition [201]. In this study the ^{73}Ge Knight shifts (in the range of ca. 100 ppm and higher) exhibited the expected $n_c^{1/3}$ concentration dependence in the metallic regime. The application of stress to the sample was expected to change the Knight shift by affecting the conduction band such that one conduction band minimum is lowered in energy relative to the other three [202, 203]. Although a longer T_1 and T_2 were observed under applied stress [204], no change in the Knight shift could be detected.

3.4.2 Sign of the Knight Shift

The question as to the sign (i.e., direction) of the Knight shifts resulting from electrons or holes is somewhat complicated, since it depends upon both the mechanism of the Knight shift (contact, dipolar, core-polarization, orbital) as well as the nature of the carriers, which in the following brief exposition following reference [205] we will now restrict to being conduction electrons. The magnetic splitting of such conduction electrons is generally given by an effective g factor g^* (also called g_{eff}), which differs from the free electron value of approximately 2.0. In an effective-mass formalism, this arises from coupling to a nearby band that is split by the spin–orbit interaction. For small bandgaps and large spin–orbit interactions the effect can be large; in InSb the $g^* = \sim -50$. The polarization of the electronic spins in a magnetic field, which is responsible for the contact Knight shift through the electronic susceptibility term χ_s in the formula for K given above, thus depends upon g^*. As derived under certain reasonable (but not invariably satisfied) assumptions [205], the Knight shift arising from the contact hyperfine interaction is given by

$$K = (4\pi/3) g\, g^{*} \mu_B^2 V |\Psi_F(0)|^2 \rho(E_F), \tag{6}$$

where V is the sample volume, the wave function at the Fermi energy is squared, and $\rho(E_F)$ is the density of states per unit volume for a single spin. One important point to draw from this is that the sign of the Knight shift is governed by the sign of g^*. As noted in a study of the ^{71}Ga Knight shift in n-type GaAs, $g^* = -0.44$, which is consistent not only with OPNMR results on GaAs mentioned in Sect. 3.2.3 but also with the negative Knight shift obtained for n-type GaAs from the MAS-NMR study mentioned below [118]. The closeness of the calculated values [206] of the (anisotropic) g^* in WZ GaN to a value of 2.0 are similarly consistent with the large positive ^{71}Ga Knight shifts demonstrated in n-type GaN [207], which are discussed below in terms of the inhomogeneous distribution of such shifts found in samples. From a ^{113}Cd NMR study of the T_1 and Knight shift in n-type CdTe between 4.2 and 300 K, the data were actually used to obtain a value for the unknown g^* [205]. This was accomplished by first establishing that at some temperature both T_1 and K are entirely due to degenerate, independent conduction electrons (this was not true at 4.2 K, where paramagnetic impurities dominated). A direct proportionality, involving only fundamental constants, between the Korringa product T_1TK^2 and g^{*2} thus enabled a value of $g^* = -1.1 \pm 0.1$ to be obtained. The sign was obtained from the sign of the Knight shift.

It should be pointed out that a somewhat different expression has been given for the Knight shift [32] and used in the analysis of PbTe data that in addition to the g^* factor contains a factor A. The factor A corresponds to the $|\Psi_F(0)|^2$ probability above except that it can be either positive or negative, depending upon which component of the Kramers-doublet wave function has s-character, as determined by the symmetry of the relevant states and the mixing of wavefunctions due to spin–orbit coupling.

The Knight shift has also been theoretically calculated for InAs and InSb, III–V compounds having strongly negative g-factors [208]. The mechanism is shown to be Fermi contact rather than orbital, but at high doping concentrations the Knight shift is predicted to decrease after reaching a maximum.

3.4.3 Knight Shifts in Compound Semiconductors

We have discussed in Sect. 3.4.1 Knight shifts and Korringa relaxation in n-type and p-type Si in some depth because it is by far the semiconductor most thoroughly studied by NMR. One important lesson should be derived from these studies, when considering the possible existence of Knight shifts in semiconductors where they have not been previously demonstrated to exist. This is that the characteristic signature of the Knight-Korringa relationship between shift and T_1 will only apply to semiconductors sufficiently doped to be in a metallic regime having degenerate and independent electron carriers, in which case the Knight shift will not depend strongly upon temperature, as is often the case with true metals. For

carrier concentrations in intermediate regimes involving the formation of impurity bands, the NMR behavior will be much more complicated, and the concentration range of this regime is usually not known for a given semiconductor. An example is given below for ^{113}Cd NMR in CdO. The small magnitude of Knight shifts at lower carrier concentrations in the semiconducting regime means that their behavior has not been studied in detail for any system. However, the higher resolution now achievable by using high field strengths, MAS, and even heteronuclear decoupling to remove broadening from scalar couplings can be expected to open up possibilities in this area.

With the detailed background for Knight shifts and Korringa relaxation in Si in mind, we can now summarize many of the Knight shift studies that have been carried out in compound semiconductors. The ^{113}Cd NMR of a powdered single crystal of CdO with $n_c = 2.6 \times 10^{19}$ cm^{-3} (from either Cd interstitials or oxygen vacancies) exhibited a constant $T_1T = 168$ seconds-°K for $T = 1.4$, 4.2 and 77–350 K, indicating Korringa relaxation in a degenerate electron semiconductor [209]. By using the Knight-Korringa relationship, a Knight shift to high frequency of 170 ppm could be deduced (the observed shift of 310 ppm measured with respect to an aqueous solution thus contains a chemical shift contribution of 140 ppm due to the covalent bonding in CdO). The probability density at the nucleus was also obtained.

The first NMR study of impurity band formation in a compound semiconductor involved the same CdO system over a wider range of carrier concentrations (3.3–44 $\times$ 10^{18} cm^{-3}) [210]. The authors discuss an impurity band forming when the concentration is high enough for electrons to move freely between donors, and which can be estimated as N_c from the Mott criterion of overlapping Bohr radii as $N_c \approx (0.25/a_H)^3$, where a_H is the impurity Bohr radius. This impurity band region can also be called semi-metallic. Above a higher impurity concentration $N_{cb} \approx (1/4\pi)(a_H)^{-3}$ the impurity band moves into the conduction band and the metallic regime exists. The value of N_{cb} was estimated to be 10^{19} cm^{-3} from the ^{113}Cd NMR data, which showed T_1 proportional to $N_e^{-2/3}T^{-1}$ and K proportional to $N_e^{1/3}$, where N_e is the carrier concentration, just as expected for a degenerate electron case. The Korringa relationship also holds. Note that for the non-degenerate electron case, with Maxwell-Boltzmann rather than Fermi-Dirac statistics, T_1 would be proportional to $N_e^{-1}\,T^{-1/2}$; in both cases T_1 is independent of frequency. For $N_e < 10^{19}$ cm^{-3} the data do not follow the above relationships, and relaxation is non-exponential, suggesting that electrons are concentrated near impurities forming an impurity band, with nuclei near the center experiencing strong contact interactions that relax them and more distant nuclei relaxed only by spin-diffusion. The nature of the localized paramagnetic moments at the impurities remains uncertain however. As pointed out, it would be interesting to pursue these studies into the semiconducting region below the Mott criterion N_c of about 2 $\times$ 10^{18} cm^{-3}, if samples with such low carrier concentrations can be made.

One of the few cases where Knight shifts for both n-type and p-type material have been studied is PbSe [211] and PbTe ([32] and references therein, and [212–214]), where both ^{207}Pb and ^{125}Te static spectra have been obtained. The

true chemical shift could be determined as the intercept of the two extrapolations of the measured shifts for both n-type and p-type material vs $n_c^{1/3}$, as shown in Fig. 9. These shifts are linear except at the highest concentrations and are of opposite slopes. Interestingly, irreversible changes in the spectra of p-type PbTe were noted after several hours of heating to the relatively modest temperature of 430 K, pointing out the need to consider the effects of thermal treatments on carrier concentrations and Knight shifts in other semiconductors as well. The ^{207}Pb NMR line shape and Knight shifts and annealing effects in 76 samples of PbTe and $Pb_{1-x}Sn_xTe$ alloys made from single-crystal ingots with measured carrier concentrations and mobilities have also been reported [215], and a theoretical interpretation made in term of band parameters [216]. There is a considerable amount of complexity and conflicting interpretations exist for the cases of PbSe and PbTe [217], quite possibly due to the presence of non-contact contributions to the Knight shifts of ^{207}Pb in n-type material and of ^{125}Te in p-type material that were attributed to an orbital hyperfine interaction [32]. Complexities of the band structure also preclude simple interpretations. The contribution of spin–orbit interactions to Knight shifts, which might be expected to be more important for heavier nuclei such as ^{207}Pb, have also been treated in a number of theoretical papers by Tripathi and coworkers [218–225], although direct predictive connection with experimental results is limited [222, 223]. A theory for the effective g-factor relevant to ternary alloys in this system has also been developed [226], and the

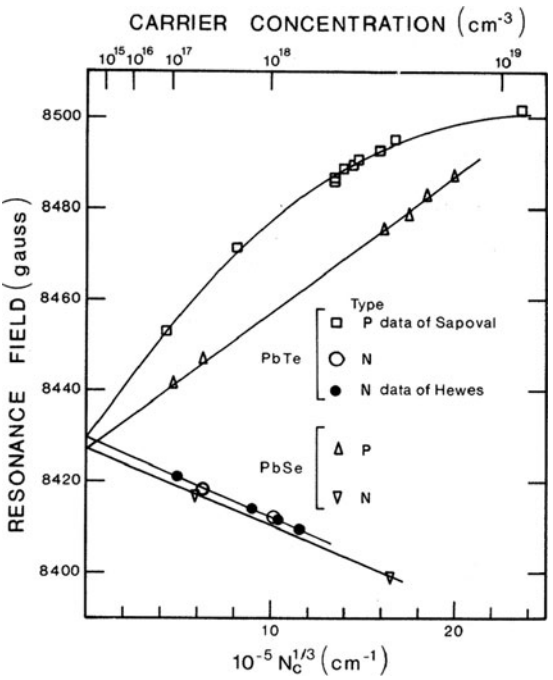

Fig. 9 Resonance field of ^{207}Pb as a function of carrier concentration in n- and p-type PbSe and PbTe at 7.5056 MHz and 1.3 K. The intercept provides the reference for zero Knight shift. In a parabolic band the shift should be linear with $N_C^{1/3}$, as it is for except for p-type PbTe, whose VB is strongly non-parabolic. Reprinted with permission from [213]. Copyright 1973 by the American Physical Society

Knight shift in p-type PbTe has been calculated based on relativistic augmented plane wave functions [227].

The Knight shifts of ^{115}In and ^{121}Sb in n-type InSb at 0.4–4.2 K and with n_c ranging from 2×10^{14} to 1.2×10^{16} cm^{-3} were measured, and oscillations in the Knight shift as a function of magnetic field strength were observed and compared to theory [228], following on an earlier report [112]. They originate from oscillations of the conduction electron DOS at the Fermi energy as a function of field due to the presence of Landau levels (cyclotron energies) of electrons in a magnetic field; similar oscillations have been observed for the Knight shifts in some metals. Knight shifts of ^{115}In and ^{123}Sb in heavily-doped n-type InSb and InAs at different field strengths at low temperature have been used to obtain information about the s-character of the wavefunctions at both nuclei in regions around the metal-insulator transition [229]. Both ^{121}Sb ($I = 5/2$) and ^{123}Sb ($I = 7/2$) T_1 values have been measured at low temperature in InSb [230], and together with ^{115}In T_1 values were used to study electron hopping in InSb [113]. The ^{115}In Knight shifts in Te-doped InP have also been reported at 77 and 4.2 K [231].

For the important and well-studied semiconductor GaAs (ZB structure), ^{71}Ga T_1 measurements have recently been reported on single-crystal samples both above and below the metal-insulator transition (MIT) as a function of both temperature and magnetic field [118]. For the most metallic sample, with $n_c = 2 \times 10^{18}$ cm^{-3} and a Korringa relaxation behavior, applying the Knight–Korringa relation to the low-temperature relaxation data yielded a calculated value for the magnitude of the Knight shift of 11 ppm, which could not be measured directly at low temperature because of the 80 ppm broad linewidth. Therefore, a MAS-NMR spectrum at 19.6 T of a powdered sample of this same wafer was obtained at 300 K, and a Knight shift of ~ -3.3 ppm (presumably defined in the conventional way as $\Delta H/H$, and therefore representing a shift to high frequency) was obtained by comparison with the shift of an SI GaAs sample. The reason for the discrepancy was not clear, especially since an expression accounting for the temperature dependence of the Knight shift predicted only a 7.5% correction on going from low to high temperature.

In this study, the need to take into account effects of Landau levels at higher magnetic fields, as in the case of InSb discussed above, was also mentioned. Interesting aspects of the T_1 relaxation mechanisms are considered in this work. At higher temperatures approaching 300 K, the T_1 relaxation curves for doping levels varying from SI to the most metallic converged, indicating the dominance of a quadrupolar relaxation mechanism at the higher temperatures. Below 30 K the relaxation in the SI sample was attributed to the shallow donors having a Bohr radius of ~100 Å, with a Fermi contact rather than the usual dipolar electron hyperfine interaction being responsible for relaxation. Rapid spin-diffusion takes place between relaxation centers just outside a diffusion bottleneck radius b, which is temperature and field dependent and of the order of ~200 Å. In order to calculate a low-temperature T_1 for the SI sample, a value for the electron correlation time τ_c was required. Two possible sources of fluctuations of the hyperfine field at the nuclear site were considered – fluctuations in donor site occupancy and magnetic exchange couplings between localized donors. The former was excluded on the

basis of the weak temperature dependence observed, and the latter calculated from a theoretical expression. The calculated relaxation rate at 4 K was in fair agreement with the experimental value. More important than the actual numbers perhaps, for studies of low-temperature relaxation by shallow donors in other semiconductors, are the considerations involved in the theoretical modeling.

Sizeable room-temperature Knight shifts in a variety of unintentionally and intentionally doped h-GaN (WZ form) samples have been observed by static ^{71}Ga and ^{14}N NMR of films [49], as mentioned in Sect. 3.2.1, as well as by MAS-NMR of polycrystalline powders [207, 232]. It is interesting to note that the ^{14}N Knight shift is only slightly smaller than the ^{71}Ga Knight shift [232], presumably due to the countervailing factors of a ca. twofold smaller atomic hyperfine constant for ^{14}N vis-à-vis ^{71}Ga [175] but a twofold higher s-orbital character of the CB (although DFT calculations of the partial DOS seem to predict more comparable s-orbital characters [233]). The ^{69}Ga MAS-NMR of GaN nanoparticles also showed Knight shifts [234] (see Sect. 4), but ^{69}Ga and ^{71}Ga MAS-NMR of HVPE h-GaN microcrystalline samples showed that Knight-shifted peaks did not generally appear as a result of heat treatment [235]. In the ZB polytype c-GaN Korringa-type T_1 relaxation with T_1 proportional to T^{-1} was observed in the ^{71}Ga static NMR for the higher electron carrier concentration of 2.5×10^{17} cm^{-3}, indicating a metallic regime, and corresponding to a Knight shift of 54 ppm [236]. For the lower concentration sample (1×10^{15} cm^{-3}) T_1 was proportional to $T^{-1/2}$, as expected for a semiconducting regime. The significance of the distributions of Knight shifts observed in ^{71}Ga MAS-NMR of h-GaN will be discussed in the next section.

3.4.4 Distributions of Knight Shifts

In the relatively few cases where Knight shifts have been clearly identified in semiconductors, the linewidths (typically observed in static NMR experiments) are typically much broader than the linewidth of the undoped sample. It is reasonable to attribute this inhomogeneous line broadening to a distribution of Knight shifts due to inhomogeneities in the sample giving rise to varying carrier concentrations. The ^{207}Pb linewidths of four samples of p-type PbTe were plotted against their Knight shifts for measurements taken at different temperatures [37] (the Knight shifts decrease with temperature, for a number of reasons [32, 216]). The plots were linear for all samples, but with different slopes, consistent with the notion that the broadening is indeed due to a distribution of Knight shifts, with the sample having the largest slope being the most inhomogeneous one (this sample was unannealed, and thus was expected to be less homogeneous than the others). It should be pointed out that an anisotropy of the Knight shift in this cubic lattice was predicted by the $\mathbf{k} \cdot \mathbf{p}$ model [216], although it represented a small contribution to the linewidths observed.

As mentioned in Sect. 3.4.3, very broad Knight shifted peaks were also observed by ^{71}Ga MAS-NMR in samples of h-GaN either with unintentionally-doped shallow donors (primarily Si and O) or intentionally doped with 0.13% Ge,

a known shallow donor [207]. By assuming that the Knight shifts in what was shown to be a degenerate electron system were proportional as discussed above to $n_c^{1/3}$, where n_c is the carrier (electron) concentration, a probability density function of carrier concentration was obtained. This function is simply the probability that a given carrier concentration exists in the sample. Lacking an absolute calibration of the Knight shifts vs *measured* carrier concentrations in this system, an indirect calibration was used based on earlier ^{71}Ga T_1 measurements for h-GaN of known carrier concentration, assuming Korringa relaxation applied.

In this approach to quantitatively analyzing the distribution of carrier concentrations, it was noted that the spatial length scale of dopant concentration fluctuations was an area for future exploration [207]. It is certainly clear that if each crystallite possessed a different dopant and thus carrier concentration, then this approach would be valid to the extent that the Knight shift followed an $n_c^{1/3}$ functional dependence as expected for a parabolic band.

However, a model previously proposed by Sundfors and Holcomb [179] in their low-temperature NMR study of Si (see Sect. 3.4.1) introduces some subtleties that should be considered when trying to obtain carrier probability density functions from Knight shift lineshapes. They attempted to account for the ^{31}P Knight shift distributions of the phosphorus dopant in the metallic regime of n-type Si at 4.2 K. The ratio of the linewidth to the magnitude of the Knight shift was found to be essentially identical for ^{31}P (0.86) and ^{29}Si (0.82), consistent with a distribution of Knight shifts as the source of the broadening. Considering the Knight shift from the expression given in Sect. 3.4.1, $K = (8\pi/3)\chi_s\langle|\Psi(0)|_{k^2}\rangle$, they wrote the electronic susceptibility per unit volume as

$$\chi_s = N(g\beta\langle S_z\rangle_{av}/H_0), \tag{7}$$

where N is the number of electrons per unit volume and $\langle S_z\rangle_{av}$ is the expectation value of the electron spin quantum number S_z averaged over all electrons. Sundfors and Holcomb argue that the T_1 of the electron spin at 4.2 K is almost certainly longer than the time for an electron to move from one ^{31}P impurity to another, a transit time they state is only about 5×10^{-14} s at 10^{19} electrons/cm^3. Thus, the polarization factor $\langle S_z\rangle_{av}$ is determined over long distances in the crystal and represents an average value for the whole crystal (the validity of this argument in general would seem to depend upon the assumed time for an electron to travel a large distance while undergoing multiple scattering events, an assumed lower limit for the unknown electron T_1, and the average crystallite size). In this formulation, the ^{31}P Knight shift K observed is proportional to the local carrier concentration N, but the *mean* value of K is still proportional to $\langle N\rangle_{av}^{1/3}$, since $\langle S_z\rangle_{av}$ is changed when $\langle N\rangle_{av}$ is changed, by a factor $\langle N\rangle_{av}^{-2/3}$.

In their model, N is the *local* electron density measured over an appropriate volume, which they argue is given by the Mott criterion discussed in Sect. 3.4.1. Thus, with the Mott radius of 20 Å for uniform spheres, these spheres will constitute the appropriate volume over which to measure the *local* electron density N.

The overlap of the wavefunction of an impurity centered on such a sphere with impurity wavefunctions for any number of impurities within the sphere will contribute electron density to the central nucleus; those impurities outside the sphere will have no effect. Because of the low probability of occupation of lattice sites by the atomically dilute ^{31}P nuclei a Poisson distribution describes the fluctuation about the average number of atoms in a given volume. In the two samples investigated, this average number of P impurity atoms was about 3 and 4. The variation in the local density N calculated from the Poisson distribution was used to predict the shape of the broad Knight-shifted ^{31}P NMR peak (with $\langle S_z \rangle_{av}$ assumed constant), and the agreement in both cases was reasonable, as long as the number of atoms in the sphere was equal to or greater than the average number (for a smaller number, the local density would render the region non-metallic).

The extent to which the Sundfors and Holcomb model of Knight shift distributions might apply to the room-temperature ^{71}Ga Knight shift distributions in h-GaN [207] is uncertain. It is not clear that it can explain the very different shapes of the inhomogeneously broadened peaks observed in many instances simply by using a different Poisson distribution. As stated previously, variations in carrier concentration from crystallite to crystallite should be well-represented by the ${n_c}^{1/3}$ model used. For variations within crystallites, the impurity band/conduction band electron T_1 values at room temperature may be extremely short, limiting the "sampling" distance. These have recently been reported to be of the order of 50 ps for much less heavily-doped ($n_c = 2.2 \times 10^{17}$ cm^{-3}) n-type h-GaN samples [237], and, since the electron T_1 is expected to be proportional to $1/{n_c}^2$ [238], extremely short values on the order of 5 fs are expected for two orders of magnitude higher dopant concentrations. The fact that ^{71}Ga is not atomically or isotopically "dilute" would not appear to be relevant, since it is the Poisson distribution of the atomically dilute shallow donor atoms that was argued to be relevant in the model. One might argue that these Poisson distributions can only produce very discrete values for the Knight shifts that would be resolved as distinct multiple peaks in ^{71}Ga MAS-NMR due to the narrow homogeneous linewidths under MAS; however, it is plausible that a less idealized model might produce some variations in shifts that would smear out such features.

To investigate the important questions raised by these considerations, it would be desirable to measure Knight shifts in single-crystal films of h-GaN (or possibly other semiconductors) that are grown to have two different dopant concentrations, both above the metallic transition, in alternating layers of varying thicknesses. The resulting Knight shift distributions would be compared with those from two separate films having the same two, but uniform, dopant concentrations.

3.5 Electron Hyperfine Couplings

The hyperfine couplings between localized electrons on paramagnetic impurities and nuclear spins often serve as the dominant source of spin-lattice relaxation for

otherwise slowly-relaxing nuclei, particularly spin-1/2 nuclei in semiconductors such as SiC [108, 239]. When spin-diffusion from rapidly-relaxing nuclei near the paramagnetic center to more remote nuclei is slow, stretched exponential relaxation may result, as mentioned in Sect. 3.2.4.

An extensive and detailed study of T_1 relaxation induced by paramagnetic donor electrons has been reported for the quadrupolar nuclei ^{69}Ga and ^{71}Ga and the spin-1/2 nucleus ^{31}P over the wide temperature range 1.8–300 K in doped GaP [240]. The donor concentrations (from Te and S) varied from 1×10^{17} to 9×10^{18} cm^{-3}, and effects of interactions between the somewhat extended wavefunctions of the donors were observed well below the metal–non-metal transition expected at 5×10^{19} cm^{-3}. Below a concentration of 10^{18} cm^{-3} the donors acted as isolated relaxation centers. For the gallium nuclei relaxation over most of the range was spin-diffusion limited, but the ^{31}P nuclei were in a fast spin-diffusion regime because of a larger barrier radius. Sharp minima in the gallium nuclei T_1 vs T plots monitored the variation of the *electron* spin fluctuation time over a wide range of 10^{-10} s to 10^{-4} s.

Electron hyperfine interactions created by optical illumination can have marked effects upon semiconductor relaxation. The ^{111}Cd and ^{113}Cd peaks in CdS at 4.2 K showed a marked reduction from 3×10^3 min to 30 min during illumination with white light, and remained at 4×10^2 min after the light was turned off [241]. Paramagnetic relaxation centers created by the light were responsible.

However, the remainder of this section will treat examples where paramagnetic centers in the form of transition metal centers have been intentionally introduced into semiconductors, and where spectral frequency shifts rather than relaxation effects have constituted the primary parameters of interest. So-called magnetic semiconductors, which include diluted magnetic semiconductors (DMS) and ferromagnetic alloy semiconductors (FAS) have been widely studied with regard to their magnetic and magneto-optical properties and potential applications in the nascent field of spintronics [242]. The DMS are II–VI or III–V semiconductors doped primarily with Mn, or less-commonly Co, Cr, Fe, etc. In the III–V case, divalent dopants such as Mn^{++} occupy primarily the cation sites and as acceptors supply holes, which can mediate ferromagnetism in p-type materials [242]. So far such ferromagnetism has been limited to temperatures well below room temperature, although Mn-doped p-type GaN has been predicted theoretically to be ferromagnetic above room temperature [243]. Although there have been numerous experimental reports of some ferromagnetic behavior in GaN samples containing Mn, the weakness of the observed magnetism renders it impossible to exclude small amounts of ferromagnetic contaminants or extraneous ferromagnetic Mn-containing phases.

Solid-state NMR offers a powerful means of directly confirming the incorporation of paramagnetic ions into semiconductors, because of their effect of increasing the rate of spin-lattice relaxation and, at high enough levels, of affecting the spectral appearance. Thus, the ^{69,71}Ga and ^{14}N MAS-NMR spectra of a GaN sample synthesized with Ge as a co-dopant to increase the Mn incorporation (1% Mn, 3.5% Ge) exhibited broad peaks shifted to higher frequency that were attributed to Knight shifts from Ge acting as a shallow donor; the ^{71}Ga spin-lattice

relaxation time was bi-exponential (21% $T_1 = 0.05$ ms, 79% $T_1 = 74$ ms), values much shorter than the 3.4 s T_1 of undoped h-GaN [232]. It was suggested that rapid relaxation of ^{71}Ga nuclei by nearby Mn^{++} ions in the GaN lattice and subsequent spin-diffusion to more remote ^{71}Ga nuclei was responsible, although at the time the effects of Korringa relaxation by conduction electrons could not be excluded. Subsequent quantitative study of the Korringa relaxation as a function of Knight shift [207] provided data that showed that the T_1 of the Mn,Ge-doped GaN was indeed much shorter than expected from Korringa relaxation alone, supporting the conclusion of Mn^{++} incorporation into the GaN lattice.

A clear example of the utility of NMR in investigating ferromagnetism in DMS is a study of $Zn_{1-x}Mn_xGeP_2$, which has a chalcopyrite structure (as discussed in Sect. 3.3.1) and has been reported to have room-temperature ferromagnetism [244]. The zero-field NMR spectra at 77 K of both MnP (known to be a ferromagnet at 77 K) and two $Zn_{1-x}Mn_xGeP_2$ samples with $x = 0.08$ and $x = 0.15$ are shown in Fig. 10 (left panel). In this example of Ferromagnetic Magnetic Resonance (FMR) at zero external field, the magnetic fields are supplied by internal fields that differ greatly for the two nuclei ^{31}P and ^{55}Mn. The ^{55}Mn ($I = 5/2$) resonance between ca. 110–125 MHz arises from nuclei that see a magnetic field generated by the contact hyperfine interaction of s-electrons polarized by the exchange interaction with unpaired electrons in the d shell; it is split into five peaks because the degeneracy of the spin 5/2 states is removed by interaction with an EFG.

The ^{31}P resonance at 74 MHz is due to the smaller magnetic field generated by the transferred hyperfine interaction, also a contact electron hyperfine interaction. No other resonances were observed in a wide range around 57 and 78 MHz, the frequencies predicted for ^{55}Mn ($I = 5/2$) and ^{31}P respectively from a first-principles calculation of the local fields in $Zn_{1-x}Mn_xGeP_2$. The identical frequencies and linewidths of the zero-field MnP and the two $Zn_{1-x}Mn_xGeP_2$ spectra show clearly that there must be clusters of MnP in the $Zn_{1-x}Mn_xGeP_2$ samples that are responsible for the ferromagnetic behavior of the samples. Quantitative comparisons of

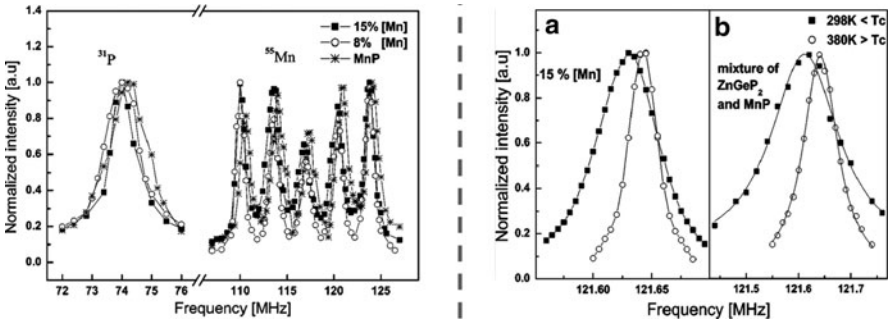

Fig. 10 *Left panel*: Zero-field NMR of $Zn_{1-x}Mn_xGeP_2$ at 77 K. *Right panel*: (**a**) ^{31}P NMR spectra at 7 T of $Zn_{1-x}Mn_xGeP_2$ with $x = 0.15$; (**b**) mixture of $ZnGeP_2$ and MnP. Reprinted with permission from [244]. Copyright 2003 by the American Institute of Physics

signal intensity showed that more than 90% of the Mn atoms of both $Zn_{1-x}Mn_xGeP_2$ samples were in the form of MnP.

One important difference between conventional NMR and FMR, besides the removal of the external magnetic field, is the enhancement of both the signal and the exciting rf pulse by the accompanying oscillation of the electronic magnetic moments (by a factor of usually 10–100 in domains and 100–10,000 in domain walls) [244]. Since the enhancement factors for bulk MnP and $Zn_{1-x}Mn_xGeP_2$ were the same, and most of the signal of bulk MnP arises from the domain walls, it was concluded that the average particle size was at least tens of nanometers. That the clusters of MnP in the $Zn_{1-x}Mn_xGeP_2$ samples were not detected by XRPD was attributed to the poor crystallinity of the MnP formed under the growth conditions used. Figure 10 (right panel) also shows the static ^{31}P NMR spectra obtained at a field of 7 T of two samples, $Zn_{1-x}Mn_xGeP_2$ with $x = 0.15$, and a mixture of $ZnGeP_2$ and MnP. Spectra were obtained both below (298 K) and above (380 K) the reported T_c of 310 K for the ferromagnetic-paramagnetic transition. The shift observed upon cooling the $Zn_{1-x}Mn_xGeP_2$ sample is too small to be due to the transferred hyperfine field of a ferromagnetic DMS, and instead is due to dipolar fields generated by MnP magnetic clusters, as shown in the spectra on the right of the finely-ground mixture. The 70 and 30 kHz linewidths of the spectra on the left could be narrowed to 1.15 kHz by MAS, although spectra were not shown.

This study convincingly illustrates an experimental NMR approach that establishes that ferromagnetism in DMS can arise from undetected ferromagnetic phases rather than from an intrinsic property of the DMS. In the case of Co-doped ZnO, the absence of a zero-field ^{59}Co NMR signal from any Co metal clusters was used along with X-ray Photoelectron Spectroscopy (XPS) data on the composition $Zn_{0.9}Co_{0.1}O$ to infer that the semiconductor exhibited room-temperature ferromagnetism [245]. A zero-field NMR search found evidence for a 0.1% level MnAs phase in the DMS Mn-doped GaAs [246].

The most detailed NMR studies of DMS have been for the II–IV semiconductors CdTe, CdSe, and CdS doped with transition metal ions. The static and MAS ^{113}Cd and ^{125}Te NMR of the ZB structures $Cd_{1-x}Fe_xTe$ [247] and $Cd_{1-x}Mn_xTe$ [248] with variable x up to $x = 0.055$ exhibit multiple peaks that are shifted mostly to higher frequency by the electron hyperfine interaction (referred to there as the transferred hyperfine interaction). The ^{113}Cd shifts for the various values of x could be assigned by assuming that the shifts depended not upon the distance of the Mn^{++} ions in the ZB lattice from a central ^{113}Cd, but rather on the number of intervening bonds. This is reasonable, since the shift is due to the Fermi contact term rather than the dipolar term. Thus, there are 12 possible sites separated by 2 bonds (and equal distances) from the central Cd (first shell), a total of 42 sites separated by 4 bonds (but 3 different distances) from the central Cd (second shell), and 80 sites separated by 6 bonds in the 3rd shell. By assuming that the hyperfine interactions are additive (e.g., the shift from two Mn^{++} ions anywhere in the first shell is twice that arising from one Mn^{++} ion in the same shell), good agreement between the observed and calculated spectra could be obtained.

The shifts in the ^{113}Cd spectra due to the electron hyperfine interaction from an Mn^{++} ion two bonds distant could then be used to obtain a transferred hyperfine interaction constant A that could be compared to the value obtained from ESR measurements. For ^{125}Te, the nearest neighbor Mn^{++} apparently broadened the NMR signal beyond detectability; the transferred hyperfine interaction constant A for Mn^{++} ions in the second shell was calculated from the ^{125}Te shifts.

The ^{113}Cd T_1 values estimated for the various peaks varied from 10 to 50 ms and obeyed the qualitative dependence upon $1/R^6$ (R = Mn–Cd distance) of the dipolar relaxation mechanism expected to be operative. The broad linewidths were also shown to have significant contributions from the T_2 relaxation induced by Mn^{++}, with both dipolar and contact terms contributing. The ^{113}Cd shifts of the peaks assigned to different shells were measured as a function of temperature, and observed to follow a linear 1/T dependence characteristic of the Curie–Weiss law, with slopes proportional to the transferred hyperfine interaction constant A.

One should note that in DMS it is the superexchange interaction between unpaired *electron* spins that is of great interest in terms of the magnetic properties; here it would be the Mn–Mn spin interaction mediated by the intervening Cd and Te atoms. However, because of the fundamental similarity noted for the superexchange and the transferred hyperfine interactions [248], measurements of the latter are informative. Indeed, it was noted that the ratio of spin-density from the Mn^{++} ion calculated from the transferred hyperfine constants in two successive Cd shells was 0.1, indicating a tenfold reduction for further-removed Mn^{++} ions; this result agreed with the ratio of first and second nearest-neighbor superexchange constants for the Mn^{++}, which was approximately 10, and suggested a similar dependence upon bonding properties in the DMS.

Qualitatively similar results and analyses were made for $Cd_{1-x}Fe_xTe$ [247], with the transferred hyperfine interaction constant A being 1.5–1.7 times larger than the corresponding ones in the $Cd_{1-x}Mn_xTe$ case, which suggestively parallels the ratio of the corresponding superexchange constants between nearest neighbors Fe pairs or Mn pairs respectively. The ^{113}Cd MAS-NMR spectra obtained with short repetition intervals also showed spinning sidebands previously observed and analyzed to arise from the magnetic moments of paramagnetic ions [249]. These were assigned to a dipolar interaction between ^{113}Cd and first-shell iron atoms at a distance of 4.56 Å, enabling the magnetic moment of the iron to be determined.

A similar approach was taken in the variable-temperature ^{113}Cd MAS-NMR study of $Cd_{1-x}M_xSe$ (M = Mn, Co, Fe) [250], which however adopts the WZ structure. Because of this, the conformations of next-nearest-neighbor (NNN) differed from those in the ZB CdTe structure, and were described in terms of trans and gauche conformations or dihedral angles. Also, because of the lack of cubic symmetry, the dipolar interactions with the unpaired electrons on the metal ions were not the only features responsible for producing spinning-sidebands, unlike the situation in $Cd_{1-x}Fe_xTe$ discussed above.

Another DMS having a WZ structure studied by ^{113}Cd MAS-NMR is $Cd_{1-x}M_xSe$ (M = Co, Fe), where assignments were made to specific NNN M-S-Cd-S-Cd conformations [251]. In the case of Co^{++} substitution, however, the

spectra could not be fitted to a random distribution of Co^{++} ions, but instead could be fitted (likely not uniquely) to a microscopic mixture where about half of the cadmium atoms do not interact with the paramagnetic Co^{++}, and the remainder interact with a more concentrated but random Co^{++} distribution.

The electron hyperfine interaction thus has important effects on both NMR relaxation and frequency shifts, and can provide valuable information on the incorporation of magnetic ions into semiconductor lattices and the resulting electronic structure as characterized by transferred hyperfine constants. Examples in Sect. 4 will show how the possible incorporation of magnetic ions into semiconductor nanoparticles can be studied by NMR.

3.6 Exchange Couplings

In principle the exchange coupling between nuclei in semiconductors carries information about electronic structure, since it involves an indirect nuclear spin coupling via the hyperfine interaction between electronic and nuclear spins [252]. In solids, the basic theory was worked out in metals, where conduction electrons provide the mediating interaction, by Ruderman and Kittel [253] and Bloembergen and Rowland [254], who also demonstrated experimental results and considered the case of insulators and anisotropic exchange interactions. The exchange (indirect, or *J*) coupling is a second-rank tensor $\mathbf{J_{jk}}$ between nuclei *j* and *k* in the Hamiltonian term $\mathbf{I_j} \cdot \mathbf{J_{j,k}} \cdot \mathbf{I_k}$, with $\mathbf{I_{j,k}}$ referring to the nuclear spin operators (the exchange coupling is sometimes written using matrix elements A_{jk}). In NMR spectra the isotropic part of the exchange coupling is also referred to as the scalar indirect coupling constant *J* and is expressed in units of Hz.

One major difficulty in utilizing exchange couplings in semiconductors resides in accurately measuring the typically small values even between directly-bonded nuclei in the presence of other broadening interactions (including the anisotropic portion of the exchange coupling) and the common situation of exchange couplings to more than one directly bonded nucleus or isotope. Using NAR, a technique relying upon the EFG alterations quadrupolar nuclei experience when subjected to acoustic waves, as well as NMR on single crystals of a number of III–V compounds, Sundfors [252] was able to determine both like and unlike and isotropic and anisotropic exchange couplings from the moments reflecting the linewidths. A MAS-NMR survey of a number of III–V compounds was able to obtain from the broadening of the Gaussian linewidths of the central peak the isotropic part of the exchange constant $\mathbf{A_{jk}}$ between directly-bonded nuclei [66].

Perhaps the most detailed studies of both the isotropic and anisotropic exchange interactions have been made for InP, where the anisotropic (pseudo-dipolar) part of the ^{31}P-^{115}In exchange coupling was shown to reduce the measured ^{31}P second moments from theoretical values calculated from dipolar couplings alone [255, 256]. Double and triple resonance ^{31}P MAS-NMR experiments have also provided much information as a result of the existence of the two nearly identical isotopes of

In, ^{113}In ($I = 9/2$) and ^{115}In ($I = 9/2$) [257]. The magnitude of $J_{iso}(^{31}P\text{-}^{115}In)$ was 225 ± 10 Hz, with an anisotropic term of magnitude either 813 Hz or 1733 Hz. The ambiguity in the latter constant arises from the inability in this (and in most cases where J couplings are measured) to determine the sign of J^{iso} experimentally, or even to deduce it theoretically reliably [258, 259]. The homonuclear ^{31}P exchange couplings have also been obtained [260] and the triple-resonance approach was applied to determine whether there was a dependence of the heteronuclear exchange coupling upon carrier concentration, as had been theoretically predicted for PbTe; none was found over the range of concentrations studied [261].

Other examples where exchange and/or pseudodipolar interactions have been studied in semiconductors include ^{115}In and ^{121}Sb in InSb [176], all the NMR nuclei in GaAs and InAs [262], ^{31}P in AlP [263] and in GaP [264], and ^{69,71}Ga and ^{75}As in GaAs [264]. The last study found a linear relationship between the exchange coupling constant in GaP, GaAs, and GaSb and the static dielectric constant, as predicted by the BOM of Harrison. Additional examples of such studies include ^{125}Te in (Cd,Hg,Pb)Te [265] and ^{111,113}Cd and ^{125}Te in a single crystal of CdTe [266]. A new technique for measuring indirect homonuclear exchange couplings in MAS-NMR based on a shift in the timing of the Hahn spin-echo has been demonstrated in GaAs [267], and the fall-off of indirect couplings with distance between the nuclei was observed to be slower than theoretical predictions.

The future utility of exchange couplings in the NMR of semiconductors may reside less in the comparison of the limited number of experimental measurements of low or modest accuracy with more refined theoretical calculations by DFT methods, and more instead in the ability to establish correlations between chemically-shifted nuclei in MAS-NMR spectra. However, dipolar couplings can also be used in such a situation by employing the recoupling methods discussed by Nielsen in another chapter of this book.

3.7 Dipolar Couplings

Dipolar couplings between nuclei differ somewhat from the other interactions described in that they can be calculated exactly for pairs of nuclei having known internuclear separations and angles of the internuclear vector with respect to the magnetic field. Even when clusters are present, an analysis can be carried out by measuring the second moments of static NMR spectra, combined with heteronuclear decoupling if appropriate and feasible. This approach has been very well developed and successful in studying the structure of glasses by distinguishing various structural models and using model compounds [268]. It should also be useful in determining the degree of ordering in semiconductor alloys as discussed in Sects. 3.3.1 and 3.8.1.

The spin dynamics of solids whose primary or sole nuclear interactions (ignoring the omnipresent Zeeman and isotropic chemical shift terms) are dipolar interactions among a very large number of nuclei present interpretive and theoretical challenges

to the NMR spectroscopist. Although a spin-spin relaxation time "T_2" is often referred to in solid-state NMR, strictly speaking it is generally not appropriate, since the dipolar-coupled spin system is undergoing a unitary evolution that can be described theoretically by a density matrix, rather than undergoing an irreversible decay as in the case of a liquid. The "T_2" behavior in a solid is not in general an exponential decay, and it depends upon the spin or spatial manipulations such as MAS that are carried out, including the pulse sequence used to measure it. In this context, it is worth citing in passing a number of studies that have examined the spin-dynamics of ^{29}Si NMR in pure or doped silicon, single-crystal or polycrystalline, some with isotopic enrichment or depletion, some with multiple pulse cycles such as MREV or CPMG: [269–273]. An interest in understanding aspects of quantum information processing (QIP) is one of the primary motivations for these studies of Si, which has been a major candidate for implementing some QIP concepts.

3.8 Nuclear Electric Quadrupole Interactions

Earlier sections of this review have already discussed results for quadrupolar nuclei in certain connections: for Knight shifts (Sects. 3.4.3 and 3.4.4), for electric-field (Stark) effects upon NQCCs (Sect. 3.1), for measurements of NQCCs in GaN by static NMR and the effects of strain upon NQCCs (Sect. 3.2.1), for obtaining exchange couplings by MAS-NMR (Sect. 3.2.2), and for characterizing polytypes and defects in cubic polytypes by chemical shifts and NQCCs obtained from MAS-NMR (Sect. 3.3.2). This section will give some further examples of information about semiconductors obtained from the NMR of quadrupolar nuclei (see also [18]).

3.8.1 NQCCs in Semiconductors: Polytypes, Alloys, and EFG Distributions

The static or MAS-NMR of quadrupolar nuclei should enable in general the distinction based upon the difference in NQCCs between polytypes of the ZB and WZ forms, as illustrated by the ^{71}Ga and ^{14}N MAS-NMR of c-GaN and h-GaN in Fig. 7 and the discussion in Sect. 3.3.2. The majority of III–V compounds, however, despite containing many quadrupolar nuclei, occur only in the ZB form under normal conditions. An example where polymorphs (polytypes having different crystal morphologies as well) can be distinguished based on their NQCC values is BN, where ^{11}B ($I = 3/2$) relaxation was also studied in BN polymorphs [274], and the ^{10}B ($I = 3$) and ^{11}B NMR obtained from cubic BN films grown by CVD [275]. Another example is the three polymorphs of titania, TiO_2, which have been distinguished based on the NQCCs obtained from second-order broadened powder patterns in the overlapping ^{47}Ti and ^{49}Ti static NMR spectra [276]. The two common titania polymorphs anatase and rutile have been distinguished based on

the ^{17}O MAS-NMR chemical shifts [277]. The ^{47}Ti and ^{49}Ti CSAs have been measured in single crystals of these polymorphs [278]. Section 4.2 discusses NMR studies of nanoscale titania.

Even in the cubic ZB form, as Fig. 7 shows, the presence of NQCCs arising from defects or dopants in the lattice can be observed and used for characterization purposes. Static quadrupole effects in disordered cubic solids arising from external stress, point defects, and dislocations have been analyzed in terms of their effects upon the zero-field and high-field NMR [279]. A theory describing NMR lineshape changes from a random distribution of point defects and resultant EFGs has been developed [280]. A similar theory for the time-domain signal predicted that the FID in a perfect crystal with zero NQCC should be scaled by $\exp(-K/t^{3/2})$ in samples having defect densities proportional to the constant K [281]. The results for ZB GaAs samples agreed with the theory for the lower defect densities.

The EFGs produced by Zn and In doping at various levels from 1×10^{18} to 2×10^{20} cm^{-3} in single crystals of GaAs were studied by static NMR of ^{69,71}Ga and ^{75}As [282]. Spin-echoes were used to observe large broadening of the ST peaks. Strain-induced EFGs were found to render ST transitions several megahertz broad within one lattice constant of the defect, and to spread the ST peaks away from the CT at distances of about one to three lattice constants from the defect. At about three to five lattice constants the ST are only slightly broadened, and further away the strain effect is negligible. However, charged defects produce long-range effects on the EFG through their electric fields (through the Stark effect discussed in Sect. 3.1). The orientational dependence of quadrupolar broadening agreed with theory, and the broadening was proportional to the defect concentration up to values as high as 10^{19} cm^{-3}. The influence of charged point defects in nonstoichiometric GaAs samples on second moments has also been reported [283]. The influence of impurity doping in a number of III–V compounds upon quadrupolar parameters has also been investigated [284]. The ^{115}In NMR of powdered InP doped with Te showed very weak ST peaks that were analyzed in terms of the EFGs produced by Te substitution in the ZB lattice [285].

The distribution of NQCCs in amorphous solids as a result of differing ionic coordination has been treated theoretically by Czjzek and co-workers in terms of a probability function for both the EFG along the z-direction, V_{zz} (related directly to C_q), and the asymmetry parameter η [286, 287], since these are not independent variables but have a joint probability. The derivation and utility of the Czjzek model for MAS-NMR of disordered solids having a CT perturbed by the second-order quadrupolar interaction has recently been discussed in insightful detail [288], with experimental examples taken from diamagnetic insulators rather than semiconductors. The principal advantages were seen to be that its parameterization of the observed lineshape provided a better estimate of the root mean square quadrupolar product than alternative methods, and that overlapping resonances could be better deconvoluted by using the knowledge of the lineshape. Further extensions of this modeling approach have been described, including a Gaussian Isotropic Model [289, 290].

The Czjzek model and these other models have also been extensively discussed in connection with a very recent major study [137] of $Al_xGa_{1-x}As$ films described below. One significant finding of this study was that, since point charge calculations of EFGs are inadequate, DFT calculations could be used to model the EFG distributions. The contributions from distant charge perturbations were additive, and calculations of V_{xx} and η were carried out for 3×10^6 configurations of a cell containing $AlGa_{255}As_{256}$. The DFT calculations reproduced the features of the Czjzek and extended Czjzek distributions observed experimentally, and enabled the conclusion that the ^{75}As quadrupolar interaction was sensitive to compositional modulations out to the seventh coordination shell in this case.

Nutation NMR of ^{69}Ga has also been used, along with ^{31}P MAS-NMR, to evaluate the quality and crystallinity of chemically-synthesized GaP [291]. The nutation NMR technique has also been applied to ^{69}Ga and ^{75}As in GaAs and In-doped GaAs in order to obtain information about lattice defects [292], and yielded asymmetry parameters η of about 1 and NQCCs of 93 kHz. The authors also reported a nuclear quadrupole resonance (NQR, or zero-field NMR) experiment showing positive- and negative-going peaks around 95 MHz, and concluded from this that this signal originated from "imperfect portions" of the sample. However, this explanation seems very unlikely in view of the enormous and rather well-defined NQCC for either nucleus it would represent, and also the extremely low concentration of such defects. The zero-field peaks observed are almost certainly due to piezoelectric ringing as described in Sect. 2.2. and reported in GaAs [40], which would disappear when the sample was removed as the authors observed, and which can produce negative-going peaks.

The study of local or long-range ordering in semiconductor alloys based upon the effects on NQCCs has been carried out in a number of cases. These studies are analogous to the study of ordering in $In_{1-x}Ga_xP$ by means of the chemical shift interaction, as described in Sect. 3.3.1.

A point charge model was applied to ^{71}Ga spin-echo NMR measurements of both random and partially ordered films of $Ga_{0.52}In_{0.48}P_2$ in order to obtain what was described as the first quantitative estimate of the local ordering parameter in a ternary III–V semiconductor [293]. Subsequent DFT calculations of EFGs in ordered $(Ga,In)P_2$ showed that the point charge method was inadequate, underestimating the magnitudes, sometimes yielding the incorrect sign, and failing to reproduce relative trends as the crystal structure changes [294]. However, comparisons of the DFT results with a tight-binding calculational method in the same system and analysis of the ^{71}Ga NMR results yielded essentially the same local order parameter as in the first study [295]. The tight-bonding approach calculated EFG changes resulting from atomic displacements about a central Ga atom in a 17 atom cluster also containing the 4 directly bonded phosphorus atoms and the 12 NNN gallium atoms.

Static ^{75}As NMR of the CT in powdered films of $Al_xGa_{1-x}As$ has been used to obtain information about possible ordering in this alloy. The milligram quantities used were obtained by an epitaxial lift-off process from the MOVPE growth substrate and subsequent pulverization. Signals from $^{75}As[Al_4]$ and $^{75}As[Ga_4]$

tetrahedra were observed with a chemical shift difference of ~180 ppm, with average NQCC values of $C\mathrm{q} = 820$ kHz and $C\mathrm{q} = 610$ kHz respectively and T_1 values under 1 s aiding sensitivity. All other mixed tetrahedra around a central ^{75}As nucleus had $C\mathrm{q} > 9$ MHz and could not be observed directly, although spin-echoes and nutation experiments were used to obtain more information. The finite NQCCs observed for the symmetrical tetrahedra clearly indicate that neighbors beyond the first coordination shell contribute to the EFGs. The results were consistent with an absence of significant ordering.

Very recently a much more detailed investigation of $Al_xGa_{1-x}As$ films by ^{75}As and ^{69}Ga NMR has been reported [137] at a very high field strength of 18.8 T and using very small rf coils to obtain very large rf fields for nutation and ^{69}Ga 3MQ-MAS experiments. The modeling of the EFG distributions by DFT calculations and comparison with the Czjzek model has been mentioned above. Although the detailed results are difficult to summarize, the lack of a good fit to the data for a long-range order parameter $S = 0$ suggested that some short-range order might exist, having a different order parameter.

The alloy $Zn_{1-x}Mg_xO$ has also been studied by NMR [296]. At levels of up to 15% Mg only weak effects are seen upon the ^{67}Zn ($I = 5/2$) MAS-NMR spectrum, but the ^{25}Mg ($I = 5/2$) resonance is greatly shifted to lower frequencies.

3.8.2 NMR of Quadrupolar Impurity Atoms

The NMR signals from quadrupolar dopant nuclei present at low concentration in semiconductors ("impurity NMR") have also been studied at high fields and at room temperature (the ^{31}P and ^{11}B NMR of these dopants in Si has already been mentioned in Sect. 3.4). The ^{27}Al and ^{69}Ga static NMR of powders of the wide-bandgap semiconductor ZnO, both stoichiometric and non-stoichiometric, doped with the shallow donors Al and Ga in the range 0.03–3 at.%, has been reported [297]. The heavily-doped material is of interest as a transparent conducting oxide (TCO). The NQCC value of 3.9 MHz for the axially-symmetric ^{69}Ga tensor obtained for the most dilute sample from the second-order broadened CT at 5.0 T was similar to the corresponding value obtained for ^{67}Zn here and in a previous single-crystal study [65], evidence that the observed ^{69}Ga nuclei substitutionally occupy Zn sites (Ga_{Zn}). The fact that the EFG q at the ^{69}Ga site is 1.40× that at the ^{67}Zn site was rationalized by assuming a further decrease of the shortest M–O distance (to the axial O) when Ga replaces Zn. The resonance position of ^{69}Ga changed by over 400 ppm going from the most concentrated to the most dilute samples, much more than the change observed for the host nuclei ^{67}Zn.

The strategy adopted to determine the true "chemical shift" of ^{69}Ga in ZnO unaffected by the Knight shift was to establish first that the relaxation was magnetic rather than quadrupolar in origin; indeed, the measured ratio of the ^{69}Ga to ^{71}Ga rates was 1.55, close to the ratio of the squares of the magnetogyric ratios, 1.61, expected for purely magnetic relaxation. By subtracting off a small estimated quadrupolar contribution to the relaxation rate and assuming a Korringa

relationship between the Knight shift and T_1, the extrapolation of a simple linear plot yielded an intercept corresponding to the chemical shift of ^{69}Ga in the ZnO matrix unaffected by the Knight shift. The value thus obtained was 220 $\pm$ 80 ppm from the aqueous reference. Using this chemical shift value, the ^{69}Ga Knight shift could be plotted vs the Ga concentration. At the highest concentration the plot converged to the theoretical $n_c^{1/3}$ dependence expected for free-electron behavior (assuming the Ga concentration is the same as the free carrier concentration n_c).

At lower concentrations of below about 1 at.% Ga (and Al), however, the carriers no longer occupy states in the free-electron-like parabolic conduction band, and formation of a narrow impurity band with an enhanced DOS and enhanced relaxation rate was suggested. However, unlike the situation for impurity bands in Si discussed in Sect. 3.4.1, for ZnO the relaxation was of the Korringa type even in the impurity band region. It was uncertain whether the situations in both semiconductors are fundamentally different, or whether the Mott criterion for estimating the concentration of carriers at the metal-insulator transition severely overestimates the concentration in ZnO. The probability density of electrons at the nucleus was also calculated and compared with the more direct ESR results from hyperfine couplings for the related compound ZnS; the approximate doubling of the density for ZnO was related to the smaller Bohr radius for its hydrogenic impurity states.

The preceding discussion was based on the behavior of the relatively sharp ^{69}Ga peak observed from the FID in stoichiometric Ga-doped ZnO due to substitutional Ga atoms. However, by using spin-echoes (presumably of the Hahn-echo $90°-\tau-180°-\tau-$Acq. variety) in a range of oxygen-deficient (to -1.2 at.%) and oxygen-rich (to +1.0 at.%) nonstoichiometric ZnO samples a very sharp rapidly-decaying signal in the time domain could also be observed that corresponded to a several-hundred kilohertz broad ^{69}Ga peak in the frequency domain spectrum that is shifted towards high frequency from the sharper signal. The fraction of the substitutional Ga_{Zn} sites characterized by the sharper peak ranged from 91% in the most oxygen-deficient sample to only 4% in the most oxygen-rich sample. Since the relaxation rate of the broad component is some three orders of magnitude less than that of the narrow component (relaxed by Korringa relaxation to conduction electrons), it was assigned to distorted diamagnetic trap sites, possibly a doubly-charged oxygen interstitial complexed with two Ga^{3+}. Paramagnetic centers such as Ga^{3+} complexed with a singly-charged oxygen interstitial could be excluded on the basis of the long T_1. In these nonstoichiometric compounds the shifts and relaxation properties of the sharp line are controlled by the amount of substitutional Ga_{Zn} sites, which provide the electrons going into the conduction band. Although the broad component does not exhibit the sharp characteristic features of a second-order quadrupolar pattern, it would be worthwhile to carry out nutation or ST population transfer experiments to determine the NQCC and compare it with theoretical calculations for the proposed diamagnetic digallium complex.

The discovery of superconductivity in heavily B-doped diamond, which produces p-type material, has provoked interest in using ^{11}B and ^{10}B NMR for characterization. The ^{11}B static NMR at 4.2 K of heavily-doped diamond (2.8–8.7 $\times$ 10^{21} B/cm^3) showed two unresolved peaks, the sharper of which was

attributed to B substituting at a symmetrical C site. The reported "Knight shift" for this peak of ~10 ppm was measured only with respect to $B(OH)_3$, which is however unlikely to have the same chemical shift as substitutional B in diamond. The decrease in linewidth at higher fields of the broad component indicated a much larger EFG, and assignment to a boron + hydrogen complex was indicated. However, a 2D ^{11}B NMR experiment, with the two axes corresponding to proton decoupling on and off, showed that such a complex did not exist in substantial amounts [298]. Further ^{11}B NMR study, both static and MAS, as a function of field up to the ultra-high field of 21.8 T, were very informative, the MAS improving resolution by removing the anisotropic interactions of CSA and magnetic susceptibility [299]. Four types of B, characterized by their differing T_1 values, including B_4C and boron powder impurities, were seen. A subsequent investigation by ^{11}B and ^{10}B MAS-NMR at up to 21.8 T using a variety of NMR techniques (decoupling/recoupling, nutation NMR, 2D NMR for ^{1}B/^{11}B interactions and ^{11}B/^{11}B spin-exchange) provided evidence against a B–H complex, and suggested instead a trigonally-coordinated B locally in a graphite-like structure but with a small NQCC [300]. The substitutional B yielding the sharp peak seems to contribute to the superconductivity. Low-temperature T_1 studies of ^{11}B in diamond provided evidence for overlap of the impurity band with the VB as a factor in the superconductivity [301].

3.8.3 Miscellaneous Studies of Quadrupolar Nuclei in Semiconductors

A number of studies not referred to elsewhere will be briefly cited here in order to indicate some of the range of nuclei and semiconductors investigated. The static ^{63}Cu ($I = 3/2$) and ^{115}In NMR of $CuInSe_2$ films has been investigated [302, 303], as well as of $CuInS_2$ [304, 305]. The ^{17}O ($I = 5/2$) static and MAS-NMR of IIA and IIB oxides, including measurements of chemical shifts and NQCCs, has been reported [306]. The ^{27}Al NMR chemical shifts in Al-V and the NQCC in AlN have been obtained [307], as have ^{11}B chemical shifts in BN and BP [308]. The zero-field ^{63}Cu NMR (NQR) of Cu_2O has been reported [309], one of the first semiconductors known and widely studied. The small NQCCs induced in a diamond lattice semiconductor by variations in isotopic composition of germanium single crystals have been analyzed from their effects on the ^{73}Ge ($I = 9/2$) CT lineshape, and modeled in terms of anharmonic motions of the isotopes [310–312].

Transparent conducting oxides are a very important class of materials for optoelectronic applications, and β-Ga_2O_3 is one relatively recent such material, with a wide bandgap (4.8 eV) but n-type semiconducting behavior due to oxygen vacancies formed when made under reducing conditions. The ^{69}Ga and ^{71}Ga static and MAS-NMR of powdered β-Ga_2O_3 [313] as well as static rotation plots of a single crystal have been reported [314]. The ^{69}Ga and ^{71}Ga NMR rotation plots and T_1 relaxation behavior of a single crystal of β-Ga_2O_3 doped with the paramagnetic ion Cr^{3+} at 0.05 mol% have recently been reported [315]. However, there

are a number of internal inconsistencies and inaccuracies in the presentation and interpretation of the T_1 behavior and chemical shifts in this paper.

3.8.4 Effects of Dynamics on Quadrupolar Interactions

Understanding self-diffusion in semiconductors as it may be affected by the presence of defects is the basis for understanding dopant diffusion processes [16]. Labeling semiconductors with radioactive isotopes or stable isotopes during the growth process to monitor diffusion has been the most widely-employed approach. Because of the typically high activation barriers normally encountered, significant atomic diffusion in semiconductors takes place only at elevated temperatures. Despite the well-known utility of solid-state NMR as a probe of atomic (and molecular) self-diffusion processes in solids via the effects of motion upon dipolar and quadrupolar couplings, chemical shift differences, relaxation times, etc., very few studies of such processes in semiconductors have been reported. This may be due partly to the limited availability of high-temperature NMR probes and reduced detection sensitivity at higher temperatures that make the study of thin films more difficult, although NMR relaxation in GaAs has been studied up to 1,425 K [120].

It would of course be possible to monitor dopant diffusion at elevated temperatures across a concentration gradient by heating samples for varying intervals and then studying them at a lower temperature more convenient for NMR. This strategy does not appear to have been employed however. Two cases where dynamics in semiconductors have been observed by NMR both involve the MAS-NMR of half-integer quadrupolar nuclei, with the effects manifesting themselves as a broadening of the ST spinning-sidebands due to modulation of the EFGs (and hence NQCCs) interfering with the formation of rotational echoes by MAS [60, 122]. The naturally p-type semiconductor γ-CuI is unusual in also being a Cu^+ ion conductor, especially in other high-temperature phases. The ^{63}Cu MAS-NMR spectra of γ-CuI exhibited a broadening of the ST peaks over the temperature range observed of 298–358 K, as shown in Fig. 11. (It should be noted that, although γ-CuI has a ZB structure that ideally would lead to a zero NQCC, the presence of defects, including the Cu^+ ion vacancies responsible for the p-type behavior, leads to a distribution of NQCC values and resulting ST.) From a simple analysis of the ST broadening that yielded a jump rate at each temperature and a subsequent Arrhenius plot, an activation barrier for Cu^+ ion hopping of 0.64 eV was obtained, in agreement with earlier static NMR studies based upon linewidths and T_1 relaxation times as a function of temperature [316].

A similar broadening of the ST spinning-sidebands in the ^{71}Ga MAS-NMR of the h-GaN component of a synthesized mixture also containing c-GaN was observed at room temperature. This observation was very surprising, since no diffusion of defects or unintentional dopants is expected at room temperature in this partly-covalently bonded semiconductor. Static Hahn-echo ^{71}Ga NMR measurements at the ST perpendicular edge of the hexagonal (WZ) form revealed a dramatic shortening of the (biexponential) T_2 with increasing temperature

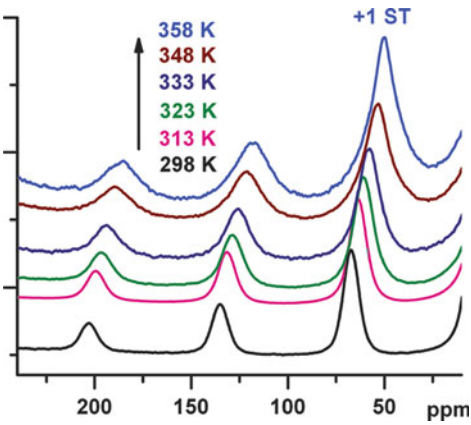

Fig. 11 ^{63}Cu MAS-NMR at 9.0 kHz spinning speed, partial spectra of γ-CuI (ZB structure) diluted in an inert matrix, showing broadening of first three STs as temperature is increased. The spectra shift to the right due to the temperature dependence of the chemical shift. Quantitative analysis of the broadening yields an activation energy for Cu^+ hopping of 0.64 eV. Reprinted from [122]

compared to a pure sample of h-GaN. Fluctuating chemical or Knight shifts were ruled out by T_2 measurements at a different field strength, and other possible interactions with the ^{71}Ga nuclear magnetic moment (dipolar, exchange, or possible electron hyperfine interactions) were excluded on the basis of the T_2 measured for the second-order broadened ^{69}Ga central transition (CT). Thus, it could be concluded that the EFGs experienced by the ^{69,71}Ga nuclei were being modulated by some dynamical process at higher temperatures that gave rise to frequency shifts of the ST and the various results observed.

Viewing the results in analogy to classic NMR chemical-exchange behavior, the ratio of the ^{71}Ga to ^{69}Ga T_2 values was used to conclude that the system was not near the fast-exchange limit, but further conclusions about the effective exchange regime could not be drawn. Since no physical motion of atoms or defects is expected to take place in h-GaN at these temperatures, the experimental observations were suggested to occur as a result of a dynamic equilibrium process involving unknown deeper-level donors that are only partially ionized: the movement of electrons from one such donor to another via the conduction band does not change bulk electrical transport properties, but does change the EFG experienced locally by a given ^{69,71}Ga nucleus. Attempts to establish the exact nature of this effect and the possible donor involved by observing these phenomena in other samples of h-GaN were not successful, but the possibility exists of seeing similar effects in other semiconductors containing quadrupolar nuclei and partially-ionized donors (or acceptors).

The nearly-identical T_1^{-1} rates of ^{115}In and ^{75}As from 300–100 K were observed to vary as T_2 over the entire range [317]. However, the addition of trace Cu (11 and 25 ppm) increased the rates above 500 K, and allowed a mean Cu jump frequency and activation barrier of 0.64 eV to be deduced.

Changes in the lineshapes of static ^{63}Cu NMR peaks at high temperatures (from room temperature to 550° C) have been observed in the chalcopyrite structure

compounds $CuInX_2$ (X = S, Se, Te) [318] and attributed to motional narrowing. Mean Cu^+ ion jump frequencies and activation barriers were obtained for all three compounds, and the effect of Cu-deficiencies in the sulfide upon the lineshape and dynamics was studied. The ^{115}In NMR was also studied. These compounds are of interest for photovoltaic and optoelectronic applications, and polycrystalline samples of the sulfide and selenide containing excess S and Se respectively have been studied by ^{63}Cu and ^{115}In NMR over the range 123–473 K [319]. Values for the NQCC and CSA were obtained, and the motional narrowing observed for the selenide yielded a diffusion constant of 3×10^{-13} cm^2/s at 473 K.

4 Nanoscale Semiconductors

4.1 General Aspects

Many of the NMR studies of semiconductors carried out in the past two decades have involved nanoscale samples, or at least nanoscale regions of differing composition within a larger macroscopic semiconductor structure (e.g., single or multiple quantum wells, SQW and MQW). Such nanoscopic materials have a wide range of potential applications, from quantum dots (QD) that when properly surface-labeled can serve as fluorescent tags in biology and medicine or as the active part of photovoltaic devices in solar cells to nanowires (NW) that can sense molecules or threat agents, or to optoelectronic and spintronic devices for combining the effects of light and either the electronic charge or spin to achieve desired applications.

Perhaps the single most salient common feature of the MAS-NMR of nanoscale semiconductors is the observation of severely inhomogeneously broadened lines reflecting a distribution of structural or electronic environments having different chemical, or possibly Knight, shifts. While not entirely unexpected, given the high surface-to-bulk ratio in nanoparticles, it presents challenges to the NMR spectroscopist similar in some ways to those involved in the NMR study of glasses [268]. One-dimensional NMR spectral editing methods based upon such characteristics as cross-polarization behavior can provide very useful information, such as the assignments of semiconductor peaks closest to the surface ligands; however, utilizing the full power of 2D NMR methods for establishing correlations between different NMR parameters of inhomogeneously broadened peaks may be required.

One practical difficulty in many studies is the limited amounts of well-characterized samples available, leading to a sensitivity problem for 2D NMR experiments. The recent development of microcoils for MAS-NMR experiments, either static [320] or rotating with the MAS rotor [321], offers much promise for

improving MAS-NMR detection sensitivity in such cases, although they are still in a developmental stage and not yet commercially available.

We can pose a number of general questions about such nano-semiconductor studies, and offer brief answers to each, before considering specific studies as examples:

1. To what extent do the insights and information obtained from measuring terms in the NMR Hamiltonian for bulk semiconductors, as discussed above, apply to nanoscale studies?

Answer: NMR characteristics observed in bulk semiconductors such as electron hyperfine effects in dilute magnetic semiconductors [322–324], Knight shifts [234], and chemical shift differences resulting from alloying [325–327] and possibly different polytypes [322, 328] have been observed at the nanoscale.

2. Can DFT calculations successfully predict NMR parameters in nanoscale systems?

Answer: Chemical shift calculations for nanoscale semiconductors by DFT methods and comparison with experimental results have recently appeared [140], and while quite challenging hold much promise.

3. What information can be obtained from NMR about the *interfaces* or *surfaces* in such systems, including crystal facets/surface planes? How do NMR parameters vary as a function of distance from the surface?

Answer: Information about capping ligand coordination to the semiconductor constituents, including different environments, and ligand dynamics has been obtained by traditional NMR approaches in a variety of studies, although identification of specific facets (surface planes and vertices) by NMR remains elusive. A combination of CP from surface protons and spin-diffusion into the nanocrystal interior has demonstrated the powerful capability of NMR to provide *depth profiling* of NMR parameters [329], although one other case provides a warning that such an approach may not always work as simply intended [330].

4. At what small dimensions do *quantum-confinement effects* begin to have manifestations in NMR, quite apart from the higher surface areas expected for smaller nanoparticles?

Answer: It is important to recognize that the size regime where such effects are manifested in optical properties such as the blue-shifted spectra vary widely depending upon the semiconductor characteristics. For optical properties to be strongly affected by confinement, the radius of a nanocrystal must be considerably smaller than the exciton Bohr radius, which is only 1 nm for CuCl, 6 nm for CdSe, 20 nm for PbS, and 46 nm for PbSe [331]. When this is the case, instead of a near-continuum of conduction band energy levels for the electrons in a QD (a 0D system) a set of discrete energy levels resembling atomic states exists, and the first excited state is of higher energy than the bottom of the conduction band in the bulk. (For a 1D system there are different levels each having many closely spaced levels

[331].) This basic behavior has been invoked to rationalize observed changes in the chemical shifts to low frequency on going from the bulk semiconductor to a QD, in the case of ^{77}Se shifts in CdSe [329, 332] and of ^{31}P shifts in InP [333]. However, there are additional factors to consider, as discussed below.

Also, for phenomena involving the localization of individual charge carriers arising from doping, such as the Knight shift in NMR, the radius of a nanocrystal must be much smaller than the typically smaller Bohr radii of the electron or hole in order to have strong quantum confinement, a situation difficult to achieve in most II–VI and III–V semiconductors with their large hole masses, but interestingly, not in PbSe [331].

5. What differences in the NMR parameters can be expected based upon the *dimensionality* [334] (e.g., zero-dimensional QD vs one-dimensional nanorods or nanowires or two-dimensional nanosheets)?

Answer: Specific effects of dimensionality upon the NMR characteristics have not yet been reported, although the NMR of some semiconductors in nanoscopic forms other than nanocrystals (NCs) has been reported.

6. Do results obtained from ODMR or OPNMR of semiconductor nanostructures such as quantum wells have relevance to the nanoscopic semiconductors synthesized and studied by chemists?

Answer: There has been little effective interplay between experimental results obtained on single nanostructures grown as quantum-wells and studied by optical-pumping methods and those obtained on bulk nanoscale semiconductors by more conventional NMR approaches. However, this situation may change, since the former studies can provide information about the effects of, e.g., charge carriers or strain or compositional interfaces upon NMR parameters such as chemical and Knight shifts and EFGs in reasonably well-defined systems.

The answers to all of these questions must be considered tentative at present, and indicate the need for further studies in this area involving additional strategies. One very important aspect that merits consideration is the potential presence of Knight shifts as a contributor to peak shifts and broadening. Although Knight shifts have been identified in nano-GaN [234], the possibility of their existence in nano-semiconductor NMR has often simply been ignored. This may possibly reflect the lack of reported Knight shifts for doped bulk samples of the same semiconductor, or it may reflect the widespread belief that it is difficult to dope semiconductor NCs [335, 336]. However, it is very difficult to characterize NCs electrically, and the presence of stacking faults and possibly other types of native defects that for instance have been identified by atomic Pair Distribution Functions (PDF) in CdSe [337] suggest that one should be cautious in assuming that no electrically-active carriers exist in nano-semiconductors. For quantum-confined NCs such as QDs the presence of any such carriers could be revealed by optical measurements.

4.2 NMR Studies of Chemically-Synthesized Nanocrystal Semiconductors

4.2.1 Nanocrystals of Cd Chalcogenides

The specific bulk nanoscale semiconductor system that has been most studied by NMR as well as by other physical methods since the early pioneering work of Brus and coworkers [338] is that of the cadmium chalcogenides, CdS, CdSe, and CdTe, where the NMR nuclides ^{111,113}Cd, ^{77}Se, and ^{125}Te have proven useful despite their low natural abundances (7–13%). At a very early stage of such studies ^{113}Cd MAS-NMR was already used to identify the ZB core nature of < 5 nm diameter CdS clusters as well as peaks due to the thiophenol surface ligand capping [339]. The first NMR results on semiconductor NCs were obtained for ^{77}Se NMR in three isotopically-enriched CdSe samples varying in size from 1.2 to 3.3 nm [332]. Interestingly, the spectra could be obtained as suspensions in pyridine solution, since as the first NMR study of a nanocrystal in colloidal suspension quantitatively showed [340], the fast rotational tumbling of nanocrystalline solids in suspension is capable of substantially averaging out the anisotropic broadening interactions in the solid.

A broadening of the ^{77}Se peak at the chemical shift position of the bulk solid and the appearance of at least two partially-resolved low frequency peaks as the NC size decreased was observed [332]. The inverse energy corresponding to the onset of UV absorption was plotted against the first moment of the line shape, representing an average chemical shift. An approximately linear relationship for the three data points, and an intercept near the inverse bandgap of the bulk material, suggested that the paramagnetic term in the Ramsey expression for chemical shielding, discussed in Sect. 3.2.6, could account for the trend if an average energy difference ΔE to the excited states in the summation could be used as an approximation. A similar linear relationship between ^{31}P chemical shift and an inverse energy corresponding to the point of inflection of the absorption curve was observed for InP nanocrystals ranging in diameter from 2.5 to 4.4 nm, and the intercept was also at the chemical shift of bulk InP [333]. Similar broad ^{31}P MAS-NMR peaks shifted to low frequency were observed for InP confined NCs formed inside the mesoporous channels of MCM-41 [341], with one preparation with an estimated size of 4.3 nm having a very similar ^{31}P chemical shift to that in a similarly-sized (4.5 nm diameter) ligand-capped InP QD in the previous study. This average energy approximation was used to explain chemical shift trends in a very recent ^{77}Se CP-MAS-NMR study of isotopically-labeled CdSe that extracted much information about surface and core sites and size-dependent reconstruction by analyzing in detail cross-polarization build-up curves [329] and modeling spin-diffusion. The high 99.66% ^{77}Se enrichment greatly increased the rate of spin-diffusion from the surface cross-polarized species into the interior. One new finding that seems significant was a difference in the *slopes* of the chemical shift dependence upon inverse energy for the core and the surface ^{77}Se nuclei. A qualitative rationalization was proposed

in terms of an increased s-character in the Se–Cd bond for those atoms nearer the surface, resulting in a decreased contribution of the Ramsey paramagnetic term.

Information about the surface and interface structures in hexadecylamine-capped CdSe NC of 2 nm size has been obtained by a variety of ^{1}H, ^{13}C, ^{113}Cd, and ^{77}Se NMR techniques [342]. The ^{77}Se CP-MAS-NMR spectrum showed five partially resolved peaks from surface or near-surface Se environments. It was possible to obtain 2D heteronuclear correlation (HETCOR) spectra between ^{1}H and the other three nuclei despite the inherent sensitivity limitations (the ^{77}Se-{^{1}H} HETCOR experiment required 504 h!). The latter experiment indicated that the methylene protons of the hexadecylamine chain interact with the surface Se atoms via a tilt of the chain toward the surface. The surface Se atoms were not seen to interact with thiophenol present, and it was suggested that thiophenol binds to a selenium vacancy at the surface.

Another study of the surface structure of CdSe NCs of 3.7 nm size used ^{31}P MAS-NMR and ^{31}P/^{77}Se rotational-echo double-resonance (REDOR) to identify overlapping broad peaks from two surface species: trioctylphosphine oxide (TOPO) at 29.3 ppm and trioctylphosphine selenide (TOPSe) at 22.2 ppm [343]. Both the isotropic chemical shift and CSA of the surface-bound TOPO were substantially different from those of the free ligand. Spin-echo experiments on ^{31}P were stated to indicate an average P–P distance of ~8–10 Å at the surface, consistent with capping at alternate atomic sites (all Cd but not Se).

A variety of Cd chalcogenide nanoparticles including alloys have been studied by ^{113}Cd, ^{77}Se, ^{13}C, and ^{31}P static and MAS-NMR [325]. The sole point that will be mentioned from this paper is the observation of broad ^{113}Cd MAS-NMR peaks for 3.2 nm and 4.5 nm CdSe nanoparticles that are shifted to higher frequency from bulk CdSe; a shift in the other direction for CdTe nanoparticles was also observed. Earlier results having a poorer signal to noise ratio from the ^{113}Cd MAS-NMR spectrum of a 5.2 nm CdSe NC also seemed to center even slightly to higher rather than lower frequency from the peak seen for the bulk [324]. Since the Ramsey paramagnetic term should dominate the chemical shifts of ^{113}Cd as well as ^{77}Se, it is difficult to explain why the quantum-confinement argument used above to rationalize the ^{77}Se shifts should not also produce shifts in the same direction for ^{113}Cd. Differences in the nature of the excited state atomic orbitals centered on the two different atom types might make some quantitative, but not qualitative, difference between the two nuclei.

Alloys of $Zn_xCd_{1-x}S$ with Cd-rich inner cores and Zn-rich outer shells have also been studied by ^{113}Cd MAS-NMR. CP-MAS-NMR was used to identify surface ^{113}Cd nuclei, which were shifted to much lower frequency [326].

Nanoparticles of dilute magnetic semiconductors have also been studied by NMR. Here one important question is whether the magnetic ion is incorporated into the NC or resides on the surface. The ^{113}Cd MAS-NMR of NCs of $Cd_{0.991}Co_{0.009}S$ with diameters from 3.5 to 29.5 nm showed peaks shifted by electron hyperfine interactions from next-nearest neighbor Co^{2+} ions, and by comparison with results from bulk samples that were discussed in Sect. 3.5 it was concluded that Co^{2+} ions occupied Cd^{2+} sites and were distributed homogeneously;

a change from a ZB to a WZ structure was inferred to take place at sizes large than around 8 nm [322]. Proton and ^{113}Cd NMR studies of precipitated CdS NCs with no capping ligands showed peaks due to surface and inner Cd atoms and water trapped in pores. In the case of Mn^{2+} co-doping the proton T_1 provided evidence that Mn^{2+} resides at the surface or in the water, and not in the core of the NC [323]. The nature of the surface water was also investigated more extensively by ^{1}H NMR [344]. The ^{113}Cd MAS-NMR of capped CdSe NCs doped with Mn^{2+} suggested that Mn^{++} was incorporated in the NC, but EPR and etching experiments indicated it resided in surface layers [324].

One difficulty with many synthetic preparations of semiconductor NCs that complicates any interpretation of NMR results is the inevitable distribution of sizes (and exact shapes or surface morphologies). Therefore attempts to make semiconductors as a sort of molecular cluster having a well-defined stoichiometry are of interest to learn potentially about size-dependent NMR parameters and other properties. One approach is to confine the semiconductor inside a template, for instance the cuboctahedral cages of the sodalite framework or other zeolite structures, which have been characterized by multinuclear NMR methods [345–347], including the mesoporous channel material MCM-41 [341, 348].

The study of ZnSe/GaP in sodalite enabled the isolated ^{31}P-^{71}Ga J-coupling in the GaP end member to be determined (712 Hz) from analysis of field-dependent spectra. Spin-diffusion measurements using the simple SPARTAN pulse sequence helped assign different ^{31}P peaks to adjacent cages, and of the four different intracage structures identified ([Zn_4Se], [$GaZn_3P$], [Zn_4P], and [Ga_2Zn_2P]) the P-containing cages were shown not to be distributed randomly by homonuclear dipolar coupling measurements [346].

Another recent approach is based on the discovery that one-pot reactions allowed to proceed for relatively long times can produce what have been termed “magic-sized nanocrystals” (MSN) or “magic-sized quantum dots” (MSQD) that are uniformly sized as a consequence of being formed more under thermodynamic rather than kinetic control. Different families of CdSe MSN have sharp bandgap absorption features shifted to higher energies and have been shown by diffusion ordered NMR (DOSY) to have a very small size range of 1.7–2.2 nm [349]. The ^{113}Cd MAS-NMR of a number of these cadmium chalcogenide MSN has been reported. The ^{113}Cd CP-MAS spectrum of CdSe MSN exhibits a peak at 422 ppm arising from ligand-bonded Cd surface atoms that has spinning sidebands reflecting a sizeable CSA. In contrast, the high-power decoupled spectra emphasize a relatively sharp peak at 680 ppm due to core Cd atoms, which is shifted only slightly to higher frequency from bulk CdSe at 657.7 ppm [350]. The lack of any conspicuous peaks due to a transition zone from surface to core is a feature to be considered in any proposed structural model for these MSN, as is the fact that the presumably inhomogeneously broadened linewidths of core and surface peaks reflect slightly different chemical environments within these regions despite the size uniformity. Similar ^{113}Cd NMR experiments on MSNs of the ternary alloy CdTeSe and its end members show that a homogeneous alloy is formed, with a ca. 1Se:1Te ratio throughout the nanocrystal [327]. The ^{113}Cd MAS-NMR of CdS MSN showed

[351], paralleling the results for CdSe, a peak at 471 ppm from surface Cd atoms and one at 792 ppm from core Cd atoms (slightly to higher frequency of the bulk CdS at 805.7 ppm [325]). It is interesting that the core ^{113}Cd resonances of MSNs are shifted slightly to higher frequency than those of the bulk, which is opposite to the direction expected from quantum confinement effects upon the Ramsey term of chemical shielding discussed above. Observing the ^{77}Se chemical shifts in these materials would obviously be very informative in view of the previous ^{77}Se NMR studies on CdSe NCs.

4.2.2 Nano-Silicon

A number of studies involving ^{29}Si CP-MAS-NMR that provide information on surface structures involving Si–H or Si–OH bonds and surface oxidation have been reported for both porous silicon prepared by electrochemical oxidation of single-crystal Si wafers in HF-based solutions [352–354] and alkyl-terminated Si nanoparticles prepared by further reaction chemistry [330, 355, 356]. Although porous silicon has attracted much attention since the early 1990s because of its high luminescence and an apparent role for quantum-confinement effects, its actual three-dimensional structure is quite complex and incompletely understood; one view is that it is a sponge-like material composed of crystalline silicon that is formed from connecting nanowires of irregular and varying diameters, and which itself can be supported on mesoscopic channels of crystalline silicon.

Only three particularly interesting points will be mentioned from the above studies. (1) No evidence of changes in the ^{29}Si chemical shift of the interior Si nuclei to low frequency due to quantum confinement effects has been seen, an interior ^{29}Si shift of -82 ppm comparing well with a -85 ppm value reported for the bulk [330]. Whether or not this is due to quantum confinement effects being smaller than in the CdSe or InP examples above is uncertain. (2) The use of CP from ^{1}H in surface alkyl groups to ^{29}Si as a means of depth-profiling the different chemical shifts was shown to produce counter-intuitive results, with the interior bulk-like ^{29}Si peak at -82 ppm actually having a higher cross-polarization rate than those ^{29}Si closer to surface ligands. Marked differences in the ^{1}H $T_{1\rho}$ values of protons responsible for cross-polarizing the different ^{29}Si may be responsible [330]. (3) No significant changes due to Knight shifts were detected in the rather broad ^{29}Si MAS-NMR spectra of porous silicon when it was produced from a heavily (5×10^{19} cm^{-3}) B-doped Si wafer [353], despite the observation of a 33 ppm Knight shift discussed in Sect. 3.4.1 for a B-doped Si sample of comparable concentration ($n_c = 8.5 \times 10^{19}$ cm^{-3}). It would be interesting to know whether the T_1 in this sample also remained unaffected by Korringa relaxation, and whether quantum confinement effects in two dimensions produced changes in the electronic structure that reduced the magnitude of the Knight shift. In this respect, quantum-confinement effects on the effective g-factor g^* of the electron that influences the Knight shift (see Sect. 3.4.2) have been theoretically predicted for semiconductor NCs [357].

4.2.3 Nanoparticles of ZnSe

Aside from the possibility discussed above of quantum confinement effects upon chemical shifts in nano-semiconductors, and the distinct possibility of effects from Knight shifts as well, there is to be expected a purely *structural chemical effect* upon chemical shifts arising from the presence of a nearby surface or interface. The termination of such a surface, whether it is reconstructed or not, necessarily involves changes in bond lengths and angles as well as in coordination from those found in the bulk material, changes that will be propagated some distance into the interior. The theoretical calculation of chemical shifts in such cases by DFT methods represents a valuable approach to accounting for the broadened and shifted experimental peaks typically observed in nano-semiconductors.

This has been shown in a recent ^{77}Se and ^{67}Zn study of capped ZnSe nanoparticles that were 9 nm diameter spheroids, 5 nm prolate nanorods, and 1.3 nm diameter nanorods [140]. The ^{77}Se spectra exhibited broadened peaks shifted by as much as 160 ppm to higher frequency for the smallest diameter nanoparticle (see Fig. 12). Although bulk ZnSe is stable only in the ZB form, the possibility of a WZ form in the nanoparticles was considered. However, the DFT calculation predicted only a 15–30 ppm low frequency shift for this form from the ZB form, indicating that surface-induced effects were responsible for the observed shifts (it should be noted however that the possibility of Knight shifts from unintentional doping or native defects was never ruled out as a factor in producing the observed shifts). The quadrupolar ^{67}Zn ($I = 5/2$) spectra of the nanoparticles also showed an unresolved asymmetric peak broadening to lower frequency, due to a combination of both chemical shift changes and second-order quadrupolar broadening. The DFT calculations of ^{77}Se and ^{67}Zn chemical shifts used supercells containing 9 or 17 ZB (100) ZnSe layers with surface capping H_3PO molecules at 50% surface coverage representing the actual TOPO ligand. The calculations show (see Fig. 12) that the ^{77}Se chemical shifts of some Se atoms in the first two layers (whose atomic positions were allowed to relax in the optimization, unlike deeper

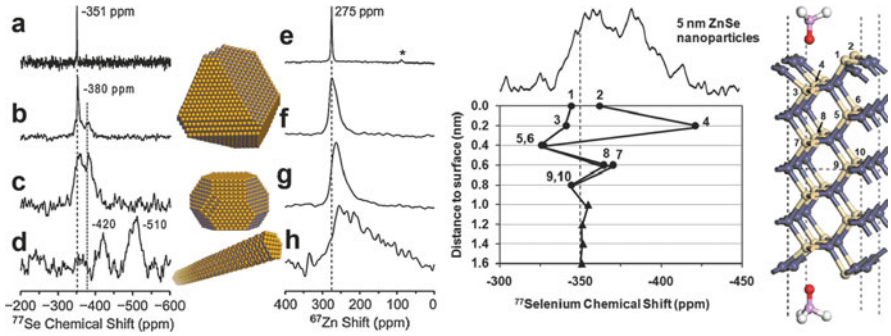

Fig. 12 *Left*: ^{77}Se (spectra a–d) and ^{67}Zn (spectra e–h) NMR of ZnSe nanoparticles with three different sizes/morphologies. *Right*: DFT calculations of ^{77}Se chemical shifts vs distance from the surface. Reprinted with permission from [140]. Copyright 2009 by the American Physical Society

layers with fixed positions) could be shifted to low frequency by as much as 70 ppm due to surface relaxation (~2–3%) as well as interactions with H_3PO molecules adsorbed on surface Zn atoms. While exact agreement is not expected given the idealized picture of the true TOPO-capped surface, the calculations are insightful in showing a damped displacement of the calculated shifts of 20 or 70 ppm on either side of the bulk signal for ^{77}Se sites 0.2–1.2 nm from the exterior surface. This means that even in the sixth or seventh layers, with no distortion of the ZB bulk lattice geometry allowed in the calculation, significant effects upon the chemical shifts are transmitted by changes in the electronic density as a result of the surface termination.

In the future improving sensitivity by studying larger quantities of nanoparticles and using isotopic enrichment may enable more detailed comparisons of DFT calculations with experimental results than in the pioneering study above. For instance, depth-profiling by a combination of CP and spin-diffusion as carried out for ^{77}Se-enriched CdSe NCs [342] provides additional information. Also, in principle measuring small CSA values such as those determined in SiC by MAT-NMR [133] would provide a valuable comparison with the DFT calculations, since electronic distortions near a surface should produce nonzero CSAs even for the cubic ZB lattice. Calculation of quadrupolar parameters for, e.g., ^{67}Zn represents another avenue to compare DFT theory with experiment.

4.2.4 Nanophase GaAs

From a very general outlook, one can argue that the NMR studies of quadrupolar nuclei present in nanoscale semiconductors should offer a more incisive look into the chemical and electronic structure than do studies of spin-1/2 nuclei. The rationale is that quadrupolar nuclei can report on the same chemical, hyperfine, or Knight shifts and dipolar or indirect couplings as observed for spin-1/2 nuclei, but also provide an additional dimension of information in terms of the NQCC and associated EFGs. Although not yet reported, DFT calculations of both chemical shifts and NQCC values for the same nuclei in nano-semiconductors should provide a more stringent comparison of theoretical and experimental results, particularly if the two parameters can be correlated experimentally, as seems feasible.

Although far fewer NMR studies of nano-semiconductors have been carried out for quadrupolar nuclei than for spin-1/2 nuclei, two examples involving ^{71}Ga, ^{69}Ga, and ^{75}As MAS-NMR of III–V nano-semiconductors can be mentioned. The first involved all three nuclei in a study of "nanophase GaAs" having small domain sizes (e.g., 2.5 nm) from XRPD broadening but not consisting of isolated nanoparticles [328]. The ZB bulk GaAs has a ^{71}Ga chemical shift of 217 ppm, whereas two broad, only partially-resolved, peaks are observed for the nanophase samples, at corrected chemical shifts of about 210 ppm (peak *a*) and 183 ppm (peak *b*). The close similarity in appearance of the ^{71}Ga and the ^{69}Ga spectra, despite the much larger second-order quadrupolar broadening and shift that would show up in ^{69}Ga spectra if the NQCC values were large, indicated that such effects were small, and that the

peak positions reflected isotropic chemical shifts. The small differences between ^{71}Ga and ^{69}Ga peak positions were used to estimate an upper limit for the ^{71}Ga NQCC value of 1 MHz for both peaks; the $\pi/2$ pulse for both peaks was exactly one half that of the bulk (ZB) GaAs, indicating that significant EFGs were present from defects or possibly surface effects.

It was suggested that peak *b* arises from a WZ form, perhaps arising from stacking faults, that is not seen in bulk GaAs. The similarity of the 15 ppm shift to low frequency for ^{67}Zn upon going from the ZB to the WZ form of ZnS to the nano-GaAs results, with an observed 27 ppm shift in the same direction going from peak *a* to *b*, was cited in support of this assignment. A subsequent report [60] of a 24.5 ppm ^{71}Ga MAS-NMR shift in the identical direction for the same two polytypes of the more closely-related III–V compound GaN provides even more compelling support for this assignment, and there has been other evidence obtained for a WZ structure in nano-GaAs [358]. The fact that a larger NQCC is observed for ^{71}Ga in the WZ form of GaN [60] than for peak *b* of nanophase GaAs does suggest that DFT calculations or more exact NMR measurements for the latter would be helpful to explain the difference. Relaxation time measurements indicated a fivefold reduction of the ^{71}Ga T_1 from the bulk value for both peaks and identical T_2 values as well (determined by isotropic homonuclear indirect couplings), suggesting a close proximity and similar electronic environment for peaks *a* and *b*. The appearance of a new peak associated with oxidation of the surface was also demonstrated [328].

These T_1 measurements in nano-GaAs, and similar measurements in h-GaN also showing a marked reduction from the bulk rate [359], appear to be the only ones reported for nanophase semiconductors, probably in part due to the limited sensitivity. There is some potential for attempting to use such measurements to learn about the lattice vibrations responsible for relaxation for both quadrupolar and magnetic (specifically nuclear dipole–dipole) relaxation mechanisms. This assumes that contributions from Korringa relaxation, electron hyperfine from magnetic impurities, and relaxation induced by the dynamics of surface groups can be controlled and eliminated. There is interest in phonons in confined structures such as QD because of the differences exhibited with respect to the bulk materials, as a result of the more discrete states forming for the various optical and acoustic modes, which affect carrier dynamics in important but ill-understood ways [360–362].

4.2.5 Nanocrystals of GaN

This first example of the utility of quadrupolar nuclei as sources of information about nano-semiconductors showed that MAS-NMR could identify a polytype that is unstable in the bulk. A second example will show that information about changes in the electronic structure of nanocrystals as a function of synthesis and treatment conditions, as well as information about different polytypes, can be obtained via measurement of Knight shifts and chemical shifts. In this extensive study ^{69}Ga

MAS-NMR of 19 samples of GaN nanopowders also characterized by XRPD were prepared by 4 different synthesis methods, and some were subjected to various treatments [234]. It also provides a warning against the attempts to interpret measured chemical shift positions in nano-semiconductors without taking into account the possible contribution of Knight shifts.

Figure 13 shows an example of how ^{69}Ga MAS-NMR was used to observe a marked increase in the intensity of the broad Knight shifted peak at ca. 420 ppm relative to the unshifted peak of h-GaN at ca. 325 ppm as a result of annealing. The annealing was carried out for hours under a flow of NH_3 at 1000–1050°C, conditions which forced a noticeable decomposition and darkening of the nano-GaN due presumably to loss of nitrogen by formation of nitrogen vacancies that can act as shallow donors, while at the same time improving crystallinity, as seen by XRPD and the slight narrowing of the unshifted peak at 325 ppm. Measuring the ^{71}Ga T_1 values across the inhomogeneously-broadened Knight shifted peaks centered around 420 ppm, as was done earlier in other h-GaN samples to establish the existence of Korringa relaxation [207], would be valuable; there is also the possibility that paramagnetic defects or other increased modes of relaxation might occur in the nano-GaN samples. Obtaining ^{14}N MAS-NMR spectra would also confirm the almost certain assignment to Knight shifts.

In addition to observing Knight shifts in nanoparticles of the usual WZ form of GaN (h-GaN), this study also observed them in the rarer ZB c-GaN form. Various proportions of c-GaN could be identified in nano-GaN prepared by nitridation of GaAs, which has a cubic (ZB) structure and therefore provides topochemical conditions favoring c-GaN. Figure 13 (right side) shows the ^{69}Ga spectra of three

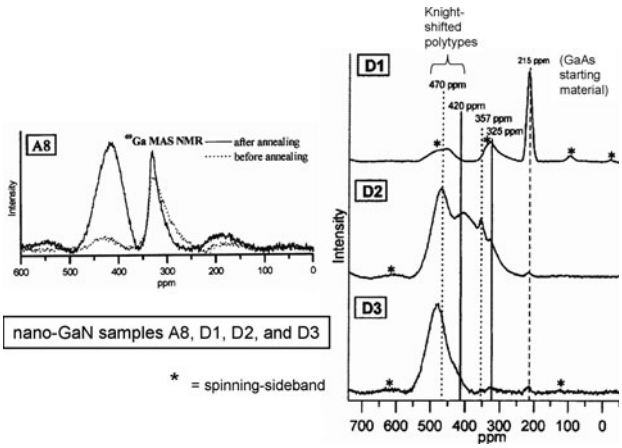

Fig. 13 ^{69}Ga MAS-NMR spectra of GaN nanopowders labeled by sample codes. *Left*: Knight shift resulting from thermal annealing. *Right*: three different samples produced by GaAs nitridation synthesis containing c-GaN (357 ppm) as well as h-GaN (326 ppm). The broad peak at 470 ppm is assigned to Knight shifts in c-GaN. Reprinted with permission from [234]. Copyright 2008 by the American Chemical Society

such samples that differ in their proportions of unshifted h-GaN (325 ppm) and c-GaN (357 ppm). From the observation that a broad peak at 470 ppm increases in relative intensity as the relative amount of c-GaN from XRPD increases, a reasonable conclusion can be drawn that the 470 ppm peak is due to c-GaN exhibiting Knight shifts as well.

The lack of confinement effects observed in this ^{69}Ga MAS-NMR study of nano-GaN can be readily understood. All of the samples had particle sizes well exceeding the Bohr radius recently estimated from EPR measurements of only ca. 3 nm [363].

Because the shift to high frequency of ^{71}Ga MAS-NMR peaks in nano-GaN has received an alternative interpretation not involving Knight shifts, it is justified here to review briefly the evidence against such an alternative explanation. Previous ^{69,71}Ga MAS-NMR studies of nano-GaN cited in [234] had observed broad peaks shifted ca. 100 ppm or more to high frequency from the sharp peak of the WZ h-GaN, which were attributed to chemical structural effects arising from nitrogen vacancies. This assignment was maintained in a ^{71}Ga and ^{15}N MAS-NMR study of labeled nano-GaN [364], even after the existence of ^{71}Ga Knight shifts to comparable high frequencies was clearly demonstrated [207] in unintentionally- and intentionally-doped n-type h-GaN and ^{14}N Knight shifts in co-doped h-GaN were shown to be nearly identical in sign and magnitude to the ^{71}Ga Knight shifts [232]. In fact, the observations of nearly identical high frequency shifts for ^{71}Ga and ^{15}N in the nano-GaN study [364] provided perhaps the strongest clue that Knight shifts were responsible. The proposal that purely structural changes in chemical coordination due to nitrogen vacancies are responsible for the observed shifts is not consistent in any quantitative sense with the large relative signal intensity of the shifted peaks nor with the lack of a large second-order broadening of the ^{71}Ga spectra due to the large NQCCs that would be expected for ^{71}Ga nuclei adjacent to nitrogen vacancies.

The most recent ^{71}Ga MAS-NMR study of nano-GaN continued to claim that structural effects rather than Knight shifts are responsible for the observed high frequency broad peaks [359]. However, two questionable lines of reasoning were used to reach this conclusion. It was argued that, since the ^{71}Ga Knight shift measured in gallium metal had some temperature dependence and the nano-GaN sample had almost none, Knight shifts were not a factor in the latter. However, Knight shifts in metals generally are rather temperature-independent in the absence of significant structural or electronic changes [25], and the same is expected to be true for doped metallic semiconductors as discussed in Sect. 3.4. Although no references to previous Knight shift measurements in gallium metal were provided in this most recent work, the reasons for its temperature (and pressure) dependence have been explored in numerous publications that will not be cited here.

The second argument offered in [359] was based on the observation of ^{71}Ga T_1^{-1} rates at different temperatures that were faster than those calculated assuming Korringa relaxation as the only mechanism. However, this observation cannot be used to exclude the presence of Korringa relaxation, since additional mechanisms can always contribute additively to relaxation rates. Indeed, exactly such behavior has been observed for ^{71}Ga MAS-NMR of h-GaN co-doped with Ge and Mn, where

the paramagnetic Mn^{++} ions in the lattice increased the relaxation rate of the broad Knight-shifted peak due to Ge shallow donors (see Sect. 3.5) [232]. In fact, we note that the T_1 reported for the unperturbed ^{71}Ga peak at 324 ppm [359] is about sixfold shorter than the corresponding value in bulk h-GaN [50], showing that additional relaxation mechanisms must be present, perhaps due to paramagnetic impurities or dangling bonds, or differences in lattice motions in the nanoscale material. Overall, none of the arguments against Knight shifts as the source of the broad ^{71}Ga MAS-NMR peaks shifted to high frequency in NCs of GaN are logically valid. To the contrary much evidence, including the ^{15}N chemical shifts [364] and the small NQCCs observed in the ^{71}Ga MQ-MAS-NMR spectra [359], supports Knight shifts as the source.

4.2.6 Other Nanoparticles

The limitations of space permit only a brief mention of some other NMR studies of semiconductors in nanoscale form. The ^{203,205}Tl static NMR peak of Tl_2Se nanorods exhibited an axially symmetric CSA arising from the tetragonal structure, and was much narrower than the signal from the bulk, which was shifted to high frequency due to Knight shifts [365]. The temperature dependence of T_1 for both samples indicated a transition from a semimetallic bulk sample to quantum-confined semiconductor nanorods. Size effects in the semiconductor SnO_2 have been studied by ^{119}Sn NMR [366] as well as the effects of Li doping upon conductivity [367]. Nanorods of ZnO have been studied by ^{1}H MAS-NMR [368]. Nanotubes of BN were studied by ^{11}B NMR lineshapes and relaxation [369]. There is widespread interest in the wide bandgap semiconductor titania (TiO_2) as a photocatalyst for environmental and decontamination applications or for utilizing solar energy in the water-splitting reaction; not surprisingly, NMR has played a significant role in characterizing these materials and reactions [370–378].

Finally, the use of DNP of shallow donors to enhance both ^{67}Zn and surface ^{1}H nuclear polarizations has been demonstrated in ZnO nanoparticles by observation of EPR features rather than direct NMR observation [85, 87]. The electronic wavefunctions of these donors in ZnO have been probed by ENDOR experiments [36, 97]. There is much potential for directly observing NMR with the sensitivity greatly enhanced by DNP not only in ZnO but in other nanoparticles as well.

5 Conclusions and Future Directions

Solid-state NMR methods have been used to characterize both elemental and compound bulk semiconductors for half a century, but a significant upturn in the level of activity and the sophistication of methods and analyses is taking place, not to mention the availability of much higher magnetic fields than were available for many of the early studies. In many cases, the availability of well-defined and optically and electrically well-characterized bulk samples will prove crucial.

Because these are often made in limited quantities as single films by a very expensive growth apparatus, only the most technologically important semiconductors will generally be available from these growth methods for NMR study.

Even for simple elemental and binary semiconductors, the Knight shift remains a parameter that has been reliably measured only in a limited number of cases and whose magnitude has not been predicted for the many other cases. It generally has not been theoretically calculated from first principles in specific instances, and its relationship to the concentration and type of carriers in specific instances is rarely known. Associated with this need for a more extensive understanding of the Knight shift in different compounds (preferably reported by the NMR isotopes of more than one element) is the need to understand the distributions of Knight shifts that manifest themselves as broadened lines. The spatial scale of inhomogeneities in the random distributions of dopants is very relevant to assessing how wide a spatial extent of electron spin polarization a given nucleus samples.

The ability of NMR to distinguish polytypes will be greatly aided, as it was in the recent case discussed of SiC, by theoretical calculations of chemical shifts and CSA values (and for quadrupolar nuclei, NQCC values). Also, MAS-NMR may succeed in identifying low levels of polytypes or new ones that have not been seen by diffraction methods.

Many of the optoelectronic applications of semiconductors, including LEDs, LDs, and photovoltaic devices, will rely on alloys of semiconductors in order to tailor bandgaps. This will present many more opportunities as well as challenges for solid-state NMR methods, since the spectra will be considerably complicated by a wider chemical shift distribution, chemical shift anisotropies, and multiple NQCC values for quadrupolar nuclei, as well as potential Knight shifts of differing magnitudes. Methods for multidimensional correlation of NMR parameters that have been successful in the study of glasses should prove important in the study of such alloys. High magnetic field strengths and techniques such as MQ-MAS-NMR for improving the resolution of second-order broadened quadrupolar CT peaks will also be important in these cases. The important role of reliable and accurate theoretical calculation of NMR parameters such as chemical shifts, CSA, and NQCC values will become more apparent.

Sensitivity limitations have often hindered the application of NMR techniques to samples available in larger quantities than typically grown by MBE, or even MOCVD, but the situation is changing. Higher magnetic fields, cross-polarization or population transfer techniques for quadrupolar nuclei, microcoils or spinning coils all may serve to improve detection sensitivity. In addition, optical pumping and DNP techniques can be anticipated to continue to develop and offer vastly improved sensitivity. The interaction of light with semiconductors in experiments not involving optical pumping, such as the marked persistent and non-persistent T_1 relaxation effects noted for ^{113}Cd in doped CdTe and CdF_2 induced by illumination with visible light, can also be expected to provide valuable information about carriers placed into metastable defects [379].

The NMR of semiconductors in a nanoscale form (QD or NC, NW, etc.) presents special problems of sensitivity, resolution, and theoretical interpretation. In

particular, the interpretation of chemical shifts as influenced by quantum-confinement effects in terms of the Ramsey paramagnetic shielding presents some puzzles.

One important area where NMR can provide information is that of semiconductor surfaces that have reacted with organic groups, a type of chemistry that has been extensively studied for technologically important semiconductors such as Si, GaAs, and InP in connection with the passivation of surfaces (which alters optoelectronic properties due to changes in surface states) or with the desire to create functionalized surfaces (e.g., for sensor applications). One of the few solid-state NMR studies of such an organic-functionalized semiconductor surface investigated para-trifluoromethylbenzylic-ether bonded to the surface of InP [77]. The specific goal was to monitor the cross-polarization efficiency for use in transferring optically-pumped InP signals to surface species as discussed earlier in Sect. 3.2.3 [76]. However, the feasibility of obtaining spectra from surface species in such relatively large semiconductor particles produced by grinding suggests that the strategy could be applied to many other interesting problems, even simply to observing the native semiconductor surfaces as they exist in air, which often results in the formation of hydrous oxide surfaces containing protons.

The use of ^{1}H NMR in this context to study NC surfaces was mentioned in Sect. 4.2.1. There also seems to be a significant, but barely exploited, opportunity for ^{1}H NMR in investigating impurity hydrogen inside semiconductors. Using muonium as essentially a radioactive light isotope of hydrogen, muon spin resonance has already been extensively used to study interstitial hydrogen in semiconductors [100]. Since hydrogen can passivate electrically-active impurities, terminate dangling bonds, act as a co-dopant that may be removed by annealing, or act as a shallow donor itself in anion vacancies [380], understanding its structural characteristics by NMR should prove valuable.

Acknowledgments This research was supported by the Office of Naval Research.

References

1. Kittel C (2005) Introduction to solid state physics. Wiley, Hoboken New Jersey
2. Pearson GL, Brattain WH (1955) Proceedings of the Institute of Radio Engineers 43:1794
3. Panich AM (2008) J Phys Condens Matter 20:293202
4. Zutic I, Fabian J, Das Sarma S (2004) Rev Mod Phys 76:323
5. Reimer JA (2010) Solid State Nucl Magn Reson 37:3
6. Coish WA, Baugh J (2009) Phys Status Solidi B 246:2203
7. Wu MW, Jiang JH, Weng MQ (2010) Phys Rep Rev Sec Phys Lett 493:61
8. van der Klink JJ, Brom HB (2000) Prog Nucl Magn Reson Spectrosc 36:89
9. Halperin WP (1986) Rev Mod Phys 58:533
10. Winter J (1971) Magnetic resonance in metals. Clarendon Press, Oxford
11. Tycko R, Reimer JA (1996) J Phys Chem 100:13240
12. Hayes SE, Mui S, Ramaswamy K (2008) J Chem Phys 128:052203
13. Yesinowski JP (2011) In: Wasylishen R, Ashbrook S, Wimperis S (eds) Encyclopedia of magnetic resonance. Wiley, Chichester (in press)

14. Tycko R, Barrett SE (2003) In: Grant DM, Harris RK (eds) Encyclopedia of nuclear magnetic resonance, vol 9. Wiley, Chichester
15. Yu PY, Cardona M (2010) Fundamentals of semiconductors: physics and materials properties. Springer, Heidelberg
16. Queisser HJ, Haller EE (1998) Science 281:945
17. Zunger A (2003) Appl Phys Lett 83:57
18. Alexander MN, Holcomb DF (1968) Rev Mod Phys 40:815
19. Zach FX (1994) J Appl Phys 75:7894
20. Koschnick FK, Wietzke KH, Spaeth JM (1998) Phys Rev B 58:7707
21. Blakemore JS (1987) Semiconductor statistics. Dover Publications, Inc., Mineola, NY
22. Madelung O (2004) Semiconductors: data handbook. Springer, Berlin
23. Yeh CY, Lu ZW, Froyen S, Zunger A (1992) Phys Rev B 46:10086
24. Phillips JC, Van Vechten JA (1969) Phys Rev Lett 22:705
25. Abragam A (1961) The principles of nuclear magnetism. Oxford University Press, London
26. Slichter CP (1990) Principles of magnetic resonance. Springer, Berlin
27. Kempf JG, Miller MA, Weitekamp DP (2008) Proc Natl Acad Sci U S A 105:20124
28. van Duijn-Arnold A, Mol J, Verberk R, Schmidt J, Mokhov EN, Baranov PG (1999) Phys Rev B 60:15829
29. van Duijn-Arnold A, Mol J, Verberk R, Schmidt J, Mokhov EN, Baranov PG (2000) In: Carter CH, Devaty RP, Rohrer GS (eds) Silicon carbide and related materials – 1999 Pts, 1 & 2 Mater Sci Forum, vol 338–342. Trans Tech Publications Ltd, Switzerland, p 799 doi:10.4028/www.scientific.net/MSF.
30. von Duijn-Arnold A, Zondervan R, Schmidt J, Baranov PG, Mokhov EN (2001) Phys Rev B 64:085206
31. Orlinskii SB, Schmidt J, Baranov PG, Hofmann DM, Donega CD, Meijerink A (2004) Phys Rev Lett 92:047603
32. Senturia SD, Smith AC, Hewes CR, Hofmann JA, Sagalyn PL (1970) Phys Rev B 1:4045
33. Smith ME, van Eck ERH (1999) Prog Nucl Magn Reson Spectrosc 34:159
34. Jerschow A (2005) Prog Nucl Magn Reson Spectrosc 46:63
35. Goldbourt A, Madhu PK (2005) Annual Reports on NMR Spectroscopy, Vol 54 (Annual Reports on NMR Spectroscopy), vol 54. Academic Press Ltd, London, p 81
36. Ashbrook S (2004) Prog Nucl Magn Reson Spectrosc 45:53
37. Ashbrook SE (2009) PCCP 11:6892
38. Amoureux JP, Trebosc J, Delevoye L, Lafon O, Hu B, Wang Q (2009) Solid State Nucl Magn Reson 35:12
39. Handbook of Quadrupolar Nuclei (2011) In: Wasylishen R, Ashbrook S, Wimperis S (eds) Encyclopedia of magnetic resonance. Wiley, Chichester, UK (in press)
40. Hester RK, Sher A, Soest JF, Weisz G (1974) Phys Rev B 10:4262
41. Gill D, Bloembergen N (1963) Phys Rev 129:2398
42. Tarasek MR, Kempf JG (2010) J Phys Chem A 114:5743
43. Tarasek MR, Kempf JG (2010) J Phys Chem A 114:10634
44. Dumas KA, Soest JF, Sher A, Swiggard EM (1979) Phys Rev B 20:4406
45. Thorland RH, Garrison AK, Duvarney RC (1972) Phys Rev B 5:784
46. Eickhoff M, Lenzmann B, Suter D, Hayes S, Wieck A (2003) Phys Rev B 67:085308
47. Grant DM, Harris RK (eds) (2003) Encyclopedia of nuclear magnetic resonance, volumes 1–9. Wiley, Chichester, UK
48. Bak M, Rasmussen JT, Nielsen NC (2000) J Magn Reson 147:296
49. Yesinowski JP (2005) phys stat sol (c) 2:2399
50. Yesinowski JP (2006) J Magn Reson 180:147
51. Samoson A, Lippmaa E (1983) Phys Rev B 28:6567
52. Park IW, Choi H, Kim HJ, Shin HW, Park SS, Choh SH (2002) Phys Rev B 65:195210
53. Mahadik NA, Qadri SB, Rao MV, Yesinowski JP (2007) Appl Phys A Mater Sci Process 86:67

54. Shulman RG, Wyluda BJ, Anderson PW (1957) Phys Rev 107:953
55. Sundfors RK (1974) Phys Rev B 10:4244
56. Guerrier DJ, Harley RT (1997) Appl Phys Lett 70:1739
57. Zwanziger JW, Werner-Zwanziger U, Shaw JL, So C (2006) Solid State Nucl Magn Reson 29:113
58. Carlos WE, Bishop SG, Treacy DJ (1986) Appl Phys Lett 49:528
59. Carlos WE, Bishop SG, Treacy DJ (1991) Phys Rev B 43:12512
60. Yesinowski JP, Purdy AP (2004) J Am Chem Soc 126:9166
61. Koch W, Lutz O, Nolle A (1978) Z Phys A Hadrons Nucl 289:17
62. Haller M, Hertler WE, Lutz O, Nolle A (1980) Solid State Commun 33:1051
63. Bastow TJ, Stuart SN (1988) Phys Status Solidi B Basic Res 145:719
64. Eckert H, Yesinowski JP (1986) J Am Chem Soc 108:2140
65. Becker KD, Berlage U (1983) J Magn Reson 54:272
66. Han OH, Timken HKC, Oldfield E (1988) J Chem Phys 89:6046
67. Timken HKC, Oldfield E (1987) J Am Chem Soc 109:7669
68. Haase J, Curro NJ, Stern R, Slichter CP (1998) Mol Phys 95:891
69. Haase J, Curro NJ, Stern R, Slichter CP (1998) Phys Rev Lett 81:1489
70. Siegel R, Nakashima TT, Wasylishen RE (2004) Chem Phys Lett 388:441
71. O'Dell LA, Harris KJ, Schurko RW (2010) J Magn Reson 203:156
72. Schurko R (2003) Chem Phys Lett 379:1
73. Dong W, Li B, Zhang Q, Tamargo MC, Meriles CA (2009) Phys Rev B 80:045211
74. Novikov S, Morris R, Kent A, Geen H, Foxon C (2007) J Cryst Growth 301–302:417
75. Morris RD, Kent AJ, Geen HL, Foxon CT, Novikov SV (2007) In: Jantsch W, Schaffler F (eds) Physics of semiconductors, Pts A and B (AIP Conference Proceedings), vol 893. Amer Inst Physics, Melville, p 1343
76. Tycko R (1998) Solid State Nucl Magn Reson 11:1
77. Goehring L, Michal CA (2003) J Chem Phys 119:10325
78. Goto A (2002) Superlattices Microstruct 32:303
79. Kaur G, Denninger G (2010) Appl Magn Reson 39:185
80. Baranov PG, Orlinskii SB, de Mello Donega C, Meijerink A, Blok H, Schmidt J (2009) Phys B Condensed Matter 404:4779
81. Baranov PG, Orlinskii SB, Hofmann DM, Donega CD, Meijerink A, Schmidt J (2010) Phys Status Solidi B 247:1476
82. Orlinskii S, Schmidt J, Baranov P, Donegá C, Meijerink A (2009) Phys Rev B 79:165316
83. Dementyev A, Cory D, Ramanathan C (2008) Phys Rev Lett 100:127601
84. Denninger G (1990) Festkorperprobleme Adv Solid State Phys 30:113
85. Denninger G, Beerhalter R, Reiser D, Maier K, Schneider J, Detchprohm T, Hiramatsu K (1996) Solid State Commun 99:347
86. Denninger G, Reiser D (1997) Phys Rev B 55:5073
87. Gotschy B, Denninger G, Obloh H, Wilkening W, Schneider J (1989) Solid State Commun 71:629
88. Reiser D, Blomker J, Denninger G, Schneider J (1997) Solid State Commun 102:359
89. Clark WG, Feher G (1963) Phys Rev Lett 10:134
90. Hoch M, Lu J, Kuhns P, Moulton W, Reyes A (2005) Phys Rev B 72:233204
91. Feher G (1959) J Phys Chem Solids 8:486
92. Baranov PG, Orlinskii SB, Donega CD, Schmidt J (2010) Appl Magn Reson 39:151
93. Denninger G (2001) J Magn Reson 148:248
94. Patterson BD (1988) Rev Mod Phys 60:69
95. Cox SFJ (2009) Rep Prog Phys 72:116501
96. Bromberger C, Jansch HJ, Kuhlert O, Schillinger R, Fick D (2004) Phys Rev B 69: 245424
97. Flinn GP, Harley RT, Snelling MJ, Tropper AC, Kerr TM (1990) Semicond Sci Technol 5:533

98. Krapf M, Denninger G, Pascher H, Weimann G, Schlapp W (1991) Solid State Commun 78:459
99. Marohn JA, Carson PJ, Hwang JY, Miller MA, Shykind DN, Weitekamp DP (1995) Phys Rev Lett 75:1364
100. Gammon D, Brown SW, Snow ES, Kennedy TA, Katzer DS, Park D (1997) Science 277:85
101. Brown SW, Kennedy TA, Gammon D (1998) Solid State Nucl Magn Reson 11:49
102. Sidles JA (1992) Phys Rev Lett 68:1124
103. Rugar D, Yannoni CS, Sidles JA (1992) Nature 360:563
104. Sidles JA, Garbini JL, Bruland KJ, Rugar D, Zuger O, Hoen S, Yannoni CS (1995) Rev Mod Phys 67:249
105. Poggio M, Degen CL (2010) Nanotechnology 21:342001
106. Thurber KR, Harrell LE, Smith DD (2003) J Magn Reson 162:336
107. Meriles C (2005) J Magn Reson 176:207
108. Hartman JS, Narayanan A, Wang YX (1994) J Am Chem Soc 116:4019
109. Narayanan A, Hartman JS, Bain AD (1995) J Magn Reson A 112:58
110. McNeil JA, Clark WG (1976) Phys Rev B 13:4705
111. Bridges F, Clark WG (1967) Phys Rev 164:288
112. Bridges F, Clark WG (1969) Phys Rev 182:463
113. Solankimoser M, Tunstall DP, Finlayson DM (1993) J Phys Condens Matter 5:1319
114. Hofland J, Honig A (1965) Phys Rev Lett 14:700
115. Mieher RL (1960) Phys Rev Lett 4:57
116. Mieher RL (1962) Phys Rev 125:1537
117. Yeom TH, Kim IG, Choh SH, Hong KS, Park YJ, Min SK (1999) Solid State Commun 111:229
118. Lu J, Hoch M, Kuhns P, Moulton W, Gan Z, Reyes A (2006) Phys Rev B 74:125208
119. Corti M, Gabetta A, Fanciulli M, Svane A, Christensen N (2003) Phys Rev B 67:064416
120. Han W-M, Gardner JA, Warren WW Jr (1992) Mater Sci Forum 83–87:971
121. Goddard YA, Vold RL, Cross J, Espe MP, Hoatson GL (2005) J Chem Phys 122:054901
122. Yesinowski JP, Ladouceur HD, Purdy AP, Miller JB (2010) J Chem Phys 133:234509
123. Ramsey NF (1950) Phys Rev 78:699
124. Ramsey NF (1952) Phys Rev 86:243
125. Ramsey NF, Purcell EM (1952) Phys Rev 85:143
126. Ramsey NF (1953) Phys Rev 91:303
127. Pyykko P (2000) Theor Chem Acc 103:214
128. Juranic N (1989) Coord Chem Rev 96:253
129. Jameson CJ (1996) Annu Rev Phys Chem 47:135
130. Eckert H, Moran K, Franke D, Hudalla C (1993) In: Tosell JA (ed) Nuclear magnetic shieldings and molecular structure (Series C: Mathematical and Physical Sciences), vol 386. Kluwer, Dordrecht, p 49
131. Hubner K (1971) Phys Status Solidi B Basic Res 45:619
132. Look DC (1972) Phys Status Solidi B Basic Res 50:K97
133. Hartman JS, Berno B, Hazendonk P, Kirby CW, Ye E, Zwanziger J, Bain AD (2009) J Phys Chem C 113:15024
134. Jeong J, Choh S, Sahoo N, Das T (2008) Phys B Condensed Matter 403:2225
135. Dietrich M, Kortus J, Cordts W, Unterricker S (1998) Phys Status Solidi B Basic Res 207:13
136. Schwarz K, Blaha P, Trickey SB (2010) Mol Phys 108:3147
137. Knijn PJ, van Bentum PJM, van Eck ERH, Fang CM, Grimminck D, de Groot RA, Havenith RWA, Marsman M, Meerts WL, de Wijs GA, Kentgens APM (2010) PCCP 12:11517
138. Yates J, Pickard C, Mauri F (2007) Phys Rev B 76:024401
139. Joyce SA, Yates JR, Pickard CJ, Mauri F (2007) J Chem Phys 127:204107
140. Cadars S, Smith B, Epping J, Acharya S, Belman N, Golan Y, Chmelka B (2009) Phys Rev Lett 103:136802
141. Franke DR, Eckert H (1991) J Phys Chem 95:331

142. Franke D, Maxwell R, Lathrop D, Eckert H (1991) J Am Chem Soc 113:4822
143. Mader KA, Zunger A (1995) Phys Rev B 51:10462
144. Chichibu SF, Uedono A, Onuma T, Haskell BA, Chakraborty A, Koyama T, Fini PT, Keller S, DenBaars SP, Speck JS, Mishra UK, Nakamura S, Yamaguchi S, Kamiyama S, Amano H, Akasaki I, Han J, Sota T (2006) Nat Mater 5:810
145. Humphreys CJ (2007) Philos Mag 87:1971
146. Tycko R, Dabbagh G, Kurtz SR, Goral JP (1992) Phys Rev B 45:13452
147. Tycko R, Dabbagh G, Kurtz SR, Goral JP (2007) Phys Rev B 75:249901(E)
148. Duncan TM, Karlicek RF, Bonner WA, Thiel FA (1984) J Phys Chem Solids 45:389
149. Humphries LJ, Sears REJ (1975) J Phys Chem Solids 36:1149
150. Vanderah TA, Nissan RA (1988) J Phys Chem Solids 49:1335
151. Sears REJ (1978) Phys Rev B 18:3054
152. Iijima T, Hashi K, Goto A, Shimizu T, Ohki S (2004) Jpn J Appl Phys 43:L1387
153. Zhang LP, Zheng Z, Liang JC, Le XY, Zou C, Liu HL, Liu Y (2008) Chin Phys B 17:4619
154. Willig A, Sapoval B, Leibler K, Verie C (1976) J Phys C: Solid State Phys 9:1981
155. Zax DB, Vega S, Yellin N, Zamir D (1987) Chem Phys Lett 138:105
156. Zamir D, Beshah K, Becla P, Wolff PA, Griffin RG, Zax D, Vega S, Yellin N (1988) J Vac Sci Technol A Vac Surf Films 6:2612
157. Beshah K, Zamir D, Becla P, Wolff PA, Griffin RG (1987) Phys Rev B 36:6420
158. Vieth HM, Vega S, Yellin N, Zamir D (1991) J Phys Chem 95:1420
159. Zax DB, Zamir D, Vega S (1993) Phys Rev B 47:6304
160. Shi JH, Wessels M, Ross JH (1993) Phys Rev B 48:8742
161. Lock H, Xiong JC, Wen YC, Parkinson BA, Maciel GE (2001) Solid State Nucl Magn Reson 20:118
162. Franke D, Banks K, Maxwell R, Eckert H (1992) J Phys Chem 96:1906
163. Franke D, Banks K, Eckert H (1992) J Phys Chem 96:11048
164. Franke D, Hudalla C, Eckert H (1992) Solid State Nucl Magn Reson 1:33
165. Franke D, Hudalla C, Eckert H (1992) Solid State Nucl Magn Reson 1:297
166. Franke D, Hudalla C, Maxwell R, Eckert H (1992) J Phys Chem 96:7506
167. Bastow TJ, Massiot D, Coutures JP (1998) Solid State Nucl Magn Reson 10:241
168. Selke H, Kirchner V, Heinke H, Einfeldt S, Ryder PL, Hommel D (2000) J Cryst Growth 208:57
169. Bloembergen N (1954) Physica 20:1130
170. Wolf D (1979) Spin-temperature and nuclear-spin relaxation in matter: basic principles and applications. Clarendon Press, Oxford
171. Selbach H, Kanert O, Wolf D (1979) Phys Rev B 19:4435
172. Gunther B, Kanert O, Mehring M, Wolf D (1981) Phys Rev B 24:6747
173. Gunther B, Kanert O (1985) Phys Rev B 31:20
174. Kanert O, Kuchler R, Recktenwald J (1980) Solid State Commun 33:993
175. Morton JR, Preston KF (1978) J Magn Reson 30:577
176. Shulman RG, Mays JM, McCall DW (1955) Phys Rev 100:692
177. Holzman GR, Lauterbur PC, Anderson JH, Koth W (1956) J Chem Phys 25:172
178. Shulman RG, Wyluda BJ (1956) Phys Rev 103:1127
179. Sundfors RK, Holcomb DF (1964) Phys Rev A Gen Phys 136:A810
180. Alexander MN, Holcomb DF (1968) Solid State Commun 6:355
181. Carver GP, Holcomb DF, Kaeck JA (1971) Phys Rev B 3:4285
182. Hirsch MJ, Holcomb DF (1986) Phys Rev B 33:2520
183. Hoch MJR, Holcomb DF (1988) Phys Rev B 38:10550
184. Hoch MJR, Thomanschefsky U, Holcomb DF (1990) Physica B 165:305
185. Hoch M, Holcomb D (2005) Phys Rev B 71:035115
186. Hirsch MJ, Holcomb DF, Bhatt RN, Paalanen MA (1992) Phys Rev Lett 68:1418
187. Dubson MA, Holcomb DF (1986) Phys Rev B 34:25
188. Fuller SE, Meintjes EM, Warren WW (1996) Phys Rev Lett 76:2806

189. Meintjes E, Danielson J, Warren W (2005) Phys Rev B 71:035114
190. Mori T, Shimazu Y, Ikehata S (1993) J Phys Soc Jpn 62:3172
191. Haase J, Oldfield E, Schmitt K (1992) Chem Phys Lett 193:274
192. Korringa J (1950) Physica 16:601
193. Brown GC, Holcomb DF (1974) Phys Rev B 10:3394
194. Alloul H, Dellouve P (1987) Phys Rev Lett 59:578
195. Alloul H, Dellouve P (1988) Journal De Physique 49:1185
196. Sasaki W, Ikehata S, Kobayashi S (1973) Phys Lett A A 42:429
197. Ikehata S, Sasaki W, Kobayashi S (1975) J Phys Soc Jpn 39:1492
198. Ikehata S, Sasaki W, Kobayashi S (1976) Solid State Commun 19:655
199. Kobayashi SI, Fukagawa Y, Ikehata S, Sasaki W (1978) J Phys Soc Jpn 45:1276
200. Jeong M, Song M, Ueno T, Mizusaki T, Matsubara A, Lee S (2009) J Phys Soc Jpn 78:075003
201. Tunstall DP, Deshmukh VGI (1979) J Phys C: Sol State Phys 12:2295
202. Tunstall DP, Sohal GS (1983) J Phys C: Sol State Phys 16:L251
203. Tunstall DP (1985) Solid-State Electronics 28:212
204. Tunstall DP (1984) J Phys C: Sol State Phys 17:1003
205. Look DC, Moore DL (1972) Phys Rev B 5:3406
206. Rodina AV, Meyer BK (2001) Phys Rev B 64:245209
207. Yesinowski JP, Purdy AP, Wu HQ, Spencer MG, Hunting J, DiSalvo FJ (2006) J Am Chem Soc 128:4952
208. Unger K (1968) Z Naturforsch A Phys Sci A 23:178
209. Look DC (1969) Phys Rev 184:705
210. Benedict RP, Look DC (1970) Phys Rev B 2:4949
211. Lee K, Liesegang J, Phipps PBP (1967) Phys Rev 161:322
212. Alexander MN, Sagalyn PL, Senturia SD, Hewes CR (1973) J Nonmetals 1:251
213. Leloup JY, Sapoval B, Martinez G (1973) Phys Rev B 7:5276
214. Weinberg I, Callaway J (1962) Nuovo Cimento 24:190
215. Hewes CR, Adler MS, Senturia SD (1973) J Appl Phys 44:1327
216. Hewes CR, Adler MS, Senturia SD (1973) Phys Rev B 7:5195
217. Sapoval B, Leloup JY (1973) Phys Rev B 7:5272
218. Tripathi GS, Das LK, Misra PK, Mahanti SD (1981) Hyperfine Interact 9:495
219. Tripathi GS, Das LK, Misra PK, Mahanti SD (1981) Solid State Commun 38:1207
220. Tripathi GS (1985) Phys Rev B 31:5143
221. Tripathi GS, Misra CM, Misra PK (1985) J Phys C: Sol State Phys 18:L935
222. Misra S, Tripathi GS, Misra PK (1985) Phys Lett A 110:461
223. Misra S, Tripathi GS, Misra PK (1987) J Phys C Sol State Phys 20:277
224. Tripathi GS, Misra CM, Tripathi P, Misra PK (1989) Phys Rev B 39:94
225. Hota RL, Tripathi GS (1991) Phys Rev B 44:1918
226. Hota RL, Tripathi GS (1991) J Phys Condens Matter 3:6299
227. Bailey PT (1968) Phys Rev 170:723
228. Miranda GA, McNeil JA, Clark WG (1974) Phys Rev B 9:495
229. Tunstall DP (1988) J Phys C Sol State Phys 21:2853
230. Tunstall DP, Harper RE (1983) Solid State Commun 48:507
231. Andrianov DG, Muravlev YB, Savelev AS (1977) Soviet Physics Semiconductors-USSR 11:411
232. Purdy AP, Yesinowski JP, Hanbicki AT (2005) phys stat sol (c) 2:2437
233. Lawniczak-Jablonska K, Suski T, Gorczyca I, Christensen NE, Attenkofer KE, Perera RCC, Gullikson EM, Underwood JH, Ederer DL, Weber ZL (2000) Phys Rev B 61:16623
234. Drygas M, Olejniczak Z, Grzanka E, Bucko MM, Paine RT, Janik JF (2008) Chem Mater 20:6816
235. Drygas M, Bucko MM, Olejniczak Z, Grzegory I, Janik JF (2010) Mater Chem Phys 122:537

236. Morris RD, Kent AJ, Geen HL, Foxon CT, Novikov SV (2007) In: Jantsch W, Schaffler F (eds) Physics of Semiconductors, Pts A and B (AIP Conference Proceedings), vol 893. Am Inst Physics, Melville, p 1339
237. Buss JH, Rudolph J, Natali F, Semond F, Hagele D (2010) Phys Rev B 81:155216
238. Buss JH, Rudolph J, Schupp T, As DJ, Lischka K, Hagele D (2010) Appl Phys Lett 97:062101
239. Hartman JS, Richardson MF, Sherriff BL, Winsborrow BG (1987) J Am Chem Soc 109:6059
240. Tunstall DP, Rogerson A (1979) J Phys C Sol State Phys 12:3105
241. Kushida T, Silver AH (1965) Phys Rev 137:1591
242. Tanaka M (2005) J Cryst Growth 278:25
243. Dietl T, Ohno H, Matsukura F, Cibert J, Ferrand D (2000) Science 287:1019
244. Hwang T, Shim JH, Lee S (2003) Appl Phys Lett 83:1809
245. Zhou XY, Ge SH, Yao DS, Zuo YL, Xiao YH (2008) Physica B Condensed Matter 403:3336
246. Hwang T, Lee S, Choi HK, Kim YS, Park YD, Chun SH (2008) J Korean Phys Soc 52:396
247. Gavish M, Vega S, Zamir D (1993) Phys Rev B 48:2191
248. Beshah K, Becla P, Griffin RG, Zamir D (1993) Phys Rev B 48:2183
249. Nayeem A, Yesinowski JP (1988) J Chem Phys 89:4600
250. Ladizhansky V, Faraggi A, Lyahovitskaya V, Vega S (1997) Phys Rev B 56:6712
251. Ladizhansky V, Lyahovitskaya V, Vega S (1999) Phys Rev B 60:8097
252. Sundfors RK (1969) Phys Rev 185:458
253. Ruderman MA, Kittel C (1954) Phys Rev 96:99
254. Bloembergen N, Rowland TJ (1955) Phys Rev 97:1679
255. Engelsberg M, Norberg RE (1970) Phys Lett A A 31:311
256. Engelsberg M, Norberg RE (1972) Phys Rev B 5:3395
257. Tomaselli M, deGraw D, Yarger JL, Augustine MP, Pines A (1998) Phys Rev B 58:8627
258. Jameson CJ, Gutowsky HS (1969) J Chem Phys 51:2790
259. Vaara J, Jokisaari J, Wasylishen RE, Bryce DL (2002) Prog Nucl Magn Reson Spectrosc 41:233
260. Iijima T, Hashi K, Goto A, Shimizu T, Ohki S (2003) Jpn J Appl Phys Part 2, Letters 42:L1411
261. Iijima T, Hashi K, Goto A, Shimizu T, Ohki S (2004) J Phys Soc Jpn 73:1045
262. Shulman RG, Wyluda BJ, Hrostowski HJ (1958) Phys Rev 109:808
263. Hwang YS, Norberg RE (1976) Phys Rev B 14:3765
264. Cueman MK, Soest JF (1976) Phys Rev B 14:13
265. Balz R, Haller M, Hertler WE, Lutz O, Nolle A, Schafitel R (1980) J Magn Reson 40:9
266. Nolle A (1979) Z Phys B Condens Mat 34:175
267. Potter LD, Wu Y (1995) J Magn Reson A 116:107
268. Eckert H, Elbers S, Epping JD, Janssen M, Kalwei M, Strojek W, Voigt U (2005) New techniques in solid-state NMR. Topics in Current Chemistry, Springer, Berlin, vol 246, p 195
269. Ladd T, Maryenko D, Yamamoto Y, Abe E, Itoh K (2005) Phys Rev B 71:014401
270. Verhulst A, Maryenko D, Yamamoto Y, Itoh K (2003) Phys Rev B 68:054105
271. Dementyev A, Li D, MacLean K, Barrett S (2003) Phys Rev B 68:153302
272. Li D, Dementyev A, Dong Y, Ramos R, Barrett S (2007) Phys Rev Lett 98:190401
273. Li D, Dong YQ, Ramos RG, Murray JD, MacLean K, Dementyev AE, Barrett SE (2008) Phys Rev B 77:214306
274. Fanciulli M, Corti M (1995) Phys Rev B 52:11872
275. Zhang WJ, Tansho M, Matsumoto S, Mori T (2001) J Appl Phys 89:1734
276. Bastow TJ, Gibson MA, Forwood CT (1998) Solid State Nucl Magn Reson 12:201
277. Bastow TJ, Stuart SN (1990) Chem Phys 143:459
278. Dmitrieva LV, Vorotilova LS, Podkorytov IS, Shelyapina ME (1999) Phys Solid State 41:1097
279. Kanert O, Mehring M (1971) In: Diehl P, Fluck E, Kosfeld R (eds) NMR basic principles and progress, vol 3. Springer, Berlin, p 1
280. Fedders PA (1975) Phys Rev B 11:1020

281. Cueman MK, Hester RK, Sher A, Soest JF, Lowe IJ (1975) Phys Rev B 12:3610
282. Mao D, Taylor PC (1995) Phys Rev B 52:5665
283. Andrianov DG, Karataev VV, Milvidskii MG, Muravlev YB (1983) Soviet Physics Semiconductors-USSR 17:57
284. Andrianov DG, Muravlev YB, Fistul VI, Shevakin AF (1978) Soviet Physics Semiconductors-USSR 12:895
285. Andrianov DG, Muravlev YB, Shevakin AF (1979) Soviet Physics Semiconductors-USSR 13:60
286. Czjzek G, Fink J, Gotz F, Schmidt H, Coey JMD, Rebouillat JP, Lienard A (1981) Phys Rev B 23:2513
287. Czjzek G (1983) Hyperfine Interact 14:189
288. de Lacaillerie JBD, Fretigny C, Massiot D (2008) J Magn Reson 192:244
289. Le Caer G, Brand RA (1998) J Phys Condens Matter 10:10715
290. Le Caer G, Bureau B, Massiot D (2010) J Phys Condens Matter 22:065402
291. Franke D, Eckert H, Kaner RB, Treece RE (1993) Anal Chim Acta 283:987
292. Takeuchi J, Nakamura H, Yamada H, Kita E, Tasaki A, Erata T (1997) Solid State Nucl Magn Reson 8:123
293. Mao D, Taylor PC, Kurtz SR, Wu MC, Harrison WA (1996) Phys Rev Lett 76:4769
294. Wei SH, Zunger A (1997) J Chem Phys 107:1931
295. Nelson C, Taylor P, Harrison W (2004) Phys Rev B 70:224207
296. Kim Y-I, Cadars S, Shayib R, Proffen T, Feigerle C, Chmelka B, Seshadri R (2008) Phys Rev B 78:195205
297. Roberts N, Wang RP, Sleight AW, Warren WW (1998) Phys Rev B 57:5734
298. Murakami M, Shimizu T, Tansho M, Takano Y, Ishii S, Ekimov E, Sidorov V, Kawarada H, Takegoshi K (2007) Jpn J Appl Phys Part 2 Letters & Express Letters 46:L1138
299. Murakami M, Shimizu T, Tansho M, Takano Y, Ishii S, Ekimov EA, Sidorov VA, Sumiya H, Kawarada H, Takegoshi K (2008) Diamond Relat Mater 17:1835
300. Murakami M, Shimizu T, Tansho M, Takano Y, Ishii S, Ekimov EA, Sidorov VA, Takegoshi K (2009) Diamond Relat Mater 18:1267
301. Baek SH, Curro NJ, Ekimov EA, Sidorov VA, Bauer ED, Thompson JD (2009) Superconduct Sci Technol 22:065008
302. Stallworth PE, de la Caillerie JBD, Maquet J, Babonneau F, Guillemoles JF, Powalla M, Lyakovitskaya V, Yakushev M, Tomlinson B (2001) Thin Solid Films 387:235
303. Aubin V (2003) J Phys Chem Solids 64:1633
304. Khabibullin IK, Matukhin VL, Ermakov VL, Gnezdilov OI, Korzun BV, Schmidt EV (2009) Semiconductors 43:1
305. Schmidt EV, Ermakov VL, Gnezdilov OI, Matukhin VL, Korzun BV, Fadeeva AA, Khabibullina IK (2009) J Appl Spectrosc 76:667
306. Turner GL, Chung SE, Oldfield E (1985) J Magn Reson 64:316
307. Sears REJ (1980) Phys Rev B 22:1135
308. Sears REJ (1981) Phys Rev B 24:4072
309. Okubo N, Igarashi M (1999) Phys Status Solidi B Basic Res 215:1109
310. Verkhovskii SV, Yakubovskii AY, Trokiner A, Malkin BZ, Saikin SK, Ozhogin VI, Tikhomirov AV, Ananyev AV, Gerashenko AP, Piskunov YV (1999) Appl Magn Reson 17:557
311. Verkhovskii SV, Malkin BZ, Trokiner A, Yakubovskii A, Haller E, Ananyev A, Gerashenko A, Piskunov Y, Saikin S, Tikhomirov A, Ozhogin V (2000) Z Naturfors Sect A J Phys Sci 55:105
312. Verkhovskii S, Yakubovsky A, Malkin B, Saikin S, Cardona M, Trokiner A, Ozhogin V (2003) Phys Rev B 68:104201
313. Massiot D, Farnan I, Gautier N, Trumeau D, Trokiner A, Coutures JP (1995) Solid State Nucl Magn Reson 4:241
314. Vosegaard T, Byriel IP, Binet L, Massiot D, Jakobsen HJ (1998) J Am Chem Soc 120:8184
315. Yeom TH, Lim AR (2009) J Magn Reson 200:261

316. Becker KD, Herzog GW, Kanne D, Richtering H, Stadler E (1970) Ber Bunsen Ges Phys Chem 74:527
317. Tasche B, Richtering H (1986) Phys Status Solidi A Appl Res 95:565
318. Becker KD, Wagner S (1983) Phys Rev B 27:5240
319. Stallworth PE, Guillemoles JH, Flowers J, Vedel J, Greenbaum SG (2000) Solid State Commun 113:527
320. Kentgens APM, Bart J, van Bentum PJM, Brinkmann A, van Eck ERH, Gardeniers JGE, Janssen JWG, Knijn P, Vasa S, Verkuijlen MHW (2008) J Chem Phys 128:052202
321. Sakellariou D, Goff GL, Jacquinot JF (2007) Nature 447:694
322. Ladizhansky V, Vega S (2000) J Phys Chem B 104:5237
323. Ladizhansky V, Hodes G, Vega S (1998) J Phys Chem B 102:8505
324. Mikulec FV, Kuno M, Bennati M, Hall DA, Griffin RG, Bawendi MG (2000) J Am Chem Soc 122:2532
325. Ratcliffe CI, Yu K, Ripmeester JA, Badruz Zaman M, Badarau C, Singh S (2006) PCCP 8:3510
326. Ouyang JY, Ratcliffe CI, Kingston D, Wilkinson B, Kuijper J, Wu XH, Ripmeester JA, Yu K (2008) J Phys Chem C 112:4908
327. Wang R, Calvignanello O, Ratcliffe CI, Wu X, Leek DM, Zaman MB, Kingston D, Ripmeester JA, Yu K (2009) J Phys Chem C 113:3402
328. Potter LD, Guzelian AA, Alivisatos AP, Wu Y (1995) J Chem Phys 103:4834
329. Lovingood DD, Achey R, Paravastu AK, Strouse GF (2010) J Am Chem Soc 132:3344
330. Giuliani J, Harley S, Carter R, Power P, Augustine M (2007) Solid State Nucl Magn Reson 32:1
331. Wise FW (2000) Acc Chem Res 33:773
332. Thayer AM, Steigerwald ML, Duncan TM, Douglass DC (1988) Phys Rev Lett 60:2673
333. Tomaselli M, Yarger JL, Bruchez M, Havlin RH, deGraw D, Pines A, Alivisatos AP (1999) J Chem Phys 110:8861
334. Yu H, Li JB, Loomis RA, Wang LW, Buhro WE (2003) Nat Mater 2:517
335. Erwin SC, Zu L, Haftel MI, Efros AL, Kennedy TA, Norris DJ (2005) Nature 436:91
336. Norris DJ, Efros AL, Erwin SC (2008) Science 319:1776
337. Masadeh AS, Bozin ES, Farrow CL, Paglia G, Juhas P, Billinge SJL, Karkamkar A, Kanatzidis MG (2007) Phys Rev B 76:115413
338. Rossetti R, Ellison JL, Gibson JM, Brus LE (1984) J Chem Phys 80:4464
339. Herron N, Wang Y, Eckert H (1990) J Am Chem Soc 112:1322
340. Yesinowski JP (1981) J Am Chem Soc 103:6266
341. Agger JR, Anderson MW, Pemble ME, Terasaki O, Nozue Y (1998) J Phys Chem B 102:3345
342. Berrettini MG, Braun G, Hu JG, Strouse GF (2004) J Am Chem Soc 126:7063
343. Becerra LR, Murray CB, Griffin RG, Bawendi MG (1994) J Chem Phys 100:3297
344. Ladizhansky V, Hodes G, Vega S (2000) J Phys Chem B 104:1939
345. Macdougall JE, Eckert H, Stucky GD, Herron N, Wang Y, Moller K, Bein T, Cox D (1989) J Am Chem Soc 111:8006
346. Moran KL, Gier TE, Harrison WTA, Stucky GD, Eckert H, Eichele K, Wasylishen RE (1993) J Am Chem Soc 115:10553
347. Moran KL, Harrison WTA, Kamber I, Gier TE, Bu XH, Herren D, Behrens P, Eckert H, Stucky GD (1996) Chem Mater 8:1930
348. Turner EA, Rosner H, Fenske D, Huang YN, Corrigan JF (2006) J Phys Chem B 110:16261
349. Ouyang J, Zaman MB, Yan FJ, Johnston D, Li G, Wu X, Leek D, Ratcliffe CI, Ripmeester JA, Yu K (2008) J Phys Chem C 112:13805
350. Yu K, Ouyang J, Zaman MB, Johnston D, Yan FJ, Li G, Ratcliffe CI, Leek DM, Wu XH, Stupak J, Jakubek Z, Whitfiel D (2009) J Phys Chem C 113:3390
351. Li MJ, Ouyang JY, Ratcliffe CI, Pietri L, Wu XH, Leek DM, Moudrakovski I, Lin Q, Yang B, Yu K (2009) ACS Nano 3:3832

352. Pietrass T, Bifone A, Roth RD, Koch VP, Alivisatos AP, Pines A (1996) J Non-Cryst Solids 202:68
353. Tsuboi T, Sakka T, Ogata YH (1998) Phys Rev B 58:13863
354. Tsuboi T, Sakka T, Mabuchi M, Ogata YH (2000) Appl Surf Sci 153:268
355. Mayeri D, Phillips BL, Augustine MP, Kauzlarich SM (2001) Chem Mater 13:765
356. Carter RS, Harley SJ, Power PP, Augustine MP (2005) Chem Mater 17:2932
357. Rodina AV, Efros AL, Rosen M, Meyer BK (2002) Mat Sci Eng C-Bio S 19:435
358. Jiang J, Schaper AK, Schafer R, Hihara T, Becker JA (1997) Adv Mater 9:343
359. Schwenzer B, Hu J, Morse DE (2011) Adv Mater 23:2278
360. Klein MC, Hache F, Ricard D, Flytzanis C (1990) Phys Rev B 42:11123
361. Inoshita T, Sakaki H (1997) Phys Rev B 56:R4355
362. Fu HX, Ozolins V, Zunger A (1999) Phys Rev B 59:2881
363. Scholle A, Greulich-Weber S, As DJ, Mietze Ch, Son NT, Hemmingsson C, Monemar B, Janzen E, Gerstmann U, Sanna S, Rauls E, Schmidt WG (2010) Phys Status Solidi B 247: 1728
364. Schwenzer B, Hu J, Wu Y, Mishra U (2006) Solid State Sci 8:1193
365. Panich A, Shao M, Teske C, Bensch W (2006) Phys Rev B 74:233305
366. Tunstall DP, Patou S, Liu RS, Kao YH (1999) Mater Res Bull 34:1513
367. Chaparadza A, Rananavare SB (2010) Nanotechnology 21:035708
368. Wang LQ, Exarhos GJ, Windisch CF, Yao CH, Pederson LR, Zhou XD (2007) Appl Phys Lett 90:173115
369. Lee CH, Park S-H, Jung JK, Ryu K-S, Nahm SH, Kim J, Chen Y (2005) Solid State Commun 134:419
370. Kleinhammes A, Wagner G, Kulkarni H, Jia Y, Zhang Q, Qin L, Wu Y (2005) Chem Phys Lett 411:81
371. Wagner GW, Procell LR, Munavalli S (2007) J Phys Chem C 111:17564
372. Chen Q, Jia Y, Liu S, Mogilevsky G, Kleinhammes A, Wu Y (2008) J Phys Chem C 112: 17331
373. Scolan E, Magnenet C, Massiot D, Sanchez C (1999) J Mater Chem 9:2467
374. Reyes-Garcia EA, Sun YP, Reyes-Gil KR, Raftery D (2009) Solid State Nucl Magn Reson 35:74
375. Pilkenton S, Hwang SJ, Raftery D (1999) J Phys Chem B 103:11152
376. Klosek S, Raftery D (2001) J Phys Chem B 105:2815
377. Hwang SJ, Raftery D (1999) Catal Today 49:353
378. Hwang SJ, Petucci C, Raftery D (1998) J Am Chem Soc 120:4388
379. Shroyer M, Furdyna JK, Ryskin AI, Warren WW (1999) Physica B 274:852
380. Du M-H, Singh D (2009) Phys Rev B 79:205201

Index